520
1-17-62

MASTER

UCRL-6438

PART I

PROCEEDINGS of the GEOPHYSICAL LABORATORY–LAWRENCE RADIATION LABORATORY CRATERING SYMPOSIUM

held at
The Geophysical Laboratory of
The Carnegie Institute
Washington, D.C.
March 28–29, 1961

LAWRENCE RADIATION LABORATORY, UNIVERSITY OF CALIFORNIA
LIVERMORE, CALIFORNIA

DISCLAIMER

Nuclear Explosions –
Peaceful Applications, UC-35
TID-4500 (16th Ed.)

UNIVERSITY OF CALIFORNIA
Lawrence Radiation Laboratory
Livermore, California

Contract No. W-7405-eng-48

PROCEEDINGS OF THE GEOPHYSICAL LABORATORY/LAWRENCE RADIATION LABORATORY CRATERING SYMPOSIUM
WASHINGTON, D. C.
MARCH 28-29, 1961

Milo D. Nordyke
(Editor)

October, 1961

UCRL-6438
Part I

Printed in USA. Price $5.50 (includes two volumes, Parts I and II).
Available from the Office of Technical Services,
Department of Commerce
Washington 25, D. C.

PREFACE

The Geophysical Laboratory/Lawrence Radiation Laboratory Cratering Symposium developed, in large part, from a suggestion of Dr. Gerald W. Johnson,* Associate Director of the Lawrence Radiation Laboratory. Dr. Johnson, as director of the Plowshare Program for industrial application of nuclear explosives, was interested in the use of large scale explosion craters for excavation purposes. This interest led to studying meteor craters on the earth and moon, and it occurred to him that a joint symposium between the scientists who were interested in explosion craters and those who were interested in terrestrial and lunar meteor craters might prove very beneficial to both groups. The proposal greatly interested Dr. Philip Abelson, Director of the Geophysical Laboratory, who promptly offered the facilities of the Geophysical Laboratory and began the task of organizing the meeting. The success of the symposium was attributable in no small measure to the participation of Dr. Abelson and the Geophysical Laboratory and we are grateful for the hospitality which they extended to the participants. Particular thanks must also go to Dr. Gordon F. MacDonald, National Aeronautics and Space Administration, and Dr. Wilmot N. Hess,† Lawrence Radiation Laboratory, who arranged the agenda and compiled the list of speakers and invitees.

The symposium was held at the Geophysical Laboratory of the Carnegie Institute, Washington, D. C., on March 28-29, 1961. Attendees included most of the experts in explosion and impact craters in the United States and Canada. Following introductory remarks by Dr. W. T. Pecora, U. S. Geological Survey, Washington, D. C., the symposium plunged into the subject

---

*Now on leave of absence to serve as Assistant to the Secretary of Defense on Atomic Energy Matters and as Chairman of Military Liaison Committee.

†Now with National Aeronautics and Space Administration.

of cratering. The symposium broke up late in the afternoon of the second day with a feeling shared by all that the two days spent discussing cratering were days well spent.

These proceedings are published in two volumes, designated Parts I and II. All the papers delivered at the meeting are included in roughly the order in which they were presented. Part I contains the papers given on the first day of the meeting, and Part II contains those given on the second day. In addition, several papers have been included which were not presented at the symposium because of time limitations, but which we felt would be of interest to the readers.

Lawrence Radiation Laboratory
Livermore, California
October, 1961

Milo D. Nordyke
(Editor)

CONTENTS

INTRODUCTION

W. T. Pecora
U. S. Geological Survey
Washington, D. C.

We are indebted to Drs. Abelson and Johnson and their co-workers for planning this symposium and for bringing together the diverse skills represented by geology and physics to focus on the problem of natural and man-induced craters. This first session is largely in the area of geology. We geologists have a different jargon from physicists and different methods of study because our science deals with natural history of rocks and minerals. In the matter of time, for example, we deal with name-words, rather than seconds, to denote duration and succession of events. In the matter of materials we deal with component minerals and their alteration products, rather than ideal systems. Geologic problems are a fertile field for the exact scientist to investigate. We know of the great progress being made by the merger of geology and physical chemistry. In the problem of craters, and other natural phenomena, experimental and theoretical physics can join with geological science and greatly increase our understanding of earth history and geological processes. We speak different languages, as you will experience throughout this symposium. As scholars in science, however, we shall attempt to learn something of each other's language and intellectual process and gauge our conclusions and future research work by attention to the contributions and skills from both our fields of science. It is our hope that geologists and physicists will join in other problem areas, as they are joining in this one on craters.

The geological papers in this morning's session will deal descriptively with surficial features and end products of impact craters caused by meteorite falls. Such items as breccia, structural deformation, normal and

inverse stratigraphy, glass (fused rock), and coesite will frequently be mentioned. Valid concepts of mechanics, absolute time, and energy of formation must come from the exact sciences. Experiment and theory of physics can rigorously explain the end products the geologists observe and measure; but we must do these things together.

Paper A

TERRESTRIAL FEATURES OF IMPACT ORIGIN

E. M. Shoemaker and R. E. Eggleton

U. S. Geological Survey

Menlo Park, California

ABSTRACT

Craters made by meteorites striking the earth are discussed, with attention given to geological evidence for discriminating them from craters formed by other structural processes. The major known meteorite craters are briefly described, as well as other features that are considered probable or possible meteorite craters on the basis of less conclusive evidence. Separate tabulations are given of (1) topographic features either known to be meteorite craters, or considered as possible meteorite craters through lack of conclusive evidence to the contrary, and (2) topographic features once considered to be possible meteorite impact craters, but which are now believed to be of other origin.

* * *

Craters with associated meteorites are now known from 11 widely scattered localities in the world (Fig. 1). Most of these craters were discovered or their meteoritic origin documented in the score of years between 1930 and 1950. The craters of Sikhote'-Aline, U. S. S. R., were formed by a witnessed fall in 1947. Only two of the established meteorite impact craters exceed 200 meters in diameter.

The craters are ephemeral features of the landscape, subject to erosion or burial. In a region of active erosion, among the first things to disappear will be the fragments of ejected meteorites; those that remain in the crater are quickly buried in the crater fill formed from the erosion of the wall. At a later stage all rock fragments thrown clear of the crater will be removed; then the raised bedrock rim, and finally all topographic vestiges of the crater, will be gone. With a steady rate of denudation, the structural features produced in the rocks will remain as mute testimony of the impact for a much

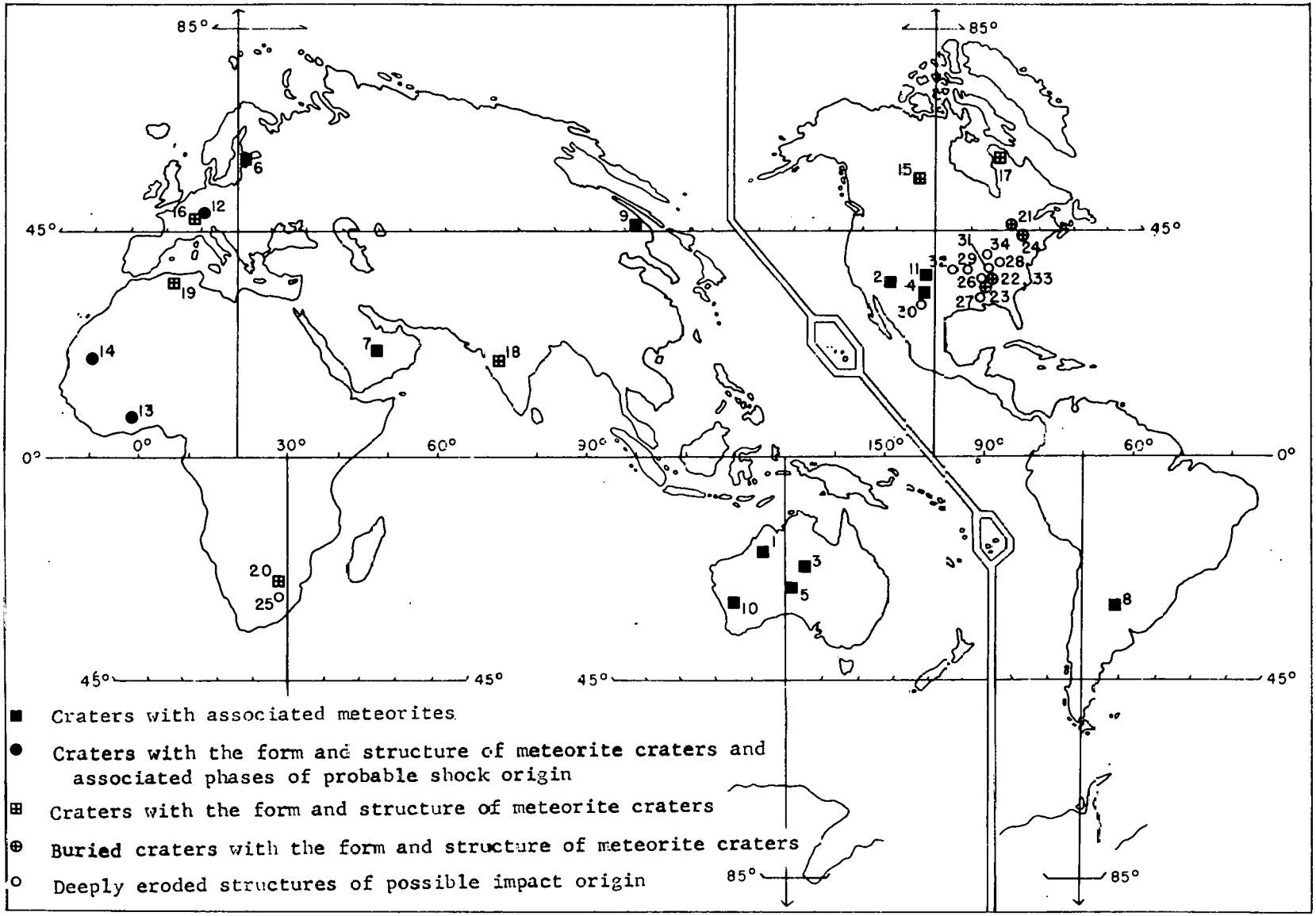

MUL-14564

Fig. 1. Index map showing location of meteorite craters and features of possible impact origin. (Locality numbers correspond to those in Table 1.)

longer time than the craters. The opposite alternative is for the crater to become gradually buried beneath stream, lake, marine, or eolian sediments. As we survey today's landscape, therefore, in addition to craters with associated meteorites we should expect to find impact craters from which the meteorites have disappeared (at least from the surface), craters which have been partially or completely buried at some time, and structures which lack any trace of a crater but which are the roots, so to speak, of impact craters.

Evidence of various kinds is accumulating which indicates there are solid nuclei of comets which may collide with the earth from time to time (Fesenkov, 1949; see also Scientific American, 1961). Such objects may form craters and structures similar to those formed by meteorites. Whether any recognizable fragments of such objects would remain in the vicinity of the impact is problematical. For the whole class of features formed by impact, Dietz (1960) has coined the term "astrobleme."

A number of craters have been found with the form and structure of meteorite craters, but from which no meteorite fragments have yet been recovered. Similarly, a number of structural features have been discovered that exhibit the essential elements of an impact structure with the crater completely removed, but proof of their impact origin is more difficult.

Studies of the size frequency distribution of asteroids (Kuiper and others, 1958) and of recovered meteorites (Brown, 1960 and 1961) indicate the frequency of collision may be expected to drop off sharply with increasing size of the impacting object. During any given period of time the small craters formed will far outnumber the large ones. But the smaller the crater, the more quickly it is buried or eroded away. There is a selective attrition of the smaller craters with time. It follows, then, that recent impact craters will be dominantly small whereas most of the ancient features preserved and exposed will be comparatively large.

The discovery of impact craters with associated meteorites has been almost entirely incidental or accidental. Attention was drawn to most of them at first by the discovery of the meteorites. The efficiency with which meteorite craters are discovered is thus probably very low.

The discovery patterns for ancient features of probable impact origin illustrate the low efficiency of incidental discovery. A certain number have been found incidentally in the course of regional geologic mapping and from aerial photography, but the systematic efforts of two groups in different areas have greatly accelerated the rate of recognition of impact features. One structure of possible impact origin in Tennessee was first noticed during reconnaissance geologic studies and reported in 1869. Starting 67 years later, in a period of 17 years C. W. Wilson, Jr., with his colleague K. E. Born, and later with students, increased the reported list of possible impact features in Tennessee to seven. The first investigation on the ground of a feature of probable impact origin in Canada was made in 1950 (Meen, 1951). Since then systematic effort by the Dominion Observatory of Canada, under the leadership of C. S. Beals, has drawn attention to 16 additional features worthy of investigation. For at least three of these, fairly good evidence of impact origin has been obtained.

The search for impact craters is complicated by the fact that several geological processes produce craters of somewhat similar form. Among these processes are volcanism; solution of limestone, dolomite, and other soluble rocks; and the collapse of pingos, or ice-cored hills, that are found in some regions of permanently frozen ground. Volcanoes of the maar type, which resemble impact craters, and solution collapse structures can generally be discriminated from impact craters by careful geological examination. It is possible, however, that certain collapsed pingos might be very difficult to distinguish from impact craters by surface examination alone.

Craters with Associated Meteorites

Approximately 50 craters with associated meteorites have been discovered (Table 1, p. A-24). The large majority of these occur as strewn fields of craters and meteorites at five localities, one each on the continents of North America, South America, Europe, Asia, and Australia. The largest known

crater is the Wolf Creek crater, Australia, which is 1300 meters in diameter, measured from rim crest to rim crest. * In general, craters less than 10 meters across are not found, though more than 100 craters less than 10 meters in diameter (not included above) were formed in addition to the larger craters by the 1947 Sikhote'-Aline fall (Table 1). There tends to be a lower limit to the size of impact craters on earth because small meteorites are decelerated by aerodynamic drag to free-fall velocity. At low impact speeds a hole with the approximate cross section of the meteorite is formed instead of a crater.

The fragmentation of the Sikhote'-Aline meteorite into a great number of pieces which formed a strewn field of craters and meteorite debris illustrates the tendency for meteorites to be broken up by large aerodynamic stresses to which a high-speed object is subjected as it traverses the atmosphere. To a first approximation the pressure on the leading face of the meteorite follows Bernoulli's equation and increases with the square of the velocity and linearly with the density of the atmosphere. In some cases major breakup occurs close to the ground, as indicated by close clustering of craters at Henbury, Australia, and in other cases the breakup probably occurs higher in the atmosphere, as is suggested by wide scattering of craters at Campo del Cielo, Argentina. The greatest separation of known craters produced by one fall may be 550 miles, the distance between the Barringer crater, Arizona, and the Odessa group of craters in Texas. The meteorites from these two localities are essentially identical and the craters may be of the same age.

The meteorites discovered in association with impact craters are preponderantly irons, but iron meteorites constitute only about 5 percent of

---

*Some uncertainty exists in this measurement. In their abstract, the diameter of the crater is given as 2800 feet (850 meters) by Guppy and Matheson (1950, p. 30), but their cross section shows this measurement as referring to the diameter of the floor of the crater, which agrees with the scale of the cross section. The rim-to-rim diameter is considerably greater than that of the floor.

observed meteorite falls. As suggested by Madigan (1940, p. 485), the explanation for this probably lies partly in the greater tendency for stony meteorites (of the size required to form craters) to be broken entirely into small pieces during their passage through the atmosphere. In addition, irons may be expected to have greater probability of surviving impact or other disruption processes in space.

An uneroded meteorite crater is a roughly bowl-shaped depression encompassed by a raised rim (Fig. 2). For convenience of discussion the various parts of the crater may be referred to as follows (see Fig. 2): (1) the crater floor, which encompasses the flat or gently sloping lower parts of the crater; (2) the crater wall, which includes the generally steep inner slope of the crater and extends to the rim crest; (3) the rim crest — the drainage divide between inner and outer slopes, also referred to in some cratering literature as the lip; and (4) the rim flank, which includes the outer slopes of the rim extending from the rim crest to the outer periphery of the raised rim. These terms are purely topographic and may be applied to eroded as well as fresh craters. Diameters given in Table 1 are all measured from rim crest to rim crest. The heights of the rims are best measured from the rim crest to the periphery of the rim flank in a direction normal to the general slope of the surrounding terrain. Similarly, the most meaningful depth of the crater is the maximum distance between the mean rim crest and the crater floor in a direction normal to the slope of the surrounding terrain.

As erosion proceeds, the diameter of the crater increases slightly, because of more rapid downcutting on the steep crater walls than on the rim flanks which generally have gentler slopes. Of all the topographic dimensions, the depth of the crater changes most rapidly owing to the combined effect of downcutting on the rim and filling on the floor. The rate of rise of the floor is fastest in the first stages of filling because a large area of the wall contributes to a comparatively small area of fill on the floor and because the ratio of thickness of fill to volume of fill is largest. The diameter-to-depth ratio, therefore, increases very rapidly at first and then more slowly as erosion proceeds. Rim heights generally decrease slowly with time.

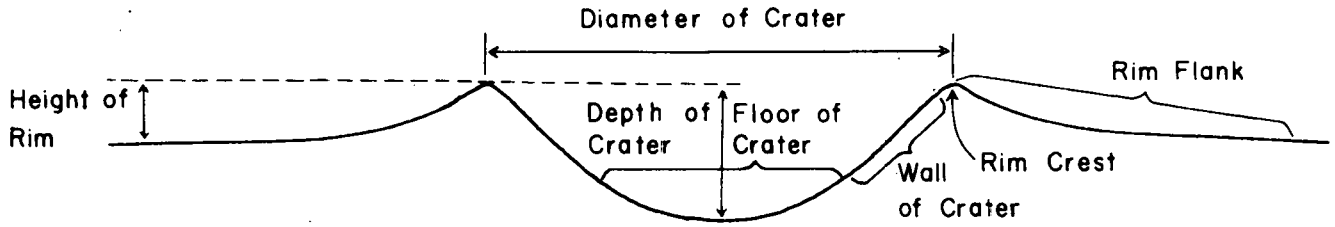

a. Uneroded Crater

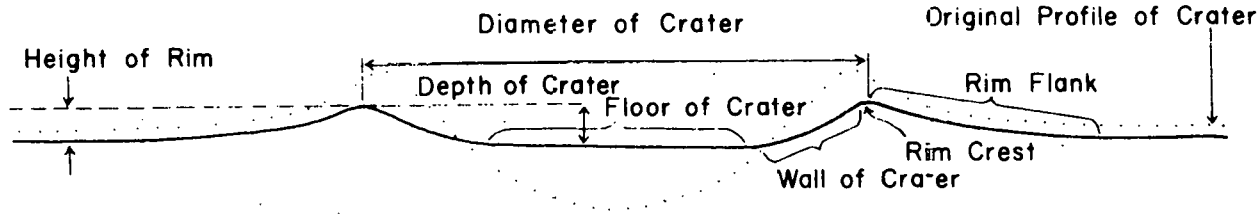

MUL-14565

b. Eroded Crater

Fig. 2. Diagrams illustrating crater terminology.

Very few craters with associated meteorites have been explored and described in sufficient detail to give a full account of their structure. Except for the Sikhote'-Aline craters, all have been modified to a greater or lesser extent by erosion and filling. Two principal structural types are represented among the larger craters, one exemplified by the Barringer crater, and the other by the main Odessa crater (Fig. 3). The chief distinguishing features are the structures exposed in the crater walls.

In both types of craters the rim flanks are underlain by rock debris thrown out along ballistic trajectories, here designated as throwout. Initially a thin layer of material, here designated as fallout, formed by free fall of pieces ejected at high angles of elevation and decelerated by aerodynamic drag, may be expected to have mantled both the inner parts and exterior rim flanks of all large craters. Such a layer is preserved beneath lake sediments at the Barringer crater and presumably in the larger of the other craters, though few craters have been explored in sufficient detail to verify its presence. The ratio of the thickness of both the throwout and the fallout to the diameter of the crater decreases with decreasing size of crater, and very small isolated craters may entirely lack the fallout layer.

Beneath the fallout and sedimentary fill in the Barringer crater is a lens of compact breccia composed of mixed fragments of rocks derived from different positions in the crater. Highly shocked fragments of rock and remains of meteoritic material, chiefly in the form of minute spherules imbedded in pieces of glass, are dispersed in the breccia. This breccia has been designated allogenic breccia (Shoemaker, 1960, Fig. 2) to distinguish it from material in the crater that has essentially been brecciated in place, which may be called authigenic breccia. A lens of fragmental rock under the floor of the Odessa crater, interpreted by Sellards and Evans (1941) as formed by the falling back of ejecta, is interpreted by us as allogenic breccia. Allogenic breccia has been found in most meteorite craters exceeding 10 meters in diameter that have been explored to sufficient depth, and in most craters the breccia contains remnants in some form of the impacting meteorites. The sum of field evidence indicates the allogenic breccia is formed entirely within the crater.

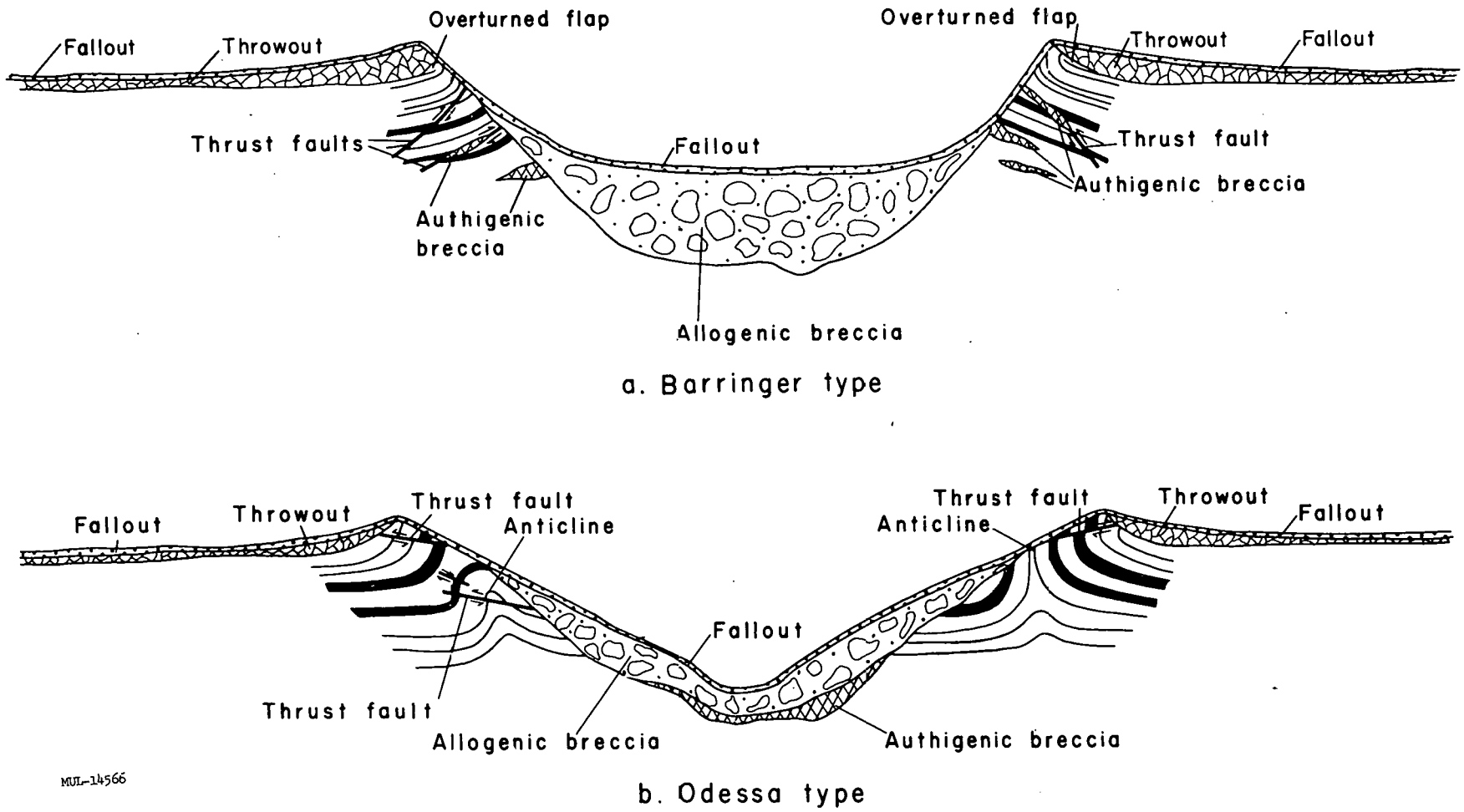

Fig. 3. Schematic cross sections illustrating the structure of Barringer and Odessa types of craters.

Beds exposed in the wall of the Barringer crater, in general, dip gently outward low in the crater and more steeply outward close to the contact with the throwout debris (Fig. 4). Locally the beds are overturned and the uppermost beds are folded back as a flap that has been rotated more than 180°. In places the flap grades outward into throwout debris, and the rock fragments in all the throwout are stacked roughly in an inverted stratigraphic sequence. The axial plane, or more properly the axial surface, of the fold along which the beds have been overturned is approximately a flat cone, concentric with the crater and with apex downward, that intersects the crater wall. The upturned and overturned strata are broken by a number of small, nearly vertical faults with scissors type of displacement. A number of outward-dipping thrust faults are also present, and locally a few inward-dipping normal faults occur that are concentric with the crater wall. Authigenic breccia is locally present along all types of faults.

Beds exposed in the wall of the Odessa crater are buckled in an anticline and locally displaced along inward-dipping faults. In a similar structure produced by a shallow nuclear explosion, the top of the anticline is sheared off and the crest of the rim is underlain by large slabs of material that have been displaced outward.

The difference in structure between the Odessa and Barringer types of craters is probably due chiefly to differences in the scaled depth of penetration of the meteorite. This is illustrated by two nuclear explosion craters in alluvium at the Nevada Test Site, formed by devices of the same yield but detonated at different depths. A burst at 16 feet per $(\text{kiloton})^{1/3}$ scaled depth produced a crater of the Odessa type (Jangle U experiment), whereas a burst at 63 feet per $(\text{kiloton})^{1/3}$ scaled depth produced a crater of the Barringer type (Teapot ESS experiment). As the meteorites at the Barringer and Odessa craters are identical and the rock types similar, the indicated difference in the scaled depth of penetration is probably to be accounted for by difference in impact velocity, the smaller Odessa meteorite mass having encountered greater atmospheric retardation than the larger mass that formed the Barringer crater.

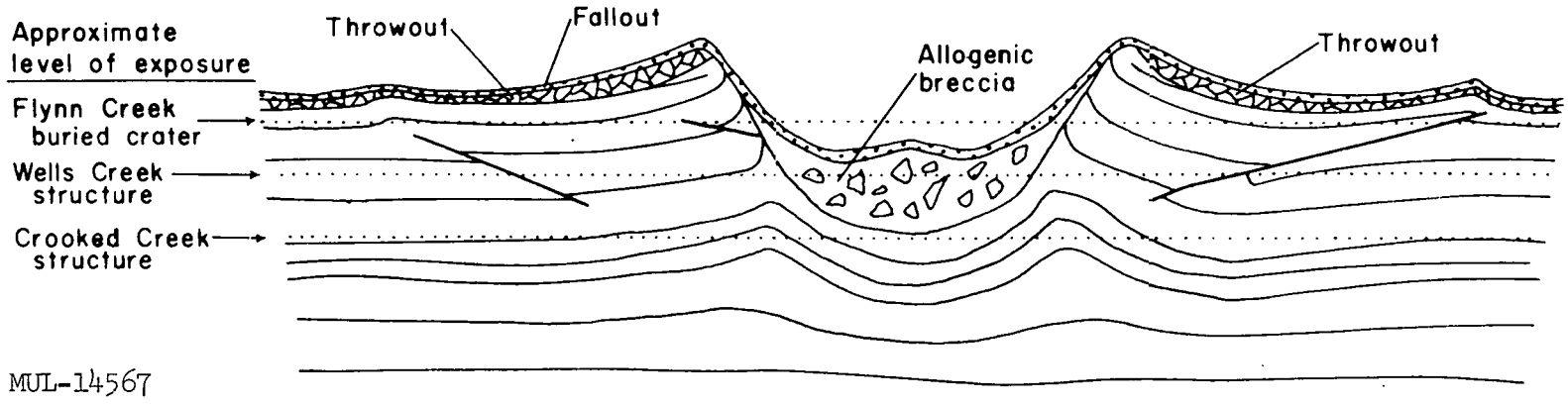

Fig. 4. Schematic diagram illustrating relation to the original crater of a buried crater and deeply eroded structures of probable impact origin.

Both the fallout and allogenic breccia at the Barringer crater contain dispersed fragments of highly shocked material. Different kinds of glass formed by sintering of the various major rock types penetrated by the meteorite are among the most conspicuous shock-produced phases. Some of the glass contains microscopic spherules of meteoritic iron and some contains new crystalline phases such as coesite, the high-pressure polymorph of silica, or a distinctive pyroxene. In addition to glass, rock fragments are present that are conspicuously crushed, shattered, and sheared. Certain types of deformed rocks, especially those exhibiting a pronounced shock-induced cleavage, contain abundant coesite, and in some pieces there are traces of glass.

At the Odessa crater, glass, if it occurs at all in the allogenic breccia or fallout, is extremely rare. Coesite has been sought in siliceous samples of breccia without success. The apparent general lack of shock-produced phases might be attributed to comparatively low impact velocity of the meteorite. Fairly abundant glass has been found around other craters of similar or smaller size at the Wabar craters, Arabia, and Henbury craters, Australia, and coesite has also been found in sheared sandstone from the largest Wabar craters, which show that these phases may be formed around craters the size of the main Odessa crater. On the other hand, the lack or rarity of shock-produced phases at Odessa may be due in part to the fact that highly siliceous beds, in which such phases are readily formed, occur only at depth, near the base of the allogenic breccia.

Craters with the Form and Structure of Meteorite Craters and Associated Phases of Probable Shock Origin

Three craters are known that are closely similar to demonstrated meteorite craters and in addition have associated phases of probable shock origin (Table 1). No meteoritic material has been definitely identified from any of these craters to date. The largest of the craters and best known, the Ries basin or Rieskessel of Bavaria, Germany, is a deeply eroded crater of Miocene age, 17 to 18 miles across. The rim flank of the crater is partly underlain by an extensive sheet of broken rock, the so-called Bunter breccia, that

appears to be precisely equivalent to the throwout around smaller craters of demonstrated impact origin. A great body of allogenic breccia underlies the crater floor. The wall, rim crest, and part of the rim flank of the crater is underlain by breccia and an imbricate series of thrust sheets. This structure has certain features in common with the Odessa type, as exemplified by both the Odessa crater and the Jangle U crater, but probably should be placed in a separate structural class. As the Ries basin is more than an order of magnitude larger than demonstrated meteorite craters of the Odessa type, some differences in structure are to be expected owing to the greater relative importance of gravity in the mechanics of cratering at this scale.

Resting on the breccias as patches both inside the crater and on the rim flank of the Ries is a lithified layer of fragmental rock and glass termed suevite. Coesite and other phases characteristic of the shock-formed glass at the Barringer crater have been found in the glass. Various patches of suevite may be interpreted as remnants of the fallout layer.

A crater 6-1/2 miles across at Lake Bosumtwi, Ghana, is in some respects a smaller version of the Ries basin. The crater wall and rim flank are underlain by structurally disordered rocks and breccia on which rest patches of suevite-like material with abundant glass. Coesite is present in the glass which, like the glass in the Ries suevite, contains an unusual variety of crystalline material. Both the Ries suevite and the suevite-like material from the Bosumtwi crater were thought to be volcanic by the original investigators, but careful petrographic examination shows they are unlike any known products of volcanism and have strong affinities to the shocked debris forming the fallout layer around meteorite impact and nuclear explosion craters.

A feature of special interest at the Bosumtwi crater is the occurrence in the breccias of shatter cones, conical slip surfaces with radiating striations, in the rock fragments.

At a small crater of the Odessa type at Aouelloul, Mauritania, pieces of glass very similar to known shock-produced glass occur both inside and on the rim flank of the crater. Search for coesite in the glass has so far been unsuccessful.

Craters with the Form and Structure of Meteorite Craters

Six craters are known at widely scattered localities in the world that resemble demonstrated meteorite craters in form and structure but from which no meteorites or probable shock-produced phases have been reported (Table 1). By far the best-described crater in this class is the Pretoria Salt Pan of South Africa. The salt pan is a crater of the Odessa type that is strikingly similar in topographic dimensions to the Barringer crater of Arizona. The crater is in a sheeted granite that was covered at the time the crater was formed with a thin veneer of sedimentary rocks. Near the base of the throwout, which is composed dominantly of unsorted granite fragments, are small blocks of the sedimentary rocks. Thus the throwout exhibits inverted stratigraphy as at the Barringer crater. Where exposed in cuts in the crater wall and rim the sheeted granite is buckled in a faulted anticline. The crater has been considerably modified by erosion and fillings; the outer part of the rim flank is largely mantled with alluvial detritus, the crater wall with talus, and the floor with lake beds. Any meteorites or fallout preserved are most likely to be found beneath the lake beds.

The Talemzane crater, Algeria, Steinheim basin, Germany, and New Quebec and Deep Bay craters of Canada are all more deeply eroded than the Pretoria Salt Pan, and the New Quebec and Deep Bay craters, in addition, are largely filled with water. Drilling to reach the fallout and allogenic breccia within these craters will probably be required to establish their origin. Sketchy published accounts of the Lonar Lake crater of India suggest that it is comparable to the Pretoria Salt Pan in degree of erosion and filling.

Shatter cones are present in breccia in the floor and wall of the Steinheim basin, which is also noteworthy for the presence of a hill of disturbed rocks in the central part of the crater floor.

Buried Craters with the Form and Structure of Meteorite Craters

Four buried craters are known which have the form and structure of partly eroded meteorite craters. All of these features were at one time

probably completely covered with sediments and are now partly exhumed by later erosion. The first such feature to be described in detail is at Flynn Creek, Tennessee. At Flynn Creek a crater in Ordovician rocks, remarkably similar to the Steinheim basin, became completely covered with sediments during Devonian and Mississippian time. The rim of the crater was eroded to the level of the surrounding terrain prior to deposition of the main part of the Devonian and Mississippian fill. At Howell, Tennessee, a crater in Ordovician rocks was extensively eroded and then filled by younger Ordovician rocks. Two craters in Ontario formed in Precambrian rocks are also filled with Ordovician beds. Each of these craters is underlain by a body of breccia similar to the allogenic breccia at the Barringer crater. As in the Steinheim basin, shatter cones occur in the breccia fragments at Flynn Creek.

Deeply Eroded Structures of Possible Impact Origin

If the terrain surrounding the Barringer meteorite crater were eroded down level with the top of the allogenic breccia at the center of the crater, a circular lens of breccia surrounded by deformed beds would remain. Among several structures of this kind that have been discovered, one at Sierra Madera, Texas, is by far the best exposed and in addition has been explored by a number of drill holes. A great lens of breccia more than a mile across and at least 1600 feet thick at Sierra Madera is nested in a collar of strongly upturned beds and underlain by less deformed beds. The surrounding rocks are folded and displaced along thrust faults as far as a mile from the margin of the breccia. Shatter cones are abundant both in the breccia and surrounding rocks. At a similar but less well-exposed structure at Wells Creek, Tennessee, a drill hole in the center shows the breccia to be about 2000 feet thick. Surrounding the breccia and enclosing upturned beds is a concentric series of faulted anticlines and synclines that extend as far as 6 kilometers from the breccia.

If the Sierra Madera and Wells Creek structures were planed down still farther to the base of the breccia, only deformed beds would remain. Just beneath the breccia in the central part of an impact structure, a central depressed region surrounded by buckled rocks should be found. Such a structure

may be represented at Crooked Creek, Missouri. The inferred relation of the structures exposed at Wells Creek and Crooked Creek to the presumed original craters at these localities is illustrated in Fig. 4. The partly eroded and buried crater at Flynn Creek, the structure at Wells Creek, and the structure at Crooked Creek are here interpreted as representing successively more deeply eroded impact structures that correspond to craters of about the same size. One feature that is common to all three structures is the presence of shatter cones.

About half a dozen other structures are known in the United States that have many features in common with the Sierra Madera and Wells Creek structures. The exposures at these other localities are generally inadequate to determine the detailed configuration of these structures or verify the presence of a central mass of breccia, even though geological maps have been prepared for several of them. The presence of shatter cones at some of these localities and of concentric patterns of folds and faults at others suggests they are similar in origin to the Wells Creek and Sierra Madera structures. The largest known structure resembling that at Sierra Madera is the so-called Vredefort dome in South Africa. At the Vredefort structure is a central mass of breccia about 40 kilometers across.

Putative Impact Craters and Structures for Which More Data are Required for Classification

In addition to the foregoing types of craters and structures, a number of other features have been suggested to be of possible impact origin, but the available data are insufficient to classify them. Some of these features are merely circular topographic depressions or lakes that have been suggested as worthy of investigation. A few are craters that have been investigated and described and for which an impact origin appears unlikely, but which cannot be rejected on the basis of present evidence. Some features listed in this putative class in Table 1 are structures that are as yet inadequately described or are known only from drill holes. Many of the features listed in the putative class in Table 1 will probably be found to have originated by other mechanisms than impact.

Putative Impact Craters Which are Probably Not of Impact Origin

Finally, it may be of interest to list some putative impact craters that have been described in the literature, but for which an impact origin now appears highly improbable (Table 2). Some of these have a superficial resemblance to known meteorite impact craters and others do not.

Table 2. Putative impact craters probably not of impact origin.

Craters	Report suggesting possible impact origin	Probable origin	Basis for classification
1. Al Umchaimin, Iraq	Merriam and Holwerda (1957)	Limestone solution sink	Evaluation of report by Merriam and Holwerda (1957)
2. Carolina bays	Melton and Schriever (1933) Prouty (1952)	Periglacial lakes	Resemblance to periglacial lakes of Alaska. An extensive literature exists on other modes of origin
3. Duckwater, Nevada	Rinehart and Elvey (1951)	Limestone solution sink	Field examination
4. Panamint, California	Humiston and others (1961)	Limestone solution sink	Dietz and Buffington (1961). Evaluation of data presented by Humiston and others (1961)

REFERENCES

Alderman, A. R., 1933, The meteorite craters at Henbury, central Australia: Mineral. Mag., v. 23, p. 19-30, 30-32 (addendum by L. J. Spencer). Reprinted in Smithsonian Rept. for 1932, p. 223-234 [1933].

Beals, C. S., Innes, M. J. S., and Rottenberg, J. A., 1960, The search for fossil meteorite craters: Current Sci. (India), v. 29, p. 205-218, 249-262.

Born, K. E., and Wilson, C. W., Jr., 1939, The Howell structure, Lincoln County, Tennessee: J. Geology, v. 47, no. 4, p. 371-388.

Branco, Wilhelm, and Fraas, E., 1905, Das kryptovulcanische Becken von Steinheim: Kgl. preussisch Akad. Wiss. Berlin Abh., 64 p.

Brown, Harrison, 1960, The density and mass distribution of meteoritic bodies in the neighborhood of the earth's orbit: J. Geophys. Research, v. 65, no. 6, p. 1679-1683.

Brown, Harrison, 1961, Addendum: The density and mass distribution of meteoritic bodies in the neighborhood of the earth's orbit: J. Geophys. Research, v. 66, no. 4, p. 1316-1317.

Bucher, W. H., 1925, Geology of Jeptha Knob: Kentucky Geol. Survey, ser. 6, v. 21, p. 193-237.

Bucher, W. H., 1936, Cryptovolcanic structures in the United States: Intern. Geol. Congr., Washington, D. C., 1933, Rept., v. 2, p. 1055-1084.

Chao, E. C. T., Fahey, J. J., and Littler, Janet, 1961, Coesite from Wabar Crater, near Al Hadida, Arabia: Science, v. 133, no. 3456, p. 882-883.

Chao, E. C. T., Shoemaker, E. M., and Madsen, B. M., 1960, First natural occurrence of coesite: Science, v. 132, no. 3421, p. 220-222.

Dietz, R. S., 1960, Meteorite impact suggested by shatter cones in rock: Science, v. 131, no. 3416, p. 1781-1784.

Dietz, R. S., and Buffington, E. C., 1961, Panamint Crater, California — not meteoritic (abstr.): Meteorit. Soc., 24th meeting, Nantucket, Mass., 1961, Program.

Eggleton, R. E., and Shoemaker, E. M., in press, Breccia at Sierra Madera, Texas: U. S. Geol. Survey Prof. Paper 424-D, p. 151-153.

Ekern, G. L., and Thwaites, F. T., 1930, The Glover Bluff structure, a disturbed area in the Paleozoics of Wisconsin: Trans. Wisconsin Acad. Sci., v. 25, p. 89-97.

Emrich, G. H., and Bergstrom, R. E., 1959, Intense faulting at Des Plaines, northeastern Illinois (abstr.): Bull. Geol. Soc. Am., v. 70, no. 12, pt. 2, p. 1596.

Fesenkov, V. G., 1949, The dimness of atmosphere caused by the Tunguska meteorite fall which occurred June 30th, 1908: Meteoritika Issue IV, p. 8-12.

Fesenkov, V. G., 1955, Sikhote'-Aline Meteorite, in Kaiser, T. R., ed., Meteors (a symposium on Meteor Physics): Special Supplement (v. 2) to J. Atmospheric and Terrest. Phys., p. 179-183.

Gèze, Bernard, and Cailleux, André, 1950, Existence probable de cratires meteoriques à Cabrerolles et à Faugères (Hérault): Compt. rend., v. 230, no. 17, p. 1534-1536.

Guppy, D. J., and Matheson, R. S., 1950, Wolf Creek meteorite crater, Western Australia: J. Geol., v. 58, no. 1, p. 30-36.

Hall, A. L., and Molengraaff, G. A. A., 1925, The Vredefort Mountain Land in Southern Transvaal and Northern Orange Free State: Verhandel. Koninkl. Ned. Akad. Wetenschap., sec. 2, pt. 24, no. 3, p. 1-183.

Hargraves, R. B., in press, Shatter cones in the rocks of the Vredefort Ring: Trans. Geol. Soc. S. Africa, v. 64.

Harrison, J. M., 1954, Ungava (Chubb) Crater and glaciation: J. Roy. Astron. Soc. Can., v. 48, no. 1, p. 16-20.

Hendriks, H. E., 1954, The geology of the Steelville quadrangle, Missouri: Missouri Geol. Survey and Water Resources, v. 36, 2d ser., 88 p.

Hoppin, R. A., and Dryden, J. E., 1958, An unusual occurrence of pre-Cambrian rocks beneath glacial drift near Mancon, Iowa: J. Geol., v. 66, p. 694-699.

Humiston, L. E., and others, 1961, Investigation of the Panamint Valley Crater (abstr.): Meteorit. Soc., 24th meeting, Nantucket, Mass., 1961, Program.

Innes, M. J. S., 1957, A possible meteorite crater at Deep Bay, Saskatchewan: J. Roy. Astron. Soc. Can., v. 51, no. 4, p. 235-240.

Janssen, C. L., 1951, The meteor craters in Hérault, France: J. Roy. Astron. Soc. Can., v. 45, no. 5, p. 190-198.

Junner, N. R., 1937, The geology of the Bosumtwi caldera and surrounding country: Gold Coast Geol. Survey Bull. no. 8, p. 5-46.

Karpoff, Roman, 1953, The meteorite crater of Talemzane in southern Algeria (CN = ∓0041, 333): Meteoritics, v. 1, no. 1, p. 31-38.

King, P. B., 1930, The geology of the Glass Mountains, Texas; Pt. 1, Descriptive geology: Texas Univ. Bull. 3038, 167 p.

Krinov, E. L., 1960, Principles of meteoritics: London, Pergamon Press, Inc., 535 p. Translated from Russian by Irene Vidziunas, edited by Harrison Brown.

Krinov, E. L., 1961, The Kaalijarv meteorite craters on Saarema Island, Estonian SSR: Am. J. Sci., v. 259, no. 6, p. 430-440.

Kuiper, G. P., and others, 1958, Survey of asteroids: Astrophys. J. Suppl. 32, v. 3, p. 289-428.

LaTouche, T. H. D., and Christie, W. A. K., 1912, The geology of the Lonar Lake: India Geol. Survey Records, v. 41, p. 266-285.

Madigan, C. T., 1937, The Boxhole crater and the Huckitta Meteorite (Central Australia): Trans. Proc. Roy. Soc. S. Australia, v. 61, p. 187-190.

Madigan, C. T., 1940, The Boxhole meteoritic iron, Central Australia: Mineral. Mag., v. 25, no. 168, p. 481-486.

Meen, V. B., 1951, Chubb Crater, Ungava, Quebec: Can. Geol. Assoc., v. 4, p. 49-59.

Melton, F. A., and Schriever, William, 1933, The Carolina Bays — are they meteorite scars?: J. Geol., v. 41, p. 52-66.

Merriam, Richard, and Holwerda, J. G., 1957, Al Umchaimin, a crater of possible meteoritic origin in western Iraq: Geograph. J., v. 123, pt. 2, p. 231-233.

Millman, P. M., 1956, A profile study of the New Quebec Crater: Ottawa, Dominion Observatory Publs., v. 18, no. 4, p. 61-82.

Millman, P. M. , Liberty, B. A., Clark, J. F., Willmore, P. L., and Innes, M. J. S., 1960, The Brent Crater: Ottawa, Dominion Observatory Publs., v. 24, no. 1, 43 p.

Mitchum, R. M., Jr., 1951, The Dycus Disturbance, Jackson County, Tennessee: unpublished Master's thesis, Vanderbilt Univ., 40 p.

Monod, Théodore, 1954, Sur quelques accidents circulaires ou cratériformes du Sahara occidental: Intern. Géol. Congr., dix-neuvième session, Alger 1952, Comptes rendus, Première partie, Fascicule XX, p. 85-93.

Nágera, J. J., 1926, Los hoyos del Campo del Cielo y el Meteorito: Publ. Dir. Minas Geol. Argentina, no. 19, p. 1-9.

Nel, L. T., 1927, The geology of the country around Vredefort; an explanation of the geological map: South Africa Dept. Mines and Industries, Geol. Survey, 134 p.

Nininger, H. H., 1938, Further notes on the excavation of the Haviland, Kiowa County, Kansas, meteorite crater (abstr.): Popular Astron., v. 46, p. 110.

Nininger, H. H., and Figgins, J. D., 1933, The excavation of a meteorite crater near Haviland, Kiowa County, Kansas: Colorado Mus. Nat. History Proc., v. 12, p. 9-15.

Nininger, H. H., and Huss, G. I., 1960, The unique meteorite crater at Dalgaranga, Western Australia: Mineral. Mag., v. 32, no. 251, p. 619-639.

Philby, H. St. J. B., 1933, The empty quarter: New York, Henry Holt and Company, p. 157-80, 365-69 (appendix by L. J. Spencer).

Priddy, R. R., and McCutcheon, T. E., 1943, Montgomery County mineral resources: Mississippi Geol. Survey Bull. 51, 116 p.

Prouty, W. F., 1952, Carolina Bays and their origin: Bull. Geol. Soc. Am., v. 63, no. 2, p. 167-224.

Rayner, J. M., 1939, Examination of the Henbury meteorite craters by the methods of applied geophysics: Australian New Zealand Assoc. Advance. Sci., v. 24, p. 72-78.

Reeves, F., and Chalmers, R. O., 1948, Wolf Creek Crater: Australian J. Sci., v. 11, p. 154.

Reinwaldt, I., and Luha, A., 1928, Bericht über geologische Untersuchungen am Kaalijärv (Krater von Sall) auf Ösel: Tartu Univ. Geol. Inst. Publ., no. 11, p. 30-42.

Rinehart, J. S., and Elvey, C. T., 1951, A possible meteorite crater near Duckwater, Nye County, Nevada (ECN = +1157, 387): Contribs. Meteorit. Soc., v. 5, no. 1, p. 44-45.

Rohleder, H. P. T., 1936, Lake Bosumtwi, Ashanti: Geograph. J., v. 87, no. 1, p. 51-65.

Scientific American, 1961, The comet did it: Volume 204, no. 1, p. 80, 83, January 1961.

Sellards, E. H., and Evans, Glen, 1941, Statement of Progress of Investigation at Odessa Meteor Craters: Texas Univ., Bur. of Econ. Geol., 13 p.

Shepard, E. M., 1904, Spring system of the Decaturville Dome, Camden County, Missouri: U. S. Geol. Survey Water-Supply and Irrigation Paper No. 110, p. 113-125.

Shoemaker, E. M., 1960, Penetration mechanics of high velocity meteorites, illustrated by Meteor Crater, Arizona: Intern. Geol. Congr., 21st, Copenhagen, 1960, Rept., pt. 18, p. 418-434.

Shoemaker, E. M., and Chao, E. C. T., in press, New evidence for the impact origin of the Ries Basin, Bavaria, Germany: J. Geophys. Research.

Shrock, R. R., and Malott, C. A., 1933, The Kentland area of disturbed Ordovician rocks in northwestern Indiana: J. Geol. , v. 41, p. 337-370.

Spencer, L. J., 1933a, Meteoric iron and silica-glass from the meteorite craters of Henbury (central Australia) and Wabar (Arabia): Mineral. Mag., v. 23, p. 387-404.

Spencer, L. J., 1933b, Meteorite craters as topographical features on the earth's surface: Geograph. J., v. 81, p. 232-33. Reprinted in Smithsonian Report for 1933, p. 307-325 [1935].

Suess, F. E., 1936, Der Meteor-Krater von Köfels bei Umhausen im Otztale, Tirol: Neues Jahrb. Mineralogie, Geologie, u. Palaontologie, B.-Bd., 72, Abt. A., p. 98-155.

Wagner, P. A., 1922, The Pretoria Salt-Pan – A soda caldera: South Africa Dept. Mines Geol. Survey Memo. no. 20, 136 p.

Wilson, C. W., Jr., 1953, Wilcox deposits in explosion craters, Stewart County, Tennessee, and their relations to origin and age of Wells Creek Basin structure: Bull. Geol. Soc. Am., v. 64, p. 753-768.

Wilson, C. W., Jr., and Born, K. E., 1936, The Flynn Creek disturbance, Jackson County, Tennessee: J. Geol., v. 44, p. 815-835.

Table 1. List of known and possible impact features on the earth.

	Lat. and long. of center	Diameter (km)	Diameter (ft)	Age Maximum–Minimum	Structural type*	Glass	Coesite	Shatter cones	Principal sources of data
Craters with associated meteorites									
1. Wolf Creek	19°18'S 127°46'E	1.3	4300	Pleistocene(?)	B(?)				Guppy and Matheson (1950); Reeves and Chalmers (1948)
2. Barringer	35°02'N 111°01'W	1.2	4000	Pleistocene	B	X	X		Shoemaker (1960); Chao, Shoemaker, and Madsen (1960)
3. Boxhole	22°37'S 135°12'E	1.75×10^{-1}	572	Pleistocene(?)					Madigan (1937)
4. Odessa craters				Pleistocene	O				Sellards and Evans (1941)
Main crater (No. 1)	31°48'N 102°30'W	1.7×10^{-1}	550						
No. 2		1.8×10^{-2}	60						
No. 3		1.6×10^{-2}	54						
5. Henbury craters				Pleistocene–Recent		X			Alderman (1933); Rayner (1939); Spencer (1933a)
No. 7 (Main crater)	24°34'S 133°10'E	1.7×10^{-1} by 1.2×10^{-1}	530 by 350						
composed of No. 7a and		1.2×10^{-1}	350						
No. 7b		8×10^{-2}	240						
No. 6 (Water crater)		9×10^{-2}	230						
No. 8		5×10^{-2}	160						
No. 4		4×10^{-2}	140						
No. 3		4×10^{-2}	120						
No. 2		3×10^{-2}	90						
No. 12		2×10^{-2}	60						
No. 1		2×10^{-2}	60						
No. 5		2×10^{-2}	50						
No. 10		2×10^{-2}	50						
No. 11		1×10^{-2}	20						
No. 13		1×10^{-2}	20						
6. Ösel craters				Recent					Reinwaldt and Luha (1928); Krinov (1961)
Kaalijärv	58°24'N 22°40'E	1.0×10^{-1}	330		B				
No. 2 composed of		5.3×10^{-2} by 3.5×10^{-2}	170 by 120						
No. 2a and		3.5×10^{-2}	120						
No. 2b		3.1×10^{-2}	100						
No. 1		3.5×10^{-2}	120		B				
No. 3		3.2×10^{-2}	110						
No. 6		2.6×10^{-2}	80						
No. 4		2.0×10^{-2}	70		B				
No. 5		1.4×10^{-2}	40						

7.	Wabar craters				Pleistocene–Recent		X	X		Philby (1933); Chao and others (1961)
	B	21°30'N 50°28'E	9.1×10^{-2}	300			X			
	A		5.2×10^{-2}	170			X			
8.	Campo del Cielo craters	28°S 62°W			Pleistocene–Recent		(?)			Nagera (1926); Spencer (1933b)
	Laguna Negra crater		7.8×10^{-2}	260						
			by 5.5×10^{-2}	by 180						
	Hoyo Rubin de Celis		5.5×10^{-2}	181			(?)			
	Hoyo de la Cañada		5.3×10^{-2}	175						
	Hoyo aislado		4.3×10^{-2}	141						
9.	Sikhote'-Aline craters	46°10'N 134°39'E			Recent					Fesenkov (1955); Krinov (1960, p. 137-154)
	Largest		2.8×10^{-2}	92						
	18 craters with diameters equal to or larger than		1.0×10	33						
10.	Dalgaranga	27°45'S 117°05'E	2.55×10^{-2}	83.7	Pleistocene–Recent					Nininger and Huss (1960)
11.	Haviland	37°35'N 99°10'W	1.7×10^{-2}	55	Recent (?)					Nininger and Figgins (1933); Nininger (1938)
			by 1.1×10^{-2}	by 36						
	Craters with the form and structure of meteorite craters and associated phases of probable shock origin									
12.	Rieskessel	48°53'N 10°37'E	2.4×10	79,000	Miocene	O**	X	X		Shoemaker and Chao (in press)
13.	Lake Bosumtwi	6°32'N 1°23'W	8	30,000	Pleistocene (?)		X	X	X	Rohleder (1936); Junner (1937); J. Littler, J. J. Fahey, R. S. Dietz, and E. C. T. Chao (unpublished data)
14.	Aouelloul	20°15'N 12°41'W	2.50×10^{-1}	820	Pleistocene	O	X			Monod (1954)
	Craters with the form and structure of meteorite craters									
15.	Deep Bay	56°24'N 103°00'W	1.0×10	33,000	Tertiary (?)					Innes (1957)
16.	Steinheim	48°02'N 10°04'E	4	13,000	Miocene		†		X	Branco and Fraas (1905)
17.	New Quebec	61°17'N 73°40'W	3.45	11,300	Pleistocene (?)	B				Harrison (1954); Millman (1956), E. M. Shoemaker (unpublished data)
18.	Lonar Lake	19°59'N 76°51'E	2	5,000	Pleistocene (?)	B (?)				LaTouche and Christie (1912)
19.	Talemzane	33°20'N 4°00'E	1.75	5,740	Pliocene or Pleistocene	B				Karpoff (1953)
20.	Pretoria Salt Pan	25°30'S 28°00'E	9.1×10^{-1}	3,000	Pleistocene (?)	O				Wagner (1922)
	Buried craters with the form and structure of meteorite craters									
21.	Brent	46°04'N 78°29'W	3.51	11,500	Late Precambrian–Ordovician					Millman and others (1960); E. M. Shoemaker, M. Dence, and J. M. Moore (unpublished data)
22.	Flynn Creek	36°16'N 85°37'W	3	10,000	Ordovician–Devonian				X	Wilson and Born (1936); Dietz (1960)
23.	Howell	35°15'N 86°35'W	2.6	8,000	Ordovician					Born and Wilson (1939)
24.	Holleford	44°47'N 76°30'W	2.35	7,700	Late Precambrian–Ordovician					Beals and others (1960)

Table 1. (Continued)

	Lat. and long. of center	Diameter (km)	Diameter (ft)	Age Maximum—Minimum	Structural type*	Glass	Coesite	Shatter cones	Principal sources of data
Deeply eroded structures of possible impact origin									
25. Vredefort	27°S 27-1/2°E	70	200,000‡	Late Precambrian—Carboniferous				X	Hall and Molengraaff (1925); Nel (1927); Hargraves (in press)
26. Wells Creek	36°23'N 87°40'W	5	15,000‡	Mississippian—Eocene				X	Bucher (1936, p. 1066-1070); Wilson (1953)
27. Kilmichael	33°30'N 89°33'W	7	25,000‡	Eocene					Priddy and McCutcheon (1943)
28. Serpent Mound	39°02'N 83°25'W	5	15,000‡	Mississippian				X	Bucher (1936, p. 1061-1064); Dietz (1960)
29. Crooked Creek	37°50'N 91°23'W	5	15,000‡	Ordovician—Pennsylvanian				X	Hendricks (1954)
30. Sierra Madera	30°36'N 102°55'W	3	10,000‡	Early Cretaceous				X	King (1930); Dietz (1960); Eggleton and Shoemaker (in press)
31. Jeptha Knob	38°06'N 85°06'W	3	10,000‡	Silurian					Bucher (1925; 1936, p. 1059-1061)
32. Decaturville	37°54'N 92°04'W	5	15,000(?)‡	Cambrian					Shepard (1904); Bucher (1936, p. 1071)
33. Dycus	36°22'N 85°45'W			Ordovician					Mitchum (1951)
34. Kentland	40°45'N 87°24'W			Ordovician				X	Shrock and Malott (1933); Bucher (1936, p. 1072-1074)

	Lat. and long. of center	Diameters (km)	Diameters (ft)	Diameters (miles)	Principal sources of data
Putative impact craters for which more data are needed for classification					
Manicouagan Lake area, Canada	51°28'N 68°37'W	6.5×10		40	Beals and others (1960)
Clearwater Lakes (2), Canada	56°10'N 74°20'W	3.2×10 2.6×10		20 16	Beals and others (1960) Beals and others (1960)
Lac Couture, Canada	60°08'N 75°20'W	1.6×10		10	Beals and others (1960)
Keeley Lake, Canada	54°54'N 106°08'W	1.3×10		8	Beals and others (1960)
Köfels crater, Austria	47°13'N 10°58'E	5		3	Suess (1936)
West Hawk Lake, Canada	49°46'N 95°12'W	5		3	Beals and others (1960)
Wells Creek Area (4), U.S.					
Cave Spring Hollow	36°29'N 87°37'W	1.4	5,000		Wilson (1953)
Indian Mound	36°32'N 87°39'W	6×10^{-1}	2,000		Wilson (1953)
Little Elk Creek	36°23'N 87°42'W	5×10^{-1}	2,000		Wilson (1953)
Austin	36°32'N 87°39'W		400		Wilson (1953)

Franktown crater, Canada	45°03'N 76°04'W	1.2		3/4	Beals and others (1960)
Le Clot crater, France	43°32'N 3°8'E	2.35×10^{-1}	770		Gèze and Cailleux (1950); Janssen (1951)
Faugères craters (5), France	43°34'N 3°11'E	5.8×10^{-2}	190		Gèze and Cailleux (1950); Janssen (1951
		5.5×10^{-2}	180		
		4.8×10^{-2}	155		
		4.8×10^{-2}	155		
		1.5×10^{-2}	50		
Putative impact structures for which more data are needed for classification					
Carswell Lake area, Canada	58°27'N 109°30'W	2.9×10		18	Beals and others (1960)
Sault au Cochons, Canada	49°17'N 70°05'W	1.1×10		7	Beals and others (1960)
Lac Michikamau, Canada	54°34'N 64°27'W	5.6		3-1/2	Beals and others (1960)
Menihek Lake area (2), Canada	53°42'N 66°40'W	5		3	Beals and others (1960)
	54°19'N 67°10'W	4		2-1/2	Beals and others (1960)
Mecatina, Canada	50°50'N 59°22'W	3		2	Beals and others (1960)
Des Plaines, Illinois	42°02'N 87°56'W	?			Emrich and Bergstrom (1959)
Glover Bluff, Wisconsin	44°11'N 89°22'W	?			Ekern and Thwaites (1930)
Manson, Iowa	42°35'N 94°31'W	?			Hoppin and Dryden (1958)

*B, Barringer type; O, Odessa type.

**May be considered a separate structural type (see text).

†Crater may be considered associated with the Rieskessel, where glass and coesite are present.

‡Estimated original diameter of crater.

Paper B

NEW EVIDENCE FOR THE IMPACT ORIGIN OF THE RIES BASIN, BAVARIA, GERMANY*

E. M. Shoemaker and E. C. T. Chao

U. S. Geological Survey

Menlo Park, California, and Washington, D. C.

ABSTRACT

The Ries basin is a shallow, nearly circular depression about 17 miles in diameter that lies between the Schwäbian and Franken plateaus of southern Germany. Great masses of breccia and a system of thrust sheets associated with the Ries have been studied by German geologists for about a century. Werner and Stutzer suggested the Ries was an impact crater, but the consensus of the principal investigators has been that the basin was formed by some sort of volcanic explosion.

The only direct evidence of magmatic activity at the Ries is the presence of glass in scattered patches of a breccia called suevit. Some of the glass has long been recognized as sintered fragments of old crystalline rocks. We have found that coesite, a high-pressure polymorph of SiO_2, and lechatelierite, SiO_2 glass, are constituents of the sintered rocks in the suevit. The occurrence of the same phases in sintered rock fragments at Meteor Crater, Arizona, suggests that the glassy components of suevit are of impact rather than volcanic origin.

* * *

The Ries basin or Rieskessel of Bavaria, Germany, is a dissected, nearly circular crater 17 to 18 miles across, located about 50 miles east of Stuttgart (Fig. 1). The town of Nördlingen is situated within the basin. Since its formation, the morphology of this basin or crater has undergone extensive

*This report concerns work done on behalf of the National Aeronautics and Space Administration.

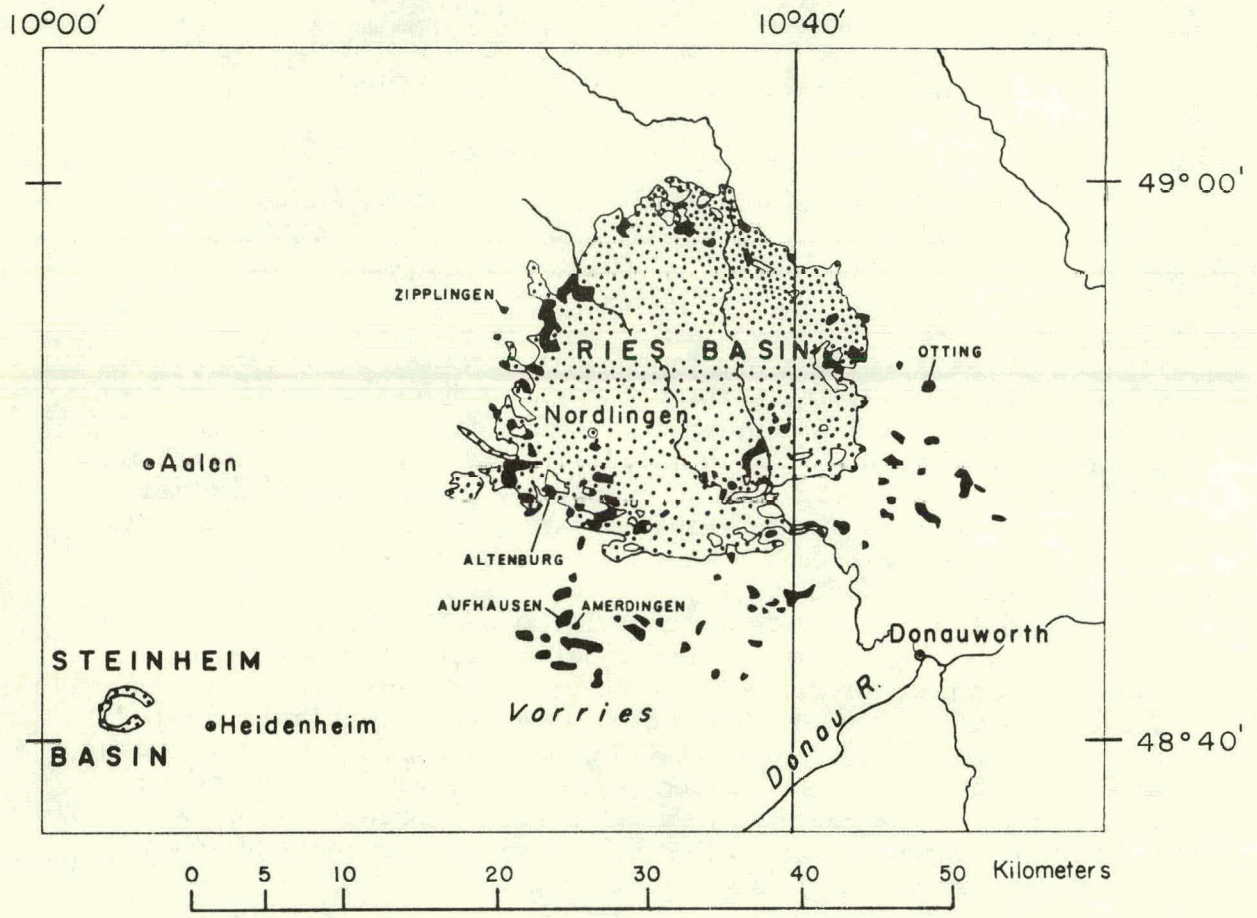

Fig. 1. Index map of the Ries Basin, Bavaria, Germany.

modification by sedimentation and erosion. Its southern rim now stands about 600 feet higher than the basin floor, and the rim is about 100 to 200 feet above the surrounding surface. The crater and associated structural textures have attracted the attention of German geologists for more than a century (Cotta, 1834; Oberdorfer, 1905; Dorn, 1948), and as long ago as 1904, the crater was suggested to be of impact origin (Werner, 1904). Review of the published data led Shoemaker to examine the structural evidence in the field in the summer of 1960. Of special interest was the occurrence of a tuff-like rock, referred to by the German authors as suevit, which we suspected to be of impact origin.

The discovery of coesite, the high pressure polymorph of silica from Meteor Crater, Arizona (Chao, Shoemaker, and Madsen, 1960) had given us a new lead towards the recognition of impact craters. It was natural that suevite from the Ries be re-examined. This paper is a preliminary report of our findings.

The Ries basin lies between the Schwäbian and the Franken Alb, limestone plateaus underlain by gently dipping and flat-lying Jurassic limestone and Triassic clastic sedimentary rocks. The original topography within the basin comprised a central depression about 7 miles across, now filled with sediments, surrounded by an irregular shelf from which rose scattered hills. Miocene lake beds up to 1000 feet thick (Reich and Horrix, 1955) and minor deposits of Pleistocene and Recent sediments have been deposited on the crater floor. The original relief between the center of the crater and the crater rim must have been more than 1600 feet. Lake level at some time in the late Miocene was above the present floor of the basin, and extensive deposits of algal tuffas, gastropod coquinas, and other forms of fresh water limestone occur on scattered hills in the basin and on the lower slopes of the crater walls.

Breccias, chiefly of old crystalline rocks, are exposed on some of the hills that rise above the floor of the Ries today. A variety of granites, interlayered granite and gneiss, aplite, amphibolite, plagioclase amphibolite, greenstone, and schist are the principal crystalline materials. Locally fragments of these rock types are mixed in varying proportion with fragments of

black and red shale of Triassic age and of limestone of Jurassic age. Elsewhere great brecciated masses of Jurassic limestone occur on the floor of the crater.

The walls of the crater and crest of the rim (the Schollen- und Schuppen-Zone of Bentz, 1927) are underlain by breccia and an imbricate series of thrust sheets composed chiefly of Upper Jurassic limestones that cap the Alb (Nathan, 1925, 1935; Dehm, 1932; Gerstlauer, 1940; Schröder and Dehm, 1950; and Treibs, 1950). Beyond, extending tens of miles to the south in the region described by Branco (1902) as the Vorries, are great masses of limestone breccia resting on the undisturbed limestone cap of the Alb and, at the outer limit, on Oligocene sediments. One far-flung fragment of limestone, measuring nearly half a meter in diameter, was found 40 miles from the crater (Reuter, 1925). In places in the Vorries and the Schollen- und Schuppen-Zone, breccias composed chiefly of Lower Jurassic and Triassic sedimentary rocks or of rocks from the crystalline basement complex rest on the breccias of Upper Jurassic limestone and the thrust slices. Locally fragments of Triassic rocks and crystalline rocks are mixed in about equal proportion. Similar breccias were found in a deep drill hole under the lake beds near the center of the Ries. Branco (1902) and later Bentz (1925) long ago concluded that the key to solving the origin of the Ries lay in explaining the mode of emplacement of these unusual breccias.

The most remarkable aspect of the geology of the Ries is the breccia, previously supposed to be of volcanic origin, that has been called suevite (Sauer, 1901). It occurs both inside the crater and on the rim and Vorries (Fig. 1). The suevite consists of a wide variety of rock fragments, most of them crystalline rocks from the basement complex, in general shattered or partially sintered, as well as bombs and smaller fragments of glass that all German authors have agreed are of a conventional igneous or magmatic origin. The glass bombs invariably carry fragments of sintered or partially sintered rocks that are recognizably derived from the crystalline basement. Some of the bombs have extraordinary shapes for volcanic ejecta such as thin sheets that have been tightly folded or curled on the edges. Although

suevite had been studied by Gümbel in 1870, Oberdorfer in 1905 and other workers such as Bentz (1925), to our knowledge no modern mineralogic or petrographic study had been published prior to this investigation. Numerous quarries and outcrops of suevite were visited to obtain samples, to study the variations in the character of the breccia, and to learn as much as possible about its structural relations. The first specimen collected, from Otting, and mailed to Chao proved to contain coesite.

In a quarry at Otting, outside the rim of the crater, suevite is exceptionally well exposed. The suevite forms a patch about 2000 feet across and rests stratigraphically on a breccia composed dominantly of fragments of red and green claystone set in a dominantly sandy matrix. These pieces of sedimentary rock are derived mainly from Triassic beds, and the material underlying the suevite is a facies of breccia that has been mapped elsewhere as Bunter breccia. The suevite itself forms a nearly massive layer about 30 feet thick with rude stratification or parting parallel to the basal contact. It is composed of a wide variety of clastic material and bomb- and lapilli-like masses of glass and partially sintered crystalline rocks that range in size from microscopic particles up to a foot across. Light-colored, partially sintered, fine-grained granitoid, and gneissic rocks are the predominant coarser fragments. Under the hand lens the quartz and feldspar grains in most of these fragments are seen to be crushed and many show varying degrees of sintering and inflation with vesicles. Tightly folded sheets of dark-colored glass (Fig. 2) are common.

One of the light-colored sintered rock fragments was selected for detailed study. It contains over 80% glass of different kinds. The remainder consists of a montmorillonitic clay mineral, magnetite, and a small but readily notable amount of coesite. Coesite, with high relief, occurs in clear silica glass or lechatelierite (Fig. 3). The silica glass is nonvesicular and may have originated by shock without actual melting. It has an index of 1.462 determined by the emersion method using sodium light at 25°C. These grains of clear silica glass were separated and examined by x ray. The x-ray diffraction photograph shows only a weak pattern of coesite, a trace of quartz,

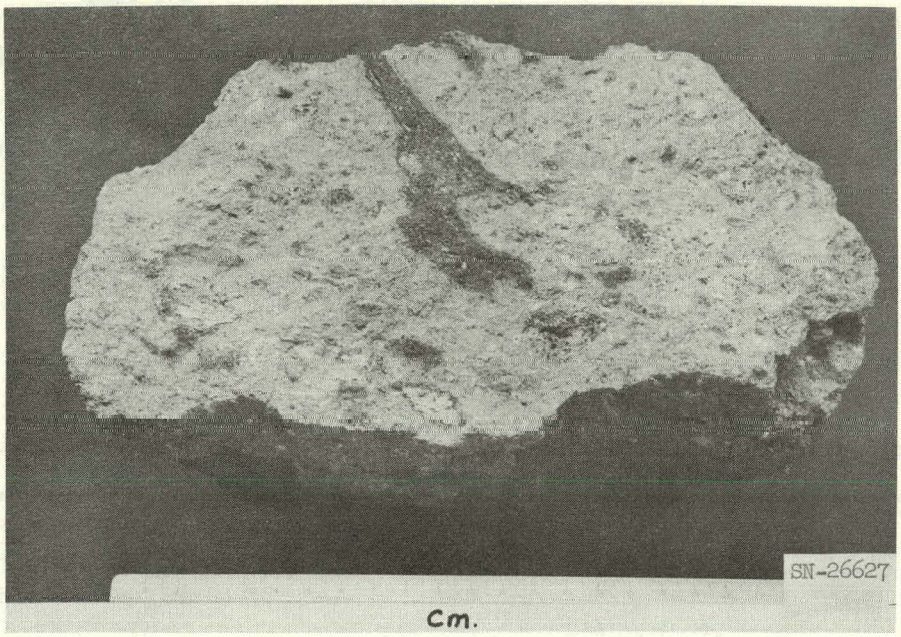

Fig. 2. Photograph of a block of suevite from Otting.

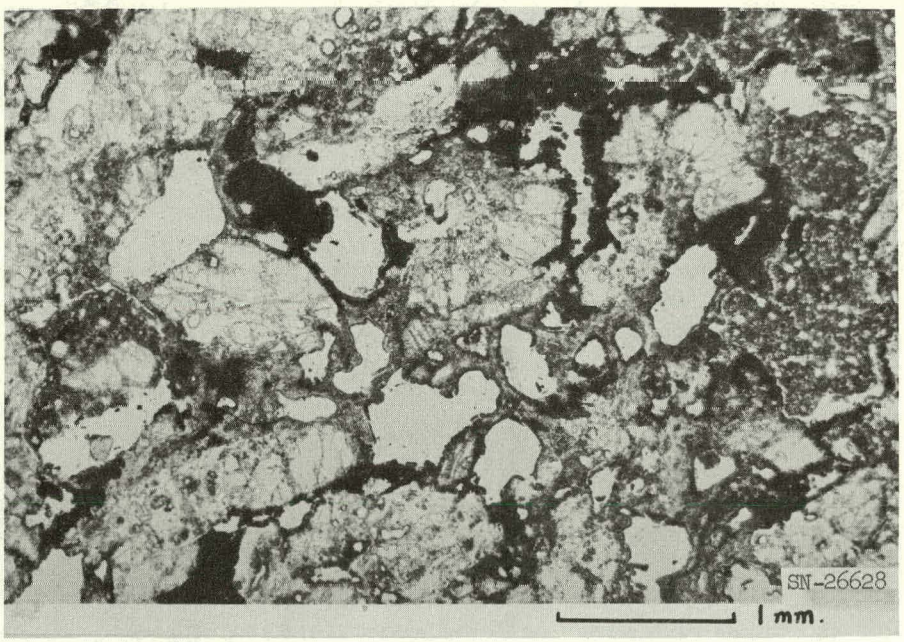

Fig. 3. Photomicrograph of a thin section of suevite from Otting (plane light).

and the darkened background of the glass. Hand-picked fractured, partially vitreous, powdery quartz gave an x-ray pattern of coesite and quartz plus some glass. Several grams of the sintered fragment studied were then dissolved in a weak HF solution to concentrate the coesite. After the coesite was concentrated, it was identified both optically by emersion oil and by x-ray diffraction. The predominant glass present in the sample is a clear vesicular glass with an index of refraction of 1.505. Secondary opaline silica is also present.

Opaque material in the light-colored fragment (Fig. 3) consists of magnetite. The rounded shape of the opaque material suggests that the preexisting iron mineral has been fused. It is strongly magnetic and its powder diffraction pattern is identical to that of magnetite. Spectrographic analysis shows that the nickel content in it is less than 0.01%.

One of the dark masses of glass studied from the suevite from Otting appears dirty grayish brown in thin section. It is chiefly glass with numerous trichites or hairlike crystallites. The glass has an index of refraction of 1.534 and the trichites are much higher in refringence. X-ray study shows that the trichites are crystallites of a monoclinic pyroxene probably isostructural with acmite. The pyroxene has not yet been identified. The only x-ray pattern which is nearly identical with it is a pyroxene yet to be described from sintered siliceous dolomite from Meteor Crater, Arizona. Some low index glass is observed as inclusions in the grayish brown glass with the trichites.

Suevite exposed in a road north of Zipplingen, on the opposite rim of the crater, contains a far larger proportion of unsintered crystalline rocks than that at Otting. Many of the larger crystalline fragments are minutely shattered, but granitic fragments tested did not contain coesite. The matrix of the breccia is characterized by a wide variety of crystalline fragments (Figs. 4 and 5). In the thin section illustrated, the larger fragment is a hornblende diorite. To the left is a fragment with garnet and pinitic chlorite which could be the alteration product of cordierite. The other poorly sorted, angular, sharp fragments are quartz, feldspar, and biotite. At least three types of glass are present: (1) a pale-brown glass

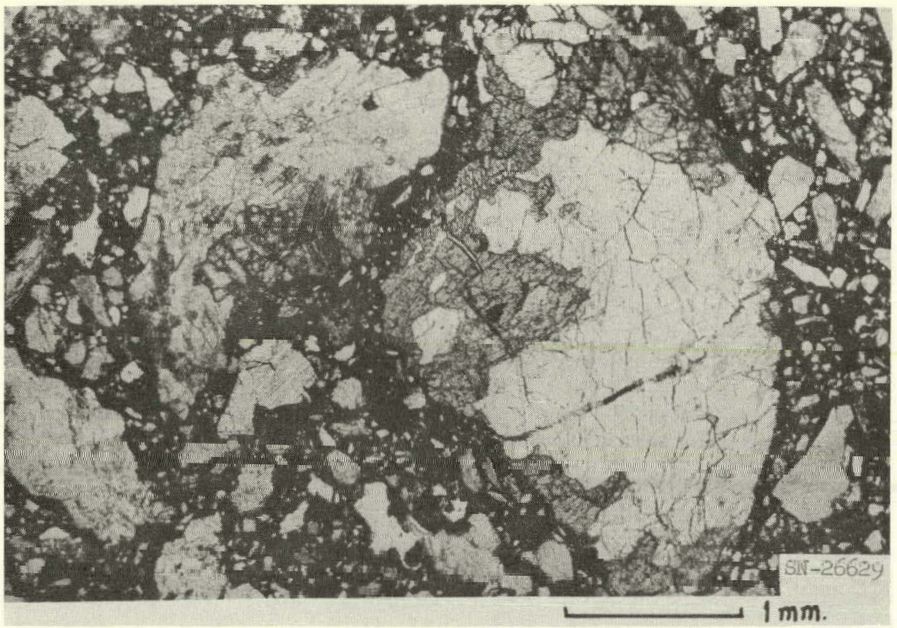

Fig. 4. Photomicrograph of a thin section of suevite from Zipplingen (plane light).

Fig. 5. Photomicrograph of a thin section of suevite from Zipplingen (crossed nicols).

with an index of 1.532, a clear glass with an index of 1.472, and a pale yellowish glass with an index of about 1.46. Some of the clear glass occurs as minute spindles, some with twisted or hooked ends (Fig. 6); the brownish glass is more massive but vesicular. Quartz grains in one of the fractured granitic gneiss fragments examined for coesite are broken by closely parallel fractures perpendicular to the grain elongation. This is a common feature of quartz grains in fractured quartzose Coconino sandstone of Meteor Crater, Arizona.

Bubbles of white glass with an index of about 1.47 occur in the suevite from both Otting and Zipplingen (Fig. 7). They resemble puffed rice and are exceedingly fragile.

A quarry at Aufhausen, south of the Ries, is developed in suevite very similar to that at Otting. The suevite is nearly massive and has many lapilli and peculiarly curved sheetlike bombs of dark-colored glass. A fragment of white glass from the suevite was found to contain coesite and abundant harmotome. In a quarry at Amerdingen, nearby, considerable dark glass is fairly common on the floor of the quarry but inconspicuous higher in the walls.

At Altenburg, within the Ries crater, the suevite exposed in a quarry is nearly massive but shows a vague subhorizontal jointing, as at the other localities, which may be nothing more than sheeting formed during weathering. Along the quarry wall the suevite has a very steep to nearly vertical contact with a giant breccia of Jurassic limestone blocks.

Nine old chemical analyses of suevite (Oberdorfer, 1905) show that the silica content ranges from approximately 56 to 68%, alumina from 8 to 16%, total iron from 4 to 6%, and total alkalies from 4 to 9%. Schowalter (Knebel, 1903) considered the suevite to be chemically related to dacite or trachyte, but the composition merely reflects the composition of the various crystalline and partly sintered crystalline rocks of which it is composed. The minutely fractured condition of much of the fragmental material and the presence of coesite, lechatelierite, and other glasses of various composition in a single small specimen all suggest the fusion was due to strong shock.

The suevite has been commonly assumed to have erupted from numerous

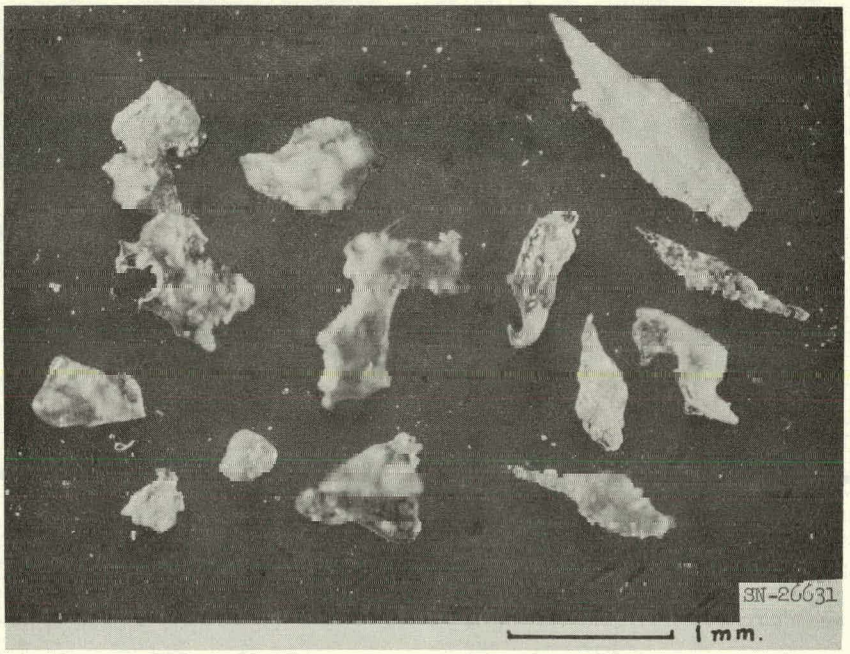

Fig. 6. Photomicrograph of spindly glass fragments from suevite.

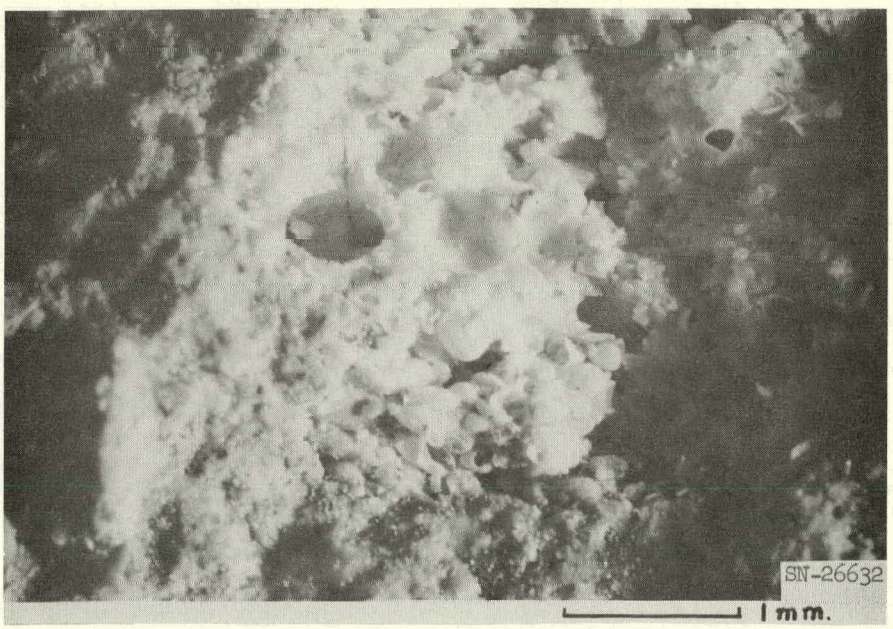

Fig. 7. Photomicrograph showing glassy bubbles in suevite.

widely scattered vents, and, because the suevite can locally be seen to rest on the other breccias, the eruptions have been interpreted as one of the latest events in the development of the Ries. On the basis of about a week's field study, Shoemaker believes that the suevite can be interpreted to rest everywhere on the other breccias; local steep contacts of suevite with other breccia within the crater are probably due to faulting or inward slumping of the breccias along crater walls. Rare dikelike bodies of suevite that have been observed may be crevasse fillings of some kind. The patches of suevite that have been preserved from erosion appear to be remnants of a layer that is analogous to a layer of mixed debris interpreted as fallout that is preserved in Meteor Crater, Arizona (Shoemaker, 1960). The fallout at Meteor Crater also fills crevices in underlying breccia, where the contacts are observed in a shaft in the crater floor.

Structurally the Ries is utterly unlike any caldera or crater of demonstrable volcanic origin. Indeed, suevite is the only material at the Ries that remotely resembles volcanic rock. Kranz (1911, 1934) has attempted to explain the Ries in terms of one large volcanic explosion, but, as Reck has pointed out (Williams, 1941, p. 303), no masses of rock even approaching the size of the thrust slices of the Schollen- und Schuppen-Zone have ever been ejected in the most violent historic volcanic eruptions. To explain the thrust slices, a variety of complicated hypotheses have been invented that involve first an uplift or doming of the central part of the Ries and a later subsidence. All of the major structural features of the crater and the ejecta, on the other hand, appear to have a straightforward explanation in terms of hypervelocity impact mechanics (Shoemaker, in press).

REFERENCES

Bentz, Alfred, 1925, Die Entstehung der "Bunter Breccie," das Zentral Problem im Nördlingen Ries und Steinheimer Becken: Centralblatt f. Mineralogie, Abt. B., p. 97-104, 141-145.

___1927, Geologische Beobachtungen am westlichen Riesrand: Stuttgart, Deutsche Geol. Gesell. Zeitschr., 79, p. 405-438.

Branco, Wilhelm, 1902, Das vulkanische Vorries und seine Beziehung zum vulkanischen Ries bei Nördlingen: Kgl. preussisch Akad. Wiss. Berlin Abh.

Chao, E. C. T., Shoemaker, E. M., and Madsen, B. M., 1960, First natural occurrence of coesite: Science, v. 132, no. 3421, p. 220-222.

Cotta, Bernhard, 1834, Geognostische Beobachtungen im Riesgau und dessen Umgebungen: Neues Jahrb. f. Mineralogie, Geognosie, Geologie, u. Petrefaktenkunde, p. 307-318.

Dehm, Richard, 1932, Geologische Untersuchungen im Ries—Das Gebiet des Blattes Monheim: Neues Jahrb. Mineralogie, Geologie, u. Paläontologie, B.-Bd., v. 67, sec. B, p. 139-256.

Dorn, Paul, 1948, Ein Jahrhundert Riesgeologie: Berlin, Deutsche Geol. Gesell. Zeitschr., v. 100, p. 348-365.

Gerstlauer, K., 1940, Geologische Untersuchungen im Ries; Das Gebiet des Blattes Offingen: München, Bayerische Oberbergamt Geol. Landesuntersuchung Abh. 35.

Gümbel, C. W., 1870, Über den Riesvulkan: Sitz.-Ber. Akad. Wiss., München.

Kranz, Walter, 1911, Das Nördlingen Riesproblem: Oberrheinische geol. Ver., Stuttgart, Jahresber. u. Mitt., N. F., Bd. 1, p. 32-35.

Kranz, Walter, 1934, Fünfte Fortsetzung der Beiträge zum Nördlingen Riesproblem: Central blatt f. Mineralogie, pt. B, no. 6, p. 262-271.

Knebel, Walther, 1903, Weitere geologische Beobachtungen am vulkanischen Ries bei Nördlingen: Deutsche Geol. Gesell. Zeitschr., Bd. 55, p. 23-44.

Nathan, Hans, 1925, Geologische Untersuchungen im Ries—Das Gebiet des Blattes Möttingen: Neues Jahrb. Mineralogie, Geologie, u. Paläontologie, B.-Bd., v. 53, sec. B, p. 31-97.

___1935, Geologische Untersuchungen im Ries--Das Gebiet des Blattes Ederheim: München, Bayerische Oberbergamt Geol. Landesuntersuchung Abh., no. 19, 42 p.

Oberdorfer, R., 1905, Die vulkanischen Tuffe des Ries bei Nördlingen: Jahrb. Ver. Naturk. Württb., p. 1-40.

Reich, Hermann, and Horrix, Wilhelm, 1955, Geophysikalische Untersuchungen im Ries und Vorries und deren geologische Deutung: Hannover, Beihefte zum Geol. Jahrb., no. 19, 119 p.

Reuter, Lothar, 1925, Die Verbreitung jurassischer Kalkblocke aus dem Ries im sudbayr. Diluvialgebiet: Oberrhein. geol. Ver., Stuttgart, Jahresber. u. Mitt., N. F., Bd. 14, p. 191-218.

Sauer, Adolf, 1901, Petrographische Studien an den Lavabrocken aus dem Ries: Jahrb. Ver. Naturk. Württb., v. 57.

Schröder, Joachim, and Dehm, Richard, 1950, Geologische Untersuchungen im Ries: Naturw. Ver. f. Schaben e. V. Augsburg, Abh., Bd. 5, 147 p.

Shoemaker, E. M., 1960, Penetration mechanics of high velocity meteorites, illustrated by Meteor Crater, Arizona: Intern. Geol. Congr., 21st, Copenhagen, 1960, Rept., pt. 18, p. 418-434.

Shoemaker, E. M., in press, Geologic interpretation of lunar craters, in Kopal, Zdenek, ed., The Moon, its astronomy and physics: New York, Academic Press, Inc.

Triebs, Walter, 1950, Geologische Untersuchungen im Ries; das Gebiet des Blattes Otting: München, Geologica Bavaria, 3, 52 p.

Werner, E., 1904, Das Ries in der Schwäb.-fränk. Alb.: Blätter d. Schwäb. Albvereins.

Williams, Howel, 1941, Calderas and their origin: Univ. California Dept. Geol. Sci. Bull., v. 25, no. 6, p. 239-346.

Paper C

THE STUDY OF FOSSIL METEORITE CRATERS WITH THE AID OF GEOPHYSICAL AND DIAMOND DRILLING TECHNIQUES

C. S. Beals and M. J. S. Innes

Dominion Observatory

Ottawa, Canada

ABSTRACT

Studies of Canadian aerial photographs have revealed the presence of three hitherto unexplained circular depressions with geographic locations and dimensions as follows: Holleford, Ont. (long. 76° 38' W; lat. 44° 27' N), diameter 7700 ft, depth 100 ft; Brent, Ont. (long. 78° 29' W, lat. 46° 05' N), diameter 12,000 ft, depth 300 ft; Deep Bay, Sask. (long. 103° 00' W, lat. 56° 24' N), diameter 40,000 ft, depth 700 ft. Gravity, geomagnetic, and seismic observations have indicated the presence under the three craters of circular volumes of rock from several hundred to several thousand feet thick, of lower density, lower magnetic susceptibility, and lower seismic velocity than the surrounding country rock. Diamond drilling at Holleford and Brent has identified this material as partly sedimentary but mainly recemented breccia assumed to be due to meteorite impact and explosion. Deep Bay has not yet been drilled, but the geophysical evidence is of so positive a character as to leave little doubt that the origin of this crater is also due to meteorite impact. Geological evidence indicates that the craters at Brent and Holleford are of Precambrian or early Paleozoic age, while the Deep Bay crater is of Mesozoic age.

In addition to the three craters for which definite evidence pointing to meteorite impact is available, there have also been observed in Canada 15 or more additional circular features ranging in diameter from 3300 ft to 300 miles for which a meteorite impact origin has been considered as a possibility. The locations of these features are given in this paper together with brief descriptions containing such information of a scientific nature as is now available concerning them.

* * *

The study of meteorite craters in Canada began with the discovery by Meen (1951, 1957) of the Chubb or New Quebec crater, 61° 41' N and 73° 41' W,

in northern Quebec Province. This impressive landscape feature (Fig. 1), 2 miles in diameter and 1300 feet deep, was at the time of its discovery the largest meteorite crater known and, next to the Barringer crater, probably the best preserved and most typical of all meteorite craters. Its location in the granite of the Canadian Shield suggested the possibility of other examples, and a search of Canadian aerial photographs was instituted which has been going on ever since. As the search proceeded it gradually became apparent that such conspicuous features as the Barringer and Chubb craters were so scarce as to be practically nonexistent and that a really effective search would have to concentrate on less obvious aspects of crater structure.

This result served to emphasize what might well have been predicted from the beginning, namely that the processes of erosion and deposition would tend to destroy or obliterate the surface features of most meteorite craters in a geologically brief space of time, leaving only inconspicuous remnants of "fossil" craters which might not at first glance appear to have any close relationship to known features.

Recent work by Beals, Innes, and Rottenberg (1960) and Shoemaker (1961) has given an indication of the underground structure of a typical meteorite crater which may reasonably serve as a guide in the location and identification of fossil meteorite craters. Rottenberg's model, in Fig. 2, shows that the circular depression and the rim associated with a recently formed crater are relatively insignificant features of the whole structure when the total volumes and masses of disturbed rock are considered. The disparity between the visible and underground structure is even more marked for the larger craters where Baldwin's well-known relationship between depth, rim height, and diameter indicates a relatively less conspicuous role for the external aspects of the crater. On the other hand, according to Rottenberg's analysis, the layers of breccia and fractured rocks should retain an approximately constant relationship to the crater dimensions, the depth of brecciated rock remaining about one-third the diameter.

On the basis of the typical meteorite crater shown in Fig. 2 and from the related suggestions of Shoemaker, it seems worthwhile to try to visualize

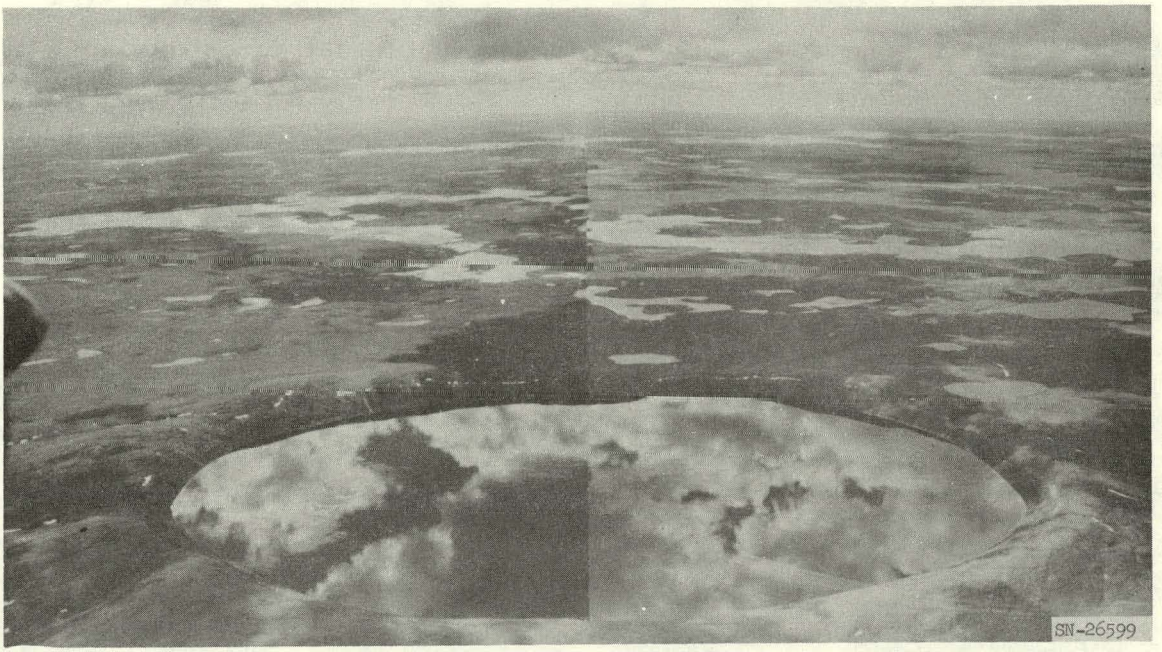

Fig. 1. The New Quebec crater. Located in northern Quebec, this crater is 11,290 ft in diameter and 1300 ft deep.

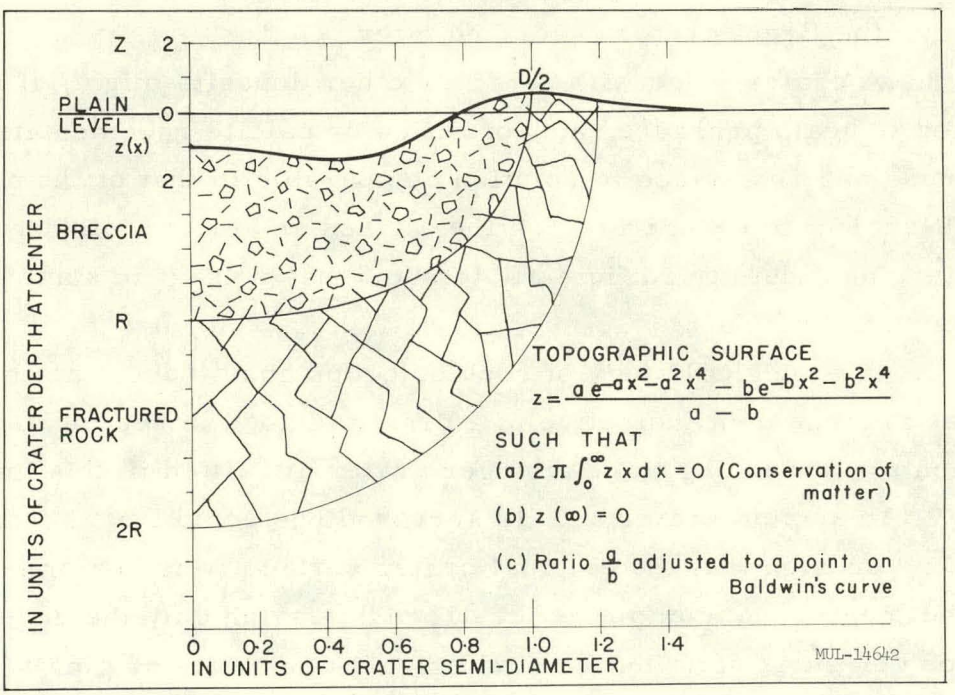

Fig. 2. Rottenberg's model, indicating both surface and underground structure of a typical impact crater.

the sort of remnants or fossil structures likely to be left after the lapse of tens or hundreds of millions of years. Some of these possibilities may be outlined as follows.

Type 1. An ancient crater could lose its rim or most of it by erosion and still remain a fairly conspicuous feature such as an approximately circular lake filled with water; the Deep Bay crater is a good example, q.v.

Type 2. A crater located in an area never covered by water could, by the ordinary processes of erosion, gradually become obliterated and cease to be a conspicuous landscape feature. Such an object might, nevertheless, be detected on aerial photographs by configurations of vegetation or drainage patterns.

Type 3. In areas covered by sedimentary rocks where the cover is thin, the circular shape and raised rim of a buried crater may influence the attitude of the sediments sufficiently to be detected; an example is the Holleford crater, q.v.

Type 4. A crater originally filled in or covered over by sediments may at a later time have the sediments eroded sufficiently to reveal a circular feature, e.g., the Brent crater described later.

Type 5. A crater filled with sandy or other deposits might, if buried and subjected to heat, pressure, and/or silica or calcite recementation, attain a hardness and resistance to solution comparable to that of the containing rock. If subject to severe erosion the altered sediments might retain their structure and identity sufficiently to stand up, at least in some degree, above the surrounding plain.

Type 6. A geological study of rock outcrops could reveal uptilted strata in a circular arrangement indicative of a crater formed in sedimentary rock. (The sediments surrounding the Barringer crater are tilted in this manner.)

Type 7. An ancient crater and its surroundings could have been subject to such severe erosion that the original crater surface (whether or not protected by sediments) was completely destroyed, leaving only the underlying breccia whose circular distribution could give a clue to its origin.

Type 8. According to G. P. Kuiper, who has carried out what are probably the most definitive modern observations of the moon, the central peaks of lunar craters may be igneous intrusions of hard basic rock. A very similar suggestion relative to earthly craters has been made by J. M. Harrison, Director of the Geological Survey of Canada. He points out that an impact of sufficient violence could act as a trigger to release latent volcanism within the earth's crust which could complicate the interpretation of fossil craters. The simplest case would be a hard central peak (of intruded igneous material) on an earthly crater which might well remain intact while the crater rim, composed of debris and shattered rock, would be removed by erosion. To judge by observations of the moon, such a situation is most likely to be encountered in a large crater of the order of some tens of miles in diameter. A combination of impact and volcanism also appears to be the most logical explanation of a number of lunar craters with rims corresponding to an impact origin and flat featureless floors probably due to lava flow.* In a similar occurrence on earth it is possible that the rim would be rapidly destroyed by erosion leaving the lava floor with no very clear indication of its origin except its circular form. There is also the possibility that the volcanic phenomena would be of sufficient magnitude to obliterate all trace of the impact, including the original circular crater form.

THE HOLLEFORD CRATER

One of the first discoveries made as a result of the study of Canadian aerial photographs was the Holleford crater, longitude 76° 38' W, latitude 44° 47' N, first noted by G. M. Ferguson and A. Landau on R. C. A. F. photograph numbers A-13969-43 and 44. A study of the aerial photographs with the stereoscope indicated a relatively shallow circular depression, with some indication

---

*Gold (1956) attributes this and other lunar phenomena to dust layers produced by impact. While impact debris undoubtedly plays a part, the writers consider that lava flows are probably more important in accounting for the large, level, featureless areas of the moon.

of raised edges, approximating 1.46 miles in diameter. The village of Holleford lies partly within the crater circumference, and several roads cross the rim in descending close to the floor of the crater. Geological studies on the site indicate that almost the entire crater area was covered by Paleozoic sediments of Ordovician age which dip gently inward toward the centre (Frarey, 1955). See Fig. 3. The area has been subject to heavy erosion, and the circular form of the feature is more clearly defined in some areas than others; but there appears to be no exception to the rule that all strata dip radially inward toward the centre. The crater thus appears to correspond to type 3 but it also has resemblances to type 4 and type 5. The general area in which the crater is located is rather thinly covered with sediments and there are numerous outcrops of Precambrian rock in its immediate vicinity. Within the circumference there appears to be only a single Precambrian outcrop, occurring as a low hillock of crystalline limestone on the northeastern sector of the crater rim. This outcrop is approximately 38 feet above the surrounding plain, suggesting that the rim of the crater had not been entirely eroded away before the deposition of sediments. The depth of the visible crater is approximately 100 feet and the surrounding hills, particularly on the south, east, and west, form a moderately impressive cirque when viewed from a point near the centre. The adopted centre is at 492 feet above sea level, about 12 feet above the surrounding plain, while the visible rim rises at its highest point in the southwest to an elevation of 600 feet above sea level. The fact that the true crater rim is covered with sediments renders its exact location difficult, but on the average its position is considered determinable within 100 feet. On the west the estimated position of the rim is on the edge of a cliff dropping steeply about 150 feet to Knowlton Lake.

A consideration of the overall geology of the area suggested the existence of a circular basin in the Precambrian basement filled with Paleozoic sediments. This hypothesis was tested by geophysical observations with the following results.

Geophysical Results. Seismological studies of the crater conducted by J. H. Hodgson and P. L. Willmore encountered difficulties due to a layer of

Fig. 3. Aerial view of the Holleford crater. Diameter 7700 ft, depth 100 ft. The open circle marks the centre. The small filled circle, lower right, is on the rim.

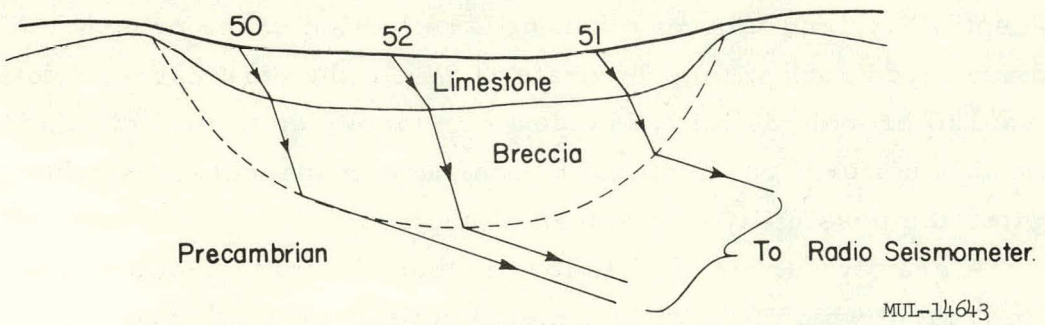

Fig. 4. Diagram illustrating ray paths of seismic shots fired inside the Holleford crater.

hard lithographic limestone about 50 feet thick on the surface of the sediments filling the crater. The characteristically high propagation velocity of this material resulted in refraction of seismic waves away from the surface, preventing the application of standard methods of refraction seismology. However, analysis of travel time curves obtained by firing a number of shots near the centre of the crater, as indicated in Fig. 4, and recording them outside at distances of 3000 to 12,000 feet from the rim showed some evidence of an underlying low velocity layer. No such layer was indicated in the records obtained at the same stations for shots fired outside and well removed from the crater to ensure that the seismic paths traversed undisturbed basement rock. While no quantitative results as to its thickness were possible, the low velocity material underlying the crater might well be identified with the zone of broken and shattered rock characteristic of impact craters.

Although no ground magnetic surveys are yet available for the crater, an aeromagnetic map of the area was made available by the Geological Survey of Canada and is reproduced in Fig. 5. The map gives anomalies of total field intensity contoured at intervals of 10 gammas and is based on measurements recorded at a flight altitude of 500 feet above terrain. The anomaly contours trend in a general northeast direction consistent with the general strike of the Precambrian rocks, and although there are marked local disturbances of as much as 300 gammas in the magnetic field within a half mile of the rim, the variation over the crater is quite uniform. There is, however, a slight widening of the contours indicating the presence of material of low magnetic susceptibility, and this may well be a reflection of the presence of sediments and shattered rock within the crater. While the aeromagnetic data can scarcely be said to provide definitive evidence in favour of an impact origin, the remarkably uniform gradient and the absence of magnetic disturbances strongly negates the possibility of a volcanic origin.

A gravity survey at Holleford indicated contours of a roughly circular form (Fig. 6) which follow the general outlines of the depression. Correcting for regional effects gives a negative anomaly of about 2.2 milligals produced by the crater. It is impossible to assess accurately the portion of the anomaly

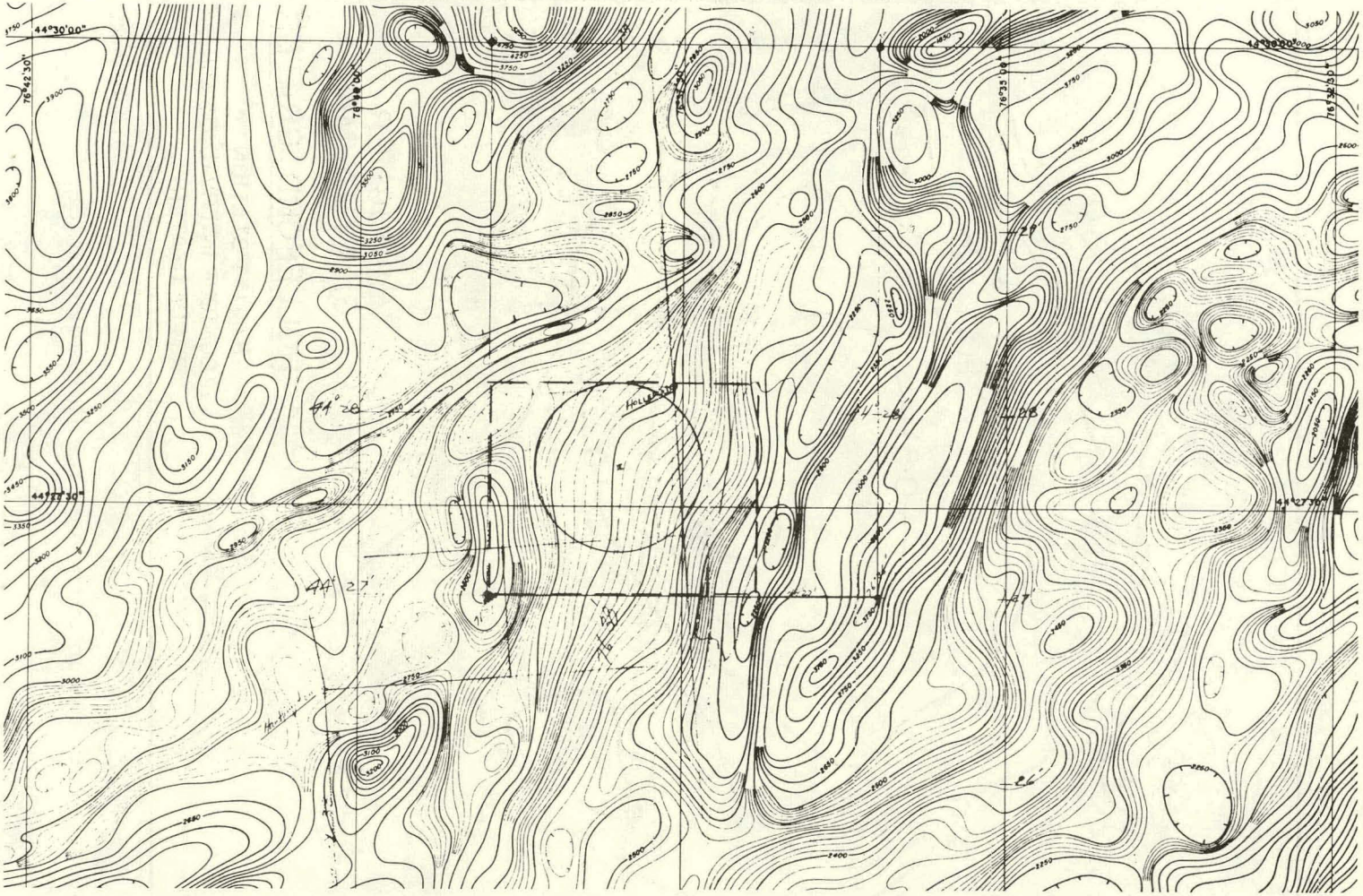

Fig. 5. Aeromagnetic map of Holleford crater area. The circle in the centre of the map outlining the inner part of the crater is 5600 ft in diameter.

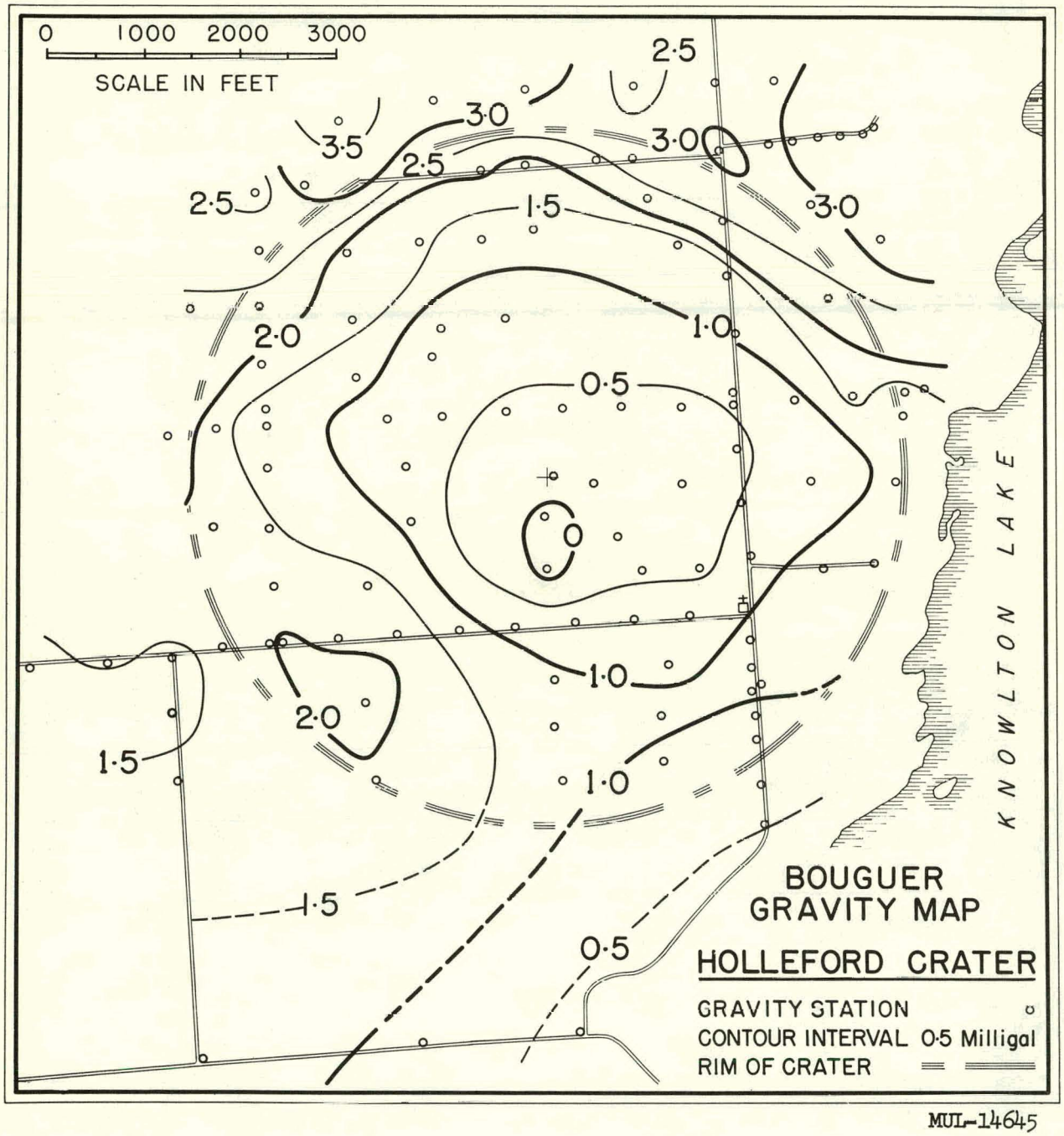

Fig. 6. Gravity contours over the Holleford crater.

that is due to the Paleozoic sediments now filling the crater and draped over the rim, or the portion due to the low density fragmental material that is believed to underlie the sedimentary strata. However, the surface exposures of the Paleozoic sediments consist of dense lithographic limestones with densities somewhat greater than those of the surrounding Precambrian rocks. As a considerable thickness of these limestones within the crater would tend to compensate for any sedimentary material of lower density at depth, overlying the crater floor, it is concluded that the total observed anomaly may be taken as a reasonable estimate of the gravitational effect of the brecciated and fractured zone. On this basis and assuming 0.16 gram/cm^3 (as observed at Brent) for the mean density contrast between the fragmental material and normal country rock, the gravity minimum indicates that the breccia zone under the Holleford crater is at least 1000 feet thick. (Bancroft, 1960.)

Diamond Drilling Program. Since the geophysical results gave some confirmation to the idea of a crater in the Precambrian basement filled with sedimentary rock, it was decided to undertake a diamond drilling program partly to ascertain the depth and shape of the crater and partly to see whether the material under the sediments would turn out to be the broken and fragmented material expected for an explosion crater. Holes were drilled at distances of (1) 1400 feet (2) 2500 feet and (3) 3750 feet from the centre of the crater. The location of hole 3 was chosen so as to be close to the top of the rim while the other two holes were located on the sloping sides at distances favourable for determining a profile. Limitation of funds prevented the drilling of a fourth hole at the centre.

The first hole (hole 1) drilled through sediments for 755 feet, at which depth rock fragments of a variety of sizes were encountered embedded in a matrix of finely divided materials which upon microscopic examination turned out to be fragments of the Precambrian basement rock. This fragmented material or breccia was drilled to a depth of 1128 feet, where the drill stuck fast and had to be abandoned. While it was a disappointment not to be able to penetrate to the undisturbed basement, the 1128 feet of drill cores recovered supplied very valuable information which was supplemented by additional

material from holes 2 and 3. In hole 2 rock breccia was encountered after 440 feet of drilling through sediments. The breccia continued to a depth of 600 feet where substantially undisturbed rock was encountered. The hole was pushed to a depth of 1486 feet in order to secure massive samples of the basement rock. Hole 3, bored on the estimated location of the crater rim, encountered a thin layer of breccia after only 65 feet of sediments had been penetrated. Undisturbed basement rock was reached at 66 feet and the hole was continued to a total depth of 443 feet. The contrast between the sediments and breccia is illustrated in Fig. 7 by a selection of cores from hole 2.

The information provided by the drill cores was very favourable to the hypothesis of a meteorite impact origin for the crater. The breccia encountered below the sediments was entirely without bedding planes and gave the impression of being formed in situ by an instantaneous event like an explosion or impact. The shape of the crater as may be seen from Fig. 8 is closely similar to that of the Barringer and New Quebec craters as well as the theoretical profile of Fig. 1. The information from hole 3 as well as the outcrop of Precambrian rock on the northeast sector of the rim already mentioned gave a definite indication of a rudimentary rim although it is reasonably certain that a large part of the rim was eroded away before the deposition of sediments. No evidence was found that could identify the crater with the processes of erosion, subsidence, or volcanism, and hence there appears little doubt that the only reasonable explanation of its origin is that of meteorite impact and explosion (Beals, 1960).

Search for Meteoritic Material. A search for meteoritic material was conducted making use of two different techniques. First, all of the drill cores were studied with the aid of a highly sensitive astatic magnetometer and those which showed indications of greater than average magnetic moment were broken up and searched for magnetic particles. In every case it was found that the excess magnetism was due to pieces of basic rock embedded in the breccia or in some cases forming the entire core. In no case was anything suggesting the presence of nickel iron discovered.

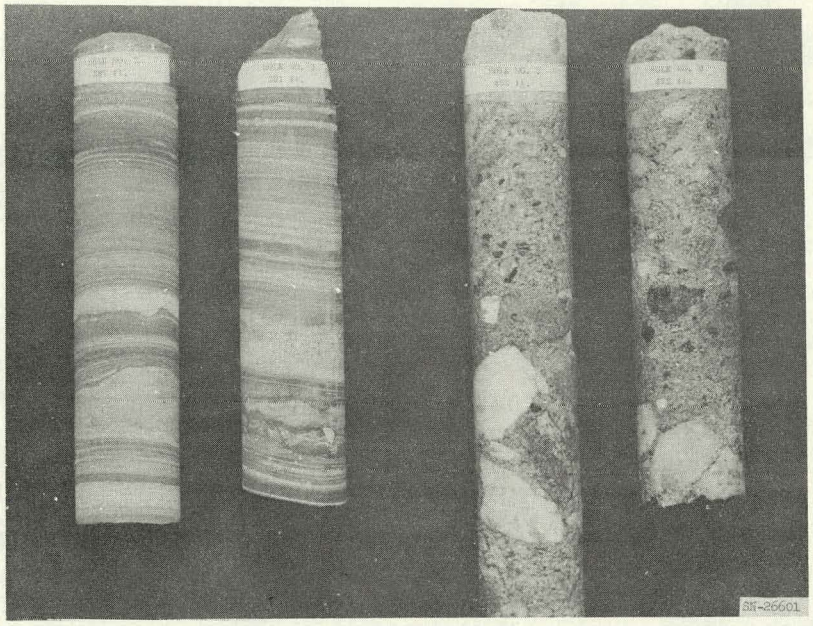

Fig. 7. Drill cores from hole 2, Holleford crater. Left, sedimentary rock; right, recemented breccia.

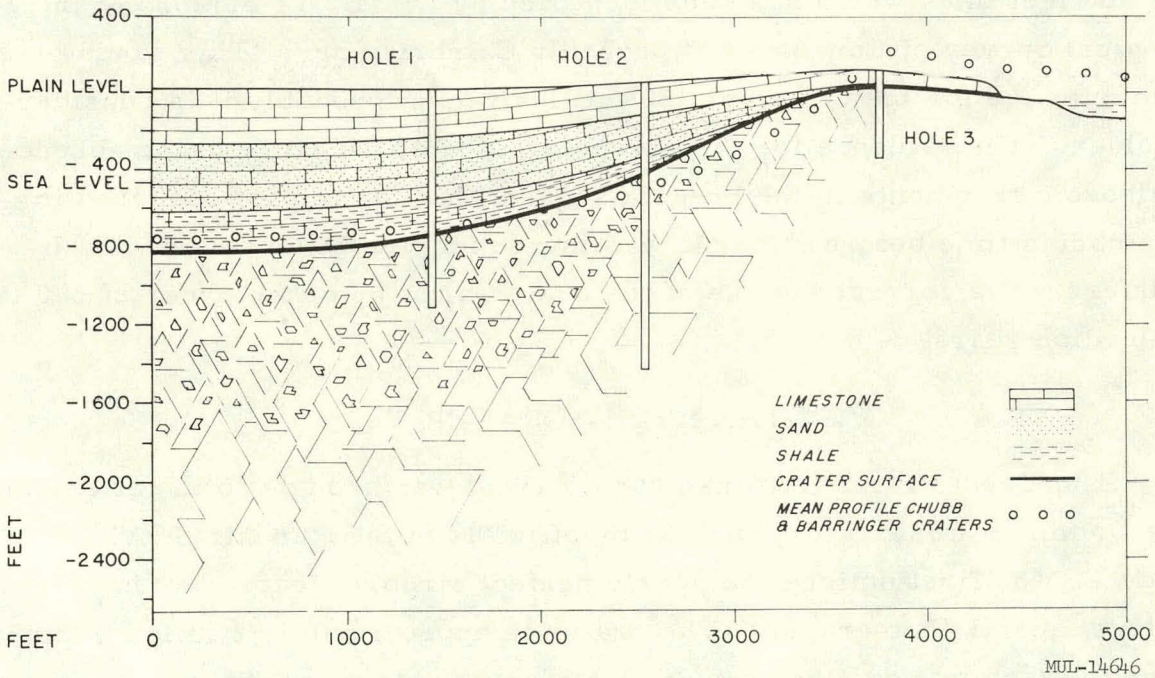

Fig. 8. Profile of the Holleford crater as reconstructed from drill hole and surface observations. The original crater dips 800 feet below the plain while the zone of fractured rock extends to an estimated depth of 2400 feet. The estimate of breccia depth at the centre depends on theoretical considerations advanced by J. A. Rottenberg.

A second procedure, carried out with the aid of the Geological Survey of Canada, was to take samples of core every 5 feet throughout the breccia and to subject them to crushing and subsequent magnetic analysis for magnetic particles. In addition to cores from the brecciated layer, numerous cores were taken from the lower layers of the sediments in contact with the breccia since the appearance of these cores suggested that they were formed of finely divided material produced by the explosion and washed back into the crater before the deposition of Paleozoic sediments. Here again the results were entirely negative and although two drill holes of small diameter are admittedly an inadequate sampling, the possibility or even the probability must be considered that the crater was formed by a stone rather than a nickel iron meteorite.

Age of the Crater. Geological investigations at the surface had indicated the presence of Black River fauna characteristic of the middle Ordovician era. A feature of the core near the bottom of the hole was a layer of whitish sandstone 400 feet thick which has been identified by Dr. B. V. Sanford of the Geological Survey of Canada as of probably Cambrian age. This would give a minimum age for the crater of 450 million years; probably it is considerably older. The evidence for the severe erosion of the rim and the absence of Paleozoic fragments in the breccia suggest that the impact occurred in Precambrian time before the area was invaded by the Paleozoic seas. If this inference is correct the age of the crater must be of the order of 500 to 1000 million years.

THE BRENT CRATER

The Brent crater (Millman et al., 1960) was brought to the attention of the Dominion Observatory in 1951 by officials of Spartan Air Services Ltd., of Ottawa, who first noticed the nearly perfect circular feature when viewing high level aerial photographs. The crater is approximately 2 miles in diameter and is located near the northern boundary of Algonquin Park in northeastern Ontario. The centre of the crater has coordinates 46° 04.5' north latitude and 78° 29.0' west longitude, and its elevation is 1150 feet above sea level. The southern boundary of the crater is about 2-1/2 miles north of

the village of Brent, Ontario, which is a divisional point on the main line of the Canadian National Railway. The crater is inaccessible by automobile but can be reached easily by light aircraft suitable for landing on small lakes, such as Gilmour and Tecumseh, which form part of the crater floor. An aerial view is shown in Fig. 9.

The circular pattern of the feature is due to the topography which forms a craterlike depression, the central portion of which has an average elevation some 300 feet below the hills that rise abruptly in places outward from the central floor. In marked contrast to the rugged terrain of the surrounding areas, there are no abrupt changes in elevation within the basin. Gilmour and Tecumseh Lakes both have about the same elevation and occupy about one-third of the crater; their western and eastern margins, together with pronounced drainage channels into them, are largely responsible for the circular pattern which first called attention to this region.

Beyond the circle and for a distance of about 2 or 3 miles, the drainage is for the most part radial and toward the depression. The only exception is the channel to the southeast, which in seasons of high water provides an outlet through Brant Lake and Cedar Lake to the south. The whole area of the Brent crater is heavily wooded. Spruce, pine, and other coniferous trees generally occupy the slopes and surrounding hills, while maples and cedars prefer the lower elevations within the crater.

Geologically the Brent crater lies in an area in which all the rocks, with the exception of a few scattered outliers of Paleozoic limestone, are of Precambrian age. The predominant rock types, which outcrop in numerous places on the rim and surrounding hills, are gneissic granites and biotite-horneblende-garnetiferous gneisses believed for the most part to be of sedimentary origin. A thick mantle of glacial drift and unconsolidated material consisting of sand, gravel, boulders, and clay obscures the crater floor and no bed rock exposures have been located. However, numerous blocks of Ordovician limestone and shale were encountered along the eastern margin of Gilmour Lake and along the north-south arcuate ridges in the centre of the basin. It was not surprising therefore that blasting operations in connection

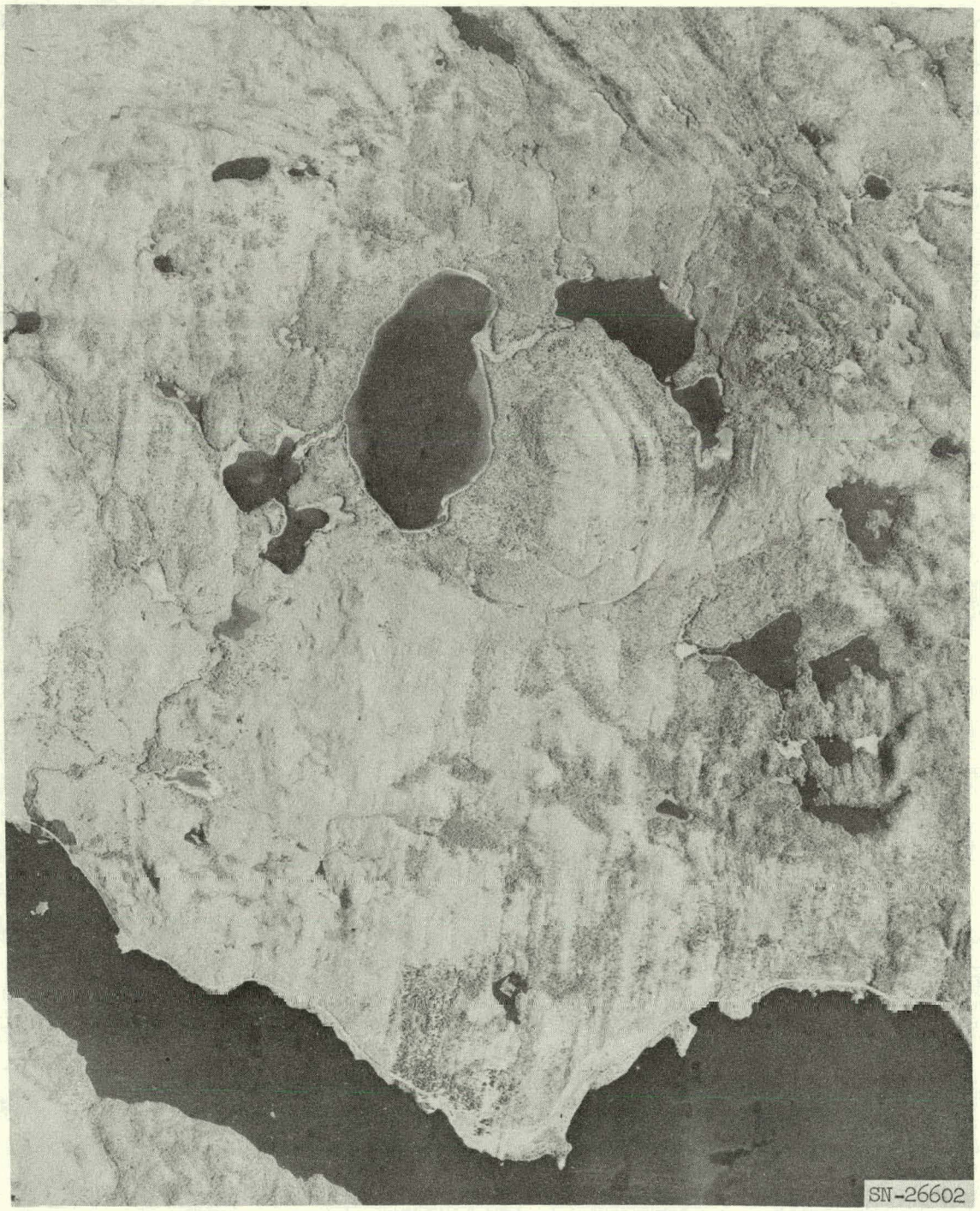

Fig. 9. Aerial view of the Brent crater. The circular pattern shown on the photograph has a diameter of 9500 ft and a depth of 300 ft.

with the geophysical investigations disclosed Paleozoic rock in situ at various depths, which makes it probable that the entire basin is underlain by sedimentary rocks.

Continental glaciation has affected this whole area with the deposition of great thicknesses of glacial debris, particularly in areas of lower elevation. The dominant structural features of the gneisses, however, may readily be observed on the ridges, and field investigation and examination of air photographs reveal no evidence to suggest a geological origin for the crater. The trends of the gneisses are generally westerly to northwesterly, and appear to be terminated by the circle defining the present crater wall. In no way do these trends appear to conform to the circularity of the feature, which seems strong evidence that the folding and deformation of the gneissic rocks antedates the crater's formation. Although the gneisses have been subject to large scale faulting, the near-perfect circularity of the crater floor indicates no differential movement and rules out the possibility of faulting and subsidence as a mode of origin. On the other hand, the drainage channels occupied by intermittent streams emptying into the crater might well be the expression of radial tensional features produced at the time of the crater's formation. It should also be remarked that any suggestion that the crater is the deeply eroded vent or caldera of an ancient volcano finds no support from the surface geology. Apart from the possibility that here as elsewhere in the Canadian Shield some of the gneisses may be of volcanic origin, no volcanic rocks are known to exist in the area.

Perhaps the strongest field evidence for an explosive origin for the Brent crater is the discovery of several outcroppings of breccia along the circular drainage channel which separates the granitic rocks from the crater floor, as well as numerous blocks of breccia within the glacial drift. The breccia is made up of angular fragments of granite gneiss of all sizes from minute particles to blocks measuring several feet across, which are indistinguishable from the paragneisses that form the surrounding hills.

The presence of Ordovician sedimentary rocks now filling the Brent depression is evidence of its great age (at least 400 million years, and

probably much older), and it is not surprising that its original form has undergone great changes through processes of erosion since its formation. If we assume an original rim diameter of 11,500 feet, which seems reasonable, then Baldwin's formula as it applies to normal explosion craters gives us values of 1555 feet and 662 feet for the total depth and rim height, respectively, and hence 893 feet for the depth of the crater floor below the original ground level.

There seems little doubt that the original rim of the crater has been almost obliterated. Its present form as marked by the height of land is much wider than that of an undisturbed crater and extends some 3000 feet beyond the well-defined 9500-foot circle that delimits the crater floor. Intensive jointing and fracturing and the formation of multiple tension fissures would tend to promote and accelerate erosion of the rim. On the other hand it seems likely that the advance of the Paleozoic seas and deposition of sediments within have contributed to the preservation of the deeper portions of the crater.

Geophysical Investigations. Obviously, if the Brent crater were a true explosion crater, the great amount of energy expended in its formation would result in marked changes in the physical properties of the country rock, not only at the point of impact but in the area surrounding the crater. Accordingly, geophysical investigations employing gravity, seismic, and magnetic methods were carried out (Millman et al., 1960) in the expectation that they might provide important information to test the validity of an explosive origin.

(a) Gravity Measurements. The gravity anomaly map (Fig. 10) gives the important results of the gravity investigation. The location of the gravity stations and their Bouguer anomalies contoured at intervals of 0.5 milligal are shown. Some topographical information which outlines the depression has been included, and it is readily seen that apart from minor variations the gravity contours are circular and form a gravity minimum of about 5 or 6 milligals concentric with the crater.

Any explanation of the gravity pattern would require a circular body consisting of material of lower density than the surrounding gneisses and

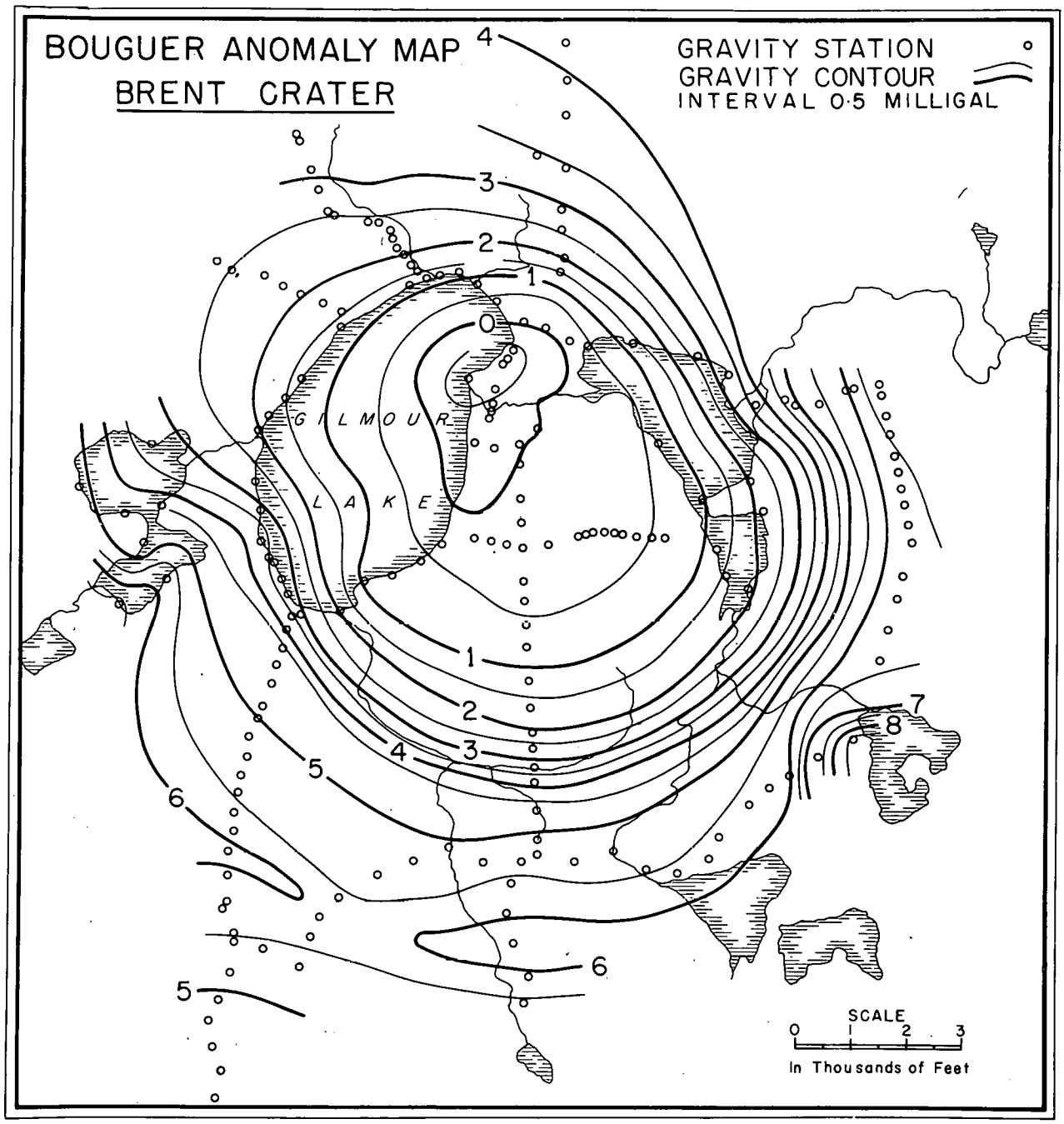

Fig. 10. Gravity contour map, Brent crater.

extending from near the surface to a considerable depth. If it is assumed that the low density body is due entirely to Paleozoic strata filling a depression in otherwise undisturbed Precambrian rocks, then some 1600 to 4000 feet of sedimentary material (depending upon its density) would have to be present to account for the total anomaly.

However, density determinations of samples of the gneiss breccia previously described yield values all lower than the densities obtained for the surrounding granitic gneisses, but which have a range similar to that of the Paleozoic rocks. This suggests that a considerable portion of the gravity anomaly is due to broken and fragmental material underlying the sediments. The assumption that the sediments extend to about 900 feet, the predicted depth to the original crater floor, leads to an estimate of 700 to 3000 feet for the thickness of the brecciated zone.

Other evidence which points to a zone of intense fracturing and uplift of the gneisses in the vicinity of the crater's rim, and which supports the higher value estimated for the thickness of the breccia zone, is apparent from the gravity anomaly map. It will be noticed that whereas the variation in gravity as indicated by the spacing of the anomaly contours is small over the central floor of the crater, the anomaly gradient is a maximum near the 9500-foot circle separating the granitic and sedimentary rocks. There are insufficient gravity observations to delimit the full extent of the gravitationally disturbed zone over the gneisses on all sides of the crater, but the measurements to the south indicate peak or normal values some 3000 to 4000 feet from the circle. This then may be taken as an indication of the outer limit of the zone of major crustal fracturing and deformation which accompanied the crater's formation.

(b) Seismic Investigation. As the velocity of seismic waves depends primarily upon the nature of the medium in which they are transmitted, seismic investigations were carried out with the expectation of obtaining significant information about the underlying structure as well as an estimate of the depth of sedimentary materials within the crater. Ordinary refraction methods were employed and shots were fired at various intervals along a north-south

diameter of the crater and on the north and south rim. Recording seismometers were located at three sites within the crater and at two sites outside, one to the north and the other to the south, each about 2000 feet beyond the 9500-foot circle. With this arrangement it was possible to record arrival times of seismic waves for shots fired at distances up to 4000 feet, sufficient to establish characteristic velocities and thicknesses of the material within the crater. In addition, one seismograph was located in the village of Brent, four miles to the south, for the purpose of determining the normal seismic velocity for this area of the Shield and to provide an estimate of the width of the zone of fracturing in the vicinity of the crater, if such existed.

Analysis of the travel time curves for the stations located within the crater and on the rim yielded wave velocities which in a broad way may be interpreted as defining three underlying layers of contrasting elastic properties. The lowest velocity, 1700 ft/sec, is considered due to a layer of glacial drift and weathered material overlying the bedrock surface with thickness as great as 100 feet. A velocity of 10,300 ± 170 ft/sec was well established on records for the three stations within the crater and is believed to represent the propagation velocity of the Paleozoic limestone and other sedimentary rocks filling the crater. Data for these stations also yield a higher velocity, 14,150 ft/sec, identified as the propagation velocity of the breccia zone underlying the sedimentary rocks and verified as such from analysis of the time-distance curves for the two long range stations located on the rim. Although considerable uncertainty remains concerning the actual form of the crater floor, the combined analysis of the seismic data from short and long range shots indicates that the sedimentary material has a thickness of about 300 feet near the rim and about 1000 feet toward the centre of the basin (Fig. 11).

Since successive seismic horizons can be identified only if the refracted wave paths are sufficiently long to verify with certainty the velocity of propagation that is characteristic of the underlying layers, a determination of the thickness of brecciated and shattered rock (14, 150-ft/sec material) underlying the sediments is dependent on the seismic data recorded for some

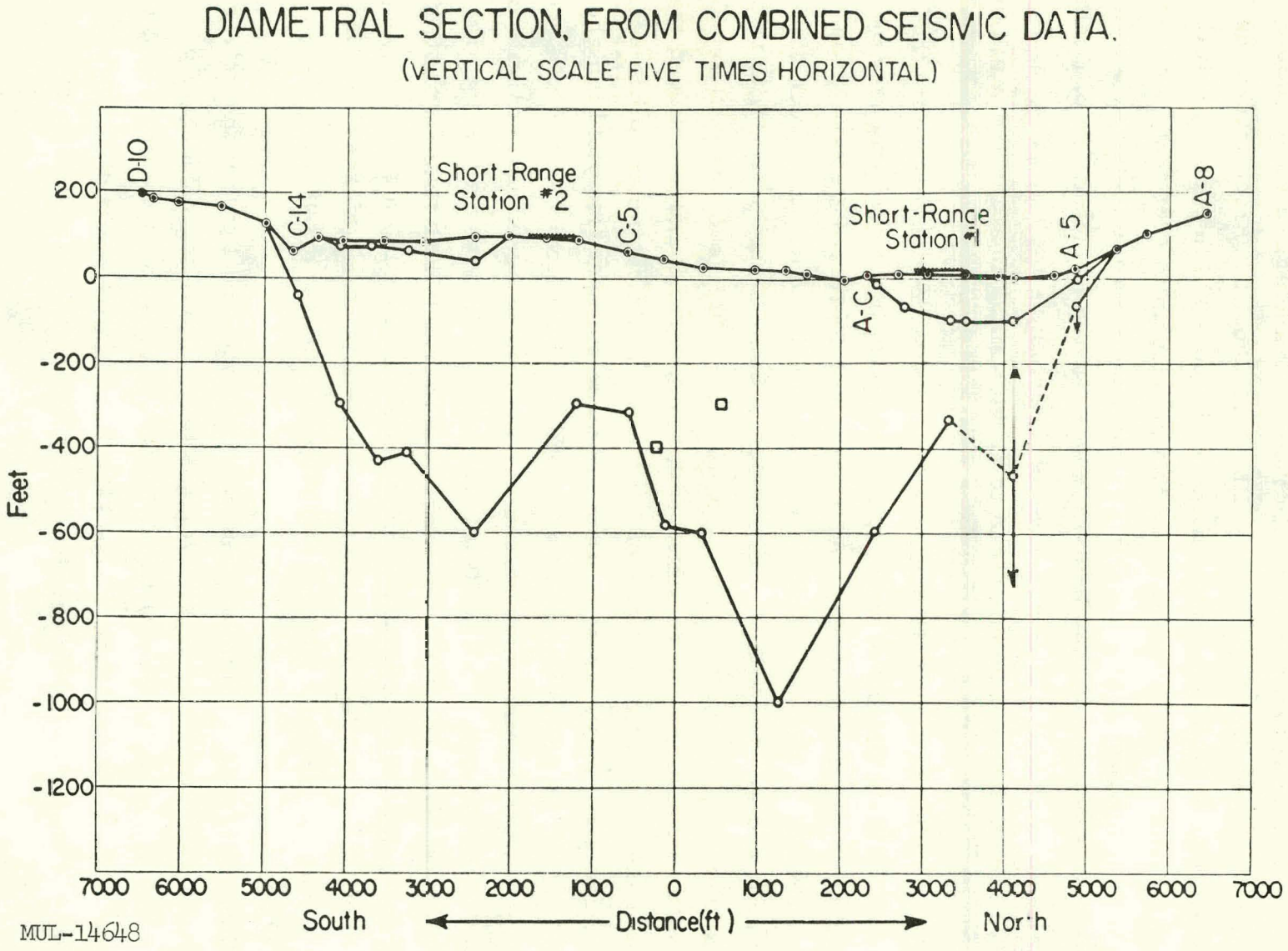

Fig. 11. Seismic profile indicating roughly the depth of sediments in the Brent crater.

distance outside the crater rim. One shot fired near the centre of the crater was recorded at the Brent station at a distance of 20,200 feet, indicating an average velocity of 15,780 ft/sec. Unfortunately, because of instrumentation difficulties, no other records were obtained to provide a firm value for the normal progagation velocity of the crustal rocks outside the crater. However, on the reasonable assumption that this value is not much different from the average value of 20,240 ft/sec for the Canadian Shield (Hodgson, 1953), and that the difference in these velocities is entirely due to low velocity materials within and surrounding the crater, the thickness of the brecciated zone is estimated to be of the order of 4000 feet.

(c) Magnetic Investigation. It is generally known that granitic gneisses of the Canadian Shield produce highly variable magnetic fields, largely due to concentrations of magnetite crystals in contact zones and along bedding planes. Apparently these crystals became polarized under the influence of the earth's magnetic field during the processes of thermal and dynamic metamorphism in which the rocks were transformed into gneisses. Contours of variations in the magnetic field, therefore, tend to follow and outline major structural features, and it was considered that magnetic surveys over the Brent crater depression might provide significant information concerning its underlying structure.

Accordingly, measurements of the vertical magnetic field intensity were made along certain traverses across the floor of the crater and on its rim by the Dominion Observatory. In addition, the Geological Survey of Canada carried out an aeromagnetic survey at a height of 500 feet, in sufficient detail to provide a contour map of the area giving the variations in the total field intensity. (See Fig. 12.) The most significant feature of the results of both surveys, which are in general agreement, is the marked contrast between the intensities observed within and outside the rim of the crater. The total variation in the airborne results over the crater does not exceed 80 gammas with a nearly uniform gradient of about 50 gammas per mile directed to the northwest. On the other hand, the magnetic intensities surrounding the crater are highly disturbed and typical of the magnetic fields

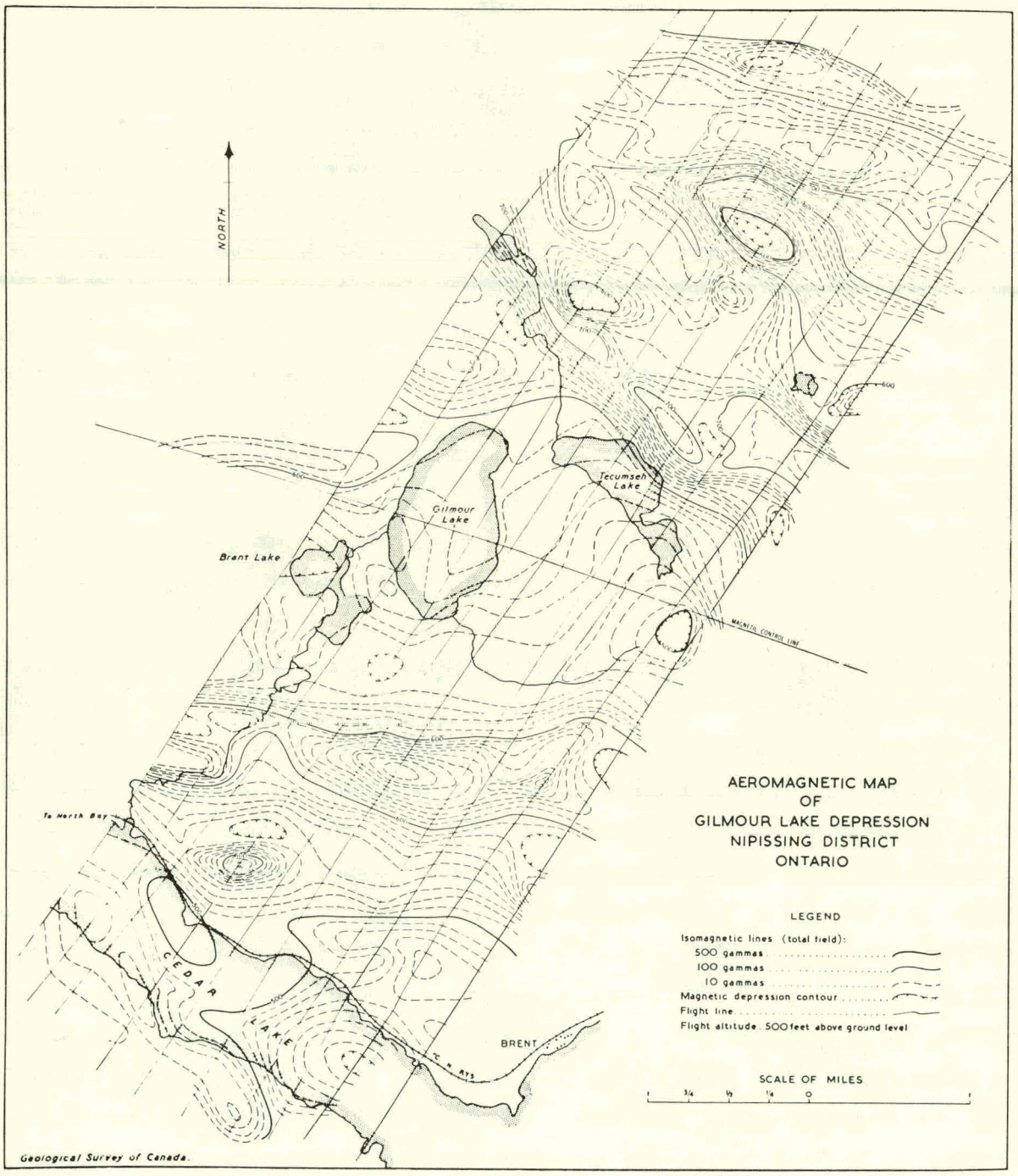

MUL-14649

Fig. 12. Aeromagnetic map of Brent crater area by Geological Survey of Canada.

associated with granitic rocks in other parts of the Shield. Here the intensities are on the average about 150 gammas higher than over the central part of the crater, with local disturbances giving rise to steep gradients as much as 600 gammas per mile.

Several factors, all of which are consistent with the hypothesis of an explosive origin, may be mentioned to satisfactorily explain the low magnetic relief associated with the central part of the crater. First of all, the aeromagnetic data are influenced by variations in the distance between the magnetic source and the magnetometer. These results are typical for deep sedimentation, the widely spaced contours and low gradients being an indication of a considerable depth to the boundaries between rocks of contrasting magnetic properties. While the thickness of sedimentary material now filling the crater would contribute considerably to the decrease in magnetic intensity because of its lower and more uniform susceptibility compared to the surrounding gneisses, the great volume of fragmental rock and breccia underlying the sediments most likely is responsible for the major effect. Impact and explosion would disrupt the systematic alignment of the magnetic materials within the gneisses to form a random distribution of magnetic poles within the brecciated zone, thus resulting in a general decrease in the magnetic field intensity.

Diamond Drilling Program. The gravity, seismic, and magnetic observations were all in remarkably satisfactory agreement in indicating the presence of a crater of considerable depth filled with material of lower density, lower seismic velocity, and lower magnetic susceptibility than the surrounding granitic rocks, all consistent with the meteoritic hypothesis of an explosive origin. A drilling program was therefore undertaken to determine the shape and depth of the crater and to examine the nature and extent of the brecciated rock which the surface geology and geophysical results suggested might underlie the Paleozoic sediments.

The first phase of the drilling program was carried out during the winter of 1955 and two holes were put down, hole 1-55 midway along the eastern shore of Gilmour Lake and hole 2-55 near the southern end of the lake and about

250 feet north of the contact between the granitic and sedimentary rocks. Unfortunately, too light equipment was used. Because of the difficulties encountered (due largely to lack of proper casing), it was found necessary to abandon hole 1-55 before penetrating to the bottom of the sediments. Although this hole did not penetrate to the breccia forming the actual crater surface, it was pushed to 570 feet indicating the presence of a relatively thick layer of sediments in the crater. Hole 2-55 near the south edge of the crater went to 190 feet, encountering 80 feet of overburden, 55 feet of sediments, and 52 feet of rock breccia, specimens of which are illustrated in Fig. 13. Although these two holes provided less information than had been hoped, the results obtained from them were in general agreement with predictions made from geological and geophysical studies and gave support to the hypothesis of an impact origin for the feature.

Additional drilling was carried out during the winter of 1959 and again in the late autumn of 1960, the results of which are shown in the diagram of Fig. 14. All of the holes, which follow roughly a diameter of the crater, are plotted on the diagram with numbers indicating the year during which the drilling was done, i.e., 1- and 2-55, 1-59, and 1-, 2-, 3-, 4-, 5-, 6-, 7-60. As has already been mentioned, one of the holes (1-55) failed to penetrate the sediments, but all of the others at least reached the surface of the brecciated zone and the points of contact with the crater surface are indicated by open circles. Also plotted on the diagram are profiles of the Chubb crater and of a hypothetical crater 14,000 feet in diameter for comparison. It would appear from the diagram that the larger crater fits the observations more closely.

With the exception of 2-60 and 7-60 all of the drill holes passed through various thicknesses of sedimentary rock outlining a lens-shaped deposit 850 feet thick at the centre, decreasing to zero near the edge. The irregularities in the present floor of the crater are probably due to the vagaries of glacial erosion and the deposition of glacial drift.

Holes 2-60 and 7-60 were drilled on the sloping sides of the depression outside the crater floor. No sedimentary rock was encountered in either of

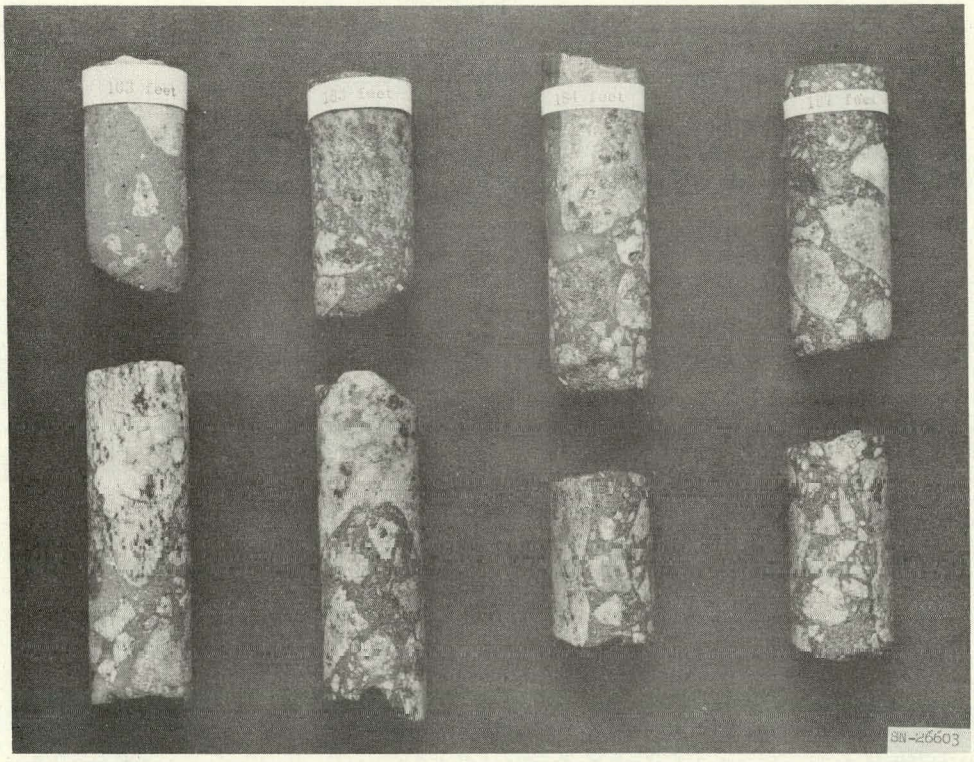

Fig. 13. Rock breccia found in hole 2-55 near the edge of the Brent crater.

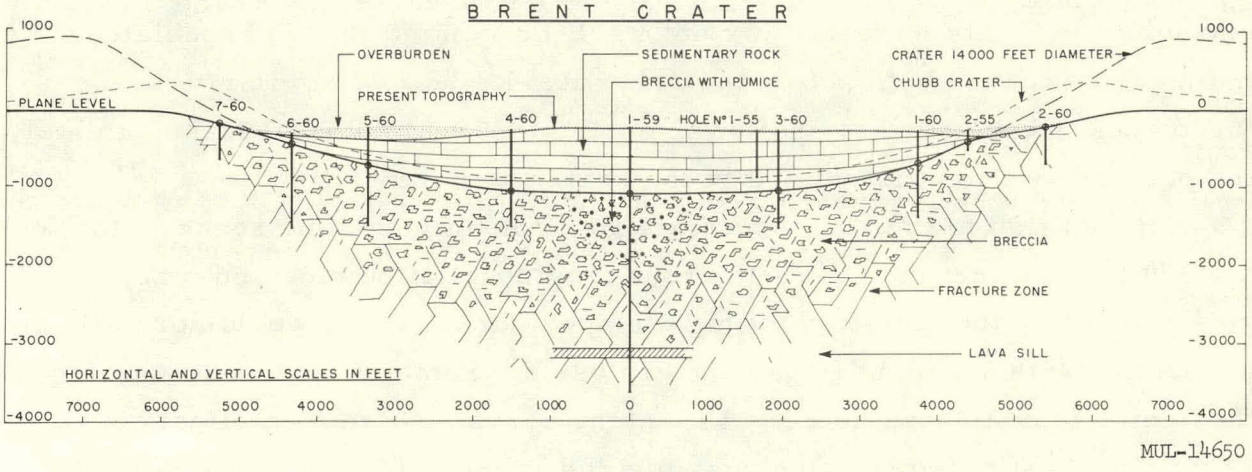

Fig. 14. Profile of the Brent crater derived from diamond drilling results. The holes are roughly on a north-south diameter with north to the left.

these two holes. The cores from these holes, especially 2-60, gave indications of the presence of macrobreccia consisting of very large fragments probably shattered in place.

Hole 1-59 was drilled to a depth of 3500 feet, and studies of the core which have so far been made indicate that this hole passed through the entire crater structure into undisturbed rock beneath the centre. The first 850 feet consisted of sedimentary rocks, mainly limestone and sandstone of Ordovician and possibly Cambrian age. At 850 feet, rock breccia was encountered consisting of a variety of fragments representing different kinds of gneiss and other rocks, some of which have not yet been identified. This breccia, consisting of small to medium fragments, continued for a few hundred feet; but as the hole went to greater depths, larger and larger fragments were encountered with sometimes short stretches of finer breccia in between. This type of material, which may be designated as macrobreccia, continued to a depth of about 3300 feet where the drill penetrated what appeared to be undisturbed gneiss. It is of course quite possible and even probable that large scale fracturing continued beyond this point, but its presence would be difficult to establish on the basis of a single hole because of the cracks and fractures commonly found in all rocks.

At 2700 feet, what is apparently a lava sill nearly 200 feet thick was encountered. This material was not itself brecciated though brecciated material was found both above and below it. Its lack of similarity to the fused rock encountered at shallower depths (850 to 1600 feet) makes unlikely the possibility that it is related to the crater structure.

In addition to the rock breccia already mentioned, the rocks in the levels 850 to 1600 feet included numerous fragments of pumice and other fused rock indicating the existence of high temperature such as would normally be associated with a violent impact or explosion. Some of the cores showing these effects are shown in Fig. 15. Many cores also showed effects suggestive of plastic deformation possibly due to the retention of the heat of the impact as a consequence of the slowness of cooling at depths of several hundred feet beneath the surface.

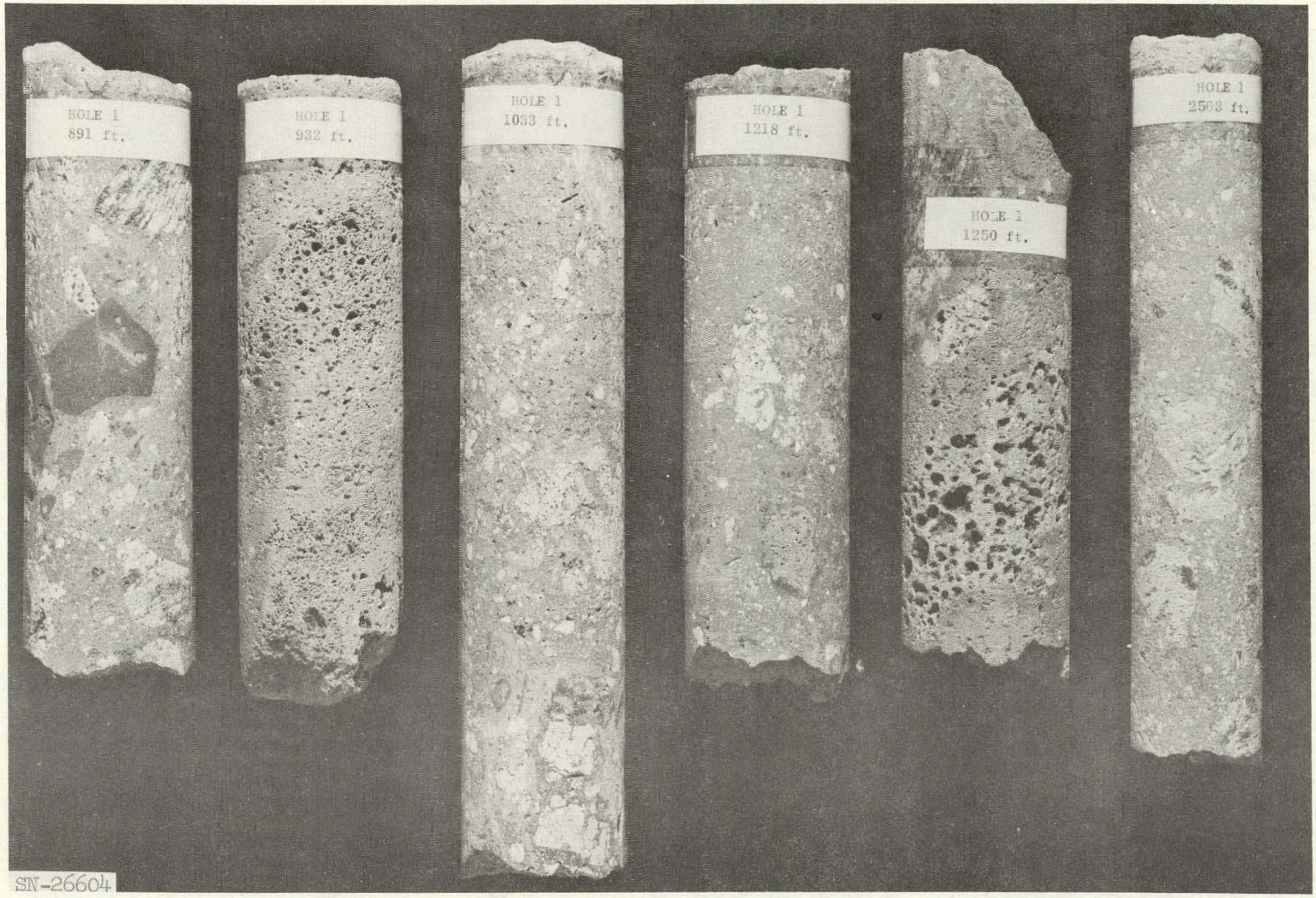

Fig. 15. Drill cores from the centre of the Brent crater. Several of the cores contain pumice, attributed to the heat generated by meteorite impact. The dark-coloured fragment in the core at 891 feet is highly magnetic.

An interesting feature of many of the cores in the upper part of the breccia zone was the presence of numerous irregularly shaped fragments of dark-coloured material that is highly magnetic, the magnetism being due to the presence of magnetite and not nickel. So far it has not been possible to investigate the cores in detail and the full significance of the magnetic material must await further study.

Of the other holes (1-60, 3-60, 4-60, 5-60, and 6-60) drilled at various locations on the crater floor as indicated in Fig. 12, all passed through various thicknesses of limestone and penetrated for several hundred feet into the breccia zone. The breccia in general was similar to that in hole 1-59 but for the most part the fragments were larger in the holes near the crater circumference. An important difference between these holes and hole 1-59 was the apparent absence of pumice or other evidence of high temperature. While a more detailed search might well make it necessary to qualify this conclusion, it is clear that the central hole is the only one where heating effects are at all conspicuous. None of the holes, except 1-59, penetrated completely through the brecciated zone and no indication of bedding planes was seen anywhere in the breccia. Up to the present, specimens of magnetic material have been found only in the central hole.

THE DEEP BAY CRATER

Following the discovery of the New Quebec crater by Meen in 1950, the Brent crater by Millman in 1951, and the Holleford crater (Beals, Ferguson, and Landau, 1956), attention was drawn (Innes, 1957) to a large circular water-filled depression known as Deep Bay, which forms the southeastern part of Reindeer Lake in northern Saskatchewan. Two separate field investigations of the feature have been completed, the first in August of 1956 during which geological and geophysical observations were carried out, and the second in the winter of 1958 during which additional gravity information was obtained by making gravimeter observations over the bay on the ice. A complete account of the results of these investigations is in preparation (Innes, Pearson, and Geuer, 1961) and will appear elsewhere.

Deep Bay, longitude 103° 00'W, 56° 24'N, elevation 1106 feet above sea level, is located in the Canadian Shield midway between the great sedimentary basin of the central plains to the southwest and Hudson Bay to the northeast. Although it lies on the principal route followed by canoes in summer and tractor trains on the ice in winter in freighting supplies to northern outposts, Deep Bay can be reached most easily by aircraft flights from the small settlement at Lac la Ronge, 120 miles to the south, and presently the northern limit of the highway system of Saskatchewan.

Topographically, the Reindeer Lake area is similar to many other places in the Canadian Shield. Flat-topped rock exposures form hills and ridges above the general level of the lakes with a maximum relief of about 150 feet. Travelling by canoe, although one might wonder at the wide expanse of Deep Bay (nearly 6-1/4 miles in diameter), the complete absence of islands, and the scarcity of sheltered beaches along its margin, one would be unlikely to notice the near-perfect circularity of the bay. From an aircraft flying at considerable height these unique features are immediately apparent and stand out in marked contrast to the main body of Reindeer Lake, with its numerous islands and irregular bays and shorelines which conform in a general way to structural trends of the underlying Precambrian rocks. An aerial mosaic of Deep Bay is shown in Fig. 16.

Although deeply eroded by glacial action, much of the bedrock portion of the crater's rim remains and stands on the average some 270 feet above the waters in the bay. To the northeast and east the rim is best preserved. It stands 400 feet or more above the lake and retains in several places steep inner slopes. The original rim diameter is estimated to have been about 40,000 feet (7.57 miles), about a mile less than its present 8-1/2-mile diameter as marked by the height of land surrounding the bay. As with the Brent crater the drainage pattern of the Deep Bay area is both concentric and radial; with the exception of three broad channels into Reindeer Lake along the northern side, the drainage is restricted to short intermittent streams no greater than 2 miles in length.

The rocks, which are well exposed in the area, are all granitic in character and are Precambrian in age. Dr. W. J. Pearson, of the Department

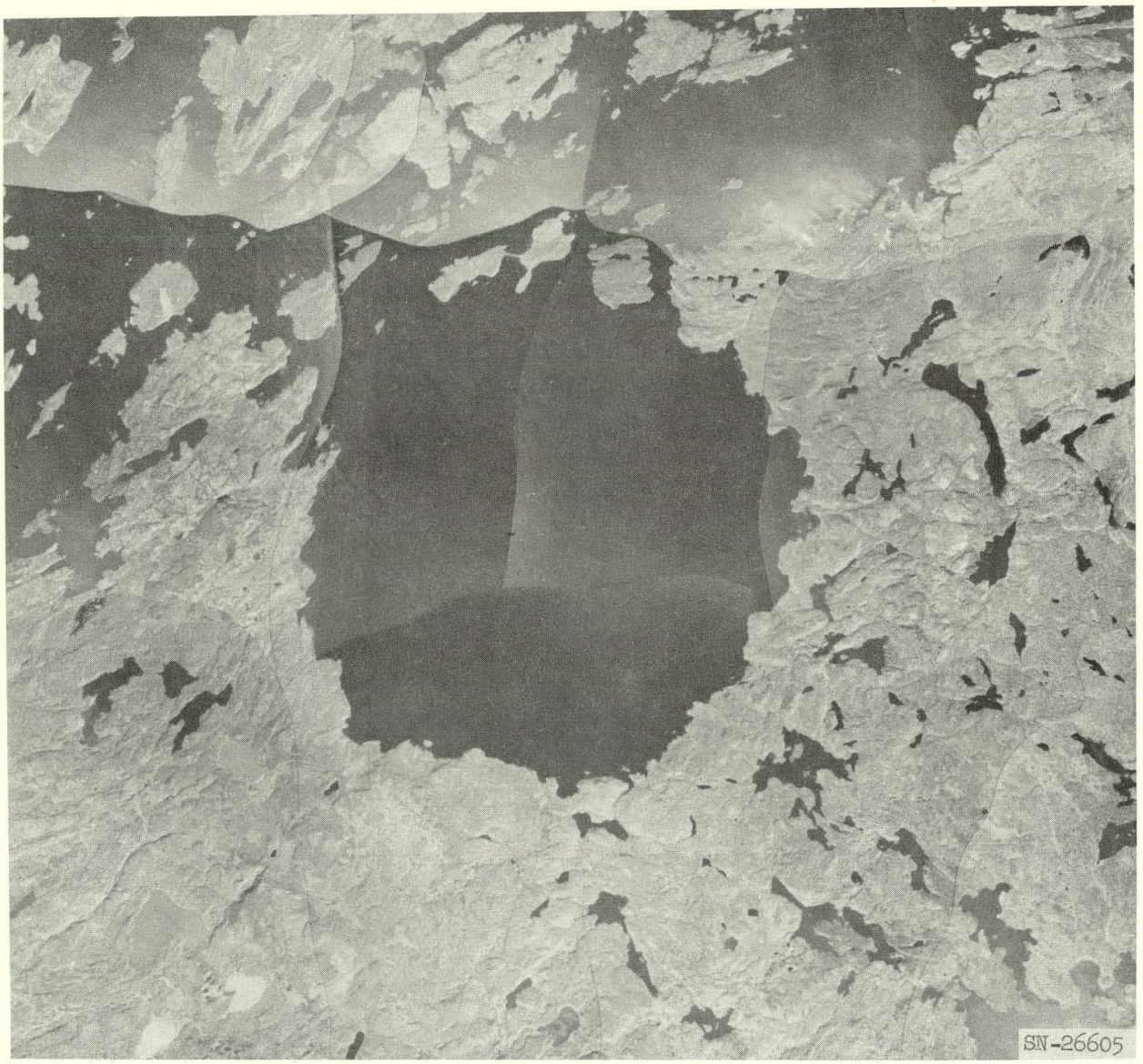

Fig. 16. Aerial mosaic of Deep Bay crater. Diameter 40,000 feet, depth 700 ft.

of Mineral Resources of the Province of Saskatchewan, has examined the rocks along the shore line and on the rim and classifies them according to the varying amounts of granitic material they contain. Three main types have been recognized as follows: a unit of injection gneisses and migmatites underlying the southern part of the area, a central unit of metamorphic gneisses of sedimentary origin, and a group of intrusive granitic rocks, chiefly granodiorites and pegmatites which occur along the northwestern and northern sides of the bay. Careful examination of the structural relations between these rock types in no way suggests a geological origin for Deep Bay. The general trend of the three units is northeasterly and approximately the same on both sides of the crater, while there is evidence that the strikes of many local structures are normal to, and are terminated at, the margin of the bay.

That Deep Bay is the result of a tremendous explosion is clearly indicated by the intense fracturing and shattering of the granitic rocks which is most pronounced in the vicinity of the shore. Large scale fracture and fault zones of various widths, now partially obscured by glacial action and deposition, cut radially and obliquely across the rim and persist for several miles from the margin of the bay. A system of concentric fractures is also well developed particularly in the area less than 3 miles from the shore line. Perhaps the most prominent feature, which may be the expression of such fracturing, is a narrow arcuate lake 3 miles in length located about 3 miles to the east of the crater. There is some evidence from the drainage pattern and dissected topography that this is the small visible part of a circular depressed zone which circumscribes the whole crater and has a diameter of about 12 miles. Within this area lie the rocks which form the now deeply eroded rim of the crater; they give the general appearance of having been shattered into huge blocks by a process involving little or no horizontal movement.

Also strengthening the meteoritic hypothesis of origin is the great depth of Deep Bay in comparison with that of Reindeer Lake, which seldom exceeds 150 feet. Numerous depth recordings show the present floor of the crater lies at an average depth of about 500 feet with an extensive depression along the

eastern margin of the bay that has a maximum depth of 720 feet. Although outcrops of sedimentary rocks are lacking, boulders and pieces of shale, identified as Mesozoic in age from fossil evidence, were discovered on a small beach near the southern end of Deep Bay. The source of this shale is uncertain, but since there are no known occurrences of this rock within hundreds of miles it is believed to have been carried by ice movement from a lake deposit on the floor of the crater. If so, and considering that 2100 feet is the depth predicted below the original plain for a crater this size, we may expect to find at least 1400 feet of sedimentary strata underlying the waters of Deep Bay.

Geophysical Results. So far, gravity and magnetic studies are the only geophysical investigations that have been carried out in the Deep Bay area. As at Brent and Holleford, the gravitational field associated with the Deep Bay crater is negative (Fig. 17) with contours of equal anomaly forming a circular pattern concentric with the feature. The amplitude of the gravity variation is, however, much larger. It reaches a minimum value, after corrections for terrain and water depths, of about 20 milligals near the centre of the bay. The 1400 feet of sedimentary material would, depending upon its density, account for about 3 to 6 milligals of the total anomaly, leaving the remainder of the anomaly to be explained by the underlying fragmental products of explosion. If the mean density of the latter is similar to the density of the breccia obtained from drill core samples at Brent (which seems reasonable, as the country rock surrounding both craters is granitic gneiss of similar composition and density), it follows that the zone of deformation under the original floor of Deep Bay crater may extend to depths as great as 10,000 feet.

An aeromagnetic map of the Deep Bay area has been compiled by the Geological Survey of Canada, giving anomalies in the total magnetic intensity. Because of the rugged topography the observations were carried out at a flight altitude of 1000 feet above general ground level. Although this is twice the height flown during the Brent aeromagnetic survey, the results for Deep Bay are equally definitive and are in qualitative agreement with the results obtained at the other craters.

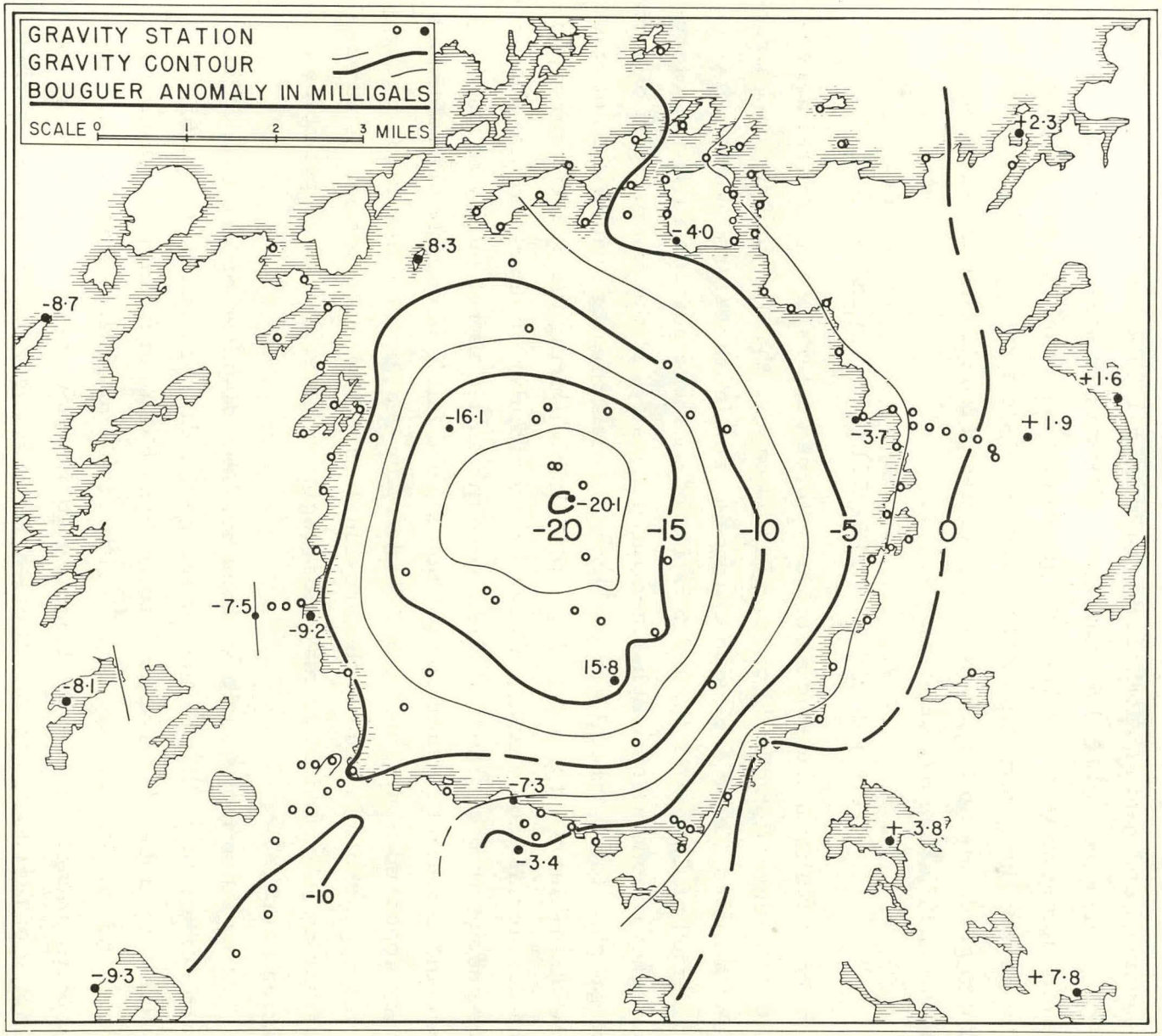

MUL-14651

Fig. 17. Gravity contours, Deep Bay crater.

As before, the most outstanding feature of the magnetic map is the small and uniform variation in intensity over the central portion of the crater when compared with the anomalies produced by the surrounding country rocks. As observed at Brent and Holleford, the regional field surrounding the crater is highly irregular. Local disturbances give rise to steep gradients, and the anomaly contours tend to follow the prominent structural trends of the gneisses. Over the bay, however, the total variation does not exceed 190 gammas with uniform gradients no larger than 50 gammas per mile, indicative of the great depth to undisturbed basement rocks.

OTHER POSSIBLE METEORITE CRATERS

The results of the studies of these three craters are in general agreement with suggestions made earlier in this paper, that the underground structure of a meteorite or explosion crater can retain its identity over a very long period of time after the obliteration of its more obvious surface features. This general conclusion emphasized the necessity, in the examination of aerial photographs, for a careful study of every circular feature which did not have some other clear-cut and definite explanation. During the present survey of Canadian aerial photographs, a great many circular or near-circular features were encountered but most of them were discarded as not justifying the expense and labour of further study. Some were fairly obviously old volcanoes. Others appeared to be sink holes, while many shallow circular lakes in boggy ground appeared to be due to the erosional effects of wave action. A number of rather small round lakes may most logically be explained as pot holes or solution cavities.

After these more obvious cases had been disposed of (and it is by no means certain that all rejections were justified) there still remained a substantial number of circular features which did not fit into any standard pattern and for which it appeared legitimate to consider the possibility of a meteorite impact origin. Preliminary studies have been made on the ground for some of these objects but others have been observed only in aerial photographs. Such information about them as is available is summarized as follows:

1. The Franktown crater: long. 76° 03.5' W, lat. 45° 03'N, about 40 miles southwest of Ottawa. This feature, about 3/4 mile in diameter, occurs in Ordovician limestone and may be an example of type 3, where the buried crater rim, or what is left of it, still influences the attitude of the sediments. The depression is approximately 25 feet deep and there is a flat area of bog and farm land in the centre which was probably once a lake. The outlines are less clear than at Holleford and in all probability only a diamond drilling program (not yet attempted) would suffice to give a clear indication of the origin of this feature.

2. Clearwater Lakes: long. 74° 20' W, lat. 56° 10' N. These lakes consist of two roughly circular bodies of water separated by a screen of islands. The larger of the two components is 20 miles in diameter while the smaller is 16 miles across. These two circular lakes stand out conspicuously in a region dominated by elongated bodies of water which presumably owe their character to the effects of glacial erosion. An interesting feature of the larger lake is an approximately circular ring of islands, 10 miles in diameter, concentric with the circular lake itself. Some of the islands are of considerable height which, combined with their circular arrangement, makes them a unique and impressive landscape feature. Geological studies of the islands indicate that they are composed of lava. In default of any other explanation it is thus possible that these two lakes constitute an example of type 8 and were formed by the impact of twin meteorites, the larger impact resulting in a lava extrusion which took the form of a ring dike. In this connection it is interesting to record that there are several twin craters on the moon roughly corresponding in size to the Clearwater Lakes. Also on the moon there is at least one crater which has a ring dike within it, concentric with the crater as a whole. This crater is 9 miles in diameter; the diameter of its inner ring is 4.5 miles. Apart from size, its similarity to the Clearwater Lake feature is quite striking.

3. The Manicouagan Lake feature: long. 68° 37', lat. 51° 28'. An approximately circular area, enclosed by Lakes Manicouagan and Mushalagan,

is a conspicuous aspect of the map of Quebec and many geologists and other students of this region have speculated as to its origin. The circle is approximately 40 miles in diameter and a mountain approximately 3000 feet high rises in the centre. Geological studies of the area (Rose, 1955) indicate that the central mountain is an igneous instrusion and that otherwise a large part of the area is covered by flat-lying lavas of somewhat different character. The possibility has been considered that this may represent an example of type 8 where a large crater has had its rim removed by erosion leaving the central mountain plus a lava floor. Some geophysical studies have been made in the region but the size of the area and the complicated nature of its geology has so far prevented any definite conclusion.

4. Stratified circular features in northeastern Quebec and Labrador. Aerial photographs in this general area have revealed five circular features ranging from 2-1/2 to 7 miles in diameter which exhibit a stratified appearance somewhat similar to that shown by the Holleford crater. The stratified structures in some cases stand up somewhat above the surrounding plain. It is considered possible that they represent examples of type 5 where an ancient crater has been filled with sediments which have subsequently been consolidated to the extent that they retained their identity when the surrounding rock suffered severe erosion. The locations and diameters of these features are given in Table I.

TABLE I

Stratified Circular Features

General area	Longitude	Latitude	Diameter (miles)
Mecatina Crater*	59° 22'	50° 50'	2
Lake Michikamau	64° 27'	54° 34'	3-1/2
Menihek Lake	66° 40'	53° 42'	3
Menihek Lake	67° 10'	54° 19'	2-1/2
Sault au Cochons	70° 05'	49° 17'	7

*Illustrated in Fig. 18.

Fig. 18. Aerial view of Mecatina crater. Diameter of the crater lake 4000 ft, depth 200 ft. The circular strata observed in the photograph may be ancient sediments transformed into granite gneiss.

5. Circular structure, Carswell Lake area, Saskatchewan: long. 109° 30', lat. 58° 27'. During the geological field season of 1957, Dr. W. F. Fahrig of the Geological Survey of Canada, working in northern Saskatchewan, discovered a feature approximately 18 miles in diameter bounded on its circumference by concentric circles of rock outcrops consisting of sandstone and dolomite sediments. These sediments, considered to be of Precambrian age, were deformed and tilted in a manner somewhat reminiscent of those on the rim of the Barringer crater designated as type 6. According to a sectional diagram provided by Dr. Fahrig, the strata give the impression of having been compressed along a radius and tilted more than 90° away from the centre of the feature. Since this is the kind of deformation expected for a meteorite crater formed in sedimentary rock, this feature is considered as having a possible meteorite origin. It is hoped to carry out some geophysical tests of this hypothesis during the 1961 field season. Although the writers consider that the available evidence is best satisfied by the meteorite impact hypothesis, it should be emphasized that there are other explanations which Dr. Fahrig, the discoverer, regards as more probable.

6. The Nastapoka Islands arc of Hudson Bay: long. 80° 02', lat. 57° 40'. These co-ordinates represent the centre of curvature of an almost perfectly circular arc on the east coast of Hudson Bay, approximately 275 miles in diameter. This is a conspicuous feature even on a world map and many scientists and others have made the suggestion that it might have been due to the impact of a giant meteorite.

On a moderately large scale map one sees that over most of its length the arc is characterized by a screen of offshore islands of which the most important are the Nastapoka Islands, a chain over 100 miles long of average latitude 57°. Geological studies of the islands (Bell, 1877-78; Low, 1900; Kranck, 1950) have indicated that they are composed of Precambrian sediments, which sometimes extend to the mainland. Throughout the length of the arc the sediments dip radially inward toward the centre at angles of a few degrees. Studies of aerial photographs have confirmed the radial direction of dip over the entire length of the arc, and have also confirmed that in

many places the sediments extend to the mainland where it is often possible to see the contact between the sediments and the granitic rock of which the mainland is largely composed. When observed from a low-flying aircraft, the seaward dip of the sediments is a very striking phenomenon which, considered in connection with the above geological and photographic evidence, suggests the existence of a deep circular basin in which great depths of sediments may well have been deposited. In addition to the offshore islands already mentioned, there are numerous other islands nearer the centre of the circle of which the most important are the Belcher Islands south and east of the centre. Where geological information is available the islands are composed of Precambrian sediments often capped or interbedded with lava flows. It appears that, in contrast to observations on the border of the arc, the sediments on the more central islands are in general either flat-lying or folded and do not correspond in dip to those on the arc (Jackson, G. D., private communication). In addition to the evidence for volcanism on the islands, lava flows are also a feature of certain areas of the mainland near the coastal arc.

On the landward side of the arc, hills normally rise to a height of several hundred feet; in places near Richmond Gulf the elevation is 1500 feet above sea level, and this is suggestive of an ancient and eroded crater rim. The incompleteness of the circle on the west is of course a handicap to interpretation and at present there is no evidence of a continuation, under water, of the visible features of the arc. It may be remarked, however, that in view of the very great age of the feature (600 to 1000 million years) it would indeed be surprising if it had remained completely intact over such an immense period of time. If this is truly a fossil meteorite crater we are fortunate in having such a substantial proportion of it remaining for study.

There is a rather striking parallel between this feature and the well-known Mare Crisium on the moon. Mare Crisium is an oval to circular feature of average diameter 318 miles and depth 8000 feet with what is believed to be a lava floor. Although measures of altitude are not available for the rim it is clear that the feature is surrounded by hills which rise to a height of

several thousand feet. When the phase of the moon is such that the line between sunlight and darkness bisects Mare Crisium, the resemblance to the Hudson Bay arc is quite striking. Unfortunately the size of the Hudson Bay feature and its great age are formidable obstacles to investigation. It would appear logical to look for a lava floor under the sediments, but their assumed great depth (3600 ft near the coast and presumably much greater farther out) would make drilling very expensive. It is also quite probable that consolidation and alteration of the sediments would make it difficult by geophysical methods to establish the existence of a boundary with the basement. In spite of these difficulties it is hoped to undertake gravity, magnetic, and seismic work in the area as soon as facilities are available for making measurements of this kind at sea.

7. Gulf of St. Lawrence arc: long. 63° 03', lat. 47° 06'. A configuration somewhat similar to the Hudson Bay arc though smaller (180 miles in diameter) is outlined by parts of the coastlines of Nova Scotia and New Brunswick in the Gulf of St. Lawrence. Prince Edward Island and the Magdalen Islands lie within the circle, and the somewhat roughly outlined arc subtends a sector of over 180°. Seismic observations within the circle have indicated the presence of sediments to a depth of approximately 20,000 ft. This result is not unfavourable to the meteoritic hypothesis, but much more extended observations will be required before it will be possible to reach any definite conclusion.

8. In addition to the circular features described above there are a number of circular lakes or bays scattered throughout Canada which for one reason or another (e.g., excessive depth, evidence of shattering around the shoreline, or simply unexplained incongruity with their surroundings) are listed as possibilities in the continuing search for old craters. These include Lac Couture, long. 75° 20', lat. 60° 08', diameter 10 miles; West Hawk Lake, long. 95° 12', lat. 49° 46', diameter 3 miles; Keeley Lake, long. 108° 08', lat. 54° 54', diameter 8 miles; and Ungava Bay, long. 67° 20', lat. 60° 00', diameter 150 miles.

We list these features and the ones described under 1 to 7 above only as interesting possibilities worthy of further investigation. They cannot yet be presented as probable fossil craters to be included in the statistics of earthly as compared to lunar features. It will no doubt be many years before the true nature of these objects is fully understood. In the meantime it is hoped that publicizing the locations will encourage the necessary investigations by geologists, geophysicists, and others interested in meteoritic phenomena.*

---

*Outside of Canada, a geographical feature of particular interest in this connection is Lonar Lake in India (long. 76° 51' E, lat. 19° 59' N), a circular feature slightly more than 1 mile in diameter and 400 ft deep. Geologists who have examined it have attributed it to a volcanic explosion, but specific evidence for volcanism appears to be lacking. Its circular form and raised rim suggest a meteorite impact origin and it may well be due to this cause. (See Newbold, 1846-48; Blandford, 1870; Medlicott and Blandford, 1879.)

REFERENCES

Bancroft, A. M., 1960, "Gravity Anomalies Over a Buried Step," J. Geophys. Research 65, 1630. (Reprinted as Contrib. Dominion Observatory 3, No. 27.)

Beals, C. S., 1960, "A Probable Meteorite Crater of Precambrian Age at Holleford, Ont.," Publ. Dominion Observatory 24, 117.

Beals C. S., Ferguson, G. M., and Landau, A., 1956, "Analogies Between Lunar and Terrestrial Topography," J. Roy. Astron. Soc. Can. 50, 203.

Beals, C. S., Innes, M. J. S., and Rottenberg, J. A., 1960, "The Search for Fossil Meteorite Craters," Current Sci. (India) 29, 205, 249; Contrib. Dominion Observatory 4, No. 4, 1960.

Bell, R., 1877-78, "Report on East Coast of Hudson Bay," Geol. Survey Canada Report of Progress, No. 128.

Blandford, W. T., 1870, Records Geol. Survey India, 1, 63.

Frarey, M. J., 1955 (unpublished). "Report on Field Study at Holleford, Ont."

Gold, T., 1956, "The Lunar Surface," Monthly Notices Roy. Astron. Soc. 115, 585.

Innes, M. J. S., 1957, "A Possible Meteorite Crater at Deep Bay, Sask.," J. Roy. Astron. Soc. Can. 51, 235.

Innes, M. J. S., Pearson, W. J., and Geuer, J., 1961, "The Deep Bay Crater," Publ. Dominion Observatory (in preparation).

Kranck, E. H., 1950, "Geology of the E. Coast of Hudson Bay and James Bay," Acta Geographica 11, No. 2, 1.

Low, A. P., 1900, "Report on East Coast of Hudson Bay," Geol. Survey Canada Report D.

Medlicott, H. B. and Blandford, W. T., 1870, "A Manual of the Geology of India," 63.

Meen, V. B., 1961, "Chubb Crater, Ungava, Quebec," J. Roy. Astron. Soc. Can. 44, 169.

Meen, V. B., 1957, "Chubb Crater, A. Meteor Crater," J. Roy. Astron. Soc. Can. 51, 137.

Millman, P. M., Clark, J. F., Innes, M. J. S., Liberty, B., and Willmore, P. L., 1960, "The Brent Crater," Publ. Dominion Observatory 24, 1.

Newbold, 1846-48, Journal of the Royal Asiatic Society, 9.

Rose, E. R., 1955, "Manicouagan Lake, Mushalagan Lake Area, Quebec," Paper Geol. Survey Canada 55, 2.

Shoemaker, E. M., 1960, "Impact Mechanics at Meteor Crater, Arizona," in The Solar System (Vol. 4, Planets and Comets, Part 2), Kuiper, G. P., Ed., Univ. Chicago Press, Chicago, Illinois (in press); also U. S. Geol. Survey open-file report, Dec. 28, 1959, 55 p.

Shoemaker, E. M., 1960, "Penetration Mechanics of High Velocity Meteorites, Illustrated by Meteor Crater, Arizona," in Structure of the Earth's Crust and Deformation of Rocks, Copenhagen, 1960, Part 18, p. 418 (reprinted from Report of the International Geological Congress, 21st Session, Norden, 1960).

Paper D

INVESTIGATIONS AT THE ODESSA METEOR CRATERS

Glen L. Evans

Midland, Texas

ABSTRACT

The Odessa craters were formed by impact of a meteoritic shower during late Pleistocene time. The main crater, 550 feet in diameter, was nearly filled by post-impact deposits, and at least four associated smaller craters were completely filled.

Extensive excavations and test drilling resulted in discovery of the previously unknown smaller craters, and in the accumulation of a large body of detailed information concerning the dimensions and characteristics of the several craters.

Maps of the main crater and a smaller, 70-foot-diameter crater have been drawn within close limits of accuracy. These maps, along with other illustrations and a brief discussion of the history of investigations, geology, and the more interesting crater features, are presented in this paper.

* * *

The Odessa craters were formed simultaneously by an ancient meteoritic shower (see Fig. 1 for distribution of recovered meteorites). They consist of the main crater, which is 550 feet in average rim diameter and about 100 feet in maximum depth; crater No. 2, which is 70 feet in diameter and 17 feet in depth; and three smaller but poorly preserved craters from 6 to 10 feet in depth. These craters are located 10 miles southwest of the city of Odessa in Ector County, Texas, in the extreme southwestern part of the Llano Estacado. The terrain of this area is remarkably flat and is covered by thin surface soils which support a sparse covering of short range grasses and localized patches of shrubbery. The climate is warm and semiarid; average temperature is about 64.2 degrees and average annual rainfall is about 15 inches.

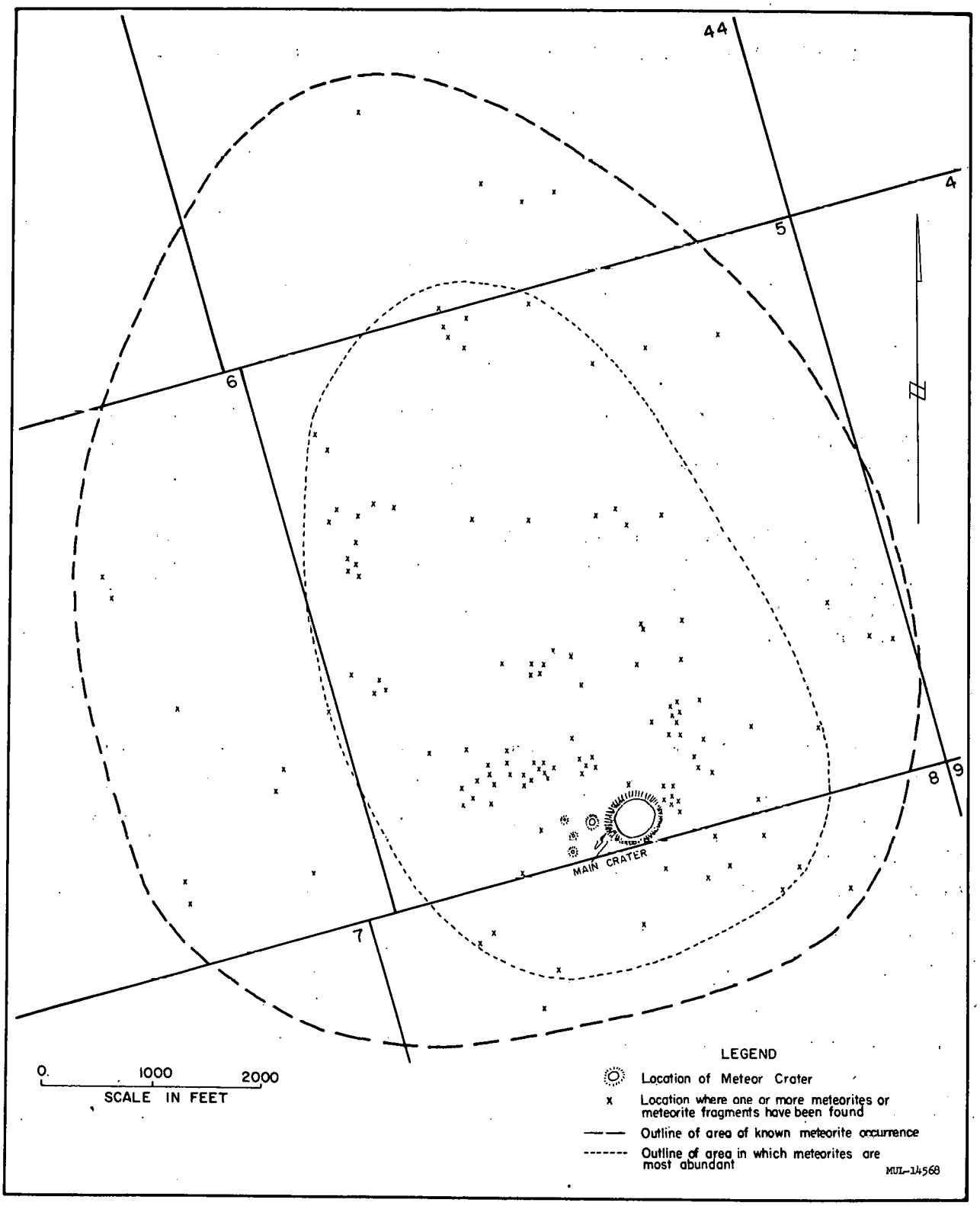

Fig. 1. Map showing distribution of meteorites recovered around the Odessa meteor craters.

In the crater vicinity, rock strata immediately underlying the plains surface consist of compact, calcareous sands and clays having an average thickness of 20 to 25 feet. A zone of hard, platy caliche, irregular in thickness, is typically present in the upper part of this unit. Underlying these near-surface deposits is a section about 50 feet thick consisting of flat-lying marine limestones and shales of Cretaceous age. These strata are in turn underlain by the Cretaceous basement sands which have an average thickness of 125 feet. The basement sands rest upon continental red beds of Triassic age. The main crater penetrates the upper formations and about 30 feet into the Cretaceous basement sands. Crater No. 2 and the smaller craters are developed entirely in the near-surface sands and clays.

It has not been possible to establish with certainty when the first meteorite was found in the crater vicinity. Local reports indicate, however, that several had been found prior to 1920. One of these was sent to G. P. Merrill who published his chemical analysis of it in 1922. The first published reference to any of the craters appeared in 1927 when E. H. Sellards described the surface features of the nearly filled main crater, and listed meteoritic impact as one of its possible modes of origin. Later, in 1929, D. M. Barringer, Jr., also described the main crater and was the first to state unreservedly that it was of meteoritic origin. It is not surprising that the crater was not recognized at an earlier date. It had been so nearly filled by sediments that the central part of its surface depression was only 6 or 7 feet below the level of the surrounding plain, and only its slightly elevated, rock-buttressed rim distinguished it from the familiar shallow blowouts of the area. Smaller associated craters in the immediate vicinity were so completely buried beneath post-impact sediments that their existence was not suspected until they were discovered some years later during the course of exploratory excavations.

The published reports engendered considerable interest in the crater area, and in 1939 a cooperative project was organized for the purpose of thoroughly exploring it. Agencies participating in the project were the Federal Works Progress Administration, the Bureau of Economic Geology of the University

of Texas, and Ector County. The Bureau of Economic Geology was responsible for the technical and scientific aspects of the work, and my participation was as the Bureau's geologist in charge of the project. The project was in operation for two years with an average labor force of 35 men. The work involved mapping, sampling, core drilling and extensive excavations — including sinking of a two-compartment shaft to a depth of 165 feet in the central part of the main crater. (See Fig. 2.) In addition to the other work, a magnetometer survey of the site was conducted for a period of 8 months. This survey was a contribution to the project by Humble Oil and Refining Company. Many of the localized magnetic anomalies developed during this survey were excavated. This resulted in the discovery of numerous meteorites and several previously unknown small meteor craters. Advent of war conditions caused the project to be suspended late in 1941 before all of the original objectives had been completed.

One of the most interesting problems which had not been satisfactorily resolved was whether or not any substantial part of the meteoritic mass which formed the main crater might still be buried at some position beneath the post-impact crater fill. During the excavation of crater No. 2, a small "satellite" crater located immediately west of the main crater, a large concentration of meteorites was found in primary emplacement in the bedrock beneath the post-impact fill. This emphasized the possibility that one or more similar occurrences might be found beneath the main crater, particularly if it had been formed by a compact cluster of masses comparable to the one that had formed crater No. 2 rather than by a single and much larger mass. Several deep trenches in the main crater's peripheral area, a shaft in the central part, and 31 test holes drilled at different locations within the crater had failed to reveal any meteorites in primary position. These explorations, however, were not conclusive, since substantial parts of the area beneath which such a mass might conceivably be resting had not been tested.

In an effort to finally resolve this problem, a new program of drilling was carried on during periods in 1958 and 1960. This work was encouraged and financed by the Barringer family of Philadelphia, owners of Meteor Crater

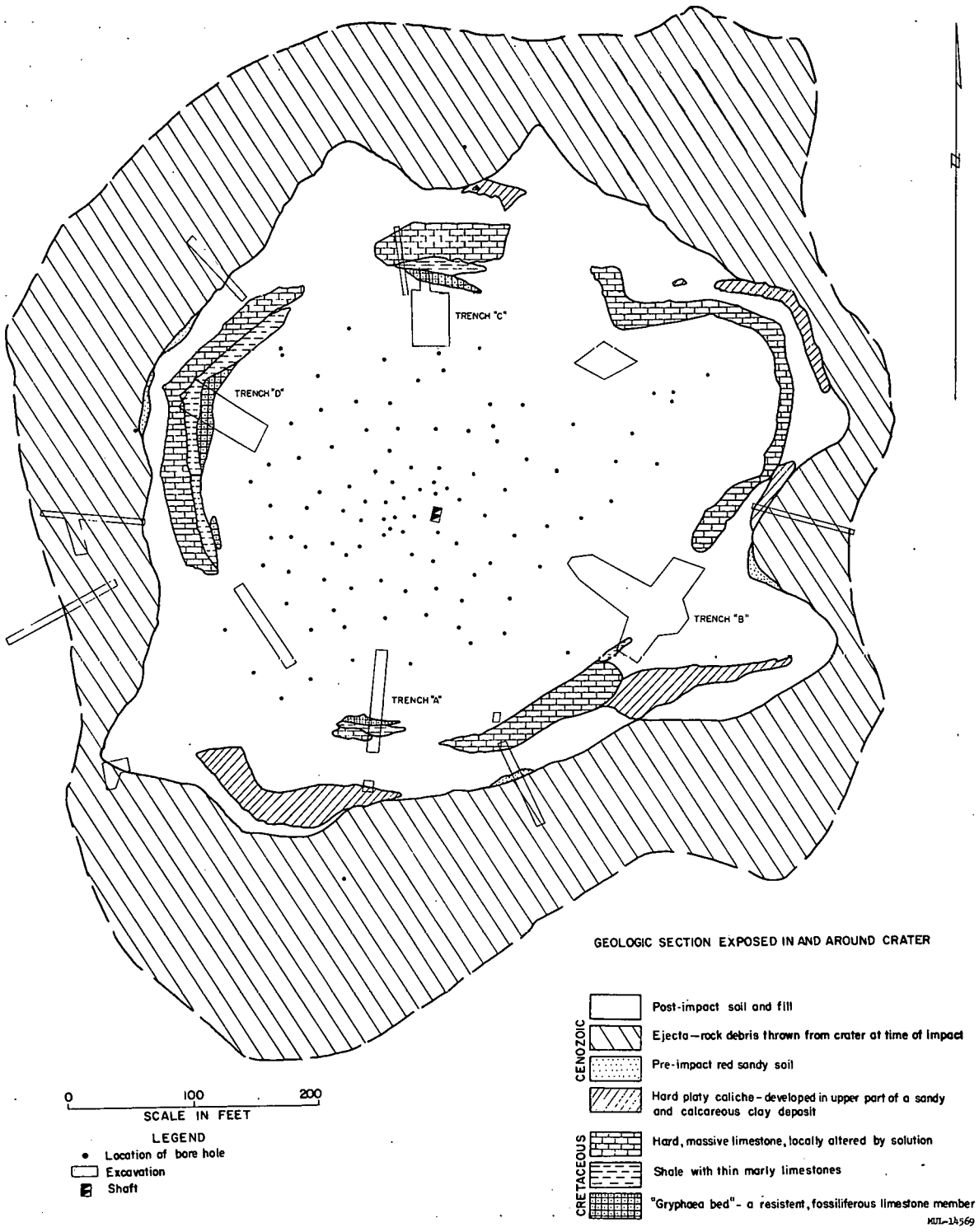

Fig. 2. Map showing exposed rock units in and around the main crater and location of principal exploratory trenches and test holes.

in Arizona. More than 80 closely spaced drill holes were sunk in all parts of the crater not adequately explored previously. With the exception of a few holes abandoned because of caving difficulties, all of the tests were sunk through the fill and well into undisturbed underlying bedrock. As was true with the testing during the 1939-41 period, numerous small oxidized meteorite fragments were found at various levels within the post-impact fill, but they clearly had washed into the crater periodically along with rock debris as a result of erosion of the ejecta rim. But again no meteorites were found in primary position. The results of these explorations lead to the inescapable conclusion that no large intact body of meteorites remains in primary emplacement within or beneath the main crater. The crater-forming mass must have disintegrated on impact, to be mostly or completely expelled along with the ejected rock debris. A structural map of the main crater is shown in Fig. 3.

The meteoritic shower which formed the Odessa craters fell on the High Plains of West Texas during the Wisconsin stage of the Pleistocene, possibly about 25,000 years ago. The meteorites are nickel-iron of the coarse octahedrite class. They are very similar — perhaps significantly similar — to those found at Meteor Crater in Arizona. The shower consisted of many thousands of individual irons which fell irregularly distributed over an area of at least 2 square miles. Very small irons weighing from a few grams to a few ounces each were most numerous and most widely distributed, but individuals weighing from a few pounds to 200 pounds each were fairly common, especially in the central and southern part of the impact area. There were also a few much larger crater-forming masses, and, so far as is now known, these fell closely grouped in the southern end of the impact area.

In addition to the main crater and associated smaller craters previously mentioned, the impact of the meteoritic shower undoubtedly also produced numerous diminutive craters, or pits, formed where individual meteorites buried themselves into the soil. As time passed, erosion on the ridges and accumulations of sheet wash and drifting sands in the lower areas either destroyed or buried all but the main crater — which was itself almost obliterated

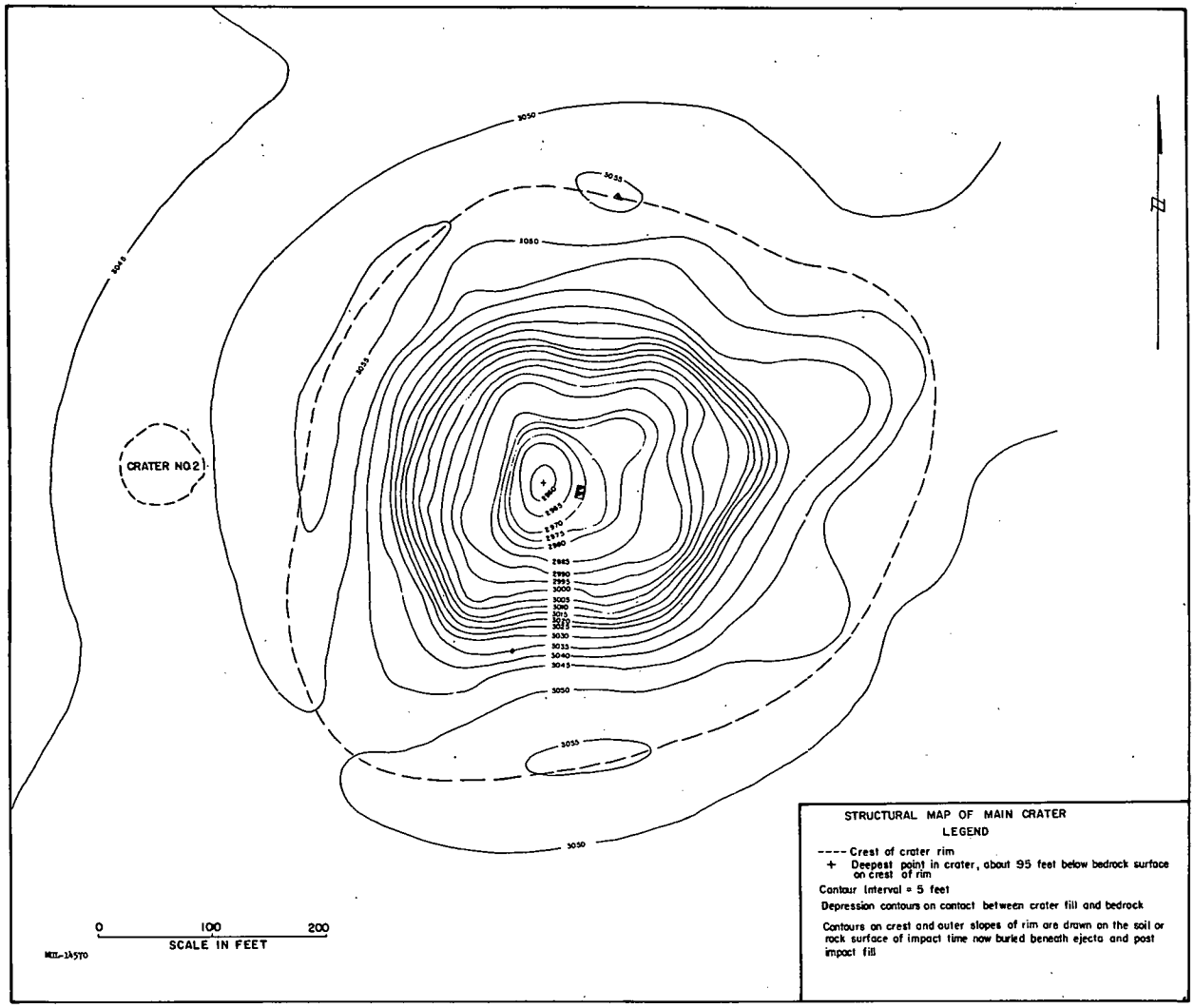

Fig. 3. Structural map of main crater based upon data from excavations and drill holes shown in Fig. 2. It should be noted that the contours in the deepest part of the crater probably fall somewhat above the actual base of the true crater. Cuttings from drill holes in the central area are not sufficiently definitive to show within close limits the contact between the fallback zone and the lithologically similar underlying bedrock. In all cases minimum datum points were used in preparing the contour map.

by filling. This illustrates the ephemeral nature of small impact craters, even when they occur in flat, dry areas where conditions for preservation seem nearly ideal. It also suggests that other old "single" craters such as Wolf Creek Crater in Australia and Meteor Crater in Arizona could also have small satellite craters similarly obliterated by filling.

The Odessa craters provide an unusual opportunity for comparing features of related impact craters of markedly different dimensions. The diameter-to-depth ratio of the main crater is about 5.5 to 1; of crater No. 2, about 4 to1; and of one of the smaller, poorly preserved craters, somewhat less than 2.5 to 1. The mass which produced the main crater evidently suffered extreme fragmentation, and perhaps partial decomposition, and was mostly or entirely expelled with ejected earth materials. The mass which produced crater No. 2 was less severely fragmented and was mostly, but probably not entirely, retained in the bedrock beneath the crater. The meteorites of the smaller crater appear to have suffered less severe fragmentation than those of crater No. 2, and, so far as could be determined, were entirely retained within the crater. This indicates that the degree of fragmentation of the impacting body is one of the factors affecting the shape of impact craters.

In no other feature do the craters differ more markedly than in the structure of their rims. The rim of the main crater is formed by strongly folded, distorted and thrust-faulted strata. The oldest strata involved in the overthrust rim folds have been uplifted as much as 50 feet from their original position, which is equivalent to one-half the depth of the crater. In crater No. 2, however, the rim exhibits only simple and comparatively slight upfolding which involved only the near-surface soil and caliche units. (See Fig. 4 for a structural map of crater No. 2.) In the preserved parts of the smaller crater rims no displacement of bedrock could be detected.

The fallback zone penetrated by the shaft sunk in the central part of the main crater has a maximum thickness of 17 feet. This zone consists predominantly of angular blocks of shattered sandstone, or "rock flour," which were disrupted from the Cretaceous basement sands in the deepest part of the crater, and only a small percentage of the material was derived from strata overlying

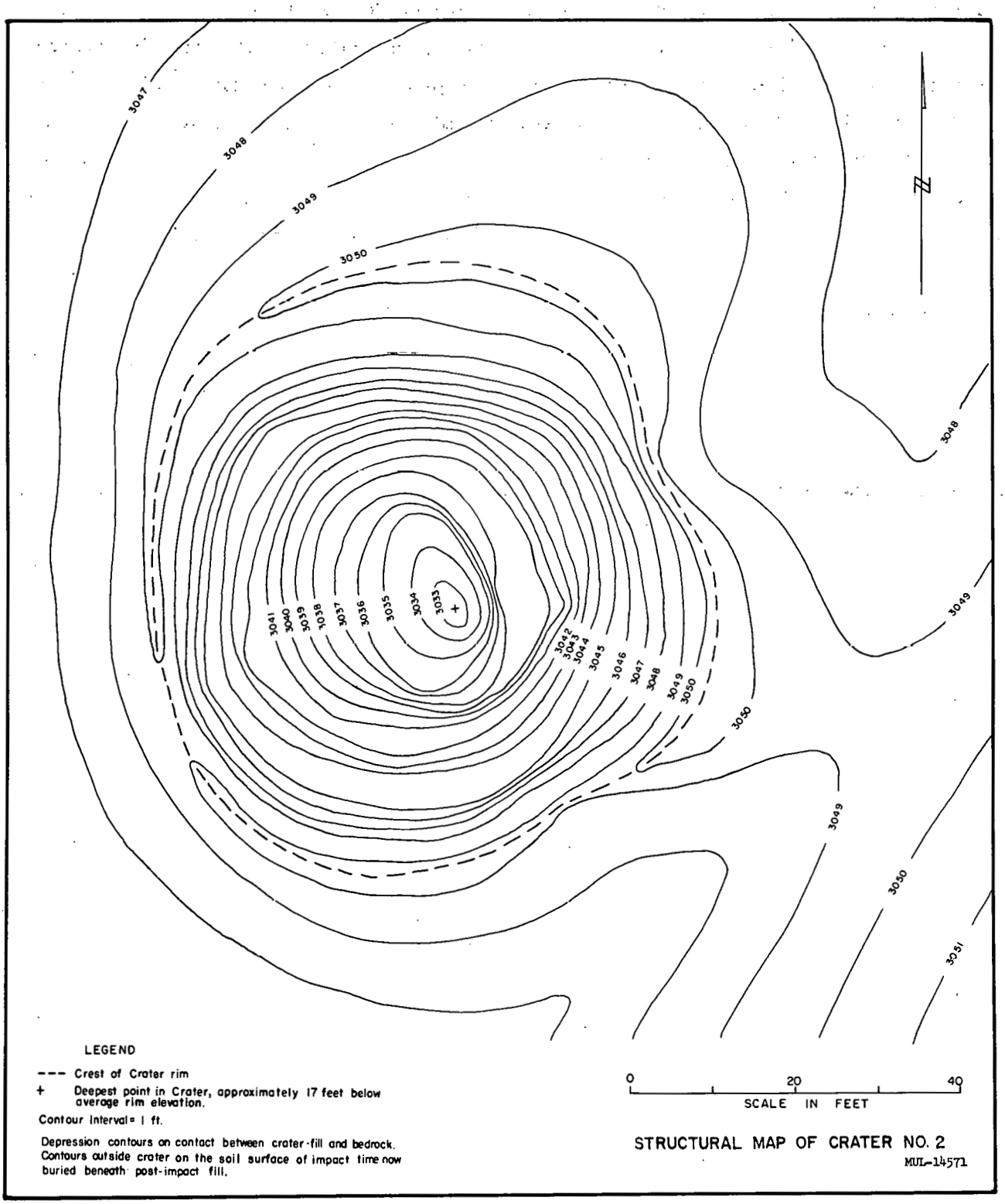

Fig. 4. Structural map of crater No. 2.

the basement sands. In crater No. 2 the fallback material did not originate in a similar fashion from the deepest strata penetrated. Rather, the crater appears to have been almost completely emptied of its own material, as the fallback in its bottom is composed largely of limestone and shale blocks which obviously were ejected from the main crater. (See Fig. 5, cross section of crater No. 2.) In the three smaller craters excavated, any fallback that may have been present could not be distinguished from post-impact fill – except for two large boulders of limestone, derived from the main crater, which presumably fell directly into one of the small craters.

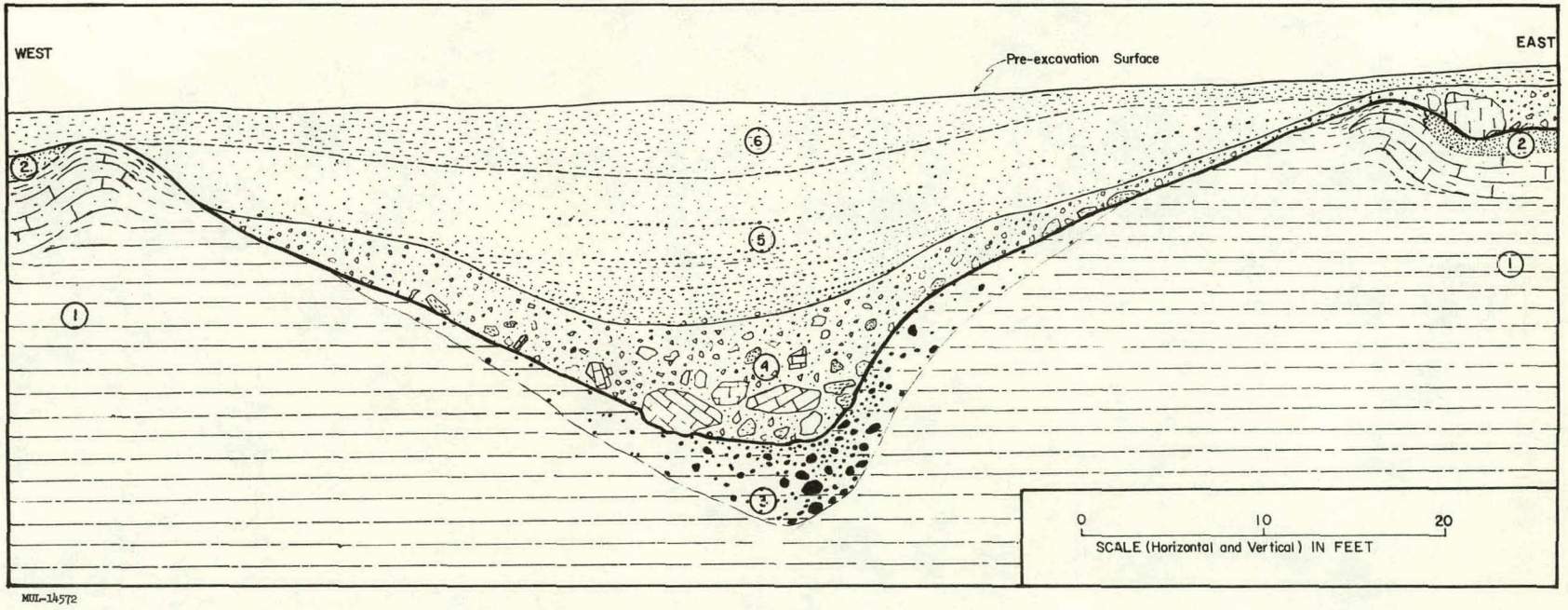

Fig. 5. Cross section through crater No. 2. The circled numbers refer to different rock units, as follows: (1) Compact, calcareous sands and sandy clays with hard, platy caliche in upper part. Except for compressional folding on the crater rim, this unit was not perceptibly affected by the meteorite impact. (2) Reddish-brown surface soil of impact time. (3) Zone of meteorites. The bedrock of this zone shows some distortion and incipient shearing, but it was not actually displaced from its original position. (4) Zone of fallback. Large limestone boulders and much of the other coarse material in this zone were ejected from deeper levels in the main crater, while blocks of reddish-brown soil and caliche appear to be fallback from crater No. 2. (5) Post-impact ponded deposits. (6) Recent sands and soil.

Paper E

PACIFIC CRATERS AND SCALING LAWS

R. B. Vaile, Jr.

Stanford Research Institute

Menlo Park, California

ABSTRACT

Crater measurements from two near-surface nuclear explosions detonated at Bikini atoll in 1954 were as follows:

Shot	Location	Approx Yield (Mt)	Crater Radius (ft)	Est. Max. Depth (ft)
1	reef	1.5	3000	240
3	island	0.1	400	75

On the basis of these and additional crater data from previous nuclear detonations, an extrapolation procedure has been developed by which crater diameters can be predicted. This procedure is based on an empirical determination of the scaling exponent, m, as a function of soil type, using

$$R = CW^{1/m}$$

where R is radius, C is a constant related to the soil type, and W is the energy release.

The range of uncertainty in the prediction of crater radius by this method is believed to be larger than a factor of 2.

* * *

The current interest in craters revolves around three somewhat interrelated questions. The military interest in craters is concerned for the most part with the question: What will be the size and shape of the crater produced by a specific military weapon detonated under specific circumstances? In the peaceful uses of explosives the question of greatest interest is, how do we make the biggest excavation? But there are others, such as

how do we minimize fallout? From a scientific standpoint, in order to answer these questions in a comprehensive and satisfactory manner, it is necessary first to address oneself to the questions: What are the detailed mechanisms of crater formation and what are the general laws specifying crater shape and size?

Military interest in craters stems from the observation that protective structures, particularly if they are buried, are likely to survive an adjacent explosion with relatively little damage if they are only a short distance outside the crater. The realities of weapons delivery have centered most of the military attention on craters formed by near-surface bursts. A major fraction of the shots in the Pacific proving ground have been in this category and I am happy to report in some detail today on those shots which have been declassified. Before reporting on the craters themselves it may be valuable to look into some aspects of nomenclature and theory.

In the investigation of craters formed by smaller explosions it has been recognized that while the crater surface apparent to the eye is relatively easy to measure, there is nevertheless a disturbance in the earth, caused by the explosion, to some depth below this upper surface. The lower boundary of this volume of disturbed earth has become known as the "true crater" in contradistinction to the upper surface, which has been called the "apparent crater." While the term "true crater" may be slightly misleading in its implications, it seems reasonably clear that for the purposes of determining the limitations of damage to underground fortifications the lower surface of the volume of disturbed earth (or true crater) is of greater significance than the apparent crater.

While for small craters it is physically and economically feasible to determine the boundaries of both the "apparent" and the "true craters," for very large craters the problem of excavation to determine the true crater becomes too extensive to be practical. The difficulty of measuring the true crater becomes even more severe when the crater is water-filled and when the level of radioactivity remains for some time high enough to prohibit extensive work.

The laws of similitude imply that the effects of an explosion of any (known) size in any medium are related precisely to the effects of an explosion of any other size in the same medium, provided the medium fulfills certain rather stringent conditions. Experimental measurements using conventional explosives such as TNT lead to some optimism that craters produced by such explosives can be predicted with an accuracy almost entirely adequate for military purposes, even though it is clear that some properties of the medium (earth) in which the explosive is fired are very sensitive parameters in affecting the crater.

The situation regarding craters produced by nuclear explosives is less satisfactory. First, the evidence is meager, since prior to CASTLE there were only three such explosions on which crater measurements were made; namely, JANGLE underground, JANGLE surface, and IVY Mike. Second, the existing evidence leads to pessimism regarding the validity of scaling from conventional to nuclear explosion effects. The failure of crater scaling from conventional to nuclear explosions is believed to result both from the enormous disparity in energy release (and this also applies between kiloton and megaton nuclear explosions) and also from the important difference in energy partition in the two types of explosions.

In general, the dimensions of the crater (radius or depth) are affected or determined by the total energy release, the depth of the charge, and the character of the medium (earth) in which the charge is fired. If these parameters operated independently, then one could write an empirical equation in the form

$$R = f(W) \cdot f(D_c) \cdot f(m)$$

or in the form

$$R = f(W) + f(D_c) + f(m)$$

where

R is the radius,

W is related to energy release, energy density, and detonation velocity,

D_c is the depth of the charge, and

m is related to the medium.

In this case the separate contribution of each of the parameters can be determined easily. If, however, the parameters are interdependent it is necessary to use the form

$$R = f(W, D_c, m),$$

and the effect of varying any one of the parameters is much more complicated because it depends on the values at which the other parameters are maintained.

There is general agreement among investigators that the parameters affecting craters are in fact extensively interrelated. The universal use of scaling concepts, particularly the scaled depth of charge, is evidence in point. Thus, in regard to the effect of energy release and depth of charge a satisfactory form for the equation is

$$R = f(W) \cdot f(W, D_c),$$

or, as a more specific example,

$$R = W^{1/k} \cdot f(\lambda_c),$$

where k is approximately 3 and $\lambda_c = \dfrac{\text{charge depth (ft)}}{[\text{weight of TNT(lb)}]^{1/3}}$. The inclusion of an additional term to represent the effect of different mediums could be in several forms, among which are:

(1) $R = f(W) \cdot f(W, D_c) \cdot f(m)$,

(2) $R = f(W, m) \cdot f(W, D_c)$.[1]

In attempting to correlate crater data from TNT blasts with those from

---

[1] The data at hand have seemed to the author to fit better into an equation of form (2) than into one of form (1), namely

$$R = (WE)^{1/m} \cdot f(\lambda_c),$$

as will be elaborated later. It is to be noted that these two forms are drastically different in the implications of extrapolation from less-than-kiloton charges up to megaton charges.

nuclear explosions, it has in the past appeared useful to include a factor less than unity (0.3 to 0.9) in the value of W assigned to nuclear charges in terms of equivalent tons of TNT, based on radiochemical data. This has been justified by the fact that the energy partition is totally different for the two types of explosives and that the nuclear weapons deliver radiant energy while conventional explosives do not. It is believed, however, that correlation will be uncertain at best, and with the advent of megaton weapons the disparity of sizes is so great that good correlation should not be expected.

The effect of charge depth (or height), λ_c, is fairly well established for TNT. If scaled crater diameter is plotted against scaled charge depth, it is clear both from experiment and physical reasoning that the curve will be concave downward, since no surface crater is produced if the charge is sufficiently high above the surface or sufficiently deep below it. For TNT, the maximum of this curve is rather broad and occurs in the range of $1 < \lambda_c < 3$, where λ_c is in ft/(lb TNT)$^{1/3}$.

The effect of the medium, f(m), has been shown to be as large as a factor of 2 in field experiments with TNT. Unfortunately, the specific properties of the medium which affect the crater are not yet established. It is postulated that strength, either shear or tension, and density are sensitive parameters. It is possible that the elastic moduli are also important. In regard to strength, it is of course the strength under shock load conditions that is important. It is very difficult to make laboratory tests under shock load conditions, and the heterogeneous character of earth makes the extrapolation from laboratory to field conditions very uncertain. Thus, while appropriate values for strength under shock load are not known, it appears clear that the strength under such conditions may differ widely from the strength under static load.

The density of the medium may in a theoretical sense affect crater size significantly. In practice, however, the range of densities found is trivial compared to the range of strengths, and hence the density is believed to be a parameter of only minor importance in affecting the crater.

As has been mentioned, the application of similitude principles places certain requirements on the medium. At a minimum for the purposes of crater investigation, it is required that the properties of the medium at equivalent locations (scaled) in two experiments must be identical. This requirement is completely met if the two media are homogeneous, isotropic, and identical. The properties of earth, however, are greatly affected by overburden pressure. Thus in a static sense the properties of earth are grossly dependent on actual (not scaled) depth below the surface, and in a dynamic sense these properties will be similarly affected by the pressure produced by the explosion. Thus one of the fundamental conditions for the proper application of simple scaling laws is violated. The greater the range of size of explosion, and hence of depth, the more serious this violation becomes.

A further difficulty with the application of theory occurs in situations such as existed on CASTLE, where two media, earth and water, were involved, and where the earth was saturated so that forces were transmitted by a complicated combination of intergranular forces and hydraulic pressures.

Pacific Craters

Most of the shots in the Pacific have been over water areas and while they may have had some influence on the bottom contours they did not produce craters in the conventional sense. Others have been fired at such high altitudes that no physical surface effects occurred. A still further group has been fired above land areas but at a height such that the craters were of the depression type rather than the scoured or throw-out type. There is a residuum of shots which have been fired on land areas and whose yields and results have been declassified. This is the group about which I will speak today.

Measurement of craters at the Pacific proving ground is fraught with considerable difficulty inasmuch as they are all water-filled and most of them have been washed by waves before it has been possible to measure them. The presence of water leads to much greater uncertainties in the actual dimensions, compared with equivalent craters fired in dry environment.

It also requires quite different techniques in measurement. These techniques in the Pacific are primarily either stereographic photography from the air or measurement of water depth inside the crater by means of a boat-carried fathometer. It is of some interest in passing that when the latter procedure is followed there is a good deal greater difficulty in determining the horizontal position of the boat than in determining the depth of water under it.

The largest crater in the Pacific was produced by shot CASTLE 1 for which the preshot aerial view is Fig. 1. This shot, which was approximately 15 megatons in yield, produced the crater indicated in Fig. 2, which as you can see is approximately 3000 feet in radius. At the time this crater was measured, approximately one week after the shot, the crater area had been washed to the extent that the fathometer showed a very flat bottom at 100 ft depth. Extrapolation of the slope of the sides where they could be measured, combined with information on the length of anchor chain required to moor a barge in the center of this crater for a following shot, led to the conclusion that the real depth at the time of formation was about 240 feet.

A similar shot fired some years earlier in the IVY Operation, IVY Mike, produced a crater with about the same radius and somewhat shallower depth. The shallower depth is undoubtedly the result of the IVY Mike shot having been fired some 20 feet above the surface while the CASTLE 1 shot was much closer to the surface.

The CASTLE 3 shot of about 100 kt was fired near the northern end of Tare Island on Bikini atoll as indicated in preshot aerial photograph Fig. 3. The result, a crater of 400-foot radius, some 75 feet deep, is shown in the aerial photograph of Fig. 4. Maps made from these photographs and from pre- and post-shot surveys are shown in Figs. 5 and 6. This crater, like all the others, was water-washed by the wave resulting from the shot which produced the crater; but this crater was washed in addition by the wave from a later shot fired on the surface of the lagoon. Thus the crater outline had been blurred to an indefinite extent before the measurement could be made.

The great sensitivity of height or depth of burst, particularly in the

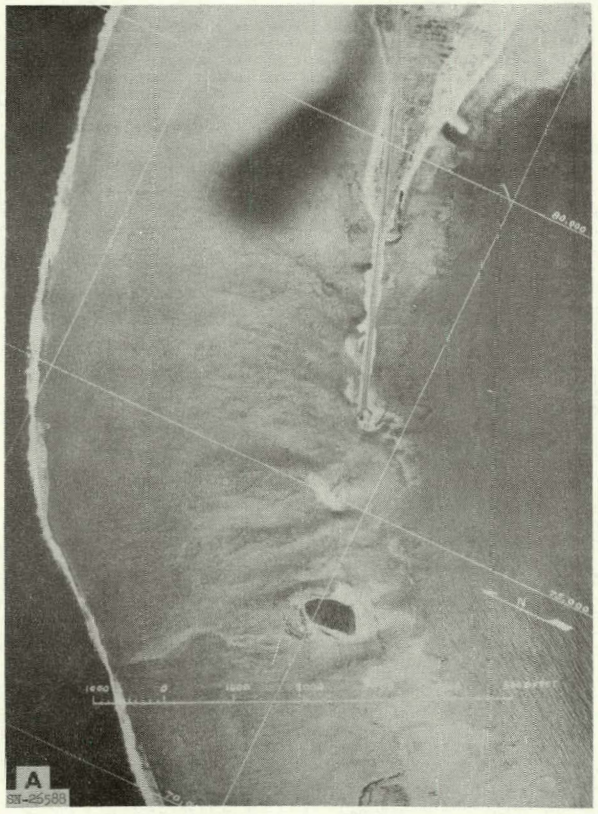

Fig. 1. Castle 1, preshot photograph.

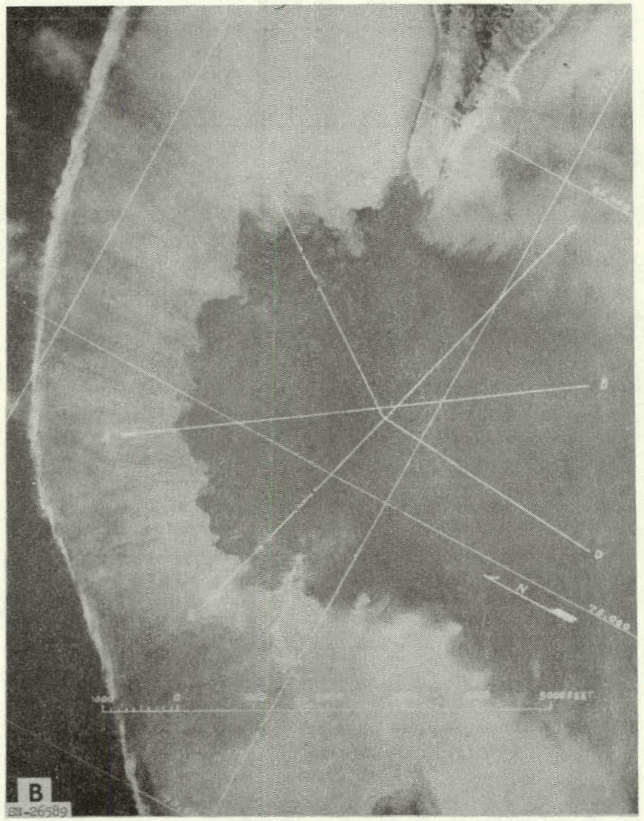

Fig. 2. Castle 1, postshot photograph.

Fig. 3. Castle 3, preshot photograph.

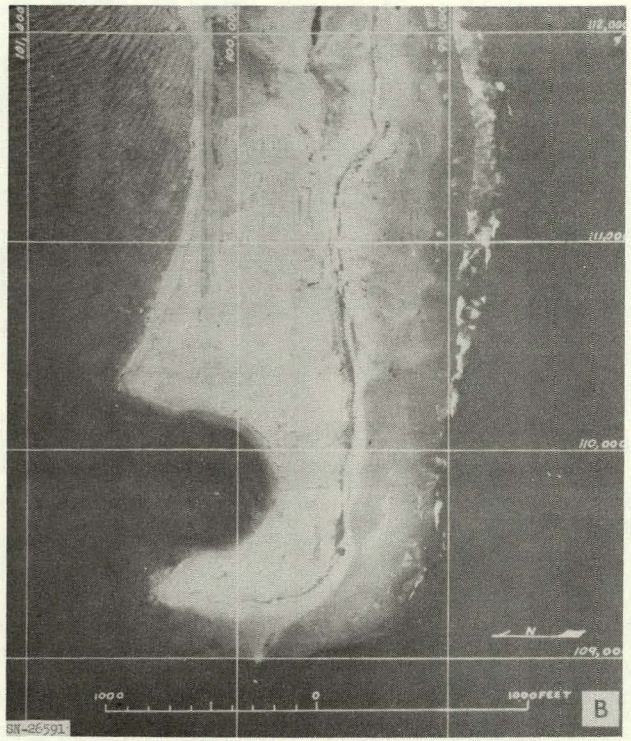

Fig. 4. Castle 3, postshot photograph.

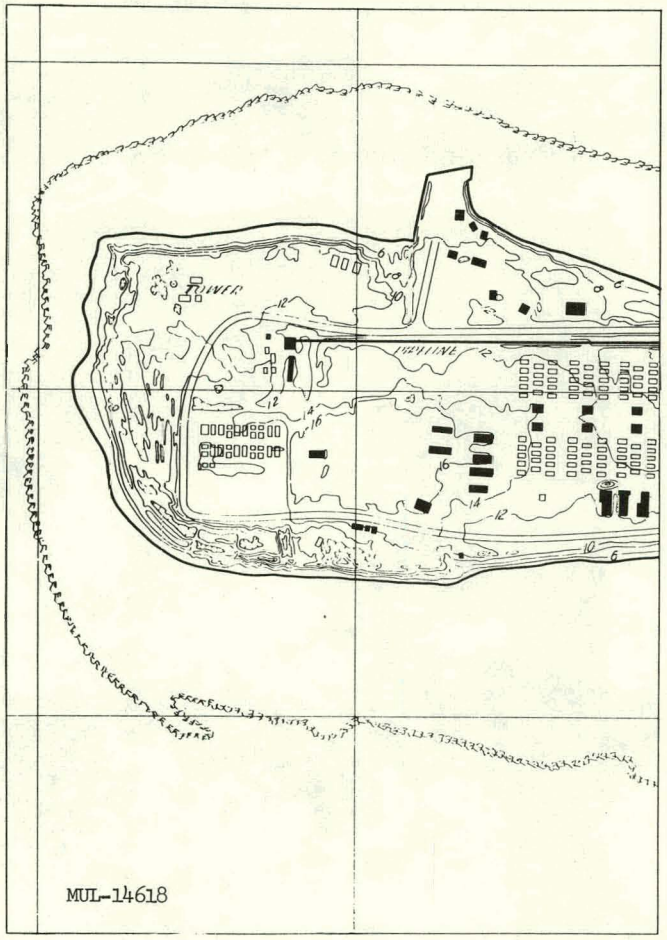

Fig. 5. Castle 3, preshot map.

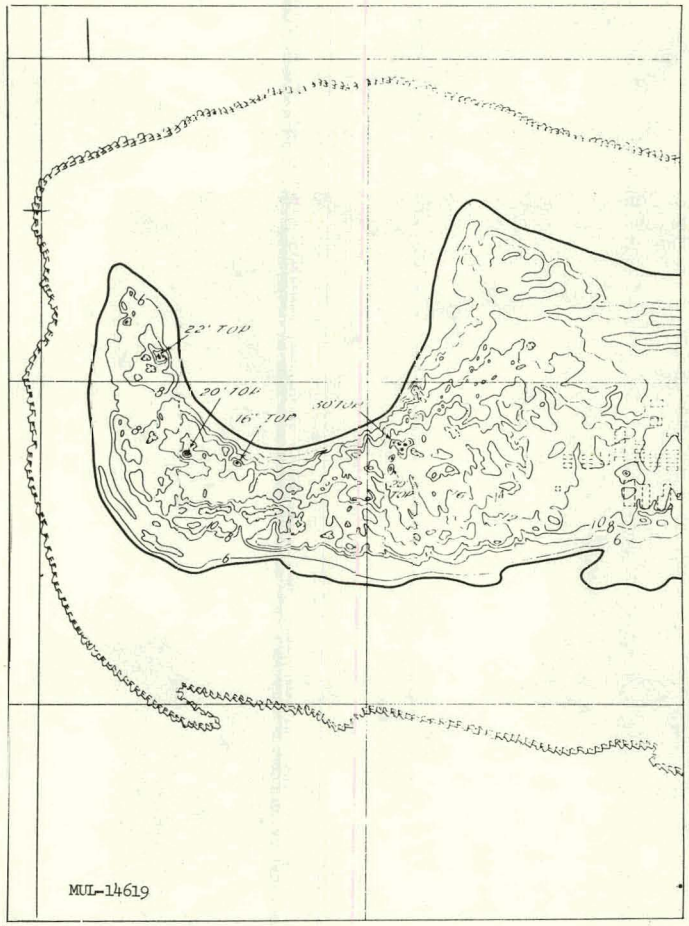

Fig. 6. Castle 3, postshot map.

region very close to the surface, is well illustrated in Fig. 7 in which the upper curves are scaled crater radius plotted against scaled depth of charge and the lower curve is scaled depth of crater against scaled depth of charge. The declassified nuclear tests in the Pacific including the ones illustrated above are shown here, and for comparison the nuclear cratering shots at the Nevada Test Site are also shown. There are two elements of interest in this figure, one the steep slope of the radius curves in the vicinity of zero depth, and the other the fact that even with this steep slope the range of uncertainty totals no more than about a factor of 3.

PREDICTION OF CRATERS

It should be pointed out that the crater prediction method presented here typifies the procedures recommended and is not as precise as it might be if more recent crater data were included. The pressure of time in the original project precluded treatment of scaling crater depth. Only crater radius is so treated.

Background

The data required in regard to any specific explosion for which a prediction of the crater is desired are (1) the yield, (2) the type of soil, and (3) the depth or height of burst. With this information, it is then appropriate to look at the existing evidence and measurements and to develop rational procedures for extrapolation or interpolation.

The craters from explosions high above the surface are significantly different from those formed by lower explosions in that they are depressions rather than excavations. Such craters are of relatively minor importance from a military standpoint and they are, therefore, not considered here.

As has been mentioned, an attempt to distinguish true from apparent craters becomes less and less realistic as larger and larger yields are considered. For this reason, only apparent craters are considered.

In previous analyses of crater data, the horizontal dimension used has sometimes been diameter and sometimes radius, and these values have been measured sometimes from lip to lip and sometimes at the original ground level. In this paper, only radius at original ground level is considered.

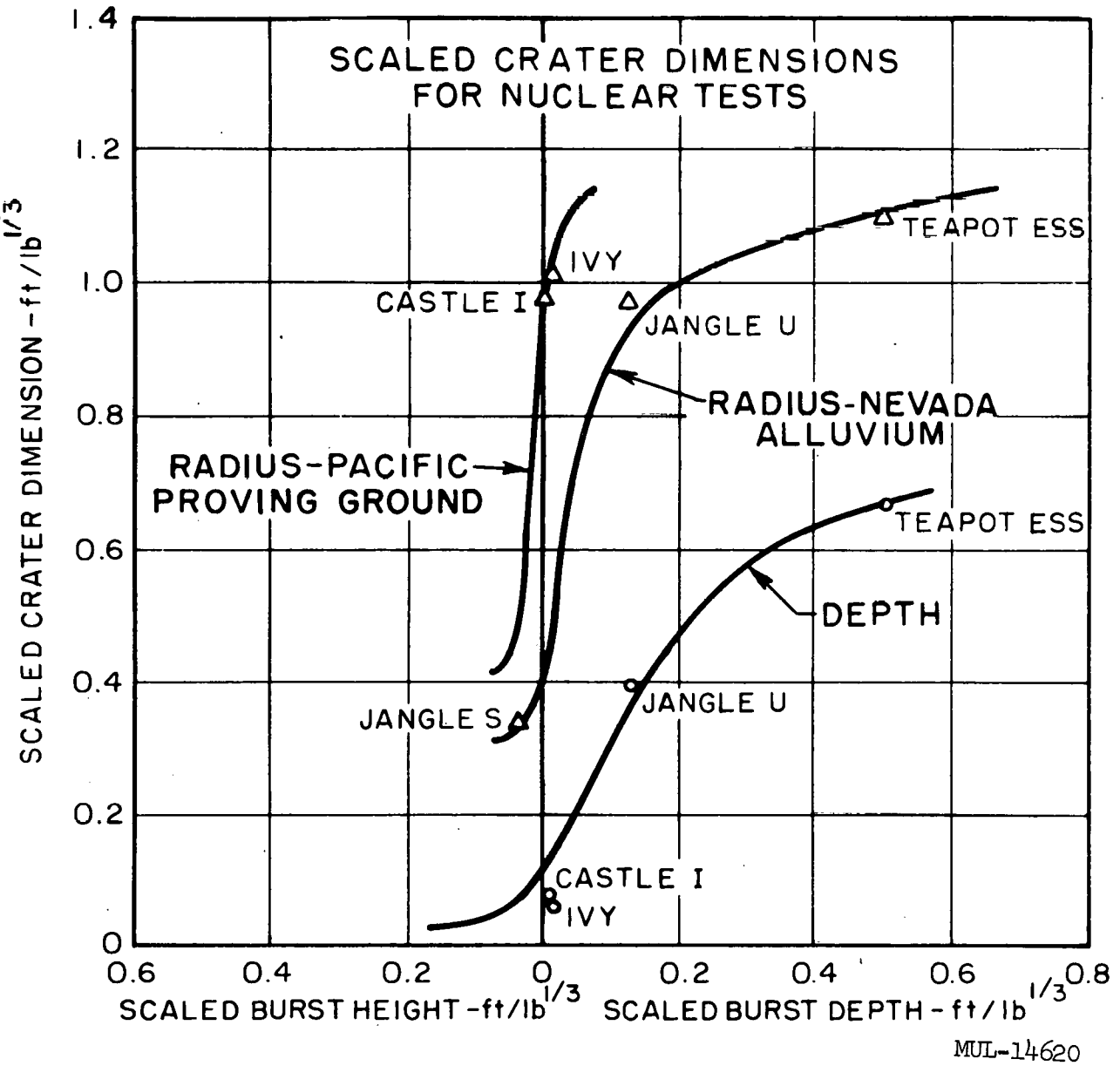

Fig. 7. Scaled radius and depth vs shot depth.

In reviewing the existing data from a broad point of view and with the objective of crater prediction for megaton explosions in mind, the following facts stand out:

1. All the data from which soils can be compared are contained in experiments involving relatively small quantities of TNT.
2. When more than one explosion has been fired under presumably identical conditions, an important scatter of the dimensions of the resulting craters is apparent.
3. The range over which these data must be extrapolated to permit prediction of megaton craters is enormously greater than the ranges of extrapolation commonly accomplished in engineering or scientific fields. The situation is roughly equivalent to an attempt to predict the penetration of the projectile from a new antitank gun through armorplate based on observation of many measurements of the penetration of BB's from an air rifle through tin cans plus a few measurements of the penetration of .45 pistol bullets through pine.

As a result of these facts any extrapolation procedure is inevitably associated with a large uncertainty in the final result. In making any extrapolation, consequently, it is of major importance to indicate the order of magnitude of the uncertainty involved as well as the extrapolation itself.

At the outset of any attempt to develop extrapolation procedures, one is faced with a philosophical choice. On the one hand he may look critically into the mechanism of the phenomenon and, on the basis of physical analysis, study the causes, the effects, and the influence of specific parameters. Alternatively, he may adopt the attitude that, in a complicated phenomenon such as crater formation, the mechanisms by which causes and effects are interrelated are so ill known as to be for the moment unknowable, and hence conclude that the appropriate approach is the empirical extrapolation of the existing data into the range of parameters where prediction is desired. It

is my opinion that the second approach is the more realistic one under the circumstances involved in the present problem, and that is the approach I have taken. The most important deviation from past thinking occasioned by this approach is that cube root scaling is, on this basis, discarded as a primary tool in the extrapolation and is used only for assistance in relatively minor aspects. In adopting an empirical approach, it would, of course, be absurd to ignore the information, however meager, in regard to the physical mechanism and, particularly, the distinction between the mechanisms occurring in TNT and in nuclear explosions. On the other hand, too much dependence on cube root scaling is likely to give the illusion of a precision in prediction unjustified by the facts.

The development described below was undertaken within the framework that the desirable result from a military standpoint is the construction of graphical or analytical relations such that knowledge of the yield, soil, and depth will permit easy prediction of the crater dimensions. It is postulated that the shape of a crater for the craters of interest is primarily dependent on its size, and hence the first attempt is to predict crater radius in terms of the three parameters just mentioned, with the exception that a later analysis can be made to predict depth and other shape aspects once the radius prediction has been accomplished.

Development of the Extrapolation Method

It was decided to study first the effect of soil type, second the effect of depth, and third the effect of yield. In looking at the available information it was at once apparent that in regard to both soil type and depth the data on megaton explosions are useless, since these shots were fired at one depth (essentially zero) and in one soil type (atoll "coral"); hence, it was finally recognized that the germane approach appeared to be to look first only at TNT data and from these data to establish an extrapolation procedure; second, to adjust the values of the parameters so that the JANGLE underground and JANGLE surface shots would be consistent; and finally, to investigate the sensitivity of the procedure and compare the results with the measurements of nuclear craters in the Marshalls.

Nevada soil is an appropriate one to look at first since there are considerable H. E. data and data from two nuclear shots. In that soil, data are available in the range λ_c = -0.13 to +1.0. Within this range greatest interest lies in the neighborhood of λ_c = 0.14. The data on the TNT shots of this scaled depth are plotted in Fig. 8, which shows crater radius plotted against yield on log paper both ways. Figure 7 is a similar plot for data on TNT at scaled depth λ_c = 0.50 and λ_c = -0.14 (minus indicates above the surface). The scatter of the points shown on these graphs is typical of the scatter shown in every case where several essentially identical shots have been fired. It is conservative to say that the uncertainty in the value of radius for any specific combination of soil type, charge size, and charge depth is at least 10%. Consequently, the ±10% limits at the maximum and minimum charge sizes shown here are marked on Fig. 8. For extrapolation purposes, the reciprocal slope, m, of the most probable line is 3.4.[2] To permit an estimate of the uncertainty in extrapolation, maximum and minimum slopes within the 10% uncertainty just mentioned have also been plotted. These slopes are m = 3.0 and m = 4.1. This elementary analysis has been undertaken with the data on Fig. 8 only, and lines of the slopes so determined have then been drawn on Fig. 9. The analysis has been limited to Fig. 8 both because the scaled depth λ_c = 0.14 is of major interest and also because a greater range of yields for TNT shots is available for this scaled depth than for any other.

It is apparent that m, the reciprocal of the slope when crater radius is plotted against yield on a log-log basis, is related to R and W in the following way:

$$R = KW^{1/m}.$$

In the remainder of the report "m" is referred to as the "scaling exponent."

Using the best fit value for m, 3.4, and the experimental data of Tables A.4 and A.6, the solid line of Fig. 10 has been constructed. On this

[2] The actual value measured on the graph is 3.39. However, the second figure is probably of somewhat doubtful validity and hence all such numbers are rounded off to two figures.

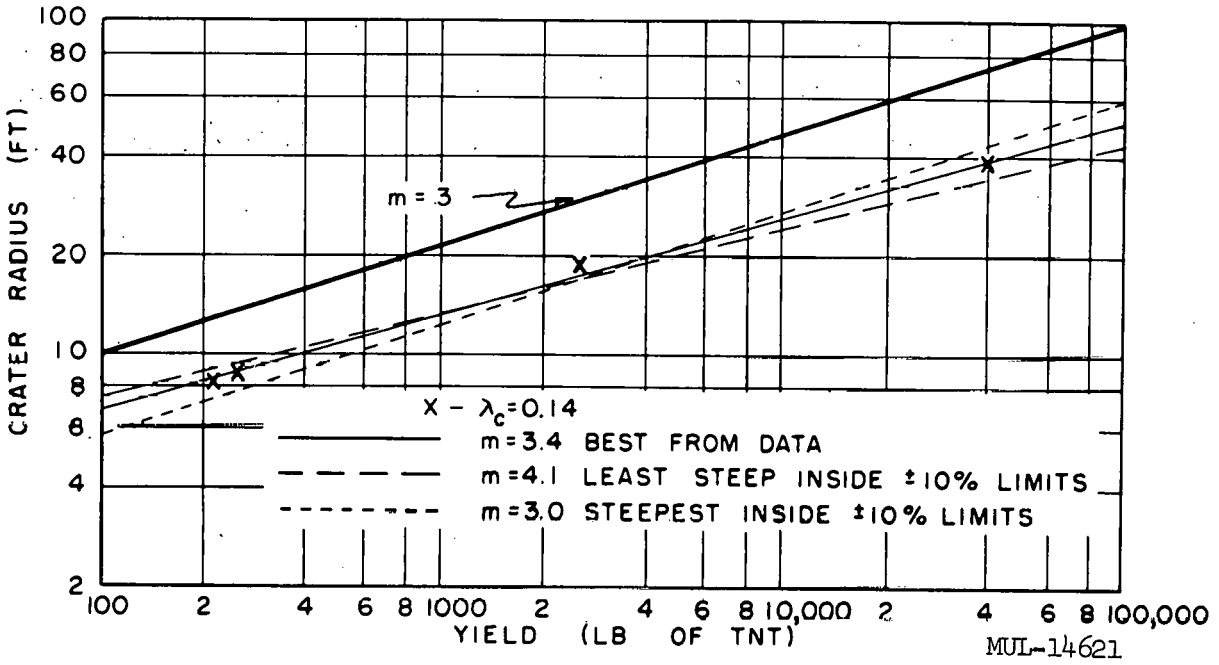

Fig. 8. Crater radius vs yield, Nevada, $\lambda_c = 0.14$.

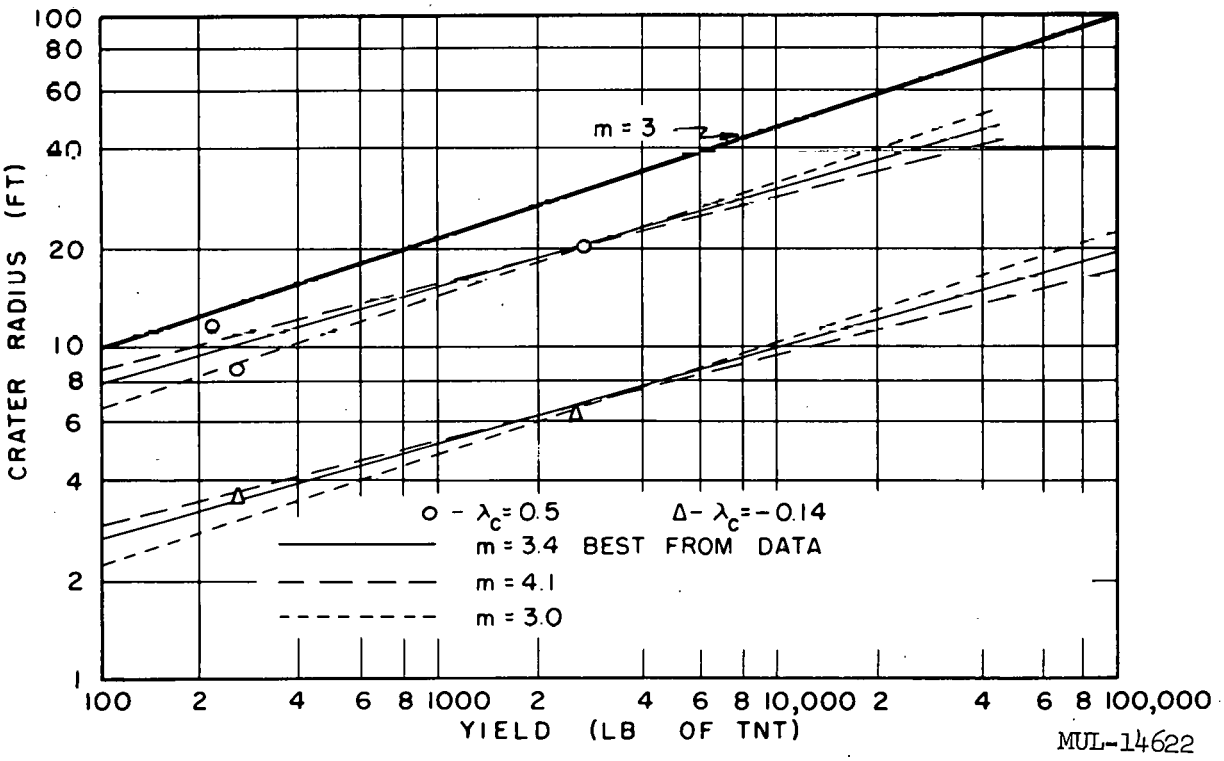

Fig. 9. Crater radius vs yield, Nevada, $\lambda_c = 0.5$ and $\lambda_c = -0.14$.

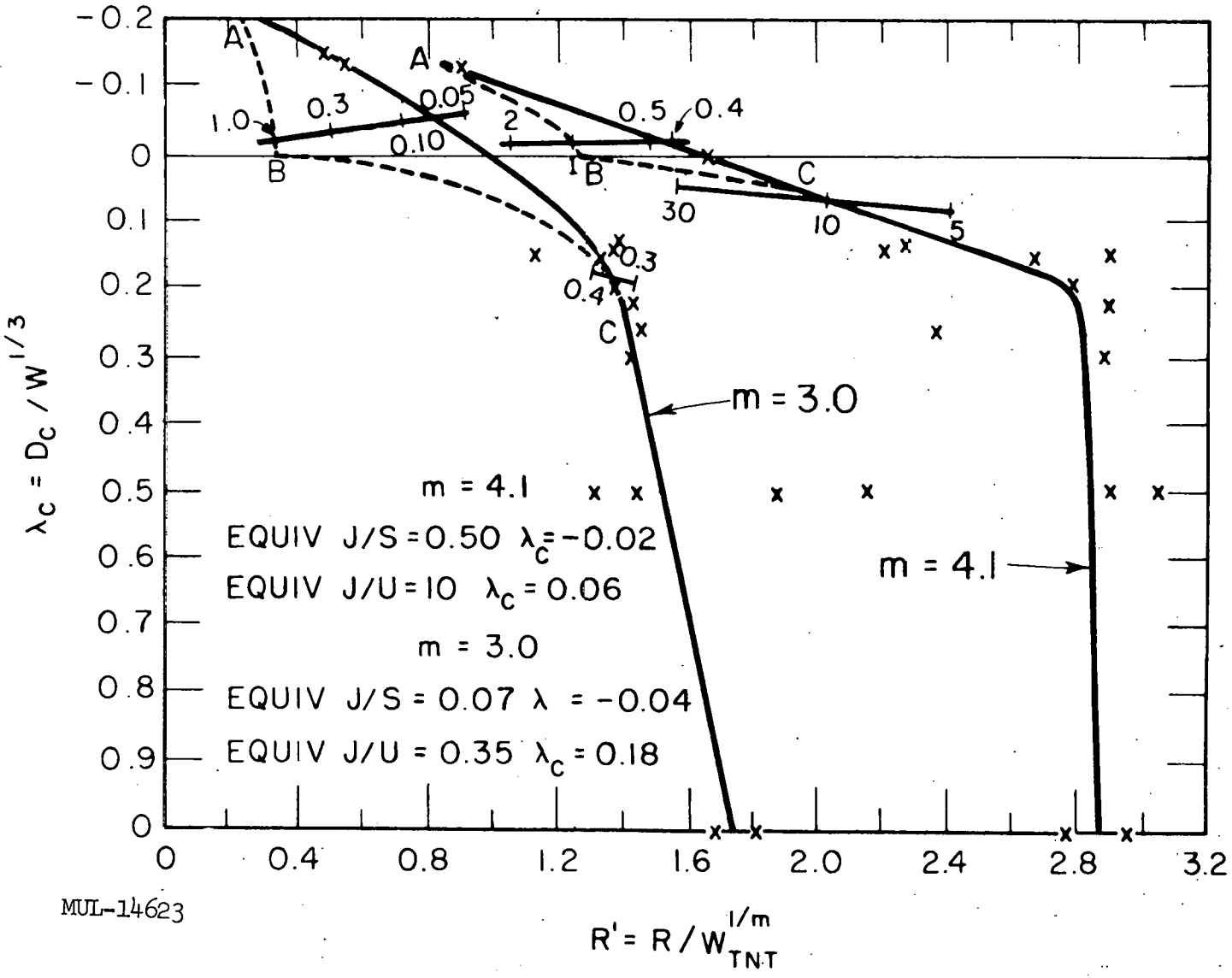

Fig. 10. Scaled crater radius vs scaled charge depth, Nevada alluvium (m = 3.4).

figure the scaled radius (on the basis m = 3.4) is plotted against the scaled charge depth (on the basis m = 3).[3]

The next step is the determination of the curve for nuclear charges based on this curve for TNT charges. In this procedure, consideration must be given to the difference in mechanism of nuclear and TNT bursts, particularly for bursts on the surface or at very low heights above the surface.

In the early stages of a nuclear explosion fired at or near the interface between air and earth, the shock wave velocity is very much higher in the air than in the earth;[4] hence, at a time when the nuclear explosion process has proceeded to the point where the average energy density[5] within the boundary of the shock wave is equal to the average energy density at the surface of a spherical TNT charge which has been detonated at its center, the envelope of the nuclear explosion is essentially hemispherical. If average energy density is a good criterion of crater size and shape, then on this basis the crater formed by a given nuclear energy release on the surface should be similar to the crater formed by a TNT charge of the same yield fired well

---

[3]Since the range of scaled depths is small in the interval of greatest interest, the distinction between determining scaled depths on the basis m = 3.0 and on the basis m = 3.4 is relatively trivial and will not affect the conclusions reached in this analysis.

[4]D. T. Griggs ("Notes on Surface and Underground Bursts," AFSWP, WT-378), in predicting the effects of JANGLE U, computes shock wave velocities in air to be approximately 25 times those in soil in the radius range from approximately $\lambda = 0.1$ to $\lambda = 1.0$. Similarly, Porzel ("Soil Pressure and Energy Transfer on Mike Shot," LA-1529), in predicting the effects of IVY Mike, estimates shock velocities in the air and water-soaked sand for high overpressures such that in the early stages of a nuclear explosion the ratio of velocity in air to velocity in soil may be as high as 1000:1.

[5]By "average energy density" is meant the total energy contained within the shock wave, divided by the total volume within it.

above the surface.[6] The crater resulting from a nuclear surface charge should differ extensively from that produced by a TNT charge whose center of gravity is at the surface, both because of the different mechanism mentioned above and because a hemispherical excavation was required before the TNT charge could be placed.

Consider a nuclear charge at $\lambda_c = -0.13$. Within its shock wave the total energy will be identically the same as that within a sphere of TNT tangent to the surface when both shock waves reach the surface. This argument can be summarized by saying that the crater radius produced by a low aboveground nuclear shot should be essentially independent of height, and (if the efficiency were 100%) should have about the same value as that produced by a TNT shot at $\lambda_c = -0.13$. On this basis the dotted curve in the region AB has been drawn on Fig. 10.

Since the energy partition in the two types of explosion is significantly different, particularly in the roughly 15% of the yield of the nuclear explosion which takes the form of prompt radiation, it seems necessary to consider an equivalence factor of less than 1 for the cratering effects of nuclear explosions. The experimental evidence on this point is very meager, being limited to the JANGLE Surface (J/S) and JANGLE Underground (J/U) shots. The data from these two shots can be placed on this graph with the equivalence factor as a parameter. Thus segment DE on Fig. 11 represents JANGLE Surface shot for a radiochemical yield of 1.2 kt times the factors shown on the line, with radius scaled on the basis of 3. Similarly the segment FG represents JANGLE Underground shot on the basis 1.2 kt times the factors shown there, using the same procedure. The intersections of these segments with the solid curve AC implies equivalence factors of 0.14 and 1.0

---

[6] Actually, as Porzel points out, at a time when the nuclear shock wave has reached the same radius as that of the TNT sphere of equivalent energy release (and hence when average energy densities are equal), there is still an enormous difference in the two situations since the mass enclosed within the shock wave in the case of TNT is some 1500 times that in the nuclear case. Hence, in the nuclear situation the pressures are very much higher and the durations shorter than in the TNT situation.

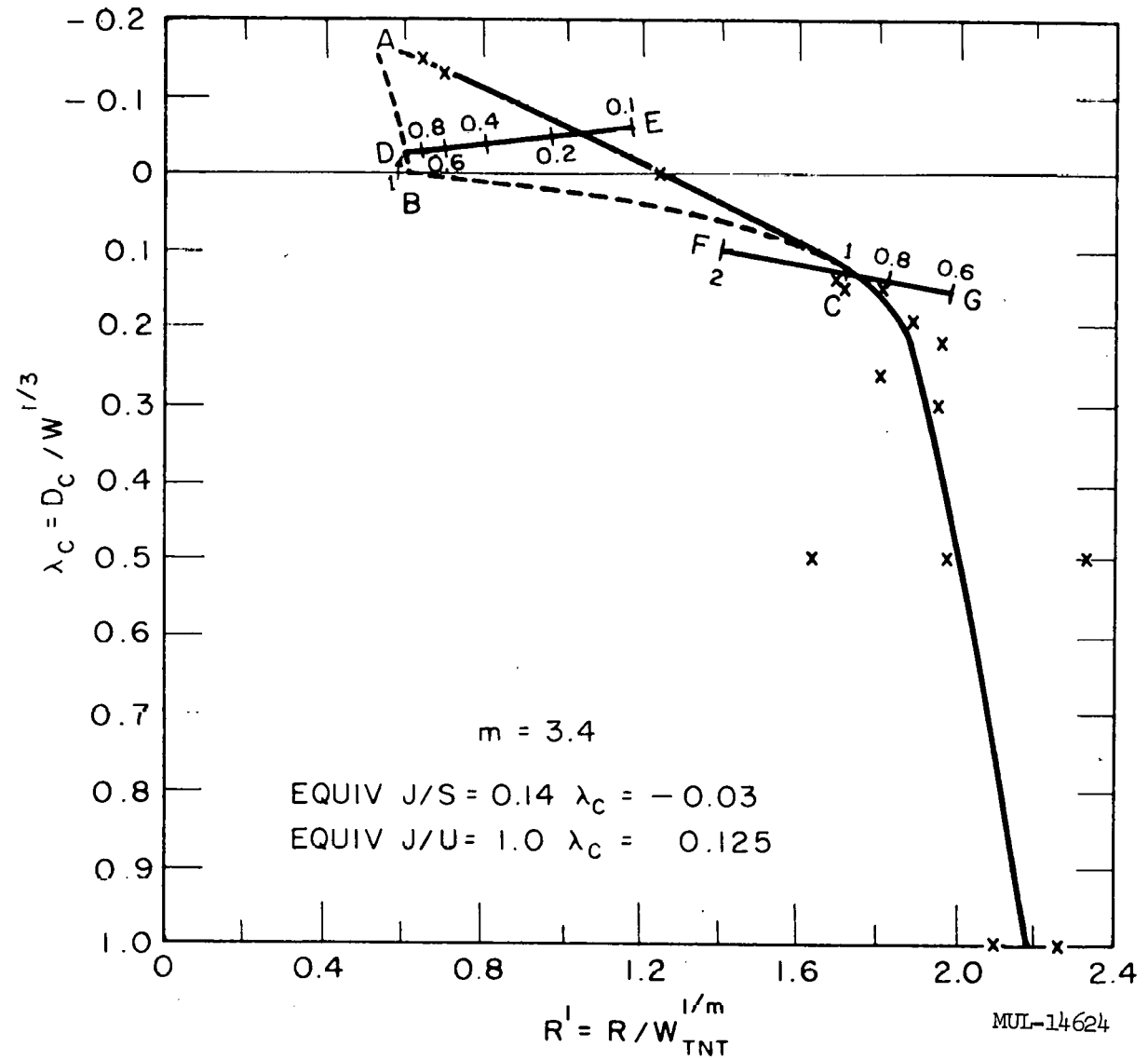

Fig. 11. Scaled crater radius vs scaled charge depth, Nevada alluvium (m = 3.0, m = 4.1).

for J/S and J/U, respectively. It is important not to attach too much precision to these numbers for the following reasons.

1. The TNT data have an important scatter which amounts to an uncertainty of the order of +10% in scaled radius.
2. The TNT curve in the neighborhood of zero charge depth has an additional uncertainty inasmuch as the radius of the TNT sphere is 0.13 on the basis m = 3.

Consideration of the difference in energy partition leads then to the qualitative conclusion that there should be gross differences in sensitivity of crater radius to changes in the charge height in the immediate vicinity of the surface between nuclear and chemical explosives. These differences should in general be that a nuclear charge placed slightly above surface will produce a crater which is relatively insensitive to further changes in height, whereas a nuclear charge slightly below the surface will have a crater radius extremely sensitive to further changes in depth. Thus the actual scaled crater radius to be expected from a nuclear explosion probably falls on the dashed curve, ABC. This has been drawn through the point representing 1.0 effectiveness factor for J/S, and may well be a more fruitful method of thinking of crater predictions from nuclear explosions than attention to equivalence factor and its variation with height or depth.

The procedure described for constructing both the TNT and the nuclear curves shown on Fig. 10 can be performed equally well using values of m other than the best fit value of 3.4. Other appropriate values of m as indicated on Fig. 8 are 3.0, representing both conventional cube root scaling and the lower limit of slope on the basis of 10% uncertainty in experimental values postulated earlier, and 4.1 representing the upper limit. Both curves have been plotted together on Fig. 11. Note that when the dashed curve ABC for these values of m is drawn through the point representing 1.0 equivalence factor for J/S, the curves are a little unrealistic in that the curve AB for m = 3 implies a larger crater for an aboveground nuclear shot than seems reasonable, and curve AB for m = 4.1 shows a smaller value than seems reasonable.

The equivalence factors for J/S and J/U as shown on Figs. 10 and 11 are rather sensitive functions of parameter m. It is also to be noted that if J/S had been precisely at the surface the efficiency factor would have been significantly different because of the acute angle of the TNT curve as it crosses the zero depth axis. The following table indicates the values of equivalence factor as a function of m for both J/S and J/U, and also the estimated value for a shot like J/S except one fired precisely at the surface.

	Equivalence Factors		
m	J/S	Surface	J/U
3.0	0.07	0.03	0.35
3.4	0.14	0.08	1.0
4.1	0.50	0.31	10.0

Since for military purposes the data for extrapolation should be available in the simplest possible form for quick use without computation, the nuclear curves shown on Figs. 10 and 11 have been replotted in the form of radius in feet against charge depth in feet, with yield as a parameter. This has been done on Fig. 12 in which, for each yield shown, both the most probable value (m = 3.4) and the limiting values m = 3.0 and 4.1 are shown.

The estimates for this soil for the most probable value of the scaling exponent, m = 3.4, are replotted on Fig. 13. Range of uncertainty (m = 3.0 and m = 4.1) is indicated by short horizontal bars attached to each of the parametric yield curves.

The same kind of analysis has been carried through for dry clay, dry sand, wet clay, and sandstone, and the results of these analyses are included in Figs. 14 through 17. For these other soils no nuclear data are available, and hence the efficiencies found in the Nevada soil have been used in the following fashion. For the most probable value of the scaling exponent m in each of these other soils, the variation of equivalence with depth at Nevada for m = 3.4 has been used. Similarly, for the lowest value of m for each of these other soils the same variation of efficiency with depth has been used

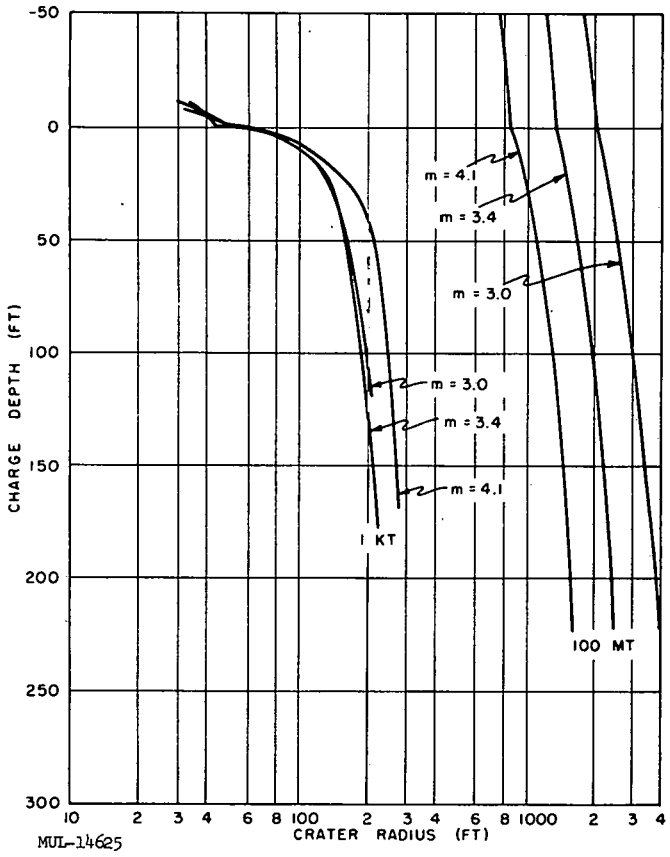

Fig. 12. Crater radius vs charge depth, Nevada alluvium, showing range of uncertainty.

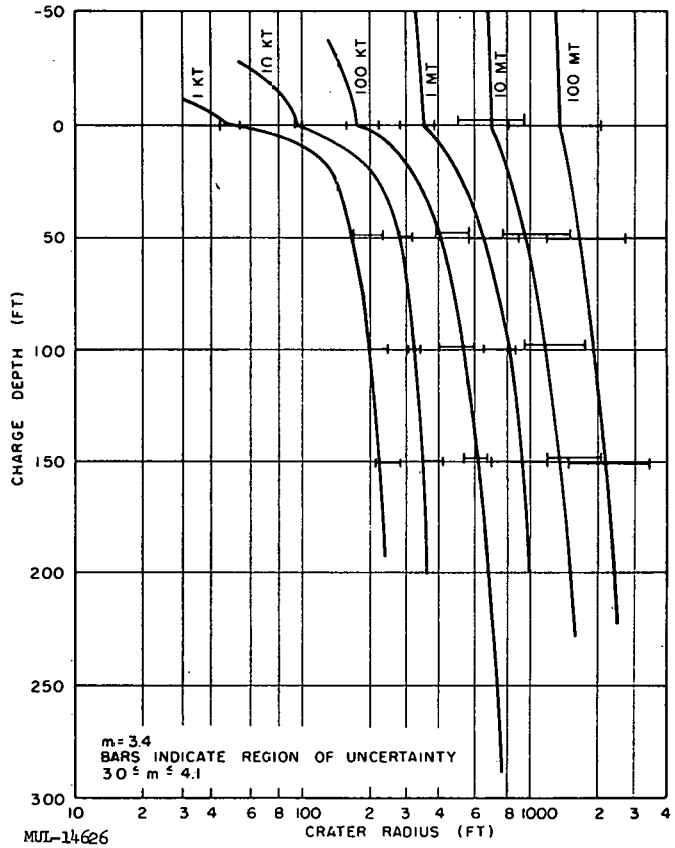

Fig. 13. Crater radius vs charge depth, Nevada alluvium.

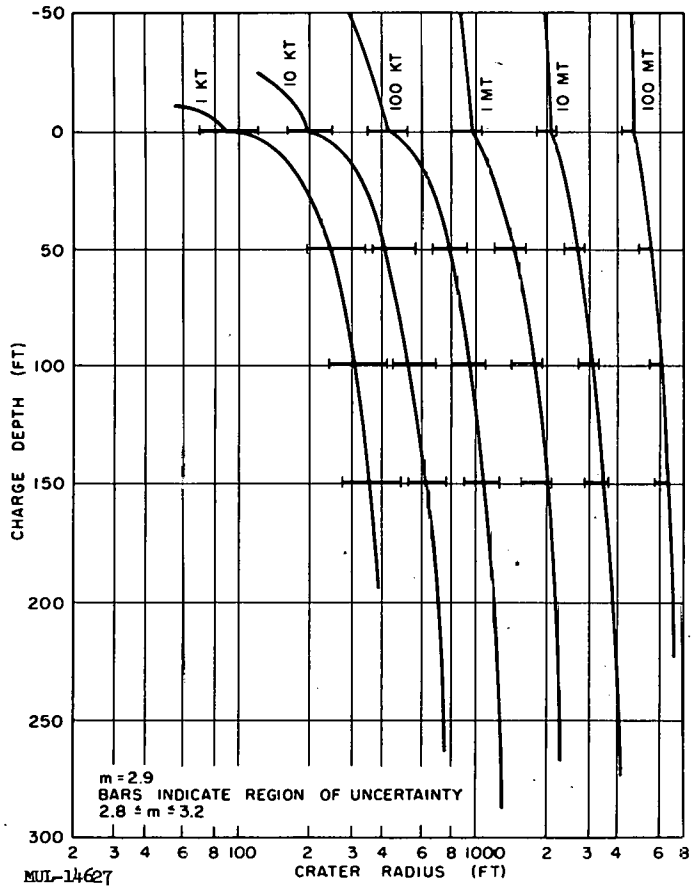

Fig. 14. Crater radius vs charge depth, dry clay.

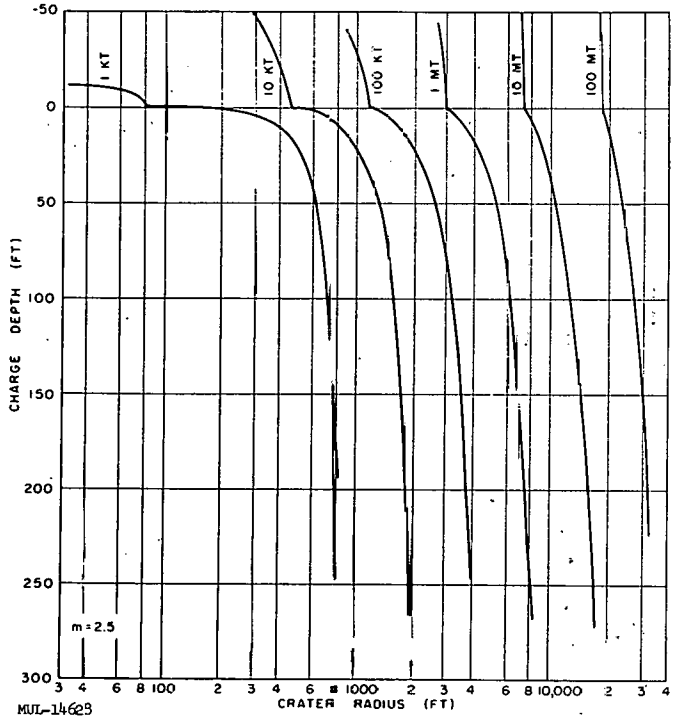

Fig. 15. Crater radius vs charge depth, wet clay.

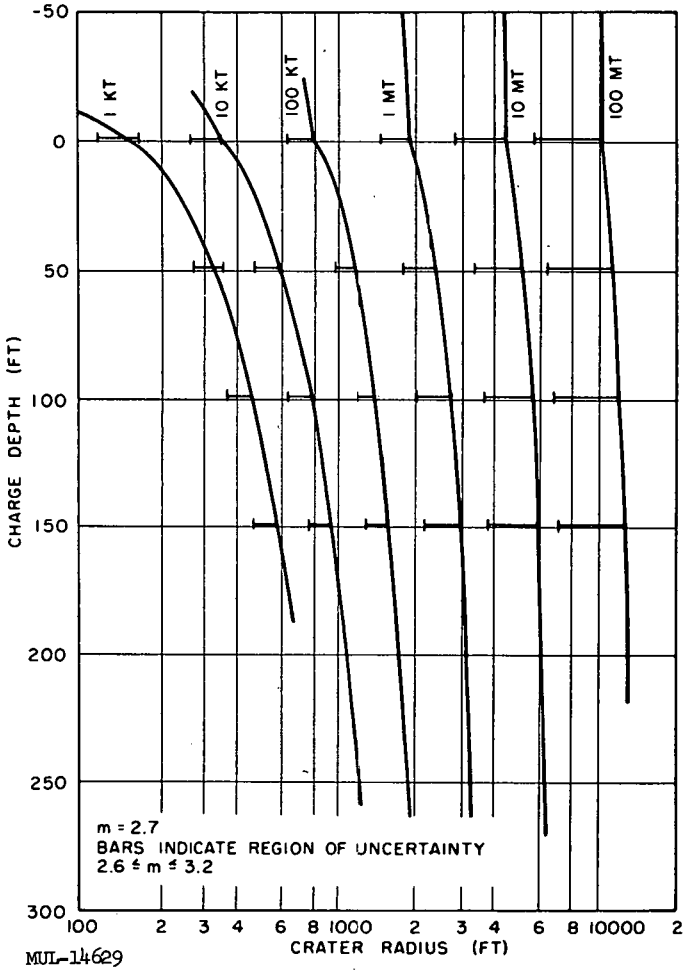

Fig. 16. Crater radius vs charge depth, dry sand.

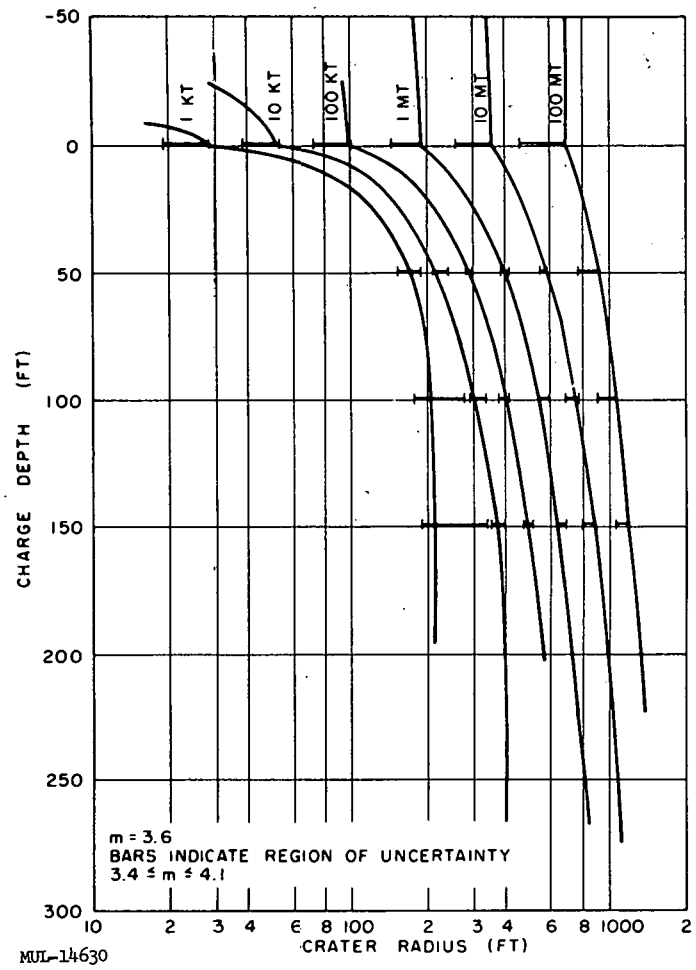

Fig. 17. Crater radius vs charge depth, sandstone.

as was found at Nevada for the lowest value of m there, namely 3.0. The corresponding analysis has been made for the upper limiting value of m.

The most probable and limiting values of m for all the soils reported here are listed in Table 1. In each, the available data have been plotted in the same form as was shown on Figs. 8 and 9, the best straight line was drawn for those points, and then values of radius 10% above and below the curve were marked at the upper and lower limits of the charge sizes considered.[7] By this procedure, the limiting values of m have the greatest range for those soils in which no large TNT charges have been fired, and this is appropriate, since in fact the extrapolation is less certain in such cases.

For wet clay, Fig. 15, so little TNT data are available that crater radius has been predicted only for the most probable value of the scaling exponent m.

Table 1. Scaling exponent, m, for several soils.

Soil	Most Probable	Minimum	Maximum
Nevada	3.4	3.0	4.1
Dry clay	2.9	2.8	3.2
Wet clay	2.5	2.0	3.3
Dry sand	2.7	2.6	3.2
Sandstone	3.6	3.4	4.1

In Fig. 18 the results for surface charges in various soils are shown. For each soil the line drawn is that for the most probable value of m. On this curve also are shown the nuclear craters for surface shots at Nevada and in the Marshalls. In plotting the results of the nuclear explosions on this figure, the equivalence factor found for a shot precisely at the surface for the scaling exponent m = 3.4, namely 0.14, has been assumed to be applicable to the explosions in the Pacific. The logarithmic grid has been adjusted in the region of 1 kt to include this equivalence for all larger yields. Hence the graph can be entered directly with the value of radiochemical yield. This graph gives a realistic indication of the uncertainty in crater prediction

[7] TNT data from charges less than 200 lb were not reviewed.

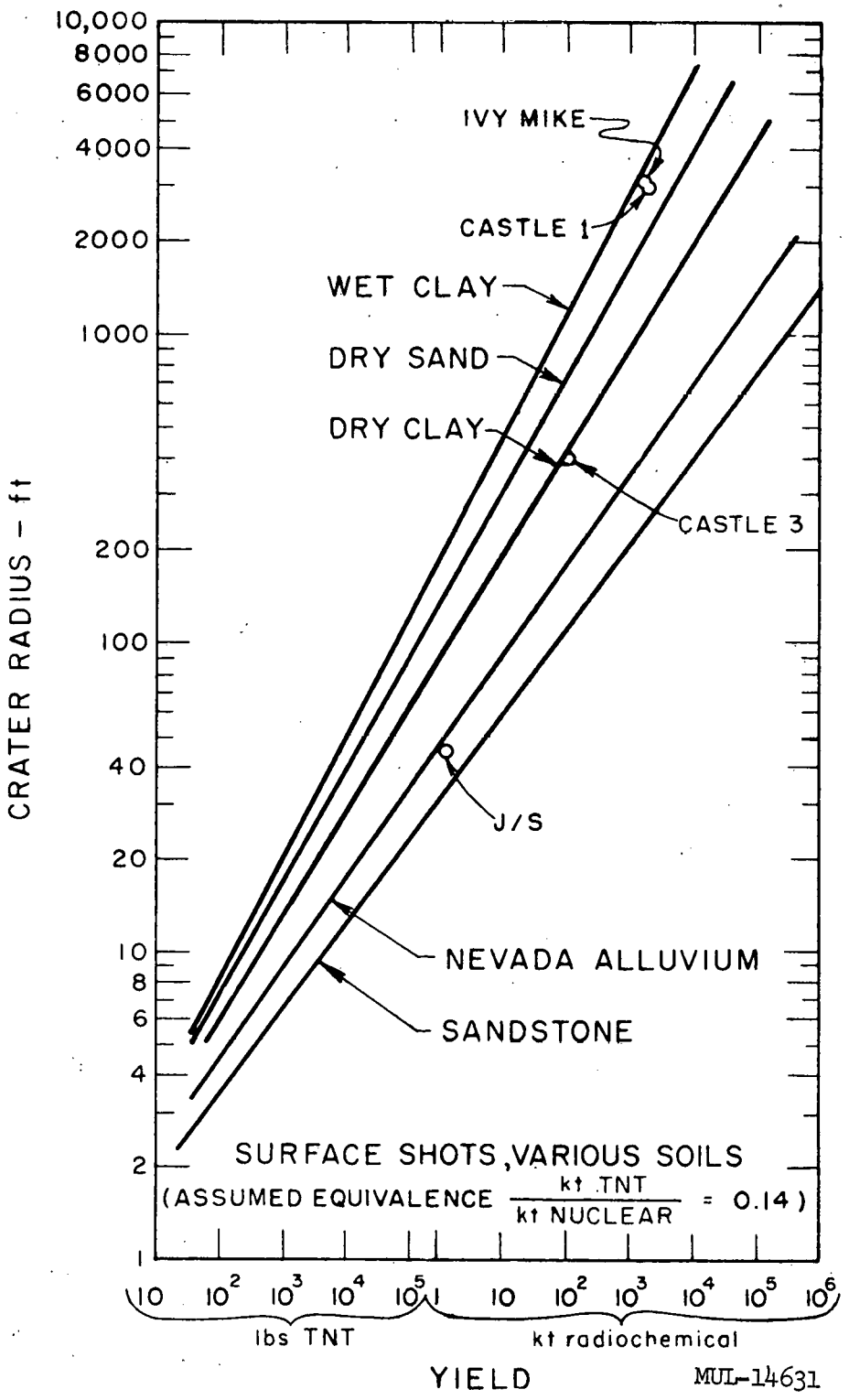

Fig. 18. Crater radius vs yield, surface shots, various soils.

depending on the properties of the soil.

All data that have been used in the development of the extrapolation method presented here are summarized in Appendix A. This appendix also includes data for some TNT shots, namely those in wet sand, as well as some nuclear charges, such as Trinity, which were not used in the actual analyses presented here.[8]

Comments on the Extrapolation Method

It should be noted explicitly that the extrapolation method described here is based on an empirical equation of the form

$$R = f(W, m) \cdot f(\lambda_c)$$

or

$$R = (WE)^{1/m} \cdot f(\lambda_c),$$

where E is an efficiency which depends on medium, scaled charge depth, and type of explosive. This is not the only form of equation which can be postulated, and defended. The available data are so meager, and their scatter around the curve representing any specific equation is so great, that it is not possible at present to establish unequivocally the relative validity of alternative forms of the empirical equation.

The suggestion has been made that an equation of the form

$$R = (WE)^{1/3} \cdot f(\lambda_c) \cdot f(m)$$

is more satisfactory.[9] When either form is used for the extrapolation of TNT

---

[8]The wet-sand TNT results were not used because data on only one charge size were found and hence a value of slope could not be established. A value for Trinity was not used because the scaled height is greater than that of interest in this report.

[9]One piece of information which has been put forward as favoring the suggested form of equation is the result of some cratering experiments in the Marshall Islands. These experiments were run under the direction of Dr. H. Kirk Stephenson, currently on the staff of the National Science Foundation. Quoting from Memorandum SWPEF 2/924 (354.2) dated 26 Nov. 1954, "1. A series of high explosive shots were fired on Elugelab (Flora) Island, Eniwetok

data to megaton nuclear explosions, a certain range of uncertainty in R is shown, resulting from reasonable values assumed for the uncertainty in $f(\lambda_c)$ and f(m). The uncertainty in R shown by the suggested equation form is smaller than that shown by the equation form used in the main body of this report.

Another and more important benefit adduced for the suggested form is that the predicted crater radii for megaton explosions have a smaller spread when soil characteristics are changed.

It is the opinion of the author that the benefits indicated are illusory and that the form used in the main body has a slightly better basis. The true value of crater radius produced by a megaton explosion in any medium other than that existing in the Marshall Islands will remain unknown until such a shot is fired and the resulting crater measured. In the meantime, it is felt that caution in stating the expected values and their uncertainties is of vastly greater military use than over-optimism.

Atoll in the spring of 1952. These shots consisted of a combination of R-7HDA(c-2)R-7-HCA (Tetrytal), primacord, and blasting caps piled in a beehive shape on the surface which had been excavated down to the high tide level. A dike was established around the charge to prevent wave interference but this proved ineffective. In addition to seismic shock information, the crater radii were determined. The crater data obtained from these HE shots at the Pacific Proving Grounds may be used to establish a soil factor for comparing saturated coral with Nevada soil. A summary of the data is as follows:

W (tons TNT equivalent)	$W^{1/3}$ $(lb)^{1/3}$	Scale height to c.g. (λ_c)	Crater radius R_c(ft)	$R_c/W^{1/3}$
1	12.6	0.06	27.5	2.18
5	21.5	0.06	32	1.49
10	27.1	0.06	37.5	1.39
15	31.1	0.06	45.5	1.47
20	34.2	0.06	50	1.47
		Overall average		1.60
		Average if first shot omitted		1.46

(End of quote.)

The corresponding H. E. data from Nevada taken from Tables A. 4 and A. 6 give a value for $R_c/W^{1/3}$ of about 0. 08. If one uses the suggested form of the equation and hence assumes that the effect of soil is independent of the effect of charge size, then one might say that craters in the Marshalls should be expected to be 1. 8 to 2. 0 times as large (in radius) as craters from identical charge sizes and depths in Nevada.

In a similar manner it is found that the value for $R_c/W^{1/3}$ for megaton surface shots in the Marshalls is about 1. 0, while that for the kiloton surface shot in Nevada is 0. 34, which implies that Marshall craters will be some three times larger than Nevada craters. Actually, if the small but finite value of $D_c/W^{1/3}$ is taken into account, particularly for the JANGLE Surface shot, the analysis suggests that scaled crater radii for nuclear charges in the Marshalls are twice as large as for those in Nevada. Since this is the same figure that was obtained for H. E. craters, it is tempting and not implausible to say that all scaled crater radii in the Marshalls will be very close to twice those in Nevada.

While the precise data quoted from the AFSWP memorandum were not at hand during the development of the extrapolation method described in the previous section, some prior discussion of them was held with Dr. Stephenson by telephone. At that time it was Dr. Stephenson's feeling that the data themselves were somewhat unreliable because all the craters were water-washed before measurement. In addition it seems improper to assume that the characteristics, for cratering purposes, of the water-saturated coral sand involved in the H. E. tests are identical with the characteristics of the more coherent water-saturated coral rock involved in the nuclear shots.

APPENDIX A

SUMMARY OF AVAILABLE CRATER DATA

Table A.1. Nuclear crater measurements.*

Shot	Soil	Radio-Chemical Yield	Height of Burst (ft)	Height of Burst (λ)	Crater Radius** (ft)	Crater Radius** (λ)	Crater Depth (ft)	Crater Depth (λ)
TRINITY	Dry sand	~20 kt	100		550		9.5	
GREENHOUSE Easy[a]	Sat. cor. sand	46.7 kt	300	-0.664	418	0.925	2.4	0.0053
JANGLE Surface	Desert alluvium	1.2 kt	3.5		45	0.336	17	0.127
JANGLE Underground	Desert alluvium	1.2 kt	-17	0.127	129	0.961	53	0.396
IVY Mike[a]	Sat. cor. sand	~14 Mt	35		3120 (2800)[b]		164	
CASTLE 1	Sat. cor. sand	~15 Mt	7		3000		240	
CASTLE 3	Sat. cor. sand	~100 kt	13.6		400		75	
TEAPOT ESS	Desert alluvium		-70		147		90	

Sat. cor. sand = saturated coral sand.

*All data except CASTLE and TEAPOT data are obtained from Cratering Produced by Nuclear Weapons, W. R. Perret, Sandia Corporation Technical Memorandum, Ref. Symbol 1922-2-(23), January 2, 1954.

**All crater radii are measured at original ground level.

[a]Due to scour from water rushing back in, and to aging (for GREENHOUSE) measured diameters may be large by 10 to 30%, measured apparent crater depths may be shallow by a factor of 2 or more.

[b]In Memorandum SWPEF 2/924 (354.2) dated 26 November 1954, the statement is made that plotting the IVY Mike data on an expanded vertical scale gives a value for crater radius of 2800 ft (λ = 1.02).

Table A.2. TNT crater measurements in dry sand, dry clay, and wet clay.* Underground Explosion Test Program. Site: Dugway Proving Grounds.

Soil	Round	Charge Weight (lb TNT)	Charge Depth (ft)	Charge Depth (λ)	Crater Radius** (ft)	Crater Radius** (λ)	Crater Depth (ft)	Crater Depth (λ)
Dry Sand	101	320	-3.5	-0.51	4	0.59	0.5	0.07
	102	320	0.0	0.0	7.68	1.12	2.5	0.37
	103	320	1.3	0.19	10.88	1.59	6	0.88
	104	320	3.5	0.51	12	1.75	6.5	0.95
	105	320	7.0	1.02	15.5	2.26	8.5	1.24
	106	320	14.0	2.04	16.75	2.45	4.5	0.66
	107	320	21.0	3.07	13.5	1.97	3.5	0.51
	108	2560	2.6	0.19	19	1.39	9.75	0.71
	109	2560	7.0	0.51	24.75	1.81	8.5	0.62
	110	320	3.5	0.51	13	1.9	7.5	1.10
	111	8	2.5	1.25	6	3	4	2
	112	2560	7.0	0.51	30	2.2	12	0.88
	113	320	3.5	0.51	14	2.0	6.75	0.99
	114	8	2.5	1.25	6	3	3.5	1.75
	115	40,000	17.5	0.51	75	2.19	23	0.67
	116	320	8.75	1.28	18.5	2.7	9	1.32
Dry Clay	301	320	-3.5	-0.51	2.5	0.37	1	0.15
	302	320	0.0	0.00	7.25	1.06	4	0.58
	303	320	1.3	0.19	9	1.3	5.5	0.80
	304	320	3.5	0.51	10.5	1.5	6	0.88
	305	320	7.0	1.02	11.75	1.72	7	1.02
	306	320	14.0	2.04	15	2.2	1	0.15
	307	320	21.0	3.07	10	1.46	1	0.15
	308	2560	2.6	0.19	20	1.46	12	0.88
	309	2560	7.0	0.51	21.5	1.57	15.5	1.13
	310	320	3.5	0.51	11	1.6	7	1.02
	311	8	2.0	1.0	4	2	2.5	1.25
	312	2560	7.0	0.51	26	1.90	15	1.09
	313	320	3.5	0.51	12.75	1.86	8	1.17
	314	8	2.5	1.25	4.5	2.25	3	1.5
	315	40,000	17.5	0.51	64	1.87	42	1.23
	316	110	2.45	0.51	9	1.87	6	1.25
	317	2560	7.0	0.51	23	1.68	15.5	1.13
	318	320,000	35.0	0.51	120	1.75	60	0.88
	319	2560	7.0	0.51	23	1.68	13.5	0.98
	Sym.	320	7.0	1.02	12.5	1.83	7	1.02
Wet Clay	401	8	2.5	1.25	7	3.5	5	2.5
	402	320	2.5	0.36	18.75	2.74	10	1.46
	403	2560	5.0	0.36	41.75	3.05	12.75	0.93
	404	320	2.5	0.36	17.5	2.56	11.5	1.68
	405	8	2.5	1.25	6	3	4.1	2.05

*Obtained from Appendix G, Underground Explosion Test Program, Final Report, Volume I, Soil, Engineering Research Associates, August 30, 1952.
**All crater radii are measured at original ground level.

Table A.3. TNT crater measurements in limestone, granite, and sandstone.* Underground Explosion Test Program. Site: Dugway Proving Grounds.

Soil	Round	Charge Weight (lb TNT)	Charge Depth (ft)	Charge Depth (λ)	Crater Radius** (ft)	Crater Radius** (λ)	Crater Depth*** (ft)	Crater Depth*** (λ)
Lime-	501	320	6.6	0.97	11.2	1.64	9.1	1.33
stone,	502	320	2.5	0.365	8.3	1.21	3.9	0.57
Granite	601	320	-2.5	-0.365	1.20	0.175	....	....
	602	320	0.0	0.00	8.43	1.23	1.7	0.25
	603	320	2.5	0.365	9.70	1.42	2.6	0.38
	604	320	5.0	0.73	14.5	2.12	5.0	0.73
	605	320	12.5	1.83	17.1	2.50	6.1	0.89
	606	320	25.0	3.65	5.20	0.76	2.0	0.29
	607	320	2.5	0.365	14.4	2.11	5.3	0.78
	608	320	2.5	0.365	14.0	2.05	4.6	0.67
	609	2560	5.0	0.365	25.2	1.84	10.2	0.75
	610	2560	5.0	0.365	23.1	1.69	8.7	0.64
	611	320	2.5	0.365	13.4	1.96	5.0	0.73
	612	320	17.0	2.49	13.2	1.93	7.6	1.11
Sand-	801	320	-2.5	-0.365	0.0	0.0	0.0	0.00
stone	802	320	0.0	0.0	5.6	0.82	2.3	0.34
	803	320	2.5	0.365	11.6	1.69	4.8	0.70
	804	320	5.0	0.73	14.0	2.04	7.6	1.11
	805	320	12.5	1.82	9.3	1.36	14.9	2.17
	806	320	25.0	3.65	0.0	0.00	a	a
	807	320	2.5	0.365	14.3	2.09	5.1 b	0.75
	808	320	2.5	0.365	13.1	1.91	5.8	0.85
	809	1080	3.75	0.365	19.0	1.85	8.6	0.84
	810	2560	5.0	0.365	32.6	2.38	9.7	0.71
	811	2560	5.0	0.365	25.1	1.83	10.5	0.77
	812	2560	5.0	0.365	23.3	1.70	11.0	0.80
	813	10,000	7.9	0.365	39.4	1.83	16.1	0.75
	814	40,000	12.5	0.365	56.5	1.65	26.9	0.79
	815	40,000	12.5	0.365	70.5	2.06	26.9 b	0.79 b
	816	40,000	12.5	0.365	53.6	1.56 c	27.5 b	0.80 b
	817	320,000	25.0	0.365	94.8	1.38 c	47.0	0.69
	818	320	2.5	0.365	17.5	2.56	6.0	0.88
	819	320	2.5	0.365	15.6	2.28	6.5	0.95

*Obtained from Underground Explosion Test Program–Technical Report No. 4, Granite and Limestone, Volume I and from Underground Explosion Test Program–Technical Report No. 5, Sandstone, Volume I, Engineering Research Associates, February 15, 1953.

**All crater radii are measured at original ground level.

***Average crater depth (D_k) is the average of the measurements of the vertical distance from the deepest point of the crater, not necessarily directly under the charge, to the surface, one measurement being made on each of the four vertical sections available for each crater. This depth is not significant unless the deepest point is below the bottom of the excavation made

Notes on Table A. 3 (Continued)
to place the charge. The charge hole was obliterated by all the detonations at the sandstone site except round 306.

[a]The damage did not extend to the surface and is not comparable with other rounds; the sides of the original charge hole were damaged up to an average slant distance of 5. 6 ft from the center of gravity of the charge.

[b]Crater shape was estimated; the breakthrough volume is not included.

[c]Average of eight measurements scaled from the vertical crater sections.

Table A. 4. TNT crater measurements in desert alluvium, Operation JANGLE. H. E. shots at Nevada Proving Grounds (Yucca Flats).

Round	Charge Weight (lb of TNT)	Charge Depth (ft)	Charge Depth (λ)	Crater Radius** (ft)	Crater Radius** (λ)	Crater Depth (ft)	Crater Depth (λ)
HE-1	2560	2. 01	0. 15	18. 2	1. 33	6. 5	0. 47
HE-2	40, 000	4. 63	0. 15	38. 6	1. 13	14. 9	0. 44
HE-3	2560	6. 79	0. 50	19. 8	1. 45	10. 8	0. 79
HE-4	2560	-2. 01	-0. 15	6. 4	0. 47	1. 9	0. 14
HE-5	2560	4. 02	0. 30	19. 6	1. 43	7. 8	0. 57
HE-6	2560	3. 00	0. 22	19. 7	1. 44	6. 7	0. 49
HE-7	2560	2. 58	0. 19	18. 9	1. 38	6. 9	0. 50
HE-8 a	216	1. 08	0. 18	b	b	b	b
HE-9 a	216	0. 83	0. 14	8. 2	1. 37	3. 5	0. 58
HE-10 b	216	3. 00	0. 50	11. 3	1. 88	5. 5	0. 92

*Obtained from Some H. E. Tests and Observations on Craters and Base Surges, D. C. Campbell, Armed Forces Special Weapons Project, Operation JANGLE Project 1(9)-3, 1 November 1951 (WT-410).
**All crater radii are measured at original ground level.

[a]Results from a corresponding 177-lb Pentolite charge are not included in this summary.

[b]Partial detonation.

Table A.5. TNT crater measurements in dry clay, Project MOLE* (by Stanford Research Institute, at Dugway Proving Grounds).

Round	Charge Weight (lb of TNT)	Charge Depth (ft)	Charge Depth (λ)	Crater Radius** (ft)	Crater Radius** (λ)	Crater Depth (ft)	Crater Depth (λ)
101	256	6.35	1.00	11.1	1.73	5.5	0.86
105	256	6.35	1.00	10.9	1.72	6.0	0.94
102	256	3.18	0.50	10.5	1.65	6.3	0.99
102A	256	3.18	0.50	9.5	1.50	5.4	0.85
106	256	1.65	0.26	9.1	1.43	6.2	0.98
107	256	0.0	0.00	6.6	1.04	3.9	0.61
104	256	-0.83	-0.13	4.4	0.69	1.5	0.24

*Obtained from Small Explosion Tests – Phase I of Project MOLE, R. B. Vaile, Jr., Stanford Research Institute, January 1953.
**All crater radii are measured at original ground level.

Table A.6. TNT crater measurements in desert alluvium, Project MOLE* (by Stanford Research Institute, at Dugway Proving Grounds).

Round	Charge Weight (lb of TNT)	Charge Depth (ft)	Charge Depth (λ)	Crater Radius** (ft)	Crater Radius** (λ)	Crater Depth (ft)	Crater Depth (λ)
202	256	6.35	1.00	11.5	1.81	5.7	0.90
212	256	6.35	1.00	10.7	1.69	6.1	0.96
203	256	3.18	0.50	8.4	1.32	4.0	0.63
204	256	1.65	0.26	9.2	1.45	2.9	0.46
205	256	0.83	0.13	8.8	1.39	2.5	0.39
206	256	0.0	0.00	6.4	1.01	1.9	0.30
207	256	-0.83	-0.13	3.5	0.55	1.4	0.22

*Obtained from Small Explosion Tests – Phase I of Project MOLE, R. B. Vaile, Jr., Stanford Research Institute, January 1953.
**All crater radii are measured at original ground level.

Table A.7. TNT crater measurements in wet sand, Project MOLE* (by Stanford Research Institute at Camp Cooke, California).

Round	Charge Weight (lb of TNT)	Charge Depth (ft)	Charge Depth (λ)	Crater Radius** (ft)	Crater Radius** (λ)	Crater Depth (ft)	Crater Depth (λ)
304 a	256	4.83	0.75	18.6	2.94 a	6.6 a	1.04 a
301	256	3.18	0.50	19.1	3.01	...	....
302	256	3.18	0.50	19.9	3.14	6.3	0.99
309	256	3.18	0.50	15.6	2.45	6.1	0.96
310	256	3.18	0.50	16.8	2.64	5.2	0.82
305	256	1.65	0.26	14.3	2.26	6.3	0.99
306	256	0.83	0.13	12.8	2.01	3.7	0.58
307	256	0.00	0.00	10.2	1.61	4.8	0.75
308	256	-0.83	-0.13	8.8	1.39	4.0	0.63

*Obtained from Small Explosion Tests – Phase II of Project MOLE, L. M. Swift and D. C. Sachs, Stanford Research Institute, May 1954.
**All crater radii are measured at original ground level.

[a]Round 304 was shot in the crater of round 303.

Table A.8. TNT crater measurements in wet clay, Project MOLE* (by Stanford Research Institute at Camp Cooke, California).

Round	Charge Weight (lb of TNT)	Charge Depth (ft)	Charge Depth (λ)	Crater Radius** (ft)	Crater Radius** (λ)	Crater Depth (ft)	Crater Depth (λ)
311	256	3.18	0.50	15.5	2.45	11.2	1.76
312	256	3.18	0.50	17.8	2.80	9.0	1.42
313	256	-0.83	-0.13	5.8	0.91	3.4	0.53

*Obtained from Small Explosion Tests – Phase II of Project MOLE, L. M. Swift and D. C. Sachs, Stanford Research Institute, May 1954.
**All crater radii are measured at original ground level.

Paper F

NEVADA TEST SITE NUCLEAR CRATERS*

M. D. Nordyke

Lawrence Radiation Laboratory, University of California
Livermore, California

ABSTRACT

Four craters have been produced by nuclear explosions at the Nevada Test Site. Three of the craters were made in loose alluvial fill by 1.2-kiloton shots at depths of burst ranging from 3.5 feet above surface to 67 feet below surface. Crater dimensions ranged from radius 45 feet and depth 21 feet for the above-surface shot to radius 146 feet and depth 90 feet for the 67-foot-deep shot. The fourth crater, made by a 115-ton shot placed 100 feet beneath the sloping side of a bedded tuff mesa, had radius 100 feet and depth 35 feet. Comparison of these nuclear craters with craters produced by high explosives shows that the two types of explosive are approximately equal (for equivalent yields) in crater-producing ability.

* * *

Four nuclear explosions at the Nevada Test Site (NTS) have resulted in large craters. Three of these were fired for studies of nuclear weapons effects and hence are at depths of burst much shallower than proposed Plowshare application, but right in the region of interest for meteoritic impact cratering explosions. All three were in the valley alluvial fill of Area 10 at NTS, a loose sand-gravel mix with a density of 1.5-1.7 and a water content (at depth) of about 10%. The fourth nuclear crater, Neptune, was made in the bedded tuff of the Rainier mesa at NTS. This medium is a weakly cemented volcanic ash in which all the deep underground nuclear explosions (i. e., Rainier, Blanca, Logan, et al.) have been fired.[1]

---

*Work done under auspices of the U. S. Atomic Energy Commission.

In Table I are given the apparent crater dimensions, measured at the original ground level for these four nuclear craters. In Fig. 1 the crater profiles have all been scaled to 1 kiloton for comparison purposes. Brief discussions of the individual craters follow.

Table I. Summary of data for nuclear craters at the Nevada Test Site.

Shot name	Jangle S	Jangle U	Teapot ESS	Neptune
Medium	Alluvium	Alluvium	Alluvium	Tuff
Yield (kt)	1.2	1.2	1.2	0.115
Depth of burst (ft)	-3.5*	17	67	100**
Apparent crater radius (R) (ft)	45	130	146	100
Apparent crater depth (D) (ft)	21	53	90	35
Apparent crater volume (yd^3)	1650	3.7×10^4	9.6×10^4	2.2×10^4
R/D	2.14	2.45	1.62	2.86
Lip height (ft)	-	8	19	-

*Detonated 3.5 ft above surface.

**Detonated 100 ft beneath a 30° slope.

Jangle S

The Jangle S event was a 1.2-kt nuclear explosive detonated 3.5 feet above the surface of the ground in late 1951. As can be seen from Fig. 1, the crater formed was very small. Hardly any loose fallback material was found in the crater. The crater and lip were formed almost entirely by

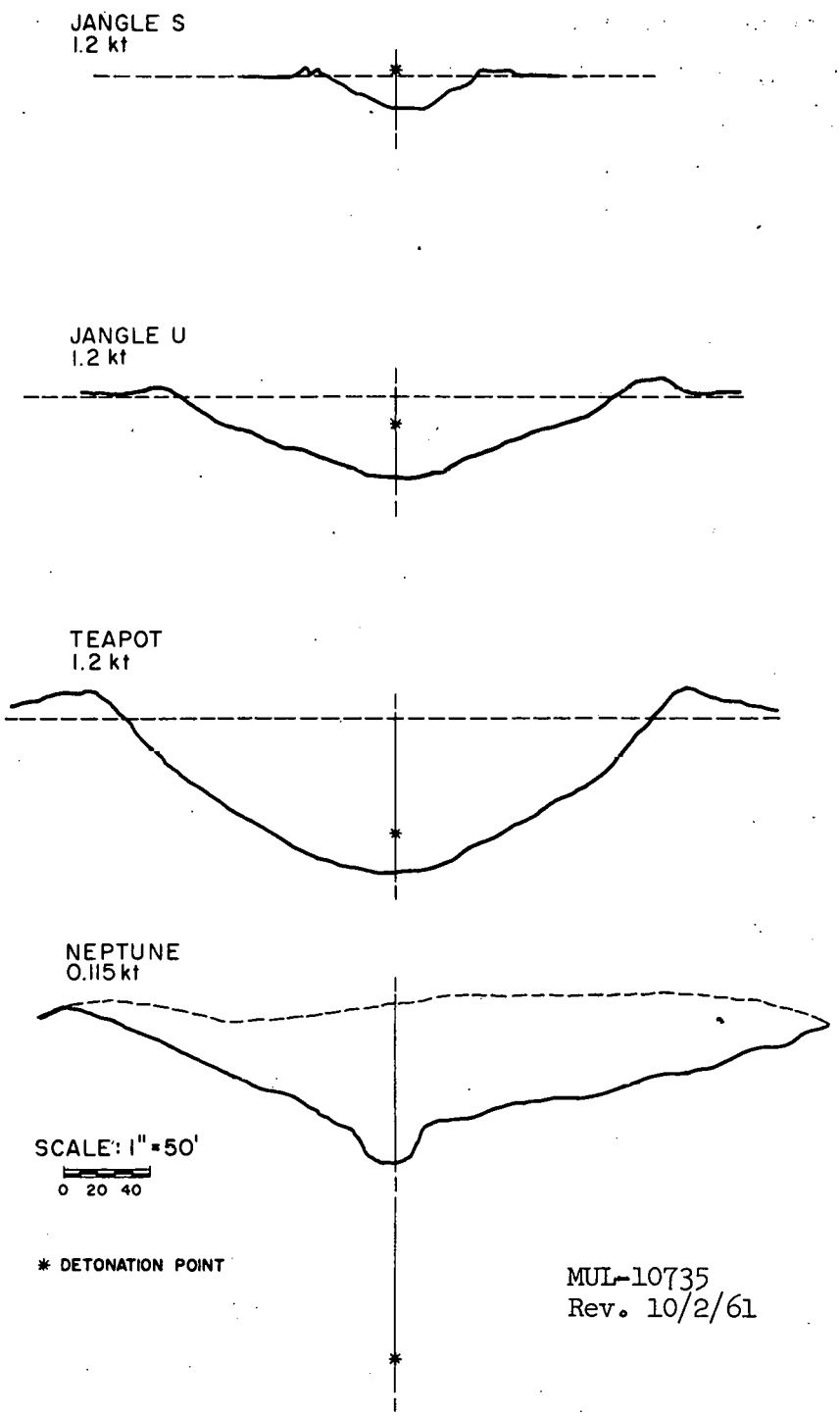

Fig. 1. Nuclear crater profiles.

plastic deformation of the ground by the action of the fireball. An additional reason for the small size is that for a nuclear device about a third of the released energy is in the form of thermal and x-ray radiation, which is lost immediately in a surface burst. In a subsurface burst this radiation energy vaporizes and melts the medium surrounding the device, and thus a portion of it is available for later utilization.

Jangle U

The 1.2-kt nuclear device used for the Jangle U event, also detonated in late 1951, was placed in a concrete-lined room 10 × 10 × 8 feet high. The hole leading from the top of the room to the surface was stemmed with a sandbag plug. The center of the device was 17 feet below the surface of the ground. The crater resulting from this explosion was considerably larger than the Jangle S crater but still much smaller than the maximum possible crater for a 1.2-kt explosion. A brief flash of the fireball was observed, but for a much shorter length of time than for Jangle S. A dense dust cloud rose to a height of about 6000 feet and a base surge was found which spread out radially to a distance of about 1 mile. Almost all the radioactivity escaped to the atmosphere and was deposited on the surface within 10 miles.

Teapot ESS

Teapot ESS was fired during Operation Teapot in March 1955 at a site very near the Jangle U crater. The 1.2-kt device was located 67 feet below the surface at the bottom of a 10-foot-diameter hole. A larger 30-foot-diameter hole was provided for personnel access prior to the explosion. The device was packed closely with sandbag plugs and both holes were filled with loose alluvial material before the detonation. A brief flash of very short duration was also observed on detonation of this device. Again a base surge about 1 mile in radius was formed. Survey of the total radioactivity after the explosion revealed that the activity was released in a manner similar to that of Jangle U. The crater had dimensions considerably larger than Jangle U because of the large depth of burst, which gave much better coupling of the

explosion energy to the ground. However, these dimensions are still much smaller than the maximum possible, based on high-explosive experimental data at large depths of burst.

An extensive program to delineate the true crater was undertaken for the Teapot event. Twenty-one colored sand columns were emplaced along a diameter to depths ranging from 50 to 200 feet in a manner shown in Fig. 2. Post-shot excavation of a trench through the crater along this diameter revealed the situation shown in Fig. 3. The true crater and rupture zones were fairly well defined by these columns. Of particular interest were the final locations of columns 9 and 13, which were extended and folded back over the edge of the true crater. The other columns show very strong effects of shear and rupture. On the basis of these data, the depth of the true crater is believed to be 128 feet and the radius 150 feet. The depth of the rupture zone can only be estimated, but its radius is believed to be 250-275 feet.

Figure 4 is an aerial view of Area 10 showing Teapot ESS and Jangle U in top center. The trench in Teapot ESS is clearly visible. The recent high-explosive craters described by Murphey,[2] including Scooter in the lower center and the three Stagecoach craters on the left, are also visible.

Neptune

The Neptune event occurred during Operation Hardtack, Phase II, on 14 October, 1955.[3] It was a 115-ton nuclear device fired at a point 100 feet below a 30° slope in bedded tuff. The vertical distance to the surface was 110 feet. The zero point room was 12 × 17 × 10 feet high with a concrete floor. The tunnel configuration was a buttonhook in shape and was stemmed before the shot in several places with sandbag plugs.

Upon detonation, the surface rose in a hemispherical dome to a height of 25-35 feet before breaking up. Then venting gas and ejected material appeared, with large rocks going 80-100 feet in the air. A large dust plume was formed which rose to a height of about 1000 feet. A large mass of rock

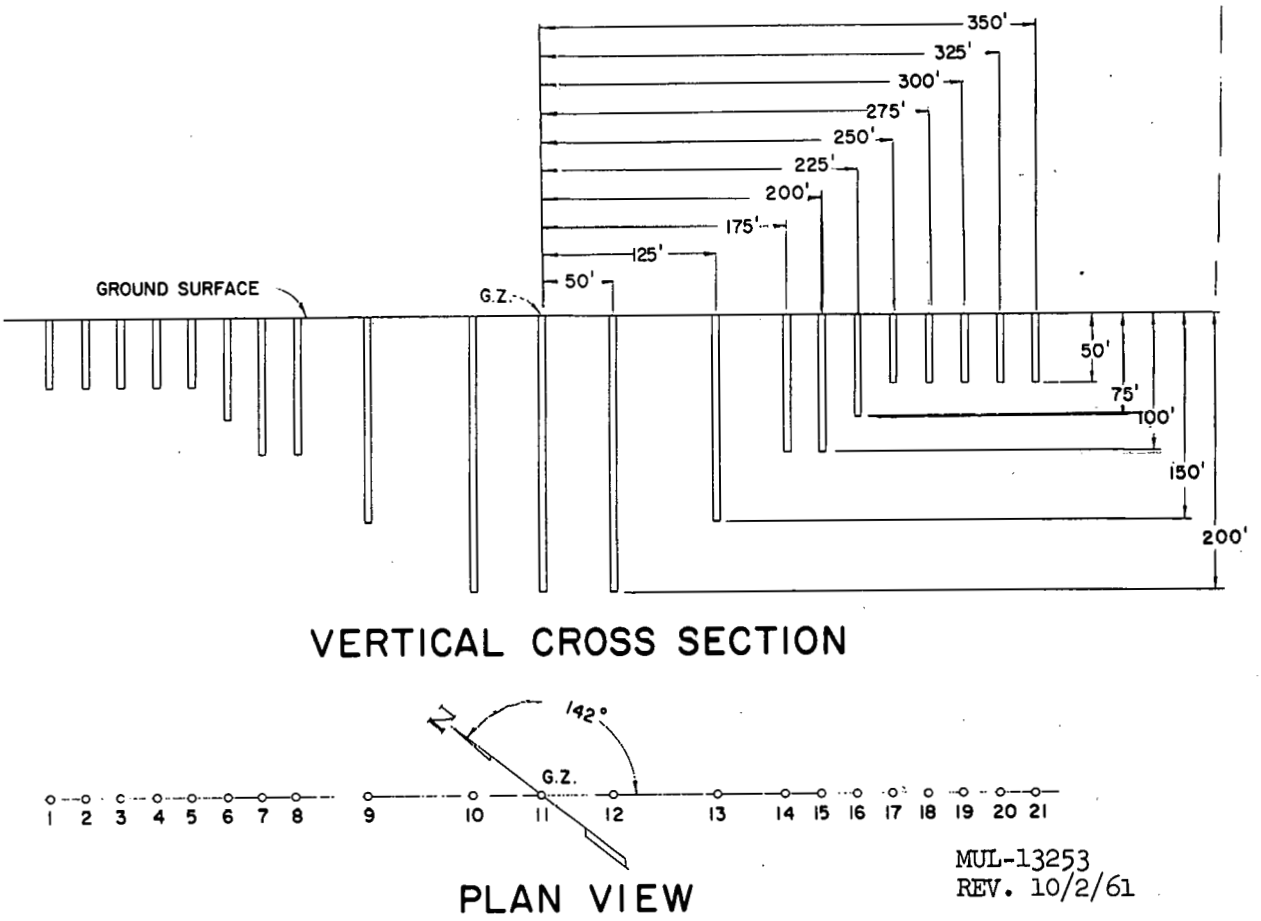

Fig. 2. Pre-shot locations of sand columns for Teapot ESS.

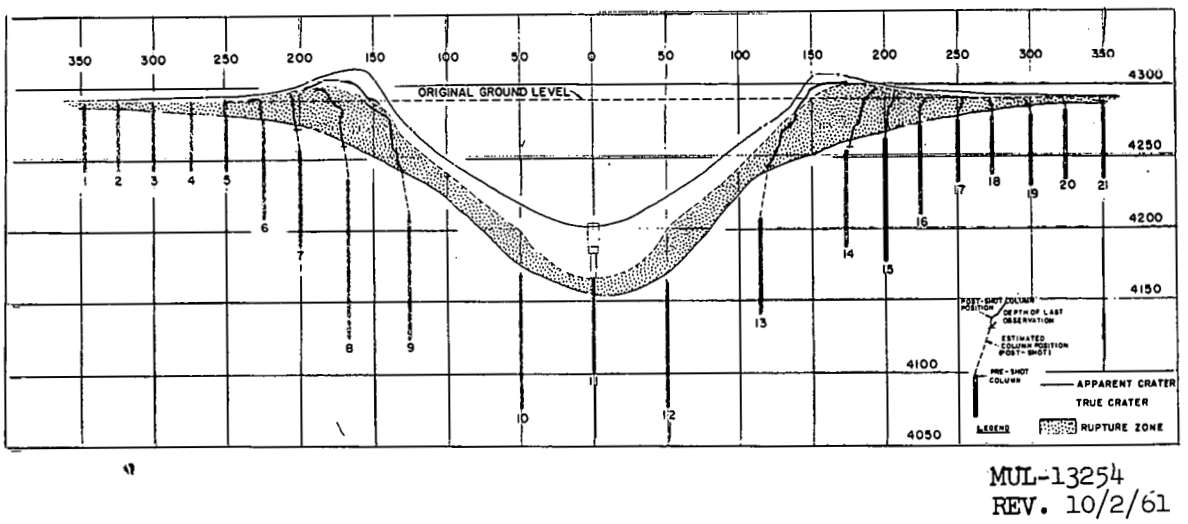

Fig. 3. Post-shot locations of sand columns for Teapot ESS.

Fig. 4. Aerial photograph of Area 10 showing craters.

and debris cascaded down the slope (upwind), carrying small amounts of radioactivity into gullies as far away as about 2000 feet.

The shape of the crater formed by the Neptune detonation was influenced by the slope of the surface in that almost all the debris formed a slide originating at the lower edge of the crater and terminating about 800 feet down the slope. The mean diameter was 200 feet, and maximum depth was 35 feet.

A total of 11 holes have been drilled into the region surrounding the Neptune detonation to determine the physical state of the rock and to delineate the radioactive regions.[4] Figures 5 and 6 show these holes and the picture of the post-shot state of the medium derived from them. Most of the layers overlying the shot retained their continuity but collapsed into the cavity produced by the explosion. The mixing that occurred was minor and the different lithologic units are still easily identifiable.

Crushing of the tuff occurred to a distance of 40 feet downward and 50 feet laterally except in the direction of the original drift where crushing extended to 80 feet. The extent of crushing was apparently influenced by bedding plane weaknesses. Fracturing of the material extended to 70 feet in the hemisphere below the zero point, according to interpretations of cores. Above the original zero point, fracturing extended to the surface, the boundary of fracturing lying on a core whose top extended slightly beyond the surface crater region.

Integration of the total fallout patterns on the surface indicates that 1-2% of the total fission product activity produced by the explosion escaped from the crater. Due to the presence of certain volatile isotopes at early times, this activity is enriched by a factor of five in Sr^{90}, Sr^{89}, and Cs^{137}.

Discussion

The results of these four nuclear-explosion craters are shown in Figs. 7 and 8, where all the pertinent high explosive data have also been plotted. Both nuclear and high explosive data have been plotted using $W^{1/3.4}$ scaling. This type of scaling has been derived on the basis of high explosive data alone as outlined by Vaile.[5]

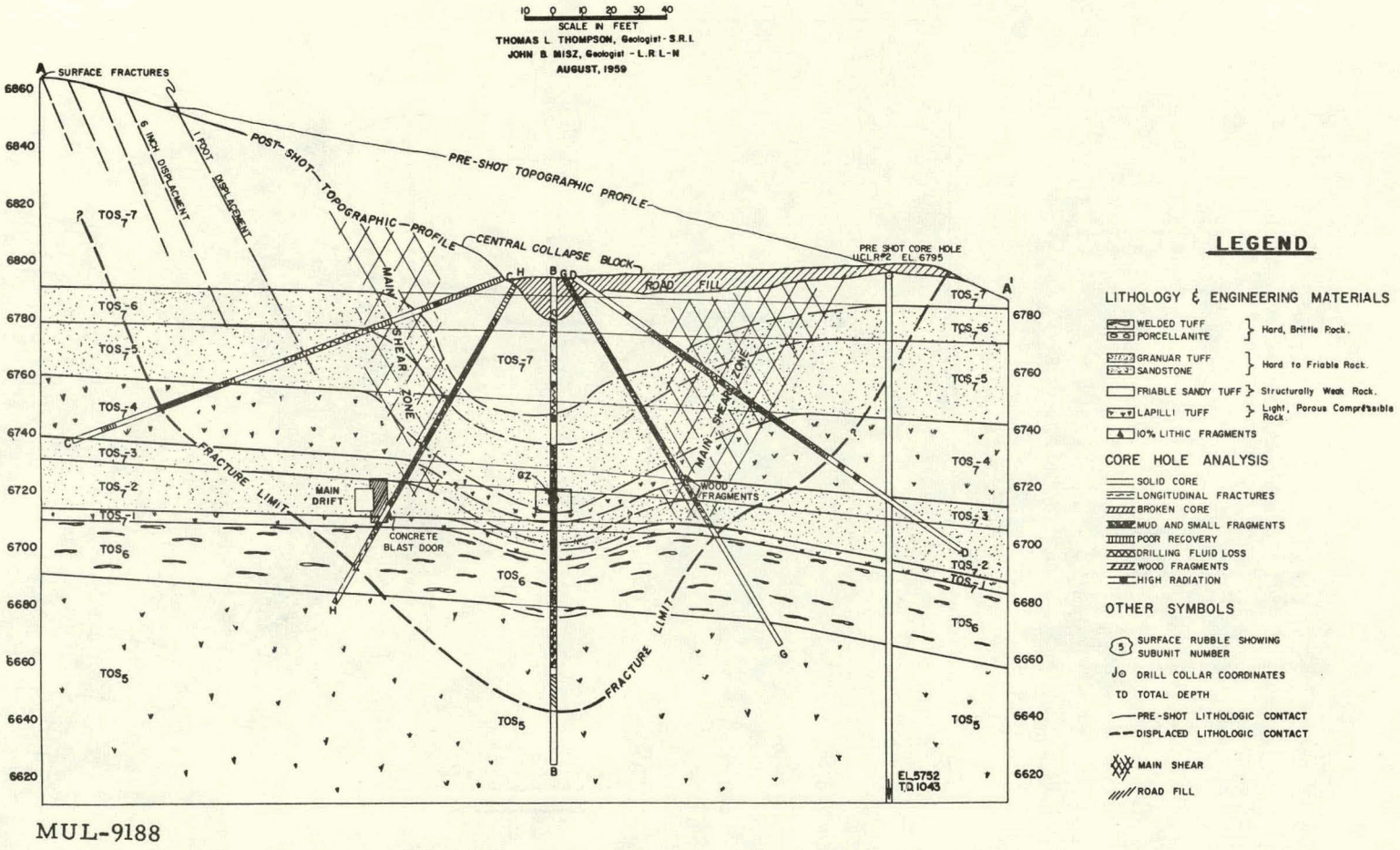

MUL-9188

Fig. 5. Post-shot exploratory drilling for Neptune.

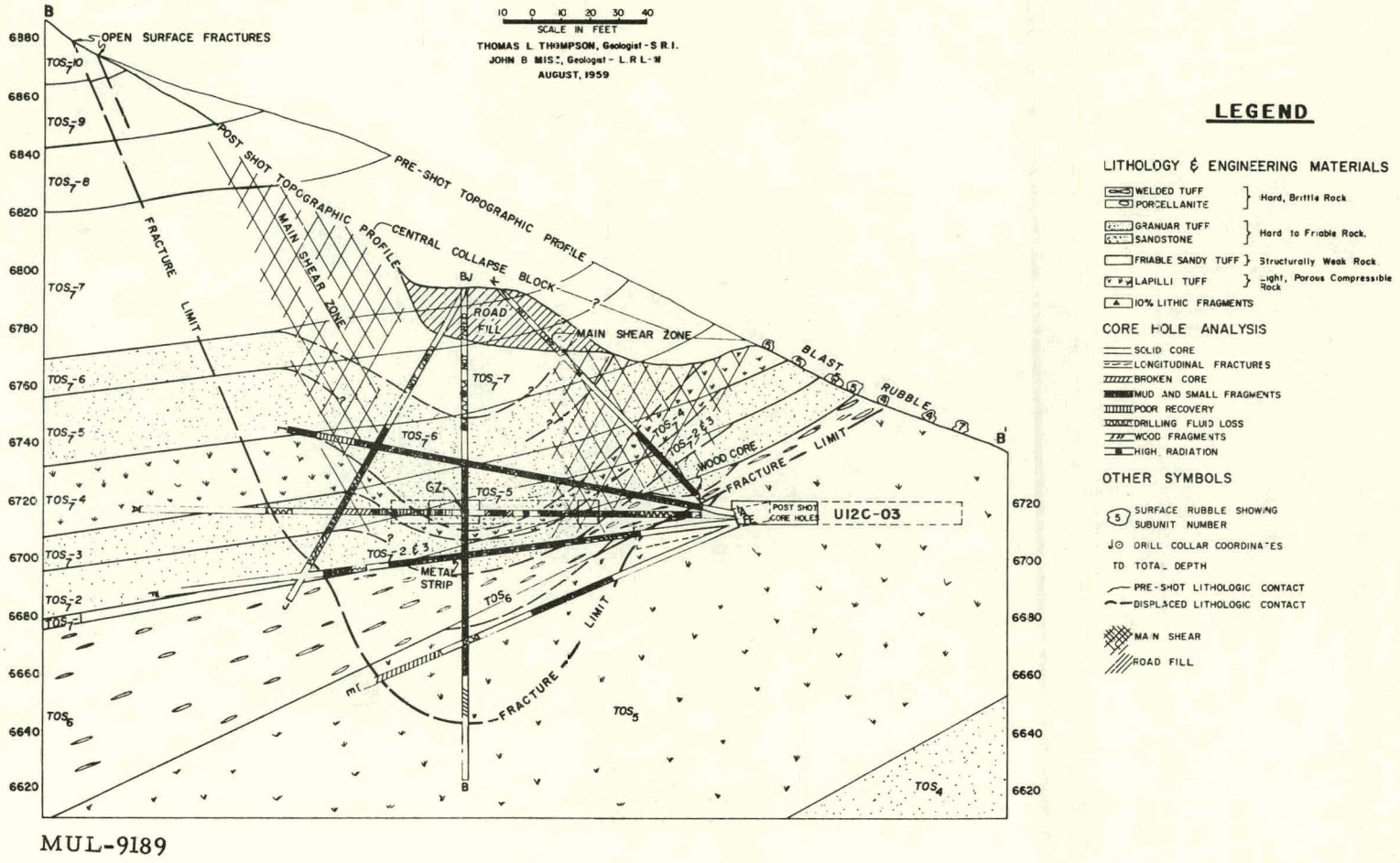

MUL-9189

Fig. 6. Effects of Neptune explosion on surrounding medium, as deduced from post-shot drilling.

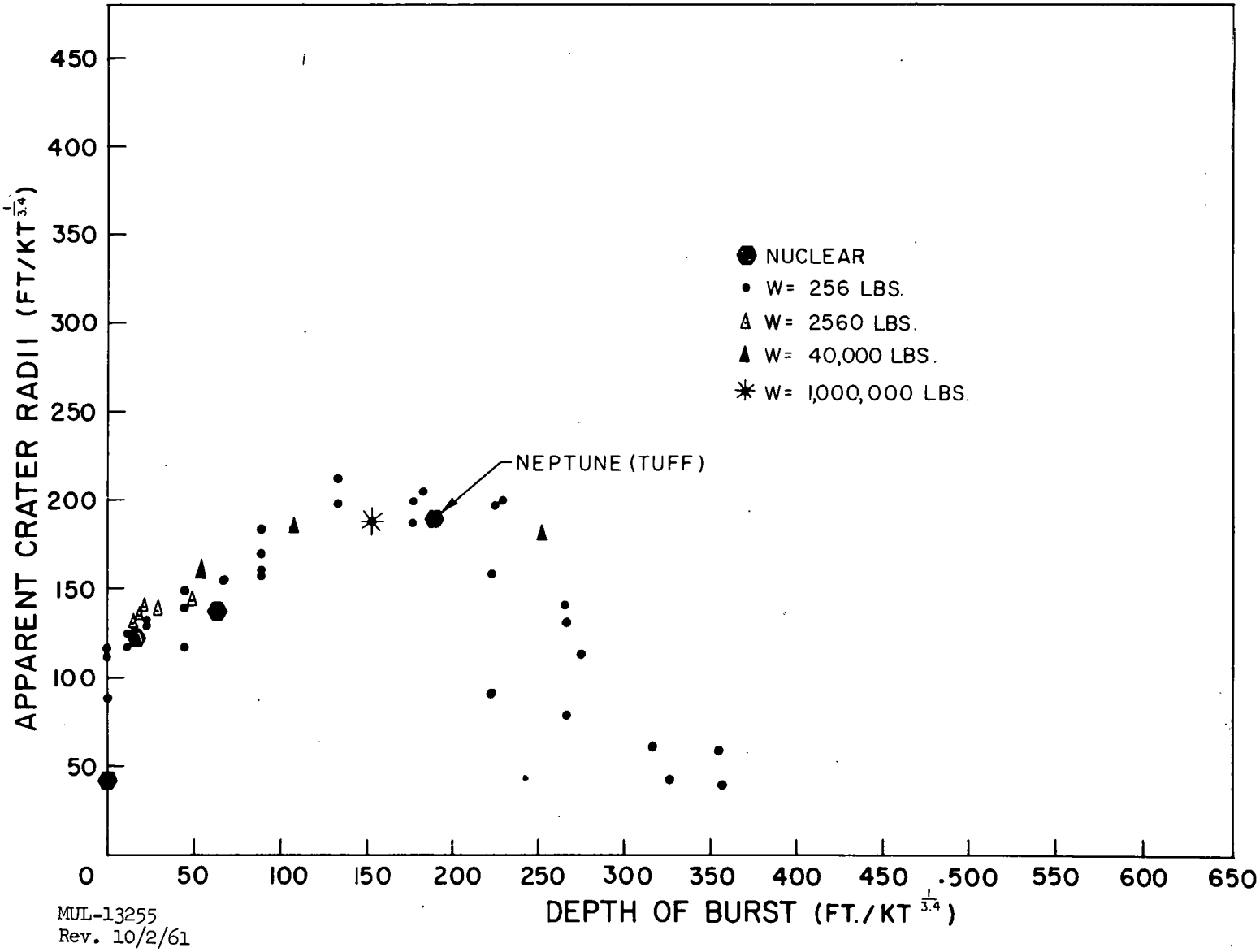

Fig. 7. Crater radius vs depth of burst for high explosives and nuclear explosives in NTS alluvium, with $W^{1/3.4}$ scaling.

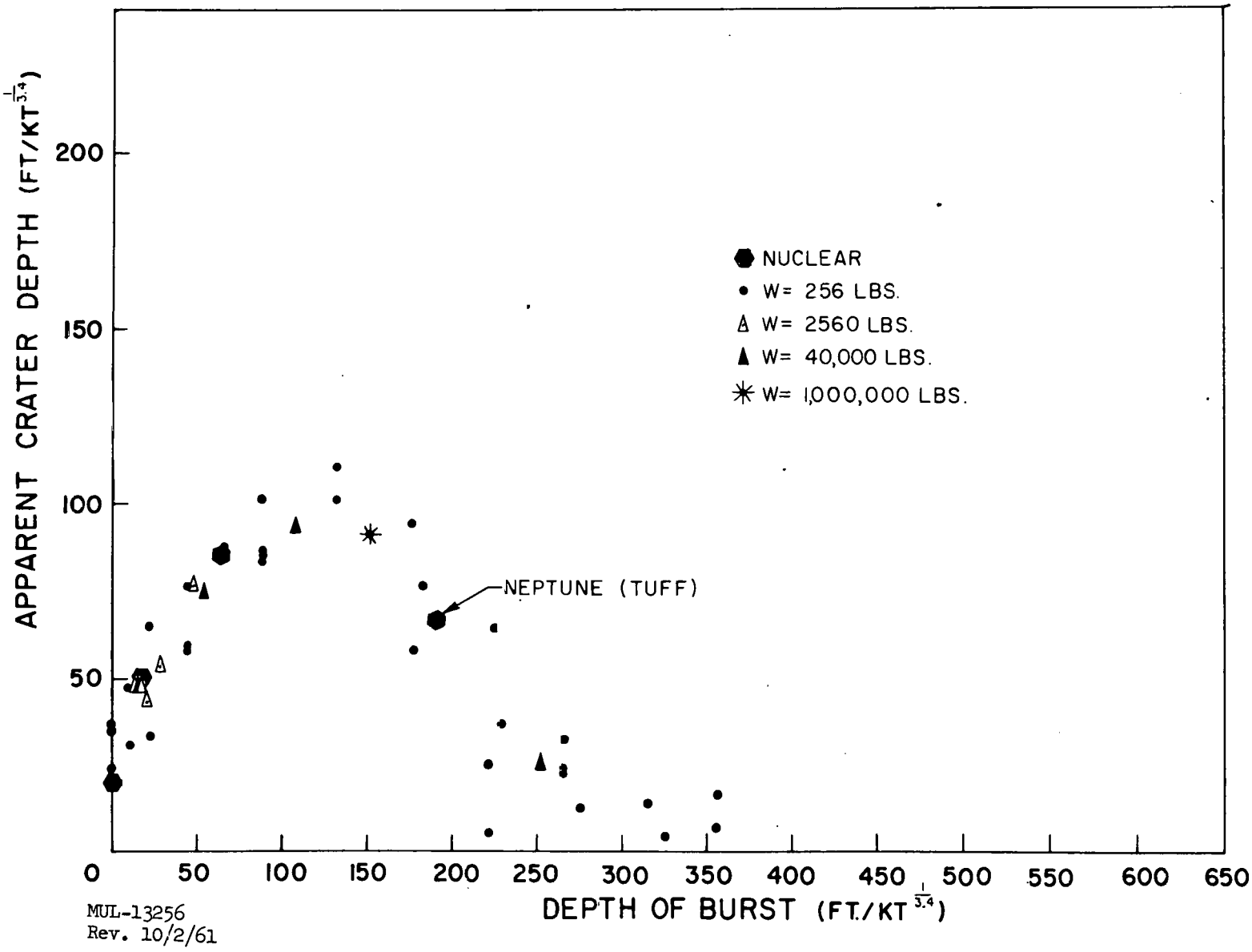

Fig. 8. Crater depth vs depth of burst for high explosives and nuclear explosives in NTS alluvium, with $W^{1/3.4}$ scaling.

The nuclear data in Figs. 7 and 8, with the exception of Jangle S, fall well within the scatter of the high explosive data. Hence one is led to the conclusion that for subsurface detonations the crater-producing efficiency of nuclear explosives is approximately 90-100% that of high explosives, when experimental errors are considered.

It is interesting to note that the Neptune point falls on the alluvium curve even though it was in tuff. The effect of the hillside may have just compensated for the decrease in crater dimensions expected for a cratering detonation in a soft rock, thus producing a crater with dimensions proper for alluvium.

REFERENCES

1. Johnson, G. W., Higgins, G. H., and Violet, C. E., Underground Nuclear Detonations, J. Geophys. Research 64, 1457-1470 (Oct., 1959).

2. Murphey, B. F., Explosion Craters in Desert Alluvium, Paper G, Proceedings of Lawrence Radiation Laboratory – Geophysical Laboratory Cratering Symposium, Univ. Calif. Lawrence Radiation Laboratory Report UCRL-6438 (June, 1961).

3. Shelton, A. V., Nordyke, M. D., and Goeckerman, R. H., The Neptune Event, Univ. Calif. Lawrence Radiation Laboratory Report UCRL-5766 (April, 1960).

4. Thompson, T. L. and Misz, J. B., Geologic Studies of Underground Nuclear Explosions Rainier and Neptune, Final Report, Univ. Calif. Lawrence Radiation Laboratory Report UCRL-5757 (Oct., 1959).

5. Vaile, R., Pacific Craters and Scaling Laws, Paper E, Proceedings of Lawrence Radiation Laboratory – Geophysical Laboratory Cratering Symposium, Univ. Calif. Lawrence Radiation Laboratory Report UCRL-6438 (June, 1961).

Paper G

EXPLOSION CRATERS IN DESERT ALLUVIUM*

Byron F. Murphey

Sandia Laboratory, Albuquerque, New Mexico

ABSTRACT

Explosion craters in desert alluvium have been formed over a range of energy releases from 256 pounds of TNT to 1 million pounds (Scooter event). Scooter crater is 307 feet in diameter and 75 feet deep. An empirical scaling law in which crater dimensions vary as the energy release to the 0.3 power best relates dimensions from small to large chemical explosions. Consideration of overburden leads to a partial explanation of the failure of cube-root scaling. Optimum depth of burst for 256-pound chemical explosions in desert alluvium is near 10 feet. Diameter-depth ratios vary from roughly 6-8 to 1 for surface bursts to 4 to 1 for bursts at optimum depth.

* * *

Craters produced by underground explosions have dimensions which depend on many parameters. I shall discuss the dependence on the charge depth and energy of the burst. The craters to be described were all produced in desert alluvium at the AEC Nevada Test Site by chemical explosives – spherically shaped charges of cast TNT. The amount of TNT used in these experiments ranged from a few pounds up to the largest shot which was 1 million pounds.[1]

The half-kiloton (i.e., million-pound) charge† was buried at a depth of 125 feet. The depth of the crater in Fig. 1 is 75 feet. The diameter at original ground level is 307 feet, which is about the length of a football field. The

---

*Work performed under the auspices of the U. S. Atomic Energy Commission.

†The Scooter explosion was part of the Plowshare experimental program.

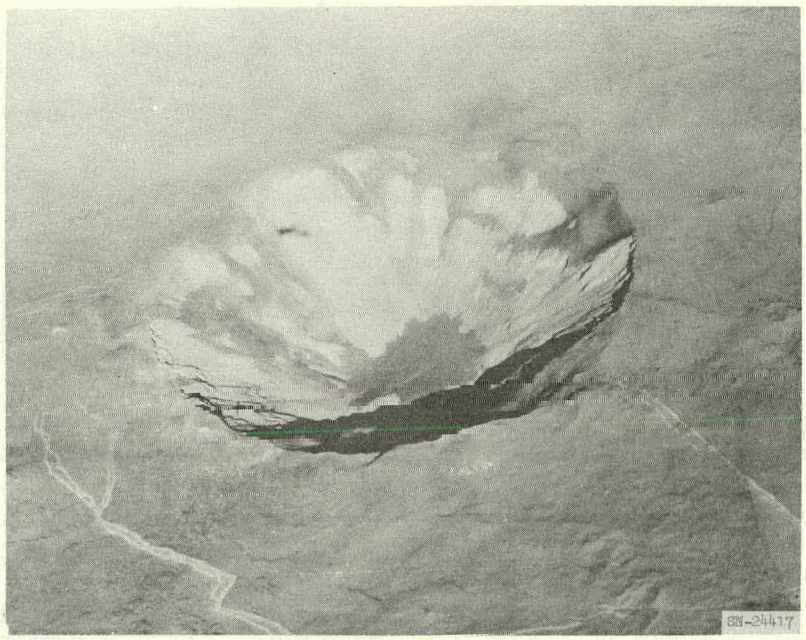

Fig. 1. Aerial view of Scooter crater.

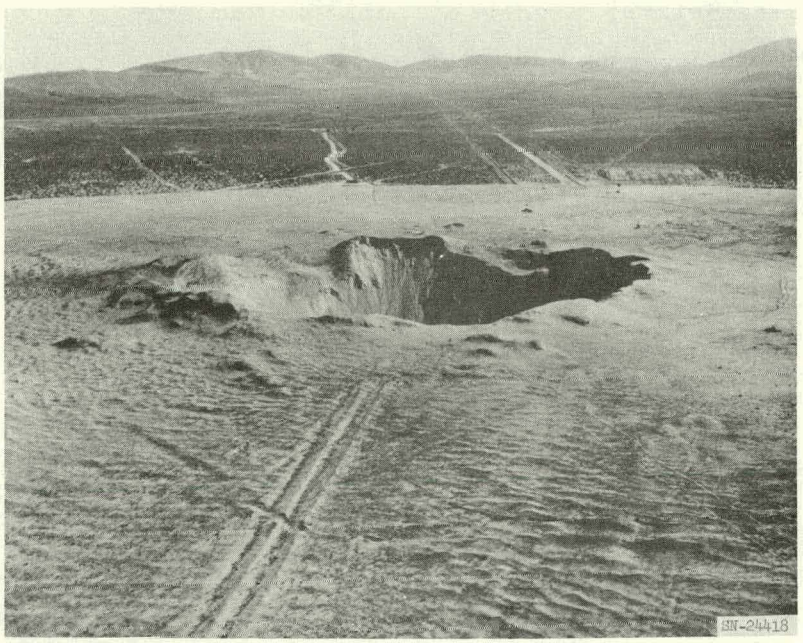

Fig. 2. View of Scooter crater lip.

flat bottom is very soft material and lies 50 feet above the position of the charge. Another view of the crater, Fig. 2, gives some impression of the lip size, which was only 8 or 9 feet. This crater is not quite as large as would be predicted by simple cube-root scaling from crater dimensions obtained from much smaller charges.

Cross sections of craters[2,3] produced by 256-lb TNT charges burst at several depths are shown in Fig. 3. The very great importance of deep, but not too deep, burial is apparent. Incidentally, the energy available in the explosive far exceeds the work done in forming any of these craters, even when required lifting of the material is taken into account. Note that no appreciable crater is formed for depths of burst beyond DOB = $3W^{1/3}$ ft (W in pounds TNT). Using cube-root scaling, I have scaled the crater which would occur at a depth of burst of 8 feet to a crater that might be obtained from 1 million pounds burst at the corresponding depth (125 feet), Fig. 4.

Quite obviously, extrapolation of cube-root scaling to large yields is not warranted; the dimensions that would be predicted are in this case too large by more than 50 percent. I hasten to add that this result had been forecast empirically from experiments with 256, 2560, and 40,000 pounds[2,4] of TNT and observations of craters from two nuclear explosions. The next three figures illustrate the data with different types of scaling.

The failure of cube-root scaling appears again in Fig. 5 in which all the crater data obtained in desert alluvium have been reduced in accordance with the cube root of the energy release of each explosion. Note the scatter of points for the smaller charges. Scatter is avoided for the large explosions by the simple expedient of not repeating shots. Seriously, effects of nonuniformity of medium are much reduced for larger explosions. These data have been fitted by trial and error to obtain the empirical scaling law illustrated in Fig. 6. The rule that $W^{0.3}$ instead of $W^{0.33}$ should be used has been obtained independently by at least four different groups.[5,6] To what extent this rule may be extrapolated to larger yields than a kiloton is not known. One possible reason for failure of cube-root scaling is, of course, simple failure to consider gravitational forces.

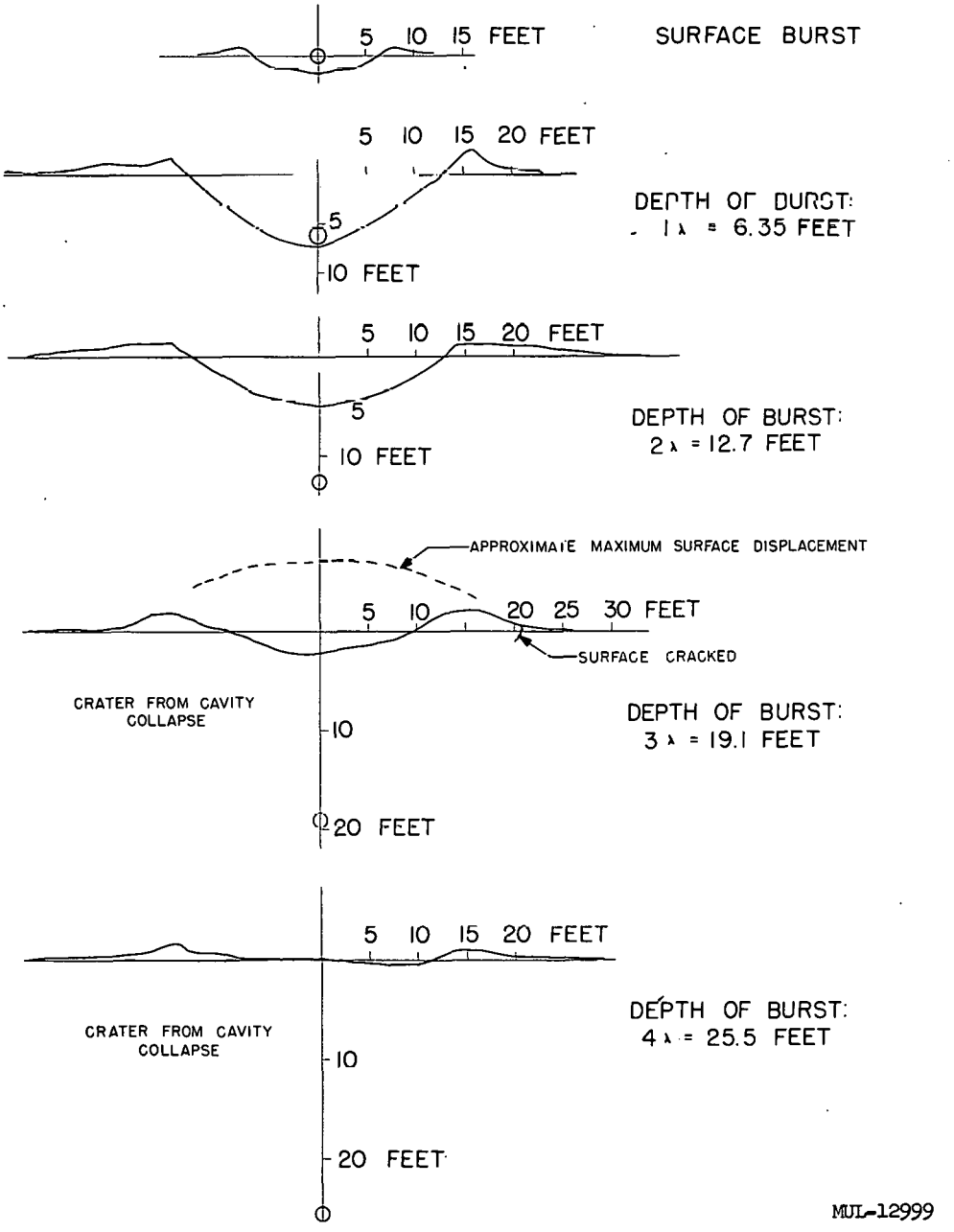

Fig. 3. Crater profiles versus depth of burst.

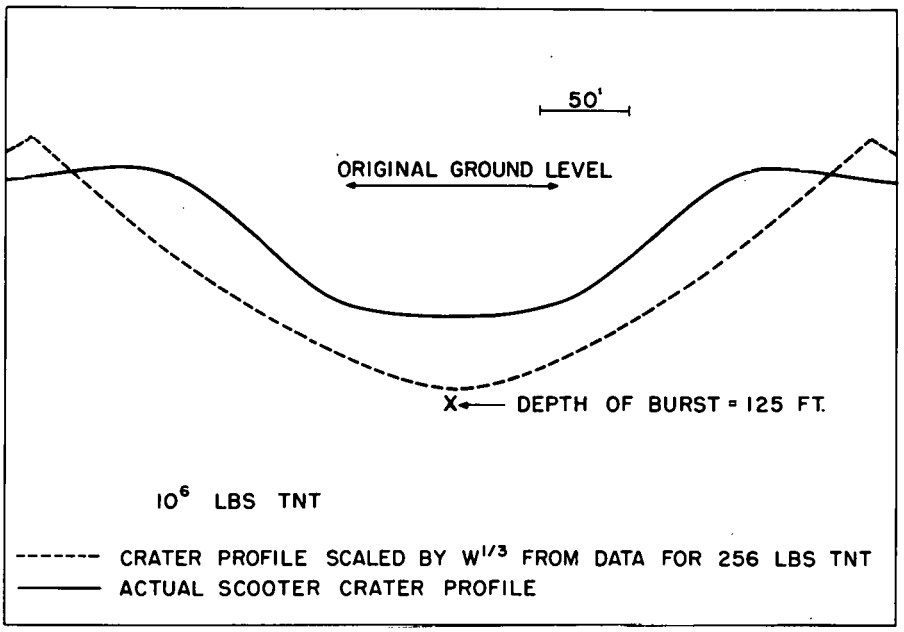

Fig. 4. Scooter crater profile compared with scaled small-charge crater profile.

If effect of gravity is included[7] in scaling, Fig. 7, nearly as good a fit is obtained as was shown in Fig. 6. It appears, therefore, that the most likely correction is the correct one.

Study of ground motion above buried explosions provides some information about the mechanism of cratering. Surface motion was photographed above the various 40,000-lb TNT charges placed at depths of burst of 17.1, 34.1, and 80 feet (Project Stagecoach*).[4]

Time scales of the deeper explosions are extended compared to the shallower. This is also true of large versus small explosions. Corresponding times are longer in proportion to the cube roots of the charge weights. The velocity and acceleration of surface movement have been obtained from motion pictures. Figure 8 illustrates early surface velocity versus time for the three 40,000-lb shots. Note that the velocity decreases very roughly as the square of the depth of burial. The corresponding accelerations are shown in Fig. 9.

---

*Supported in part by the Defense Atomic Support Agency.

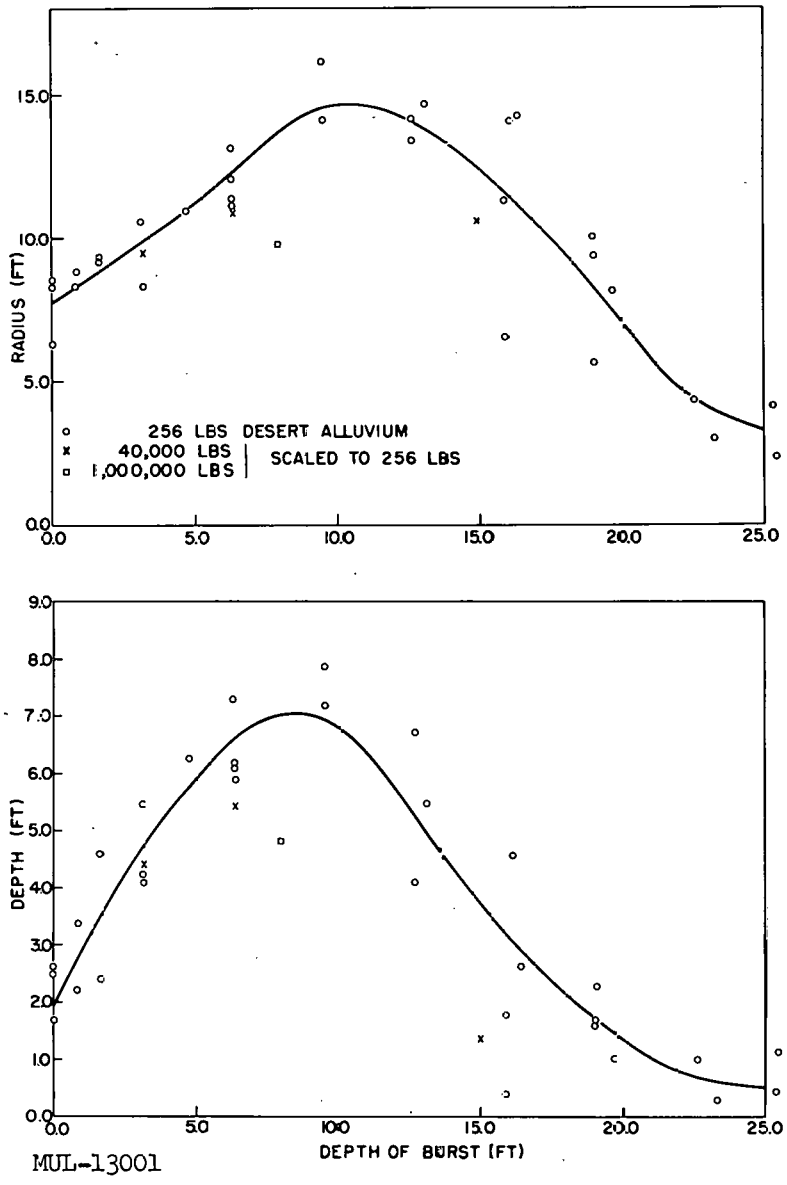

Fig. 5. Depth-of-burst curves with cube-root scaling.

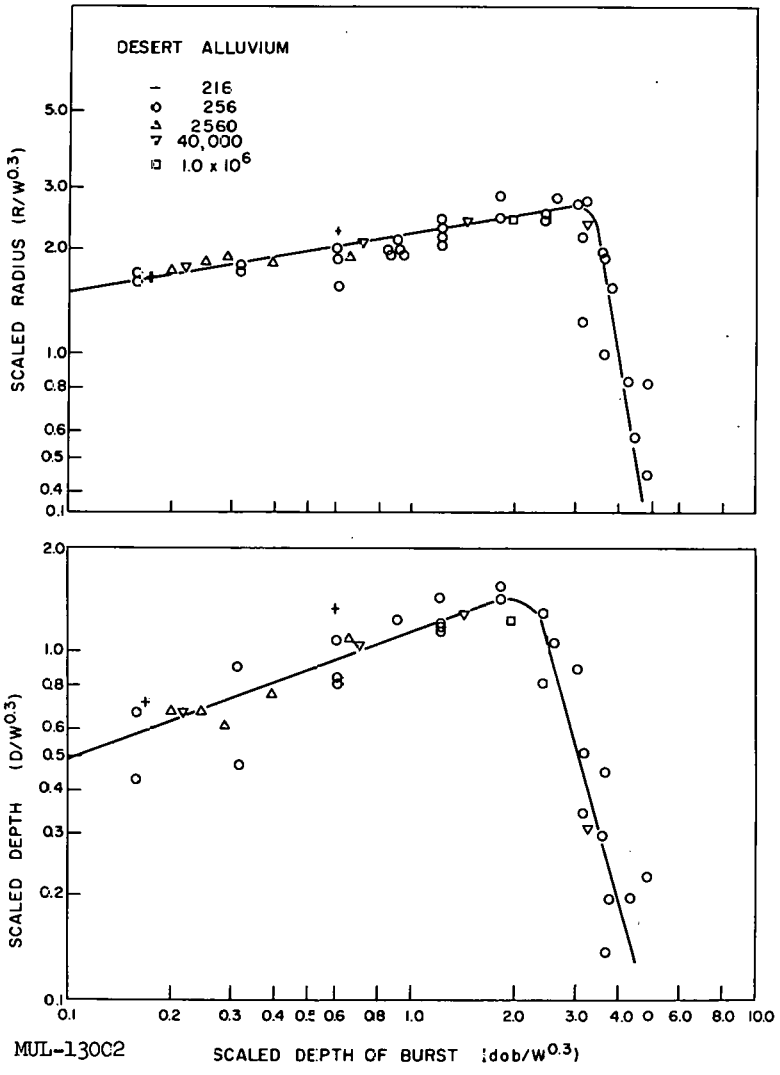

Fig. 6. Depth-of-burst curves with 0.3-power scaling.

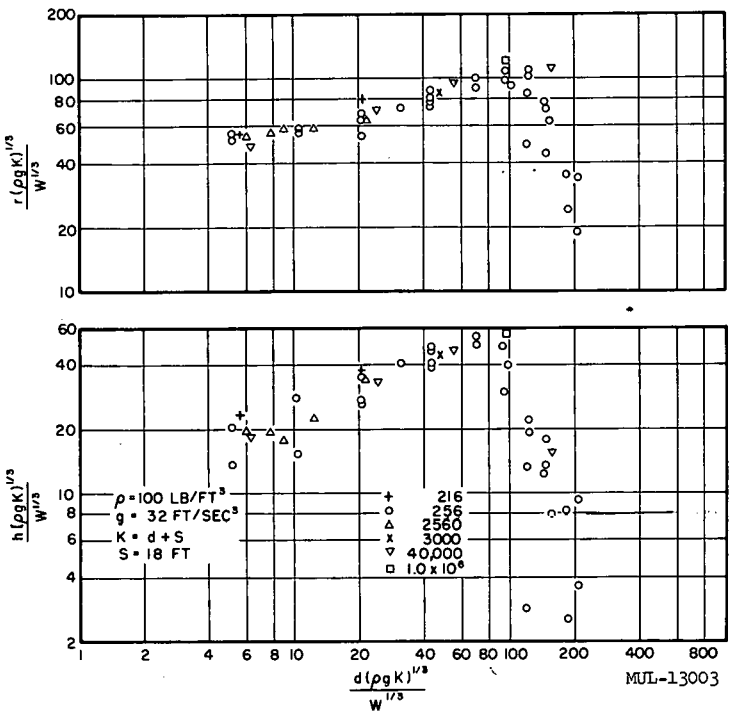

Fig. 7. Depth-of-burst curves with gravity considered.

Acceleration of the surface decreases roughly as the 4th power of the depth of burial. Thus the 20-g acceleration in evidence for the 80-foot-deep shot drops rapidly toward 1 g as the observation point is shifted away from surface zero toward the edge of the expected crater. When accelerations are geometrically scaled to larger charges, accelerations at corresponding distances will be smaller as the cube root of the ratio of the charge weights. Of course times are longer in the same proportion. Nonetheless, if scaled accelerations become less than 1 g, no cratering can occur from throwout of material.

Let us, therefore, inquire in more detail about the processes that occur. We shall take Scooter[1] as our example, because some underground particle motion data are available. An accelerometer and a velocity gage were located at shot depth on a horizontal radius at a distance from the zero point of 200 feet. The distance of 200 feet turns out to be equal to the slant distance at which the apparent crater radius eventually existed. The velocity pulse arrived at +50 msec and lasted for nearly 250 msec before changing direction.

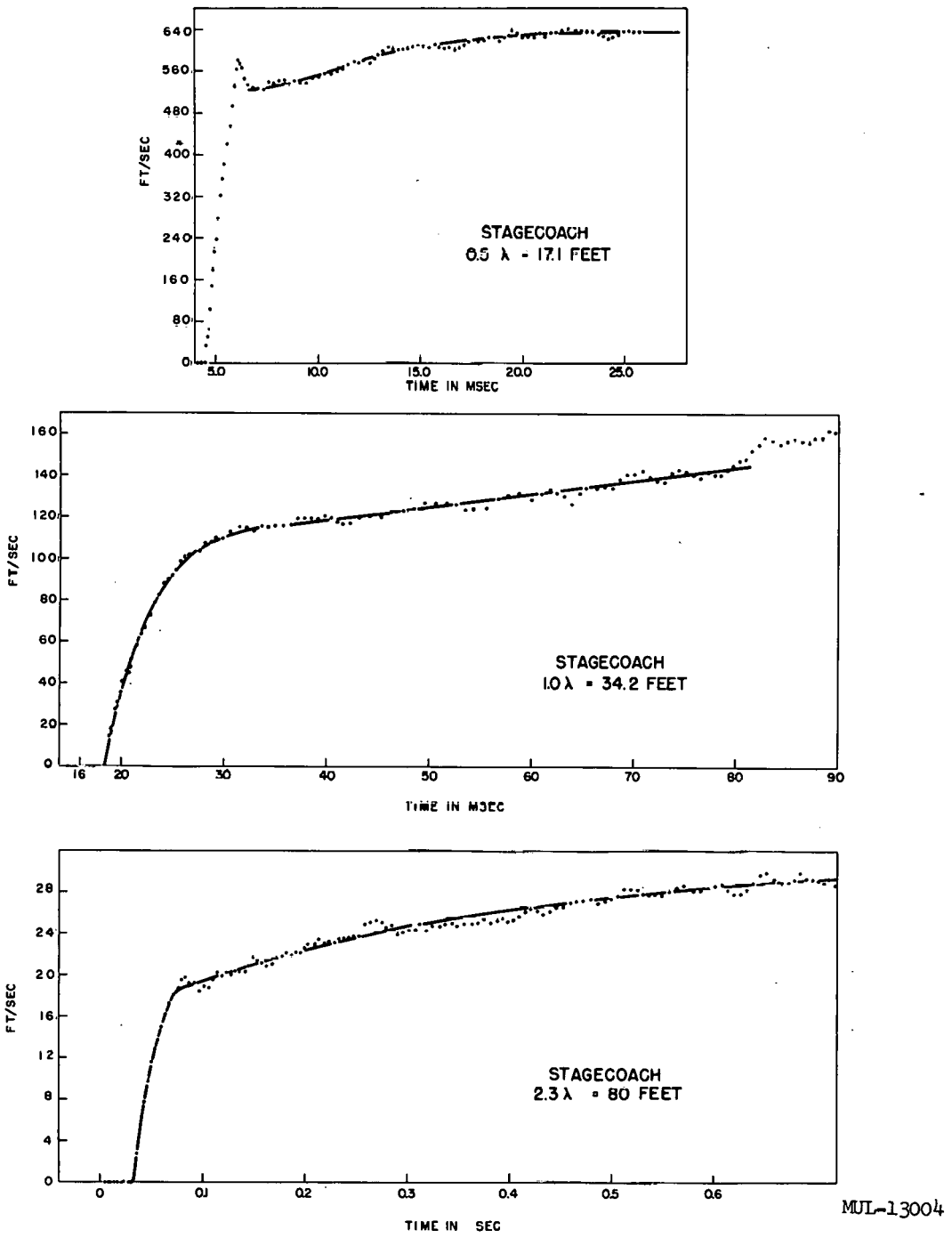

Fig. 8. Initial vertical surface velocities.

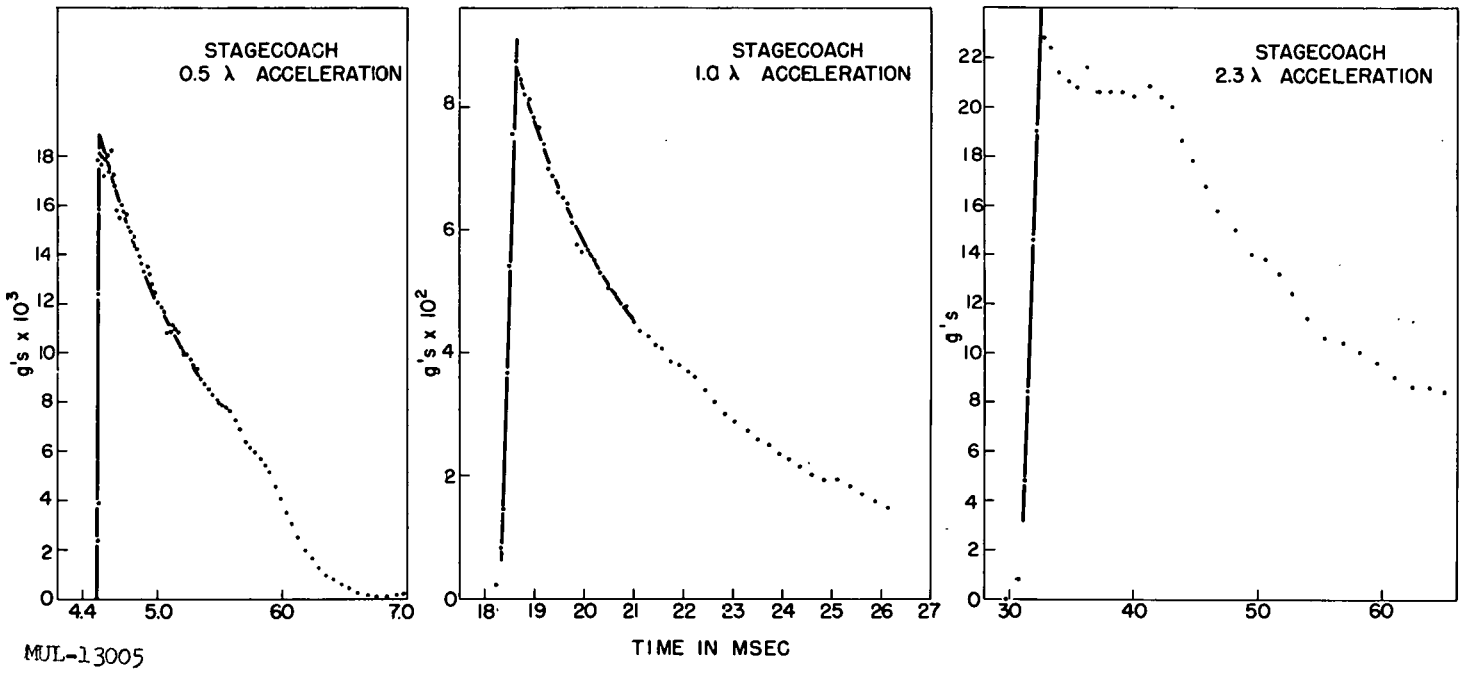

Fig. 9. Initial vertical surface accelerations.

The peak value was about 8.5 ft/sec. Accelerations involved are from 2 to 5 g. The vertical components of peak velocity and acceleration turn out to be 5.3 ft/sec and 1.3 to 3.1 g, which numbers are to be roughly doubled to account for reflection from a free surface. Under the influence of gravity, the free-surface upward velocity will drop to zero in 1/3 second, so that the surface has 2/3 second for horizontal motion. It can move about 5 or 10 feet in this time. Now consider an interior point where we were able to trace the motion of a target for 2.5 seconds. The target was on the surface at a horizontal distance of 120 feet from surface point above zero. The over-all arrangement of targets is shown in Fig. 10.

The slant range is 173 feet. Interpolating from the subsurface motion measurements at 150 and 200 feet gives a peak particle velocity in the medium of 13.1 ft/sec. The doubled vertical component would be about 14.5 ft/sec. We find from analysis of motion picture photography that the early vertical velocity is 17.5 ft/sec. We also find that this velocity is sustained for nearly 1 second, after which it drops to zero by 1.45 seconds. Obviously, something more than the initial acquired particle motion is responsible for the eventual movement. This something is, of course, residual gas pressure and trapped momentum which enlarges the original cavity in the direction of the free surface. Closer to the center of the eventual crater, the surface velocity continued to increase to the time of venting.

The displacements[8] of four of the Scooter targets are shown in Fig. 11. Venting of the black H.E. explosion products started at 0.6 second.

The above data provide some quantitative feeling for surface motions that actually took place on Scooter. We have found that just beyond 150 feet the late motions are small. Note that on the scale of 256 pounds they would still be of significance. We have found that we can scale particle motion in the medium from 256 pounds to 1 million pounds without appeal to failure of cube-root scaling. The failure of scaling for crater dimensions lies in the marginal motions near the edge of the crater. The material that starts into large motion but falls within the crater wall slumps to the bottom to fill it and decrease the apparent depth. Air drag becomes increasingly effective in this regard as the time during which it may act becomes longer.

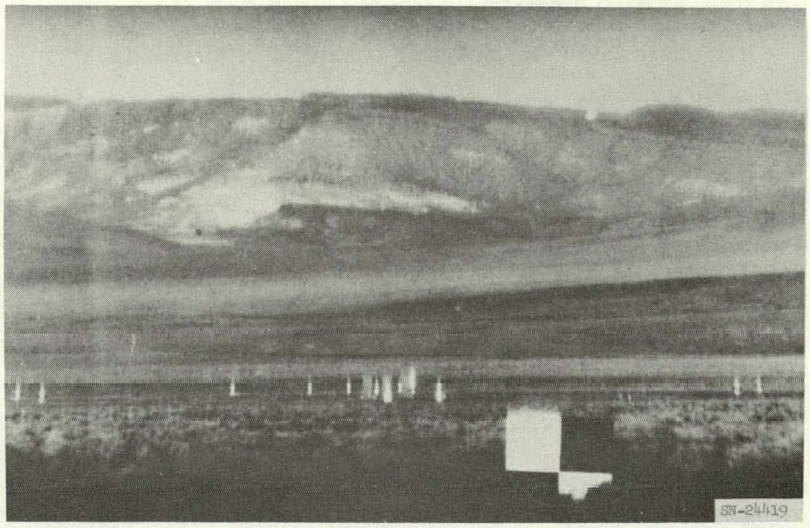

Fig. 10. Target array over Scooter at zero time.

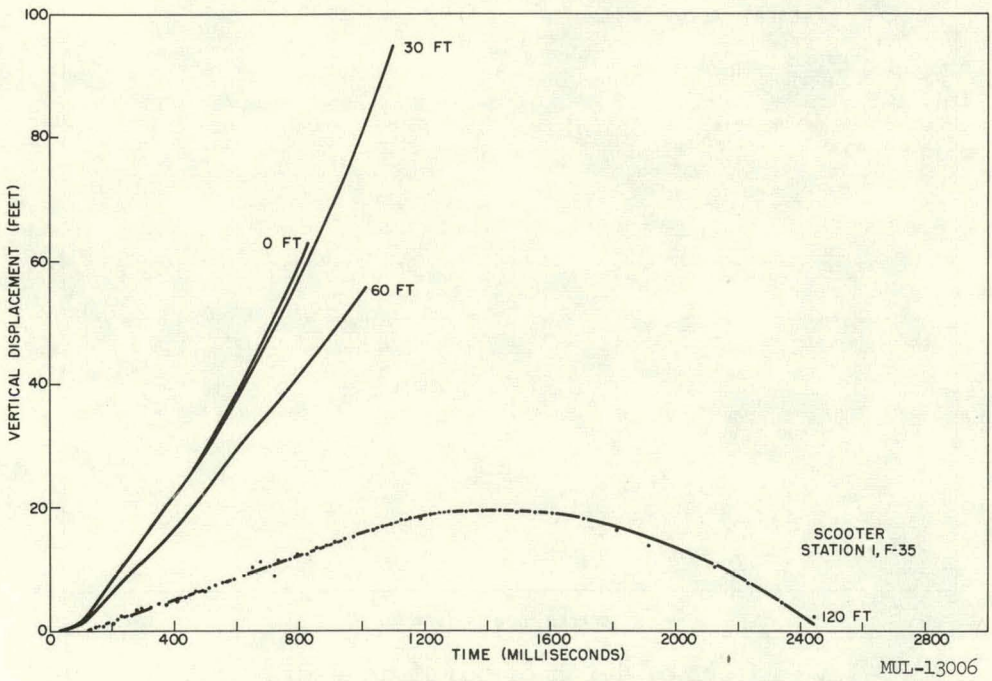

Fig. 11. Target displacements.

We can inquire also from these data into the effect of medium properties upon cratering action. The radial stress that occurred at 200 feet on Scooter would be about 600 psi. We know from the small explosion tests,[2] and Scooter data agree, that the radial stress falls off as $1/r^3$ in soil. Measured from surface zero, the vertical component of radial stress or particle velocity falls off as the 4th power of the radial surface distance. In hard rock, on the other hand, radial stress and particle velocity decrease with distance more nearly as $r^{-1.6}$. However, rock is much stronger. The cavity formed will be smaller, and the cratering action that does take place will involve higher velocities toward the center. Also, because of the greater rock strength, the gas bubble will be even less effective toward the side than in soil. As you know, these conflicting tendencies balance out somewhat so that rock craters are not so much smaller than craters in soil as one might expect.

In conclusion, a collection of radius-to-depth (R/D) ratios for most of the crater data obtained in desert alluvium is shown in Fig. 12.

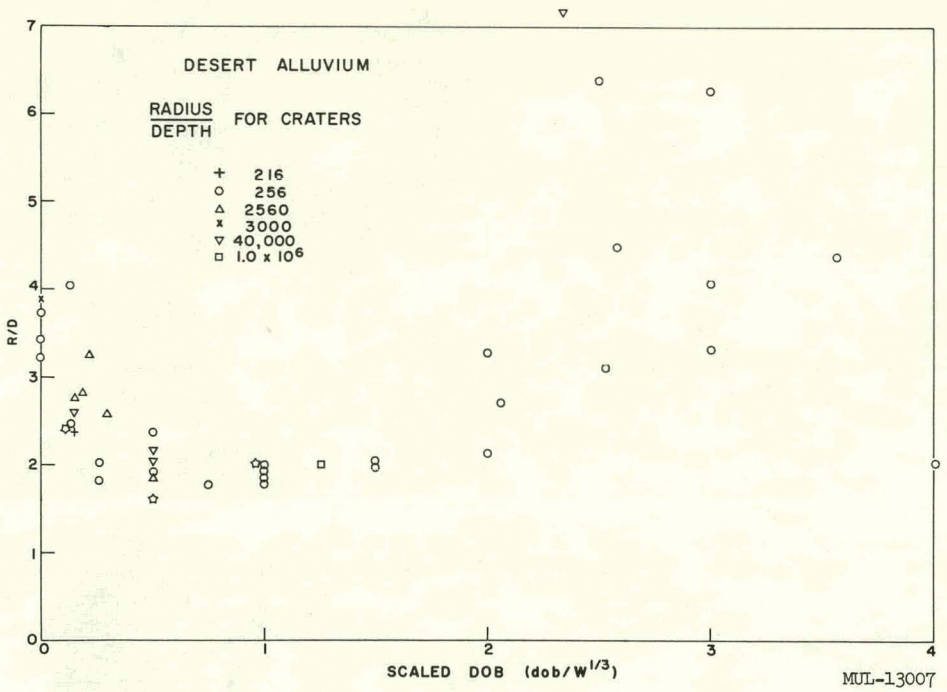

Fig. 12. Effect of depth of burst on radius-depth ratio.

R/D versus depth of burst has been plotted. Note that the ratio varies from 4 to 1 for shallow bursts to 2 to 1 over the range of depths for optimum crater size. At greater depths of burst where containment is approached, a wild scatter of large values appears.

REFERENCES

1. Perret, William R., et al., Mechanisms of Crater Formation – Project Scooter, Sandia Corporation, SC-4602(RR), to be published.

2. Sachs, D. C. and Swift, L. M., Small Explosion Tests, Project Mole, Stanford Research Institute, AFSWP-291, Vol. II, December, 1955.

3. Murphey, B. F. and MacDougall, H. R., Crater Studies – Desert Alluvium, Sandia Corporation, SCTM 119-59(51), May, 1959.

4. Chabai, A. J. and Vortman, L. J., Project Stagecoach (Interim Report), Sandia Corporation, SCTM 181-60(51), May, 1960.

5. Chabai, A. J., Crater Scaling Laws for Desert Alluvium, Sandia Corporation, SC-4391(RR), December, 1959.

6. Johnson, G. W., Excavation with Nuclear Explosives, Lawrence Radiation Laboratory, UCRL-5917, November, 1960, refs. 1 and 8.

7. Chabai, A. J. and Hankins, D. M., Gravity Scaling Laws for Explosion Craters, Sandia Corporation, SC-4541(RR), December, 1960.

8. Feigenbaum, S. A. and Wegkamp, P. L., Photographic Earth Motion Study – Scooter Event, Edgerton, Germeshausen & Grier Report L-510, February, 1961.

Paper H

HIGH-EXPLOSIVE CRATERS IN TUFF AND BASALT*

Luke J. Vortman

Sandia Laboratory, Albuquerque, New Mexico

ABSTRACT

Thirteen 256-pound charges of spherically cast TNT were detonated in volcanic tuff to determine the apparent crater dimensions. Charges were placed at six different burst depths in the region approaching containment of the explosion. Variation of crater dimensions with burst depth was determined. No crater resulted where scaled burst depth was greater than 1.75 ft/$W^{1/3}$. (W is charge weight in pounds). Ten 1000-pound charges (two at each of five burst depths) and three 40,000-pound charges (each at different burst depths) describe variation of crater dimensions with burst depth in basalt. No departures from cube-root scaling are detectable. For constant charge size, maximum and average rock size increase with increased burst depth. For constant scaled burst depth, maximum rock size increases as charge weight is increased. Cylindrical charges give larger craters than spherical charges at deeper burst depths and smaller craters at shallower burst depths. Mass of ejected dust has been related to apparent crater volume. The amount of blast suppression with charge burial is shown.

* * *

Craters in Tuff

During April of 1959 a series of cratering shots was fired in volcanic tuff at the Nevada Test Site (NTS).[1] This material and its properties have been described in detail by Warner and Violet.[2] At the site of the experiment described here, the density of the tuff ranges from 1.5 to 1.6 g/cc. Its compressive strength averages about 3900 psi, with three-fourths of the measurements falling between 2000 and 6000 psi.

---

*Work performed under the auspices of the U. S. Atomic Energy Commission. The explosions in basalt (Project Buckboard) were a part of the Plowshare experimental program.

All charges were 256 pounds of spherically cast TNT and were center-detonated. Each charge was placed in a drilled hole in the tuff and covered with about a foot of sand. The balance of the hole was stemmed with concrete similar to the tuff in density and compressive strength. A tabulation of the number of shots at each depth is given below; depth is expressed in units of feet/$W^{1/3}$, where W is charge weight in pounds.*

Number of shots	Scaled depth* (ft/$W^{1/3}$)	Number of shots	Scaled depth* (ft/$W^{1/3}$)
2	1	3	2.5
3	1.5	2	3
2	2	1	3.5

The purpose of the experiment was to determine the apparent crater dimensions in a soft rock, especially in the region approaching containment of the explosion. Figures 1 and 2 show, respectively, the scaled apparent crater radius and depth as a function of scaled burst depth. No crater was obtained at scaled burst depths greater than 1.75. At greater depths, the result was a mound of rock which is shown in Fig. 2 as a negative crater depth. As the depth increased, the height of the mound gradually decreased until, somewhere beyond a scaled depth of burst of 3.5, a point was reached at which there was very small permanent displacement of the surface. In Figs. 1 and 2, the apparent crater dimensions of the Neptune nuclear cratering shot in tuff have been included for comparison.

The early displacement of the surface as a function of time was obtained from high speed motion picture photography. The displacements measured were vertical displacements of the center of the mound immediately over the

---

* Editor's Note: In this paper, distances are normalized by "scaling" to simplify comparisons between shots of various sizes. A scaled distance is the actual distance in feet divided by $W^{1/3}$, where W is weight of the charge in pounds. For example, a 1000-lb charge with depth of burst of 15 ft would have a scaled depth of burst of 1.5 (calculated thus: $15/W^{1/3} = 15/1000^{1/3} = 15/10 = 1.5$). The unit in which these scaled distances are expressed is feet/$W^{1/3}$.

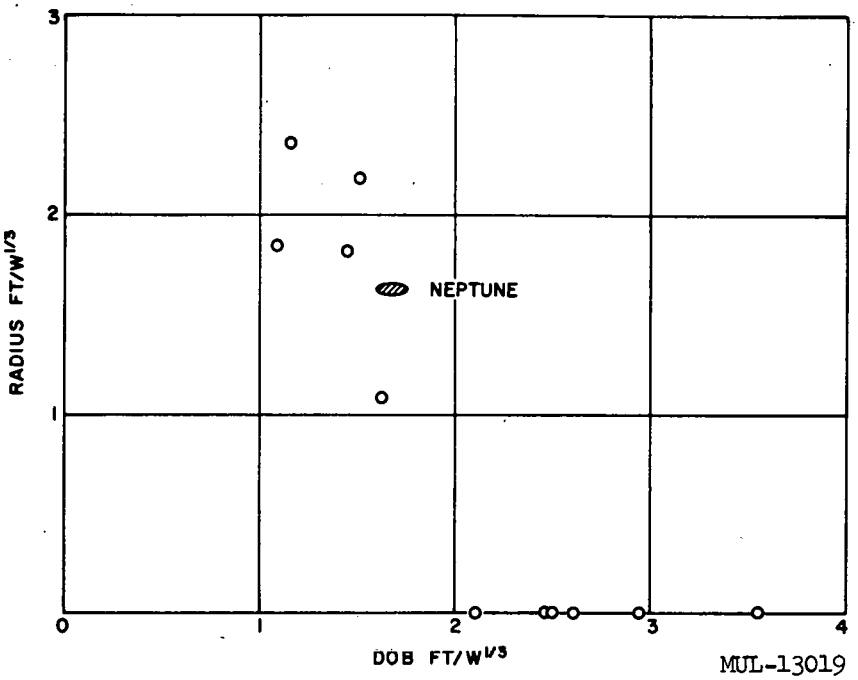

Fig. 1. Scaled apparent crater radius in tuff vs scaled depth of burst.

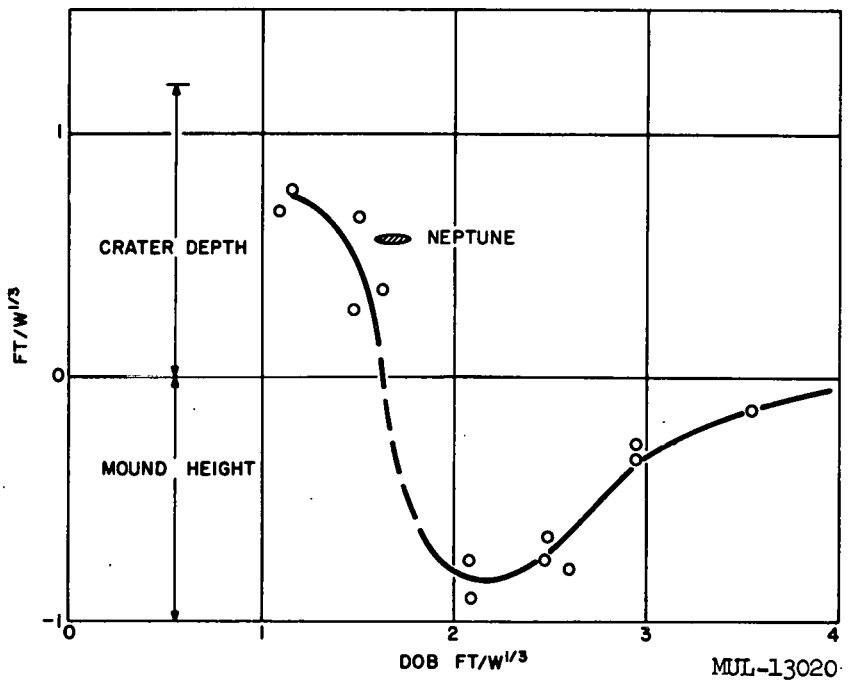

Fig. 2. Scaled apparent crater depth in tuff vs scaled depth of burst.

charge. Velocities were obtained from the displacement-time curves. At early times, the velocities are relatively constant. At later times, as the contribution of the gas bubble becomes evident, velocities increase over those at the early times. Typical values of these early time velocities are 80 ft/sec for a shot at a scaled burst depth of 1.5, and 34 ft/sec for a shot at scaled burst depth of 2. Figure 3 shows these early velocities as a function of burst depth for the 256-lb charges. The early surface velocity for the Neptune nuclear shot has been included for comparison. The surface velocities for the Neptune shot were no greater than those for 256-lb high-explosive shots at comparable burst depths, even though the Neptune crater dimensions were larger than those of high-explosive shots at the same scaled burst depths. This suggests that the slope under which the Neptune shot was fired may be one factor which accounts for the Neptune crater being larger than expected.

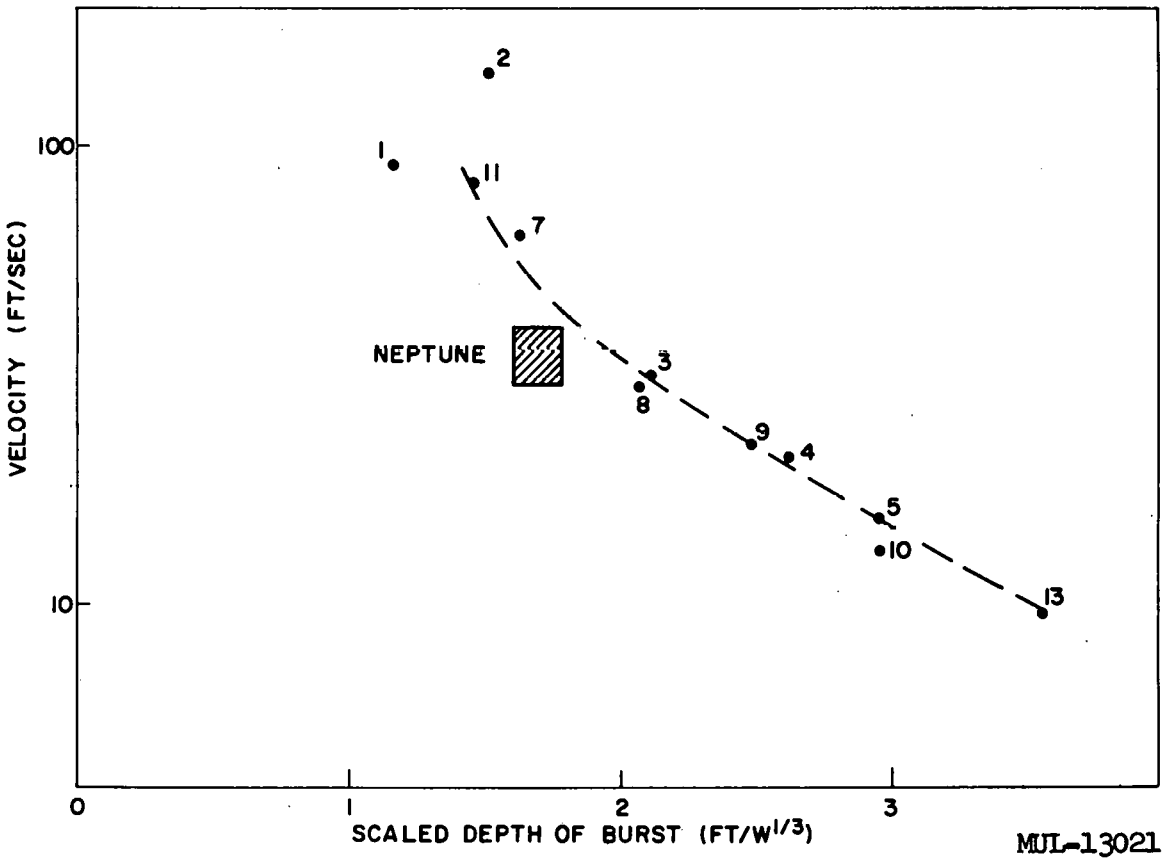

Fig. 3. Early vertical velocity at surface zero vs scaled depth of burst (for tuff).

The dimensions of the void below the surface were measured on one noncratering shot at a scaled depth of 3. A colored grout was pumped into the void and 10 holes were core-drilled into the rock and grout. The shape of the void was determined from examination of the cores. The volume of grout indicated a void of 263 ft^3, approximating that of a spherical cavity with a 4-foot radius. The mapping of the grouted area indicated a volume comparable to that of a spherical cavity with a radius of 4.6 feet.

Typical sizes of the broken rock are a nonscaling feature and are in part predetermined by natural cracks and fissures in the medium. In a single material, the distribution of rocks in each size range tends to remain relatively constant. This is especially true for the series of shots described here, all of which were the same size and placed at the relatively deeper burst depths. Thus, if larger charges had been used, they might have given craters at scaled depths greater than 1.75 because the broken rock size, being relatively smaller, might not have bridged or arched over the cavity, and an apparent crater might thus have been formed. This is a second factor which may help account for the larger-than-expected Neptune Crater.

We have concluded that larger charges are required at these deeper scaled burst depths to create craters which can be scaled with confidence to nuclear craters in tuff.

Craters in Basalt

Two series of high-explosive crater experiments have been fired in volcanic basalt. The first of these was done in 1948 by the Corps of Engineers in the Panama Canal Zone.[3] They used granular TNT in charges weighing from 8 pounds to 200 pounds. The charge shape was a cylinder whose length was twice the diameter, and the charge was placed with the long axis vertical. Because of the cylindrical charge shape, their results are used here primarily for comparison.

The second series was Project Buckboard.[4] These shots were fired to determine crater dimensions in hard rock as a function of burst depth, and to look for departures from cube-root scaling.

The program consisted of ten 1000-lb spherically cast TNT charges, each center-detonated, and three 40,000-lb charges of cast TNT blocks stacked to resemble a sphere. The latter were also center-detonated. The 1000-lb charges were placed two each at 5, 10, 15, 20, and 25 feet. The three 40,000-lb charges were placed at scaled depths of 3/4, 1-1/4, and 1-3/4. (Actual depths were 25.7, 42.8, and 60 feet.) One of the 1000-lb charges at 25 feet was a cylinder with a length-to-diameter ratio of 2. Its purpose was to provide a crater which could be compared with those of the earlier Isthmian Canal Studies experiment. All charges in Project Buckboard were covered with approximately a foot of dry sand and the charge hole stemmed with concrete.

The basalt was a Quaternary flow which had issued from a vent in the vicinity of a cinder cone near the north end of the flow and had flowed southward, presumably between two rows of low-lying hills which have since eroded. The remaining basalt-capped mesa (shown in Fig. 4) rises 400 feet above the surrounding ground on the south end of the flow (foreground) and about 80 feet above on the north end of the flow. In choosing the 13 firing sites, 37 exploratory NX holes were cored a total length of 1250 feet. Shot locations were chosen from tests on the cores such that the basalt near the depth of the charge had a density greater than 2.6 g/cc and a compressive strength of approximately 20,000 psi.

Figures 5 and 6 show craters from the three larger shots. In Fig. 5 the crater of the shallowest of the three 40,000-lb shots is shown at the center. The crater of the deepest of the three is shown in the foreground. The most striking difference between the two craters is the larger size of the ejecta in the case of the deeper shot. Rays of ejected material may also be seen surrounding the crater of the shallowest shot.

Figure 6 shows the crater from the shot at the middle depth. This was the largest of the three craters. I should mention at this point that there is some doubt whether the dimensions of this crater can be scaled with confidence since it penetrated a pocket of cinders which was not evident in pre-shot drilling. The crater was asymmetric. The deepest part of the crater

Fig. 4. Buckboard mesa.

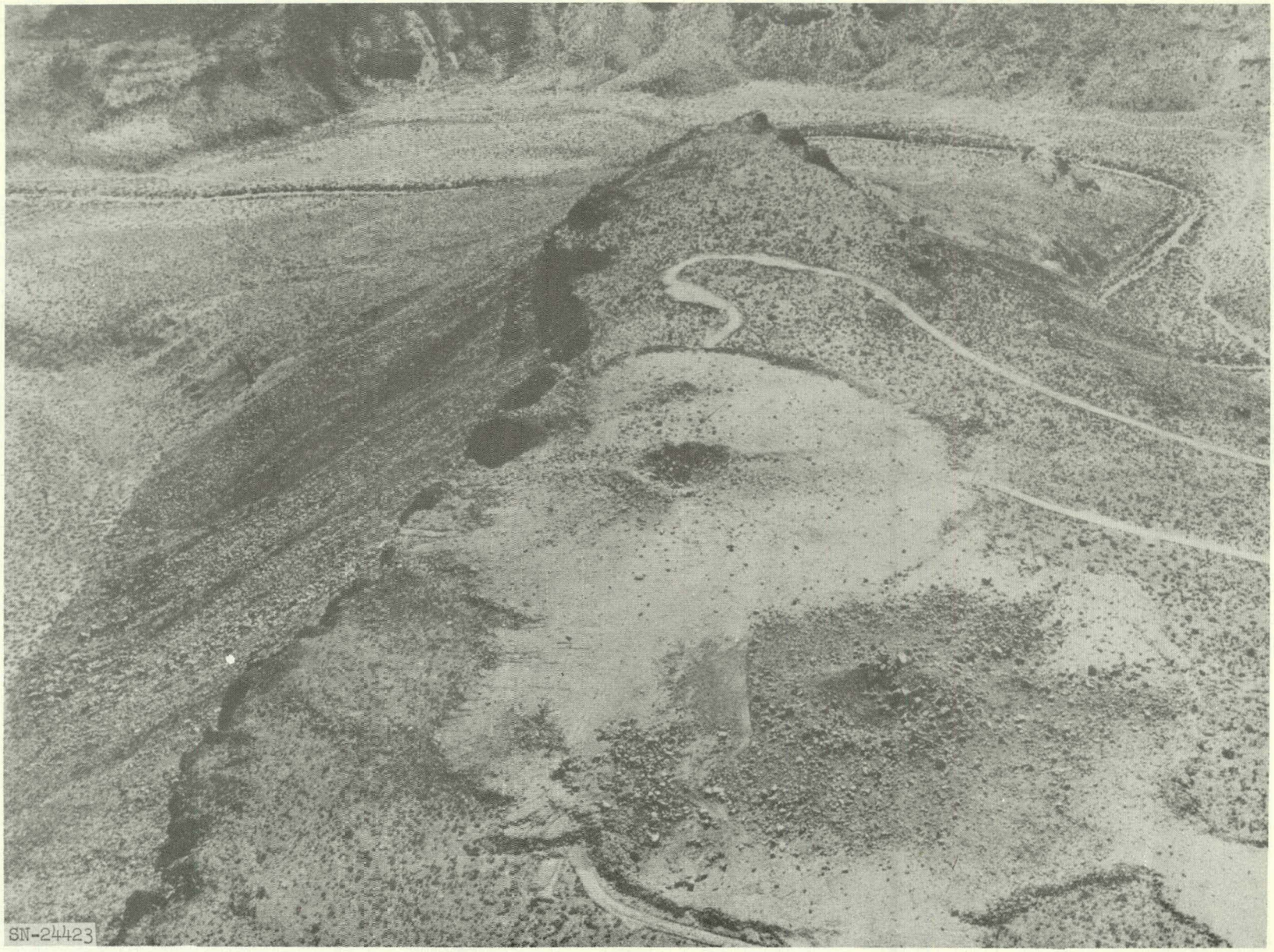

Fig. 5. Craters from deep and shallow Buckboard shots.

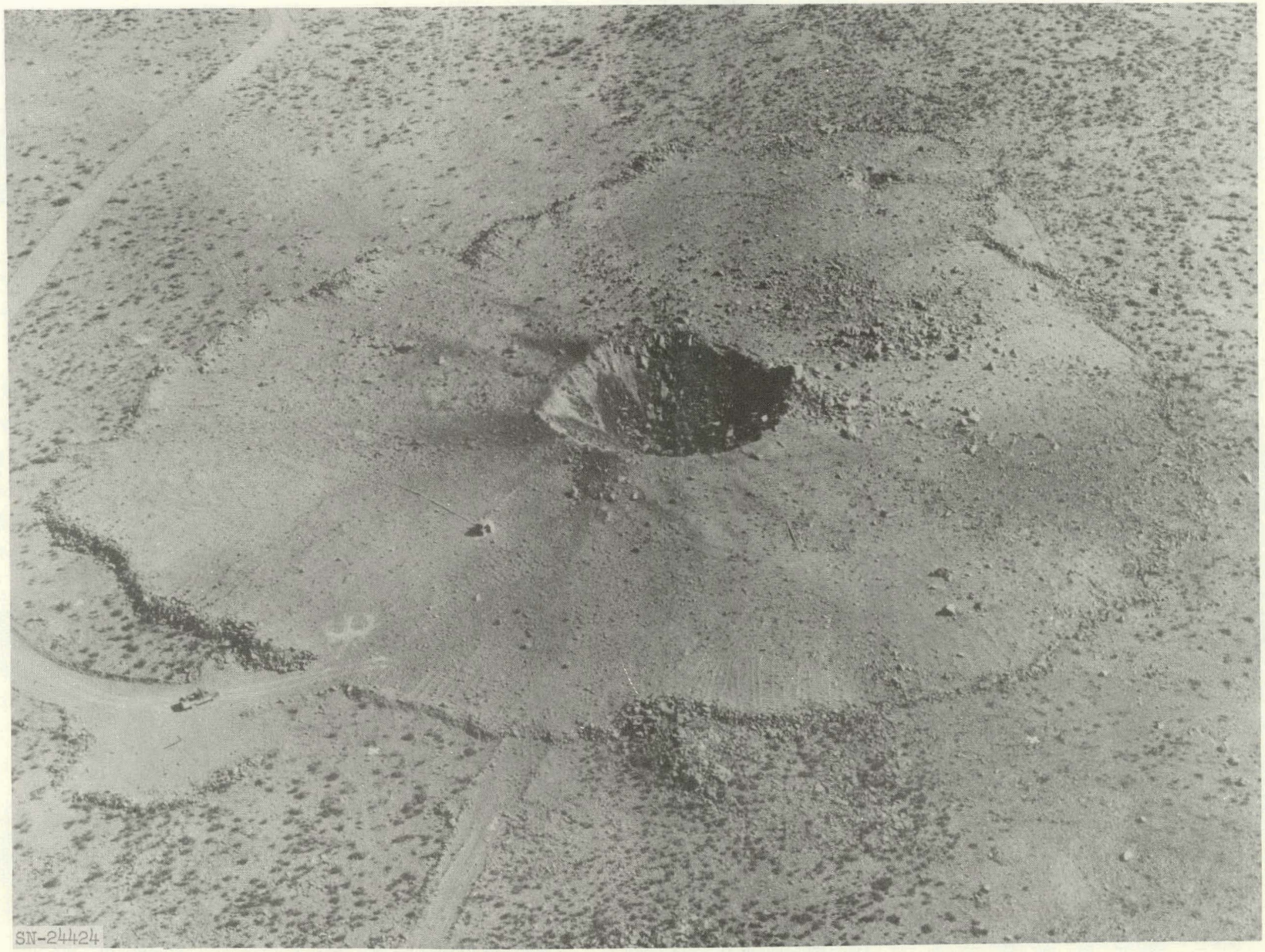

Fig. 6. Crater from Buckboard shot at 43 feet.

was located 10.6 feet from the vertical axis of the charge on a radius 9° north of east. The center of the surface contour was 3.5 feet from the vertical axis and 10° west of north. Note that because of the cinder pocket the blocks of material ejected in the more distant portion of the photograph are larger than those in the foreground.

The scaled apparent crater radius and depth as a function of scaled burst depth are shown in Fig. 7. In drawing the curves through the data points, a certain amount of judgment has been interjected. For example, the crater from the 40,000-lb shot at a scaled depth of 1.25 was considerably deeper than one would have expected. In fact, it is as deep as one would have expected had it been fired in the NTS desert alluvium. In drawing the curve, therefore, we have judged the point to be high.

Because of the scatter in the data, it was not possible to detect any departures from cube-root scaling, and without such evidence we have chosen here to continue to use cube-root scaling.

As with tuff, a nonscaling feature of the apparent craters was the size distribution of the ejected material. In the case of basalt the natural block-size distribution was partially predetermined by cooling cracks in the basalt flow. At some of the deeper burst depths, the 1000-lb charges were not large enough to eject the largest blocks of material, and these blocks fell or rolled back within the crater boundary leaving a smaller apparent crater.

These large blocks within the apparent crater greatly distort apparent crater dimensions if they are taken into account. No rocks were found in the craters of the 40,000-lb shots (which were the same size, scalewise, as the 1000-lb shots), and those which were found were no more than a small perturbation on the apparent crater. Thus, we have concluded that the 1000-lb charges were not large enough to give a crater which could be scaled with confidence, especially where scaled burst depths were greater than 1.

We did observe that, for a constant charge size, the maximum rock size (and probably average rock size also) increases with increased burst depth. Also, at the same scaled burst depth the maximum rock size increases as the charge weight is increased.

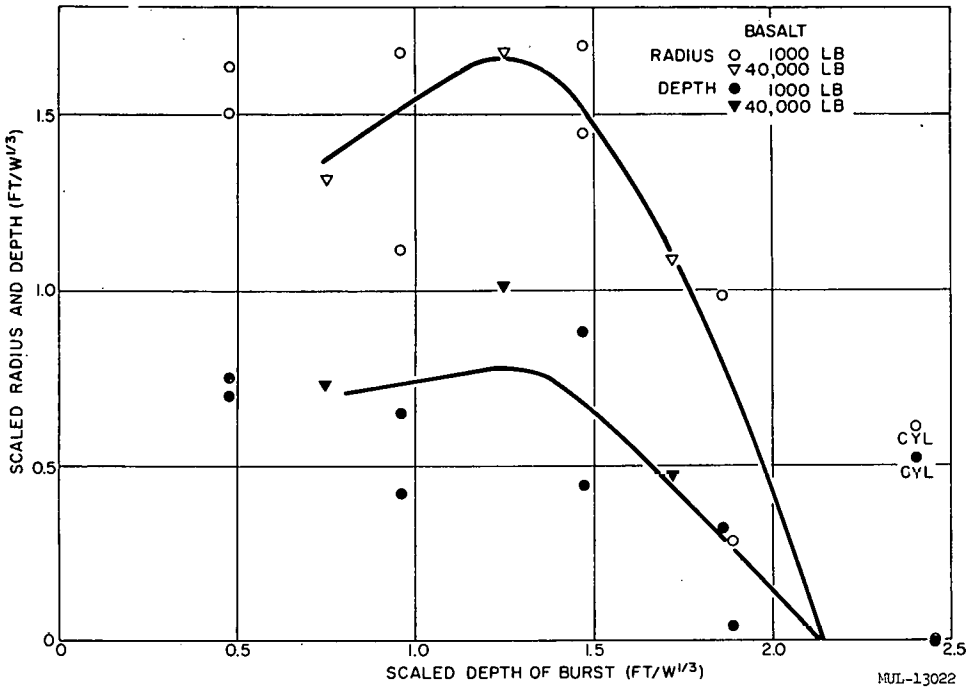

Fig. 7. Scaled apparent crater radius and depth in basalt vs scaled depth of burst.

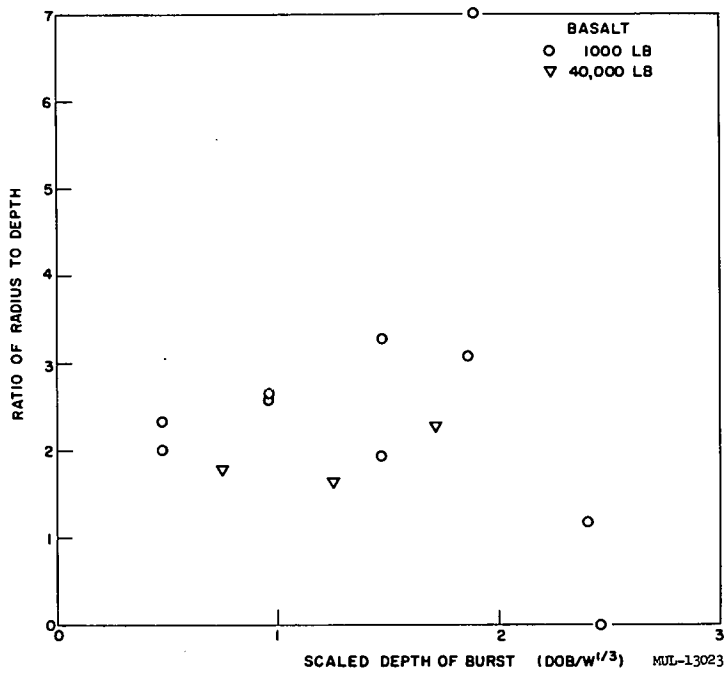

Fig. 8. Ratio of apparent crater radius to depth in basalt vs scaled depth of burst.

It should be clear that the crater dimensions in basalt are smaller than those observed for desert alluvium.

It is interesting to observe the ratio of apparent crater radius to depth for the basalt (as shown in Fig. 8). In spite of the scatter in the data, one notes that the ratios generally are in agreement with those for NTS desert alluvium. The agreement is better for the three larger charges. The larger charges gave less scatter and hence greater confidence in the crater dimensions. It is unfortunate that no surface burst charges were included in this program. They had been planned originally but were deleted because of gross irregularities in the surface of the basalt flow and because of the presence of more vesiculated basalt near the surface.

We have also concluded that charge-shape effects on crater dimensions do exist. The dimensions of the crater from the single Buckboard cylindrical charge agree well with dimensions from those of the 1948 experiment with cylindrical charges when cube root scaling is used. We can conclude only that the cylinder gave a larger crater than the sphere at the deeper scaled burst depth (2.5). One would be remiss in not calling attention to reservations regarding the cylindrical charge data of the 1948 experiment. Since in the Buckboard series we have concluded that the 1000-lb charges were not large enough to produce craters which could be scaled with confidence, the same statement must be true to an even greater extent for charge weights ranging from only 8 to 200 pounds.

To aid in throwout accountability, as well as to infer where dust-scavenged radioactivity from a nuclear shot would fall, the distribution of fine particulate material was determined. Collecting pans were placed at 8 points along each of 12 equiangular radii. Where the collecting station fell below the top of the mesa surface it was deleted from the array. The locations of the sampling stations are shown in Fig. 9. Figure 10 shows a typical isodensity contour plot for the Buckboard shot at scaled depth 1.25. It is interesting to note that the direction of most of the particulate throwout appears to be upwind. This is because wind effects were minimized by choosing firing times when wind velocities were extremely low. With wind

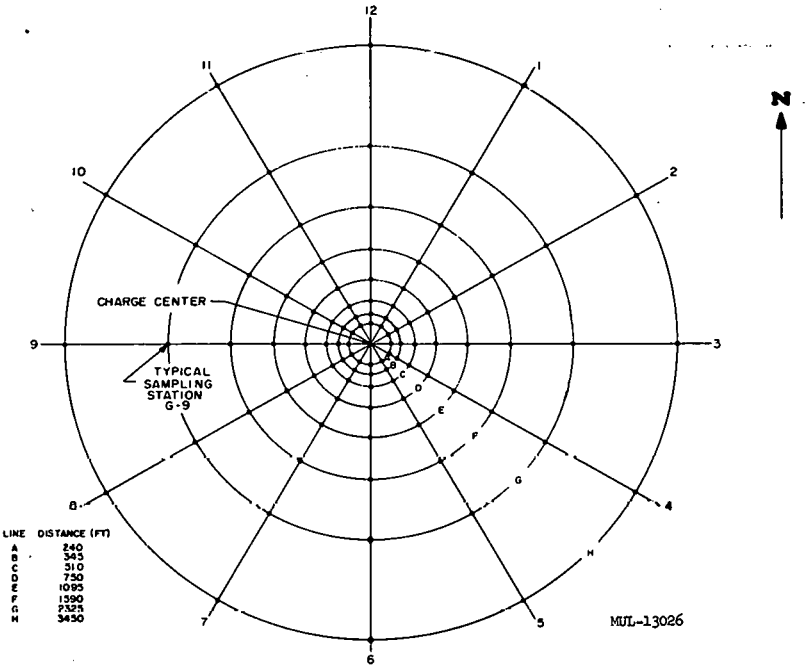

Fig. 9. Locations of dust-sampling stations.

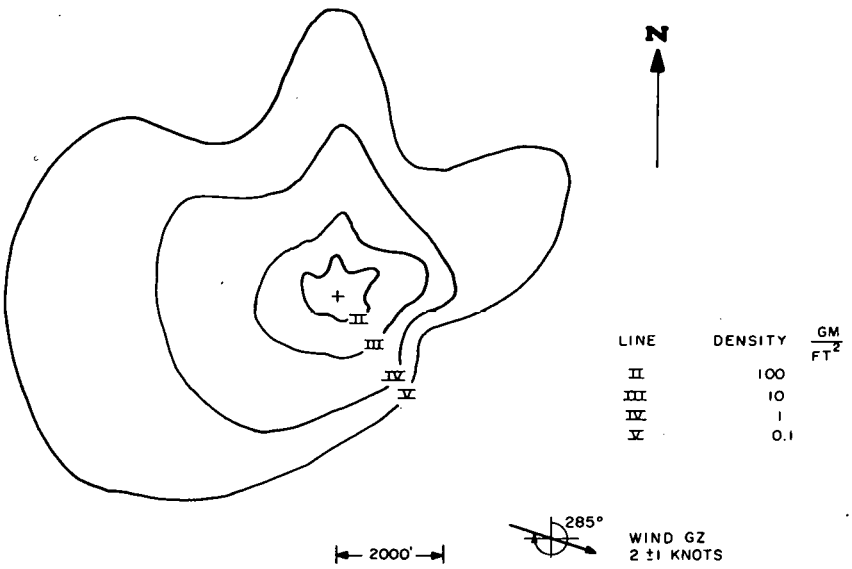

Fig. 10. Typical dust isodensity contour plot.

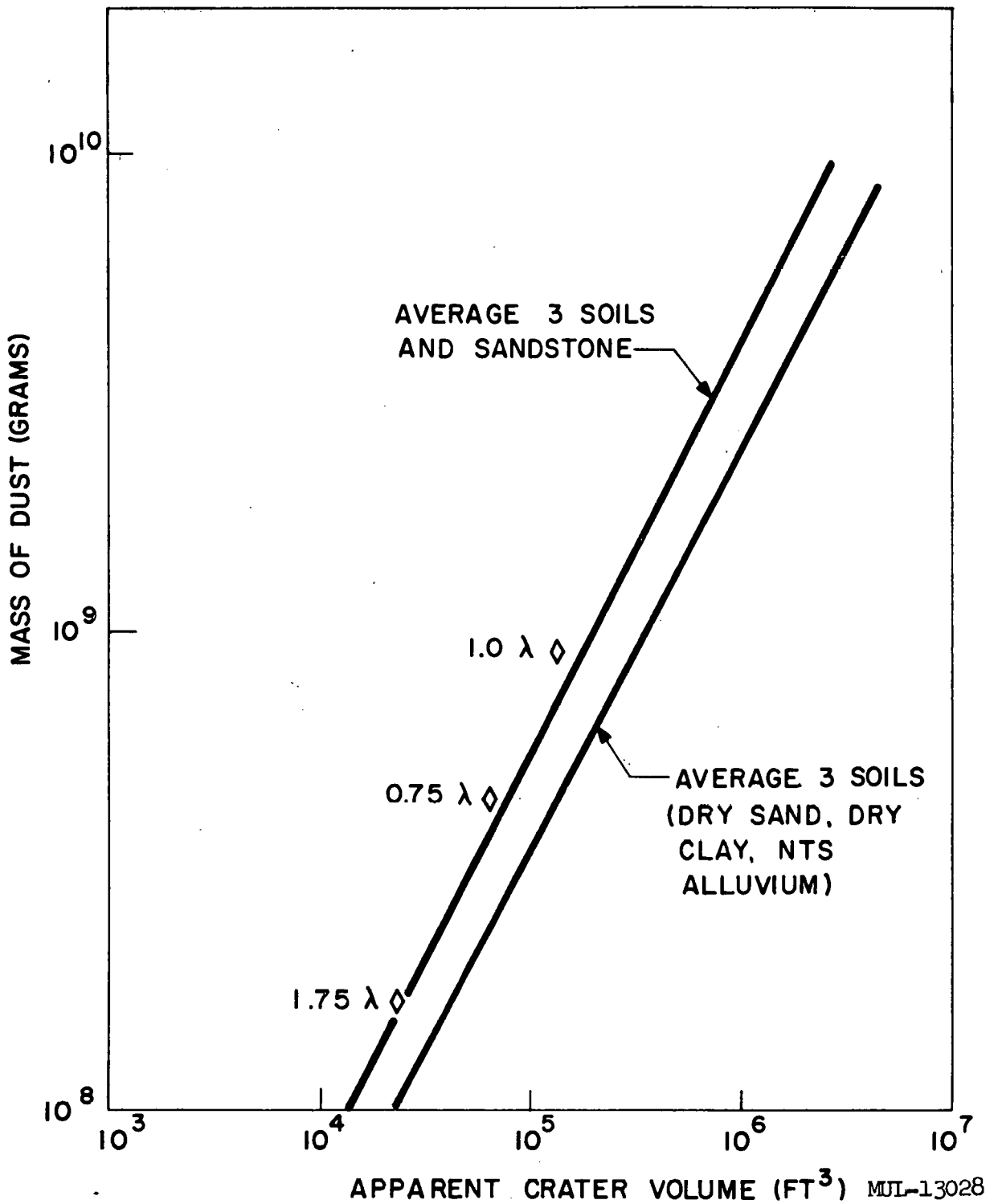

Fig. 11. Relation of dust mass to apparent crater volume.

velocities so low, wind direction was quite irregular, and the pattern of throwout did not necessarily coincide with recorded average wind directions.

Dust mass was computed by using the contours and by assuming that the density of dust was constant out to 240 feet, and that beyond 240 feet it decreased as shown in the isodensity contours. The mass of dust so determined is related to apparent crater volume as shown in Fig. 11. For comparison, Fig. 11 shows a best fit to average data from Dugway dry sand, Dugway dry clay, and the NTS desert alluvium. Adding data from Dugway sandstone to the soil data provides a shift to the left which agrees with Buckboard basalt data. The shift may not be real, but may instead be due only to inadequate data.

Note that this correlation makes no attempt to account for all of the material excavated from the crater. Rather, it establishes a relation between the crater volume and the mass of fine particulate material, and indicates that the relationship is independent of depth of burst.

On each of the three 40,000-lb shots, close-in air blast was measured between 60 feet and 630 feet along a single radius. The differences between basalt and NTS desert alluvium in suppression of close-in air blast are insignificant. The values tabulated below, measured at 250 ft, are typical.

Scaled Burst Depth ($W^{1/3}$ ft)	Percent of Surface Burst Blast
0.75	10
1.25	2
1.75	0.3

Distant air blast was measured at approximately 10,000, 25,000, and 60,000 feet from ground zero and also at off-site stations up to approximately 150 miles away. The results of the air blast suppression are summarized in Fig. 12.

In Project Buckboard, we determined the apparent crater dimensions for high explosive fired in basalt. We found that 1000-lb charges were too

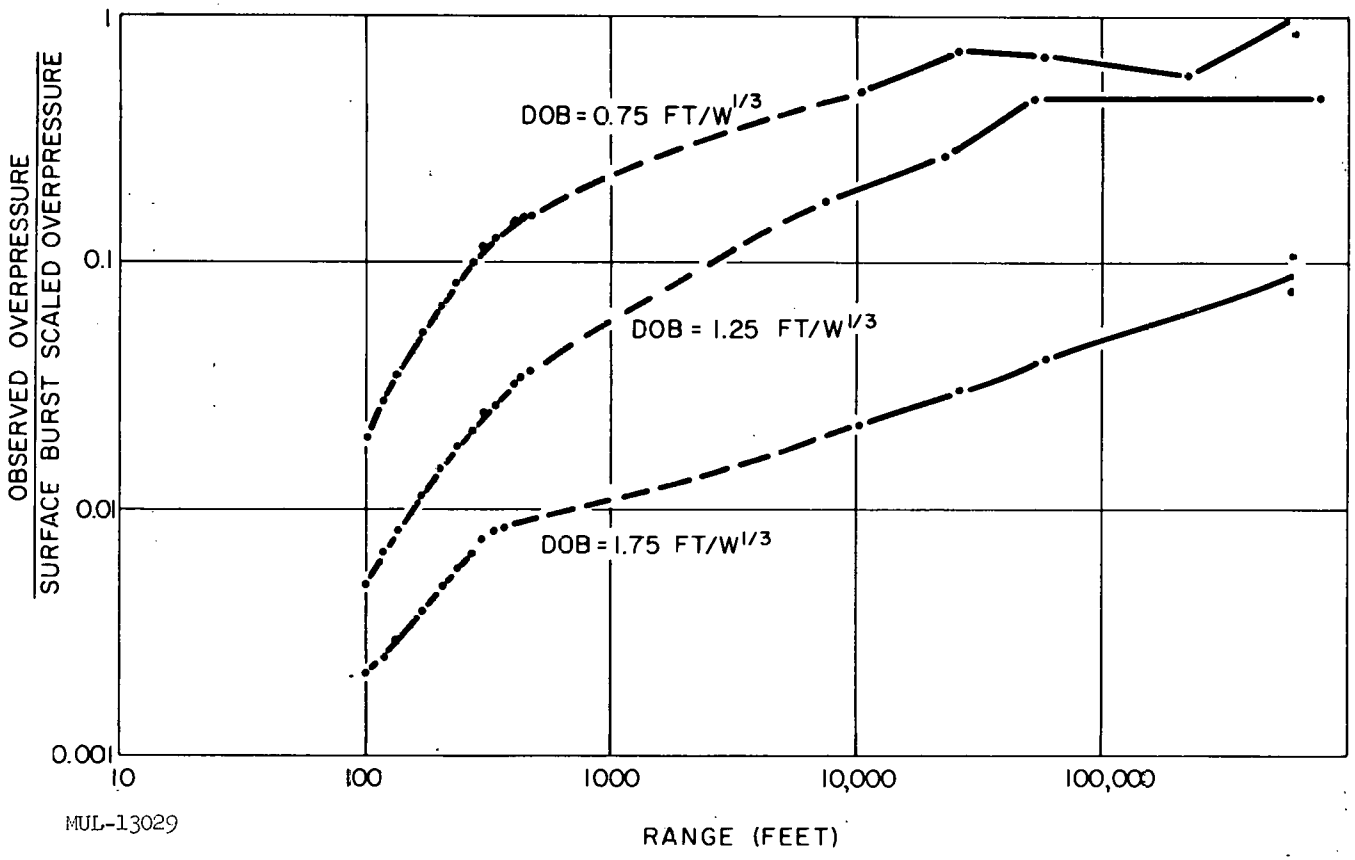

Fig. 12. Air blast suppression.

small for craters which could be scaled with confidence. It was found that charge shape effects do exist and their nature was indicated. Particulate distribution was determined and the mass of dust throwout related to apparent crater volume. The amount of air blast suppression as a function of burst depth in basalt was determined.

REFERENCES

1. Murphey, Byron F., HE Crater Studies, Tuff, Sandia Corporation Research Report SC-4574(RR), to be published.

2. Warner, Stanley E. and Violet, Charles E., Properties of the Environment of Underground Nuclear Detonations at the Nevada Test Site, UCRL-5542(Rev), April, 1959.

3. Isthmian Canal Studies, Crater Tests in Basalt, The Panama Canal ICS Memo 284-P, Diablo Heights, C. Z., April 26, 1948.

4. Vortman, L. J., Chabai, A. J., Perret, W. R., and Reed, J. W., Project Buckboard Interim Report, Sandia Corporation Research Report SC-4486(RR), November, 1960.

/wa

Paper I

A GENERALIZED EMPIRICAL ANALYSIS OF CRATERING*

Charles E. Violet

Lawrence Radiation Laboratory, University of California
Livermore, California

ABSTRACT

A general empirical analysis of chemical and nuclear explosive cratering is presented. This analysis makes use of the concepts of efficiency and scaling formalism. Efficiency is assumed to depend on type of explosive, medium, and depth of burst. Scaling formalism is generalized in terms of experimentally determined yield exponents associated with each pertinent dimension. Experimental procedures are specified which determine the efficiency and yield exponents. Applying these methods to chemical-explosive cratering data in desert alluvium, the crater radius and depth yield exponents are both 1/3.4. The standard deviation is 3 percent. The depth-of-burst yield exponent is 1/3.6 with a standard deviation of 3 percent. Thus the principle of similitude is not rigorously obeyed. Assuming nuclear craters are best described by the above exponents, the percent efficiency of nuclear cratering in desert alluvium is determined as follows:

	Based on Crater Radius	Based on Crater Depth
Jangle S	2.6 ± 1.2	4.6 ± 2.1
Jangle U	78 ± 35	146 ± 66
Teapot Ess	43 ± 19	208 ± 94

This behavior of the efficiency indicates that the relative contribution of various crater forming mechanisms differ in chemical and nuclear cratering. Therefore, the cratering capabilities of nuclear explosives cannot be related to those of chemical explosives by means of a single parameter. The prediction of nuclear crater dimensions from data obtained from low-yield chemical explosives is examined. The prediction error depends on depth of burst and yield extrapolation as well as the errors in the yield exponents and efficiency. For depths of burst near the surface or the maxima of the depth-of-burst curves, the prediction error is a minimum. The accuracy of the depth-of-burst yield exponent q is much less important than that of the crater dimension exponents p_i. The relationships between the precision that should be attempted for p_i and that for E is

---

*This work was performed under the auspices of the U. S. Atomic Energy Commission.

$$\sigma_{p_i} = \frac{\sigma_E}{|\ell_n EW|}$$

where EW is the yield extrapolation. For yield extrapolations of 10^5, the accuracy of p_i should be an order of magnitude better than that of E.

* * *

I. INTRODUCTION

A vast amount of experimental information exists on crater dimensions from chemical explosives (Pokrovskiy, 1957, Murphey and Vortman, 1959; Murphey and McDougall, 1959; U. S. Army Corps of Engineers, 1958; Vortman and Schofield, 1959; and Vortman et al., 1960). Some nuclear cratering data in desert alluvium (Lewis, 1958), wet coral sand (Vaile, 1955), and Oak Springs tuff (Shelton et al., 1960), are also available. This information has generally been described and interrelated in terms of two concepts, scaling (principle of similitude) and efficiency.

Cube-root scaling (Chabai and Hankins, 1960), states that for a limited range of energy release (yield) and for a given medium, crater dimensions can be described by the following expression:

$$R/W^{1/3} = f(H/W^{1/3}) . \qquad (1)$$

However, it is well known that cube-root scaling fails to predict crater dimensions accurately (Pokrovskiy, 1957). Previous investigators have sought to improve on cube-root scaling by retaining similitude and deriving a so-called "empirical scaling exponent." We take a more general approach here in which similitude itself can be tested.

Although cube-root scaling is an inadequate description of cratering, the formalism of Equation (1) is useful in an empirical analysis. Thus the exponents in Equation (1) can be replaced by adjustable parameters which are determined experimentally. Since these parameters are not properly scaling exponents we refer to them as yield exponents.

To compare the cratering capabilities of nuclear and chemical explosives, the concept of efficiency* has been used. To attempt to relate chemical and

---

*In this paper "efficiency" will refer to the cratering capabilities of nuclear explosives relative to chemical explosives (or a reference chemical explosive).

nuclear cratering by means of this single parameter would appear to be unreasonable in view of the vast differences in the energy densities of these explosives. Also, for surface bursts, where an appreciable fraction of the nuclear energy release is lost by radiation, the generation of the air and ground shock waves, as well as their configurations and interactions, differ greatly for the two explosives. Thus, for surface bursts, a comparison of cratering capabilities of chemical and nuclear explosives would probably require two parameters rather than one; one for crater radius and another for crater depth. However, if we make the comparison at depth rather than for surface explosions, a plausible comparison could possibly be made using one parameter.

This might be possible in terms of a phenomenon known to occur in underground nuclear explosions. This is the formation of the "gas ball." Behind the outward-moving shock wave, a region filled with gas at extremely high temperature and pressure forms (Johnson et al., 1959). This region exists for a characteristic time in a spherical volume of characteristic radius (Kennedy and Higgins, 1958). In Oak Springs tuff this radius is approximately $10\ W^{1/3}$ feet (Johnson et al., 1959) where W is in kilotons.* This radius would probably not differ markedly (less than a factor of two) for other earth materials. A gas ball of characteristic radius also exists for chemical explosives, namely the radius of the explosive itself. In the same units as above, this radius is approximately $15\ W^{1/3}$.

If the nuclear gas ball breaks above the surface, a larger fraction of its energy can be lost due to radiative processes than in the equivalent chemical-explosive case. This is due to the higher temperature of the initial nuclear gas ball. As the depth of burst increases, the fraction of the total nuclear energy release available for crater production increases from its surface value and levels off. This plateau value is associated with a critical depth of burst which is approximately equal to the gas-ball radius. We refer to this plateau value as "the efficiency." Another process which affects the efficiency is the production of noncondensing gases (e.g., water vapor) associated with the high temperature and pressure of the nuclear gas ball. Thus, in this model, the efficiency has a depth and medium dependence.

---

*A nuclear yield of one kiloton is defined as the prompt energy release of 10^{12} calories.

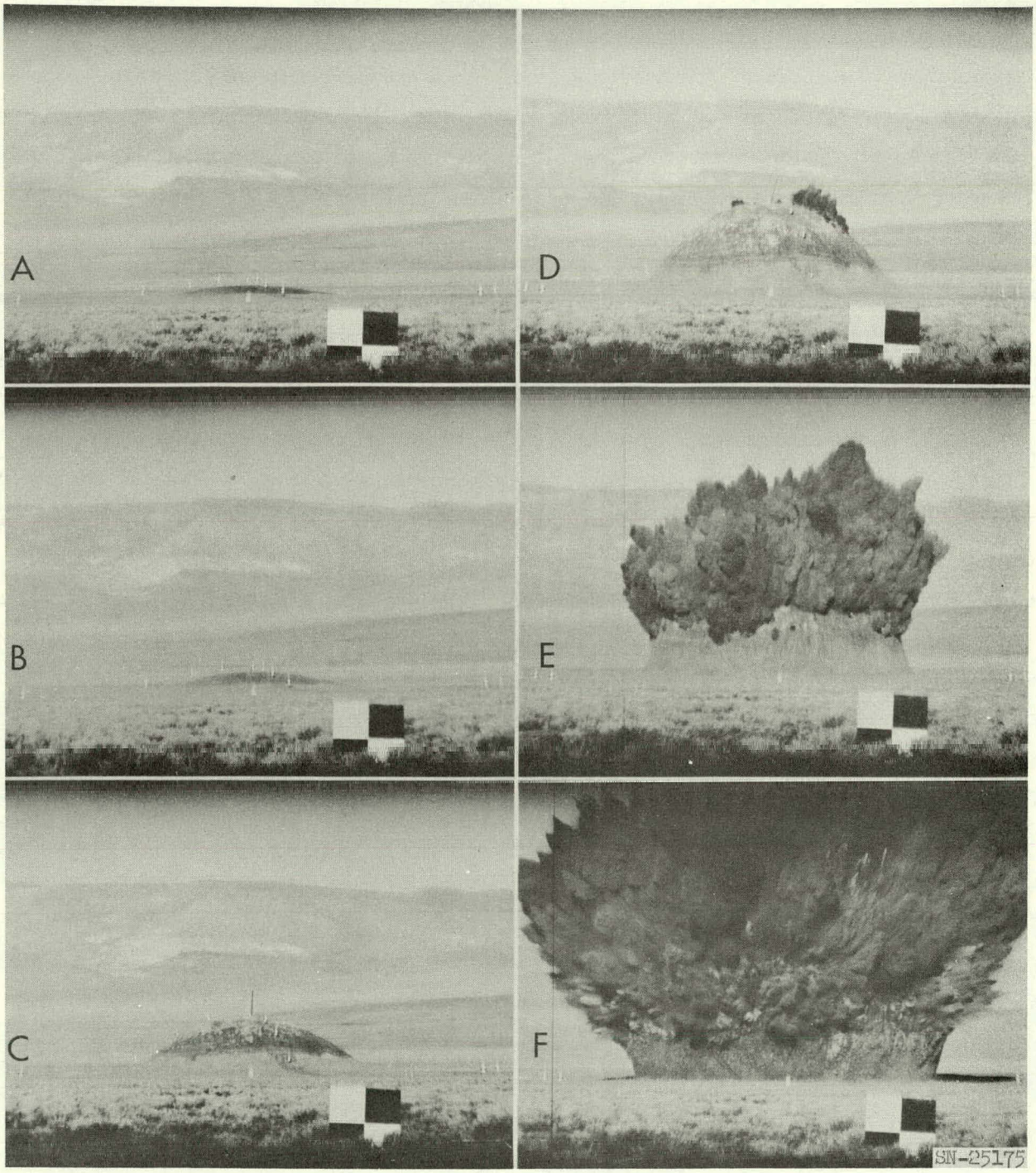

Fig. 1. Photographs of the Scooter event taken at detonation plus (A) 292 milliseconds (B) 408 milliseconds (C) 732 milliseconds (D) 1092 milliseconds (E) 1327 milliseconds (F) 2233 milliseconds.

The mechanisms for craters produced by surface bursts are crushing, compaction, and other nonelastic processes. For greater depths of burst which are of interest in this paper, the dominant mechanism is the expansion and venting of the gas ball. A striking qualitative proof of this statement is obtained from the early photography (Figure 1)* of the Scooter event (Nordyke, 1961). Although the yield exponents might have an anomalous behavior for detonations near the surface, at depths greater than the gas-ball radius the yield exponents would be expected to behave as "slowly varying constants." For the range of yields considered here, we assume these exponents to be constant.**

The gas ball for nuclear explosives is largely composed of vaporized earth materials. Since vaporization of the materials involves irreversible processes, a smaller fraction of the total yield for nuclear explosives is available for crater production than for chemical explosives. Therefore, to a first approximation, the mechanisms of nuclear cratering should be the same as those of a correspondingly smaller chemical explosion. For this model the efficiency is expressed as a coefficient of the prompt nuclear yield. We shall tentatively assume this to be a correct model. Its validity shall be explored in this paper.

The current state of knowledge with respect to chemical and nuclear cratering can be summarized as follows:

1. If the principle of similitude is retained, then the best value of the so-called "empirical scaling exponent" is 1/3.4 for both chemical and nuclear cratering.
2. The cratering efficiency of tamped nuclear explosives is somewhere between 20 percent and 150 percent (Lewis, 1958; Chabai, 1959). This range is apparently due to differences between chemical and nuclear cratering processes, in the emplacement and tamping conditions, and in the definitions of efficiency by previous investigators.
3. The efficiency for crater depth is reported to be greater than that for crater radius by about a factor of two (Chabai, 1959).

---

*Photographs provided by Edgerton, Germeshausen & Grier, Inc.

**Evidence from Baldwin (1949) indicates this to be a good assumption over a yield range of at least three orders of magnitude.

From these considerations one can conclude that the current status of cratering as a science or technology is in an unsatisfactory condition for the following reasons:

1. A theoretical treatment of cratering from first principles should be attempted. Some progress in this area is only recently apparent (Brode and Bjork, 1960).
2. All previous treatments of cratering have assumed the validity of the principle of similitude. However, since cube-root scaling is known to be inadequate the attendant failure of similitude would not be surprising. The analysis presented here provides a test of this principle by assuming an independent yield exponent associated with each dimension.
3. A meaningful definition of efficiency and a consistent method of its calculation should be adopted.
4. Experimental errors have received little attention either in experimental design or in the analysis of data. Consequently, the uncertainty in predicting nuclear crater dimensions from low-yield chemical explosive cratering is not well known.

In an attempt to meet some of these problems, we shall discuss the following subjects:

1. A general empirical analysis of cratering.
2. Experimental procedures which provide for the determination of empirical parameters.
3. An application of this analysis to provide an empirical description of chemical and nuclear cratering in desert alluvium.
4. The effect of the errors in yield exponents and efficiency in predicting nuclear crater dimensions from low-yield chemical-explosive cratering.

II. EMPIRICAL FORMALISM

We begin by stating our assumptions as discussed in the previous section.

1. Chemical- and nuclear-explosive cratering are related by means of one parameter, "the efficiency." It has low value

for surface bursts, and with increasing depth of burst it increases and levels off to a plateau value. It is also a function of medium. It is mathematically expressed as a coefficient of the total nuclear yield.

2. A yield exponent is associated with each dimension (crater radius, depth, and depth of burst). Yield exponents are independent of explosive (chemical or nuclear) and are constant for a given medium.

Generalizing Equation (1) in accordance with these assumptions, we have

$$R_i^{c,n}/(EW)^{p_i} = f_i\left[H^{c,n}/(EW)^{q}\right] , \tag{2}$$

where i denotes a specific crater dimension. For example, we let R_1 be crater radius and R_2 be crater depth; p_i and q are the generalized yield exponents. The superscripts c and n refer to chemical or nuclear explosives. The curves f_i (depth-of-burst curves) are determined by fitting convenient analytic functions to the experimental points.

A. Determination of Yield Exponents.

Equation (1) can be expressed as follows:

$$H^{c,n}/(EW)^{q} = F_i\left[R_i^{c,n}/(EW)^{p_i}\right] . \tag{3}$$

To effect a determination of the scaling exponents, the observation Equations (2) and (3) can be written:

$$\ln R_i^{c,n} = p_i \ln(EW) + \ln f_i\left[H^{c,n}/(EW)^{q}\right] , \tag{4}$$

$$\ln H^{c,n} = q \ln(EW) + \ln F_i\left[R^{c,n}/(EW)^{p_i}\right] . \tag{5}$$

If a set of observations could be obtained for constant values of the arguments of f_i and F_i, p_i and q could then be readily obtained. In general, it is impossible to choose data for constant arguments of f_i and F_i since the scaling exponents are unknown a priori. However, by a judicious choice of experimental conditions, this can be done. This is illustrated in the following sections.

B. Determination of p_i.

For the purpose of yield exponent determination, we define an "effective surface" at an actual depth of $\approx 15\ W^{1/3.4}$ feet.* If we measure actual depths from this effective surface, then Equation (4) becomes:

$$\ln R_i^c = p_i \ln W + \ln A_{i0} \ , \tag{6a}$$

$$\ln R_i^n = p_i \ln W + (p_i \ln E + \ln A_{i0}) \ , \tag{6b}$$

where A_{i0} are constants (the first terms in power series expansions of f_i). Thus, a plot $\ln R_i^{c,n}$ against $\ln W$, as obtained from chemical and nuclear explosions at the "effective surface," should be consistent with straight lines through the data. The values of p_i and E can be obtained from the slopes and intercepts of these curves.

C. Determination of Depth-of-Burst Scaling Exponents.

Knowledge of the crater dimension scaling exponents permits the subsequent determination of the depth-of-burst scaling exponent. Consider first two series of chemical cratering experiments at various depths, one series at a yield of W_1 and the other at W_2. For the conditions:

$$R_{i,1}^c / R_{i,2}^c = (W_1/W_2)^{p_i} \ , \tag{7}$$

we see from Equation (3) that

$$H_1^c / H_2^c = (W_1/W_2)^q \ . \tag{8}$$

Thus, knowledge of the depth-of-burst ratio for equal scaled crater dimensions allows one to solve for the depth-of-burst scaling exponent, q, from Equation (5).

A similar analysis could be carried out for nuclear-explosive cratering if appropriate data were available. Equation (7) and (8) are valid for nuclear

*The best a priori value of q should be chosen. Based on previous work we choose $q = 1/3.4$. From Equation (14), Figure 7, and the discussion of errors in Part IV it is evident that for depths of burst near the effective surface, the systematic error arising from this choice of q is much less than the random errors and can be neglected.

as well as chemical explosions if the efficiency is constant. Thus, to determine q for nuclear cratering, one must use depths of burst which are deeper than the critical depth.

D. Determination of Efficiency for General Experimental Conditions.

Although E can be determined under the limited conditions of (B), a more general method is necessary. Knowledge of the yield exponents permits the general determination of the efficiency if the depth-of-burst curves are expressed analytically. The functions f_i can be expressed as power series of the scaled depth of burst, h, where:

$$h = [H^{c,n}/(EW)^q] .$$

Thus:

$$f_i = \sum_{m=0}^{m=M} A_{im} h^m . \tag{9}$$

Equation (2) then becomes

$$R_i^{c,n} = (EW)^{p_i} \cdot \sum_{m=0}^{m=M} A_{im} h^m . \tag{10}$$

Carrying out the indicated multiplication we have

$$R_i^c = A_{i0} W^{p_i} + A_{i1} H W^{p_i - q} + A_{i2} H^2 W^{p_i - 2q} + \ldots , \tag{11a}$$

and

$$R_i^n = A_{i0} (EW)^{p_i} + A_{i1} H (EW)^{p_i - q} + A_{i2} H^2 (EW)^{p_i - 2q} + \ldots . \tag{11b}$$

We note that if second order and higher terms are dropped, and $p_i \approx u$, Equations (11) reduce to

$$R_i^c = A_{i0} W^{p_i} + A_{i1} H , \tag{12a}$$

$$R_i^n = A_{i0} (EW)^{p_i} + A_{i1} H . \tag{12b}$$

For equal crater dimensions and equal depths of burst, the efficiency in this approximation is the ratio of chemical to nuclear yields.

This statement has been given as a definition of efficiency (Chabai, 1959; Vortman, 1959). However, it is, at best, only a first-order approximation. Knowledge of scaling exponents and the coefficients A_{im} in a given medium as obtained from chemical-cratering data allows one to solve Equation (11b) for E from any set of nuclear-cratering data in that medium.

III. AN ANALYSIS OF CHEMICAL AND NUCLEAR CRATERING IN DESERT ALLUVIUM.

The only material for which direct nuclear scaling information is available is saturated coral sand (Vaile, 1955). Unfortunately, these data are of questionable value for the following reasons:

1. There were no detonations below the surface of the earth.
2. In some cases there were several feet of water between the center of detonation and the coral sand.
3. The craters were eroded by sea water prior to measurement.
4. The properties of the material changed to some extent with depth. The shallow craters from low-yield detonations were formed in coral sand. The deep craters from high yields occurred in partially cemented coral rock.

The nuclear crater in Oak Springs tuff is of limited value since it occurred on a hillside with a slope of about 30 degrees (Shelton et al., 1960).

Desert alluvium is the only material for which unambiguous nuclear cratering data are available. Unfortunately, all nuclear craters in this medium were produced from detonations of the same yield. Thus assumption (1) of Part II can be tested directly, but assumption (2) cannot for nuclear cratering. There is also an abundance of chemical-explosive crater data in desert alluvium obtained from center-detonated spherical charges. For these reasons we shall analyze cratering in desert alluvium in order to exemplify the methods of the previous section. A tabulation of chemical and nuclear cratering data in desert alluvium is given by Nordyke (1961).

A. Determination of p_i.

Crater dimensions for chemical explosions of scaled depths in the range of 12-18 $ft/kt^{1/3.4}$ are plotted in Figure 2. The best fit for the chemical

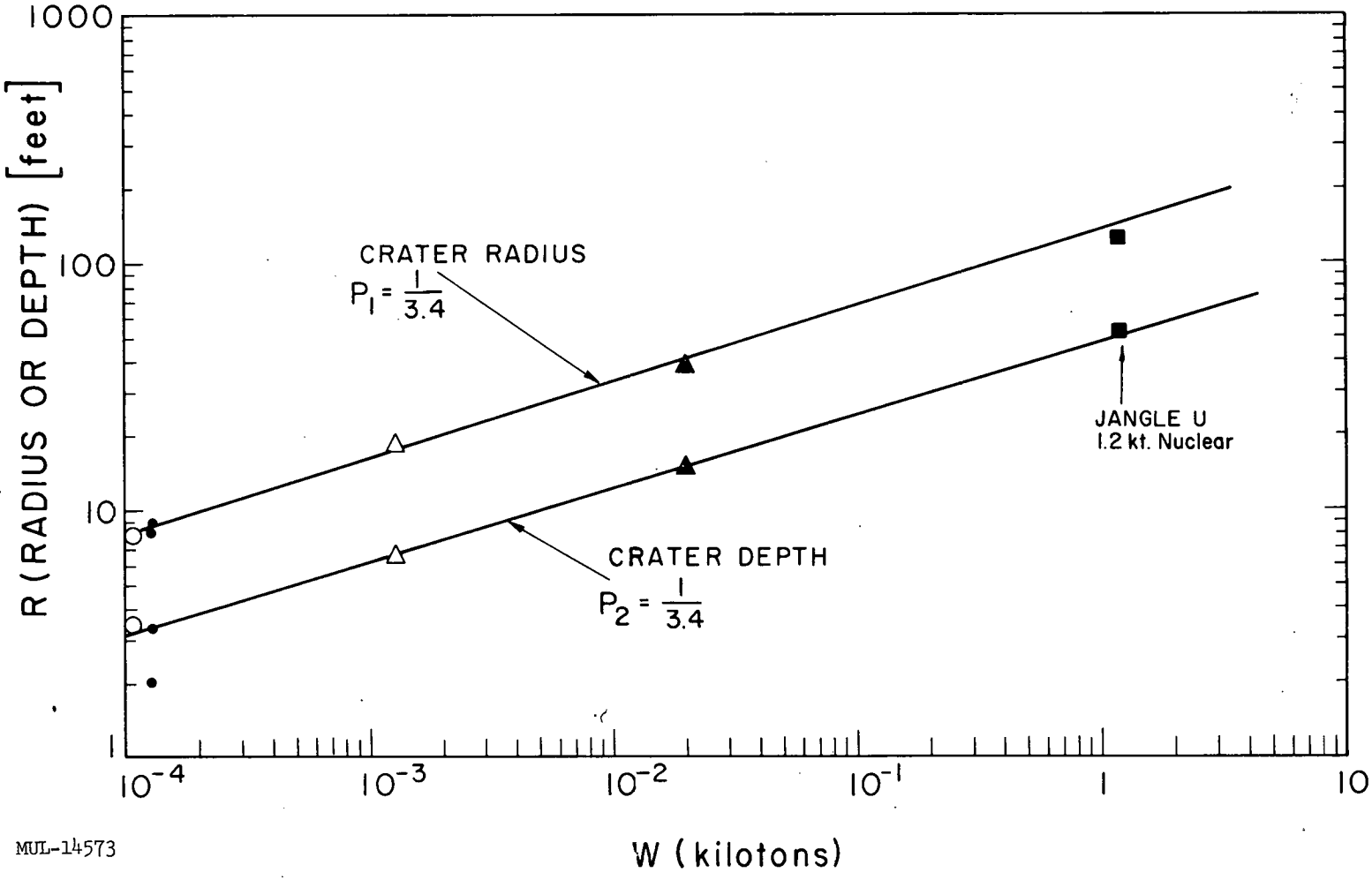

Fig. 2. Crater dimensions for chemical explosions in desert alluvium of scaled depth of burst 12-18 $ft/kt^{1/3.4}$.

crater dimensions corresponds to $p_1 = p_2 = 1/3.4$. The associated standard deviation is 3 percent. Crater dimensions for Jangle U, where the scaled depth is 16 ft/kt$^{1/3.4}$, are also plotted in Figure 2. These nuclear data appear to be consistent with the curves determined from the chemical data.

B. Determination of q.

$R_1/W^{1/3.4}$ and $R_2/W^{1/3.4}$ for 256- and 40,000-pound data are plotted as a function of absolute depth (H) in Figures 3 and 4. Curves of the form of Equation (9) could be fitted to these data. However, for the sake of clarity and convenience we fit curves to these data of the type suggested by Chabai (1959). Using Equations (4) and (5) we find that for both plots $q = 1/3.6$. The standard deviation is 3 percent.

C. Determination of f_i.

$R_1/W^{1/3.4}$ and $R_2/W^{1/3.4}$ are plotted as a function of $H/W^{1/3.6}$ in Figures 5 and 6, thus obtaining the depth-of-burst curves, f_i. The coefficients for the first four terms in the expansion of f_i are given in Table I. The errors are standard deviations.

TABLE I. Coefficients for Desert Alluvium

$A_{10} = 116 \pm 9$	$A_{20} = 33 \pm 4$
$A_{11} = 0.9 \pm 0.1$	$A_{21} = 0.8 \pm 0.1$
$A_{12} = -(1.5 \pm 0.5) \times 10^{-3}$	$A_{22} = -(1.7 \pm 0.6) \times 10^{-3}$
$A_{13} = -(6 \pm 3) \times 10^{-6}$	$A_{23} = -(7 \pm 3) \times 10^{-6}$

Using the experimentally determined exponents, the coefficients of Table I, and the crater dimensions for Jangle S, Jangle U, and Teapot Ess (Nordyke, 1961), we calculate the efficiencies shown in Table II. The errors are standard deviations (see Part IV).

TABLE II. Percent Efficiencies for Desert Alluvium

	Based on Crater Radius	Based on Crater Depth
Jangle S	2.6 ± 1.2	4.6 ± 2.1
Jangle U	78 ± 35	146 ± 66
Teapot Ess	43 ± 19	208 ± 94

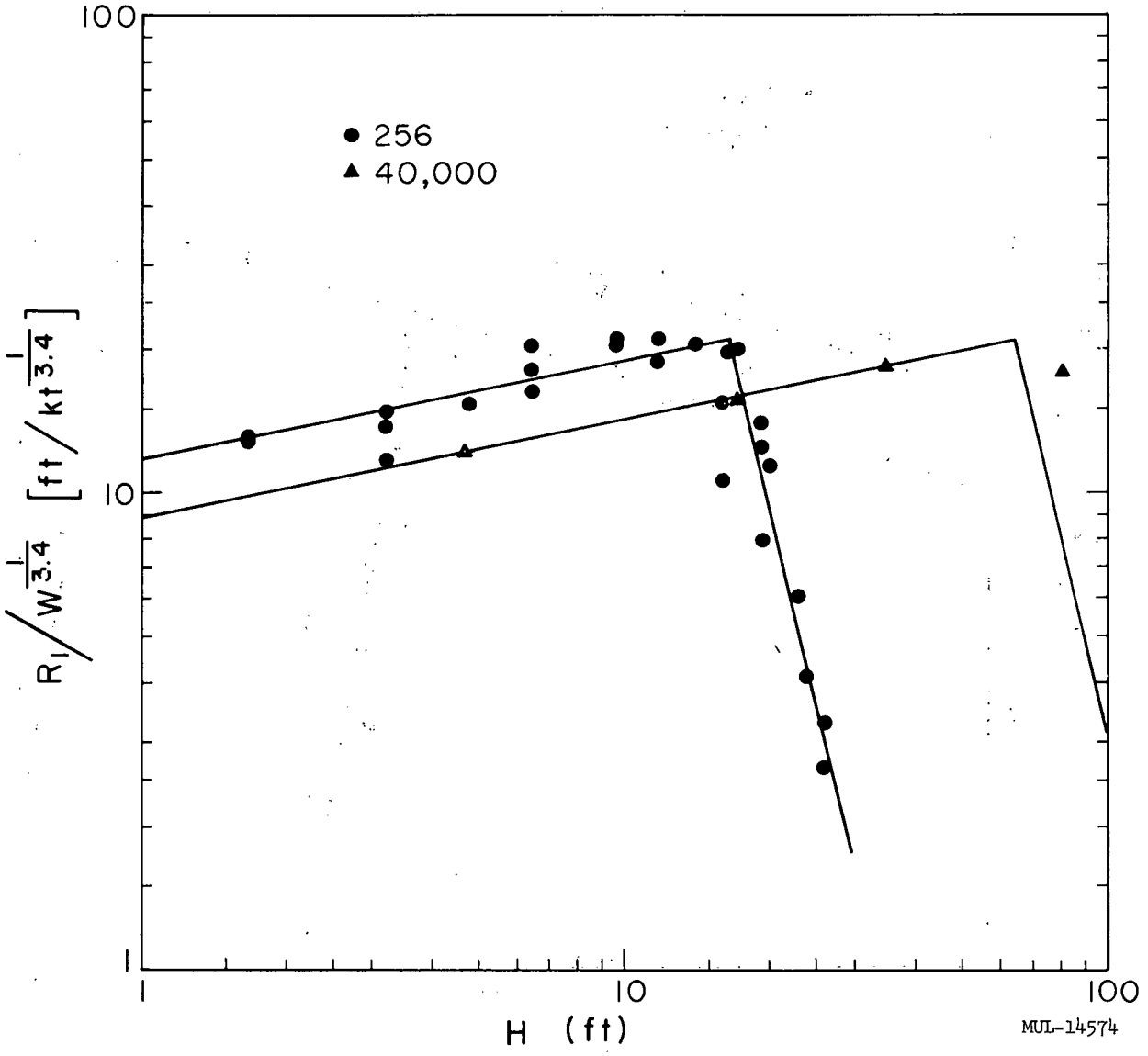

Fig. 3. Scaled crater radii for chemical explosions in desert alluvium plotted as a function of absolute depth of burst.

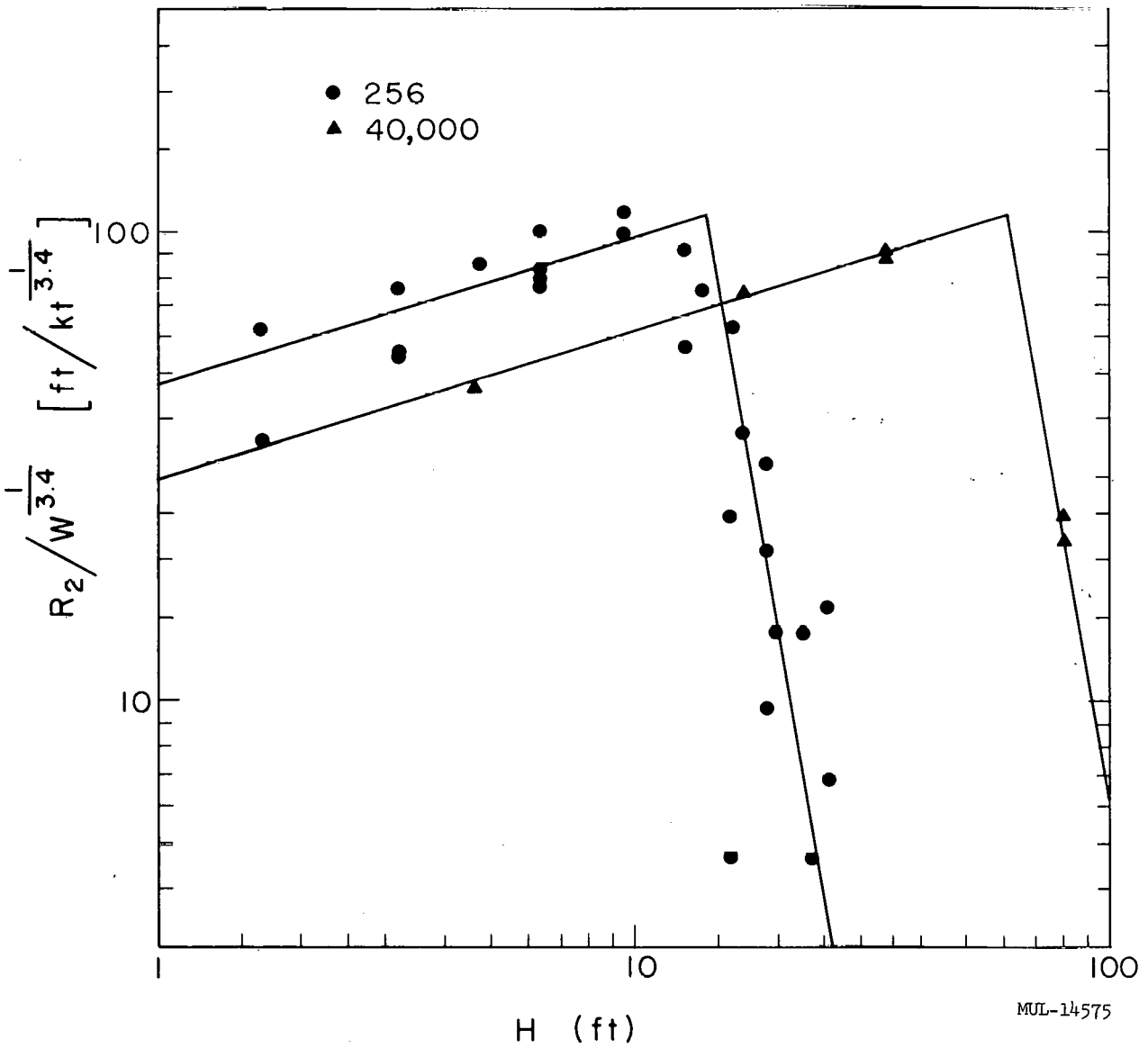

Fig. 4. Scaled crater depth for chemical explosions in desert alluvium plotted as a function of absolute depth of burst.

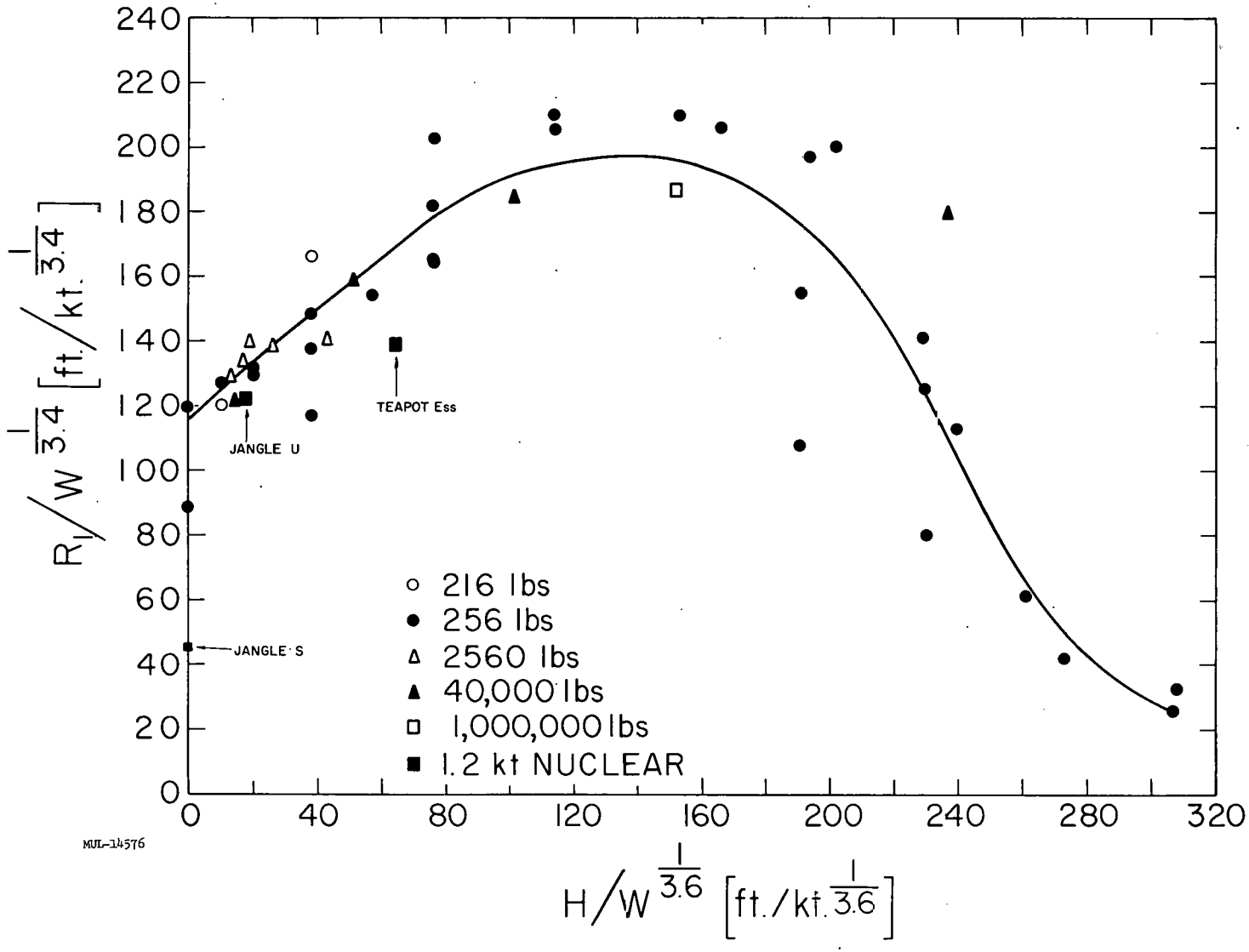

Fig. 5. Scaled crater radii as a function of scaled depth of burst for desert alluvium.

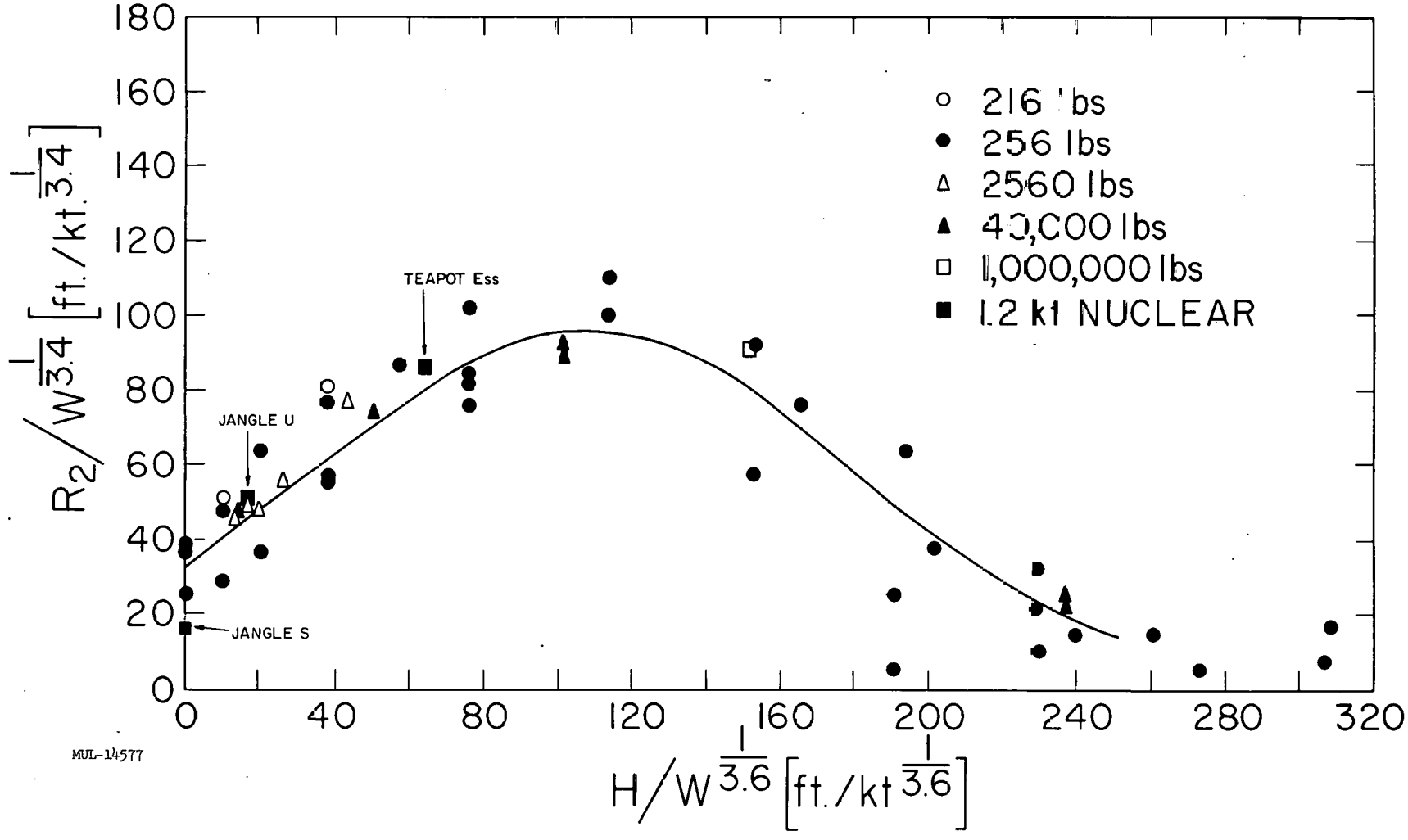

Fig. 6. Scaled crater depth as a function of scaled depth of burst for desert alluvium.

Equation (12b) is sufficient for Jangle S and Jangle U. However, second-order terms (Equation (11b)) must be included in the case of Teapot Ess.

A statistical test of the values of Table II by means of Student's t-distribution (Hoel, 1954), shows that the differences in the efficiencies of Table II are significant, with the possible exception of those based on crater depth for Jangle U and Teapot Ess. We take this to be a real effect in accordance with the conclusions of previous investigators (Lewis, 1958, and Chabai, 1959). While this behavior of efficiency based on crater radius is consistent with the simple model of Part I, that based on crater depth is not. Furthermore, its dependence on crater dimension is not consistent with this model. Thus, the relative contributions of various crater-forming mechanisms, e.g., gas-ball expansion, nonelastic deformation, and subsidence, differ in the chemical and nuclear cases, and the cratering capabilities of nuclear and chemical explosives cannot be related by a single parameter.

IV. UNCERTAINTIES IN CRATER DIMENSION PREDICTIONS

We shall examine the uncertainties in crater dimension predictions for nuclear craters in the 10^5- to 10^6-ton yield range based on chemical-cratering data obtained in the 10^{-1}- to 10-ton range. Thus, the typical yield extrapolation is a factor of 10^5. A discussion of the relative contribution of the errors in efficiency and scaling exponents to the net error follows:

The net standard deviation associated with a predicted crater dimension is:

$$\Sigma_{R_i}^2 = \sigma_{R_i}^2 + \sigma_e^2 ,$$

where Σ_{R_i} = the net standard deviation for a predicted crater dimension,

σ_{R_i} = the standard deviation in R_i resulting from the errors in efficiency and yield exponents (prediction error),

σ_e = the standard deviation of a single crater observation.

Since σ_e can be obtained from chemical explosives of a given yield, σ_e and σ_{R_i} are uncorrelated. We restrict the discussion to an evaluation of σ_{R_i} in desert alluvium. From Equation (2) we derive:

$$dR_i^{c,n}/R_i^{c,n} = \left(p_i + \left[E/f_i\right]\frac{\partial f_i}{\partial E}\right)\, dE/E + (p_i \ln EW)\, dp_i/p_i + \left(\left[q/f_i\right]\frac{\partial f_i}{\partial q}\right) dq/q \,. \quad (13)$$

In terms of standard deviations, we have:

$$\sigma_{R_i}^2 = (p_i + \varepsilon_i(h)q)^2\, \sigma_E^2 + (p_i \ln EW)^2\, \sigma_{p_i}^2 + (\varepsilon_i(h)\, q \ln EW)^2\, \sigma_q^2 \quad (14)$$

where σ_{R_i}, σ_E, σ_{p_i}, and σ_q are the fractional standard deviations in $R_i^{c,n}$, E, p_i, and q, respectively, and

$$\varepsilon_i(h) = \left(1/q\right)\left(E/f_i\right)\frac{\partial f_i}{\partial E} = \left(1/\ln EW\right)\left(1/f_i\right)\frac{\partial f_i}{\partial q} \,.$$

Evidently the prediction error depends on depth of burst and yield extrapolation as well as the errors in p_i, q, and E. The dimensionless quantity, $\varepsilon_i(h)$, is plotted in Figure 7 in the case where $f_i(h)$ is represented by Equation (9) and the coefficients A_{im} are taken from Table I.

For depths of burst near the surface or the maxima of the depth-of-burst curves, the following condition holds:

$$|\varepsilon_i(h)| << 1 \,. \quad (15)$$

(Compare Figures 5, 6, and 7.)

For this condition and with the aid of Equation (14), we observe that:

1. E and q are least accurately determined,
2. The prediction error is a minimum.

We next calculate the error in E. From Equation (2) and under the condition of Equation (15) which is valid for the nuclear data in desert alluvium, we derive:

$$\sigma_E^2 \approx \left(1/p_i^2\right)\left[\sigma_e^2 + (p_i \ln EW)^2 \sigma_{p_i}^2\right] \,. \quad (16)$$

The curves of Figures 5 and 6 are essentially based on data from 256-pound explosions. Thus the appropriate yield extrapolation is $\approx 10^4$. Taking the values for p_i and σ_{p_i} from Section III and $\sigma_e = 0.10$ (see the spread of data in Figures 5 and 6) we have:

$$\sigma_E \approx 45 \text{ percent.}$$

Using these values we can now calculate the prediction error for a yield extrapolation of 10^5 and for the condition of Equation (15) from Equation (14).

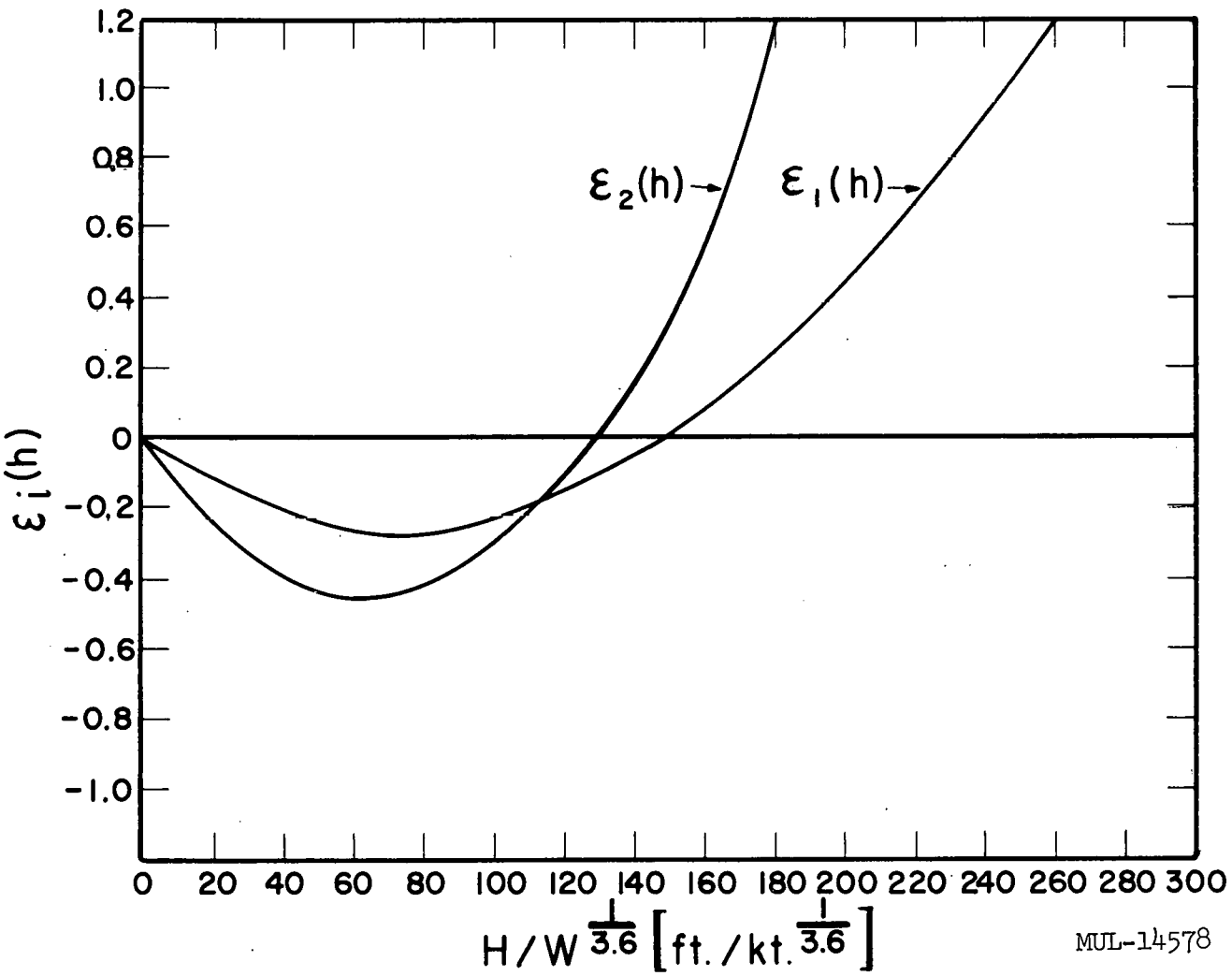

Fig. 7. The function ε_i (see text) versus scaled depths of burst.

Thus, $\sigma_{R_i} \approx 17$ percent. Therefore, the net standard deviation for a predicted nuclear crater dimension in desert alluvium involving a yield extrapolation of 10^5 is $\Sigma_{R_i} \approx 20$ percent.

For an experiment designed to provide data for predicting nuclear crater dimensions in a new material, the following relationship among crater parameter uncertainties should hold under the condition of Equation (15).

$$|\sigma_E| \approx |\sigma_{p_i} \ln EW| \approx |\sigma_{q\varepsilon_i(h)} \ln EW| . \tag{17}$$

We draw the following conclusions from Equation (17):

1. The accuracy of the depth-of-burst yield exponents (q) is much less important than that of the crater-dimension yield exponents.
2. The relationship between the precision that should be attempted for p_i and the precision of E so that approximately equal uncertainties will be introduced in the calculations of R_i, is given by

$$\sigma_{p_i} \approx \frac{\sigma_E}{|\ln EW|} . \tag{18}$$

Clearly, the precision of the yield exponents is much more important than that of efficiency. For our assumed extrapolation range of 10^5 in yield, the accuracy of p_i should be more than an order of magnitude better than that of E. In desert alluvium the scaling exponents are known to an accuracy of about three percent. To explore cratering phenomena in another medium to this same extent would require a knowledge of the efficiency to about a factor of one-third. Thus, it would appear that medium effects could be adequately explored using chemical explosives only.

V. CONCLUSIONS

A. A general empirical analysis, such as that presented here, provides a powerful tool for describing and interrelating chemical- and nuclear-explosive cratering. Such concepts as the principle of similitude and the efficiency as represented by one parameter can be readily tested by this analysis.

B. The analysis of chemical cratering in desert alluvium gives the following yield exponents for yields in the range 256 pounds to 40,000 pounds:

$1/p_1 = 3.4$ (crater radius),

$1/p_2 = 3.4$ (crater depth),

$1/q = 3.6$ (depth of burst).

The standard deviation associated with p_1 and p_2 is 3 percent; that for q is 3 percent. Thus, for these phenomena, the principle of similitude is not rigorously obeyed.

C. Assuming nuclear cratering is best described by the same yield exponent as chemical cratering, the percent efficiencies for nuclear cratering are then,

	Based on Crater Radius	Based on Crater Depth
Jangle S	2.6 ± 1.2	4.6 ± 2.1
Jangle U	78 ± 35	146 ± 66
Teapot Ess	43 ± 19	208 ± 94

Thus, the relationship between chemical and nuclear cratering capabilities (the efficiency) cannot be given in terms of one parameter.

D. The prediction error depends on depth of burst and yield extrapolation as well as the errors in the yield experiments and efficiency. For depths of burst near the surface or the maxima of the depth-of-burst curves:

1. E and q are least accurately determined,
2. The error in predicting nuclear crater dimensions from low-yield chemical explosives is a minimum,
3. The net standard deviation for a predicted nuclear crater dimension in desert alluvium involving a yield extrapolation of 10^5 is approximately 20 percent.

E. The relationship between the uncertainties in cratering parameters are summarized as follows:

1. The accuracy of the depth-of-burst yield exponent q is much less important than that of the crater dimension yield exponents p_i.
2. The relationship between the precision that should be attempted for p_i and the precision of E is given by:

$$\sigma_{p_i} = \frac{\sigma_E}{|\ln EW|} ,$$

where EW is the yield extrapolation.

F. For yield extrapolations of the order of 10^5 or more, the accuracy of p_i should be more than an order of magnitude better than that of E. Thus, for these conditions, medium effects could be adequately explored with chemical explosives.

ACKNOWLEDGEMENTS

I am indebted to Drs. G. W. Johnson and M. D. Nordyke for their helpful advice and encouragement. The preparation of the manuscript by Mrs. Wilma McGurn is gratefully acknowledged.

REFERENCES

Baldwin, R. B., Face of the Moon, University of Chicago Press, Chicago, 1949.

Brode, H. L., and R. L. Bjork, Cratering from a Megaton Surface Burst, RM 2600, The RAND Corporation, June 30, 1960.

Chabai, A. J., Crater Scaling Laws for Desert Alluvium, SC 4391 (RR), Sandia Corporation, December 1959.

Chabai, A. J., and D. M. Hankins, Gravity Scaling Laws for Explosion Craters, SC 4541 (RR), Sandia Corporation, December 1960.

Hoel, Paul G., Introduction to Mathematical Statistics, 2nd ed., John Wiley & Sons, Inc., New York, 1954.

Johnson, G. W., G. H. Higgins, and C. E. Violet, Underground Nuclear Detonations, J. Geophys. Research, October 1959.

Kennedy, G. C., and G. H. Higgins, Temperatures and Pressures Associated with the Cavity Produced by the Rainier Event, UCRL-5281, July 1958.

Lewis, John G., Private Communication, July 1958.

Murphey, B. F., and H. R. McDougall, Crater Studies in Desert Alluvium, Sandia Corporation, SCTM 119-59 (51), May 1959.

Murphey, B. F., and L. J. Vortman, Cratering with Chemical Explosives, Proceedings of the Second Plowshare Symposium, May 13-15, 1959, UCRL-5676, 5-19.

Nordyke, M. D., On Cratering, UCRL-6578, August 1961.

Pokrovskiy, G. I., Diffusion Blasting: Coal Mining, Military Aeronautical Engineering Academy, Moscow, Priroda No. 8, August 1957, 81-83.

Shelton, A. Vay, M. D. Nordyke, and R. H. Goeckermann, The Neptune Event, A Nuclear Cratering Experiment, UCRL-5766, April 1960.

U. S. Army Corps of Engineers, Cratering Effects of Surface and Burial H.E. Charges in Loess and Clay, Technical Report No. 2-482, Waterways Experiment Station, Vicksburg, Mississippi, June 1958.

Vaile, R. B., Stanford Research Institute, Private Communication, June 1955.

Vortman, L. J., Relative Cratering Efficiency of Nuclear Explosives, SCTM 114-59 (51), Sandia Corporation, Albuquerque, New Mexico, April 1959.

Vortman, L. J., and L. N. Schofield, High-Explosive Cratering in Fan Delta Alluvium, SCTM 60-59 (51), Sandia Corporation, October 1959.

Vortman, L. J., A. J. Chabai, W. R. Perret, and J. W. Reed, Project Buckboard, Interim Report, SC 4486 (RR), Sandia Corporation, November 1960.

/cc

520
1-17-62

MASTER

UCRL-6438
PART II

PROCEEDINGS of the GEOPHYSICAL LABORATORY–LAWRENCE RADIATION LABORATORY CRATERING SYMPOSIUM

held at
The Geophysical Laboratory of
The Carnegie Institute
Washington, D.C.
March 28–29, 1961

LAWRENCE RADIATION LABORATORY, UNIVERSITY OF CALIFORNIA
LIVERMORE, CALIFORNIA

Nuclear Explosions –
Peaceful Applications, UC-35
TID-4500 (16th Ed.)

UNIVERSITY OF CALIFORNIA
Lawrence Radiation Laboratory
Livermore, California

Contract No. W-7405-eng-48

PROCEEDINGS OF THE GEOPHYSICAL LABORATORY/LAWRENCE RADIATION LABORATORY CRATERING SYMPOSIUM WASHINGTON, D. C. MARCH 28-29, 1961

Milo D. Nordyke
(Editor)

October, 1961

UCRL-6438
Part II

Printed in USA. Price $5.50 (includes two volumes, Parts I and II).
Available from the Office of Technical Services,
Department of Commerce
Washington 25, D. C.

PREFACE

This is the second volume of the Cratering Symposium proceedings. It contains principally the papers delivered on the second (final) day of the meeting. For the papers delivered on the first day and for general information on the symposium, see the companion first volume (UCRL-6438, Part I).

CONTENTS

Paper J

CALCULATIONS OF UNDERGROUND EXPLOSIONS

George Maenchen and John Nuckolls

Lawrence Radiation Laboratory, University of California

Livermore, California

ABSTRACT

The described calculations are an attempt to predict underground explosion phenomena from physical conservation laws and laboratory measurements of the properties of the materials. Analytic solutions for nontrivial cases are usually impossible to obtain because of the nonlinear behavior caused by the simultaneous existence of and dynamic transitions between gaseous, liquid, plastic, fractured, and elastic states. We have therefore chosen to integrate the equations numerically on a digital computer. In the two "codes" developed for this purpose the calculation is simplified by restricting the problem to spherical or cylindrical symmetry. Inelastic effects like plasticity and fracture are treated by imposing simple restrictions on the stress tensor.

* * *

General Description. In order to predict underground explosion phenomena without recourse to simple scaling of past explosions, a method of calculating the motion of elastic, plastic, and fluid materials is required. Such a calculation involves the solution of a set of coupled partial differential equations derived from the conservation laws for mass, momentum, and energy together with a reasonable mathematical model of the response of the materials concerned. Since analytic solutions for nontrivial cases are difficult and frequently impossible to obtain, we have chosen to integrate the equations numerically on a digital computer. Two "codes" have been developed for this purpose. In both codes the necessary number of variables is reduced by requiring some degree of symmetry in the problem. The older code, UNEC, describes spherically symmetric motion; it is one-dimensional in that there is only one permitted direction of motion (radial). This code has been in use for over two

years and results of some calculations have been published.[1] Recently a two-dimensional code, TENSOR, has been developed to study cylindrically symmetric problems (e.g., craters) where two spatial variables are required. This code is still being tested, and has given satisfactory agreement with UNEC results and with some analytic solutions. The following description of the calculations is expressed in terms of the TENSOR code; the UNEC code, of course, follows the same general lines.

TENSOR is a cylindrically symmetric two-dimensional Lagrangian elastic-plastic-hydrodynamic code for the IBM 709/7090. The equations describe the motion of material under the influence of a stress tensor (in contrast to the usual scalar pressure in hydrodynamic calculations). The distinction between purely elastic and plastic, cracked, and fluid materials is made by imposing certain restrictions on the stress tensor. It is assumed that the materials are homogeneous and isotropic. The basic difference equations are derived from the differential equations for conservation of momentum and energy:[2]

$$\rho\dot{u} = -\frac{\partial}{\partial R}(P+Q-\tau_R-Q_R)+\frac{\partial}{\partial Z}(\tau_{RZ}+Q_{RZ})+\frac{1}{R}(2\tau_R+2Q_R+\tau_Z+Q_Z)+G_R,$$

$$\rho\dot{v} = -\frac{\partial}{\partial Z}(P+Q-\tau_Z-Q_Z)+\frac{\partial}{\partial R}(\tau_{RZ}+Q_{RZ})+\frac{1}{R}(\tau_{RZ}+Q_{RZ})+G_Z,$$

$$\dot{E} = (2\tau_R+\tau_Z+2Q_R+Q_Z)\dot{e}_R+(\tau_R+2\tau_Z+Q_R+2Q_Z)\dot{e}_Z+(2\tau_{RZ}+2Q_{RZ})\dot{e}_{RZ}-\frac{(Q+P)\dot{V}}{V^0},$$

where

R, Z = radial and axial coordinates,

u, v = radial and axial velocities,

ρ = density,

P = pressure = the negative of the isotropic component of the stress tensor,

τ_R, τ_Z, τ_{RZ} = radial, axial, and shear components of the deviatoric stress tensor,

Q, Q_R, Q_Z, Q_{RZ} = viscous damping terms,

G_R, G_Z = R and Z components of gravity,

E = internal energy per unit original volume,

V = volume,

η = compression = $\frac{V^0}{V}$ (V^0 is original volume),

$\dot{e}_R$, $\dot{e}_Z$, $\dot{e}_{RZ}$ = components of deviatoric strain-rate tensor.

The stress tensor was expressed in deviatoric form in order to facilitate calculation of plastically deformed material (since plastic yielding limits only the effective shear stress but not the average pressure).[3] In the case of a fluid material the deviatoric stress tensor vanishes and the equations of motion reduce to the familiar hydrodynamic case. The possibility of plastic deformation also requires that the stress-strain relationship be expressed in incremental form, since one cannot define a meaningful absolute strain (in terms of coordinates at t = 0) in a material which has at some previous time deformed inelastically. In this form, Hooke's law becomes

$$\dot{P} = -k\dot{\theta}$$

$$\dot{\tau}_i = 2\mu\dot{e}_i + \text{rotation term}, \quad i = R, Z, \text{ or } RZ,$$

where

k = bulk modulus = $\lambda + \frac{2}{3}\mu$,

λ, μ = Lamé constants,

θ = dilatation,

and the rotation terms account for stress changes caused by rotation of already stressed material.

In the code itself the derivatives in the above equations are expressed as finite differences. The spatial distribution of material is described in terms of a mesh of finite quadrilateral zones, which is integrated in time over many finite time-steps. The use of a Lagrangian mesh automatically conserves mass. After each time-step the stress in each zone is recalculated. Here inelastic behavior (like plasticity) may be taken into account by testing and suitably modifying the stress in the zone.

Plasticity. Plastic yielding arises from the inability of real materials to support arbitrarily large shear stress. While several proposed yield criteria may be found in the literature, the differences between them are considerably smaller than the uncertainties of the applicable material constants. In the

code a generalized form of the von Mises yield criterion is used: $f = J_2 - K^2$. Here J_2 is an invariant of the deviatoric stress and K corresponds to the shear strength which may be made a function of pressure and also of the work done in previous plastic deformation (work hardening). When $f < 0$ the material behaves elastically, but when $f > 0$ the shear strength has been exceeded and the stresses are adjusted to bring f to zero.

Cracking. When the tensile stress across some element of material exceeds the material's tensile strength a crack forms normal to the direction of the stress. This direction is not, in general, parallel to either of the RZ coordinate axes used in the code. It can be shown that for any local stress system there exists a coordinate system such that the stress tensor, when transformed to this system, is diagonal. The elements of this transformed tensor correspond to the greatest (and least) normal stress experienced by the material. Thus it is this greatest stress which will cause the first crack to form, and the orientation of the transformed coordinate system corresponds to the direction of the crack. In the code the three elements of the diagonalized stress tensor (sometimes called "principal stress components") are calculated and compared with a stored constant tensile strength. If the tensile strength is exceeded, the stresses are adjusted by an amount sufficient to reduce the stress normal to the crack surface to zero. In this adjustment it is assumed that only the principal strain normal to the crack can change (i.e., that formation of the crack causes no sudden material motion parallel to the crack surface). This adjustment is then translated to an adjustment of the deviatoric and isotropic stress components in the RZ coordinate system. The code keeps track of the crack width and, until the crack closes again at some later time, continues to adjust the stresses in order to maintain the principal stress component normal to the crack at zero. It is, of course, possible that two or even three mutually perpendicular cracks exist simultaneously in the same element of material. In the case of three simultaneous cracks all the elements of the stress tensor are zero (which physically corresponds to something like uncompressed gravel), and the code relabels the material with a different equation of state.

Hydrodynamic Fluid. The code has provisions for treating some material as a hydrodynamic fluid with a simple polynomial equation of state:

$$P = a_0 + a_1\mu + a_2\mu^2 + a_3\mu^3 + (b_0 + b_1\mu + b_2\mu^2)E$$

where $\mu = \eta - 1$. More elaborate equations of state can be added if necessary. In this material the deviatoric tensor elements are of course set to zero.

Transitions. The code has provisions for relabeling the material in each zone to permit the treatment of the zone to be changed according to its individual history. For example, an initially elastic material may have enough work done on it to cause it to melt and subsequently be treated as a fluid. Similarly one may wish to treat elastic zones differently according to whether any crack has ever formed (since the presence of a crack may also weaken the material in other directions). There is an option to permit brittle failure to occur when the shear strength is exceeded (rather than the ductile plastic flow described above). The transitions presently in the code are summarized below.

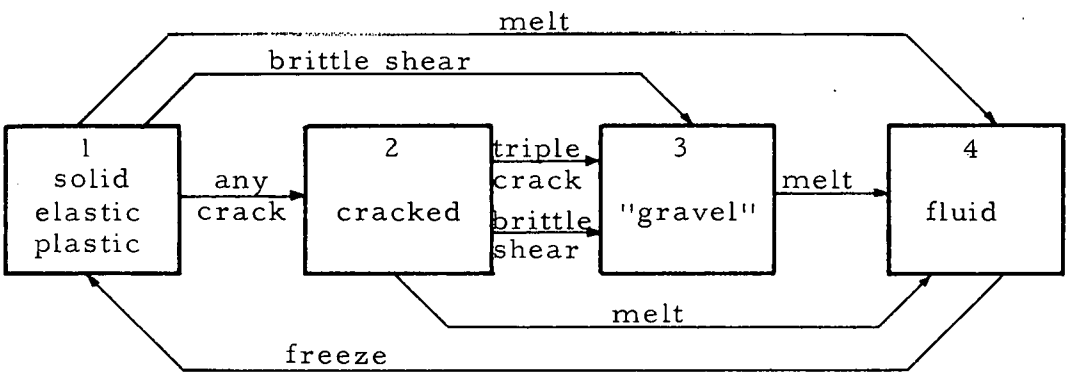

Damping. To ensure stability some kind of viscous damping is needed. Like the stress tensor the damping has been expressed as a scalar Q and a deviatoric tensor (with elements Q_R, Q_Z, Q_{RZ}). To permit flexibility in experimenting with the type of damping appropriate to this kind of calculation, four

forms of Q are available (although they certainly would not all be used simultaneously).

Scalar Q:

$$Q = Q_1 + Q_2 + Q_3 ,$$

where

$$Q_1 = C_0 \rho^0 \eta (\Delta \vec{U})^2 ,$$

$$Q_2 = \left(C_1 c \rho^0\right) \eta [(\Delta \vec{U})^2]^{1/2} ,$$

$$Q_3 = (C_2 c \rho \Delta X) \frac{1}{V} \frac{\partial V}{\partial t} .$$

Here Q_1 is the usual (quadratic) von Neumann Q, Q_2 is a linear form of Q_1 (effective at low velocity only), and Q_3 is a volume viscosity which together with Q_i corresponds to the stress tensor in viscous flow.

Tensor Q:

$$Q_i = (C_3 c \rho \Delta X) e_i , \quad i = R, Z, \text{ or } RZ,$$

where

C_0, C_1, etc. are constants (typically ~ 1/2),

$\Delta \vec{U}$ = rate of collapse of the zone,

ΔX = a typical zone size,

c = sound speed.

REFERENCES

1. Proceedings of the Second Plowshare Symposium, Part I: Phenomenology of Underground Nuclear Explosions, University of California Lawrence Radiation Laboratory (Livermore) Rept. UCRL-5675, May 1959, pp. 120-134.
2. See also I. S. Sokolnikoff, Mathematical Theory of Elasticity (McGraw-Hill Book Co., Inc., New York, 1946).
3. R. Hill, The Mathematical Theory of Plasticity (Clarendon Press, Oxford, 1950).

Paper K

PRELIMINARY NOTES ON THE MECHANICS OF EXPLOSIVE CRATER FORMATION

M. D. Nordyke

Lawrence Radiation Laboratory, University of California

Livermore, California

ABSTRACT

Experimental data from nuclear and chemical explosive cratering programs and theoretical machine calculations of the behavior of underground explosions have been used to construct a picture of the major mechanisms that contribute to the formation of explosion craters. These mechanisms include compaction and plastic deformation of the medium immediately surrounding the explosion, spalling of the surface above the explosion by the tensile wave generated at the free surface of the ground, and acceleration of the fractured material overlying the explosive cavity by the gases trapped in the cavity, before and during their escape. The role that each of these mechanisms plays changes with the scaled depth of burst of the explosion and to some extent with the surrounding material. The contribution that each makes is outlined for four typical craters representing surface, shallow, optimum, and deep burial depth. For surface burial, plastic deformation and compaction are the principal actions; for shallow burial depth, spall is the dominant feature; for optimum depth, gas acceleration becomes the most important mechanism; and for deep depth of burial, subsidence of overlying material into the cavity produced by plastic deformation and compaction is the major factor. The differences to be expected between explosion craters and craters resulting from impact explosions such as those produced by meteors are examined. An estimate of the relative contribution of each of these mechanisms is also made for apparent crater depth versus depth of burst.

* * *

The general subject of cratering has been studied for many years by many investigators. Much of the work has been of a qualitative nature, with a few notable successes for quantitative analysis of isolated phases of the processes involved. Much of the analysis has been based upon empirical

relationships or dimensional-analysis arguments which, while providing a useful bridge, have not given much insight into the basic problems involved. This will certainly not be a quantitative discussion either, but I hope to set down a few ideas relating to the mechanisms involved in the formation of explosive craters, together with some estimates of their relative orders of magnitude. The analogy between explosive craters and impact craters, such as result from meteors hitting the earth or the moon, is not, in my mind, complete. I will attempt to point out some of the differences in this discussion.

The ideas expressed in this paper are based on many sources, ranging from the experimental data derived from cratering programs such as Teapot ESS,[1] Scooter,[2] Bureau of Mines[3] work, and Neptune re-entry and reconstruction,[4] to theoretical advances made possible through the development of machine calculations such as the UNEC code described by Maenchen and Nuckolls.[5]

Definitions

For the purpose of this paper, definitions of several of the terms to be used should be made. Unfortunately there is no uniform terminology in the field of elastoplastic behavior, and each writer is forced to define his own terms for his purposes. This difficulty, of course, arises to a great extent because of the tremendous range of properties of materials — causing definitions that are adequate for one material to break down for another.

Figure 1 is a schematic drawing of a typical crater cross section showing the pertinent parameters. The apparent crater is defined as the crater visible on the surface; its dimensions are measured with respect to the original ground level. The true crater is defined as the boundary between the loose, broken fallback material and the material that has been crushed and fractured but has not experienced significant vertical displacement. The products of the explosion are widely dispersed throughout the fallback material that rests in the true crater after the explosion.

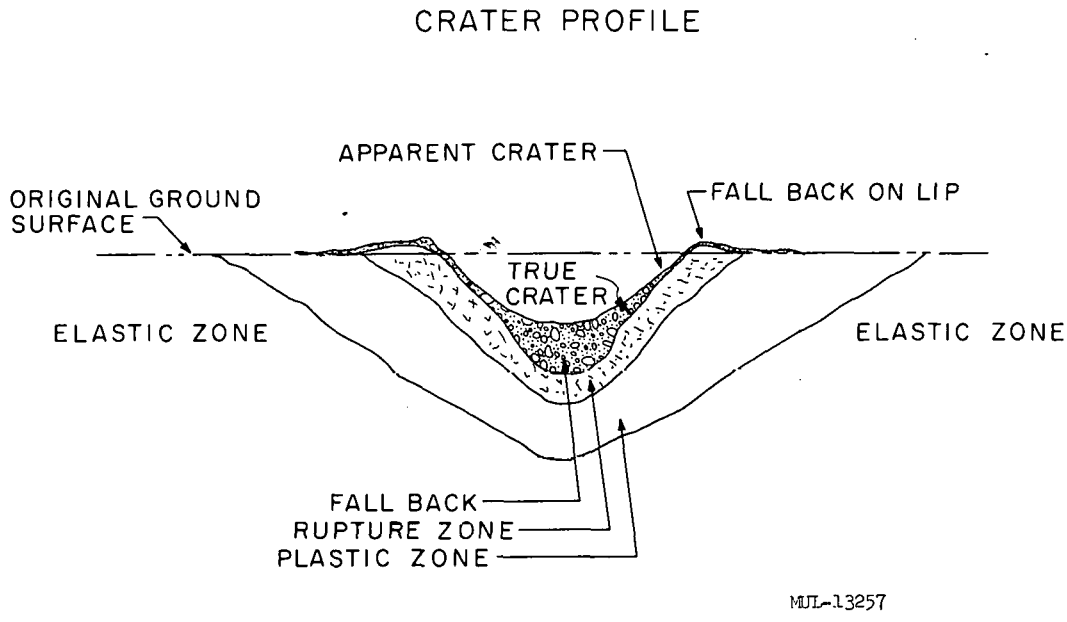

Fig. 1. Schematic drawing of a typical crater.

The rupture zone is perhaps the most difficult to define, particularly with regard to differentiating it from the plastic zone. There is, of course, a gradual transition from one zone to the other. In the rupture zone near the true crater interface, large amounts of fracturing and crushing by shear failure and gross displacements by faulting and underthrusting are generally seen. Their severity decreases as one goes farther down into the rupture zone, until near the rupture zone/plastic zone interface only small-scale shear failures (of the order of an inch) are found. This zone gradually shades into the plastic zone, in which there are small uniform permanent displacements which decrease to infinitesimal values as one goes into the elastic zone.

The extent of these zones is very dependent on the material in which the crater is made, varying widely for different materials in the range between alluvium and basalt. The definitions given here have been derived principally for soft materials such as alluvium, and there would have to be some redefinitions of these terms for a discussion of cratering in hard rock.

I should hasten to add at this point that I have discussed this entire problem as a physicist, and as is well known, there is a distinct difference in the approach of physicists and geologists. Recognizing this, I hope the geologists in the audience will not take me to task for some of my terminology.

Mechanisms of Crater Formation

One phenomenon that is present in all underground explosions to varying degrees is the crushing, compaction, and plastic deformation of the medium immediately surrounding the source of the explosion, whether it be a chemical explosion, nuclear explosion, or impact explosion. As the high pressure gases generated by the explosion push on the walls of the cavity, a shock wave is generated across whose spherical surface there is a sharp discontinuity in the physical state of the material. This discontinuity propagates outward at a velocity that, for high pressures, is faster than the speed of sound in the medium. For chemical explosives the initial pressures are of the order of 100-200 thousand atmospheres; for a nuclear explosive they are as large as 10-100 million atmospheres, depending on the initial cavity; and for a meteor impact explosion they can have any value ranging between these two, depending on the meteor velocity and the type of material it hits. For explosions where the pressures are greater than 500 thousand atmospheres, the medium is melted and vaporized when the shock passes through it. As the shock wave moves outward in a spherically diverging shell, the peak pressure in the shock front drops because of spherical divergence as well as energy expenditure in doing work on the medium. For pressures above the dynamic crushing strength of the material, this work appears in the form of crushing, heating, and physical displacement. In regions outside the limit of crushing, the shock wave will still produce permanent deformation by plastic flow until the peak pressure in the shock front has decreased to a value equal to the plastic limit for the medium. This plastic limit marks the boundary between the elastic and plastic zones described for Fig. 1. As with the definitions given for Fig. 1, the limits of crushing and plastic deformation vary widely from material to material.

The above picture of the first few milliseconds of an explosion neglects the effects of any free surface, effects which are exceedingly important. As a compressive wave encounters a free surface, it must match the boundary condition that the pressure, or more correctly the longitudinal stress, be zero at all times. This results in the generation of a negative stress wave or rarefaction which propagates back into the medium. This process is shown schematically in Fig. 2 where a triangular-shaped stress wave $\sigma_n(t)$ has been assumed for simplicity instead of the more correct exponential shape. At some depth, such as P in Fig. 2, the sum of the two stress waves is equal to the dynamic tensile strength of the medium; hence the medium breaks in tension at P, with a piece flying off at a velocity characteristic of the total momentum trapped in it. This produces a new free surface that will break at P' and again at P''. For a loose material like alluvium, this process, called "spall," makes almost every particle fly into the air individually, whereas in a rock such as basalt the thicknesses of the slabs are generally determined by presence of pre-existing joints and zones of weakness. For the case of a small sample or where there is a very massive block, the dynamic tensile strength of the rock determines the thickness of spall. As the distance from the explosive to the free surface gets larger, the peak pressure decreases and so the maximum possible tensile stress decreases until it no longer exceeds the tensile strength of the medium. In addition, the velocity given to the spall decreases in proportion to the peak pressure. For ranges beyond the point where spall occurs, the negative stress in the rarefaction wave will decrease the shear strength of the medium, which results in ruptures and large plastic deformations. This makes the rupture zone extend a considerable distance along the surface and contributes to the formation of the lip. Ultimately the surface expression of a deep underground explosion is only a small elastic excursion of the surface. Spalling of the free surface is probably the most important phenomenon in cratering, especially for shallow depths of burst, and is the easiest mechanism to observe and to calculate.

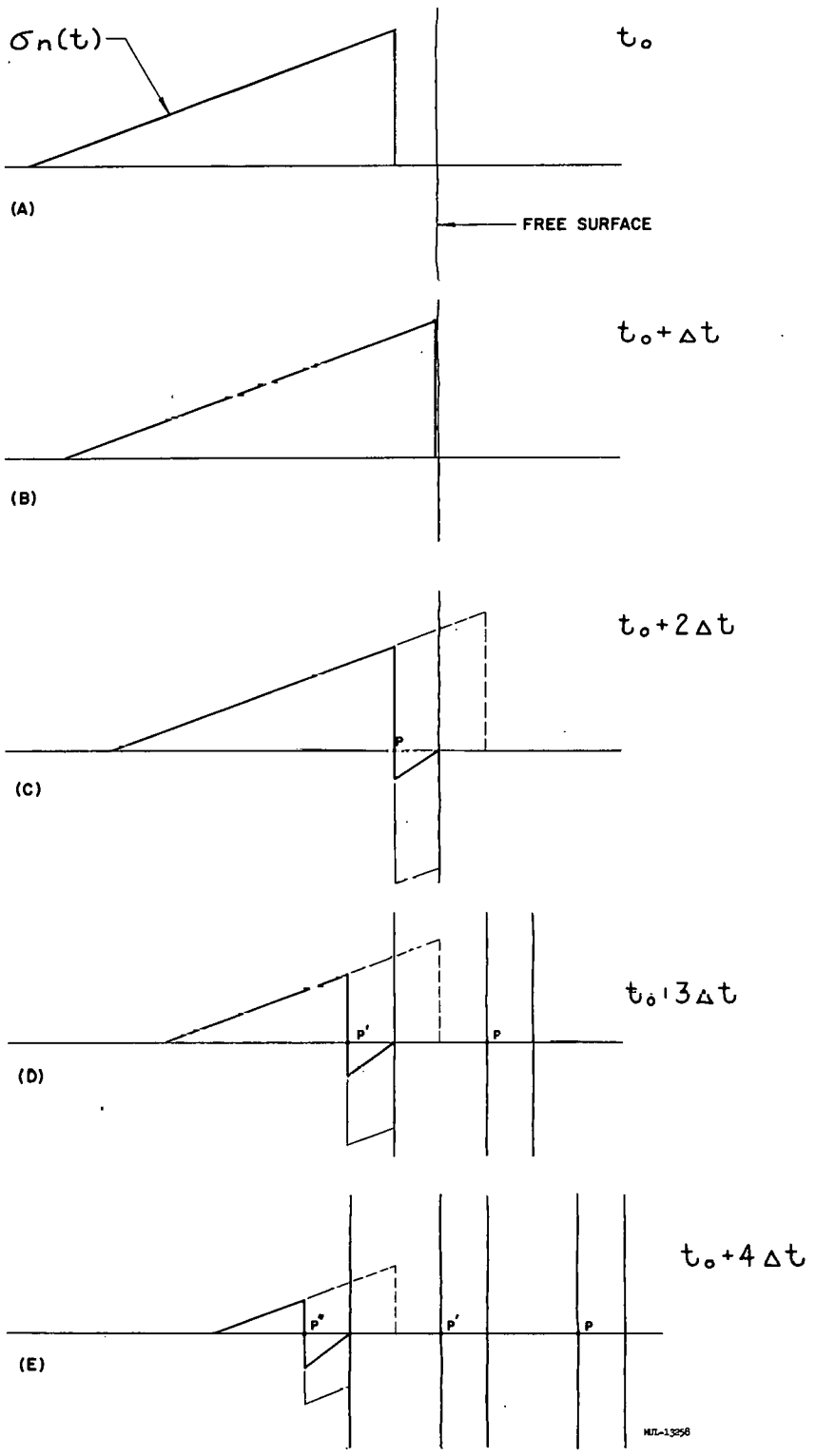

Fig. 2. Schematic drawing illustrating the spall mechanism.

The third mechanism of importance in cratering, particularly for craters deeper than some critical depth, is what I have termed "gas acceleration." This is a long-period acceleration given the material above the explosion by the adiabatic expansion of the gases trapped in the cavity. For some cases, particularly for deep depths of burst, this gas also gives appreciable acceleration during its escape through cracks extending from the cavity to the surface. For very shallow depths of burst the spall velocities are so high that the gases are unable to exert any pressure before venting occurs. For very deep explosions, the acceleration given the overlying material is so small as to be negligible. I will go into more detail on this process in a later section.

Subsidence is the last remaining major process that makes a significant contribution to the formation of the apparent crater. It is very closely linked to the first process of compaction and plastic deformation, without which there would be no void into which material could subside. Subsidence occurs when the spall or gas acceleration has so distended the overlying material that large cracks are produced through which the gases from the explosion escape. It is most important, of course, for very deep explosions.

Effect of Depth of Burst

The part each of the above mechanisms plays in producing a crater is very strongly dependent on the scaled depth of burst of the explosion. The effect of the depth of burst of a 1-kiloton (10^{12}-cal) explosion in alluvium on the radius and depth of the apparent crater is shown in Fig. 3. These curves are based on chemical explosion data taken by many investigators,[6-9] using $W^{1/3.4}$ scaling which Vaile[10] and other investigators[11,12] have shown best represents the high explosive data. These data for alluvium, along with much other information, have been used to draw the sketches in Fig. 4 of four typical craters in cross section. The small dashed circle about the detonation point indicates the size of the original TNT sphere. Explosions in other media would give different dimensions; for example, dimensions would be as much as 20-30% smaller for rock[13-15] and 20-50% larger for water-saturated media.[16]

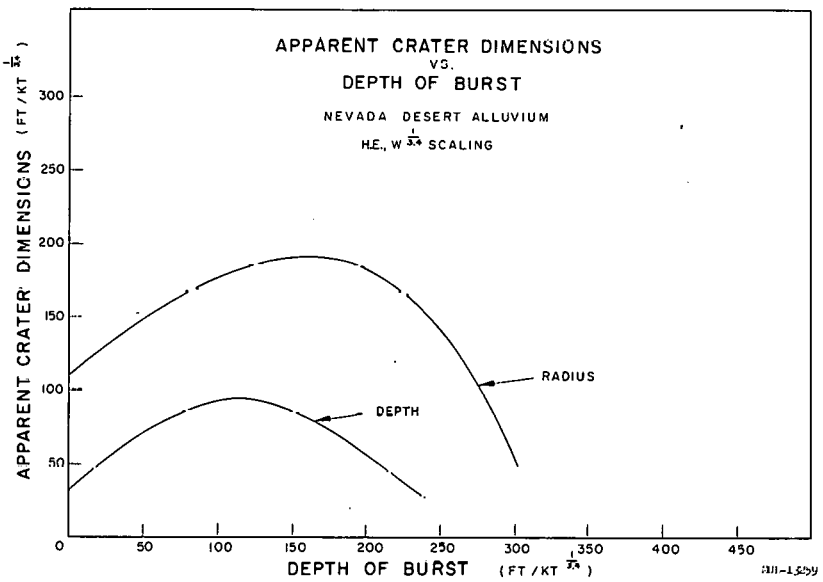

Fig. 3. Apparent crater dimensions vs depth of burst.

Surface Burial

Figure 4a shows the crater resulting from the detonation of an explosion very near the surface of the ground. As can be seen, the crater is produced to a large degree by compaction and plastic deformation. There is scouring action by the gases in the initial gas sphere which erodes the surface of the crater, but this is not a significant mechanism in the formation of the crater. The radius is extended to its limit by spalling action resulting from a horizontally diverging shock wave, but the major process for the depth of the center and for lip formation is the plastic deformation and flow of the material in the rupture zone. Very little fallback is found in a crater of this kind, and the true crater and apparent crater are almost the same.

The picture shown in Fig. 4a is based on data from the nuclear crater Jangle S.[1] It has dimensions somewhat smaller than would be expected from a chemical explosive at the same depth of burst, because of the large fraction of the energy from a nuclear explosion that is released in the form of thermal

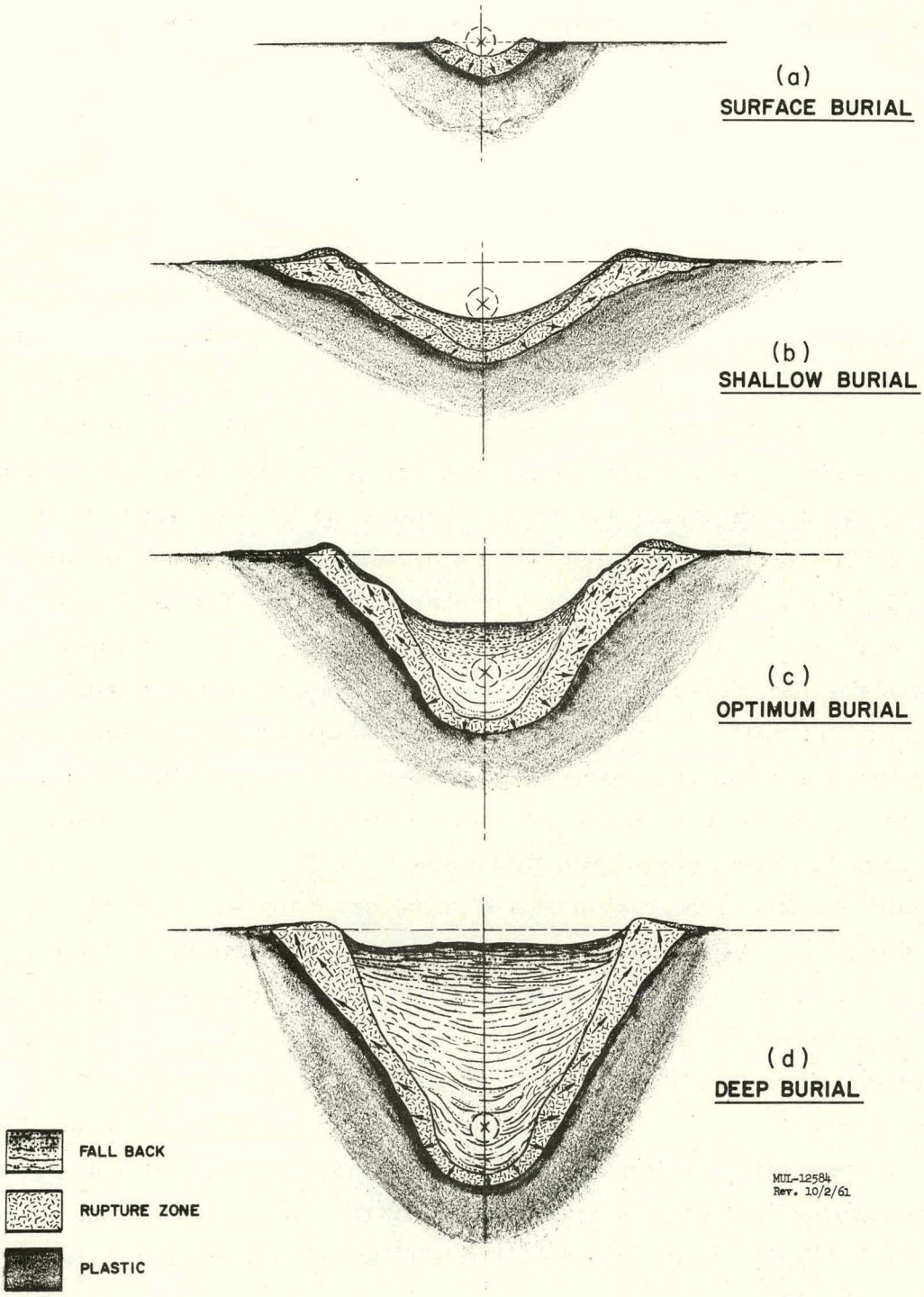

Fig. 4. Typical crater profiles vs depth of burst for alluvium.

and x-ray radiation. For meteoritic impact, the resulting explosion could be considered analogous to a surface burial only for very low velocity meteors. In this case, the pressures involved would be more like those occurring in a chemical explosion than a nuclear explosion, with the result that dimensions more like those shown in Fig. 3 for a surface burst would be expected. However, the mechanisms involved would be essentially the same.

Shallow Burial

A cross section of the crater resulting from shallow burial of the explosive is shown in Fig. 4b. This scaled depth of burst corresponds roughly to the scaled depth of the nuclear explosion Teapot ESS (66 ft). Spalling of the free surface has now become the dominant process for the formation of the crater. Gas acceleration and scouring action are of only minor importance because of the high velocities given to the material by the spalling process. The radius of the crater is determined by the limit of the spalling process, whose velocities decrease rather rapidly with increasing surface radius and thus cause the "folding back" of the material on the edge of the crater to form the lip that is evident in many craters including Teapot ESS and Meteor Crater, Arizona.[17] Below the original surface the radius of spall decreases because of the increased total path length the shock and the rarefaction must travel. This results in a roughly parabolic-shaped true crater. The extent of the fallback and rupture zone for a crater from a shallow depth of burst were very well defined by the sand column techniques used on Teapot,[1,8] and Fig. 4b is based very closely on this work.

The impact and explosion of a high velocity meteor is probably most closely simulated by a nuclear explosion at a shallow depth of burial. For example, Shoemaker's analysis of Meteor Crater[17] showed an approximate scaled depth of burial of 45 feet. Further, most of the general features noted in meteor craters are found in explosion craters for shallow scaled depths of burst. A nuclear explosion would more closely simulate the meteor impact explosion than would chemical explosions, because of the very high initial pressures and energy densities which are found in both nuclear and meteor explosions. Both are characterized by relatively small amounts of

condensable explosion products and by vaporization of considerable quantities of the medium surrounding the explosion. However, experience has shown that for shallowly buried nuclear explosions in alluvium, there are very small differences between chemical explosive and nuclear explosive craters. This is believed to be because (1) gas acceleration is not important for shallow depth of burst, and (2) there is 10-20% water in the alluvium, which produces noncondensable gases in the cavity when vaporized. The virtually complete venting of the radioactive material from the Teapot ESS explosion leads one to the conclusion that, if the high pressures and temperature predicted by Shoemaker are true, the meteoritic material from a meteor impact would also be completely vaporized and vented to the atmosphere and be spread over the surrounding countryside. One should add that there is undoubtedly not an exact correlation between an impact crater and an explosion crater because the meteor's energy is released in the form of a line source as opposed to a point source for an explosion. Thus, deviation from the dimensions predicted for explosion craters should be expected.

Optimum Burial

For an explosion at optimum depth, i. e., at a depth that results in maximum apparent crater dimensions, the resulting crater would appear as shown in Fig. 4c. The apparent crater dimensions shown are taken from the Scooter crater.[2] The Scooter event was the detonation of a 1-million-lb TNT sphere buried 125 feet deep in desert alluvium, a scaled depth of burst of 153 feet. The true crater and rupture zone for both this sketch and the deep burial (Fig. 4d) are estimates. For craters at these depths of burst, all three phenomena – plastic deformation, spall, and gas acceleration – are important, but the latter has become the dominant feature of the cratering process. When the shock wave reaches the surface it has decayed to the point where, although it is still capable of fracturing the material in tension (since most media have very small tensile strengths), the velocities given the spalled material are relatively small. Since the maximum height to which a particle will go is proportional to the square of the initial velocity, if spalling were the only process the throwout would not go any appreciable distance into the air.

The inadequacy of the spall mechanism and the necessity for some kind of gas acceleration is best seen from the surface motion data from Scooter. Taking the displacement-versus-time data given by Feigenbaum and Wegkamp,[18] which was obtained from high speed motion pictures of seven surface targets on Scooter, and computing vertical velocities we get the plots shown in Fig. 5. The straight lines are least-squares fits to the data over the ranges of 80-350 msec and above 350 msec, respectively. General venting at about 1.2 sec obscured the targets. As can be seen from Fig. 5, the data very easily can be broken down into these two regions, one with a negative acceleration and the other with an approximately uniform positive acceleration. The data from the graphs in Fig. 5 are summarized in Table I where the initial velocities and the velocities at 1.2 sec are given along with the accelerations derived from the slopes of the lines in Fig. 5. In addition, the maximum heights are computed for the initial velocity and the 1.2-sec velocity, based on the equation $h = v^2/2g$. The heights based on the 1.2-sec velocity are quite consistent with observed particle trajectories, indicating that there was no appreciable acceleration after venting occurred.

Table I. Summary of data on motion of Scooter surface targets.

Target Number	2	3	4	5	6
Distance from surface zero (ft)	60	30	0	30	60
Initial velocity (ft/sec)	50	74	73	73	54
Acceleration, 80-350 msec (ft/sec^2)	-8	-46	-34	-27	-20
Acceleration, 350-1200 msec (ft/sec^2)	+39	+102	+133	+100	+17
Velocity at 1.2 sec (ft/sec)	85	145	177	150	70
Maximum height from initial velocity (ft)	39	86	83	83	46
Maximum height from 1.2-sec velocity (ft)	106	328	490	352	77

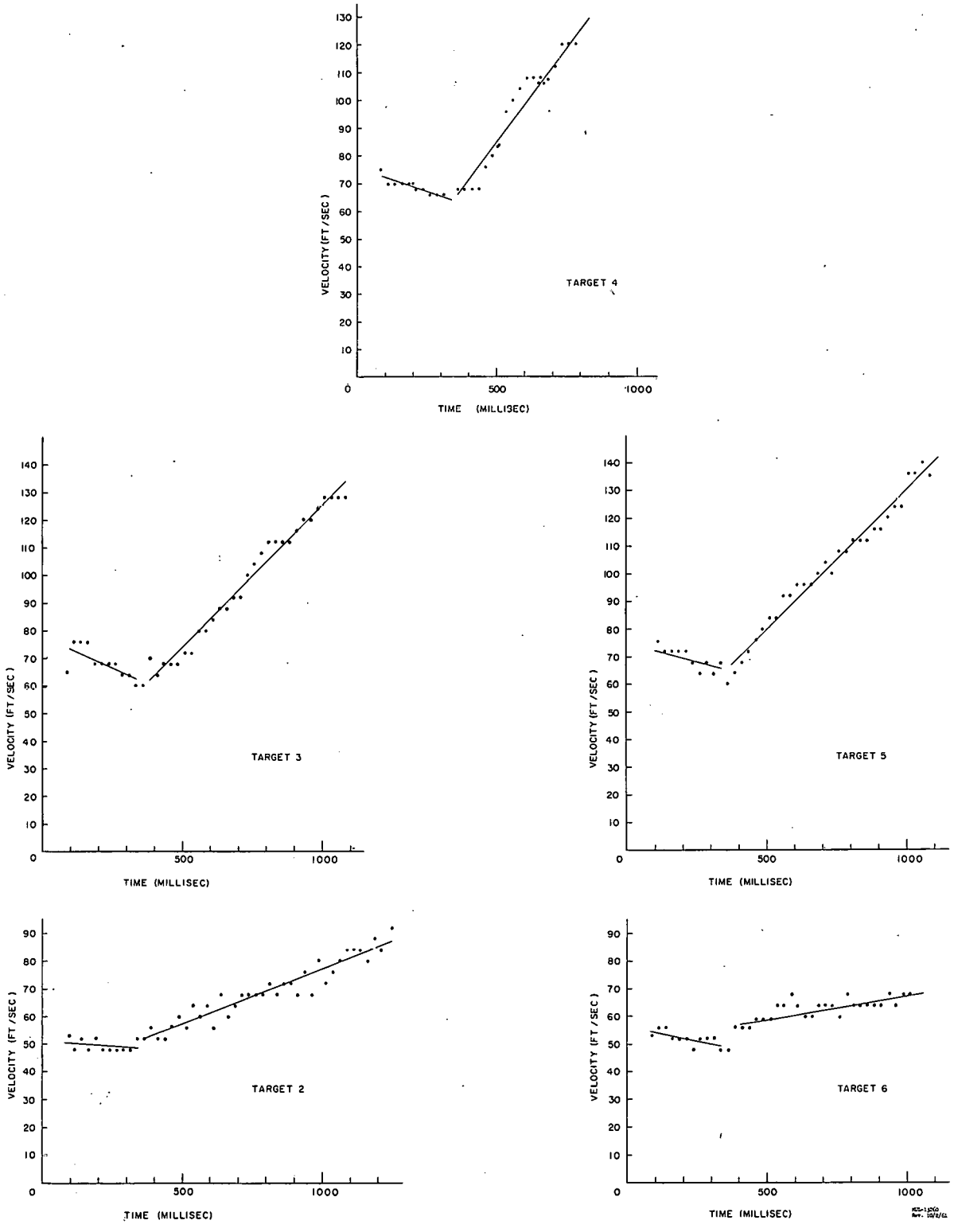

Fig. 5. Velocities of surface targets vs time, Project Scooter

The picture presented by the data of Table I is fairly clear. The first motion experienced by the surface of the ground is that produced by spall. The highest spall velocities of about 70-75 ft/sec are realized at surface zero, decreasing as one goes away from this point because of the increased travel length for the shock wave. As the rarefaction propagates back toward the cavity, all the material is given an upward velocity which decreases in magnitude with depth. After the passage of the shock, the material falls in approximately free fall as shown by the magnitude of the negative acceleration in the period from 80 to 350 msec. When the rarefaction reaches the cavity, the cavity begins to expand very rapidly, pushing on the loose and broken layers above it, picking up each layer as it moves upward, bringing them all to the same velocity in much the same manner that an engine of a freight train accelerates its cars when it reverses direction. Ultimately this second push reaches the surface and all the earth or rock above the explosion is moving as one mass. In Scooter, the hemispherical surface set in motion by spall experienced a relatively uniform positive acceleration starting at about 350-400 msec. The rate of acceleration was very dependent on the distance from surface zero. Finally, radial divergence of the hemispherical plug leads to the opening of large cracks from the cavity to the surface, through which the high pressure gas escapes. During its escape it gives appreciable acceleration to the material through which it is passing. This results in the surface layers experiencing a much longer period of acceleration than the deep layers. Much of the material immediately above the cavity does not attain the high velocity of the surface and falls back in place with very little mixing or disruption of the stratigraphy.

An order-of-magnitude estimate can be made of the validity of this picture, based on the results of a UNEC calculation[5] and some simple concepts. The UNEC code is a program for the IBM 7090 which can make a one-dimensional elastic-plastic-hydrodynamic calculation of the early history of an underground explosion. These calculations lead to the result that at the time when the shock wave reaches the surface of the ground, the pressure of the gas in the cavity is approximately 175 bars. The cavity radius

is about 36 ft versus an initial radius of about 15 ft for the TNT sphere. The initial surface velocity predicted by UNEC is 103 ft/sec, in fair agreement with the observed values of 70-75 ft/sec. This agreement is particularly encouraging when one considers the difficulties of making an elastic-plastic calculation for a sand-gravel mixture.

With these numbers an estimate can be made of the magnitude of the gas acceleration by considering the material contained in the solid angle, Ω, above the cavity. This solid angle is defined by the approximately hemispherical surface which is the first evidence of surface motion. Figure 6a shows a sketch of the situation at 350 msec if the material above the cavity continues to move but the cavity remains at the 36-ft radius. Numerous voids are opened up whose total volume equals the volume of the hemispherical segment. Figure 6b shows the configuration if the cavity is allowed to expand to take up all these voids. The new cavity volume is now $V_0 + \Delta V$, where ΔV is the volume of the spherical segment. Thus

$$\Delta V = \frac{\pi h^2 (3R-h)}{3}$$

where R = radius of hemisphere = depth of burst + h, and h = height of hemispherical segment. The new pressure in the cavity after this adiabatic expansion is given by

$$P = P_0 \left(\frac{V_0}{V_0 + \Delta V} \right)^{\gamma},$$

where P_0 = original pressure in cavity.

If we now assume that this conical mass moves as one under the influence of the gas in the cavity, we have

$$PA = Ma$$

where

$$M = \text{mass of cone} \approx \frac{R^3 \rho \Omega}{3},$$

$$A = \text{area of the truncated cone} = \Omega \left(\frac{V_0 + \Delta V}{4\pi/3} \right)^{2/3},$$

$$a = \text{acceleration experienced by conical mass.}$$

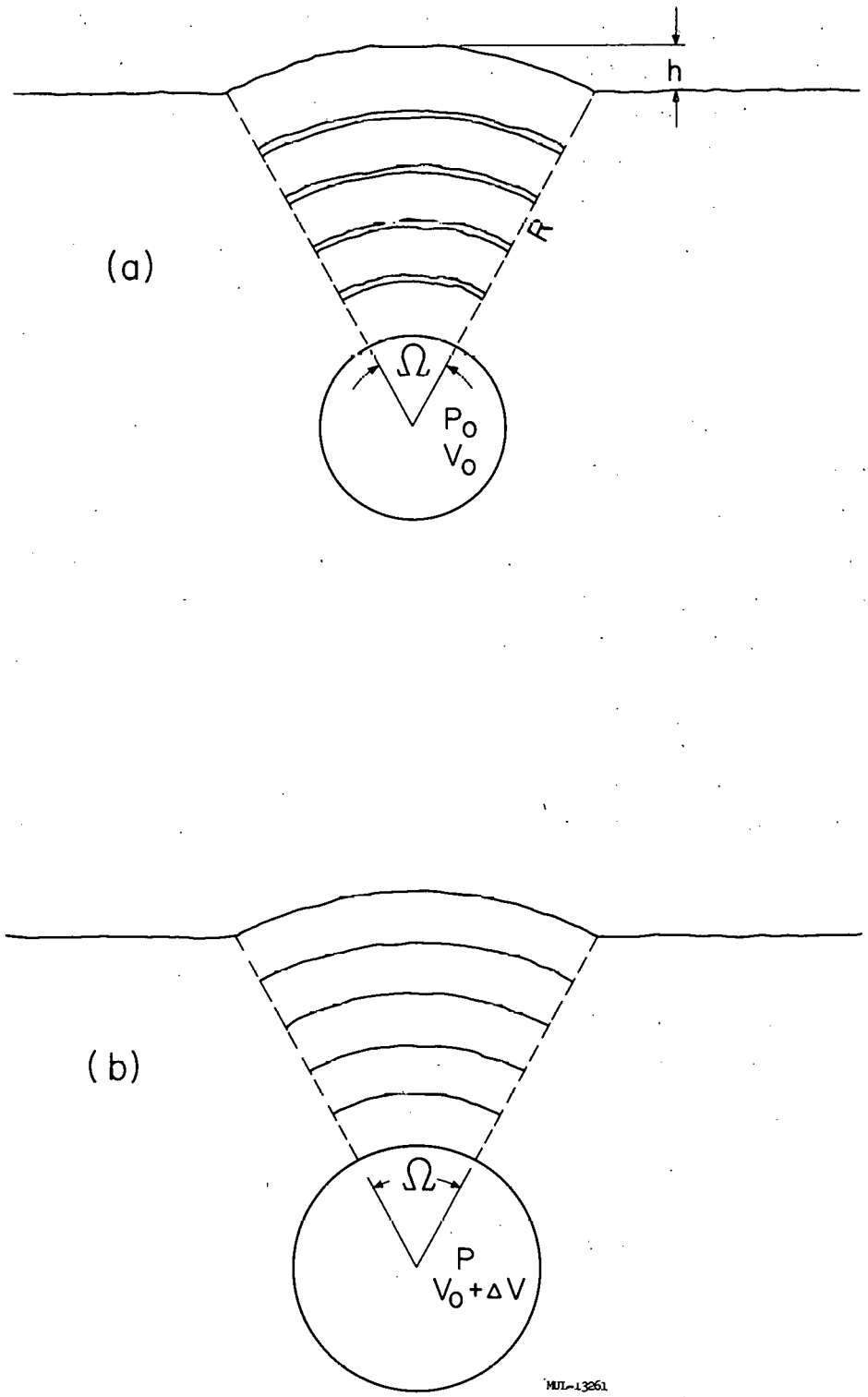

Fig. 6. Schematic drawing of optimum depth of burial for (a) no expansion of cavity, (b) cavity expanded to take up voids.

Thus we have

$$a = \frac{\Omega P_0 \left(\frac{V_0}{V_0 + \Delta V}\right)^{\gamma} \left(\frac{V_0 + \Delta V}{4\pi/3}\right)^{2/3}}{\frac{R^3 \rho \Omega}{3}}$$

$$= 1.15 \frac{P_0 \left(V_0 + \Delta V\right)^{2/3}}{R^3 \rho} \left(\frac{V_0}{V_0 + \Delta V}\right)^{\gamma}.$$

At 350 msec the observed height of the spherical segment for Scooter was approximately 16 ft (490 cm). Using 125 ft (~3810 cm) for the depth of burst, we have R = 4300 cm and

$$V_0 = 5.55 \times 10^9 \text{ cm}^3,$$

$$\Delta V = 3.12 \times 10^9 \text{ cm}^3.$$

The density of alluvium is about 1.6 g/cm^3. The γ for TNT at 175 kilobars, obtained from Jones and Miller,[19] is about 1.3. Using P_0 = 175 bars (1.75×10^8 dynes/cm^2), we have

$$a = 1.15 \frac{1.75 \times 10^8 (8.67 \times 10^9)^{2/3}}{1.6(4.3 \times 10^3)^3} \left(\frac{5.55}{8.67}\right)^{1.3}$$

$$= 6.68 \times 10^3 (0.64)^{1.3} = 3.74 \times 10^3 \text{ cm/sec}^2$$

$$= 123 \text{ ft/sec}^2.$$

This calculated acceleration is remarkably close to the accelerations observed (see Table I) for the period from 350-1200 msec, particularly for the central targets. It is considerably above the observed accelerations of targets 60 feet from surface zero, even when one considers that the numbers given in Table I are vertical components. One would not, of course, expect the acceleration to be constant in time but to decrease with time because of the dropping pressures in the cavity. However, the continued acceleration of the surface layers by the gas escaping through cracks and fissures gives additional acceleration to compensate for this drop. Obviously such a picture is inadequate but it does indicate the correct order of magnitude of these effects.

The sequence and magnitude of events described above apply only for a medium such as alluvium. For other media the numbers, and consequently the relative importance of the various mechanisms, are greatly different. Preliminary results from high speed motion pictures of ground motion at surface zero for the three large Buckboard detonations[20] provided some interesting information for another medium. This was a cratering program in basalt conducted at the Nevada Test Site which included three 40,000-lb detonations. These were designated shots 11, 12, and 13, and were buried at depths of 25.5, 42.7, and 58.8 feet, respectively. These correspond to scaled depths of burst of 80, 135, and 186 feet, using $W^{1/3.4}$ scaling for ease of comparison with the alluvium data.* The surface motion data for these three shots are given in Table II along with the spall velocities that were calculated by the UNEC code.

Table II. Surface motion data for 40,000-lb Buckboard shots.

Shot Number	11	12	13
Scaled depth of burst (ft)	80	135	186
Observed initial velocity (ft/sec)	330	150	120
Calculated initial velocity (ft/sec)	340	164	100
Residual cavity pressure (kilobars)	10	9	8

The agreement here is excellent. The higher velocities (compared with alluvium) are due to the much greater strength and competence of the basalt. A shock wave is attenuated much less in traversing a foot of basalt than a foot of alluvium. The result is that for a scaled depth of burst equal to Scooter's, the spall velocities for basalt are over twice as large as for

*Scaled depth of burst for a 40,000-lb (20-ton) shot is obtained by multiplying the actual depth by the factor

$$\left(\frac{1000 \text{ tons}}{20 \text{ tons}}\right)^{1/3.4},$$

thus obtaining the corresponding depth for a 1-kiloton shot.

alluvium. This means that the mechanics of cratering for an optimum depth of burial in basalt are much more like those for a shallow depth of burial in alluvium. The gas acceleration does not have a chance to accelerate the rock, and the crater is formed almost entirely by spalling. For deep depths of burial in basalt the spall velocity is not so high, but the mass of material to be accelerated by the gas is so large that the acceleration would be very small.

When considering impact cratering mechanisms, it is obvious that gas acceleration must play a much less significant role since the hole made by the entry and explosion of the meteor would not permit entrapment of the gases produced by the explosion. There has been a small amount of work done on the effects of stemming a cratering charge,[20] all at relatively shallow depths of burst, which indicates that apparent crater dimensions are reduced by something like 15-30% by eliminating stemming. This work produced no data on the effect of stemming at depths of burst near optimum, where the effect of gas acceleration would be most important, but it did suggest that the effect of stemming increases with depth of burst.

Deep Burial

Figure 4d depicts the cross section of a crater resulting from an explosion at a depth well beyond the optimum depth of burial. The apparent crater profile here is taken very closely from the deepest Stagecoach[2] crater (scaled depth = 253 ft). The spall velocities are now very small, about 10-15 ft/sec. The direct gas acceleration is almost an order of magnitude smaller than for optimum and is in general difficult to identify. The acceleration resulting from frictional drag by the escaping gases is probably more important for this situation. The fallback within the crater should be well ordered with little or no disruption of the stratigraphy, as indicated in the sketch. The lips are produced to a very large extent by the rupture and plastic flow of the material in the rupture zone. About 50-75% of the apparent crater volume can be attributed to subsidence, depending on the exact depth of burial.

Analysis of Neptune

Based on the above picture, an analysis of the Neptune detonation[4] has been undertaken to try to explain the observed phenomena. Neptune was a 115-ton nuclear device which was exploded about 100 feet under a 30° slope in bedded tuff. The vertical distance to the surface was 110 feet. The zero-point room was 12 × 17 × 10 feet high with a concrete floor. Based on a post-shot geological study of the regions surrounding the detonation point,[21] core holes drilled into the active region, and machine calculations of the expected behavior of underground detonations, a history of the Neptune event has been reconstructed, including the mechanisms that led to formation of the crater.

A few microseconds after detonation, all of the material surrounding the device was vaporized and the mixture of hot air and vaporized material had filled the shot room. Since the volume of the room was approximately 5.8×10^7 cm^3 and there was about 10^6 g of material in the room (assuming the concrete floor was one face of the room), the gas would be at a temperature of about 150,000°K and a pressure of 25,000 atmospheres (bars). At this temperature the gas would be only partially ionized. (The temperature and pressure are estimated on the basis of a Thomas-Fermi-Dirac equation of state for the material in the room. The radiation pressure is completely negligible.) The 25-kilobar pressure in the room would not generate a shock strong enough to melt or vaporize the surrounding rock, but the shock would crush and fracture the tuff, permanently displacing the material near the room and allowing the cavity to expand. The high temperature gas in the cavity would vaporize and melt the inner surface of the spherical cavity by conduction and produce a thin molten lining. Such a picture is confirmed by samples recovered from the Neptune area which show that the fused material occurs only as thin layers, a fraction of an inch thick, in contrast to the fused material from Rainier,[22] which was several inches thick.

As the shock wave traveled outward it decreased in strength, ultimately propagating as an elastic wave. The shock wave reached the sloping face of the mesa, 100 ft from the device, at about 12 msec after the detonation.

The rarefaction from the free surface, traveling back to the cavity at close to sonic speed, reached the liquid-lined sphere at about 25 msec.

The initial spall velocity of the surface material as measured on Neptune near the region of maximum rupture was 30-40 ft/sec.[23] If these pieces moved in free fall, under the influence of gravity alone, they would have gone only 15-25 ft in the air. Since large rocks were observed going much higher, it is clear that some sort of late-time gas acceleration occurred. Expansion of the cavity after the arrival of the rarefaction, followed by the outward rush of hot gases from the gas bubble, accelerated the upward flight of the broken rock fragments, blowing them out of the crater. Venting occurred through cracks in the overlying strata with no general upheaval or mixing of the strata above the cavity, as evidenced by the clear delineation of the pre-shot geologic structure.[21]

Due to the low overburden pressure for the Neptune detonation and the large gradient in the overburden pressure horizontally in the direction of the face of the mesa, the cavity expanded asymmetrically, with fractures extending large distances from the cavity. Hot gases penetrating these cracks produced fused layers of rock on the surface of the cracks which resulted in evidences of radioactivity throughout the region surrounding the cavity. Such widespread distribution of the radioactivity and heat from the detonation have made determination of the final cavity radii very difficult. Significant amounts of radioactivity have been found up to 30 ft from the detonation in the direction away from the face of the mesa and up to 50 ft toward the face. In general, the zones of maximum radioactivity define a maximum radius for the cavity of 15-20 ft. The large amount of radioactivity found up to 50 ft away toward the face is probably due to early venting of the cavity along bedding planes in that direction. This is indicated by films that show venting from the surface of the slope occurring at a point well below the point of maximum rupture and before the venting at the point of maximum rupture is visible.

Following the venting and collapse of the cavity, a chimney or subsidence was formed which propagated to the surface. If all of the volume of

the cavity had been transmitted to the surface by the chimney, it would have contributed approximately 640 cubic yards to the apparent crater volume of 22,000 yd^3.

Summary

In an attempt to give an overall picture of the effects of these four mechanisms and their relative importance at various depths of burst, I have constructed a schematic diagram showing their effect on one crater dimension. For the purpose of this example I have chosen to use apparent crater depth because the role played by each mechanism is comparatively simple. Figure 7 shows, in a dimensionless graph, these relationships. The contribution from compaction and plastic deformation and subsequent subsidence is a maximum for a surface detonation and decreases somewhat asymptotically with depth because of the increasing overburden pressure. The effect of spall is, of course, directly proportional to the depth of burst for shallow depths of burst; it peaks and then decreases as shown for larger depths of burst because of the decrease in surface velocities. The effect of gas acceleration does not become significant until the spall phenomenon starts to lose its effectiveness. It then increases somewhat to a peak, and tails off as shown. The effectiveness of even this tail is dramatically illustrated by films of the Blanca[22] nuclear event, an event somewhat similar in geometry to Neptune except that the scaled depth of burst was about 50% greater. The surface spall created no crater at all for this shot. However, a large cavity or camouflet was produced which collapsed, with subsidence progressing toward the surface. This collapse required 15 seconds before it reached the surface, at which time the gases trapped in the cavity vented to the surface with a very startling plume of gas which went about 1000 feet in the air. When this venting first evidenced itself, some of the surface rocks were ejected several hundred feet in the air by the escaping gas, showing the capabilities for particle ejection of the gases during their venting phase even for such a large scaled depth of burst. Summarizing these individual contributions to the crater depth gives the heavy line shown in Fig. 7.

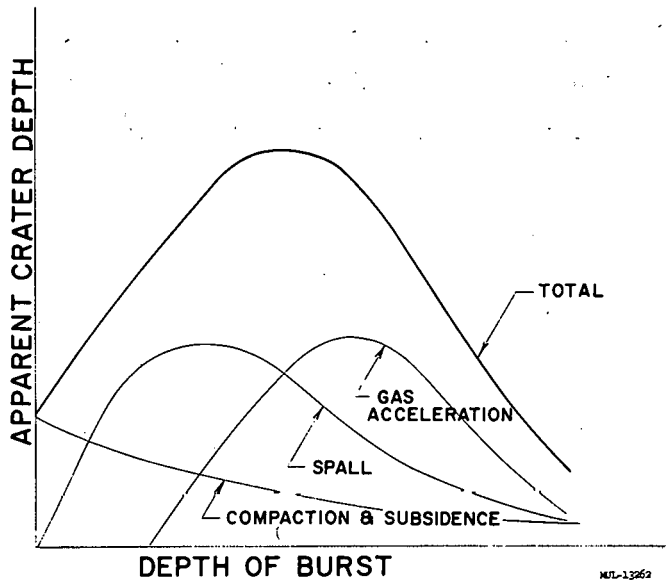

Fig. 7. Relative contributions of various mechanisms to apparent crater depth for explosion crater.

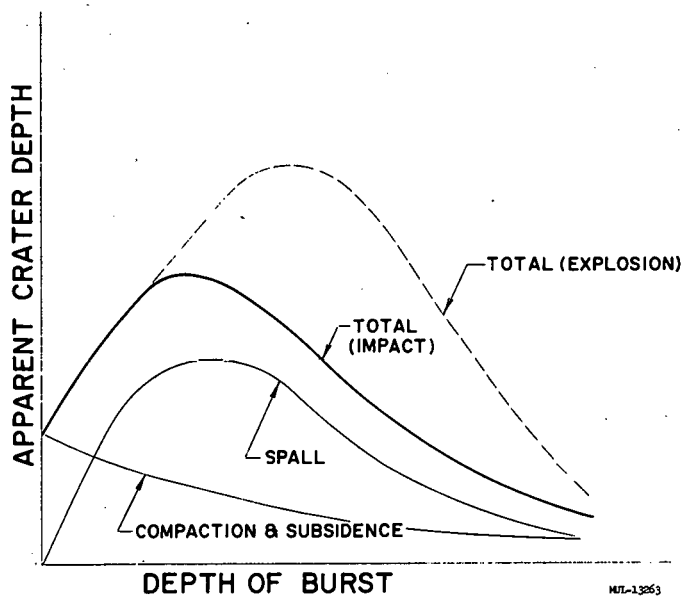

Fig. 8. Relative contributions of various mechanisms to apparent crater depth for impact crater.

If we make the assumption that the principal difference between impact craters and explosion craters is the effect of gas acceleration, we should eliminate this contribution and draw the picture shown in Fig. 8. Thus for surface and shallow depths of burst the craters should be quite similar; but for depths of burst somewhat deeper than Teapot ESS, for example, one would expect serious differences to appear. However, most impact explosions are equivalent to surface or shallow-depth explosions, so one would expect relatively good comparison of existing experimental data. For a set of conditions that would result in a deeper equivalent depth of burst for an impact explosion, one would expect the above-indicated deviations to occur.

A similar set of curves could be drawn for crater radius, but it is very difficult to untangle the various effects. For surface detonations spalling undoubtedly contributes to the radius to some extent. Gas acceleration is probably less important at all depths of burst in determining radius than in determining depth.

Conclusion

This discussion has been largely qualitative in nature but I believe the model outlined is basically correct. Further development of this theory will require additional theoretical work as well as more experimental studies. The UNEC code has the limitation of being one-dimensional. This means that it is valid only in the vertical direction and only until such time as the rarefaction arrives back at the cavity. Work is presently being done on a two-dimensional version of UNEC which will be much more useful for cratering purposes. This code will allow accurate calculation of the true crater and give initial spall velocities for all the material that is ejected into the air, and should adequately treat the early stages of the gas acceleration. Calculational treatment of the late stages, when venting occurs, is impossible with present codes, and attempts are being made to develop a treatment that will handle this problem. Further experimental work, directed toward exploring existing craters such as Scooter, the three Stagecoach craters, and the three large Buckboard craters, should be undertaken.

Geologic mapping of craters has proved invaluable in analyzing the mechanics of cratering in the past and will be even more useful in the future as we gain experience with it.

We are on the edge of constructing a quantitative picture of cratering, and we are hopeful that future experimental and theoretical programs will allow the construction of a complete theory for the mechanism of explosive crater formation.

REFERENCES

1. Nordyke, M. D., "Nevada Test Site Nuclear Craters," Paper F, Proceedings of Lawrence Radiation Laboratory/Geophysical Laboratory Cratering Symposium, Univ. Calif. Lawrence Radiation Lab. Rept. UCRL-6438, June, 1961.

2. Murphey, B. F., "Explosive Craters in Desert Alluvium," Paper G, Proceedings of Lawrence Radiation Laboratory/Geophysical Laboratory Cratering Symposium, Univ. Calif. Lawrence Radiation Lab. Rept. UCRL-6438, June, 1961.

3. Duvall, W. I. and Atchison, T. C., "Rock Breakage by Explosives," U. S. Bur. Mines, Rept. Invest. 5356, 1957.

4. Shelton, A. V., Nordyke, M. D., and Goeckermann, R. H., "The Neptune Event, A Nuclear Explosion Cratering Experiment," Univ. Calif. Lawrence Radiation Lab. Rept. UCRL-5766, April, 1960.

5. Maenchen, G. and Nuckolls, J. H., "Calculations of Underground Explosions," Paper J, Proceedings of Lawrence Radiation Laboratory/Geophysical Laboratory Cratering Symposium, Univ. Calif. Lawrence Radiation Lab. Rept. UCRL-6438, June, 1961.

6. Sachs, D. C. and Swift, L. M., "Small Explosion Tests, Project Mole, Final Report," Stanford Research Inst. Rept. AFSWP-291, Dec., 1955.

7. Doll, E. B. and Salmon, V., "Scaled H. E. Tests, Operation Jangle," WT-350, Nov., 1951.

8. Lewis, J. G., "Crater Measurements, Operation Teapot," Engineering Research and Development Lab. Rept. WT-1105, July, 1958.

9. Murphey, B. F., Sandia Corp., private communication.

10. Vaile, R. B., "Pacific Craters and Scaling Laws," Paper E, Proceedings of Lawrence Radiation Laboratory/Geophysical Laboratory Cratering Symposium, Univ. Calif. Lawrence Radiation Lab. Rept. UCRL-6438, June, 1961.

11. Chabai, A. J., "Crater Scaling Laws for Desert Alluvium," Sandia Corp. Rept. SC-4391 (RR), Dec., 1959.

12. Pokrovskii, G. I. and Fedorov, I. S., "Effect of Shock and Explosion on Deformable Media," Gos. Izd., Moscow, U.S.S.R., 1957.

13. Vortman, L. J., "High Explosive Craters in Tuff and Basalt," Paper H, Proceedings of Lawrence Radiation Laboratory/Geophysical Laboratory Cratering Symposium, Univ. Calif. Lawrence Radiation Lab. Rept. UCRL-6438, June, 1961.

14. Panama Canal Company, "Crater Tests in Basalt," Isthmian Canal Studies, Memo 284-P, April, 1948.

15. Panama Canal Company, "Crater Tests in Gatun Sandstone," Isthmian Canal Studies, Memo 285-P, May 1948.

16. Panama Canal Company, "Crater Tests in Marine Muck," Isthmian Canal Studies, Memo 286-P, May, 1948.

17. Shoemaker, E. M., "Impact Mechanics at Meteor Crater, Arizona," Open File Report, U. S. Geological Survey, July, 1959.

18. Feigenbaum, S. A. and Wegkamp, P. L., "Photographic Earth Motion Study, Scooter Event, Final Report," Edgerton, Germeshausen & Grier, Inc., Rept. L-510, Feb., 1961.

19. Jones, H. and Miller, A. R., "The Detonation of Solid Explosives," Proc. Roy. Soc. (London) A194, 480-507 (1948).

20. Martin, D. L. and Hinze, W. J., "Energy Partition of Underground Explosions," Engineering Research and Development Lab. Rept. AFSWP-789, March 1958.

21. Thompson, T. L. and Misz, J. B., "Geologic Studies of Underground Nuclear Explosions Rainier and Neptune, Final Report," Univ. Calif. Lawrence Radiation Lab. Rept. UCRL-5757, Oct., 1959.

22. Johnson, G. W., Higgins, G. H., and Violet, C. E., "Underground Nuclear Explosions," Univ. Calif. Lawrence Radiation Lab. Rept. UCRL-5626, July, 1959.

23. Morris, R. H. and Schneiderhan, R. C., "Earth Motion Studies, Operation Hardtack, Phase II," Edgerton, Germeshausen & Grier, Inc., Rept. ITR-1706, Feb., 1959.

/mr

Paper L

CRATERING FROM A MEGATON SURFACE BURST*

H. L. Brode and R. L. Bjork

The RAND Corporation

Santa Monica, California

ABSTRACT

Assuming a hydrodynamic model, the authors have calculated the stresses and early motions associated with the cratering of a rock medium (tuff) from a 2-megaton surface burst. The results demonstrate the basically two-dimensional geometry of such an explosion, and offer preliminary values of the pressures and motions involved. The excavating action is found to be associated with the direct shock from the bomb, and not due to the loading developed by the air overpressures in the early fireball. A limited description of the method, inputs, and equation of state of rock is included. Graphical results, together with some discussion of the salient features and the various physical assumptions and limitations associated with the calculations make up the body of this report.

* * *

I. INTRODUCTION

The cratering action of large-yield explosions is an important part of both peaceful and warlike applications of nuclear weapons effects. It is a dominant feature in any earth-moving application, such as in the proposed harbor and canal digging (Plowshare) operations. In protective construction for the military, the crater boundaries define a sensible if perhaps extreme limit inside which survival cannot be expected. For an increasing number of applications more exact knowledge of expected craters and the associated ground shocks has become a vital factor.

* This work was sponsored by the U. S. Air Force and supported in part by the U. S. Atomic Energy Commission.

An improved understanding of cratering must come from theoretical work coupled with field work using scaled or small-yield explosions. Ideally, theory and experiment should be combined at the yields of interest, but for several overriding reasons, no large-yield surface (or shallow-buried) bursts have been shot or are contemplated in a site of dry soil or rock, and it is necessary to rely on extrapolation from small nuclear shots and from chemical explosive work for the experimental aspects. Without benefit of adequate theoretical work, the extension of small-yield field data to large-yield situations is at best approximate and at worst may be quite wrong. A clear physical basis for predictions and scaling is particularly desirable at this time, and it is toward that goal that the calculations covered in this report were aimed.

In constructing a reasonable theoretical model of the cratering action, several factors stand out as being immediately necessary: Since the early phases of either chemical or nuclear explosions involve pressures far in excess of the shear or viscosity stresses characteristic of any natural materials, and since the resulting strong shocks induce appreciable compression and heating in the surrounding matter, a hydrodynamic model is not only reasonable but is a necessity at early stages. Furthermore, since the geometry of the burst relative to the interface separating ground and air figures dominantly in the formation of any crater, the hydrodynamics must be carried out in two space dimensions, i.e., must include vertical and radial motions. A program for numerical computation of hydrodynamic motions in two dimensions has existed at RAND for some time, and is particularly appropriate for use on the nuclear cratering problems. The scheme was originally generated by Bjork[1] in an investigation of high-speed impact craters in metals. The programming was done by N. J. Brooks.

Although the hydrodynamic assumption is basic to the model, two further features are of importance, if less obviously so. In order to properly follow the cratering action of a surface-burst nuclear explosion, it is necessary to know with considerable precision the early history of a nuclear bomb explosion. The exact amount of energy (and its form) that enters the ground, and how much

energy goes in or out across the surface of the ground at later times, will depend critically on the bomb energetics and the early fireball and air-blast history. Recent detailed calculations by Brode[2] have made easy the definition of initial and boundary conditions to approximate the influence of the complex dynamic loading induced by a surface-burst nuclear weapon.

One further factor of prime importance involves the equation of state of the earth material. A cratering problem is sensitive to the relation between energies and sound speeds in the two media on either side of the interface. In the air above, the ambient sound speed is about 330 meters/sec, while seismic velocities in natural earth materials vary from typical soil seismic speeds around 600 meters/sec to a speed in granite near 3700 meters/sec. Air is quite compressible and very heat-absorbent at the high pressures in a nuclear explosion, while solid materials are much less compressible and tend to be much less dissipative at comparable stress levels. The extent to which these inequalities matter in such a cratering calculation can easily be appreciated.

As the stress in the soil or rock sinks below a level where hydrodynamics can properly be considered the dominant force in producing motions and transporting energy, the calculation should embrace such physical features as plasticity and elasticity and should then deal with real solid-state features of the material. Although something of this sort has been done in the simpler case of spherically symmetric explosions by Nuckolls,[3] it was not attempted in any comparable sense here in connection with the two-dimensional cratering calculations. Furthermore, since the forces far exceed the force of gravity in the pressure regime where the model is considered valid, gravitational forces were not carried in this program.

II. NUMERICAL METHOD

The motion of the ground itself is assumed to be governed by the compressible, hydrodynamic equations. Written in terms of Eulerian variables, these are

$$\rho \frac{\partial \bar{u}}{\partial t} + \rho \bar{u} \cdot \text{grad } \bar{u} + \text{grad } P = 0 \qquad (1)$$

$$\frac{\partial \rho}{\partial t} + \bar{u} \cdot \text{grad } \rho + \rho \text{ div } \bar{u} = 0 \qquad (2)$$

$$\rho \frac{\partial e}{\partial t} + \rho \bar{u} \cdot \text{grad } e + P \text{ div } \bar{u} = 0 \qquad (3)$$

$$P = P(\rho, e) \qquad (4)$$

where the variables are

$\bar{u}$ particle velocity
P pressure
e specific internal energy
ρ density
t time.

The effects of viscosity and heat conduction are neglected in the above equations. It is possible to show by order-of-magnitude arguments that neglecting heat conduction is a good approximation. However, not enough is known of the viscous properties of materials under high pressures and densities to make such a positive statement relative to neglecting viscosity. Viscosity is really omitted from the framework of these calculations for the practical reason that no good estimates of it are available.

The nature of the problem renders the solution of these equations particularly difficult. Portions of the ground suffer large distortions, so that a Lagrangian description fails after a short time. The Eulerian formulation suffers from the continual diffusion across interfaces.

The numerical technique employed was one previously developed by Bjork[1] to treat problems of high-velocity impact, where similar difficulties occur. Briefly, the method treats mass points moving through an Eulerian mesh. Integration is carried out on time, starting from the initial conditions (described in Section III) and imposing the appropriate boundary conditions. The advance over Δt is carried out in two steps. In the first step, the

transport terms in Eqs. (1) through (4) are neglected, and the integration is performed by solving the difference analog of the resulting differential equations. In the second step, the transport terms are accounted for by noting which masses changed cells in the first step.

To get the new mass of the cells affected, one merely sums the masses now present in each cell, which accounts for the mass transport term in Eq. (2). A mass which changes cells is assumed to carry with it an increment of internal energy given by the product of the mass in question and the specific internal energy of the cell which it left. This accounts for the internal energy transport term in Eq. (3).

A mass, in changing cells, also brings with it an increment of momentum given by the product of the mass and the velocity present in the cell which it left. This momentum is added to the cell entered by the mass, and that cell is given a new velocity equal to the new momentum divided by the new total mass. Thus the momentum transport term of Eq. (3) is taken into account.

The process described conserves mass, internal energy, and momentum. However, it is easily shown that kinetic energy is always lost in this repartitioning unless the velocities of the two cells involved are equal. This is accounted for by arbitrarily adding the loss in kinetic energy of the two cells to the internal energy of the entered cell. Thus, total energy is conserved, but a small fraction of the kinetic energy is converted to internal energy in the process. This conversion may be shown to be equivalent to an artificial viscosity of the Landshoff type,[4] and its presence precludes the necessity of adding any further artificial viscosity to the problem.

In both the previously treated impact problems and the present ground motion calculations, the magnitude of the viscosity is ideal in the sense that it spreads the shock jumps over about three mesh spaces.

The method was tested in two ways. The first was to compare the solution generated for one-dimensional impacts with analytical solutions which are available in this case. This test showed that the method gave correctly the jumps in pressure, density, and velocity across a shock, and also the velocities of the shocks themselves. This means that the jump in entropy

across the shock is given correctly, placing the final state on the Hugoniot rather than the adiabat connecting the initial and final states.

The second test was to calculate with this two-dimensional code a spherically symmetric nuclear air burst previously calculated by Brode[5] with a one-dimensional code. The agreement was checked in the vertical direction, the horizontal direction, and at an angle of 45° between the two, and found to be satisfactory in all cases.

The calculations were performed by an IBM 704 which possessed a 32,000-word fast memory. The memory size was the limiting factor in the resolution. In order to obtain an adequate mass resolution, 20 mass points per cell were used. This meant that on the average a cell's density could change in 5% increments. This choice of the number of mass points restricted the number of space grid points to 400, which were arranged in a 20 by 20 rectangular array. Using fewer mass points per cell would have resulted in a larger number of space grid points, but it was not deemed feasible to coarsen further the mass resolution.

By an artifice known as "grid changing," the 400 grid points were always arranged to encompass only the region of activity and its immediate environs. In a "grid change," the points were laid down in such a manner as to encompass the shock front plus about an equal extent of undisturbed media. Within the shock, the dependent variables were given the values existing at the end of the previous grid, and outside they were assigned values appropriate to the undisturbed media. The new grid was then used until the program detected the first faint movement on the grid's boundary caused by the approaching shock, at which time a new grid change was effected.

In the present calculation, it is possible to gain only a very rough idea of the crater dimensions, as the forming crater is covered only by very few space grid points. The reason for this is that the ground shock is several times as deep as the crater bottom and the grid spacing is uniform in the vertical direction. In this sense the present calculation emphasizes the information relative to the deep ground motion. It will be possible to emphasize the cratering information by using a gradation of grid sizes in the vertical direction, so that there will be many points near the surface and only a few deep underground.

III. INITIAL AND BOUNDARY CONDITIONS

The problem to which we address ourselves is that of calculating the crater and ground motion due to a 2-megaton surface burst. The nature of the problem is contained in the specification of the boundary conditions. These initial and boundary conditions were based on results of calculations by Brode[2] of the early phases of a nuclear explosion. From these calculations at 1 microsecond after initiation, one finds that approximately half the bomb energy has radiated out of the bomb into the surrounding air, and most of the energy remaining in the bomb is in directed kinetic energy of the bomb materials. At this time it is reasonable to characterize the explosive input to the ground as due to both the impact of the bomb mass on the ground directly below it and to the pressure on the surface from the initially extended and rapidly growing fireball or strong shock in air. The pressures generated by this air blast are initially several orders of magnitude less than the pressures created directly by the bomb vapors, since the energies in the air and in the bomb are comparable, but the volume of air is many times larger than that occupied by the bomb itself.

These initial conditions lead to a specification of velocities of the order of 1700 m/ms in the first few zones of the rock, representing the mass and kinetic energy of the lower half of the bomb. In these zones an appropriate internal energy was included. These conditions, together with the initial choice of grid spacings, lead to the following initial configuration:

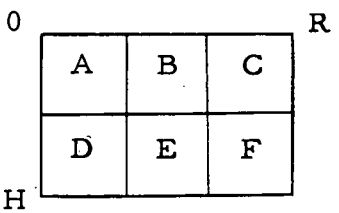

In the grid, each initial zone was 1/4 meter both across and deep, representing rings of mass in the cylindrical coordinates used. Each of the six "bomb" zones had a specific internal energy (and a pressure associated with it) corresponding to 8.05×10^5 in the meter-millisecond-megagram system

of units used here (i.e., in 10^{16} ergs/10^{6} gm). Each of these zones also had an initial velocity of 1670 m/ms, directed radially, so that the initial velocity components were as in Table 1.

Table 1

	Vertical Velocity V	Horizontal Velocity U	E	ρ_0
A	1181	1181	8.05×10^5	1.7
B	528	1584	"	"
C	327	1638	"	"
D	1584	528	"	"
E	1181	1181	"	"
F	859	1432	"	"

Energies, pressures and velocities were all initially zero outside of the six bomb zones. These bomb zones represented only the lower half of the bomb in a "true" surface burst position (i.e., with the center of gravity located on the plane of the surface between rock and air). The upper half of the bomb had been carried in the calculations in an early version, but proved to have an entirely negligible effect on the subsurface behavior. Since it added to the complexity of the problem to follow the upper masses as they flew off at high velocity, they were omitted from subsequent computations.

The surface pressures due to the air blast were included in the form of a boundary condition on the uppermost masses. An analytical form representing the air pressures as a function of time and radius was developed from the detailed calculations of an air-burst megaton explosion.[2] The fit is approximately correct from earliest times until around half a second, after which it increasingly overestimates the pressures. At half a second the peak overpressure in the air shock should be about 145 psi (at a shock radius of more than one kilometer) while the fit gives about 180 psi. A comparison

between the detailed calculation overpressures and the fit used is made in Fig. 1. The impulse from this overpressure in its positive phase is generally too high by a factor of 1.5 over the applicable range of distances. Since nearly all of the observed ground motions were directly attributable to the direct impulse from the bomb vapors and not at all from the air blast impulse, the use of an air overpressure formula which overemphasizes the air impulse is conservative in the present calculations, and emphasizes that no appreciable change would have resulted had the air overpressure been completely ignored.

The formula employed for the air overpressure boundary condition is the following:

$$\Delta P = \frac{0.62}{0.1 + t^{1.15}} \left[1 + 1.6\left(\frac{t_s}{t}\right)^6\right] 10^{10} \text{ dyne/cm}^2$$

where t_s is the time of shock arrival, t is the time (both in milliseconds), and $t \geq t_s$.

$$t_s = 7 \times 10^{-5} + 7.24 \times 10^{-20} R_s^{10}, \text{ for } R_s \leq 56,$$

$$= \frac{7.24 \times 10^{-20} R_s^{10}}{1 + 0.637 \times 10^{-14} R_s^{7.5}}, \text{ for } 56 < R_s < 200,$$

$$= \left(\frac{R_s}{95}\right)^{2.5}, \text{ for } R_s \geq 200 \text{ m},$$

in which R_s is the shock radius in meters. At times before shock arrival the overpressure is zero.

For a low air burst, in which the bomb materials do not get close enough to the ground to shock it strongly, the main mechanism for inducing ground motion would be just the air blast. The above form could also represent the approximate pressure history on the surface from a burst at about 100 meters above the surface. At that burst height the direct bomb shock would be

negligible, but the air shock would be quite similar to that from a true surface burst for horizontal ranges greater than about 100 m.

Since the compressions in the ground from such a low air burst would be quite small, the particular numerical scheme used here is not appropriate. It may be more reasonable to carry out such a calculation using a Lagrangian scheme, more adapted to propagations with small density changes. It is fairly clear that the nature of the air-slap loading is such that no conventional crater will occur from it alone in rock or in most soils. Its load is applied so rapidly over such a wide area and is relieved so rapidly that the main response is a tendency to compact, and very little excavating motion would be generated. On the other hand, the induced ground shock will not be entirely in the vertical direction, and will be quite divergent, i.e., will not be a plane wave. These trends as stated here were substantiated by two calculations which used only the air-slap input. Unfortunately these same calculations used unreal equations of state, and so are not useful beyond their indications of a general geometric nature.*

IV. EQUATION OF STATE

The influence of the equation of state on the results of such calculations has been only partially explored. A preliminary problem using an ideal gas of specific heat ratio three ($\gamma = 3$) was run, but at the lower pressures it suffered most from the fact that the computation treated all shocks as strong shocks. In the region where the ground shock is properly strong, the comparison with a more nearly correct equation of state shows an expected greater effective explosion energy for the ideal gas case. Since, for real gases, much more energy is involved in the ionization and dissociation of the hot gas behind

* The first was an ideal gas, strong shock case, and the second used an unusually "soft" fluid. The second problem was not restricted to the strong shock limitation and did have a reasonable seismic speed (~2000 ft/sec), but was too compressible to be realistic. (A pressure of 20 Kbars would cause a compression to twice the original density.) A more appropriate problem will be carried out soon.

the shock front, the shock in a real gas very quickly drops to a lower strength than the corresponding shock in an ideal gas of high specific heat ratio.

The best equation of state used so far represents a soft volcanic rock called tuff (the rock in which some underground nuclear explosions at the Nevada test site were shot). This equation of state was represented by an analytical formula fitting three general regions of information. At the high-temperature end, the fit was to data from a Fermi-Thomas-Dirac calculation for an appropriate mixture of elements representing the chemical constituents of tuff. We are indebted to Bill McMillan of RAND for this data, and to Forrest Gilmore and Arthur Smith of RAND for some thermodynamic interpretation. In the region between 80 and 300 kilobars, the Hugoniot data from high explosive experiments on tuff were used as guidance for the fitting. These data were a part of experimental work carried out by a group at the Livermore Laboratory of the AEC, and were called to our attention by Arthur Smith.

In carrying the fit to lower pressures, the observed speed of sound in tuff was used as a limiting condition. The fit, while only approximately satisfying all of these restrictions, is considered compatible with the accuracy limits imposed by other physical approximations involved in the calculations.

Expressed in terms of the specific internal energy (E) and the density relative to the standard density for tuff ($\eta = \rho/\rho_0$), the pressure, according to the resulting fit, was defined as

$$P = 0.425\eta E + 0.113\eta^{3/2}E + 5.30\eta E^{1/2} + 0.707\eta E^2/(10^5 + E),$$

P in 10^{10} dyne/cm^2,

E in 10^{10} erg/gm,

$\eta = \rho/\rho_0$,

$\rho_0 = 1.7$ gm/cc.

Of course, the solid state properties of the rock which become important at stress levels below about 10 Kbars are not realistically covered by the concepts of thermodynamic equilibrium implicit in the equation of state. But further, the above equation includes no special consideration for phase

changes — melting and vaporizing. It appears unlikely that the inclusion of phase changes would cause the equation-of-state behavior to be radically different from that assumed, however. In the first place, both the melting and vaporization points occur in about the same temperature range, and neither would occur at a precise temperature but would be spread over a factor of two or so in temperature. It is questionable that a melting point would even exist under explosive loading. The shock pressure at the melting temperature should be somewhat less than 100 kilobars, and the above fit covers this region by bridging smoothly the gap between Thomas-Fermi-Dirac results and high-explosive experimental results.

Tuff is a rock which contains an unusually high amount of voids. It is not likely that the collapse of the voids creates a permanent change in the tuff density at the high pressures, since at the highest temperatures the material is violently excavated, and at more modest temperatures (near melting) the voids seem to reconstitute themselves. At the lowest stress levels (below 10 Kbars) where this hydrodynamic model is already inapplicable, permanent void collapsing is likely. No such hysteresis was included in the treatment here. The equation of state for tuff used in these calculations is graphically illustrated in Fig. 2.

V. THE RESULTS

Although the boundary and initial conditions specified accurately both the bomb-vapor residual energies and the impulse from the air-blast slap, it is a striking feature of the results that only the former plays an important role in the excavation process. The air slap does indeed send a shock into the ground, but over a wide area and at pressures several orders of magnitude less than those at the same time in the direct bomb shock. Out along the surface beyond the region of the crater, of course, the air-blast slap exceeds the direct shock (which arrives later), but for the cratering action, and for shocks immediately below the crater, one could validly omit the air slap.

In Fig. 3, the early pressure field is displayed as a map of isobars (at 0.1026 ms). The bomb shock has created a nearly hemispheric shock front

with peak pressures of around 7000 Kbars in the 90° solid angle downward about the vertical axis (darkened area). The lack of a sharp front to the shock at this stage is due to the nature of the computation scheme which spreads shock discontinuities over about three zones of the chosen space grid. Such spreading does not seriously affect the Hugoniot or shock values of the various hydrodynamic variables. At this time, about one-tenth of a millisecond, the direct shock has progressed only some 7 meters, while the air shock aided by radiation diffusion has gone out more than 50 meters. The 7-megabar ground shock pressures are to be compared with the peak overpressure in the air shock at this time of some 30 kilobars. The shaded box at the origin represents the volume of rock in which the initial kinetic and internal energy was put, to approximate the bomb. It is already clear at this time that the ground shock is no longer dependent on the geometrical details of the source.

Figure 4 displays the velocity vectors of various rock masses at this same early time. Here the symmetrical nature of the strong shock generated by the bomb energy becomes even more evident. All the compressed region of the shock front is rapidly expanding spherically. The topmost rock is being blown off into the air (in this case into the fireball above) at extreme velocities. This upward flying rock is of course not a true vapor and is already at fairly low density. The same is true of that material below the surface and well behind the shock front, although the motions are more nearly random below a couple of meters depth.

At 10 times this early time, at 1 millisecond, the shock has advanced to some 18 m deep and has dropped to a peak pressure (in the vertical cone) of the order of 500 Kbars (Fig. 5). The shock front is still fairly uniformly spherical out to 45° from the vertical, dropping an order of magnitude from there to the surface. The pressure behind the shock appears more chaotic.

Later, at 3.4 ms, the shock has progressed down to 32 m and fallen to a peak pressure of around 125 Kbars in the same 90° vertical cone (Fig. 6).

The subsequent progress is illustrated at various times (at about 10, 21, 50, 80, and 100 ms) in Figs. 7 through 14. Throughout these figures one can follow the hemispherical shape of the shock. At all times the peak pressures

along the vertical are largest and extend fairly uniformly out to a point 45° from the vertical before a serious drop in pressure begins as one follows the shock front further toward the surface. At the later times (> 40 ms) the calculation has been illustrated beyond a point where all pressures are below 10 kilobars, and so beyond a time when the hydrodynamic assumption is reasonably rigorous. It is interesting to note that at these late times, when the shock is no longer strong enough to make a fluid of the rock, the velocity maps (Figs. 10, 12, and 14) indicate a fairly sharp cleavage at around 70 m deep. Above that point the material is moving up and continues to go up. Below that depth the material continues to move down. This "crater bottom" persists at the same depth after the 50-ms time. Since this is a fluid model, and since we have claimed no rigor for the model at late times and low pressures, this evidence of a crater depth approximately equal to that predicted by conventional scaling laws[6] can be considered at least in part as a gratifying coincidence. It should be noted, however, that conservation of mass, momentum, and energy in the correct geometry are still appropriate and are in fact responsible for the motions illustrated, and it may well be that the plastic and elastic properties of the rock play secondary roles in determining crater depths.

Pressures as a function of time at fixed vertical positions fairly close beneath the source display the usual strong shock type of bimodal decay in which the pressure, after rising to a peak and falling rapidly for a time, follows a more gradual decay rate (Fig. 15). At greater distance less structure is evident in the pressure histories (Fig. 16), and only rough values of peak stress and total impulse are derivable from them. A similar description applies to the pressure histories at positions along the line inclined at 45° from the horizontal (Figs. 17 and 18), but the pressure-time relations at points along the surface are quite different. Along the surface, air pressures arrive first, dropping from a peak air overpressure (not shown in Figs. 19 and 20) to a "slowly" decaying fireball pressure. Later the direct ground shock arrives, driving the pressure up one or more orders of magnitude for a short time. At distances beyond a few tens of meters (Fig. 20), it is clear that in

surface pressure histories the direct shock rapidly drops out of importance, and at horizontal distances much greater than 100 meters, the direct shock can be ignored. But it does not follow that the direct shock can be ignored at depths below the surface at the same horizontal distances. Referring to Fig. 13, it is evident that the direct shock brings pressures up to 2 kilobars out to a distance larger than 200 meters, but at depth of some 100 meters. Even at a 50-meter depth one would expect 1 kilobar, and perhaps 1/2 kilobar (> 7000 psi) at depths less than 20 meters and at ranges better than 200 meters. At distances much beyond 200 meters, however, and at depths of less than 100 meters (or more nearly correctly, at depths such that a direct line to the point of explosion makes an inclination from the horizontal of less than about 20°), it is the air blast alone which creates the pressure pulse. The peak overpressure from the air blast will be almost an order of magnitude higher than that from the direct shock at 100 meters, while the air blast impulse is already a little larger than the impulse in the direct shock at the surface at that distance.

In Fig. 21, the peak pressures in the direct shock are shown versus the radial distance from the point of burst for the three directions, as solid curves labeled vertical (V), horizontal (H), and diagonal (D). In the early, strong shock region the decay of pressure is approximately as the inverse cube of the distance, while at lower pressures the decay is less rapid, approaching the inverse three-halves power of the radial distance. The pressures along the surface (H) continue to drop rapidly even at large distances, since a rarefaction wave propagates downward from the surface on which the air pressure is at every instant much lower than the vertical ground shock pressures. The air was not always at a lower pressure, since at an earlier time the air shock created surface pressures much higher — about as indicated by the small circles. The dashed curves are from the ideal gas calculation. These begin at higher pressures but continue to drop rapidly at low pressures because of the strong shock restriction involved in the ideal gas calculations. The shock compression in the vertical and horizontal directions is indicated by the curves labeled $10(\eta - 1)$, where $\eta = \rho/\rho_0$. Thus at 10 meters the vertical shock has a density of $2\rho_0$ and the horizontal shock a density of $\sim 1.5\rho_0$.

Figure 22 illustrates the maximum components of velocity as a function of distance down the vertical and also horizontally. From this one observes that the velocities along the vertical are dominantly vertical (V_v) but have some slight radial component (U_v) indicating some hemispherical divergence. The velocities along the horizontal are both upward ($-V_v$) and outward (U_n), and of comparable magnitudes at most distances.

As the problem progressed, and as it was necessary to include more material into which the shock could run, new and larger sets of zones were arranged and the hydrodynamic variables adjusted to the new grid according to the conservation laws. When such new grids were introduced, those masses above the initial surface and having high-speed motions upward were omitted. In excluding these jettisoned materials some energy and mass is lost to the system. Slightly less than 50 kilotons of mass were ejected by this procedure (in the 100 milliseconds covered). (It is estimated that altogether something on the order of megatons of material are carried aloft and tossed out of the crater from such an explosion.) Figure 23 shows this mass loss as a function of time along with the energy changes.

A study of the energy-time relations shown in Fig. 23 leads to the following observations: The downward kinetic energy, initially half a megaton, decreases rapidly as the shock develops in the surrounding rock. The heat or internal energy builds up rapidly at the expense of the initial kinetic energy, but begins to return to kinetic energy as surface material blows off. The sharp drops in energy occur as blown-off masses and their associated energies are eliminated at grid changes. Note (Fig. 23) that the biggest drop is in the kinetic energy. The total energy drops both because of such periodic (and arbitrary) mass losses and because of the work done continuously against the high-pressure air of the fireball above. At the beginning the total energy is 600 kilotons (30% of 2 megatons), but by the time the direct shock is out some 50 m, the energy is down to less than 100 kilotons (< 5%), and must drop further by both mechanisms.

The seemingly strange behavior of the internal energy at late times (Fig. 23) is an unfortunate consequence of the treatment of energies and

pressures at low densities. Although negative pressures were not allowed (replaced as zero) in the calculation, negative internal energies did arise in low-pressure, low-density zones as these zones did work on their surrounding zones. The lack of consistency here is considered to be due to undamped and nearly random kinetic motions which absorb the energy and thus cause it to be recorded as kinetic rather than as internal. It is perhaps only a misidentification which makes the energy partition motions artificial, but it may also be a source of real error since if energies were allowed to become consistent with a simple gas pressure, the pressures might well have been higher, causing further accelerations. This effective transfer of energy did not become seriously "out of line" until times after 10 ms, so that although late-time information may be of doubtful accuracy, the early history should still be correct.

An investigation of ways to avoid this trouble is still in progress, although it is currently expected that the general features of the present calculation will remain unaltered by the correction of this inconsistency.

VI. CONCLUSIONS

Perhaps the most significant result to come out of these preliminary calculations, aside from the general observation that the method seems capable of offering an interpretation of cratering phenomena, is that the kinetic energy in the bomb debris when it reaches the ground is the most important mechanism in inducing the ground motion below the crater, as well as in the formation of the crater itself.

This fact implies that the crater size should be very sensitive to the height of burst near the ground. For if the debris must travel even a short distance through air before contacting the ground, its energy may be seriously reduced as it drives a strong air shock. This energy is quickly radiated away to the periphery of the fireball and contributes to increasing the air blast at the expense of cratering efficiency.

Moreover, it implies that the cratering is sensitive to the details of the bomb disassembly in that this process determines the partitioning of bomb

energy between the debris' internal and kinetic energy and that radiated away to air. This indicates that shallow burial or denser case should enhance cratering efficiency.

It also shows that comparisons with high-explosive bursts in this regime would seem particularly unfruitful, since the early energy partitions between explosive gases, air, and earth are vastly different.

A further remarkable quality is that the presence of a nearly free surface causes the stress patterns below the burst to be elongated along the vertical axis. The fact that the pressures along the shock front are far from uniform at any given time is understandable in terms of the geometry of the surface burst, but was not always a recognized factor in previous analysis of ground shocks generated by nuclear bursts at low heights above the surface, on the surface, or shallowly buried.

A further feature worthy of reiteration is the nature of the continuous loss of effective energy in the ground medium due both to the work done by the expanding ground against air overpressure and to the essential disassociation of jetting material from the main body of soil or rock.

It would appear that further investigations should include studies of

(1) Subsurface bursts.

(2) Bursts in other materials, both hard rock and dry soil. (It may prove interesting to consider some cases of bursts on wet soils or even water.)

(3) High explosive bursts for the sake of comparison and to illustrate more clearly the differences in the action between nuclear and chemical explosions.

(4) Special geometries of high explosive charges with a view to modeling the stress wave history of a nuclear explosion (an investigation of this possibility is currently under study at SRI with DASA sponsorship).

These preliminary calculations were intended to reveal the basic nature of the cratering process and the formation of ground shocks. That the hydrodynamic model was used should always be kept in mind. This limits the strict

applicability of these results to pressures greater than 8 kilobars (which corresponds to compressions of greater than 10%) for the soft rock, tuff, which was the only material considered. It is believed that above this compression and pressure, the results are substantially correct, although the various uncertainties could easily lead to errors of about a factor of two.

Even recognizing this, it is of interest to examine the results of the present model beyond the region of its strict applicability, for it is not unreasonable to expect that at least the first motions are given correctly by it, leading to roughly correct values of peak pressure and peak velocity. However, the energetics at late times are questionable, and are subject to further interpretation.

It is hoped that the results presented here will furnish useful guidance and inputs to further studies at lower stress levels, which are very important to the design of protective structures. At these lower stress levels, the present hydrodynamic model must be replaced by one which considers the tensor nature of the equation of state.

ACKNOWLEDGMENTS

The authors wish to credit Mrs. Nancy J. Brooks of the Computer Sciences Department at RAND with recognition for her truly professional management of the entire computing program of this problem. In addition to her competent organization of the numerical work, Mrs. Brooks participated enthusiastically in discussions and decisions concerning the progress of the overall effort. Our appreciation extends also to Miss Linda Larson, Mrs. Margaret Cohen, and Mrs. Rosemary Plue for aid in the analysis and preparation of report graphs.

Although this study was initiated primarily to satisfy a need in military applications, the method and some results are of significance to several proposals for peaceful uses of nuclear explosions under the Plowshare program of the Atomic Energy Commission. For this reason the study was funded in a small part under Contract No. AT(11-1)-135 with the University of California Lawrence Radiation Laboratory at Livermore, California.

REFERENCES

1. Bjork, R. L., and N. J. Brooks, A Numerical Technique for Solution of Multi-Dimension Hydrodynamic Problems, The RAND Corporation, Research Memorandum RM-2628 (to be published).
2. Brode, H. L., Weapon Effects for Protective Design, The RAND Corporation, Paper P-1951, 31 March 1960.
3. Nuckolls, John, in Proceedings of the Second Plowshare Symposium, Part I: Phenomenology of Underground Nuclear Explosions, University of California Lawrence Radiation Laboratory (Livermore) Rept. UCRL-5675, May 1959, pp. 120-134.
4. Landshoff, Rolf, A Numerical Method for Treating Fluid Flow in the Presence of Shocks, Los Alamos Scientific Laboratory (1955).
5. Brode, H. L., "Numerical Solutions of Spherical Blast Waves," J. Appl. Phys., Vol. 26, No. 6, June 1955, pp. 766-775.
6. Glasstone, S. (Ed.), The Effects of Nuclear Weapons, AEC and DOD, pp. 209-213, June 1957.

/bs

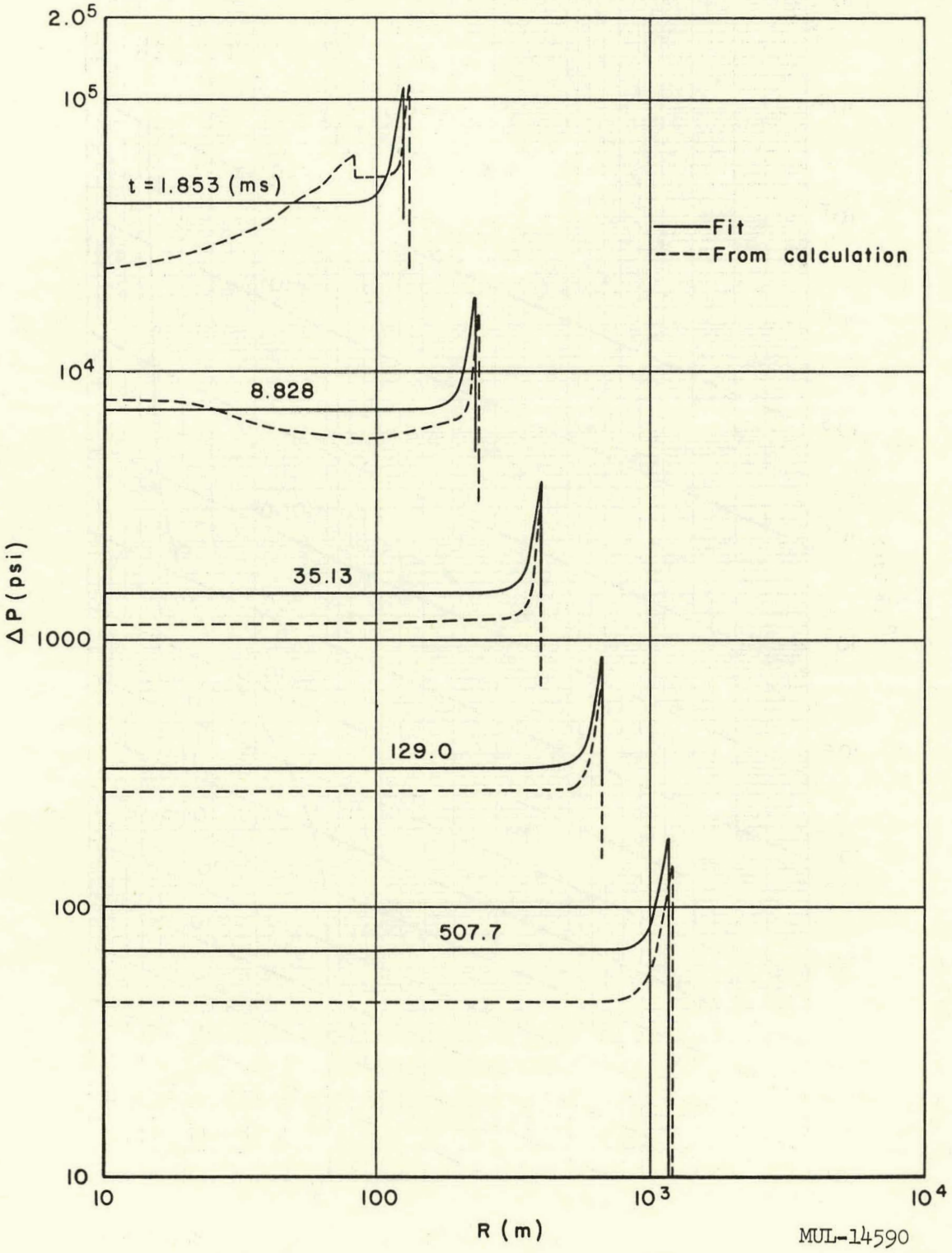

Fig. 1—Comparison of air overpressure approximate analytical form (——) with detailed numerical results (– – –)

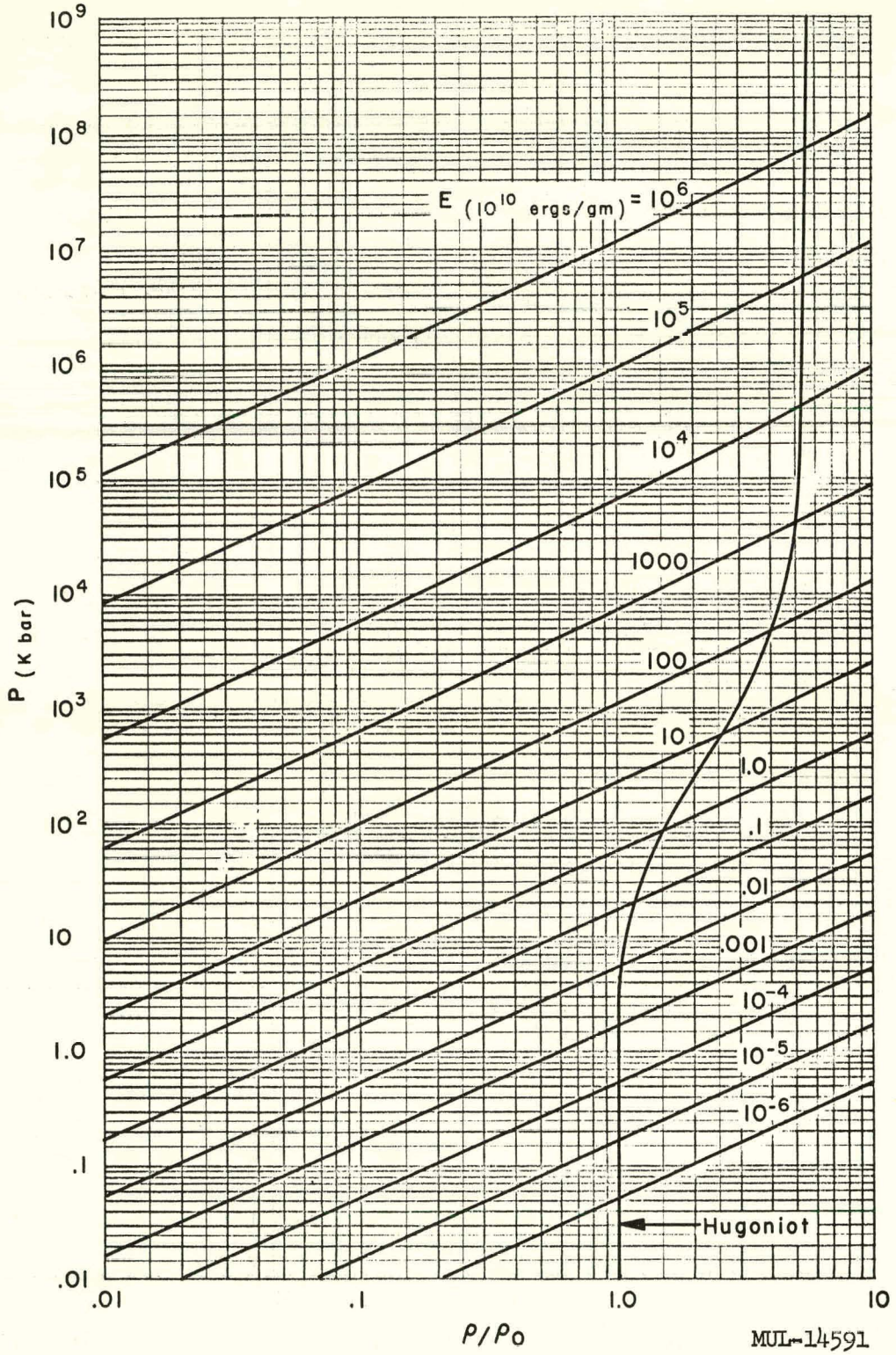

Fig. 2—Equation of state for Tuff

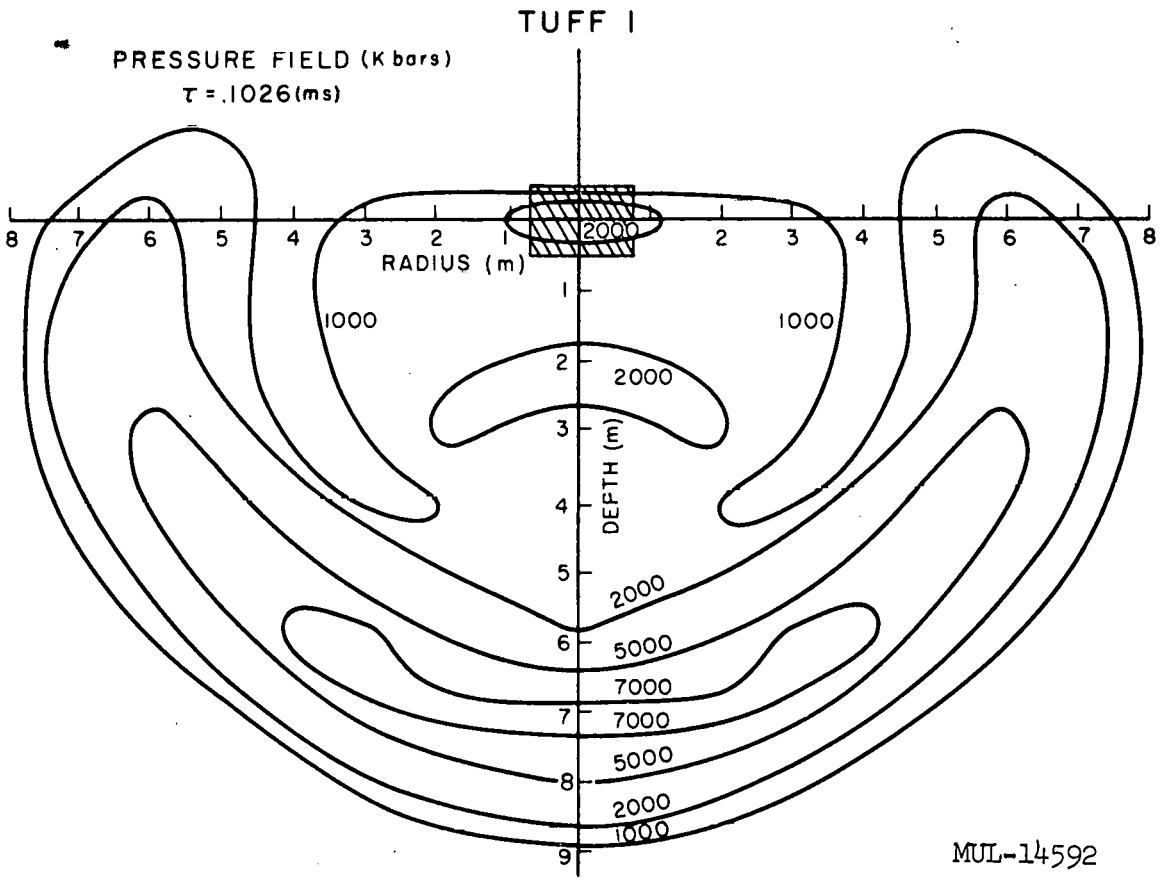
TUFF I
PRESSURE FIELD (K bars)
τ = .1026(ms)
RADIUS (m)
DEPTH (m)
2000
1000
1000
2000
2000
5000
7000
7000
5000
2000
1000
MUL-14592

Fig. 3

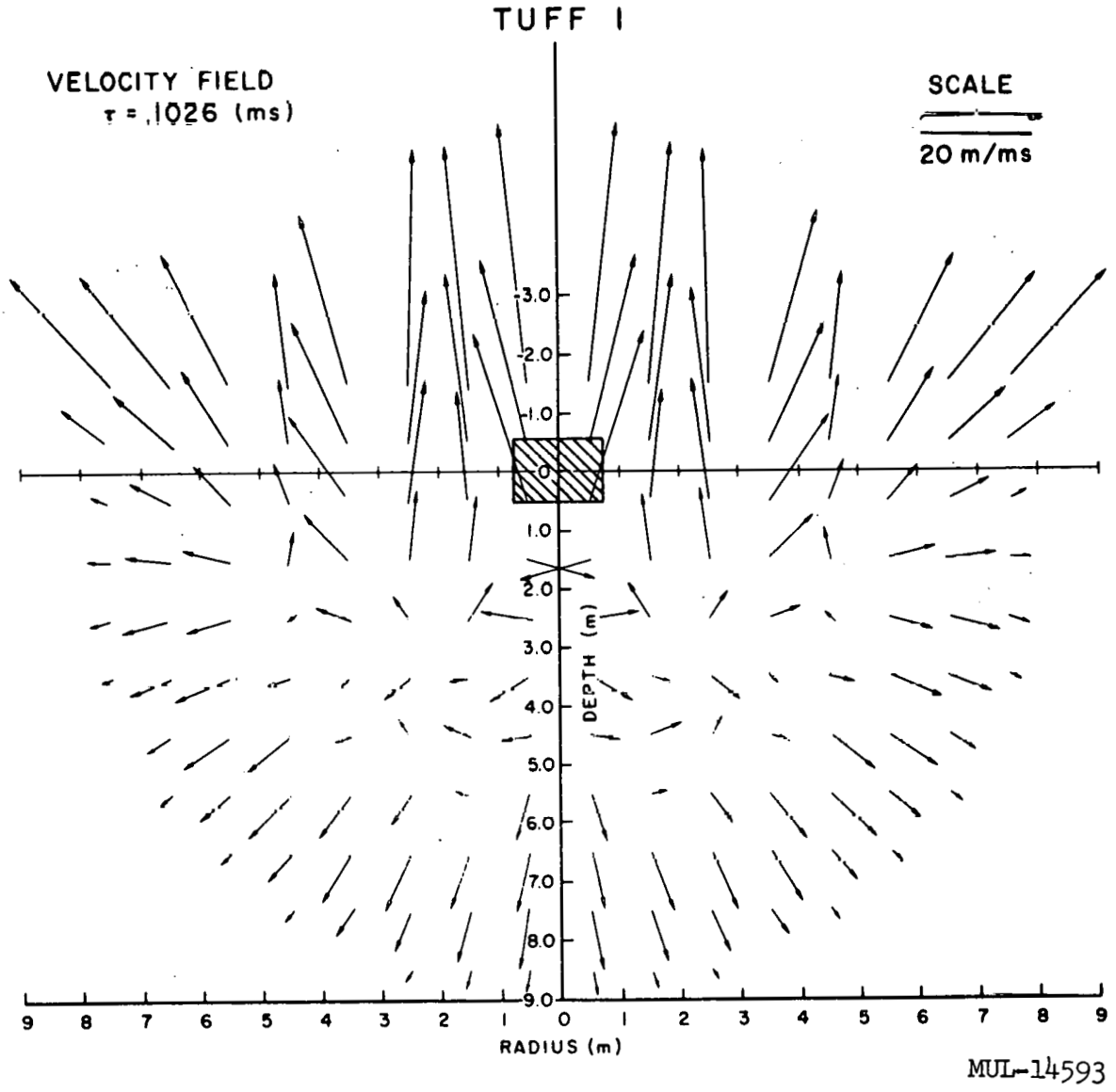
TUFF I
VELOCITY FIELD
τ = .1026 (ms)
SCALE
20 m/ms
DEPTH (m)
RADIUS (m)
MUL-14593

Fig. 4

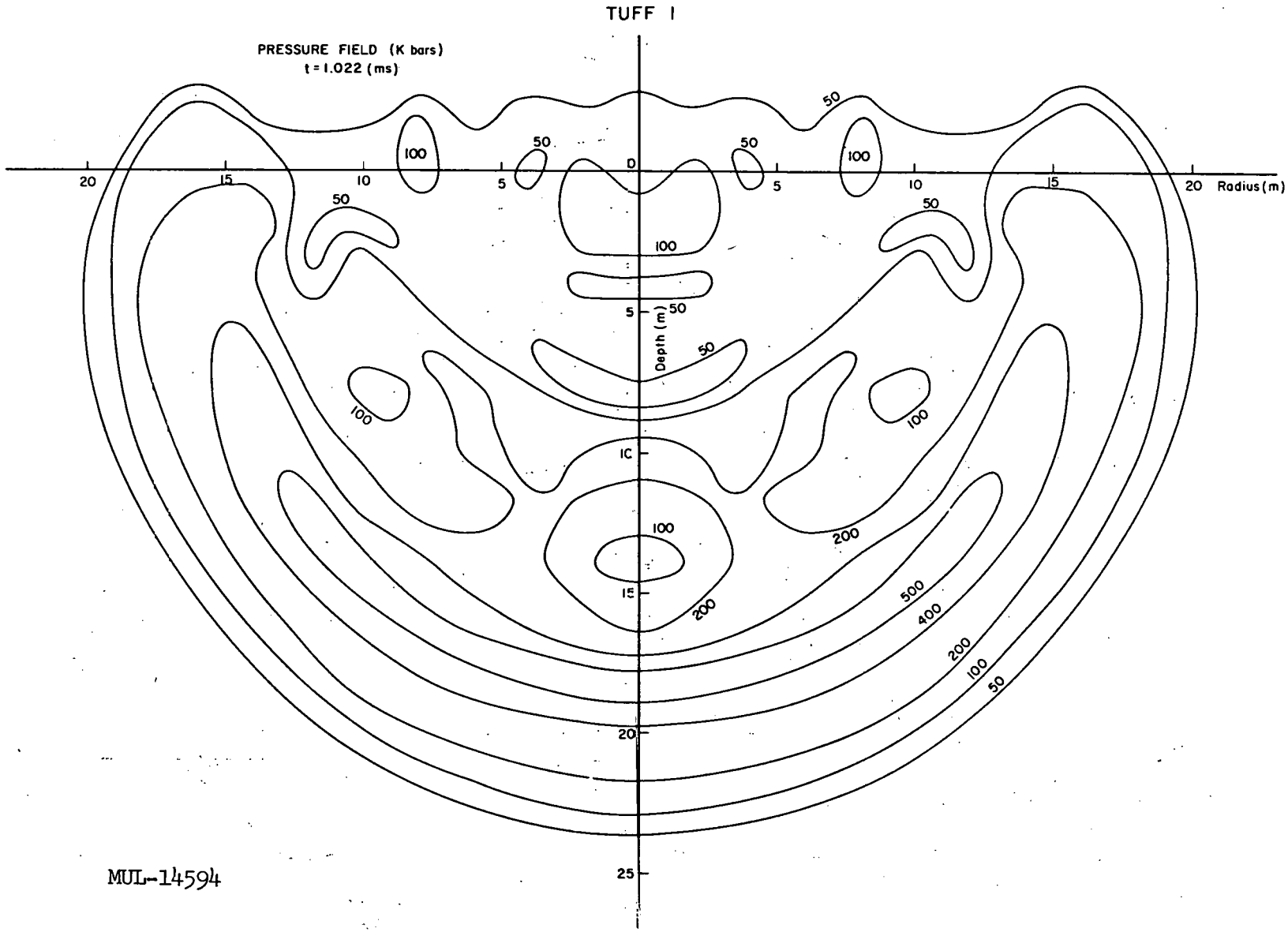
TUFF I
PRESSURE FIELD (K bars)
t = 1.022 (ms)
Radius (m)
Depth (m)
MUL-14594

Fig. 5

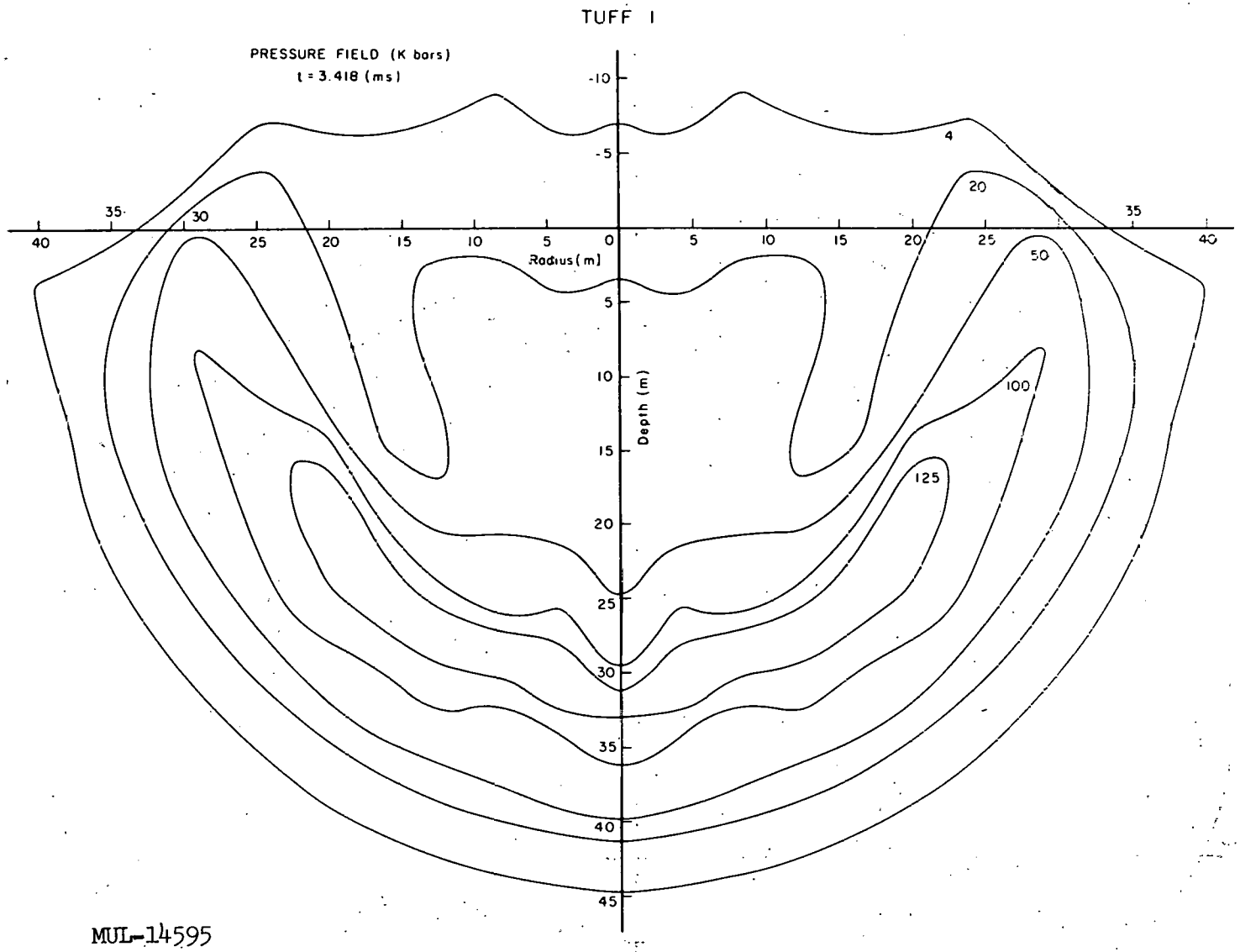

MUL-14595

Fig. 6

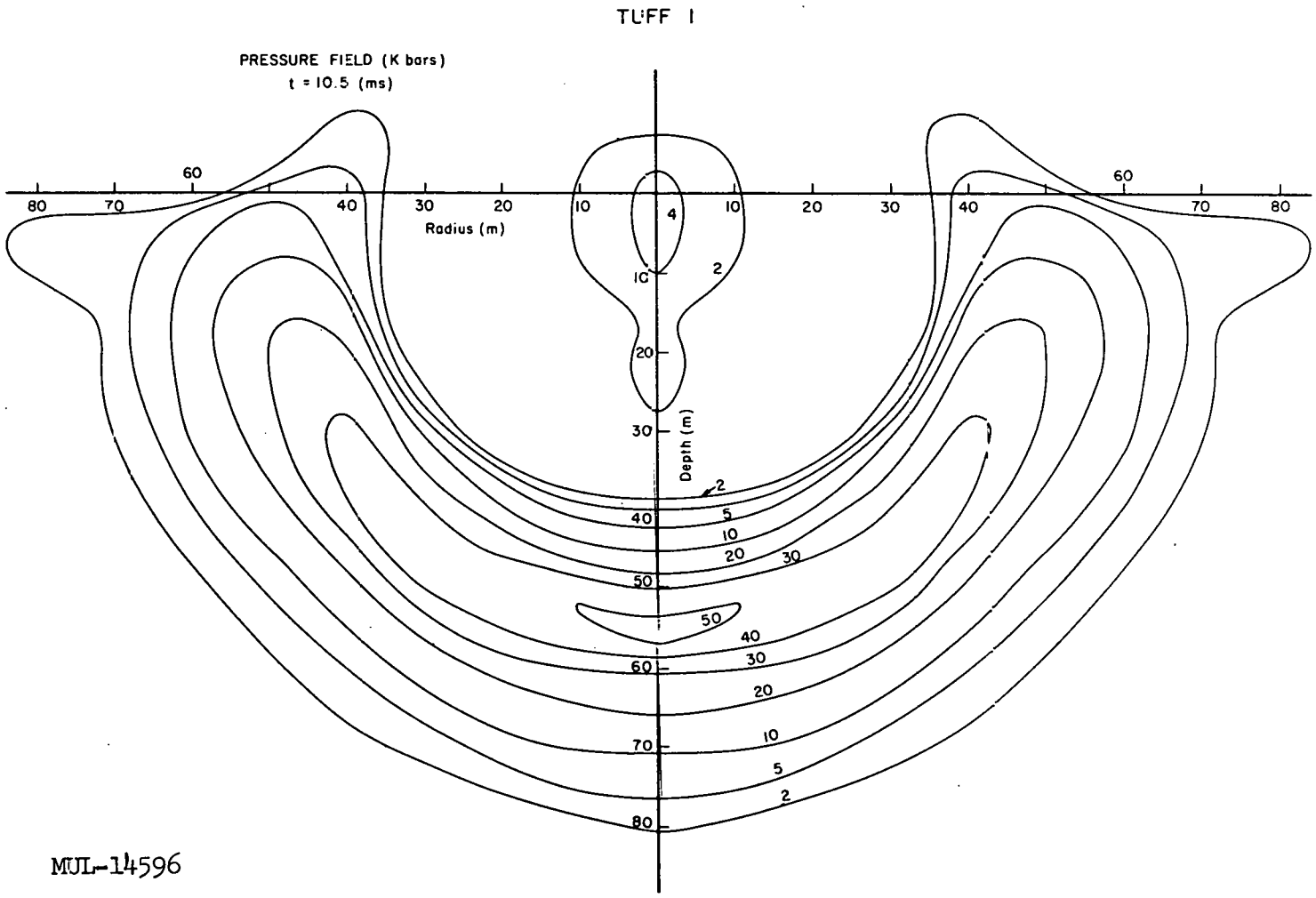
TUFF I
PRESSURE FIELD (K bars)
t = 10.5 (ms)
Radius (m)
Depth (m)
MUL-14596

Fig. 7

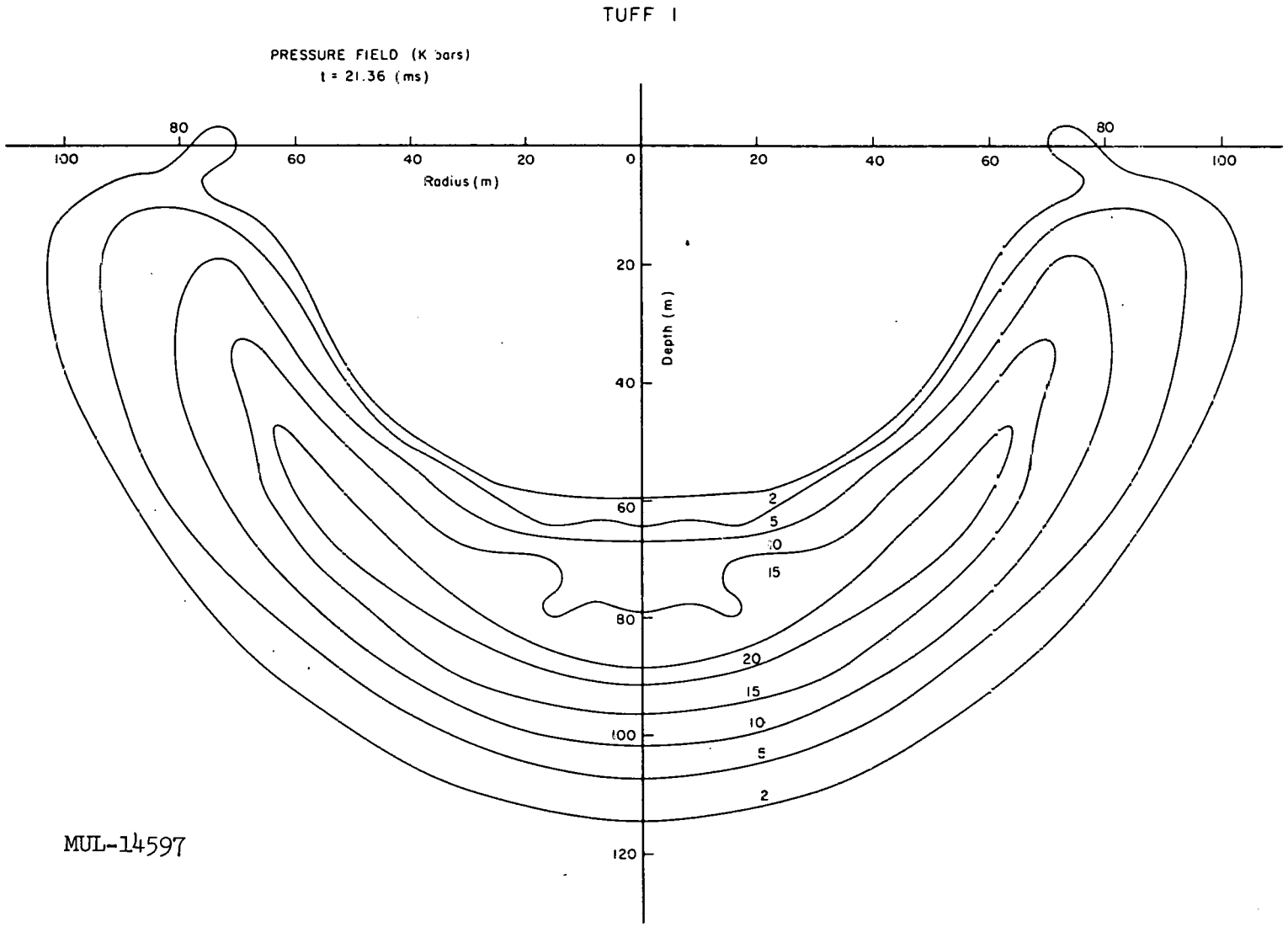
TUFF 1
PRESSURE FIELD (K bars)
t = 21.36 (ms)
Radius (m)
Depth (m)
80
100
60
40
20
0
20
40
60
80
100
20
40
60
80
100
120
2
5
10
15
20
15
10
5
2
MUL-14597

Fig. 8

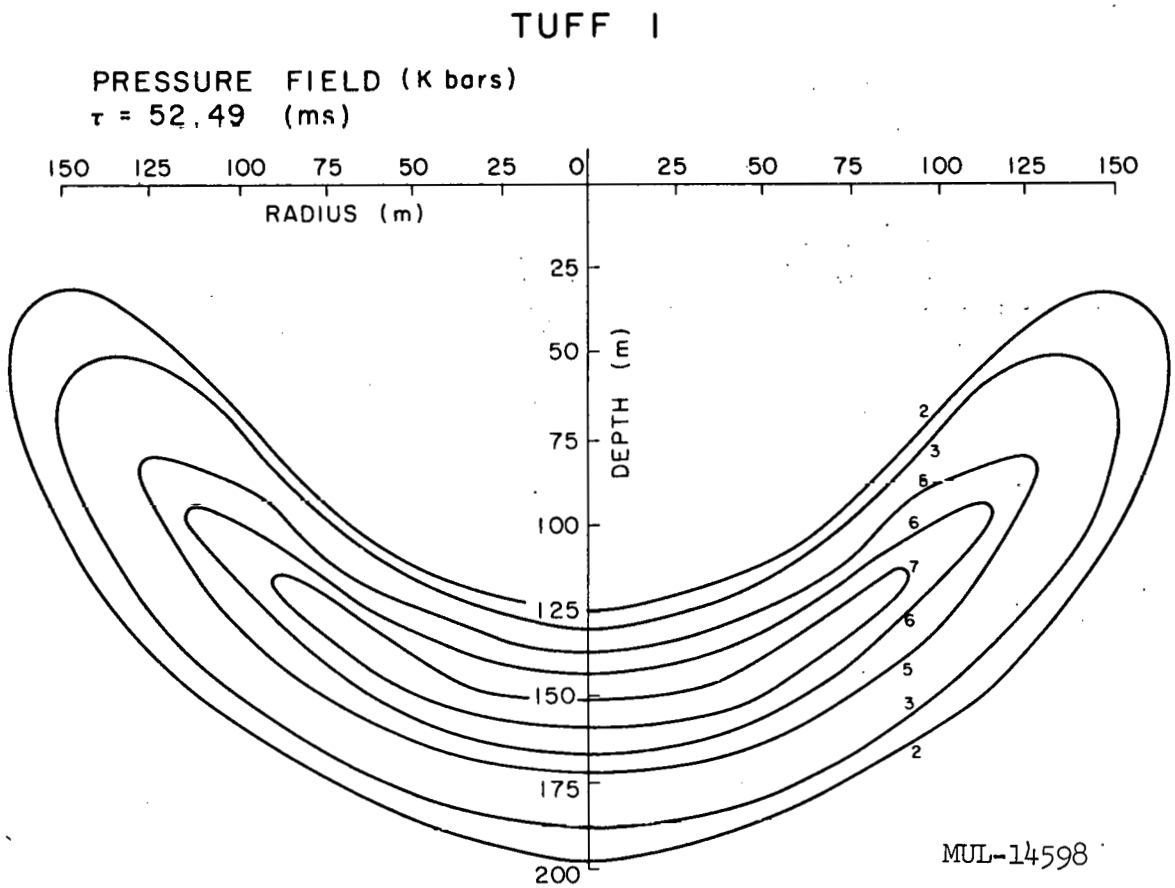
TUFF I
PRESSURE FIELD (K bars)
τ = 52.49 (ms)
150 125 100 75 50 25 0 25 50 75 100 125 150
RADIUS (m)
25
50
75
100
125
150
175
200
DEPTH (m)
2
3
5
6
7
6
5
3
2
MUL-14598

Fig. 9

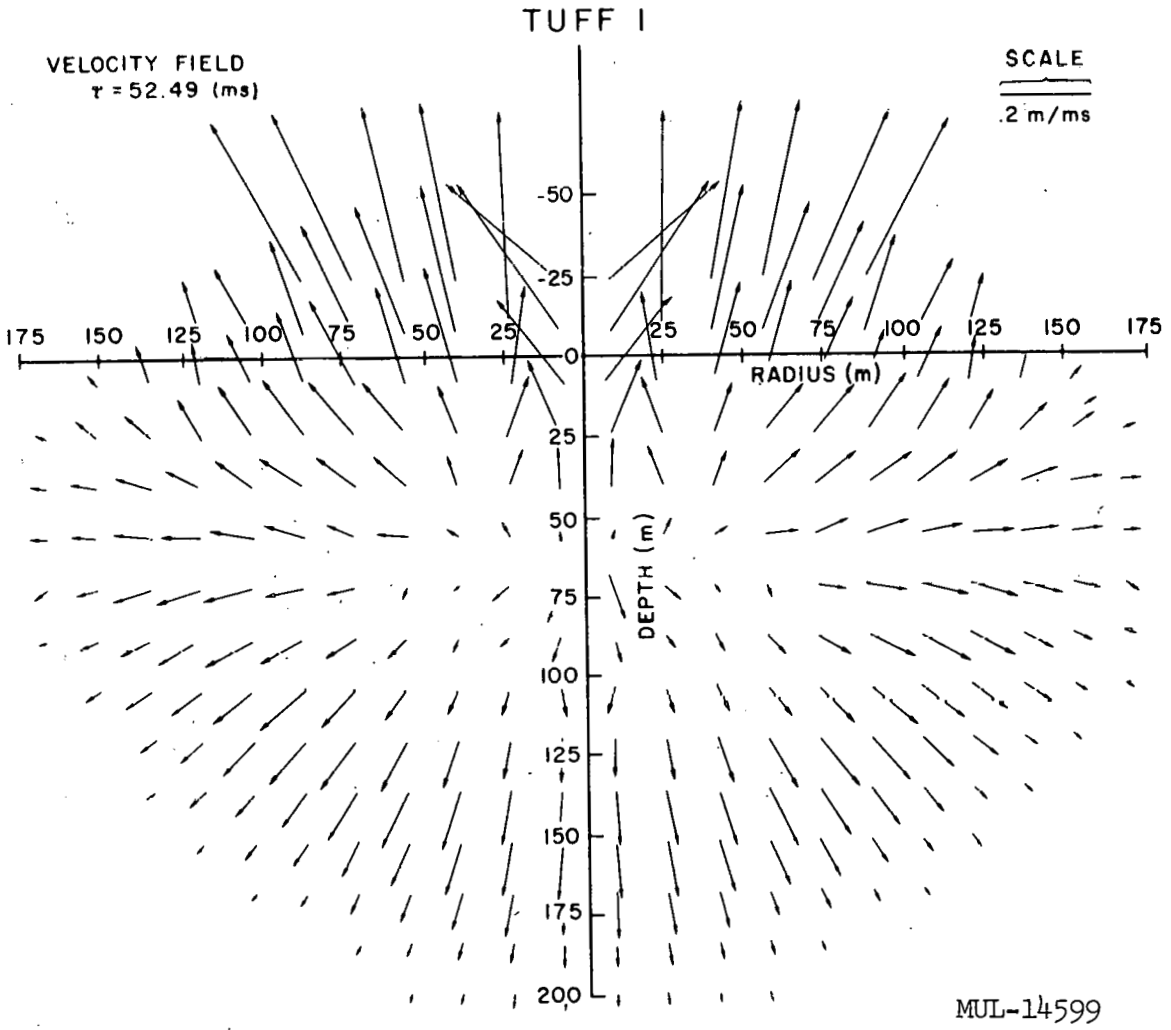
TUFF I
VELOCITY FIELD
τ = 52.49 (ms)
SCALE
.2 m/ms
-50
-25
175 150 125 100 75 50 25
0
25 50 75 100 125 150 175
RADIUS (m)
25
50
75
100
125
150
175
200
DEPTH (m)
MUL-14599

Fig. 10

TUFF I

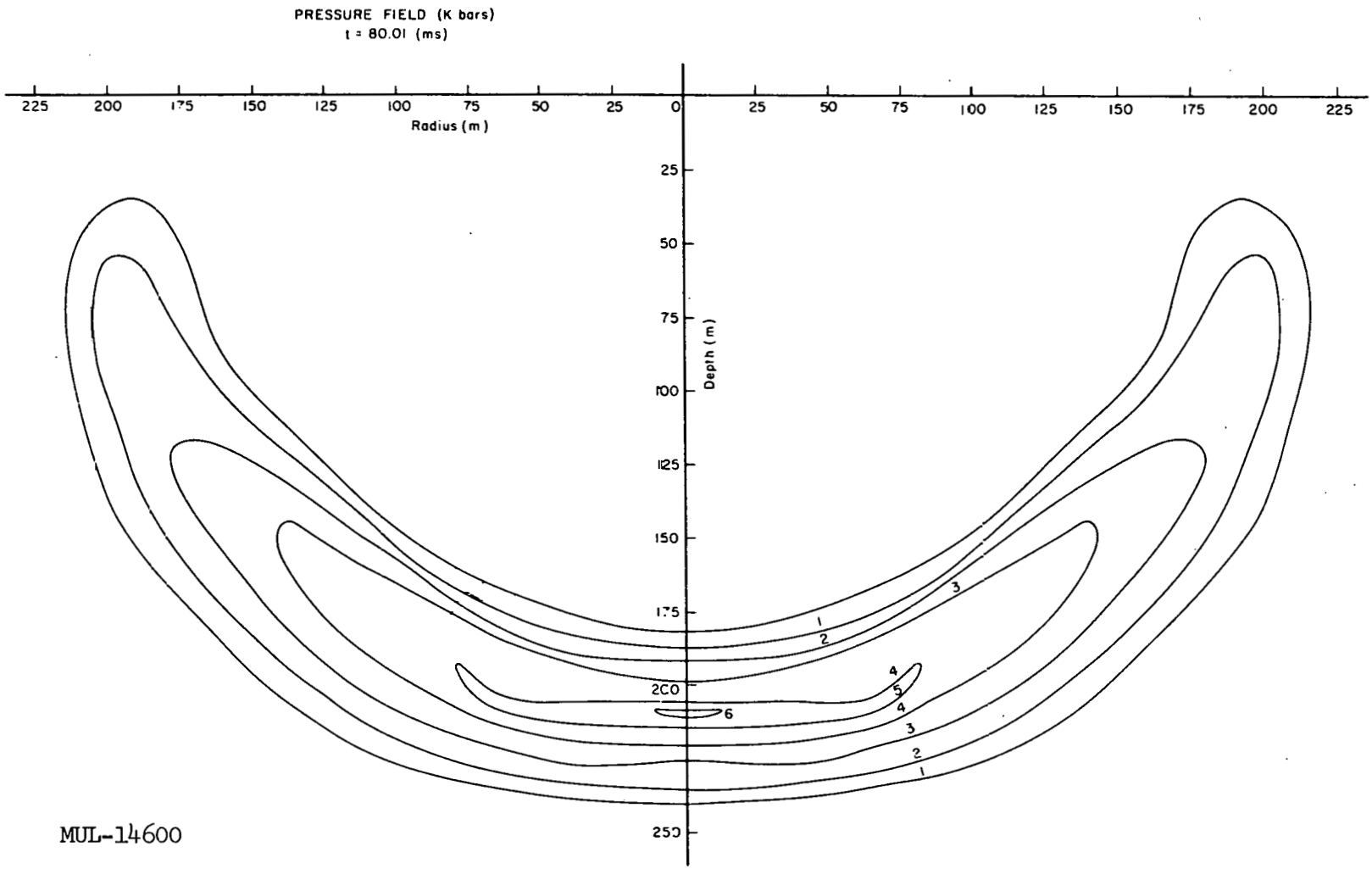

MUL-14600

Fig. 11

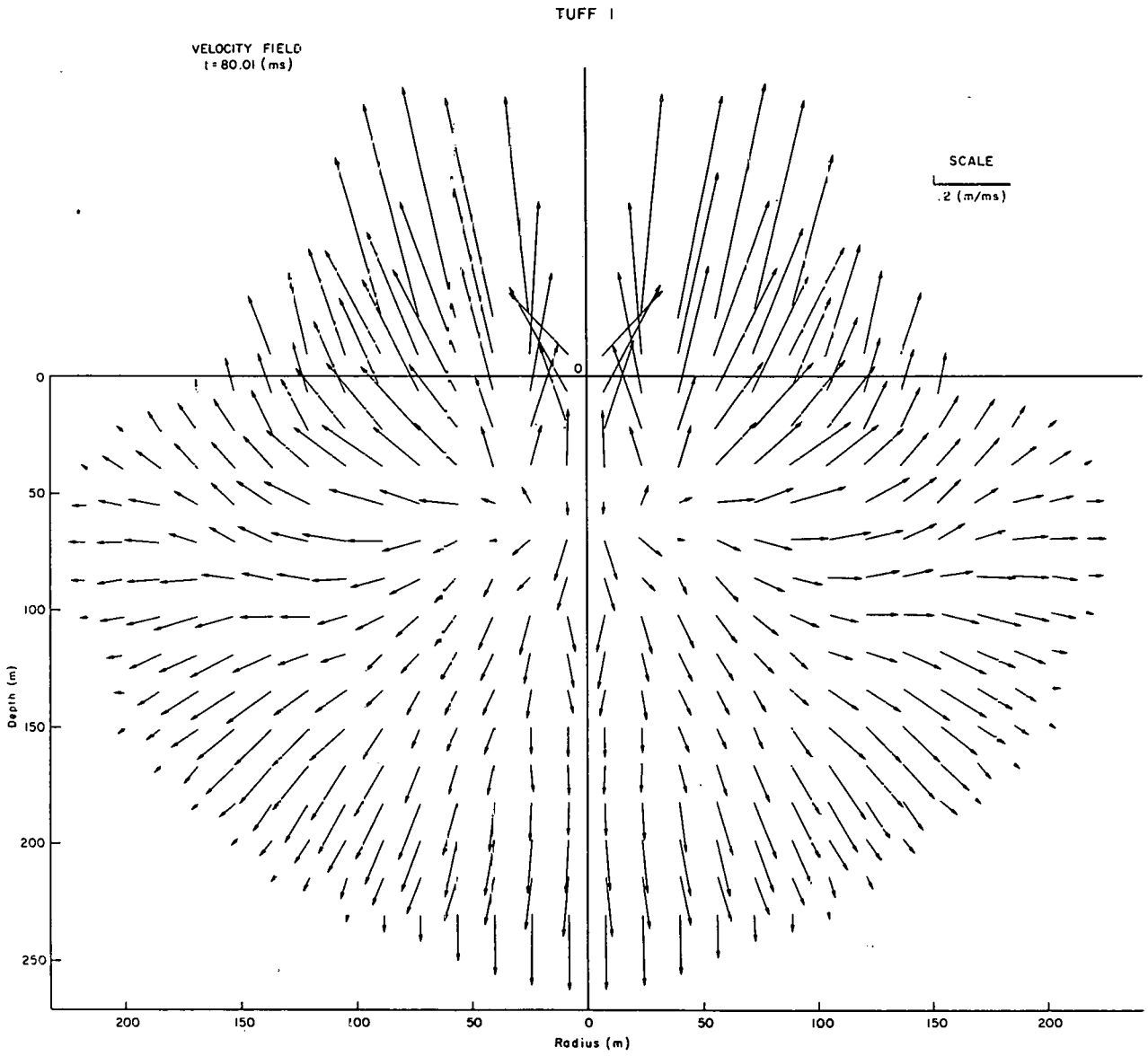

MUL-14601

Fig. 12

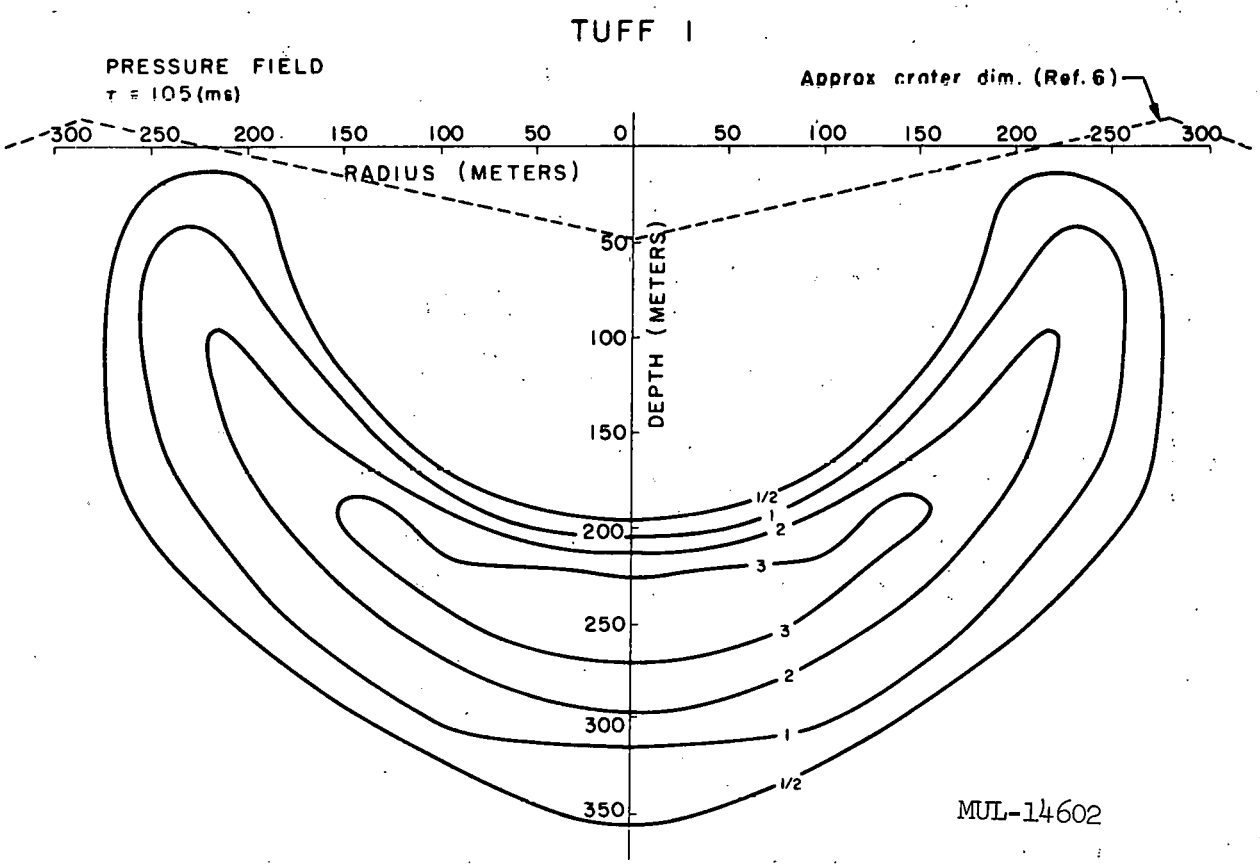
TUFF I
PRESSURE FIELD
τ = 105 (ms)
Approx crater dim. (Ref. 6)
300 250 200 150 100 50 0 50 100 150 200 250 300
RADIUS (METERS)
DEPTH (METERS)
50
100
150
200
250
300
350
1/2
1
2
3
3
2
1
1/2
MUL-14602

Fig. 13

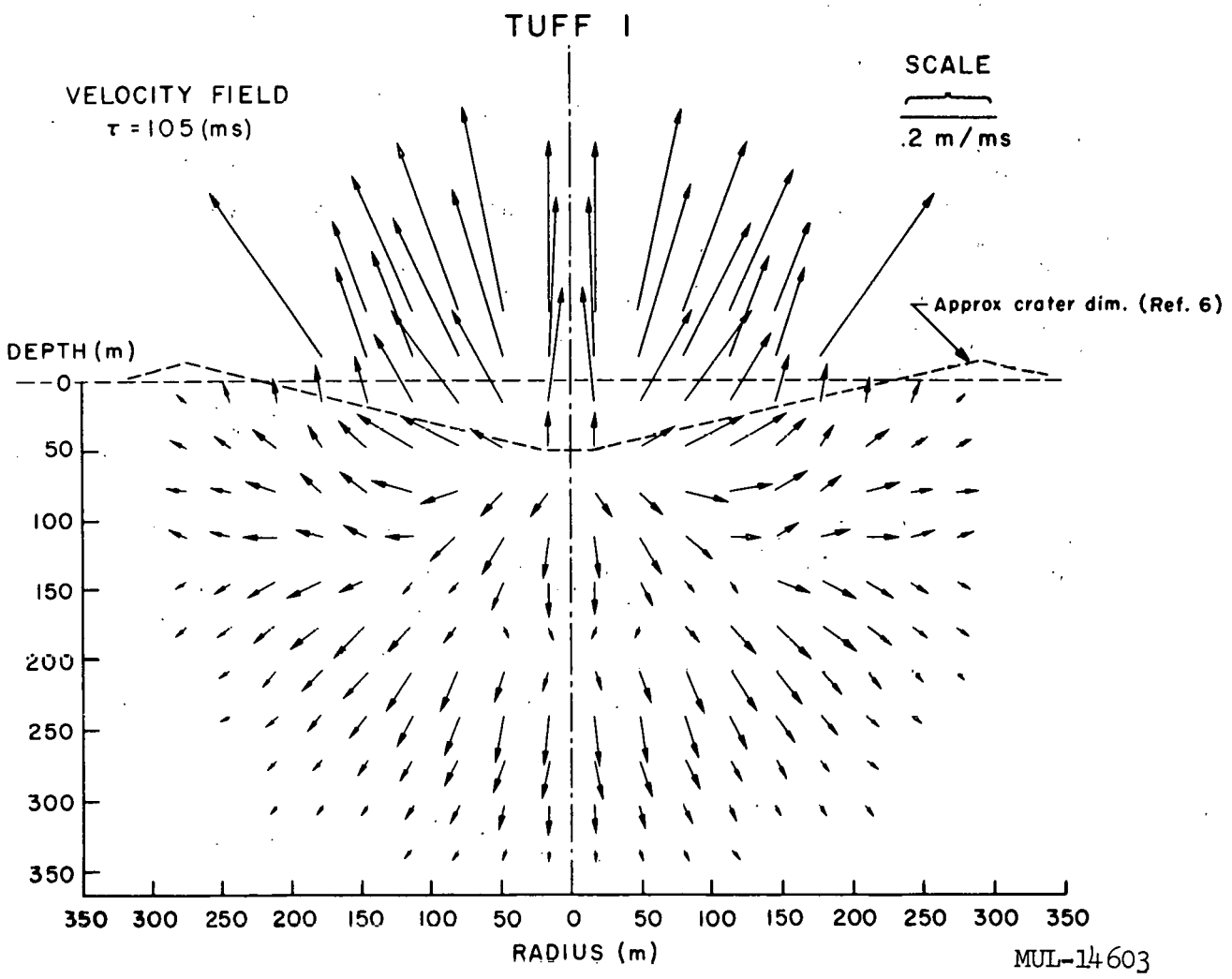
TUFF I
VELOCITY FIELD
τ = 105 (ms)
SCALE
.2 m/ms
Approx crater dim. (Ref. 6)
DEPTH (m)
0
50
100
150
200
250
300
350
350 300 250 200 150 100 50 0 50 100 150 200 250 300 350
RADIUS (m)
MUL-14603

Fig. 14

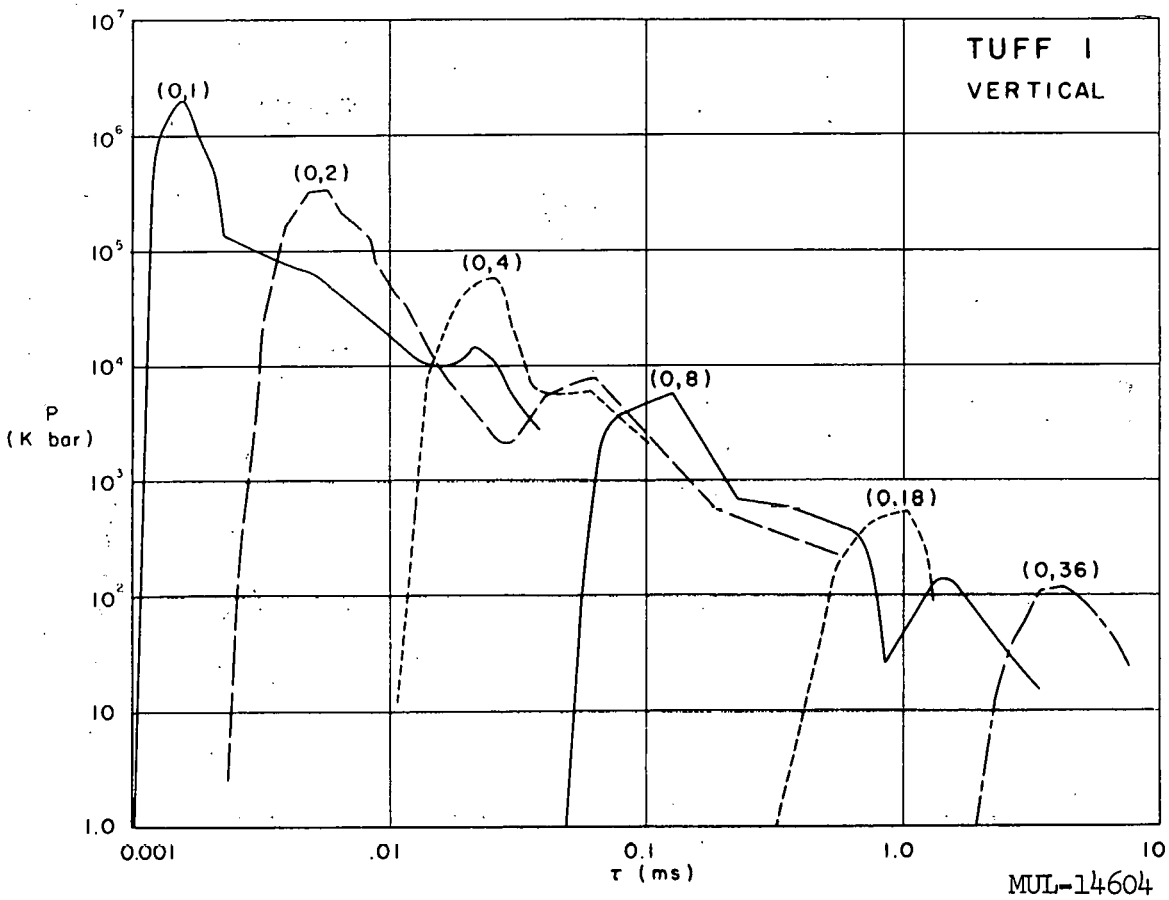

Fig. 15 — Pressure vs time at indicated depths (m) below burst point

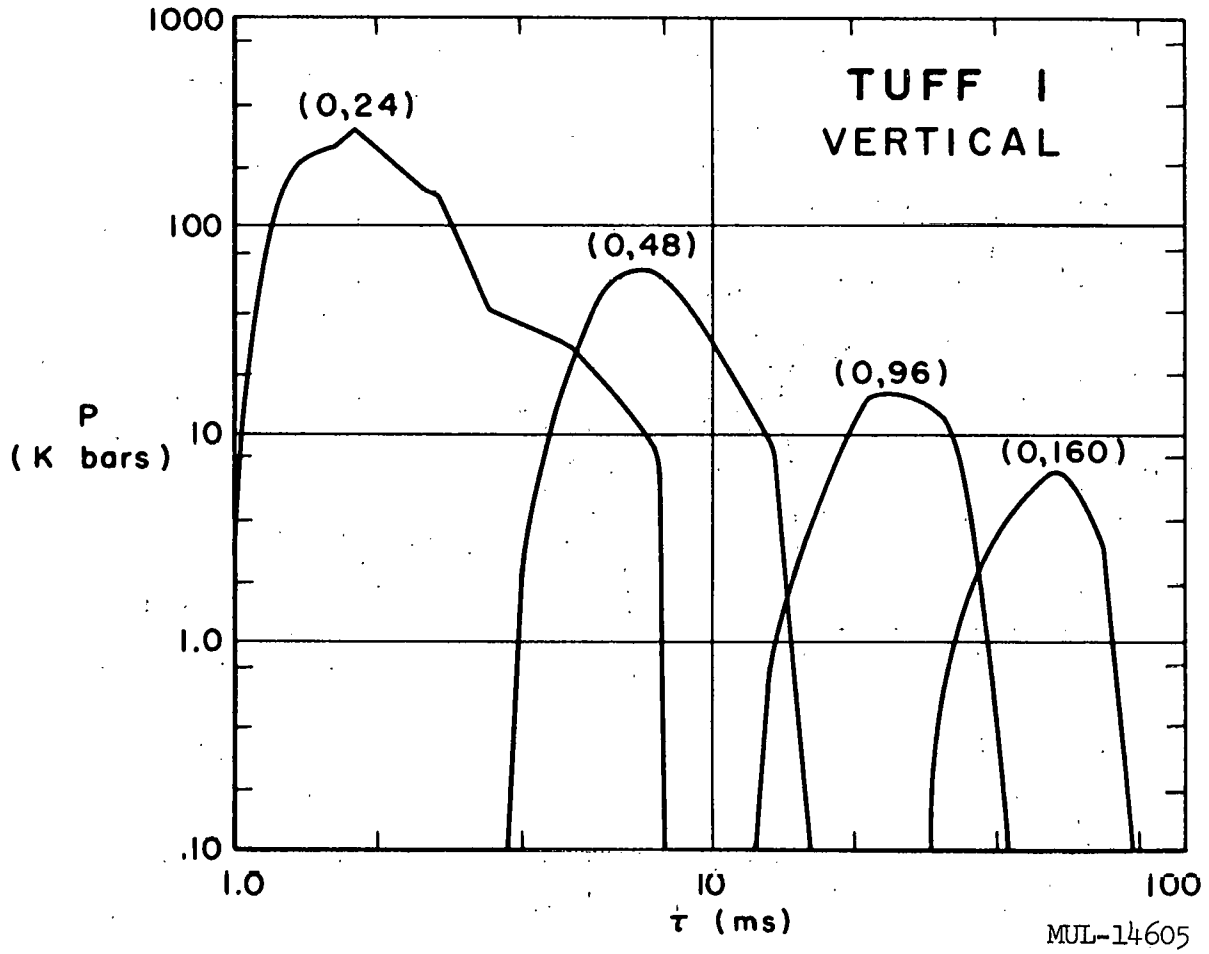

Fig. 16—Pressure vs time at indicated depths (m) below burst point

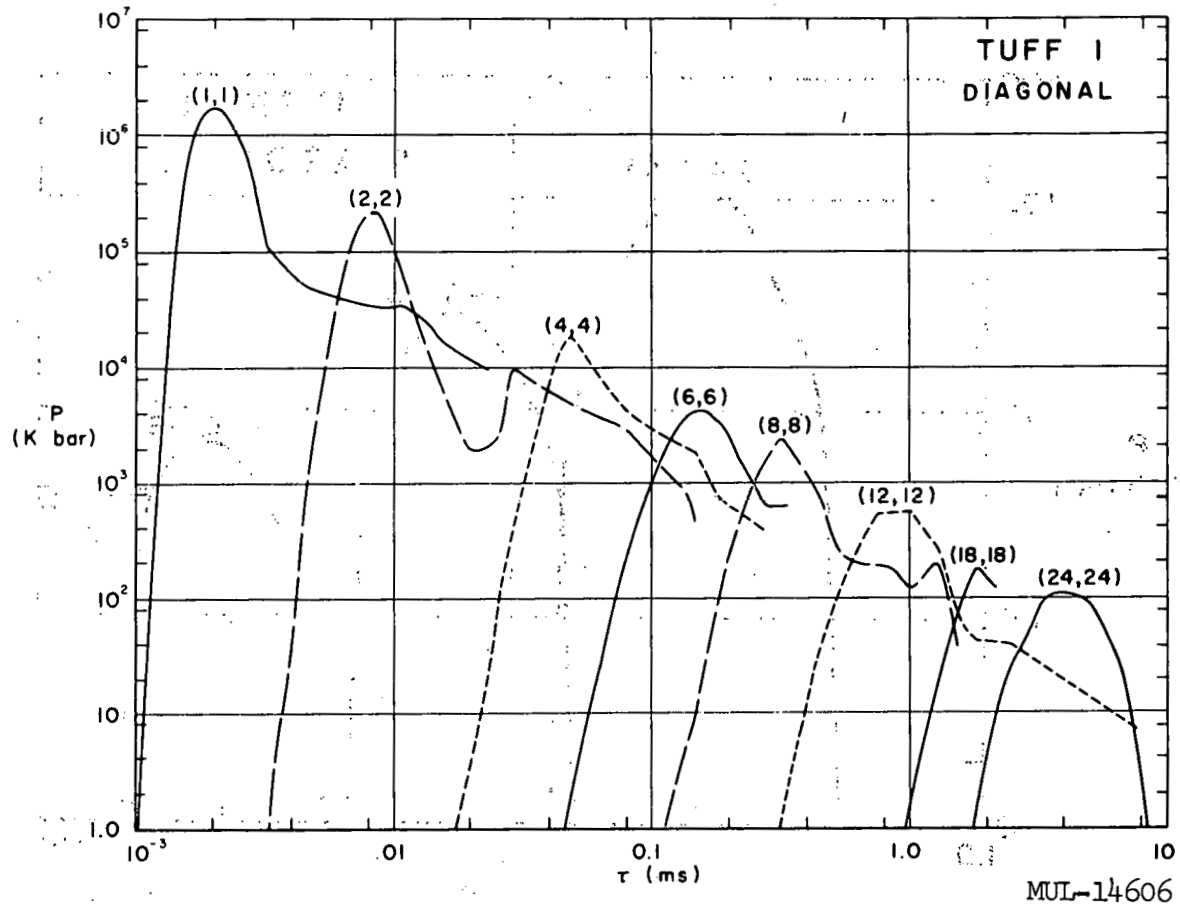

Fig. 17 — Pressure vs time at points with radii and depths indicated in meters

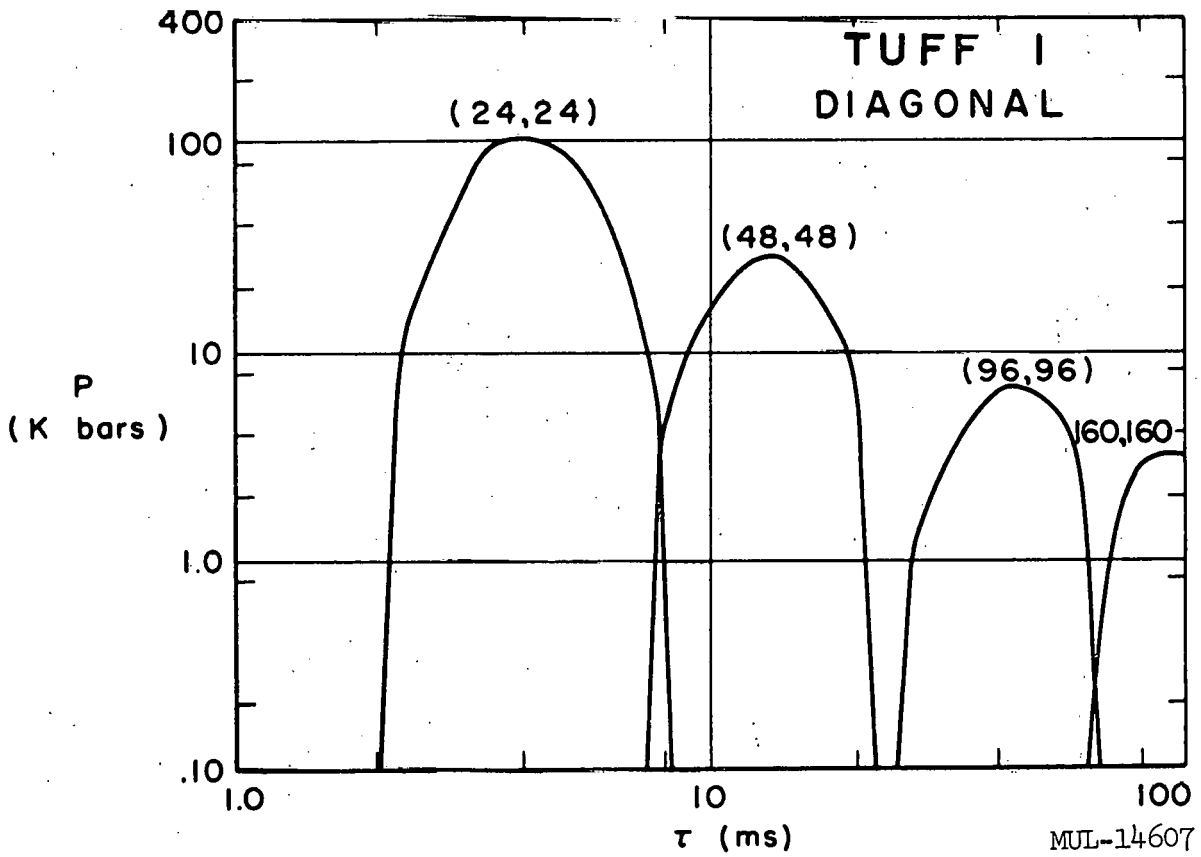

Fig. 18 — Pressure vs time at indicated positions (m)

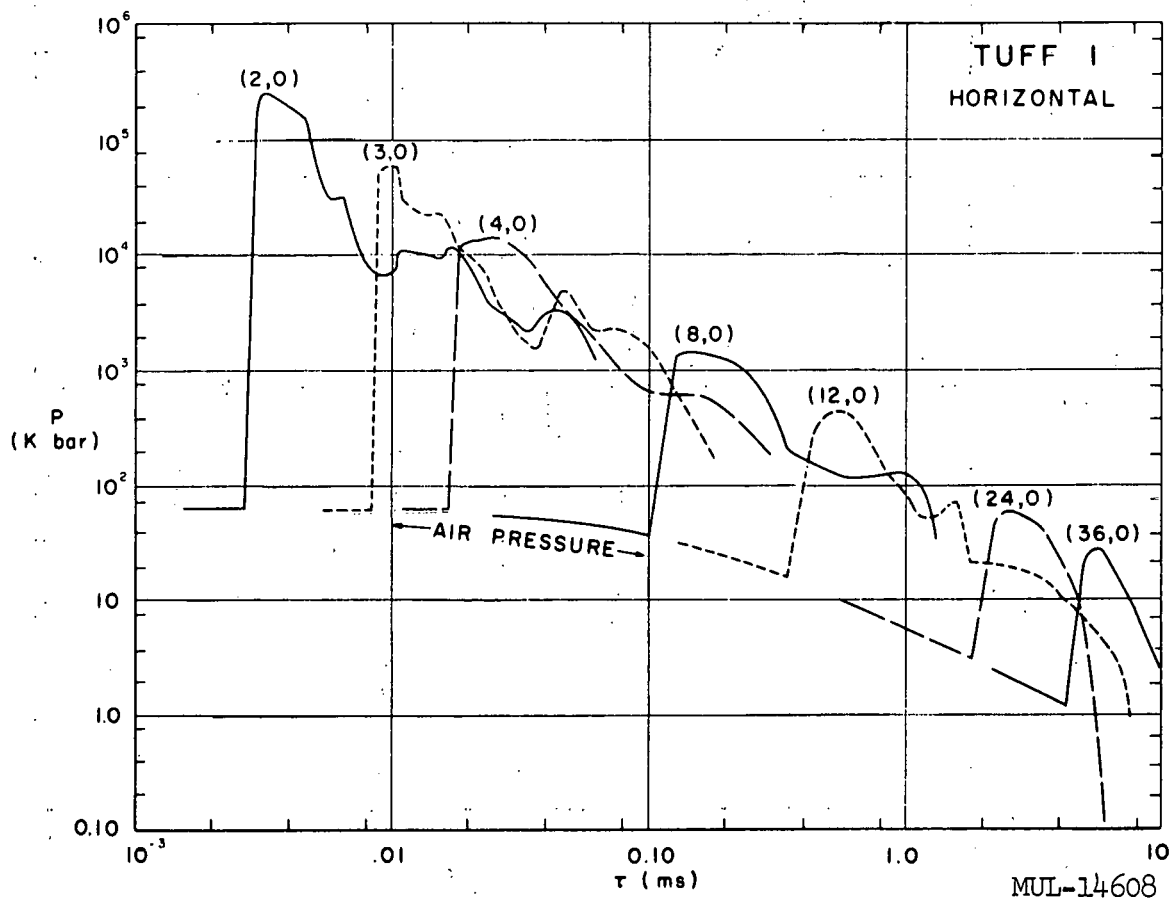

Fig. 19 — Pressure vs time at indicated radial distances (m) at the surface

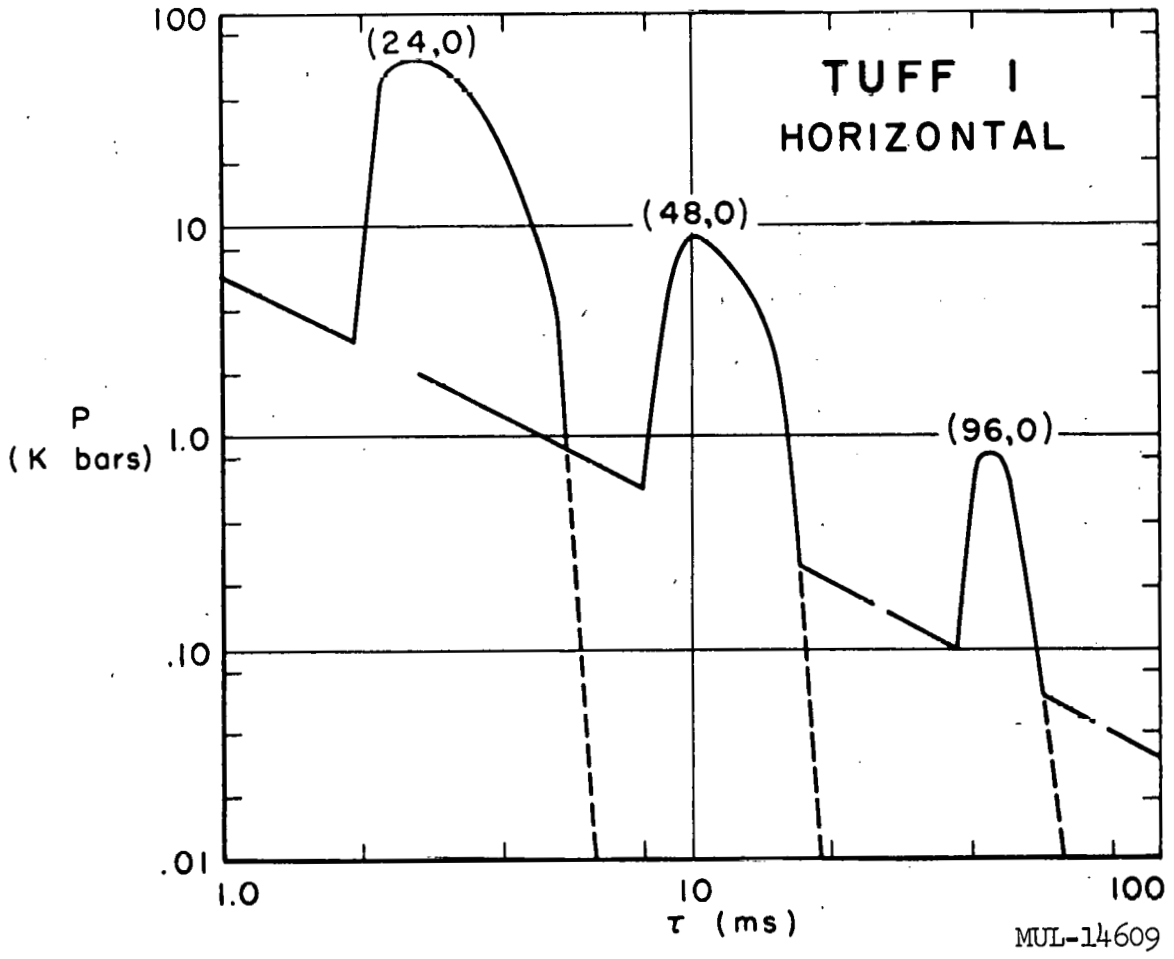

Fig. 20—Pressure vs time at indicated radii (m) along the surface

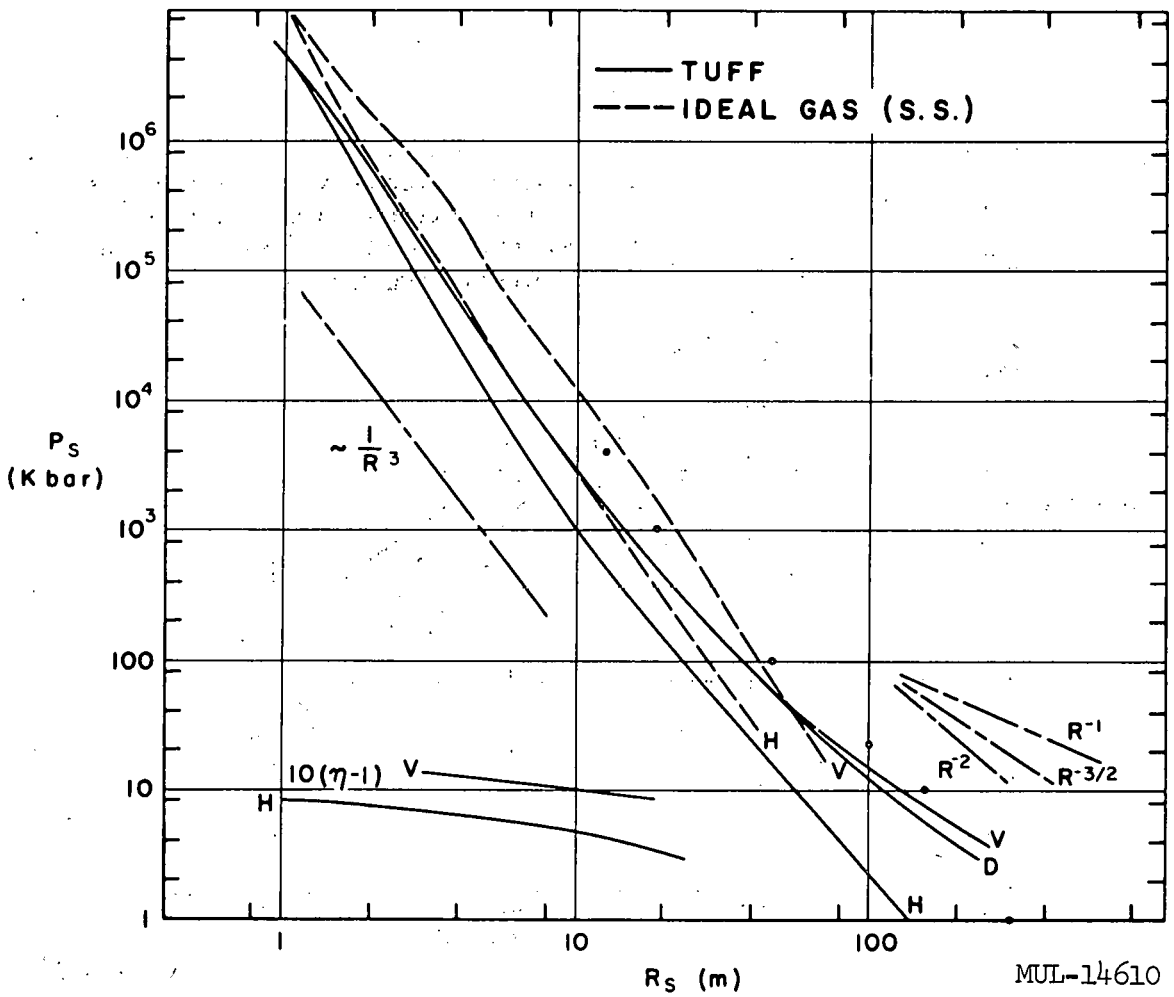

Fig. 21—Peak pressures and compressions (η-1) vs range along vertical (V), horizontal (H), and diagonal (D), from burst point

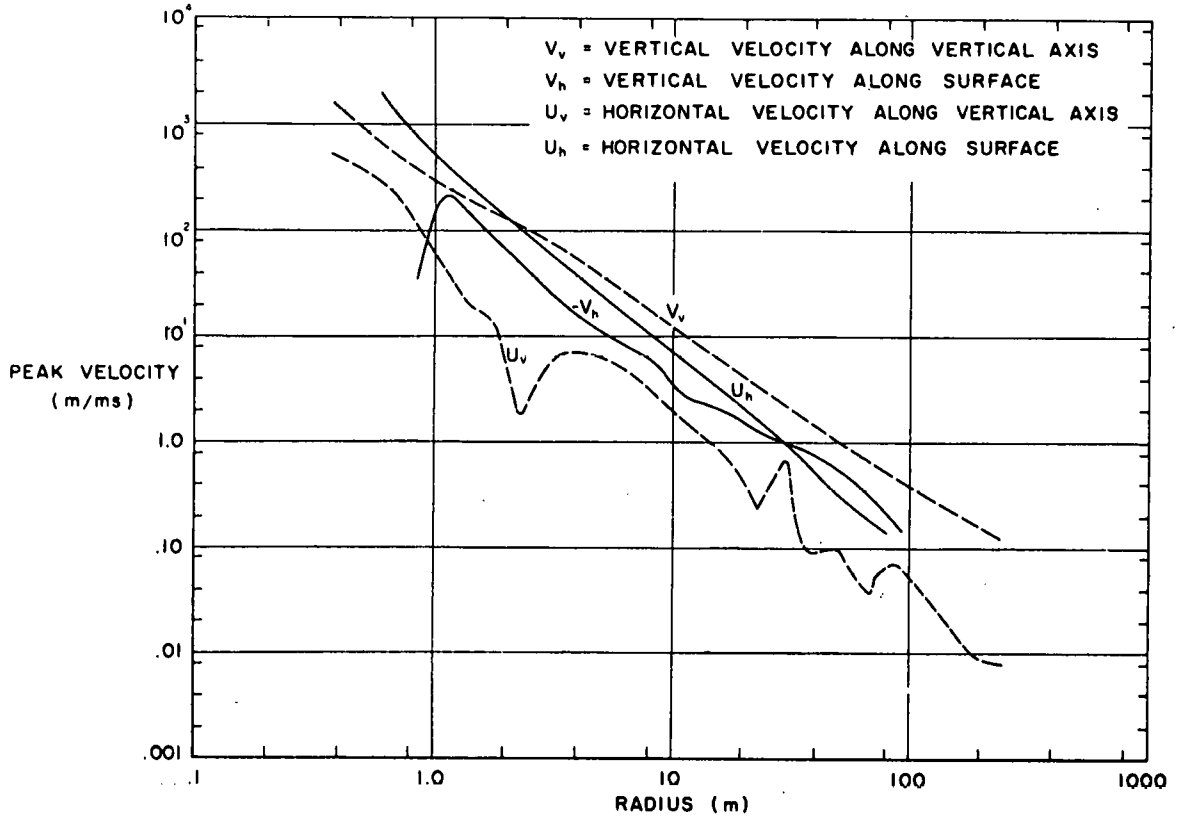

MUL-14611

Fig. 22

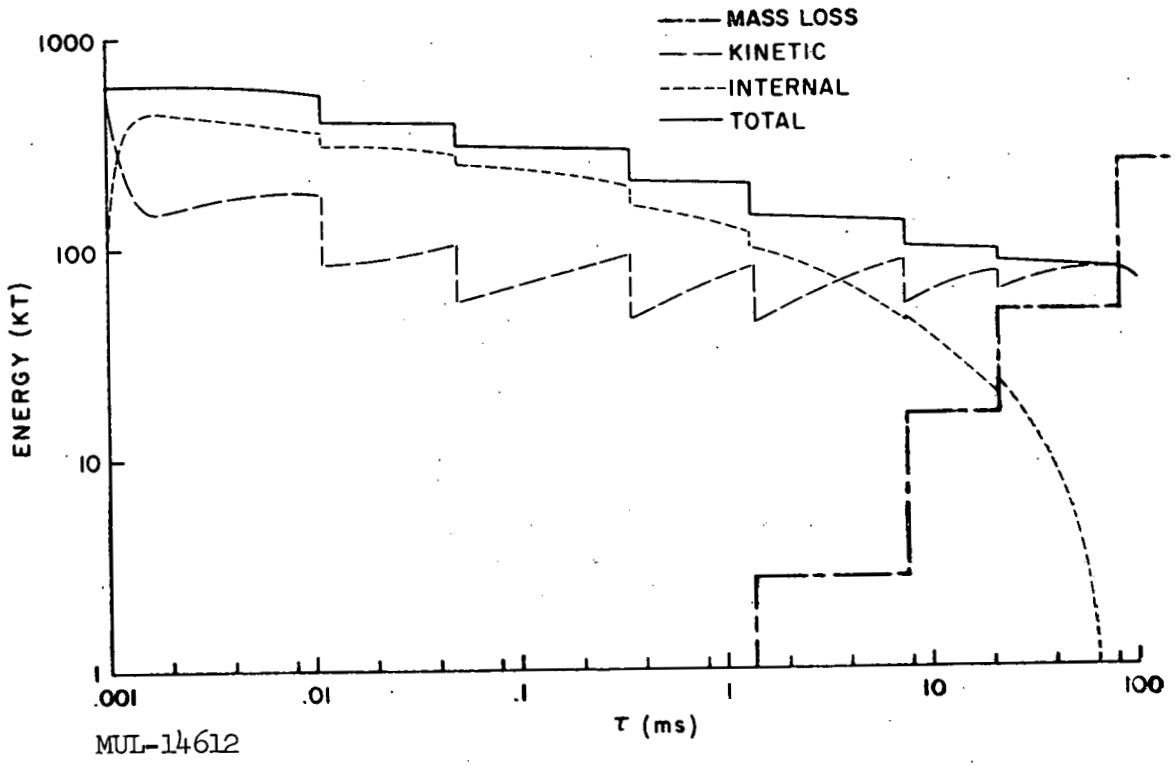

Fig. 23 — Energies and mass loss vs time

Paper M

ANALYSIS OF THE FORMATION OF METEOR CRATER, ARIZONA: A PRELIMINARY REPORT

R. L. Bjork

Aero-Astronautics Department

The RAND Corporation

ABSTRACT

A theoretical study is made of the cratering process accompanying the impact of a 12,000-ton iron projectile on a semi-infinite half-space of soft rock at a velocity of 30 km/sec. The constituents and velocity approximate those involved in the formation of Meteor Crater, Arizona. The assumption is made that the process is hydrodynamic in nature, since the pressures generated so far exceed the strengths of the materials. At these high pressures, the compressibilities of the materials must be taken into account with the result that shocks are generated. The motion is solved by numerical means, and graphs showing details of the motion are presented. The conclusion in this preliminary report is that the meteorite had a mass of between 30,000 and 194,000 tons, the range being due to the uncertainty in the impact velocity.

* * *

I. INTRODUCTION

The Arizona Meteor Crater, situated in the Canyon Diablo region of north-central Arizona, is a well-publicized geological feature which has captured the fancy of many a scientist. Its enormity calls up visions of the fantastic violence which must have accompanied its creation. Its present depth, about 570 feet from rim to bottom, is somewhat greater than the height of the Washington monument and its diameter of approximately 4000 feet could comfortably accommodate three long holes of golf laid end to end. As the meteor hurtled through the atmosphere, it released a thunderclap containing the energy of a score of Hiroshima-type atomic bombs, and upon reaching the earth blasted its tremendous crater in a time on the order of a second. An Indian, viewing this event about 50,000 years ago, is likely to have been so impressed as to never again question the word of his medicine man.

Greater details of the geometry and geology of the crater and its environs are available in a report by Shoemaker,[1] who also gives an extensive bibliography on the subject.

Remnants of the meteorite itself are scattered about the crater. By far the greatest mass identified is in the form of small iron particles scattered throughout the soil within a few miles of the crater. In a 1956 expedition sponsored by the Smithsonian Institution, Rinehart[2] made a careful sampling of these, concluding that about 12,000 tons of meteoritic iron is present in this form, the majority of particles being between 0.5 and 2 mm in dimension. In addition, Rinehart cites that between 20 and 30 tons of larger meteorites had been previously recovered from the immediate vicinity, these ranging in size from a few ounces up to about 2000 pounds.

In attempting to analyze the creation of the crater, one is immediately confronted with two major uncertainties, viz., the mass and impact velocity of the meteorite. The evidence is fairly conclusive that the meteorite was composed mainly of iron, and had a mass of at least 12,000 tons. It is also extremely likely that its impact velocity was between 11 and 72 km/sec. Of the thousands of velocity measurements made on meteors, all lie in this range, which corresponds to earth escape velocity on the one hand, and the maximum velocity any member of our solar system could have with respect to the earth on the other. Assuming that it had the average meteor velocity of 30 km/sec could thus lead to an error of at most a factor of 2.7. Previous studies on hypervelocity impact lead one to suppose that the mass deduced from such an assumption is in error by the same factor as the velocity.[3]

The possible velocity error is small compared with the range of previous estimates of the meteorite mass. This extends from the 10,000 to 15,000 tons estimated by Rinehart[4] to the 5,000,000 tons estimated by Öpik[5] and later by Rostoker.[6]

It is unfortunate that impact velocities of meteoric magnitude have not so far been achieved in the laboratory under circumstances which enable one to make quantitative measurements on the crater produced. However, some fairly recent results have been obtained which enable one to deduce that the

mass estimate of 5,000,000 tons is substantially too high. For an iron sphere of this mass would have a diameter of about 100 meters, and the implication would be that in striking earth at at least 11 km/sec it produced a crater only two sphere diameters in depth. However, experiments have shown that iron spheres at the much lower velocity of 6 km/sec produce craters of about 2 sphere diameters depth even in steel targets.[7]

II. MODEL

To simulate the creation of the Arizona Meteor Crater, we treat the case of a 12,000-ton iron projectile striking a semi-infinite target of tuff, a soft rock. The impact velocity is taken to be 30 km/sec directed at right angles to the ground's surface. The whole problem has axial symmetry if the projectile does. Accordingly, the geometry chosen for the projectile is a right circular cylinder having the same length as its diameter. For the mass chosen, both dimensions turn out to be 12 meters. The cylinder axis is in the direction of the initial motion.

Hypervelocity impact experiments have shown that the size and shape of the crater is not strongly dependent on the geometry of the projectile as long as it is not extreme, such as a long, pencil-shaped jet traveling along its axis. If all dimensions of the projectile are of the same order, it does not matter greatly whether it is spherical, cubical, cylindrical, or irregular. Therefore, the material and geometry of the projectile are felt to be well-chosen.

The target is not so well approximated. The actual target structure consists of strata, roughly parallel to the ground surface, whose chief members are a 270-foot layer of Kaibab limestone underlain by a 700- to 800-foot slab of Coconino sandstone.[1] Tuff, a porous volcanic rock, is less dense and somewhat softer than these materials, and is used only because its equation of state was available to the author, having been worked out by Brode in connection with another problem.[8]

The velocity provides another area of uncertainty, but, fortunately, fairly concise limits may be placed upon it. Of the thousands of meteor

velocities measured, all lie between 11 and 72 km/sec. The lower limit corresponds to the earth escape velocity. The upper limit is the greatest velocity any member of our solar system could have with respect to Earth. The average of measured meteor velocities is about 30 km/sec, and by choosing it, one is confident that the error is at most a factor of 2.7, and is probably much less.

The angle of incidence is also unknown. However, experiments have shown that the crater dimensions depend only on the normal component of velocity up to angles of incidence of about 55°,[9] so that the case we are treating is that of a meteorite having a normal velocity component of 30 km/sec.

In the regime of pressures generated by impact at meteoric velocities, materials behave in ways which are contrary to most of our intuitions. One is used to thinking of massive iron as a very strong substance, which under the most extreme forces might be slightly distorted. However, in the case at hand, the massive iron projectile is immediately squeezed into only half its original volume by the pressure generated on impact. The softer tuff is compressed to less than a fourth of its normal volume. This feat is accomplished by a pressure of 10.5 megabars (one megabar is about a million atmospheres).

In the light of this information, it is understandable why the strength of both the iron and the stone may be neglected in calculating the motion induced by the impact. The pressure exceeds the strength by such a vast amount that any pressure gradients will cause the material to literally flow like a fluid. Therefore the approximation is made that the compressible hydrodynamic equations govern the motion.

In this framework, the material properties are described by an equation of state which specifies the pressure as a function of density and internal energy. Only pressure-type forces are considered, since the material has insufficient strength to support any shear comparable to the pressure. In arriving at the equation of state valid over the requisite pressure range, two bodies of information are used. At pressures above about 10 megabars, the

quantum-mechanical Fermi-Thomas-Dirac theory is felt to be valid. Experimental data are available between about 80 and 300 kilobars for tuff, and between about 50 and 5,000 kilobars for iron. These data are obtained by using high explosives to generate shocks in the materials under consideration. The equations used in these calculations are

Tuff:

$$P = 0.425\,\eta e + 0.113\,\eta^{3/2} e + 5.30\,\eta e^{1/2} + \frac{0.707\,\eta e^2}{(10^5 + e)}$$

Iron:

$$P = \frac{a_1\mu + a_2\mu|(\mu)| + \epsilon(b_0 + b_1\mu + b_2\mu^2) + \epsilon^2(c_0 + c_1\mu)}{\epsilon + \epsilon_0} \; *$$

The units for the above equations are the megagram, millisecond, meter system, and the symbols are:

ρ = density $\qquad$ $\mu = \eta - 1$

P = pressure $\qquad$ e = specific internal energy

$\eta = \rho/\rho_0$ $\qquad$ $\epsilon = \rho_0 e$

ρ_0 = normal density (1.7 for tuff, 7.86 for iron).

The values of the constants are:

$a_1 = 7.780 \times 10^4$ $\qquad$ $b_2 = 463.4$

$a_2 = 31.18 \times 10^4$ $\qquad$ $c_0 = 0.3984$

$b_0 = 959.1$ $\qquad$ $c_1 = 0.5306$

$b_1 = 1568$ $\qquad$ $\epsilon_0 = 900$

---

*This equation of state was furnished by F. Harlow of the Los Alamos Scientific Laboratories. The constants were determined by Osborne and associates in group W-4.

The initial conditions for the problem are set at the instant the cylindrical projectile first contacts the ground. At this time, the pressure and internal energies are everywhere zero, and all materials have their normal density. The meteorite material is all given a velocity of 30 km/sec. These are the only inputs to the problem besides the constants specifying the equations of state.

Subject to these initial conditions, a numerical solution of the compressible hydrodynamic equations is generated on an IBM 7090 computer.[10] During the calculation a boundary condition is imposed, namely that the pressure at a solid-vacuum interface is zero. The results are discussed in the following section.

III. RESULTS

Figure 1 illustrates conditions 0.17 milliseconds after the initial contact between the meteorite and the ground. The original cylindrical meteorite had a radius of 6 meters and a length of 12 meters. The y-axis corresponds with the axis of symmetry of the problem, the velocity field being presented on the right and the field of pressure contours on the left. Each vector represents the velocity of the particle situated at the tail of the vector. For clarity, only one-fourth of the available velocity data are presented, every other row and column having been excluded. It is clear that near the axis of symmetry, the velocity vectors remain parallel to the axis, so that the flow is still one-dimensional in nature. For such a flow analytical solutions are available, and it is possible to compare the machine solution with them to see how well the program is doing.

The comparison of velocities is made in Fig. 2. The analytical solution predicts the presence of two shocks, i.e., surfaces across which discontinuities in pressure, density, internal energy, and velocity appear. The projectile material moves unimpeded at its original velocity of 30 km/sec until it reaches the upper shock, shown as the left one in the figure. At the time of 0.317 msec, the shock is at a depth of slightly more than 4 meters. The projectile material is slowed discontinuously to a velocity of 21.84 km/sec

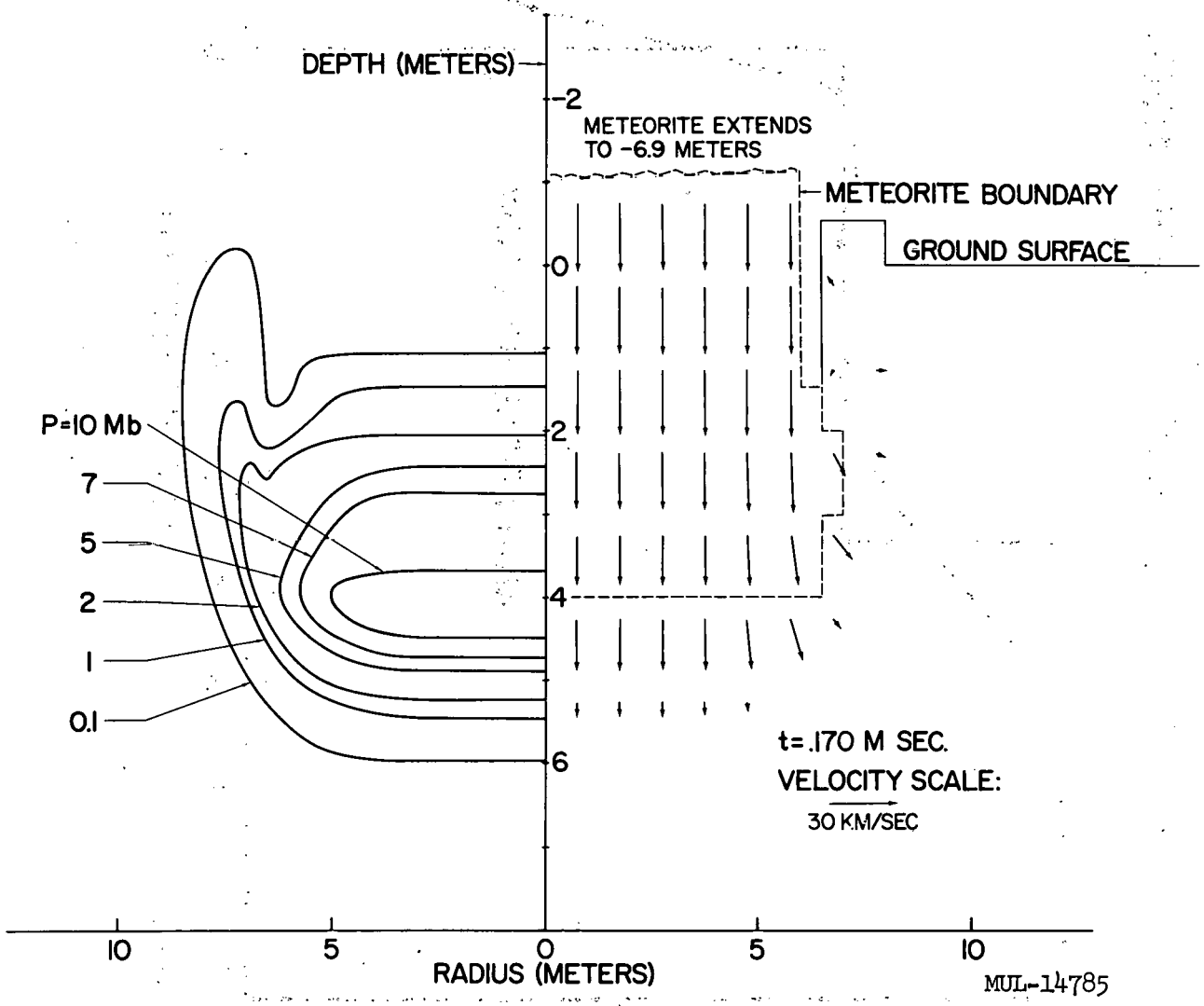

Fig. 1. Pressure and Velocity Field at 0.17 msec.

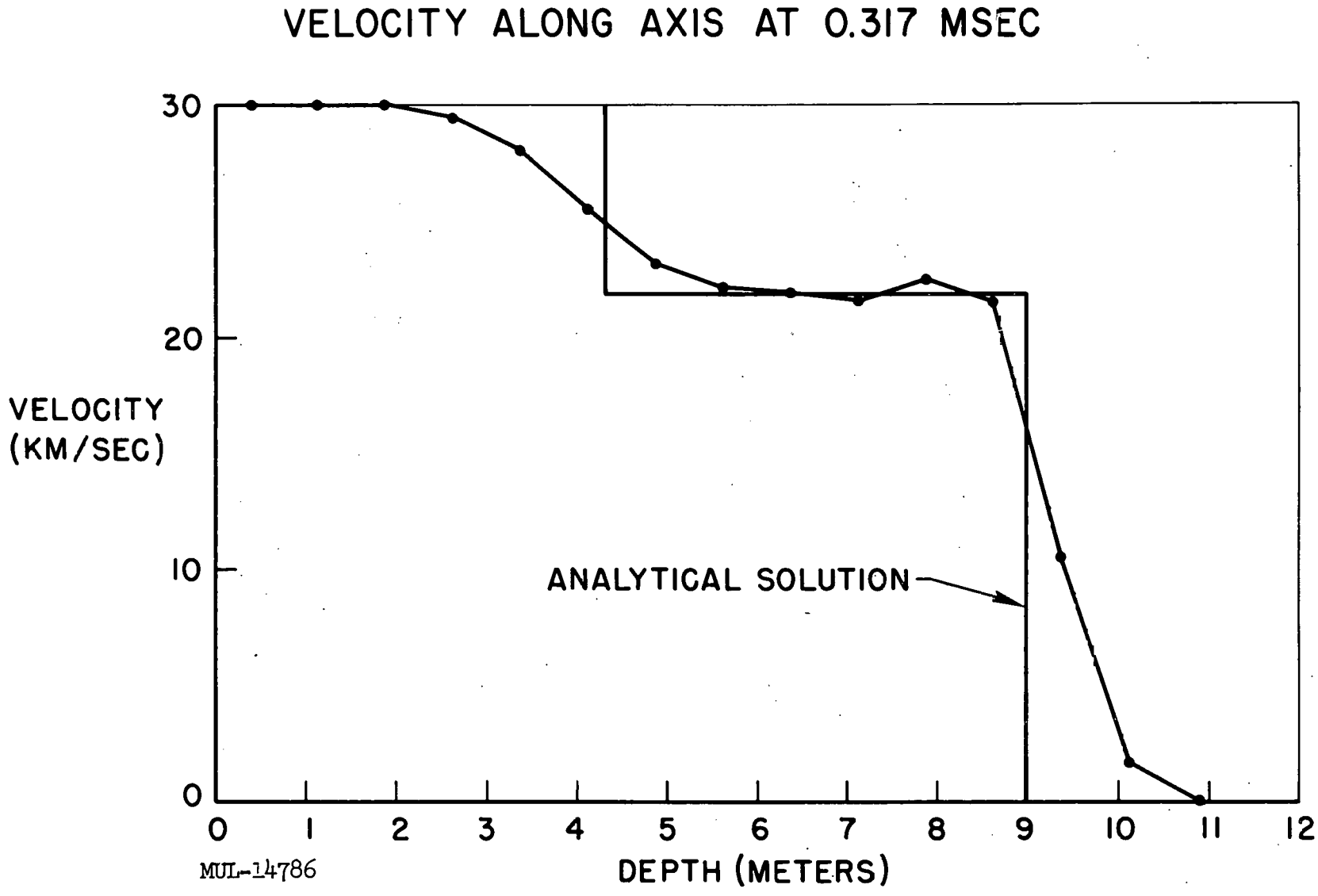

Fig. 2. Velocity Along Axis at 0.317 msec.

as it crosses the shock, being simultaneously compressed and brought to a high pressure and internal energy. Similarly, the target material remains at rest until the leading shock reaches it. At 0.317 msec, the leading shock is at a depth of almost exactly 9 meters. As the shock engulfs it, the target material is suddenly given a velocity of 21.84 km/sec, the same as the shocked projectile material. The continuity of material velocity across the interface between the two materials (which at this time is at about 7 meters) is always preserved in the one-dimensional case.

The numerical solution, shown by the broken line in Fig. 2, does not match the analytical solution exactly. The most salient feature is that the velocity increase does not take place discontinuously, but requires on the order of three grid spaces to occur. This feature is required in order for the numerical solution to be stable. However, it is seen that the velocity increments are nearly correct, and that the transition corresponds well with the position predicted for the shocks.

Figure 3 shows a comparison of the pressures. In the analytical solution there is no pressure outside of the shocked region, emphasizing that the projectile and target material remain in their initial velocity state until a shock is encountered. A uniform pressure of 10.5 Mb is predicted for the shocked material. Again, the numerical solution rises rapidly, but continuously, to simulate the shock, the transition occurring about where the shocks should be, and approximately the correct pressures being obtained behind the shocks. Oscillations are seen to occur in the numerical solution. If one follows the pressure history of an individual particle, he sees that its pressure oscillates in time about the correct value, the average pressure being such as to maintain the correct shock and particle velocities.

The comparison of specific internal energies is made in Fig. 4. Both the iron and the tuff are brought to the same pressure behind the shock, but the tuff undergoes a far greater volume change. One can see intuitively that the PdV work done on it must therefore be far greater than in the case of iron. In addition to this effect, there is a smaller mass of tuff per unit volume. Both things contribute to tuff's acquiring a greater specific internal energy than iron in the shock compression.

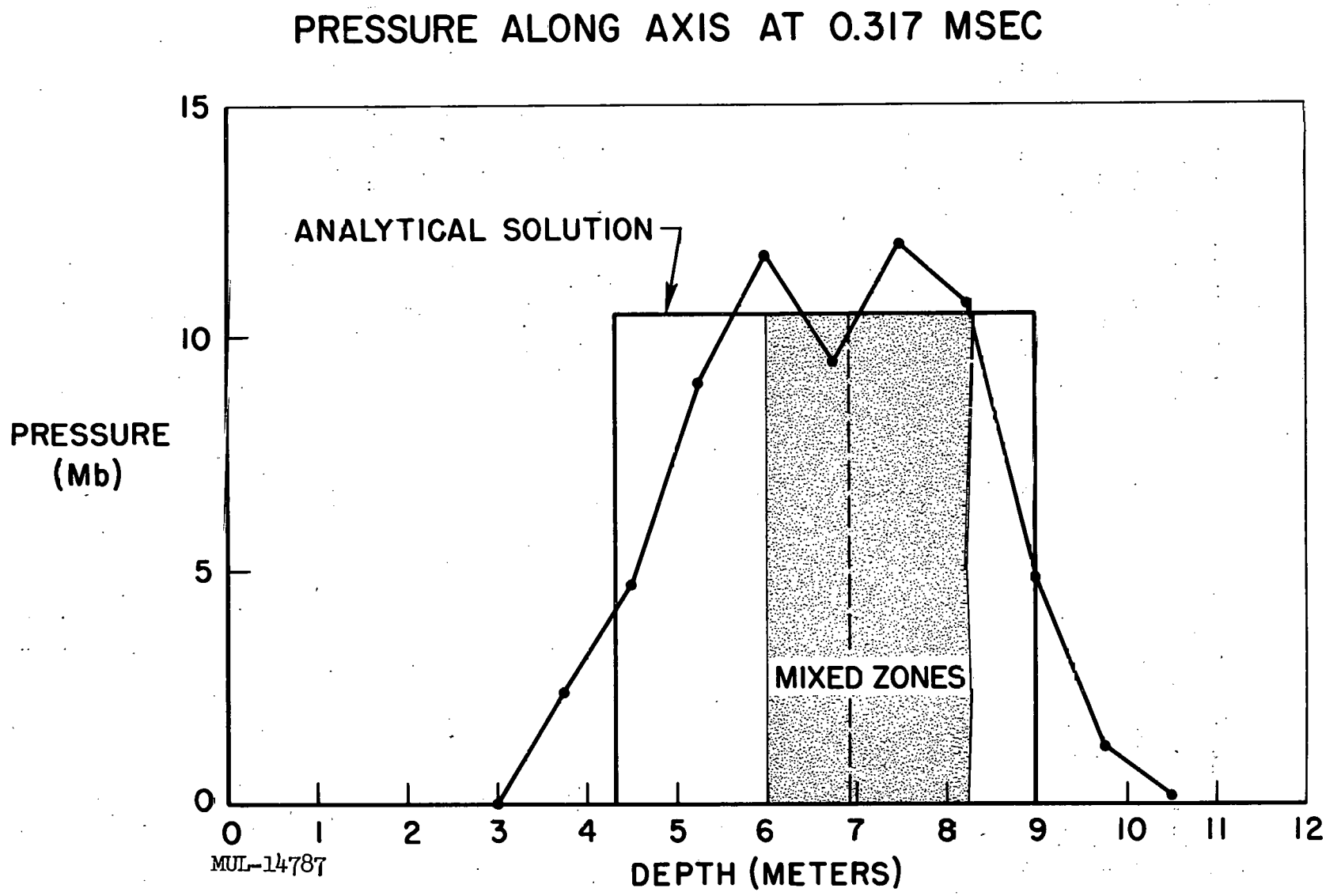

Fig. 3. Pressure Along Axis at 0.317 msec.

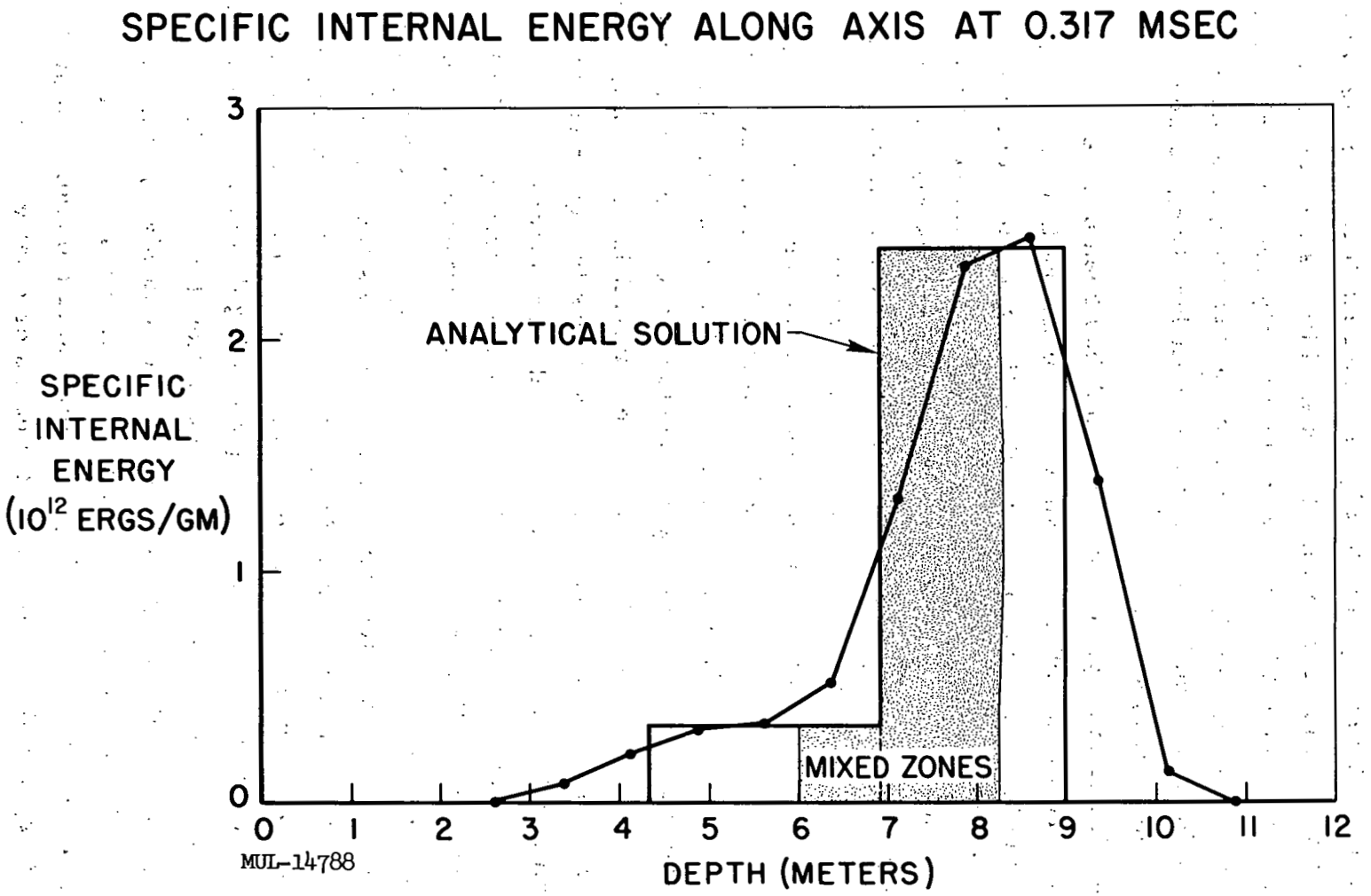

Fig. 4. Specific Internal Energy Along Axis at 0.317 msec.

The iron's density behind the shock is 1.99 normal, and the tuff's is 4.38 normal. Referring back to Fig. 1, one sees that the material interface is at about 4 meters depth. The dashed line is the boundary between iron and tuff. Since it is clear from the velocity field that only a slight amount of lateral spreading has occurred at this time, a 4-meter cylinder of tuff has been wadded into a one-meter cylinder, lying between about 4- and 5-meters depth at this time.

Outside of this cylindrical hole which has been punched in the tuff, the ground has recoiled radially, generating a pressure field described by the wings in the 0.1 and 1 Mb contours. Recalling that the acceleration is proportional to the pressure gradient, one can see the reason for the tuff starting to "rebound" into the zero pressure region corresponding to the space between the side of the meteorite and the tuff, and for the upward acceleration of the tuff into the air above the ground surface.

This feature of the motion continues, as shown in Fig. 5. Here the ground has rebounded into the side of the meteorite and more of it is being hurled into the air. More lateral spreading of the meteorite has occurred, with the result that the high-pressure contours are shrinking as rarefaction waves proceed into them. The meteorite material is proceeding unimpeded below the ground surface level until it encounters the upper shock which, at this time of 0.36 msec, is at a depth of about 5 meters.

By 3.44 msec, as shown in Fig. 6, extensive mixing of the iron and tuff has occurred. The front portions of the meteorite are continually peeling off and being driven laterally into the ground. Then as the ground rebounds toward the axis, they are carried back. As the rebounding material reaches the axis, it builds up a high pressure and is deflected upward or downward. What might be termed a stagnation point exists at a depth of about 12 meters, material above this point being deflected upward, and below that point being deflected downward to follow the meteorite. In the machine program, three types of regions are recognized, viz., pure iron, pure tuff, and a mixture. At this time only two types exist, pure tuff and mixture, the dashed line denoting the interface of the two. The meteorite material is spread throughout many times its original volume.

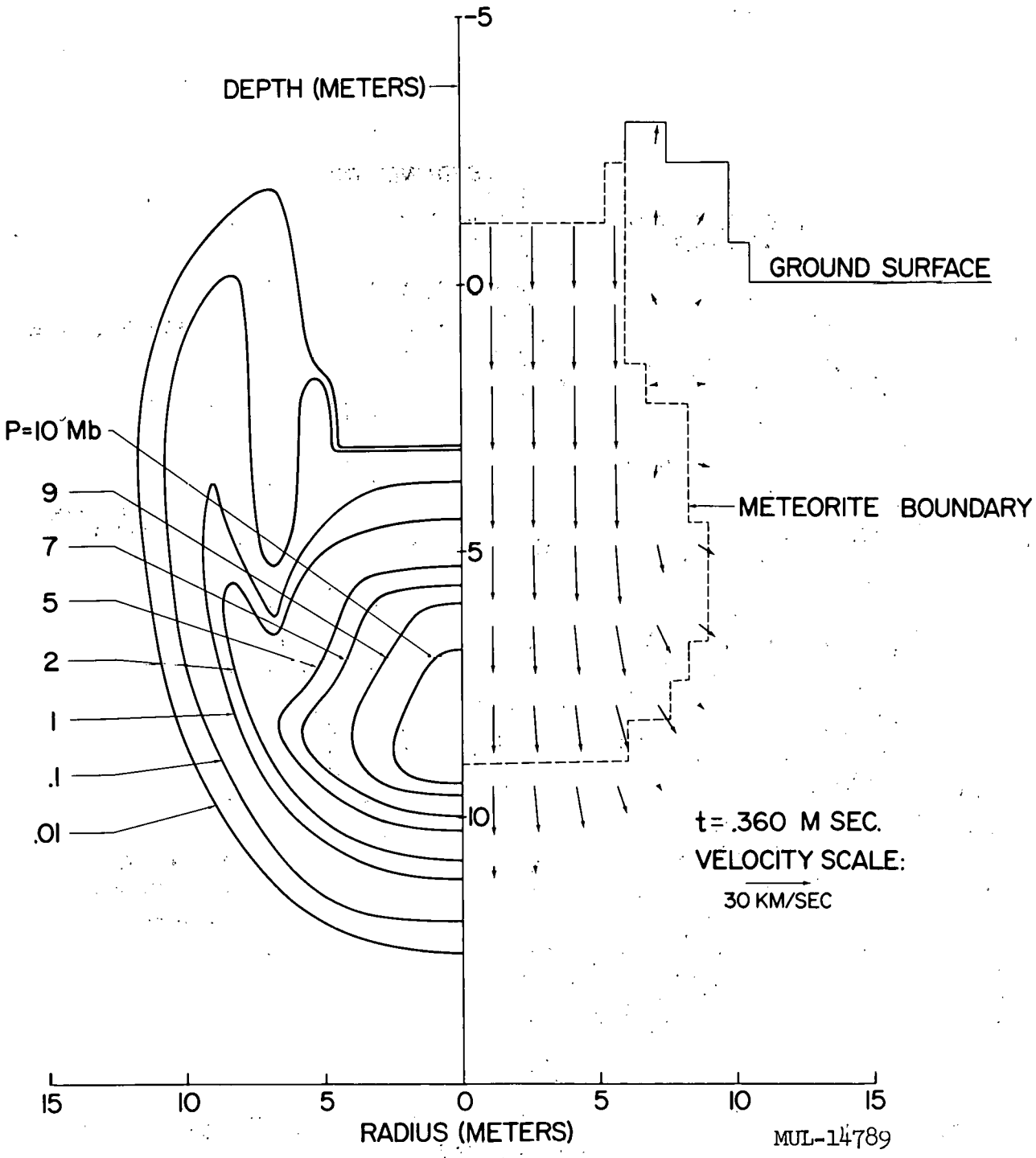

Fig. 5. Pressure and Velocity Field at 0.360 msec.

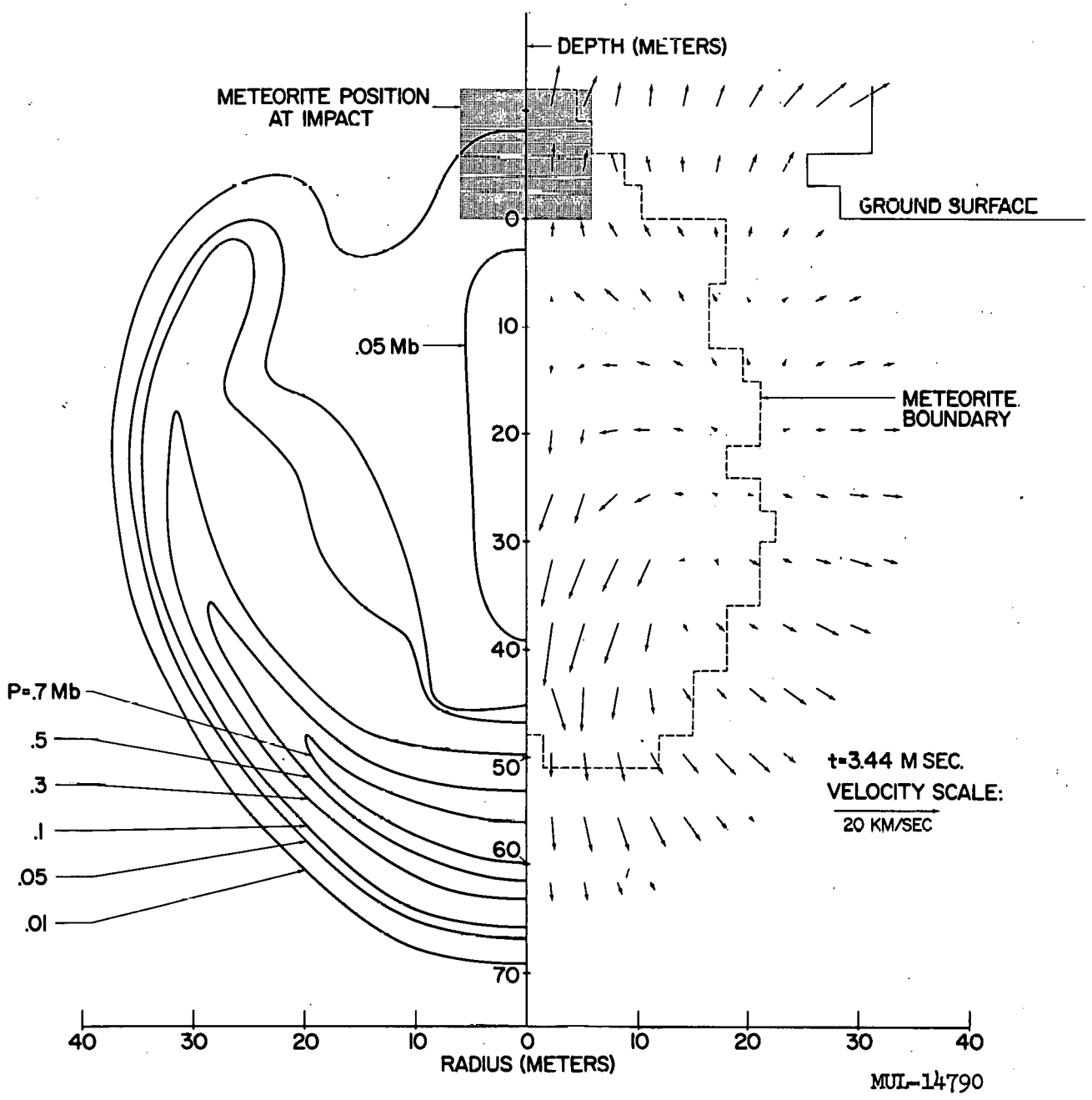

Fig. 6. Pressure and Velocity Field at 3.44 msec.

In Figs. 7 and 8 the mixing motion is seen to continue, the stagnation point moving lower and lower, so that an increasing amount of material is hurled upward. Another important feature of the motion during this time period is the shock which is being driven into the tuff and the flow induced behind it which occupies an ever-increasing volume.

In Figs. 9 and 10, the mixing has essentially stopped, and the flow in the tuff has been generated which will lead to the crater. It is estimated in this preliminary report that the final crater will be about 150 meters deep and have a radius of about 500 meters. In Fig. 10 it is seen that intense shocks penetrate substantially deeper than the crater bottom, and these are believed to account for the brecciated region beneath the crater cited by Shoemaker.

IV. CONCLUSIONS

The solution indicates that the meteorite will be thoroughly pulverized and mixed with the ground material, so that no major portions of it are expected to be found intact. It is planned to reduce the final data to decide how much of the meteorite is flung into the air, and how much is distributed beneath the surface of the crater, but this information is not available for this preliminary report.

The meteorite's energy is delivered into the ground across the surface of a deep, relatively narrow hole, acting more like a line source than a point source. The top portions of the line are loaded first and then the force is released. The ground then rebounds to the axis, and the converging flow generates additional shocks which then proceed radially outward. This complicated flow is very different from that which is generated by an explosive detonated at a point. Consequently, descriptions of the crater formation modeled on explosive experiments are liable to be in considerable error.

A preliminary estimate of the theoretical crater's size as given by these calculations is a depth of 150 meters and a radius of 500 meters. These dimensions are each about 20 percent less than those of the actual crater. Since the theoretical results scale with the meteorite dimensions,

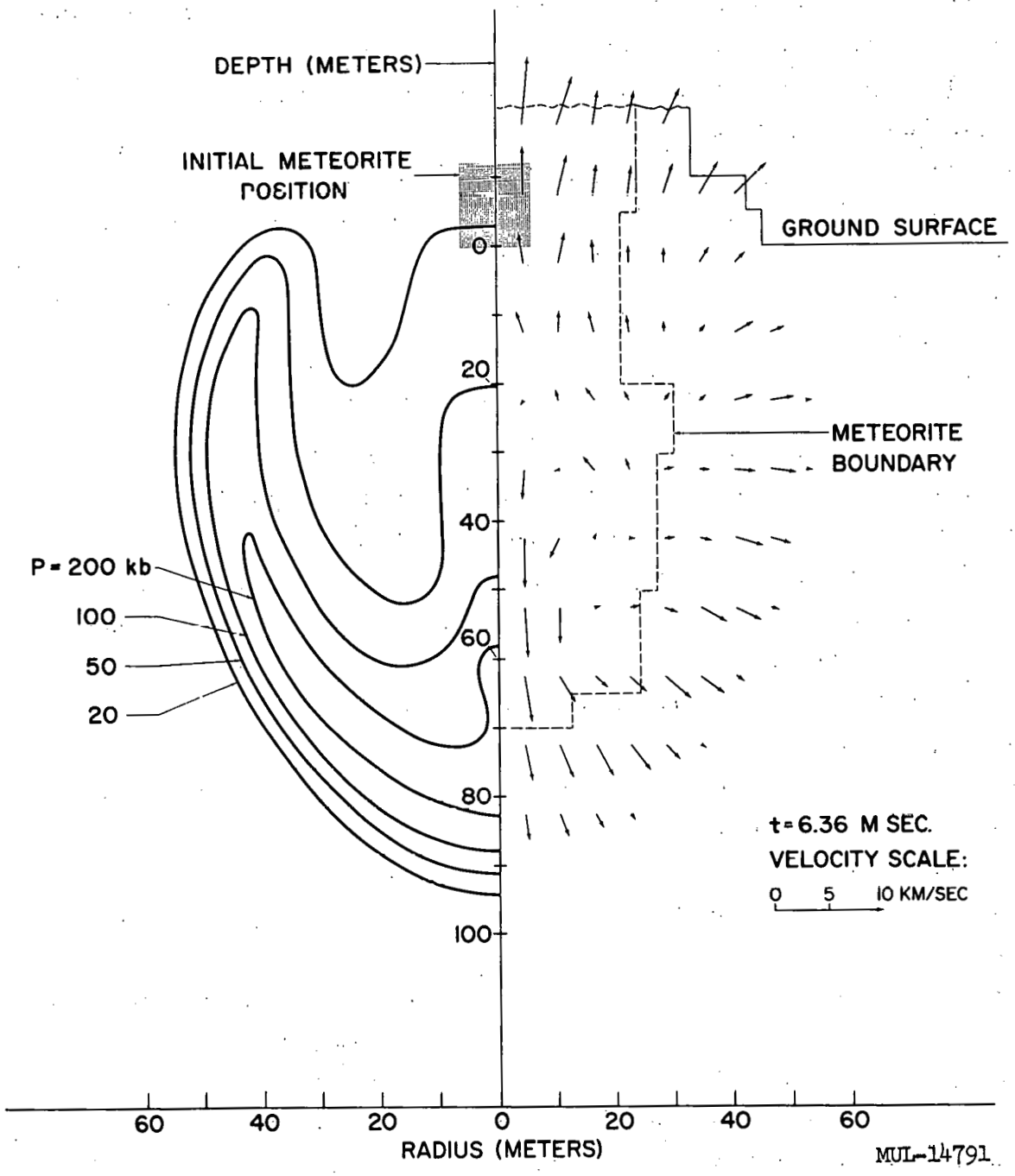

Fig. 7. Pressure and Velocity Field at 6.36 msec.

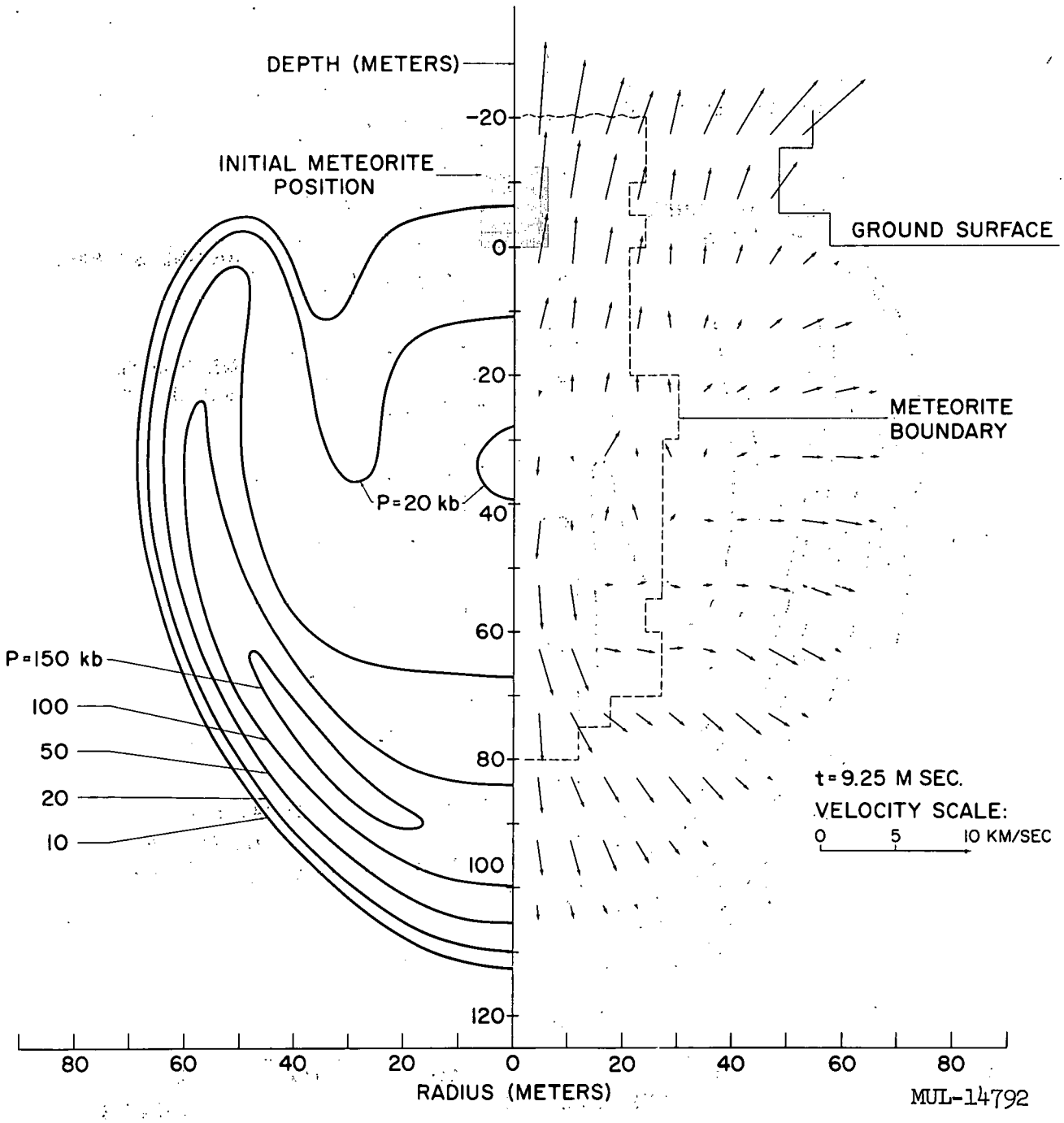

Fig. 8. Pressure and Velocity Field at 9.25 msec.

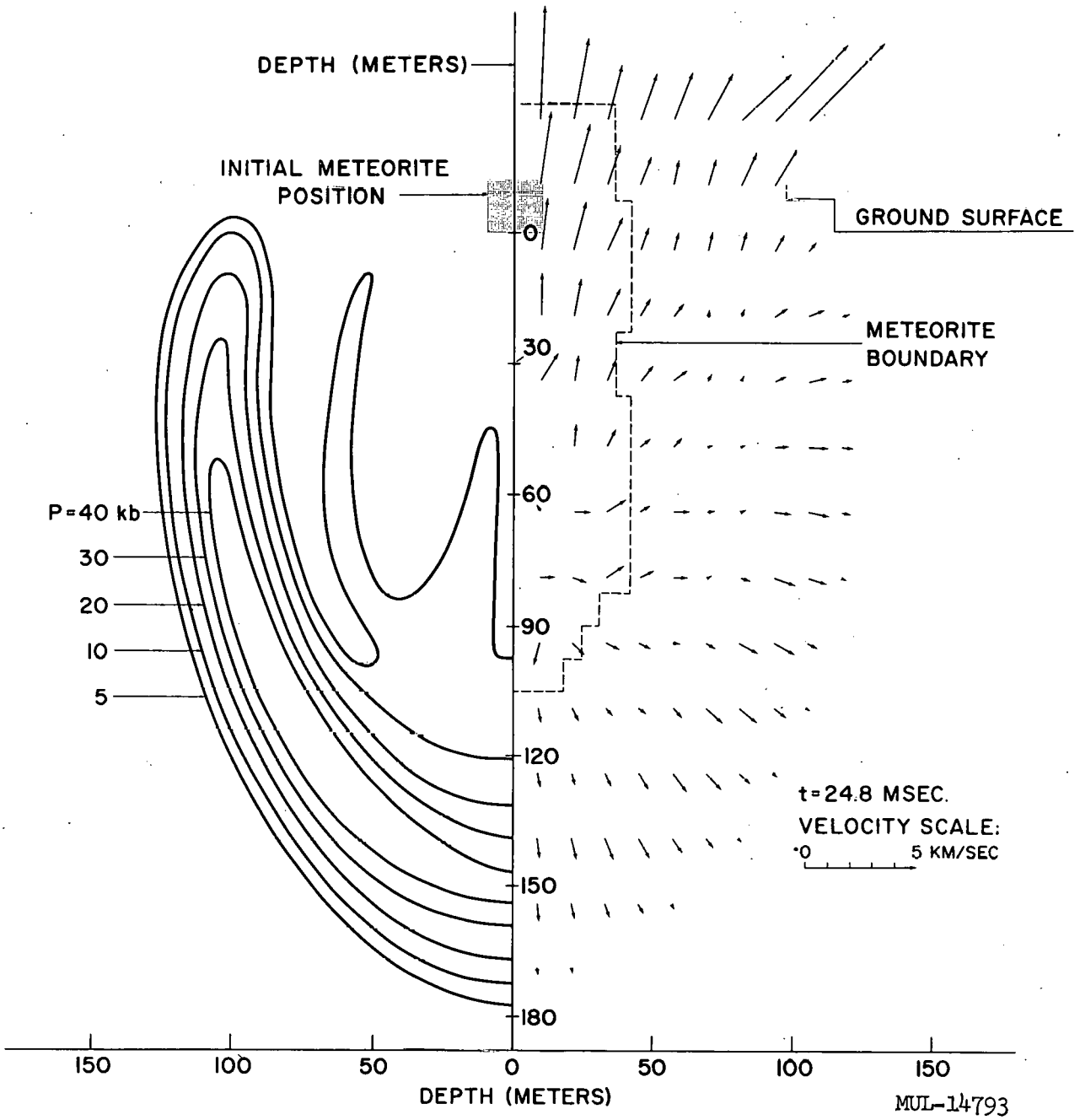

Fig. 9. Pressure and Velocity Field at 24.8 msec.

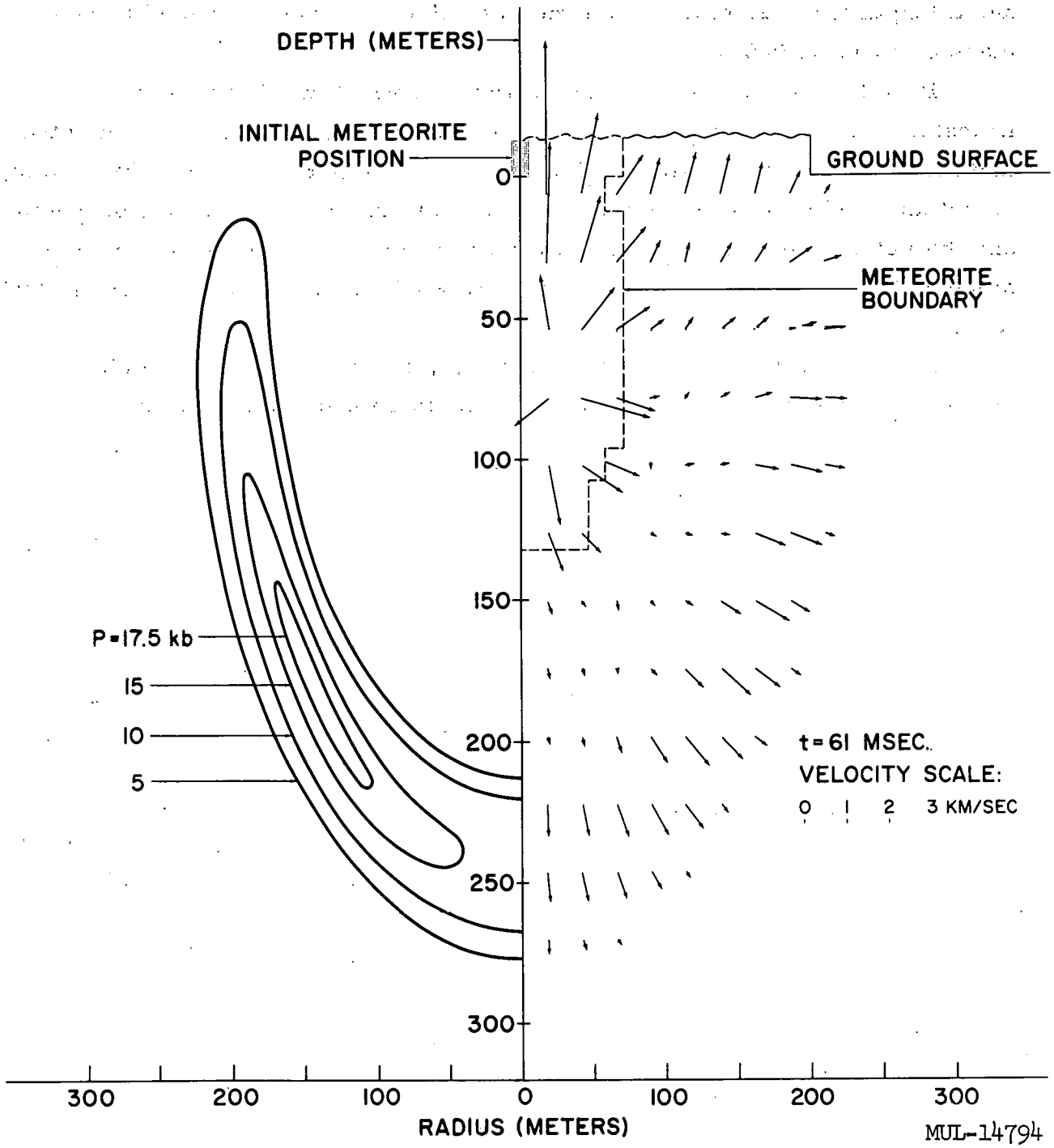

Fig. 10. Pressure and Velocity Field at 61 msec.

the two may be brought into correspondence by assuming that the meteorite had a length and diameter of 14.4 meters. Such a projectile would have a mass of about 21,000 tons.

It is difficult to estimate the crater size which would be calculated if limestone and sandstone were used instead of tuff. However, a rough estimate is that the crater calculated here is about 50 percent larger than would be obtained using these materials. This would indicate that a body of length and diameter 21.6 meters would be required to produce the crater in limestone and sandstone, and such a meteorite would have a mass of about 71,000 tons.

If the impact velocity were 11 km/sec, the required mass would be 194,000 tons and if it were 72 km/sec it would be about 30,000 tons.

BIBLIOGRAPHY

1. Shoemaker, E. M., "Penetration Mechanics of High Velocity Meteorites, Illustrated by Meteor Crater, Arizona," Report of the International Geological Congress, XXI Session, Norden, 1960, Copenhagen, 1960.
2. Rinehart, J. S., Smithsonian Contributions to Astrophysics, Volume 2, (1958), page 145-160.
3. Bjork, R. L., "Effects of a Meteoroid Impact on Steel and Aluminum in Space," The RAND Corporation, Paper P-1662, December 16, 1958.
4. Rinehart, J. S., Popular Astronomy, Volume 58, (1950), page 458.
5. Öpik, E., Publ. de L'Observatoire Astronomique de L'Universite de Tartu, Volume 28, (1936) 27 pages.
6. Rostoker, N., Meteoritics, Volume 1, (1953), page 11.
7. Partridge, W. S., Utah Research and Development Corporation, Salt Lake City, Utah, personal communication.
8. Brode, H. L., and R. L. Bjork, "Cratering from a Megaton Surface Burst," The RAND Corporation Research Memorandum, RM-2600, June 30, 1960.
9. Summers, J. L., and A. C. Charters, Proceedings of the Third Symposium on Hypervelocity Impact, edited by F. Genevese, Armour Research Foundation of Illinois Institute of Technology, Chicago, Illinois (1959), page 101.
10. Bjork, R. L., and N. B. Brooks, "A Numerical Technique for the Solution of Multi-dimensional Hydrodynamic Problems," The RAND Corporation, Research Memorandum RM-2628, August 10, 1960.

Paper N

HYPERVELOCITY IMPACT OF STEEL INTO COCONINO SANDSTONE*

By H. J. Moore, D. E. Gault†, R. V. Lugn, and E. M. Shoemaker

U. S. Geological Survey, Menlo Park, California

ABSTRACT

Impact of a 0.4019-g steel sphere at 4.27 km/sec into Coconino Sandstone from Meteor Crater, Arizona, produced a crater 11 to 12 cm across and 2.45 cm deep. The ejecta consisted of sandstone fragments, disaggregated sand, splinters of sand grains, strongly shocked aggregates of crushed sandstone grains, and chips, splinters, and minute spheres of steel. Part of the shocked steel was melted and some of the melted and unmelted steel occurred as impregnations in the strongly shocked sandstone. No conclusive evidence was found that new phases were produced from the sandstone by the shock. The fusion of the steel cannot be due to compressive heating alone, but can be accounted for partly by conduction of heat from the shocked sandstone and by production of heat by viscous drag and friction along the sandstone-projectile interface and along shear planes in the projectile.

* * *

INTRODUCTION

The occurrence of phase changes has occupied a prominent place in the discussion of meteorite impact for the past 50 years. Beginning with the work of Merrill (1908), the concept was developed (Ives, 1919; Gifford, 1924 and 1930; Moulton, 1931; Wylie, 1933 and 1934; Spencer, 1935; Baldwin, 1949;

---

* Work performed on behalf of the National Aeronautics and Space Administration.

† Ames Research Center, National Aeronautics and Space Administration, Moffett Field, California.

Gilvarry and Hill, 1956a and 1956b; Hopkins and Kolsky, 1960) that a meteorite would vaporize upon sufficiently high-speed impact into rock, and that the explosive expansion of the vapor produces the resultant crater. So frequently has this concept been stated, that meteorite craters are now commonly referred to as explosion craters.

The concept of explosion originated in a simple calculation in which all the kinetic energy of the meteorite was assumed to be converted into internal energy in the meteorite; for common geocentric velocities of meteorites it was found that the specific internal energy would exceed the enthalpy required for vaporization. It may readily be shown that such a calculation, which neglects the partition of energy in the shocks produced by impact, is grossly in error (Shoemaker, 1960). The idea of explosion, however, fortified by statements concerning the vaporization of the meteorite at Meteor Crater, Arizona (Nininger, 1956), is peculiarly persistent.

After the discovery of coesite, a high-pressure polymorph of silica, in sintered Coconino Sandstone from Meteor Crater (Chao, Shoemaker, and Madsen, 1960), an experiment was designed by members of Ames Research Center of the NASA and the U. S. Geological Survey to examine the production of new phases under known conditions of hypervelocity impact. A block of Coconino Sandstone from Meteor Crater, Arizona, was selected for the target and a steel sphere was fired into the target at a velocity greater than 4 kilometers per second. Most of the ejected debris was recovered, and the debris and the crater produced in the target were examined minutely. This paper presents the results of this study; to our knowledge this is the first detailed description of the effects of experimental high-speed impact in rock or a granular medium.

The steel sphere was launched under the supervision of D. E. Gault, at the Hypervelocity Ballistic Range of Ames Research Center; a map of the crater was prepared at greater than natural scale by use of photogrammetric techniques by R. V. Lugn; and the ejecta were studied by H. J. Moore, E. M. Shoemaker, and E. C. T. Chao. Gault and Shoemaker are responsible for the theoretical considerations of the fusion of the steel.

THE SANDSTONE TARGET

A block of Coconino Sandstone 11 cm deep, 16 cm wide, and 18 cm long, collected from an adit in the south wall of Meteor Crater, Arizona, was used for the target. The target block is a laminated, yellowish gray, weakly cemented, fine-grained sandstone composed of about 97% quartz, 3% feldspar, and a fraction of a percent of clay and heavy minerals. The sandstone is free of the effects of surface weathering but its physical properties have probably been affected to a minor degree by the event that produced Meteor Crater.

Average and modal grain size of the sandstone is between 0.117 and 0.149 mm in diameter; the grains range from less than 0.062 to 0.71 mm across (Fig. 1). Subparallel laminae 5.0 to 17.5 mm thick are separated by thin laminae 0.5 mm thick containing more than average amounts of silt and clay-sized grains. The bulk density, measured from rectangular-sawed blocks, is 2.26 g/cm^3, the grain density is 2.67 g/cm^3, and the calculated porosity is 15.2 percent. The sandstone is only weakly to moderately well cemented with silica, mainly in the form of quartz overgrowths on the sand grains. Some laminae can be disaggregated with finger pressure. Unconfined crushing strengths measured perpendicular to the bedding of three 2.2-cm by 2.2-cm by 5-cm blocks under load applied in the long direction were 320 and 371 kg/cm^2 for water-saturated specimens.

CONDITIONS OF THE SHOT

The projectile, a 4.76-mm-diameter sphere of high carbon steel weighing 0.4019 grams, was accelerated to a velocity slightly greater than 4.3 km/sec with a light gas gun (Charters, Denardo, and Rossow, 1957) employing hydrogen as the propellant medium. The projectile was launched and impacted the target in an atmosphere of air at a nominal pressure of 25 mm of mercury. During the launch, the sphere was mounted in a supporting four-piece nylon sabot which guided it down the bore of the gun; after launch, aerodynamic drag acted to separate the sabot from the projectile and deflect the pieces away from the target area. Time measurements and spark photographs of the sphere in flight were obtained at four stations along the trajectory; the resultant time-distance history permitted evaluation of the impact velocity within

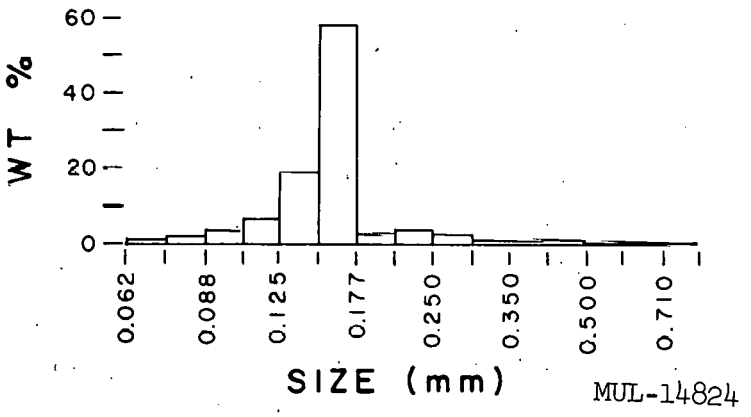

Fig. 1. Grain-size distribution of sandstone of the Coconino Sandstone.

± 0.05 km/sec. Impact velocity on the sandstone target was 4.27 ± 0.05 km/sec.

To prevent reflected-wave induced fracturing and spalling along the sides and back of the sandstone block, the block was cast in concrete to form a cylindrical target 30-cm diameter by 15-cm long. The target face was finished flat to provide a plane reference surface and the projectile struck this surface at perpendicular incidence.

Material ejected from the crater was collected in a rectangular tank approximately 25-cm square and 50-cm long constructed from sheet aluminum. One end of the tank was open and fitted flush against the target face. The opposite end was closed except for a 5-cm diameter entry hole for the projectile. High-speed fragments ejected from the crater at angles of about 45° to 55° formed a 5-cm wide belt of conspicuous small pits along the walls of the tank. About 5 percent of the ejecta from the crater was lost through the entry hole for the projectile.

SHAPE AND STRUCTURE OF THE CRATER

A crater with two distinct topographic parts was produced by the impact (Figs. 2 and 3). The crater resembles a sherbet glass with a thick vertical stem and a shallow sloped cup. The lip of the cup is 11 to 12 cm in diameter, and the stem varies from 4 to 4.5 cm across; the total depth is 2.45 cm, the surface area of the cup is 12.6 cm^2, the total crater volume is 72.7 cm^3, and the calculated total mass ejected to form the crater is 164.3 g. The volume increased slightly after the crater was first formed, owing to sloughing of loose sand in the lower part of the crater.

The cup part of the crater owes its form primarily to a set of fracture surfaces which dip toward the center of the crater. These fracture surfaces cut across the sedimentary laminae of the sandstone, which are nearly parallel to the reference surface of the block. Small-scale relief on the cup surface has a shagreen pattern with isolated sharp bumps and irregularities. Such features show that the fractures were produced as tensile breaks, rather than by shear. No slickensides or other evidence of shearing is present on these surfaces. Subordinate features in the cup part of the crater are controlled by fractures nearly perpendicular to the surface of the block with roughly radial arrangement with respect to the axis of the crater. Some radial fractures were found to intersect the inward-dipping fractures that form the cup slope. Some fractures were also formed, beneath the cup part of the crater, that are mainly parallel to the lamination of the sandstone. Locally these fractures cut across the sandstone laminae near the crater and near the margins of the sandstone block.

All fractures preserved in the crater appear to have formed mainly in response to tensile stresses. The inward-dipping fractures that bound the cup and the fractures parallel with the lamination were probably produced by a rarefaction wave reflected from the upper free surface of the block. The radial fractures were probably propagated during divergent displacement of material in the shock wave.

At the base of the crater is a lens of partially crushed sandstone (Fig. 3). The partially crushed sandstone is composed mainly of undamaged detrital

Fig. 2. Slightly oblique photograph of hypervelocity impact crater formed in sandstone by a projectile like that on the black square.

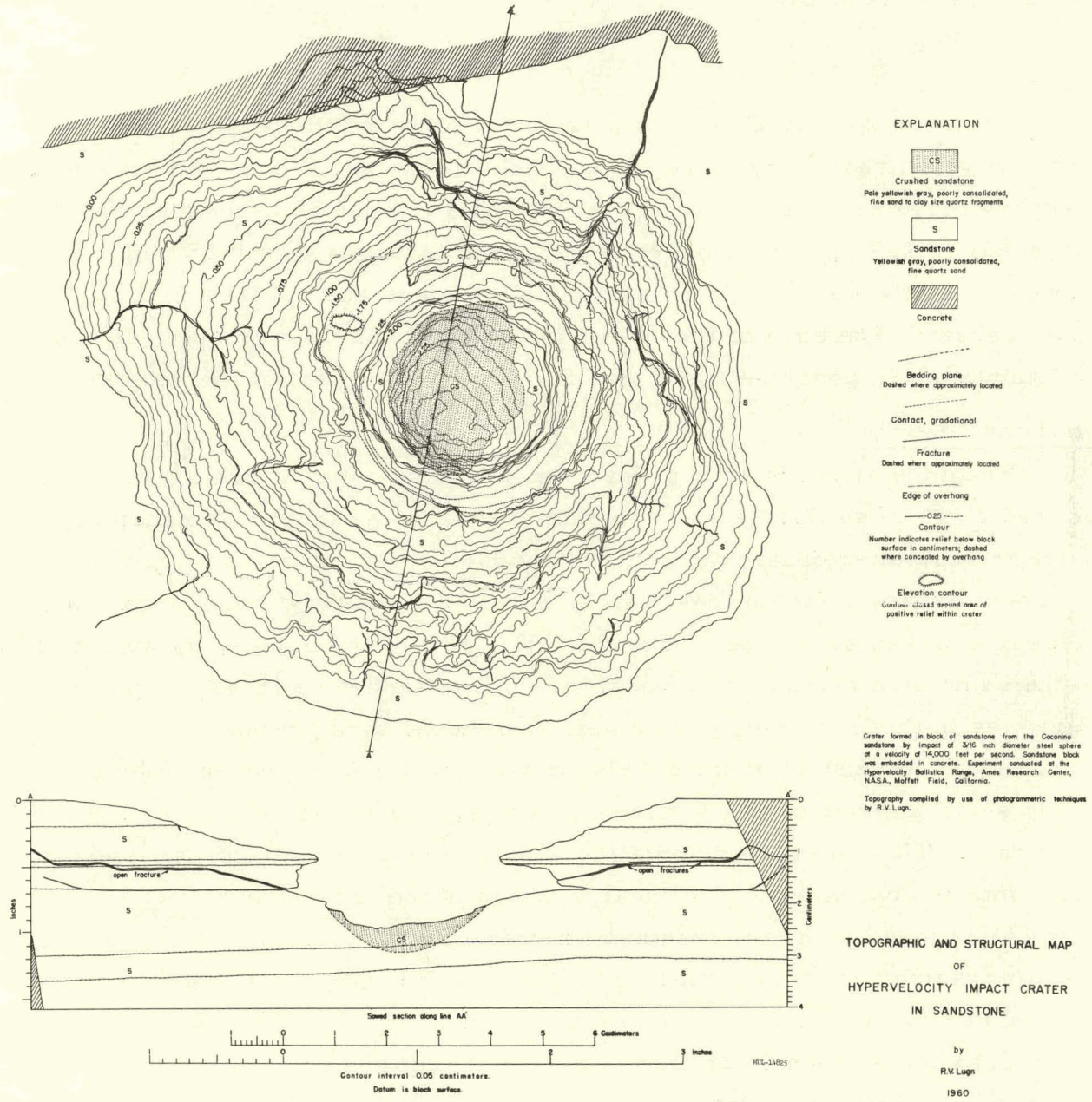

Fig. 3. Topographic and geologic map of hypervelocity impact crater in sandstone.

sand grains among which are scattered packets of splinters of the original sand grains. The partially crushed material was easily identified by its pale yellowish gray color which contrasts with the darker yellowish gray color of the uncrushed sandstone.

THE EJECTA

Fragments derived from both the sandstone and the projectile were recovered which show varying degrees of shock damage. About 94 percent of the ejected sandstone debris was recovered (154.9 g), and 52 percent of the steel projectile (0.209 g) was recovered as fragments larger than 0.25 mm. Part of the projectile was dispersed as minute splinters and spheres in the sandstone debris. The edge of the crater intersected concrete on one side and fragments of the concrete make up a fraction of a percent of the debris.

Sandstone debris

Fragmental products derived from the sandstone include relatively unaltered chips of sandstone up to 66 mm across in the longest dimension, smaller equidimensional fragments of sandstone, individual sand grains, splinters of grains (some less than 0.04 mm in diameter), and compact aggregates of crushed sandstone. Approximately half of the debris, by weight, falls in the same size class as the modal size of the sandstone (Figs. 4 and 5). Particles in this size range are chiefly individual sand grains.

About 36 percent of the debris, most of which is represented by a relatively small number of large sandstone chips, lies in the size range of 0.177 mm to 64 mm. The log of the cumulative weight percent of fragments larger than 0.177 mm is approximately a linear function of the log of the particle size (Fig. 6) as found by us for fragment distribution in other impact experiments and for fragmentation experiments by Grimshaw (1959). A line fitted by the method of least squares has a slope of +0.70.

Grains less than 0.125 mm across make up 11 percent of the total debris. Comparison of the size distribution of all debris less than 0.84 mm in diameter with the original grain size distribution of the sandstone (Fig. 5) shows that

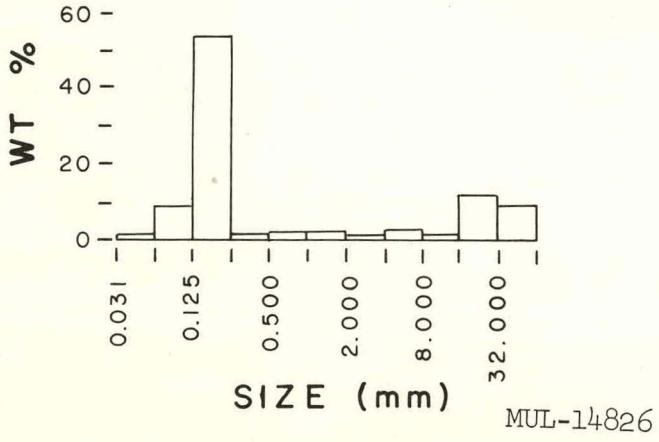

Fig. 4. Size distribution of fragmented sandstone of the Coconino Sandstone.

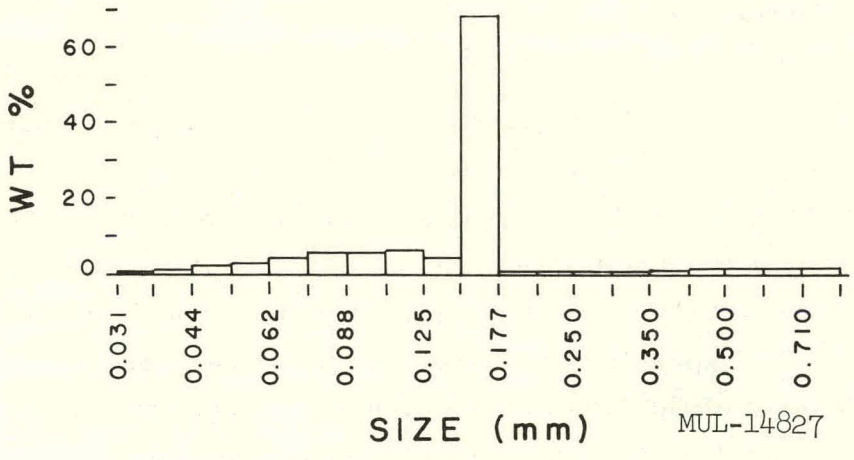

Fig. 5. Size distribution of fragmented sandstone of the Coconino Sandstone (below 0.840 mm).

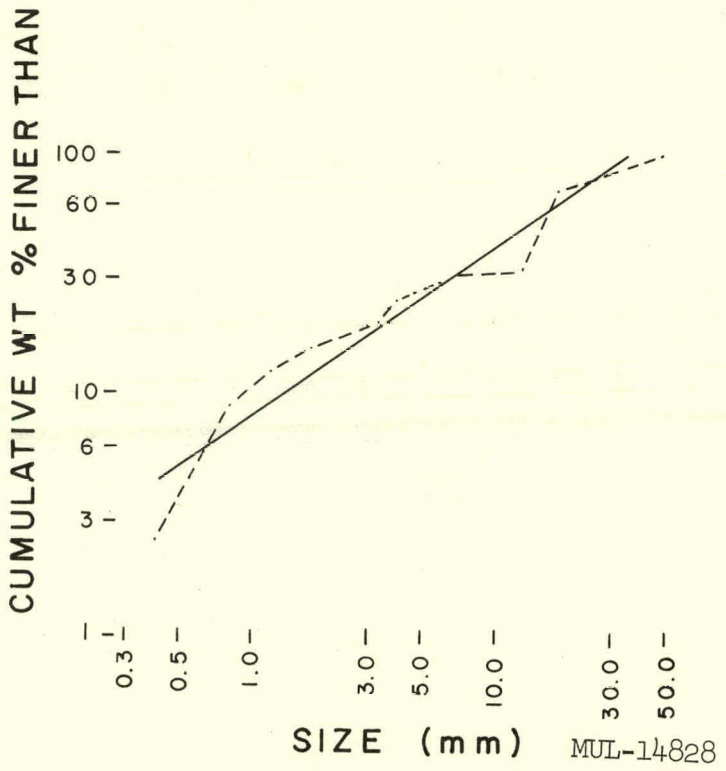

Fig. 6. Cumulative size distribution of fragmented sandstone of the Coconino Sandstone (above 0.177 mm).

more than half of the material less than 0.125 mm in diameter consists of splinters of pieces of the original grains.

The largest fragments of sandstone are pie-shaped or platy with long dimensions typically 5 to 10 times the thickness of the plates; their shape has been controlled mainly by intersecting radial and inward-dipping fractures along which they separated from the crater and each other.

About 20 percent of the fragments in the size range from 0.15 mm to 2 mm and about 13 percent of the total ejecta consist of compact aggregates of crushed sandstone grains. These aggregates resemble pieces of crushed, sheared Coconino Sandstone from Meteor Crater described by Merrill (1908, p. 473-475), Barringer (1910, p. 6-8), and Chao, Shoemaker, and Madsen

(1960). Most of the original quartz grains in the aggregates are broken down into angular slivers, plates, and equidimensional pieces which have remained weakly bonded together. The largest fragments or aggregates of crushed material, up to 5 mm across in long dimension and 1.5 mm thick, exhibit a crudely developed cleavage and are partly bounded by shear surfaces with divergent striations or slickensides. About 5 percent of the crushed aggregates are locally impregnated on one side with steel, part of which is in the form of minute spheres ranging in diameter from a few microns to about 15 or 20 microns.

Most of the crushed sandstone aggregates represent the most strongly shocked parts of the target and are clearly derived from a region close to the path of penetration of the projectile. The total mass of crushed aggregates recovered would form a cylinder about 2 cm deep and 1.2 cm in radius if restored to an original bulk density of 2.26. The lens of partially crushed sandstone preserved in the floor of the crater is apparently a remnant of an envelope of partially crushed sandstone that surrounded the more strongly shocked region. Crushed aggregates impregnated on one side with steel have a total weight on the order of 1 gram and would form a cylinder about 1 cm deep and 0.4 cm in radius. The mean thickness of these fragments is of the order of 0.2 mm, and the area of the steel-sandstone interface developed during cratering, therefore, is of the order of 25 square centimeters, which would correspond to a hemisphere about 2 cm in radius.

Close petrographic examination and x-ray diffraction of the crushed sandstone aggregates failed to yield any conclusive evidence of the presence either of glass or the high-pressure silica polymorph, coesite, such as has been found in the natural crushed sandstone from Meteor Crater. Rare grains with optical indices appropriate to silica glass and to coesite were observed in oil immersion under the microscope, but were so small and few in number as to preclude positive identification. An attempt was made by E. C. T. Chao to extract coesite from 0.257 grams of the crushed aggregates with a 0.5-normal HF leach, but without success. Microscopic study of the fine fraction

of the ejecta also failed to reveal the presence of any new silica phases produced by the impact.

Projectile debris

Steel derived from the projectile was dispersed in the debris as chips up to 2.8 mm across, as minute splinters and ragged fragments, and as spheres ranging in diameter from a few microns to about 200 microns. Slightly more than half of the original mass of the projectile was recovered from the coarse fractions of the debris by extraction with a hand magnet. The bulk of the remainder was present partly as free steel particles in the fine fractions, and partly as impregnations in crushed sandstone aggregates. A quantitative separation was not attempted because of intimate mixing of crushed sand and steel particles in the aggregates. All gradations may be found between crushed sandstone with sparse steel particles and aggregates of steel particles with traces of quartz. Individual spheres of steel are also common in the fine fraction (Fig. 7).

The coarser chips of steel are angular fragments bounded, in general, by a set of curved surfaces. Three types of texture are present on these surfaces: (1) hackly texture formed, as shown by scattered inclusions of crushed quartz, at the interface between the steel and the sandstone; (2) fine parallel grooves and striae (Fig. 8), formed by shear displacement of individual parts of the projectile; and (3) irregular to smooth texture composed of rivulets, globules, and irregular smooth patches (Fig. 9), in short, the forms assumed by a liquid under the influence of surface tension. Droplets and rivulets occur locally on the striated surfaces. Isolated spheres generally have a smooth specular surface like a welding bead. The specular surfaces are generally steel gray or tarnished slightly yellow, whereas the striated surfaces display an iridescent array of colors from yellow to red to gun-metal blue.

Selected chips of steel showing evidence of fusion on the surface were submitted to R. H. Thielemann of the Stanford Research Institute for metallographic examination. Thielemann reports as follows:

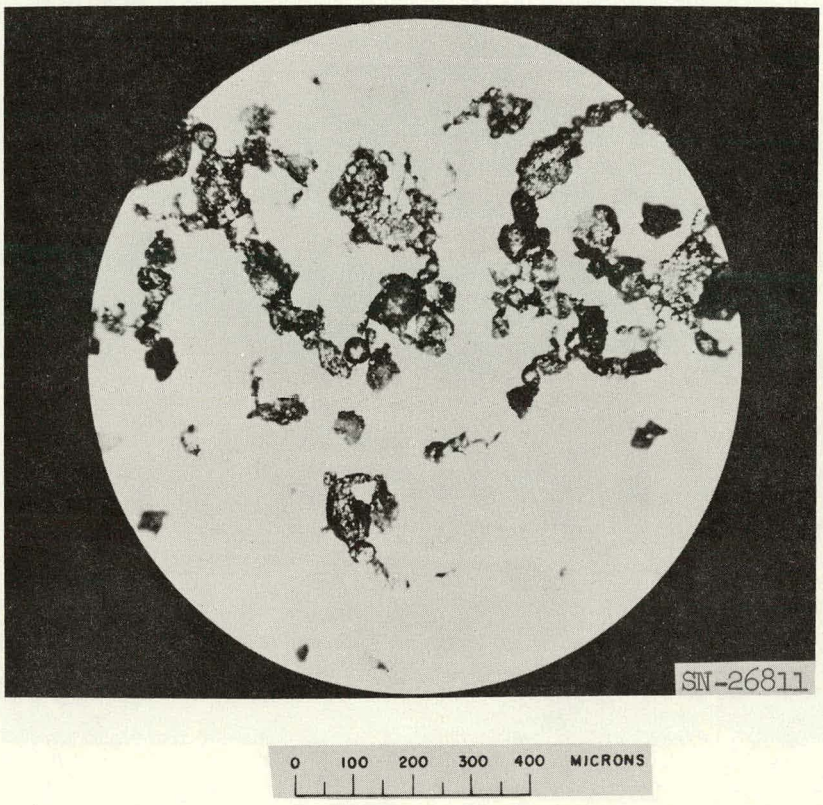

Fig. 7. Photomicrograph showing spheres and irregular slivers of steel in ejecta.

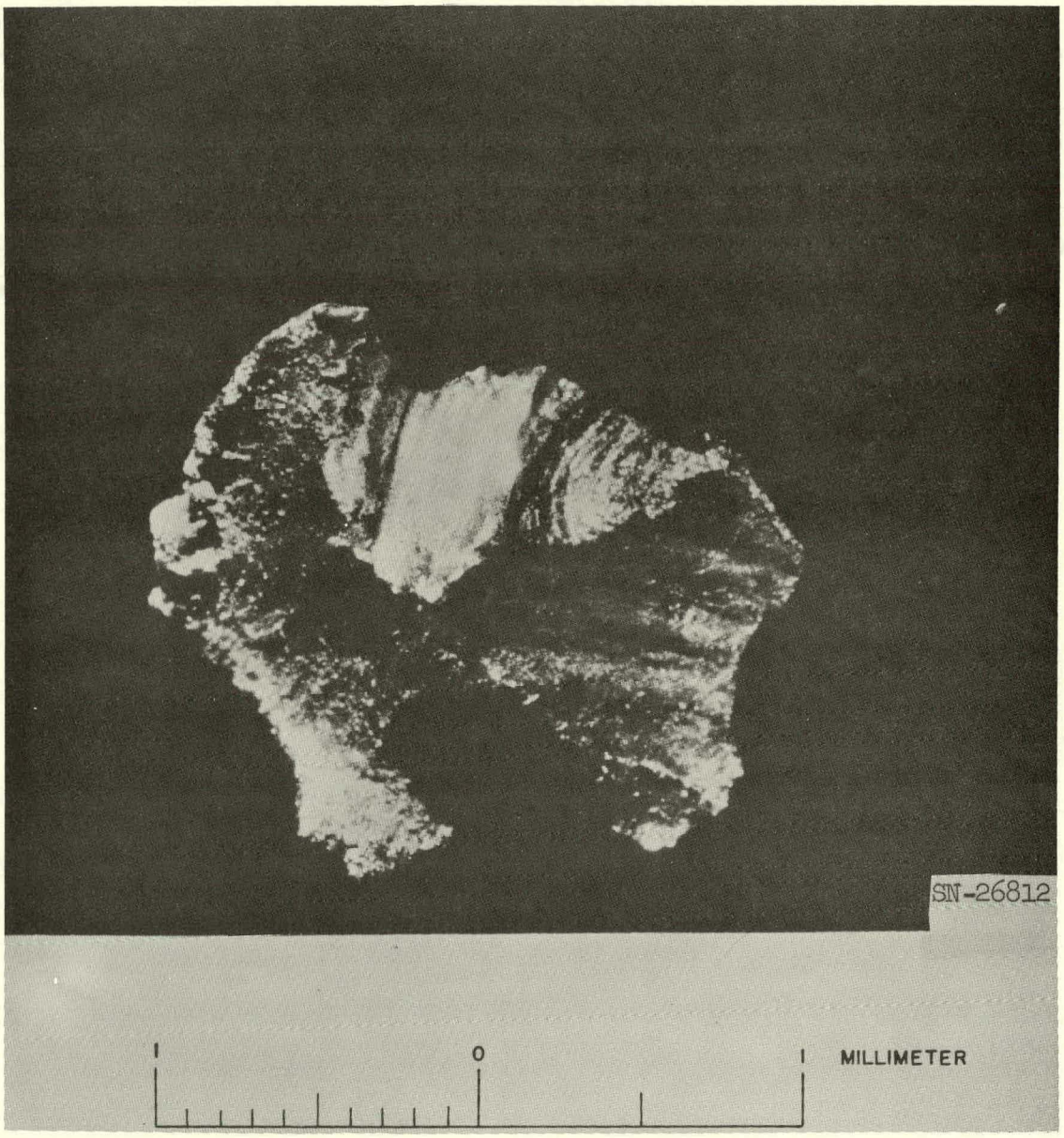

Fig. 8. Photomicrograph showing grooved and striated curved surfaces on projectile fragment.

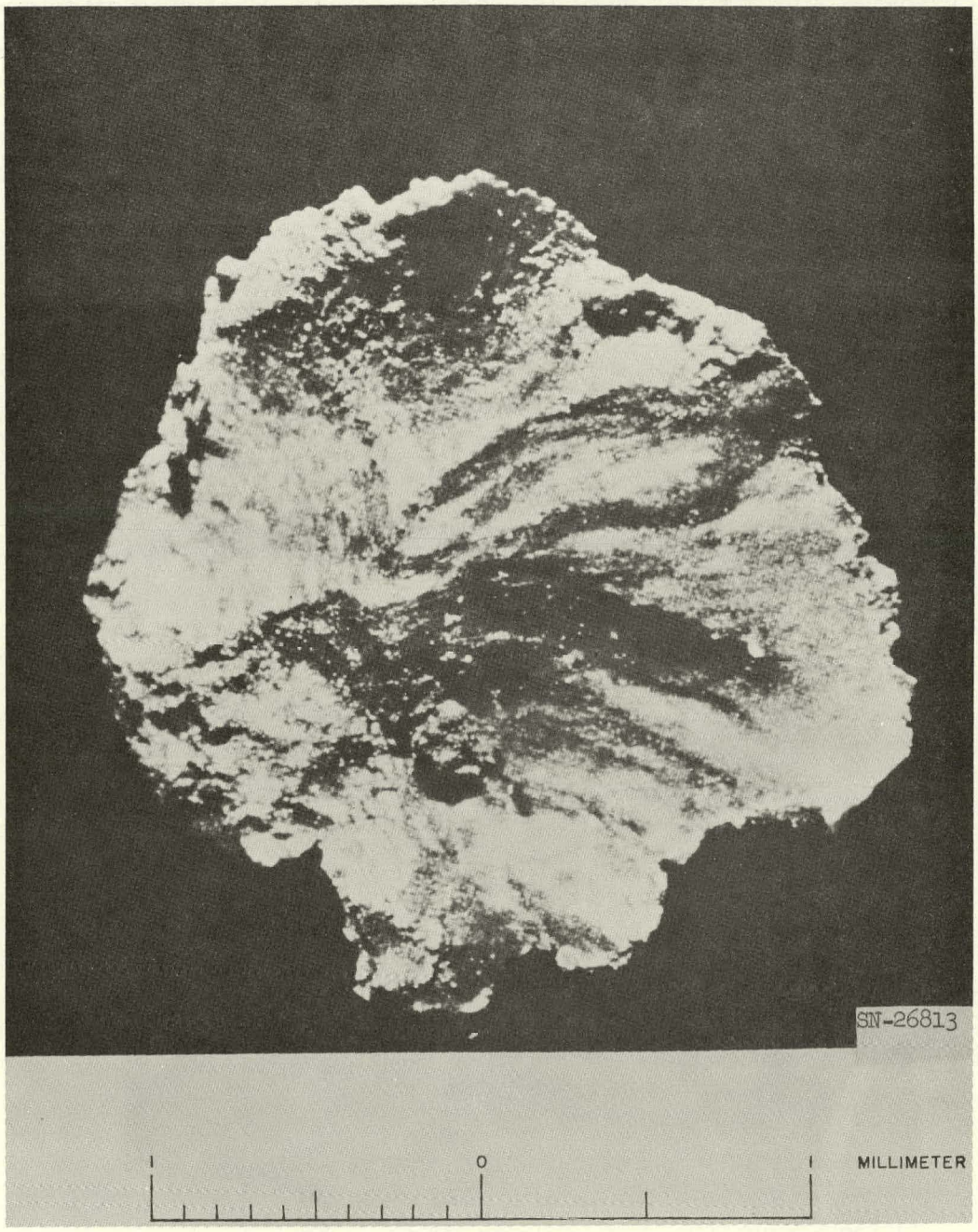

Fig. 9. Photomicrograph showing irregular textured surface with smooth patches where striae have been obliterated by melted material.

"Our findings indicate that the fragments had reached a temperature of around 2400° to 2500°F, which is the liquid plus solid, or mushy, stage for a steel of this composition. Particles were cooled slowly enough so that the excess iron carbide, or cementite, precipitated around the austenite grain boundaries, and on cooling to room temperature this cementite network enclosed pearlitic grains.

"Because of the high degree of fragmentation and because the particles had reached the semi-liquid state, the grain boundary structure was extremely heterogeneous and, hence, difficult to study. Practically every structure obtainable in an alloy of this composition seemed to be present in the microstructure. Because of this our analysis took into account the average structures of the fragments which seemed to be most uniform."

Typical microstructure of the shocked steel is shown in Fig. 10.

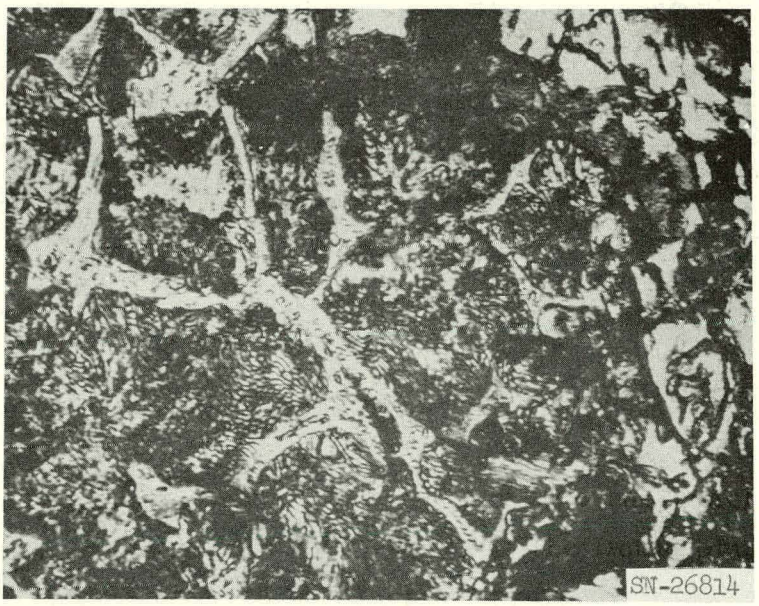

Fig. 10. Microstructure of typical steel fragment showing iron carbide (cementite) network around prior austenite grains and pearlite. Magnification 800×.

THEORY FOR FUSION OF THE STEEL

The presence in the ejecta of steel spherules and projectile fragments with surfaces covered by forms assumed by true liquids, and the analysis by Thielemann, show that temperatures exceeding the minimum melting point of the steel were reached at least locally. Only steel can definitely be shown to have melted, but it is likely that a small amount of the quartz in the target sandstone was also fused, which may, in part, account for the bonding of the most finely crushed aggregates. At most, however, only a very small fraction of the strongly shocked sandstone reached fusion temperatures. Probably not more than 10 percent of the projectile was fused.

Compressive heating

It may be shown on the basis of a simple hydrodynamic model that the temperature of the bulk of the projectile would not have been raised to a temperature of complete fusion, in keeping with the observed experimental result. Using a simple one-dimensional model for the flow during the early stages of the impact, when the maximum temperature and pressure occur (Shoemaker, 1960, p. 426-429), the peak impact pressure is found to be 440 kilobars (one bar = 10^6 dynes/cm^2). The calculations are based on measurements of Altshuler and others (1958) of the hugoniot for iron, and on determination by Dr. R. Schall at the Institut Franco-Allemand de Recherches de Saint Louis (written communication 1960) of the hugoniot for a dry quartzose sandstone with a bulk density of 2.06 g/cm^3. The difference in bulk density between sandstone studied by Schall and that of the target specimen used in this experiment (2.26) would not significantly alter the calculations nor the conclusions. The peak pressure will be slightly underestimated. The chief error will lie in overestimating the temperature of the sandstone. For a pressure of 440 kilobars, the total increase in internal energy is 0.5×10^{10} ergs/g for the projectile, and 5.5×10^{10} ergs/g for the target sandstone. Only a fraction of these increases in internal energy, however, can be manifested as an increase in temperature.

For the projectile, the data of McQueen and Marsh (1960, p. 1264) indicate that the maximum temperature of the compressed steel would be of the order of 400°C at 440 kilobars pressure. At a pressure of 440 kilobars iron may be expected to melt at about 2100°C (Strong, 1959). About 5 percent of the total internal energy is expended in raising the temperature of the iron to 400°C. After decompression to atmospheric pressure the estimated residual temperature is of the order of 100°C as compared to a fusion temperature of 1500°C. Heating by shock compression thus fails by an order of magnitude to account for partial fusion of the projectile.

Using Schall's hugoniot for sandstone, the energy irreversibly expended as heat in the most intensely shocked part of the target sandstone is calculated as 3.1×10^{10} ergs/g for the peak impact pressure of 440 kilobars (56 percent of the total increase in internal energy). Because of a permanent decrease of about 15 percent in the specific volume of the shocked sandstone, due to the closing up of the intergranular pore space of the sandstone, the heat is taken as the difference between the peak internal energy and the integral of the hugoniot from one atmosphere to peak pressure. The hugoniot, in this estimate, is considered a close approximation of the decompression adiabat of the shocked sandstone. Adopting a mean specific heat of 1.25×10^{7} ergs/g °C for quartz, this heat would raise the quartz to a residual temperature after decompression of approximately 2500°C. This temperature estimate is undoubtedly too high because the porosity of the sandstone for which the hugoniot was determined is somewhat greater than that of the target block of Coconino Sandstone, but it strongly suggests that some quartz in the sandstone target may have been raised to temperatures above the quartz melting point (1500°) or the cristobalite melting point (1700°).

It should be noted that the peak pressure in the sandstone exceeded that calculated for experiments in which DeCarli and Jamieson (1959) obtained an amorphous or glassy form of silica by shock loading single crystals of quartz with high explosives. As the calculated temperatures in their experiments did not exceed 1100°C, the presence of glass in the ejecta from the sandstone target would not necessarily indicate temperatures exceeding the melting point of quartz.

The localization of heat required to fuse part of the steel might be attributed to two processes: (1) conduction of heat across the interface between the target sandstone and projectile, and (2) dissipation of internal energy as heat by viscous drag and friction, primarily along the steel-sandstone interface and along shear surfaces formed during deformation and breakup of the projectile. The probable relative importance of these two processes may be evaluated in the following manner.

Conduction of heat

Most of the conduction of heat will probably take place under relatively low pressure during expansion of the projectile-sandstone interface. Consider a semi-infinite block of steel at a temperature, T_F, of 100°C placed instantaneously in contact along a plane interface with a semi-infinite body of shocked sandstone heated to a temperature, T_Q, of 2500°C, the maximum possible temperature of the quartz after decompression. From heat conduction theory, the approximate distance from the interface, d, to which significant changes of temperature will penetrate either medium after an interval of time, t, is given by

$$d = 2\sqrt{(K/\rho c)t}, \qquad (1)$$

where $(K/\rho c)$ is the thermal diffusivity of the medium; K is the thermal conductivity, ρ is the density, and c is the heat capacity. The following approximate physical constants may be used for the range of temperatures of interest:

K_Q (mean conductivity of heated quartz) $\approx 3 \times 10^{-2}$ watt/cm deg,

c_Q (mean heat capacity of heated quartz) ≈ 1.3 joules/g deg,

ρ_Q (mean density of heated quartz) ≈ 2.6 g/cm^3,

K_F (mean conductivity of steel) ≈ 0.7 watt/cm deg,

c_F (mean heat capacity of steel) ≈ 0.5 joule/g deg,

ρ_F (mean density of steel) ≈ 8 g/cm^3.

The diffusivity of the heated sandstone is of the order of 10^{-2} cm^2/sec, and that of the steel is about 20 times greater. The time interval for growth of the interface is of the order of 10^{-5} sec. During this time, cooling of the sandstone will penetrate to a depth of the order of 10^{-3} cm and the steel will be heated through a distance four times as great, or approximately the thickness of the layer of steel that would be formed by spreading the projectile uniformly over the estimated maximum area of the interface. The heat transferred across the interface per unit area, ΔH, during 10^{-5} sec may be approximately estimated from the formula

$$\Delta H \approx d \rho_Q c_Q \left(\frac{T_Q - T_F}{2} \right). \qquad (2)$$

Substituting the appropriate quantities, the total heat flow across the interface is found to be about 4 joules/cm^2. Spread evenly through the mass of the projectile, this heat would raise the temperature of the steel on the order of 10° to 20°C.

On the basis of the model of two semi-infinite bodies in contact, the maximum increase in temperature in the steel, ΔT, which would occur at the interface is given (Carslaw and Jaeger, 1959, equation 5, p.88) by

$$\Delta T = (T_Q - T_F) \frac{\sqrt{K_Q \rho_Q c_Q}}{K_F \rho_F c_F + \sqrt{K_Q \rho_Q c_Q}} \qquad (3)$$

This equation applies until the thermal disturbance reaches the back side of the layer of steel. During this interval of time, which was found to include approximately the period of growth of the steel-sandstone interface, the maximum increase of temperature in the steel is found by substitution of the appropriate quantities to be only about 400°C. As the fusion temperature of the iron is about 1500°C, conduction alone can contribute heat to the steel but cannot possibly account for melting of parts of the larger chips, which became disengaged from the sandstone on ejection from the crater. If the temperature of the most strongly shocked quartz was significantly above the fusion point of the steel, however, the steel present as minute spheres

impregnating the crushed quartz aggregates could have been fused by conduction of heat from the sandstone after the aggregates had been ejected from the crater.

(Please turn to p. N-20. The blank areas on this page and page N-20 are due to a last-minute revision.)

Frictional heat

An order of magnitude estimate can also be made for the contribution of frictional heat. For a pressure, p, in dynes/cm^2, a friction coefficient, f, and a slip distance of h, the energy per unit area, H_f, absorbed by friction along shear planes (as heat) can be expressed

$$H_f = pfh . \tag{4}$$

In contrast to conduction, the major contribution by shear will probably occur under conditions of high local pressures. Substituting $p = O(10^{11})$ and $f = O(10^{-1})$

$$H_f = O(10^{10})h . \tag{5}$$

The shearing distance, h, through which p remains on the order of 10^{11} will be on the order of the projectile diameter or less, $O(10^{-1})$. This yields $H_f = O(10^9)$ ergs/cm^2 or $O(10^2)$ joules/cm^2. As the heat required for fusion is of the order of 10^3 joules/g, the frictional heat may be adequate to melt on the order of 10^{-1} gram of steel per square centimeter of shear surface. The thickness of the fused layers produced by frictional heating along the shear surfaces would be on the order of 100 microns.

Thus, frictional heating appears adequate to account for the fused steel recovered in the experiment independently of the possible contribution of heat from the target sandstone. In particular, frictional heating appears to offer the best explanation for the local occurrence of fused steel on the surfaces of the larger recovered chips of the projectile. This explanation is essentially the same as that offered by Abbott (1960, p. 15) for the occurrence of thin

layers of very fine untempered martensite along slip planes in the vicinity of a crater in a steel target by impact of an aluminum projectile at 3.554 km/sec.

In conclusion, it may be noted that spheres of melted steel were produced by experimental high-speed impact which closely resemble spheres of meteoritic nickel-iron found in abundance at Meteor Crater, Arizona. The spheres produced by natural impact at Meteor Crater have been interpreted as formed by condensation of nickel-iron vapor (Nininger, 1956, p. 100-105). But abundant spheres can be produced under conditions that preclude the formation of any significant amount of vapor. More definitive evidence is required, therefore, to show that a significant fraction of the meteorite which struck the earth at Meteor Crater was vaporized.

REFERENCES

Abbott, K. H., Metallurgical observations of high-speed impact, Hypervelocity Impact, Fourth Symposium, Eglin Air Force Base, Florida, 2, No. 24, 22 pp., 1960.

Altshuler, L. V., K. K. Krupnikov, B. N. Ledenev, V. I. Zhuchikhin, and M. I. Brazhnik, Dynamical compressibility and equation of state for iron under high pressure, Soviet Phys. JETP, 7, 606-614, 1958.

Baldwin, R. B., The Face of the Moon, University of Chicago Press, Chicago, 239 pp., 1949.

Barringer, D. M., Meteor Crater (Formally Called Coon Mountain or Coon Butte) in Northern Central Arizona, Published by the author, Philadelphia, Pa., 24 pp., 1910.

Chao, E. C. T., E. M. Shoemaker, and B. M. Madsen, First natural occurrence of coesite, Science, 132, 220-222, 1960.

Charters, A. C., B. P. Denardo, and V. V. Rossow, Development of a piston-compressor type light-gas gun for the launching of free-flight models of high velocity: Natl. Advisory Comm. Aeronautics, Tech. Note 4143, 95 pp., 1957.

DeCarli, P. S., and J. C. Jamieson, Formation of an amorphous form of quartz under shock conditions. J. Chem. Phys., 31, 1675-1676, 1959.

Gifford, A. C., The mountains of the moon, New Zealand J. Sci. and Technol., 7, 129-142, 1924.

Gifford, A. C., The origin of the surface features of the moon, New Zealand J. Sci. and Technol., 11, 319-327, 1930.

Gilvarry, J. J. and J. E. Hill, The impact theory of the origin of lunar craters: Publ. Astron. Soc. Pacific, 68, 223-229, 1956a.

Gilvarry, J. J. and J. E. Hill, The impact of large meteorites, Astrophys. Jour., 124, 610-622, 1956b.

Grimshaw, H. C., The fragmentation produced by explosive detonated in stone blocks, in Walton, W. H. (ed.), Mechanical Properties of Nonmetallic Brittle Materials, Interscience Publishers, Inc., New York, 380-395, 1959.

Hopkins, H. G. and H. Kolsky, Mechanics of hypervelocity impact of solids, Hypervelocity Impact, Fourth Symposium, Eglin Air Force Base, Florida, 1960.

Ives, H. E., Some large-scale experiments imitating the craters of the moon, Astrophys. Jour., 50, 245-250, 1919.

McQueen, R. G. and S. P. Marsh, Equation of state for nineteen metallic elements from shock-wave measurements to two megabars, J. Appl. Phys., 31, 1253-1269, 1960.

Merrill, G. P., The meteor crater of Canyon Diablo, Arizona; its history, origin, and associated meteoritic irons: Smithsonian Inst. Misc. Collections, 50, 461-498, 1908.

Moulton, F. R., Astronomy, Macmillan Co., New York, 549 pp., 1931.

Nininger, H. H., Arizona's Meteorite Crater, World Press, Inc., Denver, Colo., 1956.

Shoemaker, E. M., Penetration mechanics of high velocity meteorites, illustrated by Meteor Crater, Arizona, 21st Internat. Geol. Cong., Copenhagen, 1960, Rept., pt. 18, 418-434, 1960.

Spencer, L. J., Meteorite craters as topographical features on the earth's surface, Smithsonian Inst. Ann. Rept., 307-326, 1933.

Strong, H. M., The experimental fusion curve of iron to 96,000 atmospheres, J. Geophys. Research, 64, 653-659, 1959.

Wylie, C. C., On the formation of meteoric craters, Pop. Astronomy, 41, 211-214, 1933.

Wylie, C. C., Meteoric craters, meteors, and bullets, Pop. Astronomy, 42, 469-471, 1934.

Paper O

THROWOUT CALCULATIONS

Wilmot N. Hess

Lawrence Radiation Laboratory, University of California

Livermore, California

ABSTRACT

This paper presents a study of the throwout from an explosion crater. Starting with particles in motion in the crater, the lip buildup is followed until all particles have landed. We have worked with experimental information from a 500-ton H. E. explosion and attempted to calculate the apparent crater and lip shape and characteristics. This has been done only roughly so far and the data are preliminary. We have changed g and also the size of the crater to try to see how craters on the moon would look. Some scaling laws have been developed, based on this work.

* * *

In order to achieve a more detailed understanding of the cratering process, we have attempted to calculate the throwout from a crater and the subsequent buildup of the crater lip. In this process we have taken a simple approach. We consider the material in the true crater as being divided into zones and give a mass and velocity to each zone. We follow the particles through their parabolic orbits until they hit the ground, and then observe the construction of the lip.

Experimental Information

There is considerable experimental information that we can use to help in this calculation. An example is the data available from the 500-ton Scooter TNT explosion carried out this past year at the AEC test site in Nevada. Several measurements were made in connection with this test that are of direct use to us here.

(1) The motion of several targets near ground zero was recorded photographically. This provides us with surface velocities at several positions,

until gas venting obscures the targets at about 1 second after the explosion (see Fig. 1).

(2) From the photographs made at late time, we can follow individual rocks in the air and determine their velocities shortly before they hit the ground.

(3) From the photographs we can determine a value for the maximum velocity of ejecta by observing how high the cloud goes at early times (before thermal effects are important).

(4) Twenty radioactive pellets were buried in the earth at known positions near ground zero before the explosion. After the explosion, they were found (by using a counter to locate the activity) and their final positions were measured. This information is shown in Fig. 2.

(5) The final lip height was measured. Part of the increase in height close to the crater is caused by the upthrust of rock resulting from the explosion and part is caused by the throwout of material.

(6) One particular feature of the throwout is apparent from the photographs and agrees with information on terrestrial craters. The strata in the crater body appear inverted in the crater lip, at least close in to the crater. This means that the material thrown out of the crater from the top of the ground landed first, and material from beneath it landed later. With all of this information, we can learn a good deal about the throwout process.

Scooter Calculation

Our objective in this study is to reproduce the Scooter throwout in detail. If we are successful in this, our understanding should allow us to calculate the throwout from other cratering explosions.

Our results of the Scooter calculation are preliminary. So far, we have considered that all particles are given an initial velocity and then undergo free fall, under the action of gravity alone. This "impulsive" model we know to be wrong, as is shown by the early velocity history of one of the targets from Scooter in Fig. 3. After the initial shock acceleration, the target slows down with 1 g deceleration due to gravity until, at about 0.35 sec, a second acceleration starts which continues until the record is obscured.

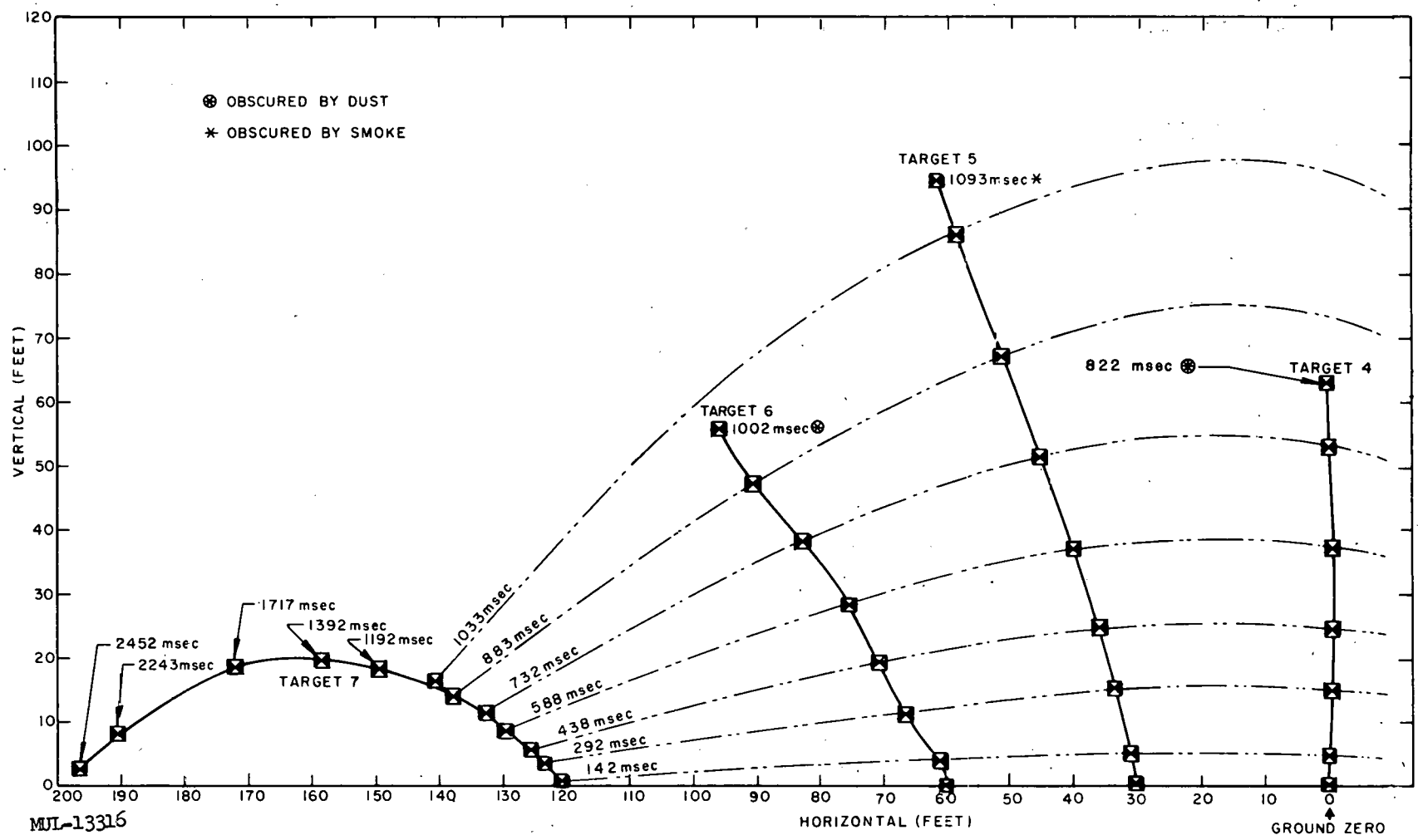

Fig. 1. Displacements of targets on the ground surface above the Scooter explosion versus time.

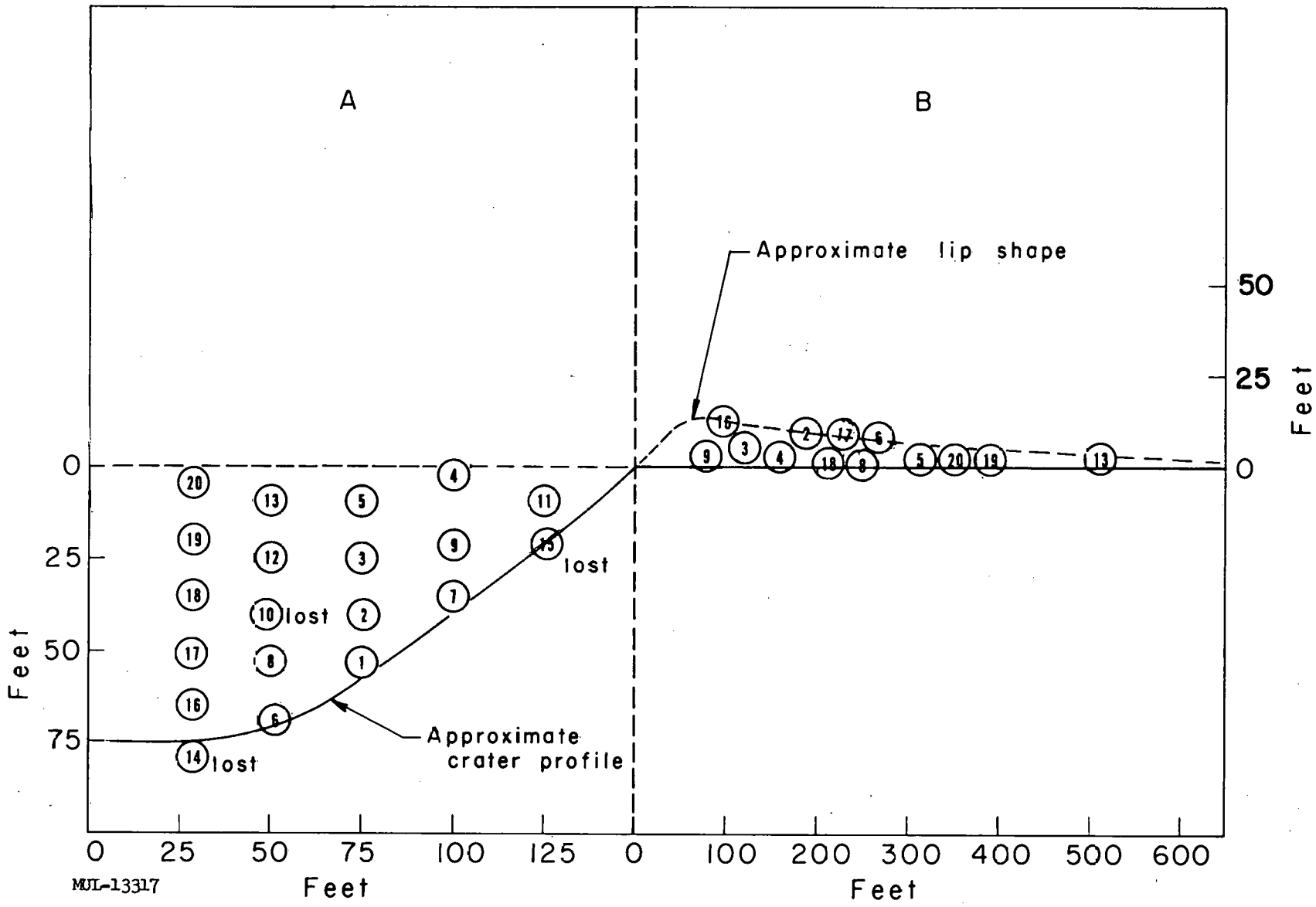

Fig. 2. Positions of the radioactive pellets before and after the Scooter explosion, showing (A) the pellets in place in the ground before the explosion, and (B) the approximate final positions of the pellets, with a different length scale. Pellets 1, 7, 11, and 12 remained in the crater and traveled only short distances.

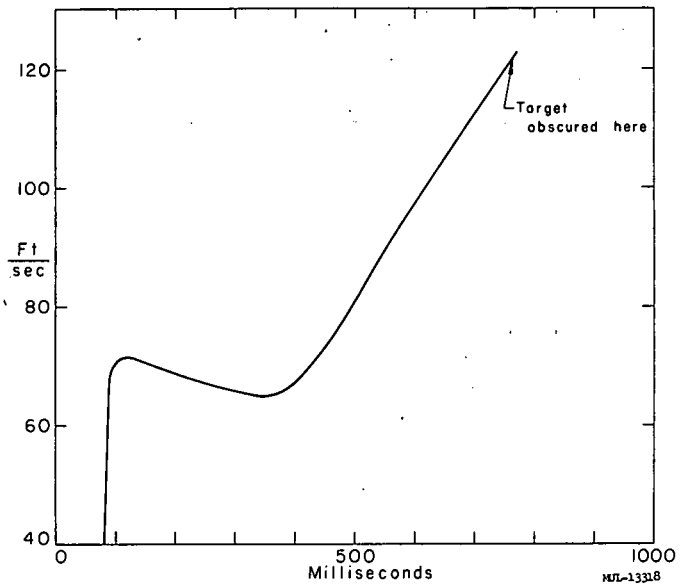

Fig. 3. Velocity history of a surface target at ground zero from the 500-ton Scooter TNT explosion.

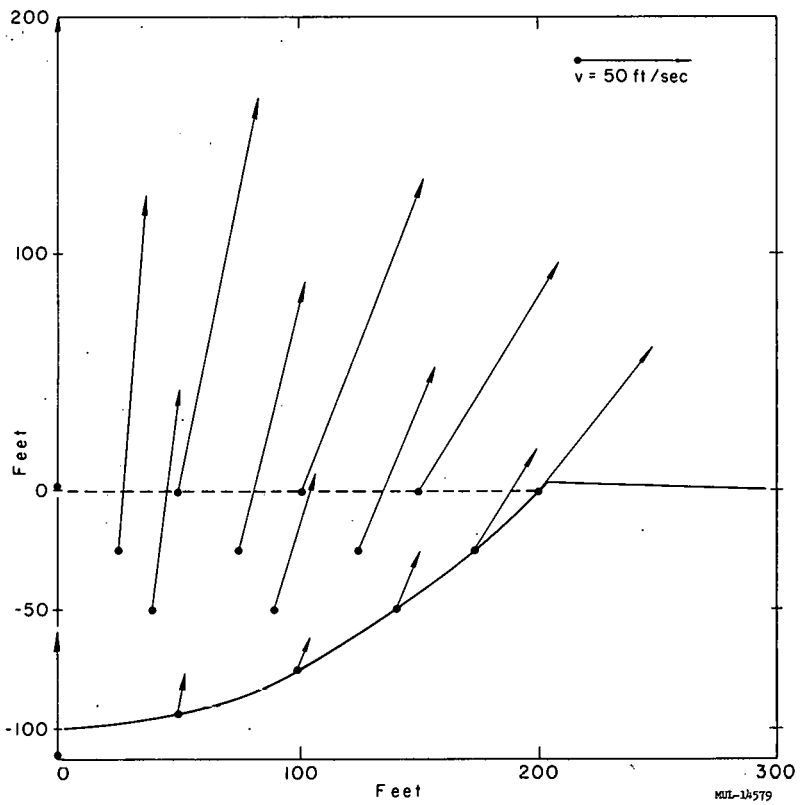

Fig. 4. The velocity field used in the throwout calculations. The ground-zero surface velocity is the largest at 200 ft/sec. The other velocities are to scale.

Nordyke has already discussed this second acceleration caused by gas venting. We have also neglected aerodynamic drag and wind effects. All of these effects can and will be included in future calculations. Our machine code can treat a velocity that changes continuously with time.

In selecting the initial velocities in our impulsive model, we used experimental data from (1) and (3). We have used a ground-zero surface velocity of 200 ft/sec which gives a cloud height of about 600 ft; this is about the observed value. The velocities used decreased monotonically with radial distance from ground zero and also decreased with depth.

For positions away from ground zero, we must decide what direction to use for the velocity vector. We might instinctively make the velocity vectors radial outward from the explosion point. After a little thought, however, we might think that particles would leave the surface vertically because of the shock reflection conditions (see sketch below).

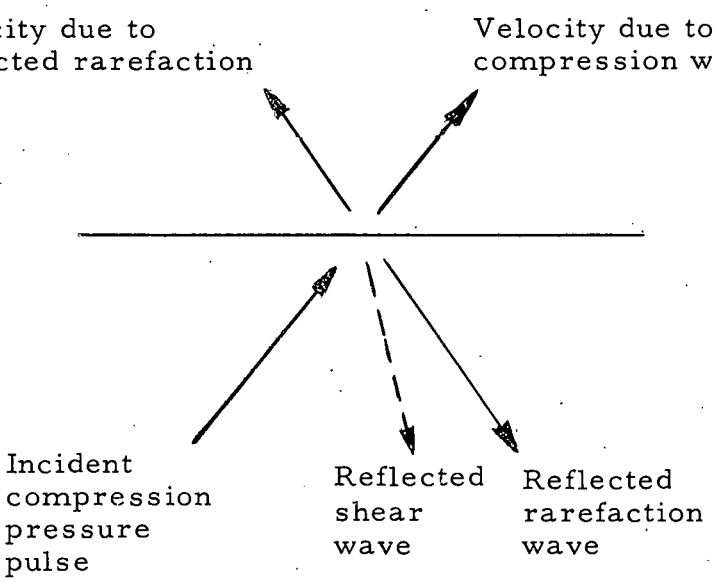

Adding the velocity vectors due to the incident compression wave and reflected rarefaction should result in the particles moving vertically. But this still does not account for all factors affecting the velocity vector. When reflection

occurs, shear waves and surface waves are generated which complicate the problem. This problem has been considered in the elastic case by Cagniard. Seidl has solved Cagniard's equations and found that the velocity vectors are nearly radial. Experimentally, the early velocities from Scooter are also radial, and the later velocities, when gas acceleration has occurred, are nearly radial as well.

In this, our first problem, we have used velocities that are more vertical than radial, but for later problems we probably will use radial velocities. The velocity field used for this problem is shown in Fig. 4.

The calculation starts with all particles in the crater in motion, and the lip of the crater partly formed by upthrust (see Fig. 5A). The bottom of the velocity field is only roughly the true crater of Scooter. We have assumed that material below this line doesn't move any appreciable distance. We calculate where all the particles are after short steps in time and, as particles hit in the crater or on the crater lip, we spread out the mass to cover the proper range of positions and keep track of what particle lands where, and on top of what other particle. Steps in the crater buildup are shown in Fig. 5. In Fig. 5E we see the final apparent crater after all particles have landed.

We know that there are several things in Fig. 5 that don't agree with the actual Scooter throwout: (a) not enough material falls back into the crater, therefore some of the velocities are too high; (b) we do not get inverse stratigraphy, therefore some of the velocities near the edge of the crater are ordered wrong; and (c) the radioactive pellet positions from Scooter are not accurately reproduced. All of these can be corrected by properly modifying the velocity field in future problems.

Other Calculations

We have run several more problems, starting with the same velocity field and varying other parameters. Even though we know this velocity field is not really correct, it is not radically wrong and scaling problems based on these velocities should be roughly correct. Figure 6 shows the apparent crater formed when the acceleration of gravity is reduced to 3.2 ft/sec^2 compared with the case for g = 32 ft/sec^2. Most of the material gets out of the crater here, and the apparent crater is nearly the same as the true crater.

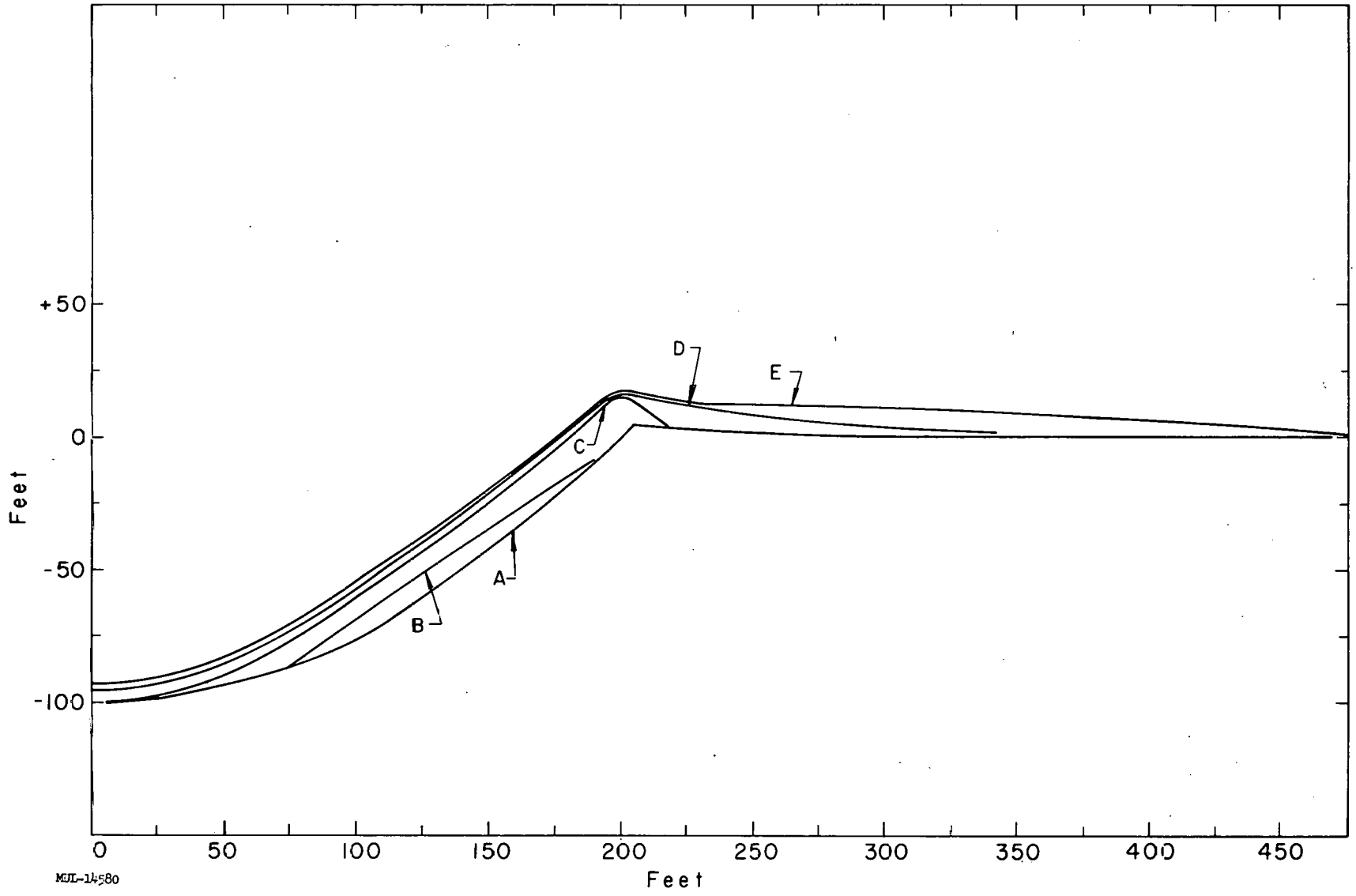

Fig. 5. The calculated Scooter crater profile as a function of time during the throwout period. Curve A is the true crater profile. Curves B, C, and D show the crater buildup at successively later times. Curve E is the final calculated crater shape.

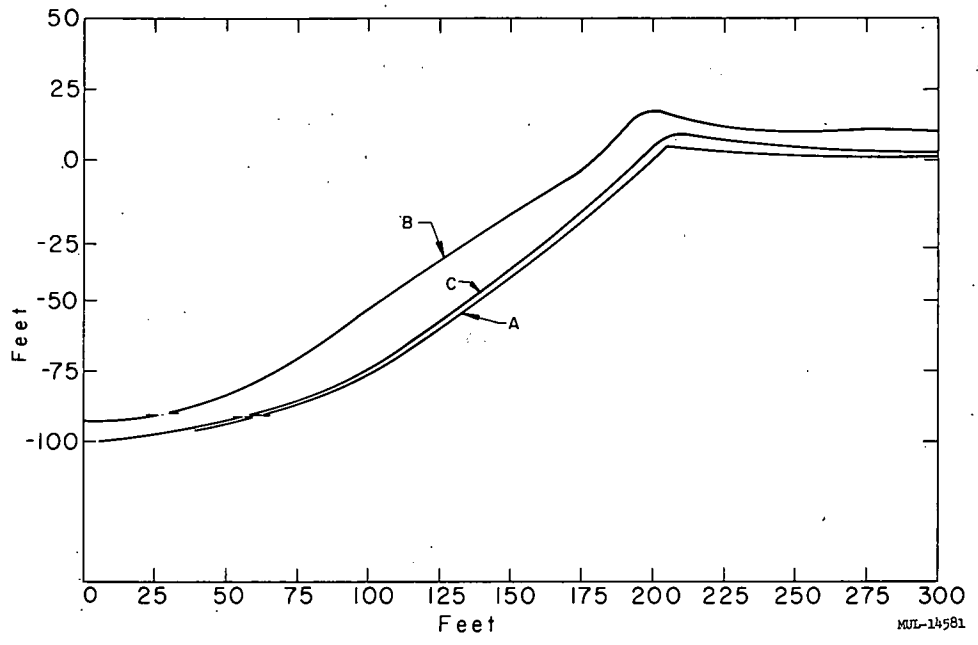

Fig. 6. A comparison of the calculated Scooter crater profile using normal earth gravity g (curve B) with the calculated profile using gravity of $g/10 = 3.2$ ft/sec^2 (curve C). The true crater profile is shown by curve A.

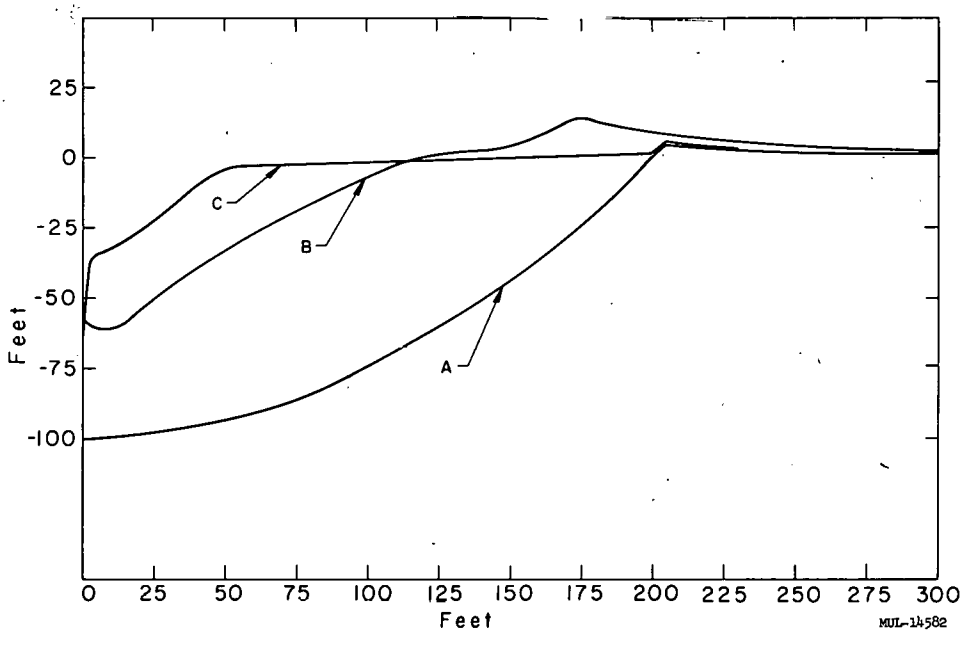

Fig. 7. A comparison of the apparent crater profiles for true craters 2000 ft in radius (B) and 20,000 ft in radius (C), calculated on the assumption that the velocities of the particles were the same as for Scooter at comparable positions in the crater. The true crater is shown in A. Note that the upthrust lip shows through the fallback in C.

We have also changed the scale of the problem in order to see how larger craters would look. In other problems we have used 2000 ft and 20,000 ft as the diameter of the true crater while keeping the velocities the same as for Scooter. We think that, for the same scaled depth of burial, the velocities should stay constant for different size explosions. The reason for this is that time and distance scale the same way; therefore velocity, which is the ratio of these, should not change. The apparent craters from these explosions are compared with Scooter in Fig. 7. For the larger explosions, the apparent crater is smaller. This is to be expected because the particle velocities stay constant and the particles, therefore, move a smaller fraction of the crater radius. Thus, more of the particles land in the crater. Figure 7C shows the upthrust lip exposed and a fairly flat region inside it. This looks interestingly similar to a walled plain on the moon.

Scaling

The dimensions of the true crater should vary as $W^{1/3}$, the cube root of the explosive yield. The true crater shape depends on the strength of materials and it should therefore behave similarly to the underground effects of explosions, which vary as $W^{1/3}$. Starting with this behavior for the true crater, we can get the apparent crater scaling law from Figs. 6B and 7. This gives a $W^{1/3.6}$ variation for both the apparent crater depth and radius, scaling from Scooter (0.5 kt) up to 0.5 Mt. If we extend the range of scaling from 0.5 kt to 500 Mt we get a $W^{1/3.9}$ scaling law. Even though we know the original velocity field isn't too good, this scaling law probably is nearly right.

We can also consider the similarity of lunar and terrestrial craters. Starting with

$$h = V(ab \cos \eta)t - \frac{g}{2}t^2,$$

$$x = V(ab \sin \eta)t,$$

where h and x are vertical and horizontal displacements, v is the ground-zero surface velocity, a and b are functions that describe the change of velocity with radius and depth, and η is the zenith angle of the velocity vector,

we can get

$$gh = gx \cot\eta - g^2x^2\left(\frac{1}{2V^2a^2b^2\sin^2\eta}\right).$$

An interesting feature here is that dimensions x and h are both multiplied by g. For two apparent craters to be similar, we need $(\ell/R_{true})_1 = (\ell/R_{true})_2$, where the dimension ℓ is either x or h. If this condition is satisfied, all the throwout particles fall to earth at the same fraction of the true crater radius. Then the total throwout distribution, scaled to the same true crater radius, will be identical for the two craters. We can achieve this by

$$\frac{\ell}{R_{true}}(1\text{ kt},\ 1\text{ g}) = \frac{2\ell}{2R_{true}}\left(8\text{ kt},\ \frac{g}{2}\right),$$

where R_{true} has been doubled by increasing the explosive yield eightfold and ℓ has been doubled by halving g. Because ℓ and g appear as a product in the equation, decreasing one of them increases the other one.

For the moon we get

$$\frac{\ell}{R_{true}}(1\text{ kt},\ 1\text{ g}) = \frac{6\ell}{6R_{true}}\left(216\text{ kt},\ \frac{g}{6}\right).$$

That is, on the moon where g is about 1/6 that on earth we could make a crater similar to one produced on earth by using 216 times the explosive yield used on earth. The dimensions of the lunar crater would be six times those of the terrestrial crater, but the scaled sections of both craters would be identical.

One more point can be made about the relationship of terrestrial and lunar craters. For small vertical displacements ($h \approx 0$) we can write,

$$x = \frac{2V^2}{g}a^2b^2\sin\eta\cos\eta.$$

If on the moon there is no second acceleration due to gas venting (because no gas-producing materials such as water or carbonates are present), then we

might take the initial velocity of Scooter for explosions on the moon and the final velocity of Scooter for explosions on the earth. We get from this

$$\frac{x_{earth}}{x_{moon}} = \left(\frac{V_e}{V_m}\right)^2 \left(\frac{g_m}{g_e}\right) = \left(\frac{V_{final}}{V_{initial}}\right)^2 \left(\frac{1}{6}\right) \approx (2.5)^2 \left(\frac{1}{6}\right) \approx 1 .$$

This says that a crater on the moon from a certain explosive yield should be about the same size as a crater on the earth made by the same explosive yield. There may, of course, be some second acceleration on the moon which would make the lunar crater larger than the crater on earth.

Paper P

EVALUATION OF MISSILE HAZARD, UNDERGROUND SHOT

R. B. Vaile, Jr., and V. Salmon

Stanford Research Institute

Menlo Park, California

ABSTRACT

The missile experiment performed as a part of the JANGLE underground explosion test demonstrated that reinforced concrete walls and highways located 40 feet to 140 feet from ground zero were broken and thrown out as missiles. Material nearer than 40 feet (or perhaps 50 feet) was vaporized or pulverized to the extent that it was largely windborne.

Missiles of military significance were found 400 feet to 3300 feet from ground zero. Those of major significance were in the range 400 feet to 1500 feet.

Analysis has permitted estimates of the missile hazard from an underground explosion of roughly 25 times the energy release of the JANGLE underground explosion (and at the same scaled depth, $\lambda_c = 0.15$) fired under a continuous reinforced concrete runway 18 inches thick. It is predicted that missiles would produce serious damage to buildings out to a radius of 1100 feet and to airplanes out to 3000 feet. These figures should be compared to estimates that the air blast from such an explosion would damage buildings to 2200 feet and airplanes to 6000 feet.

It is concluded that for large shallow underground explosions, damage by the mechanism of air blast will extend farther than damage by the mechanism of missiles. This conclusion is sufficiently firm that no further missile experiments appear necessary.

* * *

INTRODUCTION

1.1 Historical

The hazards of missiles from underground explosions became of interest in 1950 during a time when an underground nuclear test was proposed for Amchitka Island where the soil contains rocks and boulders. Because of this interest an experimental study of missiles was added to the underground (HE) explosion tests at Dugway in 1951.

The Dugway tests revealed such large ranges for missiles that a further experimental study of missiles was added to the program of the JANGLE underground explosion at the Nevada Test Site in December 1951 as Project 4.5.

1.2 Objective

The over-all purpose of Project 4.5 was to obtain data leading toward the determination of the damage produced by missiles as a result of underground nuclear explosions. Evaluation of the damage to be expected from missiles is important to the extent that it affects the choice of an underground weapon rather than an air-burst weapon against any class of target.

The specific objective of Project 4.5 was to obtain data on the underground shot of Operation JANGLE in regard to the range, size, and source location of potentially damaging missiles produced from a typical concrete highway or landing strip, and a typical concrete wall of a type that might be used in a small factory building of several stories.

BACKGROUND DISCUSSION

2.1 Interior Ballistics

The design of the JANGLE missile experiment was particularly difficult because of the extremely meager quantitative information available regarding missiles from underground explosions. It was desired to obtain, both before the experiment and as a result of the test, information on (1) the formation and ejection of missiles from target sources (interior ballistics) and (2) the ballistic behavior of whatever missiles are formed (exterior ballistics).

The formation of missiles is primarily a matter of the breakup of materials under shock conditions and, in the case of nuclear explosions, of their response to temperature shock as well.

While quarrying operations using high explosives have been carried on for many years, the intent in such explosions is to minimize the production of missiles, and no quantitative information on the size and ballistic characteristics of missiles incidentally produced has been found. A considerable amount of work on the fracture of solids has been carried out for use in problems of coal handling and ore crushing, and the possible application of this work to missile formation is of interest. However, the shock intensity produced by nuclear explosions is of a different order of magnitude than that produced by any of the methods considered in the literature and hence there was no reason to expect previous experience to be particularly useful in planning this experiment. As a result, an important component objective of this test was the determination of the extent of breakup of ordinary concrete construction when subjected to a nearby underground nuclear explosion.

2.2 Exterior Ballistics

In regard to the ballistic behavior of whatever missiles are produced, some information was available prior to the design of this test. That information consisted of the results of an experiment with artificial missiles salted in the backfill of the underground HE explosions in dry clay at Dugway during May of 1951. At Dugway, one of the most difficult elements of the experiment was the detection of missiles for recovery after the explosion,* and this experience influenced the design of the JANGLE missile experiment.

The Dugway tests confirmed the expectation that missiles would follow trajectories lying approximately in vertical radial planes passing through the charge center and the missile in the backfill; this finding is also reflected in the design of the collection strips at JANGLE.

---

* These experiments are reported in Technical Report No. 5, dated November 15, 1951, "Behavior of Missiles in Underground Explosions at Dugway," by Stanford Research Institute, under Contract N7onr32104 (Project 317, Rabbit) for the Office of Naval Research; classification, SECRET.

It had been estimated that missiles would be thrown out with initial velocities approximately the same as those of the surface particles in their path and that their external ballistic behavior would be adequately predictable if their size, shape, and density were known. The results of the Dugway experiments were consistent with this estimate.

The analysis procedure developed in the cited Dugway report was used for prediction of missile behavior in the JANGLE underground shot. This analysis is given on pages 23 to 26 of that report. In it the expected ranges are computed for possible missiles composed of Portland cement concrete of sizes from 2 inches to 8 inches and with initial zenith velocities between 5000 and 20,000 feet per second. Detailed analysis based on photographic evidence has indicated that the drag coefficient assumed for the Dugway analysis was too high; downward revision of it has yielded a changed formula (with smaller values) for the initial velocities of missiles at Dugway: $v = 750 \sin^2\theta$, where v is the initial velocity of a missile in feet per second and θ is the elevation angle of the slant radius from the charge to the initial position of the missile in the backfill. Similar correction of drag coefficients and initial velocities assumed for JANGLE might affect the range and density predictions, but certainly to a far smaller extent than the other uncertainties involved, particularly those concerning the nature of the breakup.

Discussion with personnel of the Armed Forces Special Weapons Project and the Technical Operations Squadron before the test led to agreement that the source of missiles of greatest interest was concrete highways (or landing strips) of typical modern reinforced concrete construction. It was also agreed that a missile source of secondary interest was a reinforced concrete wall such as might be used in a low, multistoried, reinforced concrete building.

2.3 Extrapolation

Extrapolation of the results of one experiment to what may be expected from a larger scale experiment requires consideration of both exterior and interior ballistics.

In general, the scaling laws for interior and exterior ballistics will be different. Breaking of missile source material presents a problem for which

very little direct information exists. Newmark has shown* that the failure of reinforced concrete beams, when subjected to the blow of a falling hammer, depends on the energy absorbed from the hammer and utilized in cracking the concrete and rupturing the reinforcing material. While this method of loading the concrete is much slower than the process by which an explosion breaks up missile source material, it furnishes a criterion of breakup which has some experimentally demonstrated validity. Thus on this basis the extent of breakup is proportional to the energy absorbed during the breakup process which, in turn, may be considered proportional to the energy density in the shock wave in the earth. Since the unit of energy density has the same dimensions as pressure it scales in the same manner. Hence on a series of ideal scaled experiments, the same energy density in the shock wave will exist at the same scaled distances from the charge. Thus,

$$S = \left[\frac{W_2^{1/3}}{W_1^{1/3}}\right] = \frac{E_2^{1/3}}{E_1^{1/3}} \quad ,$$

$$(ED)_1 = \beta \frac{E_1}{r_1^3} \quad ,$$

$$(ED)_2 = \beta \frac{E_2}{r_2^3} = \beta \frac{S^3 E_1}{r_2^3} \quad .$$

If $(ED)_1 = (ED)_2$, then

$$\beta \frac{E_1}{r_1^3} = \beta \frac{S^3 E_1}{r_2^3} \quad ,$$

---

* "Methods of Analysis for Structures Subjected to Dynamic Loading," N. M. Newmark, prepared for Physical Vulnerability Branch, Air Targets Division, Directorate of Intelligence, USAF, March 1951.

or $r_2^3 = S^3 r_1^3$;

therefore $r_2 = S r_1$, where

S = the scale factor,

W = weight of charge in equivalent pounds of TNT,

E = energy,

ED = energy density,

β = a factor of proportionality,

r = distance in feet from ground zero.

It can be postulated that the breaking up of a solid body depends on the stresses which accelerate the internal parts of it when the whole body is subjected to unbalanced external forces. On this basis peak acceleration is a criterion of breakup. If scaling laws are combined with experimental evidence regarding the variation of peak acceleration with distance on any one explosion, it can be shown that as the charge size is increased the scaled radius for a given value of acceleration decreases. Further analysis of this point is presented in Chapter 5 and a complete discussion of scaling laws may be found in an early report by Lampson.*

Accompanying breakup is the ejection of the missiles. For the calculation of the exterior ballistics portion of the problem it is necessary to know the velocity and the angle at which missiles are initially ejected. Experience with missiles at Dugway indicates that the velocity-angle relation is of the form

$$v = \frac{V_{00}}{\lambda_c^{\,n}} (\sin \theta)^n .$$

In this, λ_c is the scaled depth of charge; θ is the elevation angle of the radius vector from charge to missile; n is an exponent of the order of 1 or 2; and

---

* "Final Report on Effects of Underground Explosions," C. W. Lampson, Division 2, National Defense Research Committee of the Office of Scientific Research and Development, NDRC Report No. A-479, OSRD Report No. 6645, March 1946.

V_{00} is a constant, presumably dependent largely on some characteristics of the soil. Implicit in this relation is the assumption that missiles are ejected radially from the charge.

From the velocity and elevation angle of ejection, together with the drag coefficient of the missile, it is possible to calculate by the standard methods of external ballistics the horizontal range, the maximum altitude, the time of flight, and the angle of striking of the missile. In a series of scaled experiments, missiles originating at the same angle will originate at constant scaled distance from ground zero. (See diagram.)

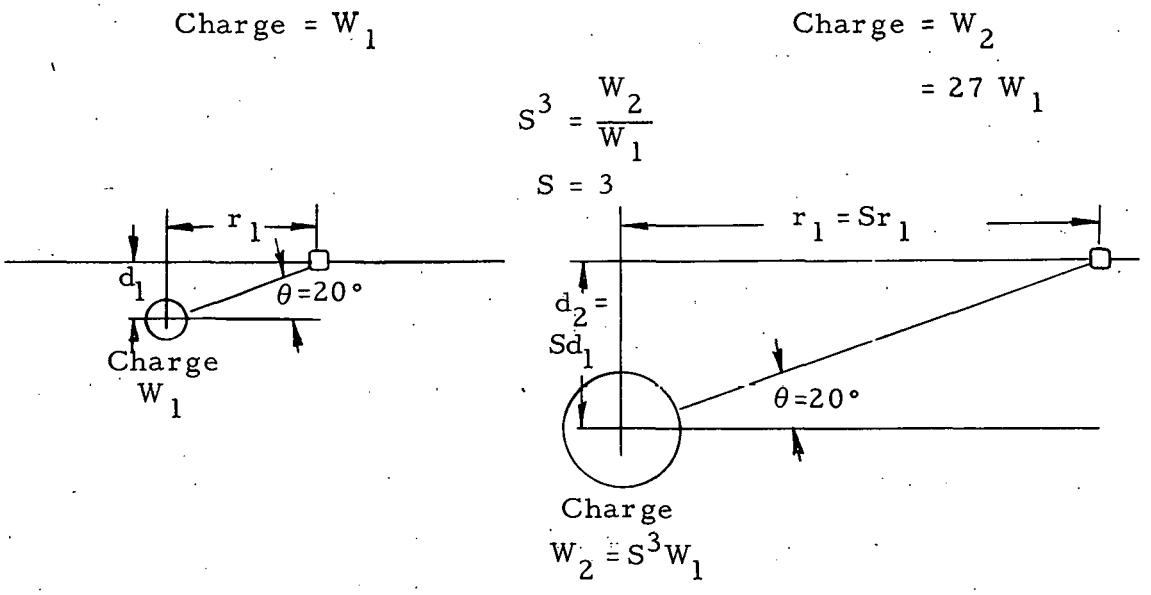

Since λ_c would be held constant in a series of scaled experiments, the ejection velocity, v, is independent of the scale of the experiment. Thus the horizontal ballistic range is independent of the scale of the experiment. The total range, as measured from ground zero, will consist, however, of the sum of this ballistic range and the distance from ground zero of the point of origin of the particular missile considered. This may be expressed by $R = \alpha r_c + r_b(\theta)$, where R is the total range; αr_c is the distance from ground zero to point of origin of the missile, expressed as a fraction, α, of the crater radius r_c; and $r_b(\theta)$ is

the ballistic range which depends only on θ, the elevation angle of the slant radius from charge to missile source.

In a series of scaled experiments α is held constant and r_c is believed to be proportional to the scale factor. When the scale of an experiment is increased, this relation indicates that the total range, R, will increase, but not as rapidly as the scale factor, because r_b is constant. The point at which the two components of the range are equal must be determined by experimental evidence.

2.4 Calculation of Potential Damage

After conclusions are reached about missile behavior, and extrapolations are made to other situations, a criterion of damage must be established for assessing the importance of missiles. It is considered important and valuable to know under what circumstances missiles might be sufficiently concentrated and possess sufficient velocity to cause actual demolition of buildings. For this purpose data obtained at Dugway on the amount of throwout which actually caused collapse of test structures were used to develop such a damage criterion.

In regard to airplanes, it is ultimately necessary to know both the concentration and size of missiles which will damage airplanes, as well as the concentration and sizes of missiles which will arrive at any specified radius from ground zero. During the analysis reported here, no quantitative information regarding the effectiveness of missiles in damaging airplanes has been available, and common sense estimates have therefore been used in determining the limiting size and concentration of missiles considered.

Final conclusions regarding missile hazard must be based on comparison with the hazard produced by other mechanisms, such as air blast and ground motion.* In estimating the hazards of air blast and ground motion, extrapolation

---

* Data for these comparisons has come primarily from two preliminary reports of phases of Operation JANGLE. The two reports, both by E. B. Doll and V. Salmon of SRI in April, 1952, are: "Ground Acceleration, Ground and Air Pressures for Underground Test, Project 1(9)a," Contract N7onr32104, for the Office of Naval Research; "Scaled HE Tests, Project 1(9)1," Contract DA 49-129-eng-119, for the Office of the Chief of Engineers.

to larger charges requires careful consideration of the effect of soil characteristics. Information from Dugway and from the HE-1, HE-2, and HE-3 shots at JANGLE as to levels of peak air-blast pressure and impulse have been used as a basis for comparison with missile damage.

DESCRIPTION OF THE EXPERIMENT

3.1 General

As a result of the considerations just enumerated, a group of concrete highway strips was laid out together with a collection area along the central radius, in accordance with the plans shown in Figures 3.1 and 3.2. These are the A targets and collection area. A similar array of walls and collection area was laid out as shown in Figures 3.1 to 3.5, under the designation of B targets and collection area. As a result of the Dugway experiments, it was estimated that the missiles having the greatest range would come initially from locations where they would have elevation angles of 45 to 60 degrees (assuming that their initial velocity was along the slant radius from the charge to the target).

3.2 Construction

To permit determination of the source location of missiles that were recovered after the explosion, the highway slabs were poured in small sections, each containing a different combination of pigment and aggregate. Similarly, each of the walls contained a different pigment. Since the greatest interest was thought to lie in the highway slab nearest ground zero, designated A1, that slab was divided up into five subsections, as indicated in Figures 3.1 and 3.3. While each of these subsections had a different pigment, the reinforcing steel was continuous across the section boundaries and the concrete was placed in rapid sequence (this whole target was poured in one day) so that a good mechanical bond was obtained even though there was color separation. In order to make certain of the identification of missiles stemming from the A1 targets, all of these were poured with special aggregate. The aggregate consisted of crushed red brick plus 50 pounds of 3d aluminum nails per cubic yard of concrete. In addition, specific pigments were used to designate the separate

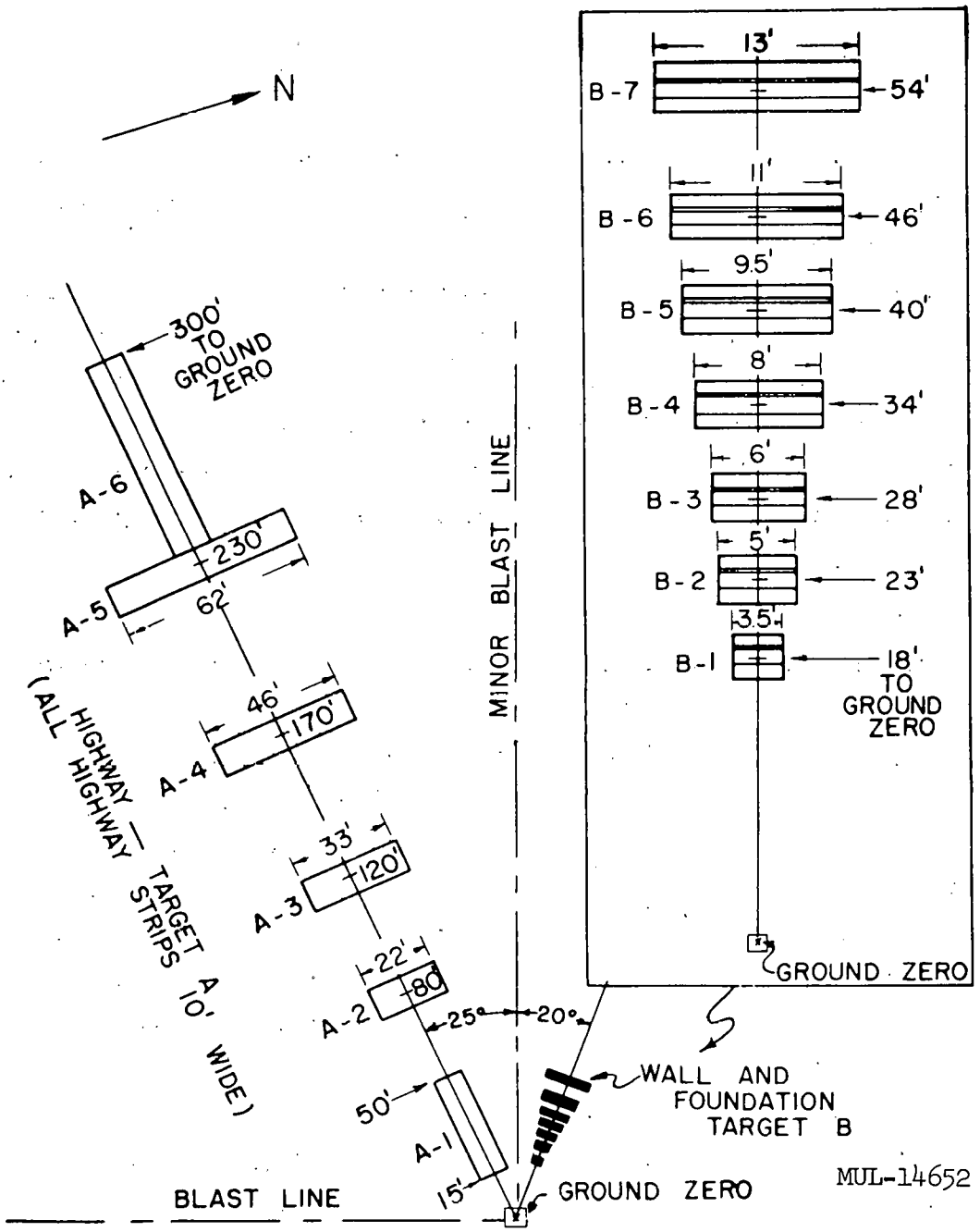

Fig. 3.1. Target (missile source) layout.

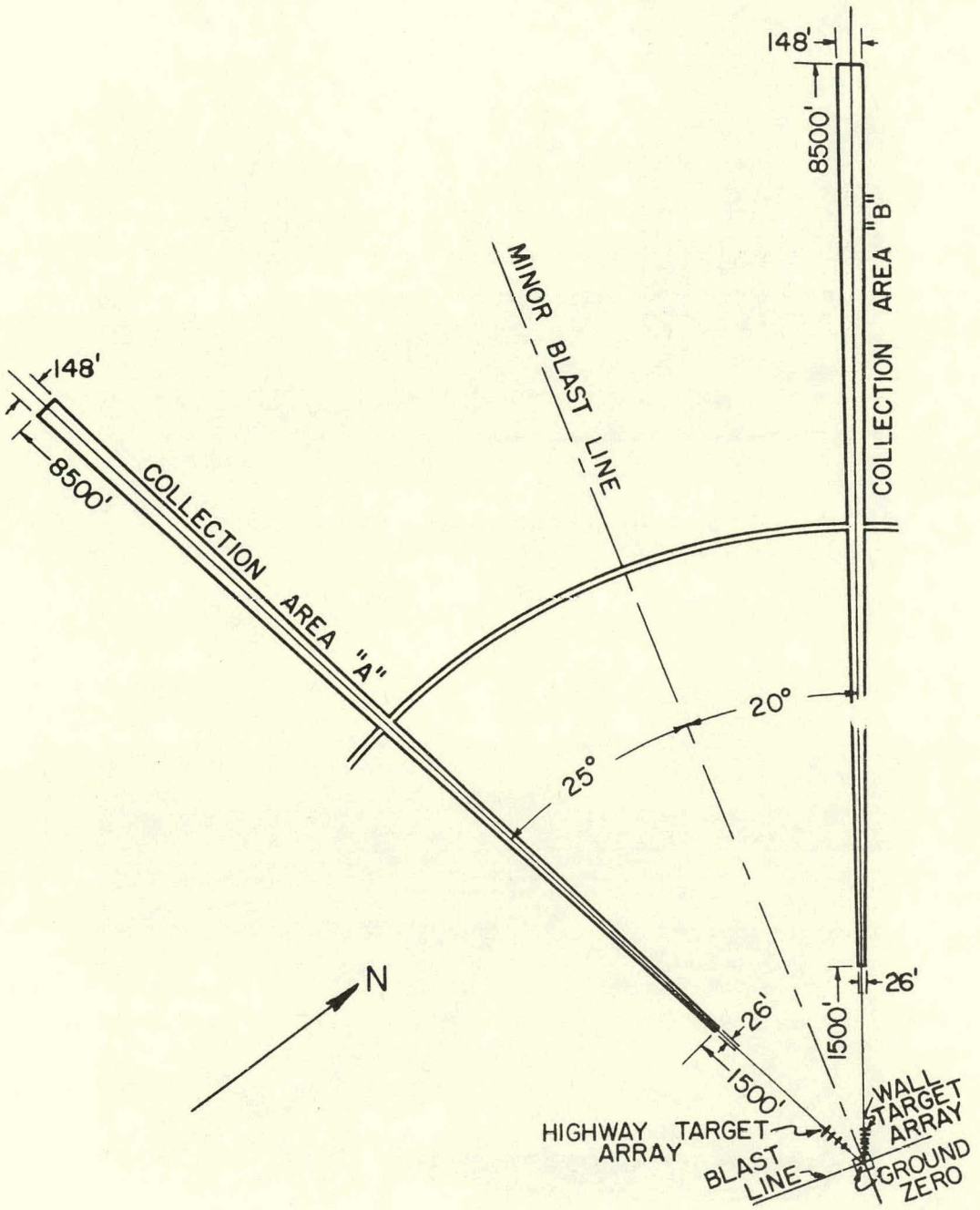

Fig. 3.2. Collection strip layout. MUL-14653

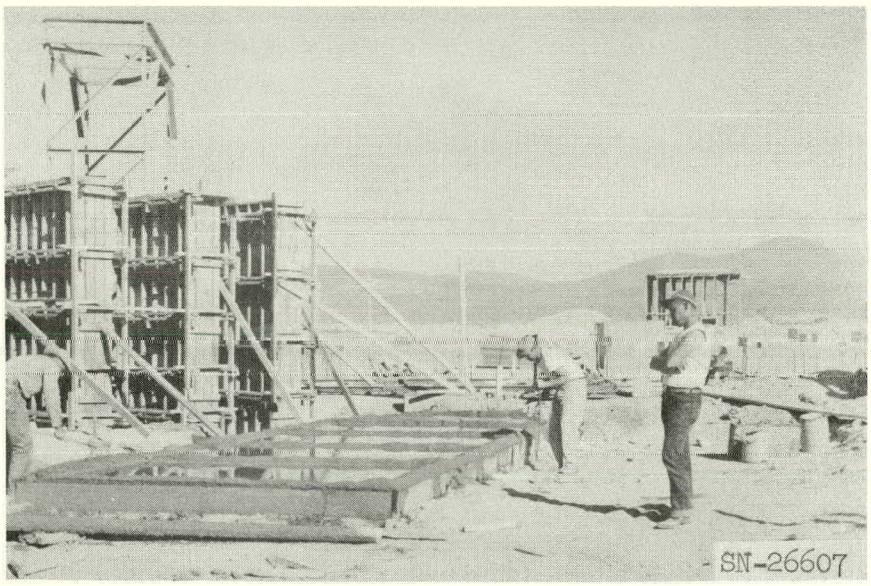

Fig. 3.3. Target A-1 in preparation.

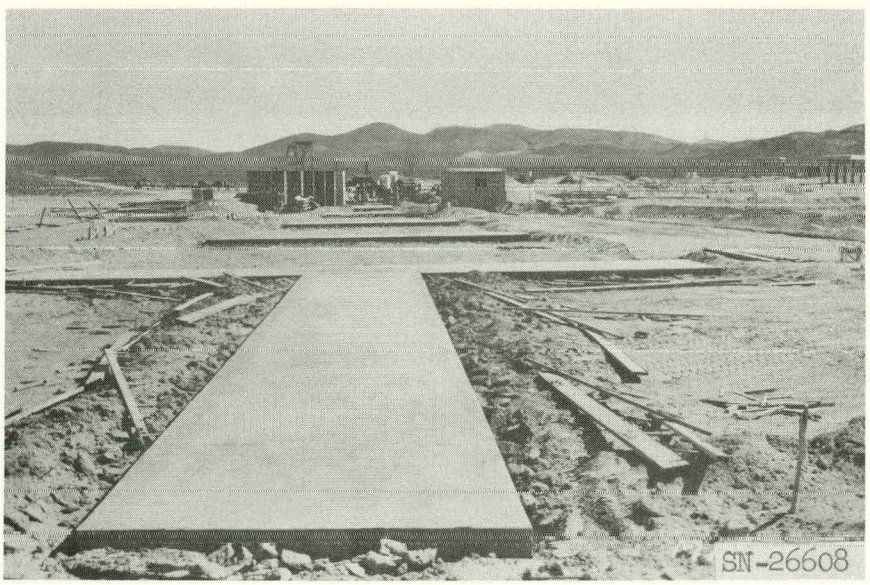

Fig. 3.4. View of highway and wall targets.

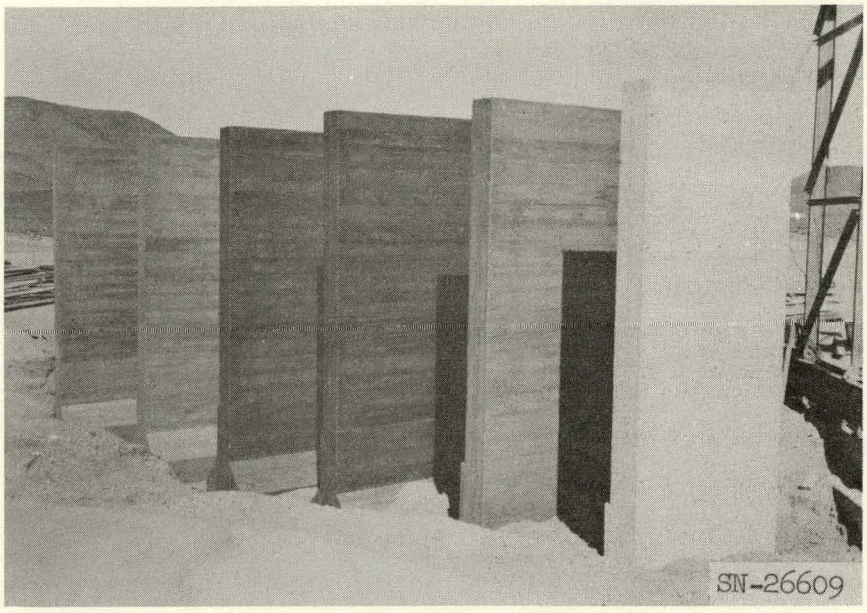

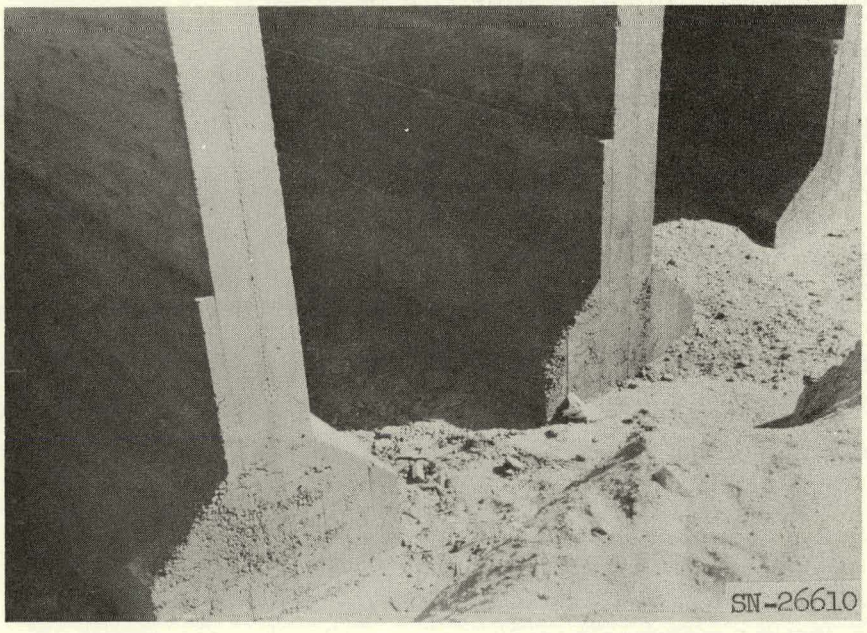

Fig. 3.5. Pigmented wall targets.

sections of this target. The remaining A targets (A2 to A5) were poured with the ordinary gravel aggregate used in all the construction at the site, and this aggregate was also used on all the walls which comprised the B targets, as shown in Figure 3.6.

Test samples were poured at the same time all these targets were placed and additional test samples were obtained by coring after the targets had been in place for at least 28 days. All these test samples were given compression tests by the Pittsburgh Testing Laboratory and all were found to have strengths in the range 3000 to 4000 psi (California State Highway Specifications require 3000 psi in primary highways). These tests demonstrated that the special aggregate (brick and aluminum nails) used in the A1 targets had no effect on the compressive strength under slowly applied load. However, the possibility that they may have affected adversely the strength when subjected to shock loads cannot be neglected.

The collection areas were laid out as specified in Figure 3.2 and then cleared, leveled, and oiled. Both collection areas extended from 1500 feet to 8500 feet in radius. They were surveyed with marked stakes on each side of each collection area at 100-foot intervals in radius.

The construction of the targets and the collection areas was accomplished precisely as specified, and the fact that after the test it became apparent that a somewhat different design of experiment would have given more information implies no criticism of the AEC Field Office or the contractor.

3.3 Postshot Operations

After the shot, missiles of diameter larger than 2 inches and less than 12 inches were collected. Visual observation made it apparent that the total number which actually landed on the collection strips was much smaller than had been expected and so missiles as far as 50 feet to the sides of collection strip B were also noted and, in many cases, collected, in order to increase the total number available for analysis.

Collected missiles were placed in labeled containers and shipped to NRDL, Hunter's Point, for later weighing on December 20, 1951.

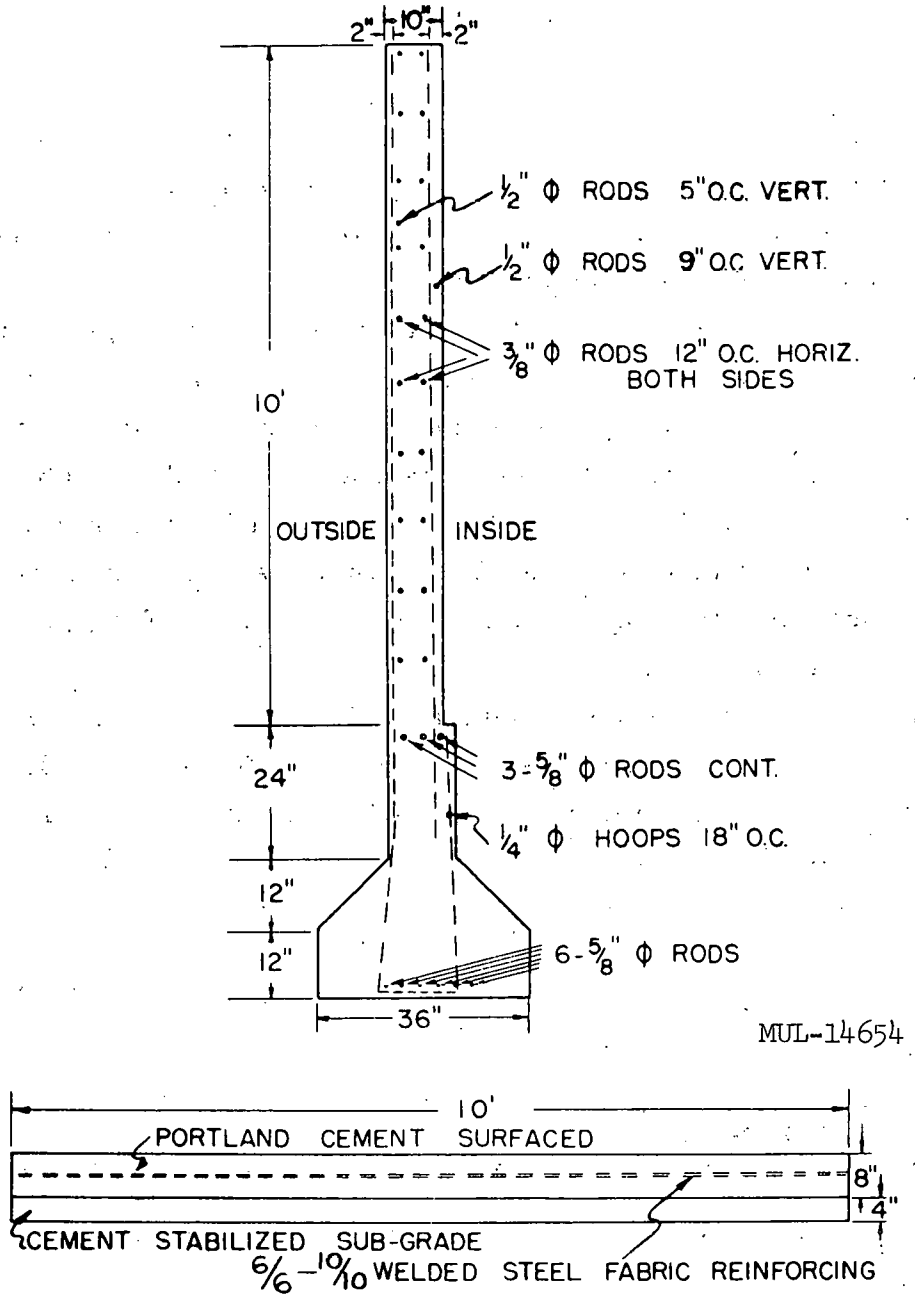

Fig. 3.6. Specifications for wall and highway target construction.

Later analysis disclosed that the large missiles from the white slab at r_0 = 80 feet which fell closer to ground zero than the beginning of the collection strip were of special interest, and so an actual survey of these was made on April 14, 1952.

RESULTS

4.1 General

An over-all survey after the shot revealed a very low density of missiles on the collection strips with almost none beyond a range of 3300 feet.* By and large, the missiles found between 1500 feet and 3300 feet were originally between 30 feet and 50 feet from ground zero.

On the A strip about 20 missiles were collected at ranges between 1500 and 3000 feet. These are shown in Table 4.1. As indicated, most of these were yellow, with the brick aggregate and aluminum nail content identifying them as from source A-1-e. All these missiles were badly fractured and crumbly. It is presumed that the shock actually produced failure in many fracture planes but the missiles hung together during their ballistic flight because of slight geometrical interlocking of the fracture surfaces. Examples are shown in Figures 4.1, 4.2, and 4.3.

Only about 15 missiles were found actually on the B collection strip. It was therefore decided to collect missiles some 50-60 feet to the left and right of the strip as well.** This yielded a total of about 130 and permitted some more detailed analysis. Table 4.2 is a description of the collected missiles from wall sources and Table 4.3 shows their range distribution. Examples appear in Figures 4.4, 4.5, 4.6, and 4.7.

---

* The exceptions were a 792-gram yellow missile at 3350 feet; a 1500-gram black missile at 3500 feet; a 578-gram yellow missile at 4150 feet; a 5000-gram yellow missile at 5380 feet; and a 10,000-gram red missile at 5500 feet.

** Throughout this report, left and right are specified as the directions when viewed from the charge.

TABLE 4.1

Size Distribution of Missiles Recovered on Collection Strip A.

	Size Categories*			
a: 100-400 g	b: 400-700 g	c: 700-1400 g	d: 1400 g up	

Range	Missile Color and r_0											
	Green (23 feet)				Black (34 feet)				Red (41 feet)			
(100's of feet)	a	b	c	d	a	b	c	d	a	b	c	d
15-16	1								4			
16-17									8			
17-18												
18-19												
19-20												
20-21												
21-22												
28-29												

Range	Missile Color and r_0											
	Yellow (47 feet)				White (80 feet)			
(100's of feet)	a	b	c	d	a	b	c	d
15-16	3		1					
16-17	3							
17-18	3		1					
18-19			1					
19-20		1						
20-21								
21-22			1	1				
28-29				1				

* Corresponding sizes are: 100-400 g, 400-700 g, 700-1400 g, 1400 g up.
Diameter (inches): 1.7-2.8, 2.8-3.3, 3.3-4.2, 4.2 up.

TABLE 4.2

Size and Number of Missiles Recovered from Wall Target Sources

Color of Wall	White	Green	Black	Red	Yellow	Blue
Average Original Distance from Ground Zero	19 feet	24 feet	30 feet	36 feet	42 feet	50 feet
No. missles collected	0	4	7	15	5	102
Av. wt of " "(grams)	0	266	227	252	1275	1175
Total wt " " "	0	1065	1589	3782	6374	119,828
Smallest wt picked up (grams)	0	77	30	26	29	85
Largest wt found (grams)	0	436	806	677	5000	11,800

TABLE 4.3

Number of Missiles Recovered from Wall Target Sources*

a: 100-400 g	b: 400-700 g	Size Categories c: 700-1400 g	d: 1400 g up

Wall Color (r_0)	White (19 feet)				Green (24 feet)				Black (30 feet)				Red (36 feet)				Yellow (42 feet)				Blue (50 feet)			
Size	a	b	c	d	a	b	c	d	a	b	c	d	a	b	c	d	a	b	c	d	a	b	c	d
Range in 100's of feet																								
15-16	2				1								2								3	3	3	
16-17	1												1								5	3	1	
17-18	1								3				3								3	5	2	3
18-19													1								7	5	3	2
19-20																					2	3	7	2
20-21													1								5	3	1	2
21-22									1				2								3	1	1	1
22-23																	1				2		2	7
23-24													2				1				2	4	1	1
24-25					3	1							1				1						1	2
25-26									1					1							1		1	1
26-27																							2	1
27-28									1				1	1			2	1					1	3
28-29														1			1							
29-30																								
30-31									1					1				1						1
31-32																								
32-33										1							2							2
33-34																		1						
34-35																								
35-36										1														
36-37																								
37-38																	1							
41-42																	1							
48-49																	1							
53-54																		1						
55-56															1									

* Collection area = approximately a 5° sector, including Collection Strip B (1°).

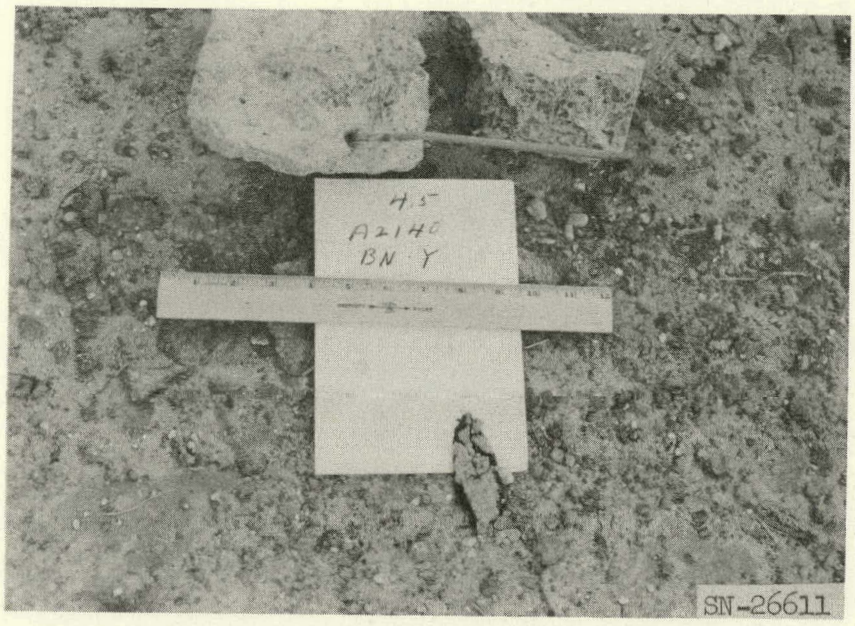

Fig. 4.1. Highway missile, recovered at 2140 feet; originally at 45 feet.

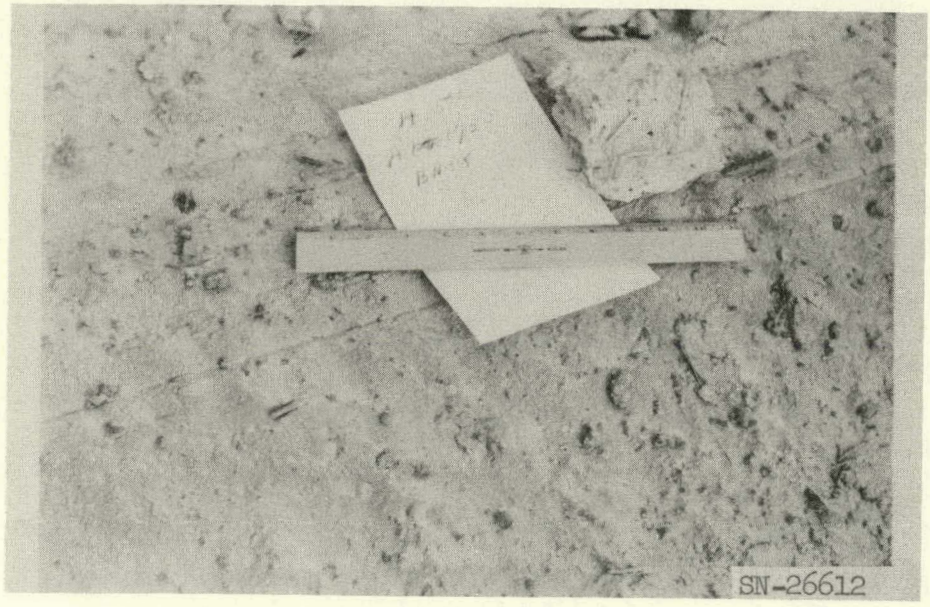

Fig. 4.2. Highway missile, recovered at 1750 feet; originally at 45 feet.

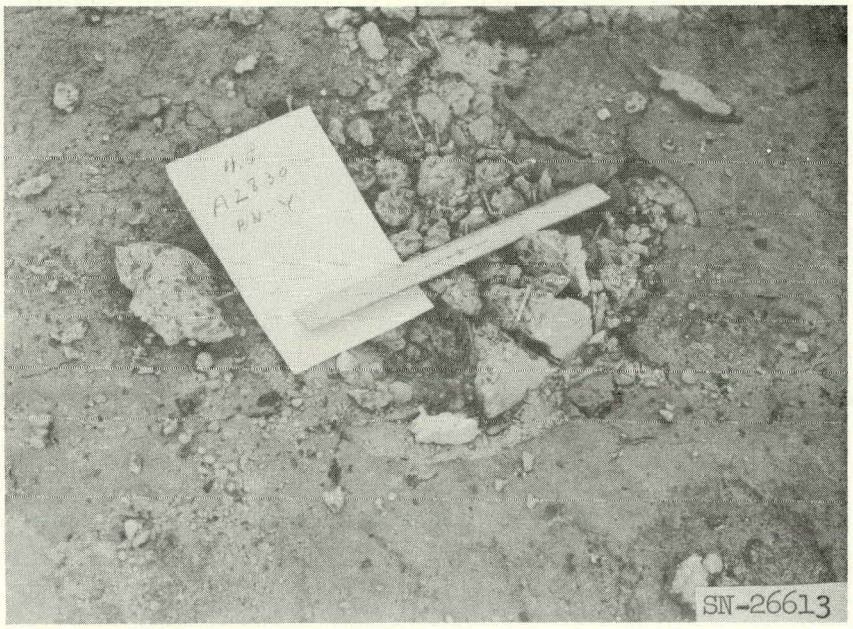

Fig. 4.3. Highway missile, recovered at 2830 feet; originally at 45 feet.

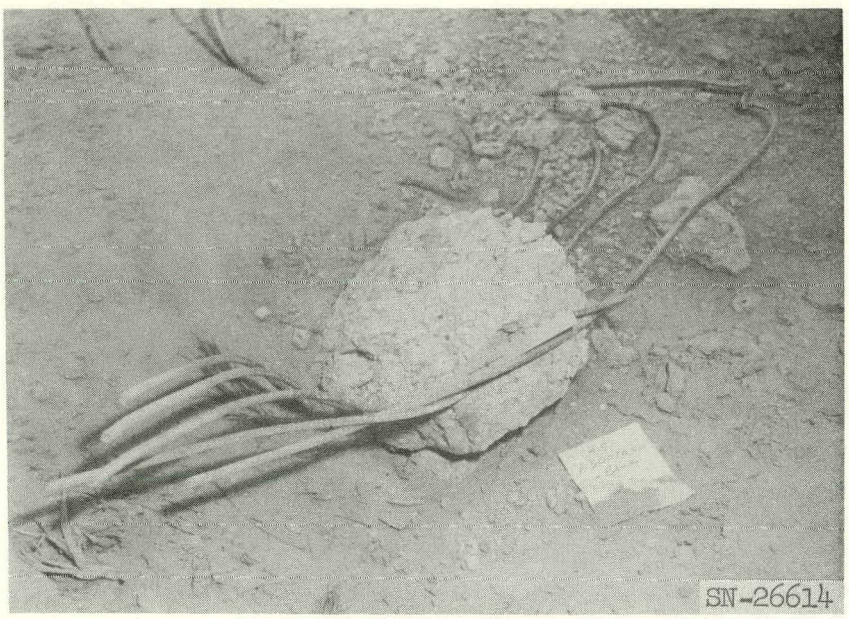

Fig. 4.4. Wall missile, recovered at 4001 feet, about 50 feet to right of collection strip; originally at 50 feet. Note twisted but unbroken reinforcing.

Fig. 4.5. Wall missile, recovered at 3350 feet, to left of collection strip; originally at 42 feet.

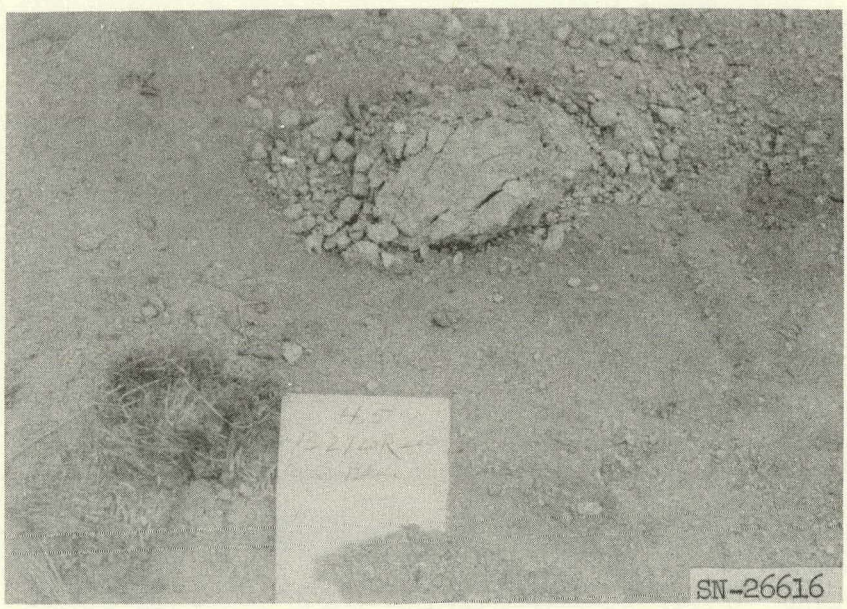

Fig. 4.6. Wall missile, recovered at 2720 feet, 200 feet to right of collection strip; originally at 50 feet. Note friability.

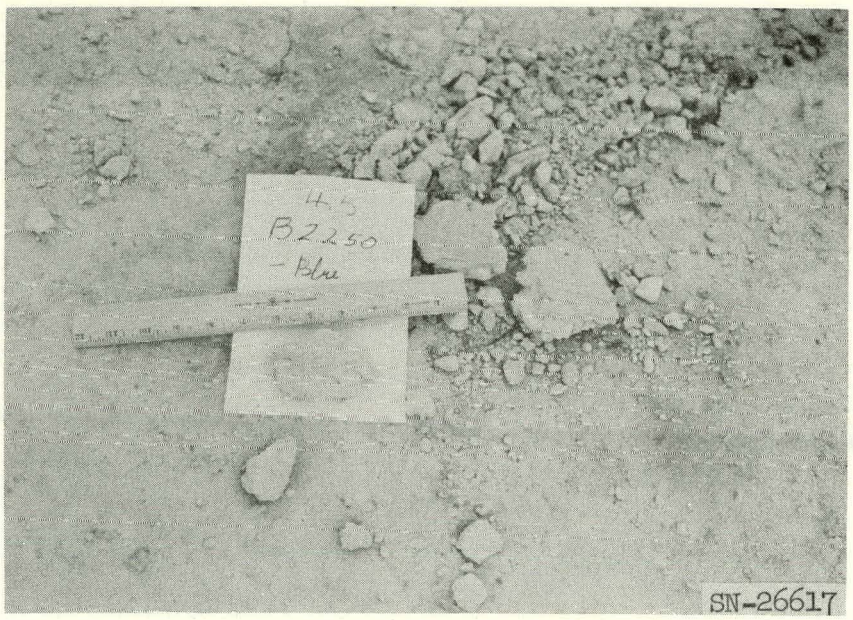

Fig. 4.7. Wall missile, recovered on collection strip at 2250 feet; originally at 50 feet. Note extensive fracture.

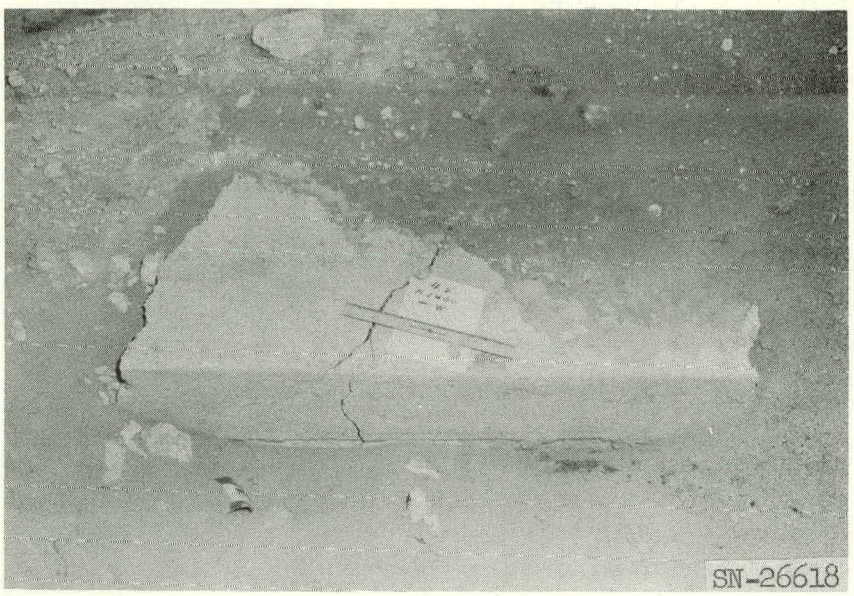

Fig. 4.8. Highway missile, found at 1400 feet; originally at 80 feet.

A sketch showing the location (as determined by stadia survey) of large missiles from white slab A-2 is shown in Figure 4.9. Photographs of several of these large pieces of slab appear in Figures 4.8, 4.10, 4.11, and 4.12. The three corners which were identified are of special interest because they are the only missiles whose origins can be precisely located within a target. These provide a means of checking the variability both in lateral location and range. If a terminal location of each corner is predicted on the assumption that its flight was in a radial plane in accordance with the ballistic behavior of such missiles as predicted by Paxson,* then the deviations from their predicted locations are as follows (refer to Figure 4.9):

Corner a, 250 feet long, 0.5° left ;
Corner b, 175 feet short, 4.5° left ;
Corner c, 125 feet short, 4.9° right ;
Corner d, not found .

These deviations are believed to represent the uncertainties to be expected of missiles from underground explosions. Deviations of the same order were observed at Dugway.

4.2 Summary

a. Almost all the missiles recovered originated in the three targets having initial locations between 40 feet and 85 feet from ground zero. Less than 5% of the nearer targets (40 to 50 feet) is accounted for in the missiles recovered, while more than 70% of the farther target (75 to 85 feet) is accounted for. Apparently most of the source material within a radius of about 50 feet of ground zero was either vaporized or pulverized to such fine sizes that it was carried by winds, whereas material beyond 85 feet had such short flight that it was covered by the throwout material around the crater rim.

b. The resulting missiles were thrown to distances between 400 feet and 3300 feet from ground zero. The nearer targets were thrown to the greater

---

* "The Trajectories of Surface Fragments Subsequent to an Underground Explosion," E. W. Paxson, Report RM-743, The RAND Corporation, Santa Monica, California, December 1951.

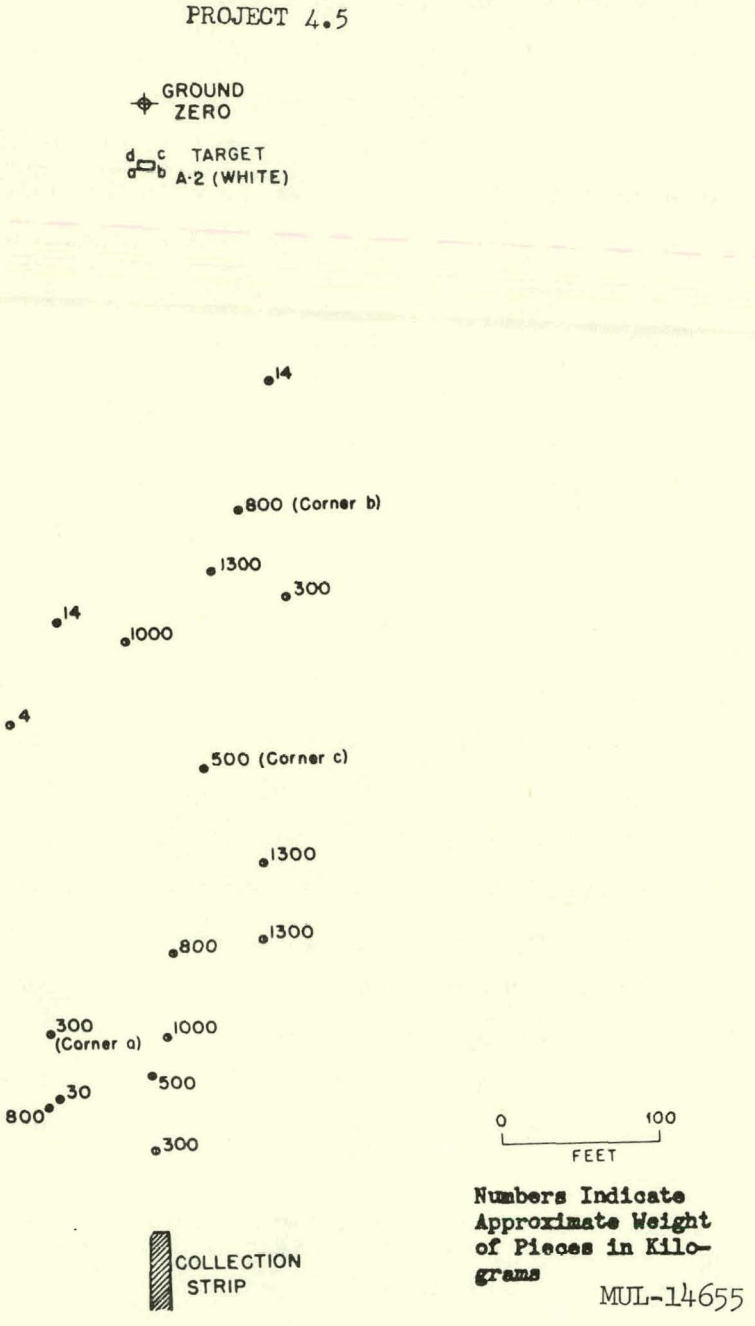

Fig. 4.9. Sketch of location of missiles from white highway slab, target A-2; originally at 75 feet to 85 feet.

Fig. 4.10. Highway missile, found at 800 feet; originally at 80 feet.

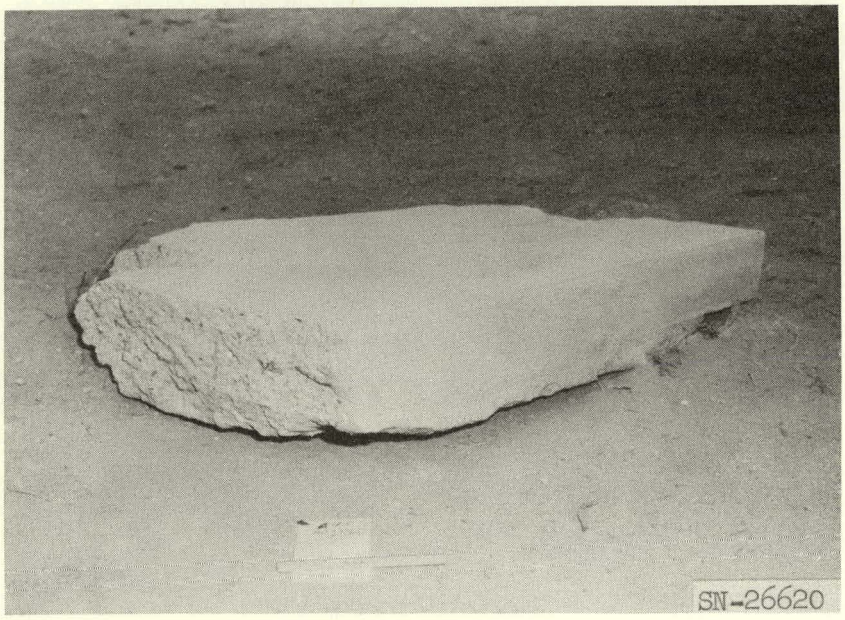

Fig. 4.11. Highway missile, found at 1000 feet, about 100 feet to left of center line; originally at 80 feet.

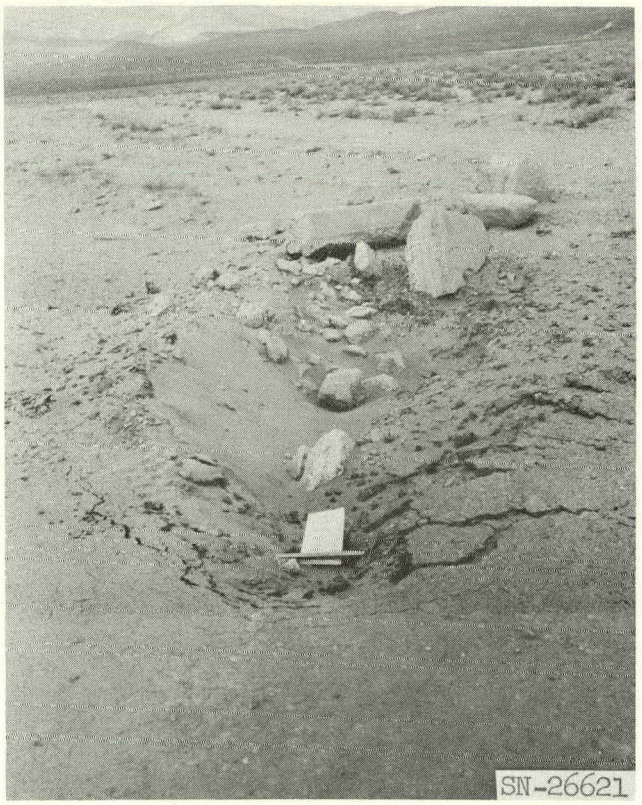

Fig. 4.12. Highway missile, found at 1200 feet; originally at 80 feet.

ranges; missiles from these sources were all smaller than about 6 inches. The farther target produced very large missiles (up to 5 feet) which were thrown to locations between 400 feet and 1500 feet.*

DISCUSSION

5.1 Interior Ballistics

The formation of missiles is the most important element in interior ballistics. The breakup of materials such as is produced in rock crushers has occasioned a great deal of study. It seems clear that a single blow should be expected, in a statistical sense at least, to produce a whole range of sizes and most of the published work is aimed toward the analysis or prediction of the distribution of sizes so produced. Enough contradictory publications have been found so that the technical situation for present purposes is definitely not clear. However, both experimentally and from the literature it is plain that missile source material very close to an explosion will be broken into small pieces, while missile source material at great distances will be broken into large pieces or not at all. Superimposed on this over-all picture, however, is the expectation that at any one radius a wide range of sizes will be produced.

Some impression of the way these sizes are thought to be distributed can be obtained from Figure 5.1, in which the log-log of the reciprocal of the percent of total weight of missiles (from a given source) larger than a specific size is plotted against the log of the created surface area for that size. Theoretically, a slope of 0.5 is predicted for such data on the basis of the "Ideal

---

* It should be remembered that the missile sources at JANGLE were not continuous. It is believed that if the intervening spaces (50 to 75 feet and 85 to 115 feet) had contained missile source material, the behavior of the resulting missiles would have been intermediate to that described above and that the concentration of falling missiles would have been considerably greater, particularly at the shorter ranges.

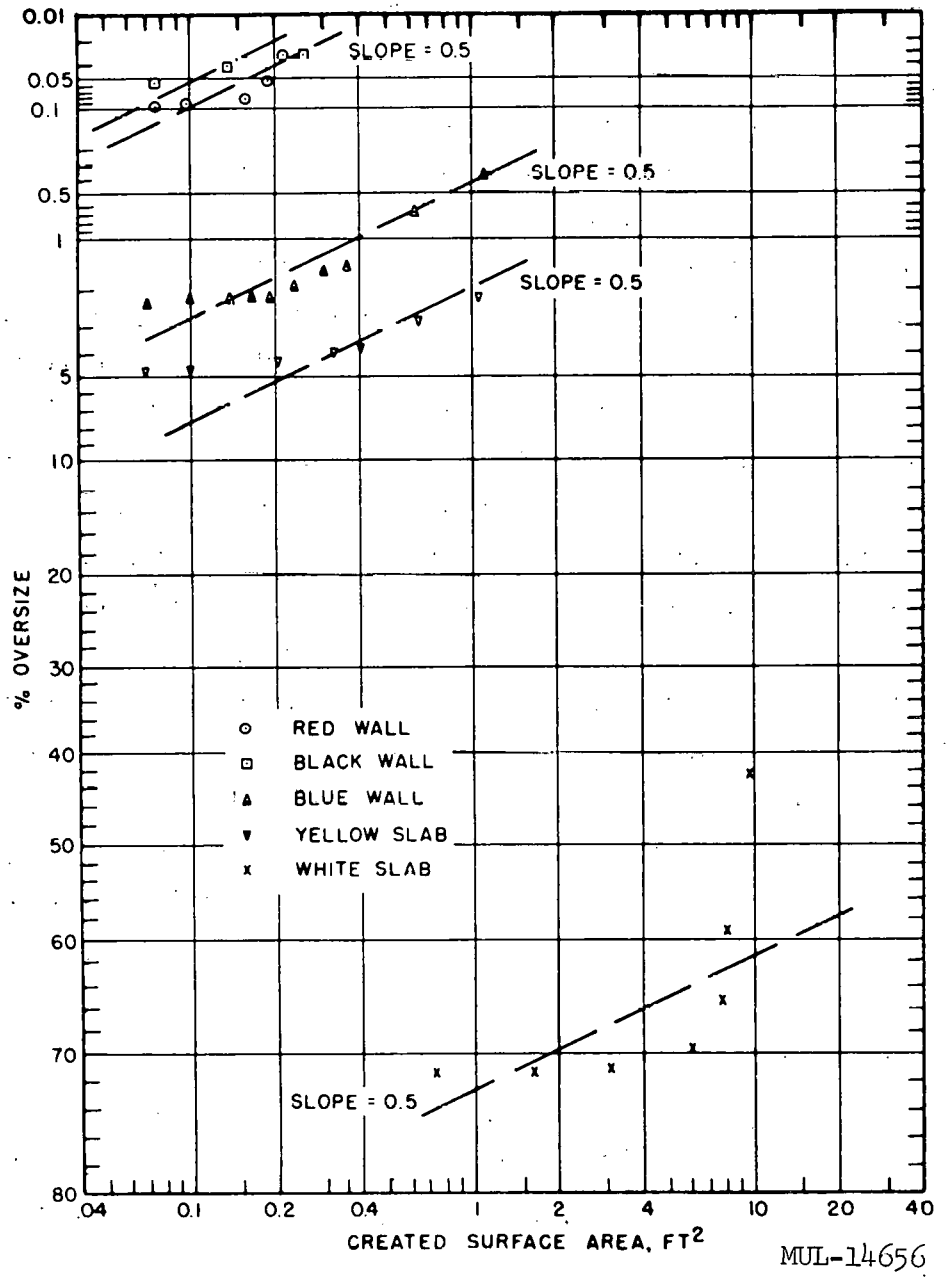

Fig. 5.1. Size distribution of missiles. Theoretical slope = 0.5.

Breakage Law"* and, in experimental situations where the original material is completely collected and accurately measured, excellent fit is usually obtained. At JANGLE, small sizes were not collected at all, and large sizes are always expected to deviate because there is not an infinitely large amount of available material. Thus, all that can actually be stated is that the JANGLE data do not preclude the possibility that the breakup of concrete source material caused by a nuclear shot obeys the same laws as does coal in a mine or ore in a crusher.

As a minor part of the interior ballistics or early behavior of missiles the high temperature close to the explosion is of interest. It appears probable that an important fraction of missile source material is vaporized and in addition small fragments are still further reduced in size by the high temperature; some fragments of size 1 inch to 6 inches show a great loss in strength as well as change in color (note Figure 4.6). These effects are probably due to the high temperature. The over-all result of this high temperature is to reduce the damage caused by missiles. This is true because that part of the missile source which would otherwise be thrown out with any but small elevation angles is instead vaporized and hence airborne.

The final aspect of interior ballistics to be considered is the initial velocity which is imparted to missiles. As a result of the Dugway experiments it was concluded that missile velocities are related to the elevation angles of exit approximately by the relation $v = V \sin^2\theta$, where v is the initial velocity of the missile, V is the velocity of the earth directly over the charge, and θ is the elevation angle of the slant radius from the charge center to the missile. However, in extrapolating to the JANGLE shot, it must be noted that the missiles of importance at JANGLE were those which had very small values of θ, while the Dugway missiles to which most attention was directed in developing the equation were relatively high angle missiles. In fact, the low angle missiles at Dugway deviated rather significantly from this relation.

---

* "Broken Coal II," J. G. Bennett, B. L. Brown, and H. G. Crane, J. Inst. Fuel 14, III (1941). The "Ideal Breakage Law" specified is

$$M(x) = 1 - e^{-x/\overline{x}},$$

where M is the fraction of the total weight in pieces smaller than size x, and $\overline{x}$ is the "characteristic" size.

A further assumption made at Dugway needs reconsideration in extrapolation of the JANGLE results. This is the assumption that the initial velocity of missiles is along the slant radius from the charge center to the initial location of the missile source. Both photographic evidence and analysis indicate that at least in the later stages of the throwout process there is a scouring action by which material originally lower than the charge center is thrown out around the lip of the crater. This material undoubtedly has a greater elevation angle than that indicated by the slant radius. Presumably missiles which are originally on the surface are thrown out at an earlier stage in the process and hence this consideration may not be pertinent.

Finally, it is entirely possible that the gross differences in soil characteristics at Dugway and at JANGLE may have important effects on many aspects of missile formation and ejection.

5.2 Exterior Ballistics

The behavior of missiles after they have left the immediate vicinity of an underground explosion has been established by the experiments at Dugway and at JANGLE with a reliability which is probably adequate in view of the gross uncertainties in the interior ballistics. Figures 5.2 and 5.3 are elevation drawings of the highway and wall targets. The missiles of a size to be of military importance at JANGLE all had elevation angles less than 20° and initial velocities less than 600 feet per second. For this group of missiles the air drag is not of major importance and calculations based on vacuum ballistics would be almost adequate. The most important consideration is that trajectories are very flat and the maximum height of the missiles is less than 200 or 300 feet.

Considerable support for the practical accuracy of both the breakup and range assumptions was derived from a detailed analysis carried out on missiles from the blue wall. In outline, the analysis consisted of the following steps:

a. Data on the 102 blue missiles were plotted, number vs size.

b. The curve so obtained was assumed to apply to the whole wall.

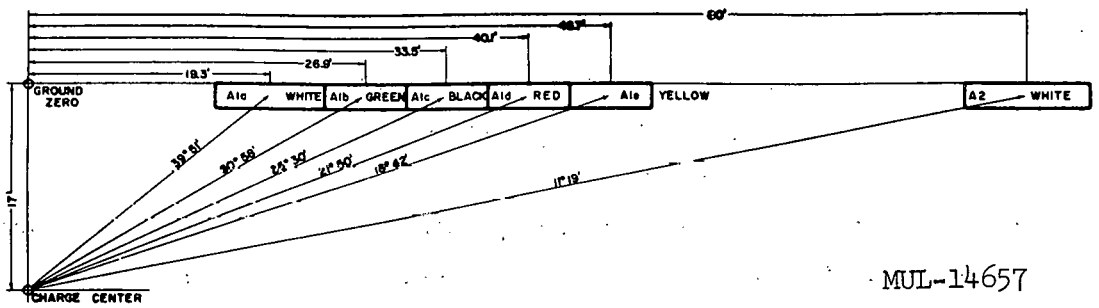

Fig. 5.2. Elevation of highway slab targets A-1 and A-2.

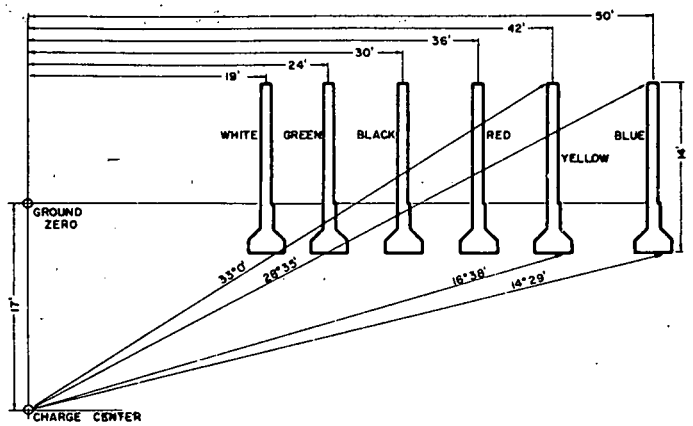

Fig. 5.3. Elevation of wall targets.

c. The mass of the wall (in the 5° sector from which missiles were collected) was calculated for each 1° increment of θ from the bottom to the top, taking into account the dimensions of the wall. (See Figure 5.3.)

d. This mass was divided into four weight categories (of equal numbers of missiles) according to the distribution described in "b" and the probable range determined for each weight group in each 1° θ-interval.

e. The predicted relative concentration of each size at each range was then plotted.

f. This plot was compared with that for the missiles actually picked up. Figure 5.4 shows this comparison between calculated and actual distribution for the largest weight category.

The coincidence seems remarkably good: A double-peaked distribution for each size was predicted, with one peak occurring inside the 1500-foot minimum for the collection strip and the other peak occurring on the beginning of the strip. The first peak could not be checked, of course, but the second, in the case of the two weight categories analyzed, actually occurred within 200 feet of the location predicted by the analysis.

Since the total weight of the blue missiles picked up was only about 3% of the weight of the wall in that 5° sector, it would not have been surprising if this small sample had behaved very differently from a prediction made for the whole wall sector.

5.3 Extrapolations

Since the causes of breakup are not well established, there is considerable uncertainty when one attempts to extrapolate the JANGLE results to a larger explosion. Specifically, one might assumc that it is the maximum energy density at a given point which is the determining factor in breakup. On the other hand, it might be argued that it is the peak acceleration produced in the soil which is crucial.

If one assumes that breakup depends on peak energy density (and it is believed that this is the most tenable assumption), then a missile source at a given scaled radius (λ_0) will be broken up into the same distribution of sizes

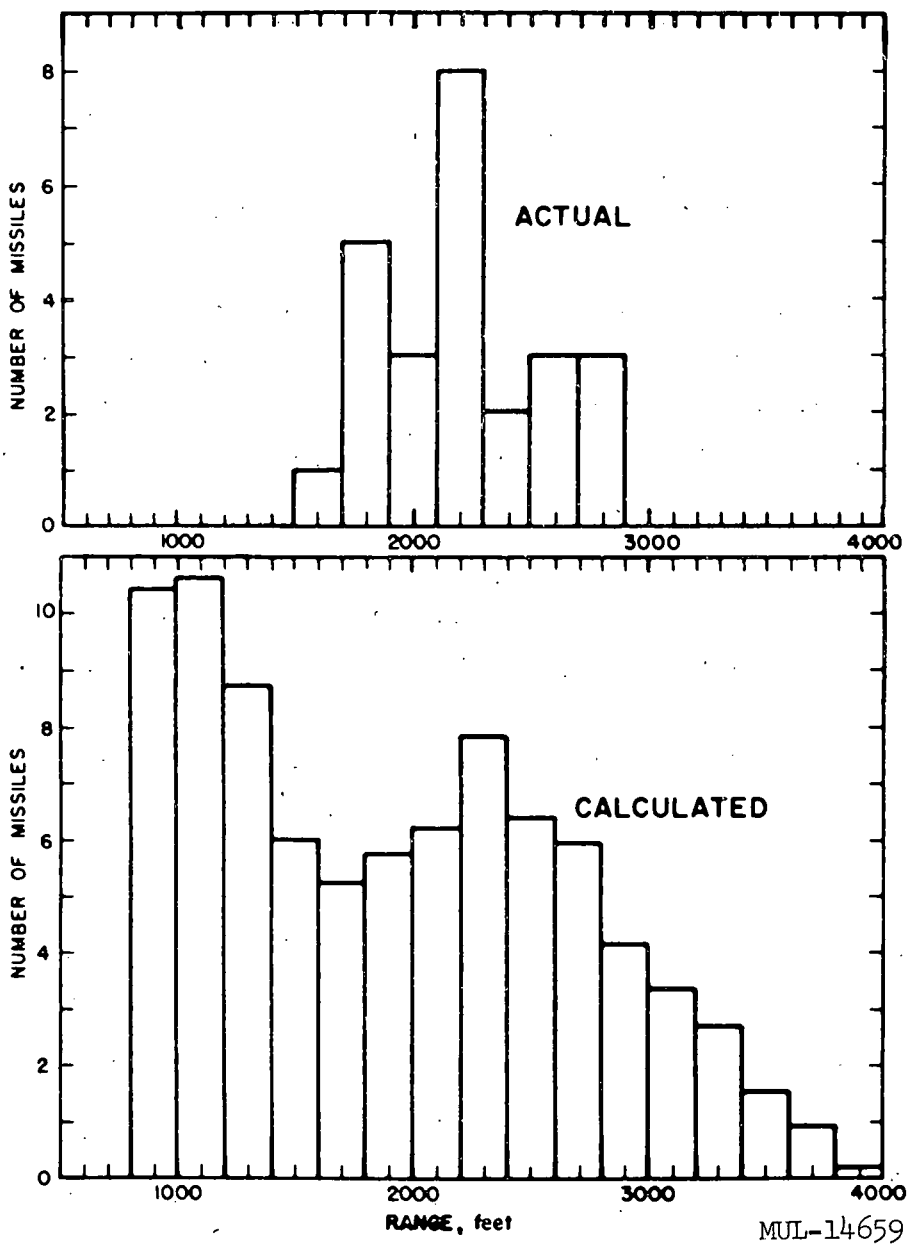

Fig. 5.4. Calculated and actual range distributions of large blue wall missiles.

on two scaled explosions (that is, where λ_c is the same). These missiles will have exterior ballistic flight identical to those at JANGLE. Since 1- to 4-foot missiles were thrown to distances of 1000 to 1200 feet from the rim of the crater at JANGLE, missiles of this size should then be found at the same actual distance from the new crater rim (not scaled) on any size explosion (at the same λ_c).

If breakup depends on peak acceleration, then when the JANGLE test is scaled up to an energy release S^3 times as large, missiles having a size of military importance will be produced at a smaller scaled radius than if the other assumption of breakup is made.* These missiles will have higher elevation angles and greater ranges (if they survive thermal destruction), but the density of missiles arriving will be very much less, both because the source of missiles is smaller (at a smaller radius) and because the interval of ballistic flight, and therefore dispersion, is greater due to the higher elevation angle.

5.4 Calculation of Potential Damage

The results of the JANGLE test have been studied and analyzed so as to obtain the firmest possible answers to two questions: First, what damage can be expected by missiles from a large underground explosion (and how does this compare to the damage produced by air blast or ground shock)? Second, should a missile experiment be included if another underground test is performed?

While it is not the purpose here to discuss in definitive terms the military aspects of the JANGLE experiment, it appears useful to outline the military context into which the conclusions of this experiment must fit.

---

* The scaled radius at which the peak acceleration is identical will depend both on scaling and on the fall-off of acceleration with radius in any explosion. By scaling laws $A_2 = A_1(1/S)$ where $\lambda_2 = \lambda_1$. If on any one explosion $A = k\lambda^{-n}$, then the acceleration will be the same on two scaled shots when $\lambda_2 = \lambda_1(S)^{-1/n}$. ($A = k\lambda^{-n}$ is based on experimental evidence.)

If $n = 2$ and $S = 3$ then $\lambda_2 = \lambda_1(3)^{-1/2} \approx 0.6\lambda_1$.

As was mentioned in the Introduction, the over-all function of the missile study was to assist in evaluation of the usefulness of an underground weapon versus an air-burst or surface-burst weapon. Three types of targets merit consideration in this connection (under the assumption that other types of targets are surely better attacked by air or surface bursts). These three are:

a. Deep fortifications,
b. Urban areas,
c. Air fields.

In attacking deep fortifications it seems clear that underground weapons are important. However, against such targets essentially no damage is produced by missiles and hence the evaluation of the missile situation is unimportant.

Against urban areas, particularly business or industrial areas, air-burst weapons are believed to give greater radius of important damage than underground bursts. If an underground weapon is detonated in such an area, there are sufficient buildings to constitute an important source of missiles, but by the same token there will be surrounding buildings which will absorb all of the low trajectory missiles early in their flight. High trajectory missiles, if they survive thermal destruction, would land at great distances and therefore at very low densities which would not be a source of important damage to buildings. Both because the air burst seems more effective and because the highly concentrated missiles formed from an underground burst will be stopped quickly, precision in the evaluation of the effectiveness of missiles against urban built-up areas is not warranted.

In attacking air fields the primary military objective is ordinarily to deny use of the air field for the maximum possible time. In general this requires gross damage to the airstrip itself. Secondary objectives may be destruction or damage to airplanes and surface buildings. To produce gross damage to an airstrip, an underground burst is undoubtedly the most effective weapon. In regard to the airstrip itself, the residual damage caused by missiles is altogether trivial. In regard to airplanes and buildings, the damage

due to missiles may be as large as or larger than that produced by ground shock or air blast. It appears that this is the only situation in which precise knowledge of missile behavior might be of significant value. Since missile damage to planes and buildings is still of secondary importance, it is doubted that the precise evaluation of such damage is worth more than a minor expenditure of effort.

Under some circumstances damage to planes or buildings may be the primary objective. In this case an air burst would be more effective and hence again precise evaluation of missile damage is not important.

5.4.1. Damage to buildings. Assessment of the damage to buildings produced by missiles involves several intangibles. Steel frame or concrete buildings may be pierced by large missiles but would probably not be damaged beyond easy repair unless more than one major column was buckled by impact with a large missile or unless the total momentum of material striking the building was sufficient to produce its collapse. Actually, in producing collapse, the total moment of momentum is probably more significant than the momentum itself, since in such cases failure may be expected to occur first at the bottom of the columns, and it is clear that the momentum of a group of missiles striking the side of the building near its top will produce twice the overturning moment that the same momentum of missiles striking the building halfway up will produce. On the other hand, the effect of missiles, particularly those with flat trajectories, will produce much the same forces as are produced by wind, and taller buildings are designed with greater resisting moments in the column joints.

The best means immediately available for estimating the total momentum of missiles required to collapse a building is contained in the Surface Structure Tests at Dugway.*

---

* Final Report, "Surface Structure Program, Underground Explosion Tests at Dugway," Stanford Research Institute. Prepared for Sacramento District Office, Corps of Engineers, U. S. Army, March 1952. CONFIDENTIAL SECURITY INFORMATION.

In these tests several structures collapsed as a result of the impact of throwout material. While the structures were far from typical buildings, they were intended to have roughly the same strengths, and while the missiles under discussion are considerably different from the throwout material at Dugway, it is believed appropriate to consider the total momentum the most important parameter. Looking at the Dugway experiments, it is estimated that Structures A, D, and E were struck with throwout having about three times the momentum required to produce collapse. By assuming (1) a frontal wall for these structures and (2) that one-third of the actual missile (or throwout) momentum was distributed over it, it is estimated that the momentum density required to produce collapse is roughly 150 slug feet per second per square foot.

Consideration of all the available information suggests that a peak of missile momentum density will always occur at the crater lip because, if source material is available there, it will have the lowest possible trajectory and therefore the greatest concentration. If the slant radius to the crater rim has an elevation angle greater than, say, 15° the trajectory will be high enough so that simple radial dispersal as well as elevational dispersal of the material there will quickly reduce its density below a critical level. However, if the crater size is such that the slant radius from charge to rim forms an angle of 15° or less with the horizontal, intensive missile damage can be predicted (assuming the presence of source material) in an area just outside the rim. This damage area increases with increasing charge size, but far less rapidly than the scale factor.

The results of the JANGLE experiment indicate that a peak of missile momentum density would probably have occurred at around 140 feet from ground zero (i. e., at the crater lip) if the highway slab had been continuous. This would have been about five times as much as necessary to demolish an ordinary building.

Beyond this peak the density could be expected to taper off so that at about 1000 feet from ground zero the density is only one-third the amount

necessary for severe building damage, with the critical distance being about 600-800 feet from ground zero. Peak air-blast pressure at 750 feet from ground zero was about 10 psi, which is also considered critical for ordinary buildings.

Extrapolation to an explosion having an energy release S^3 times as large, along with the assumption of breakup determined by energy density, results in the calculation of a maximum density of missile momentum at the rim of the larger crater which is roughly S times that for JANGLE, if S is of order 3 (that is, if $S^3 \approx 25$). Similarly it is expected that the critical distance for severe damage would now be of order 1100 feet from ground zero. This should be compared with 10 psi air blast predicted at 2250 feet from ground zero, or with 20 psi at 1100 feet. Thus buildings should be expected to sustain damage by the mechanism of air blast out to roughly twice the distance where they will sustain damage by the mechanism of missiles.

Extrapolation to a shot having S^3 times the energy release under the assumption that breakup depends on peak acceleration results in very similar conclusions. Here too, although breakup would be very different, the only location where missile trajectories would be flat enough to yield high concentrations of missile momentum would be again at the crater lip. Large pieces might be predicted to travel at velocities in the neighborhood of 100 feet per second essentially along the ground and to do considerable damage to anything in their paths nearer than 1000 feet or so. There is no evidence for this theory of breakup, however.

Comparison of the critical damage radius by missiles with the critical damage radius produced by ground motion was considered pertinent before the experiment, but has been found to be unimportant because the critical radius due to air blast from such shallow explosions is definitely larger than that due to ground motion.

5.4.2. Damage to airplanes. Since damage to airplanes may be a secondary objective of an attack on an airfield with an underground weapon, the effect of missiles in this regard needs to be considered. Several differences from the analysis of damage to buildings are at once apparent. Among these are:

a. Airplanes, particularly high speed planes, may sustain important damage as a result of impact by even a few relatively small missiles. Thus the momentum of missiles or momentum density is not an appropriate criterion of damage.

b. Airplanes around airfields are commonly protected by revetments, which are particularly effective against missiles having flat trajectories.

Thus under the assumption of breakup determined by energy density, the missiles at JANGLE to which attention was devoted for building damage would be ineffective because they would be stopped by the barricades. However, since it is possible that even missiles smaller than 2 inches might produce some damage to airplanes, analysis was carried on to estimate the incidence of individual missiles at much greater distances. Predictions are difficult because the smallest missiles were not extensively studied at JANGLE.

However, using all the available data, the ballistic curves developed from the Dugway experiment and from the RAND studies, together with the present knowledge with regard to scaling, it has been estimated that an underground nuclear explosion with an energy release about 25 times as large as that at JANGLE (S = 3) fired under a continuous concrete slab would produce very roughly the following missile concentrations at the specified ranges:

Underground Nuclear Explosion: S = 3 (JANGLE, S = 1), $\lambda_c = 0.15$

Approximate Number of Missiles Predicted to Fall in a 100-ft^2 Area

	Missile Size and Angle of Entry					
Range	Small		Medium		Large	
1700 feet	300	40°-50°	2	20°	1	13°
2200 "	75	45°	3	25°	1	14°
2700 "			1	40°	<1	14°
3200 "					<<1	25°

Typical wing area of planes is about 200 ft^2 for a single-engine plane to over 2000 ft^2 for a heavy four-engine bomber.

Small: 0.8 inch to 2.8 inches in diameter. Medium: 2.8 inches to 6.4 inches in diameter. Large: 6.4 inches to 30 inches in diameter.

These values must be considered in the light of extrapolated predictions for air-blast values on such a shot: 3 psi peak at 6000 feet and 8 psi peak at 3000 feet. On this basis airplanes should be expected to sustain damage by the mechanism of air blast out to roughly twice the distance where they will sustain damage by the mechanism of missiles.

The comparison of the critical damage radius due to missiles with that due to air blast may be modified by the effect of soil characteristics. Comparison of the air blast from HE-3 at the Nevada Site with Round 315 at Dugway (both 2560 pounds TNT at $\lambda_c = 0.5$) shows that the air blast at Dugway was roughly one-half that at Nevada. While comparative figures at other depths are not available, it seems obvious that the air blast due to charges on the surface ($\lambda_c = 0$) will be unaffected by the soil characteristics. From this presumption and the comparison just mentioned at $\lambda_c = 0.5$, it is felt to be safe to predict that the air-blast pressure produced by an underground explosion as shallow as $\lambda_c = 0.15$ will not be significantly affected by soil characteristics. Experimental information on this point will be obtained on programs currently in progress.

CONCLUSIONS AND RECOMMENDATIONS

6.1 Conclusions

It is concluded that an underground explosion having 25 times the energy release of the JANGLE underground shot at the same scaled depth of burial ($\lambda_c = 0.15$), fired beneath a continuous concrete runway 18 inches thick, would produce missiles which would seriously damage or destroy buildings out to a radius of about 1100 feet or airplanes on the ground out to about 3000 feet.

The same underground explosion would, as a result of air blast, produce major damage to buildings out to a radius of about 2200 feet and damage to airplanes out to a radius of about 6000 feet.

For still larger underground explosions the damage radius of missiles increases at a slower rate than the damage radius of air blast, which is proportional to $W^{1/3}$.

6.2 Recommendations

Further study of the missile problem is not justified unless corrections are found to be necessary in either (a) the discussion of military aspects contained in this report, or (b) the radius assumed here of significant damage to buildings or airplanes by the mechanism of air blast from underground explosions.

ACKNOWLEDGMENT

Acknowledgment is made to the Naval Radiological Defense Laboratory for transporting the samples from Nevada, and for making available facilities for weighing the samples.

Paper Q

BALLISTICS AND THROWOUT CALCULATIONS FOR THE LUNAR CRATER COPERNICUS

Eugene M. Shoemaker

U. S. Geological Survey

Menlo Park, California

ABSTRACT

Discrimination between lunar craters of impact origin and volcanic origin may be possible on the basis of the distribution pattern of the ejecta, a feature observable from the earth. The ejecta from a maar type of volcano (one whose crater resembles lunar craters) are almost invariably thrown out along high-angle trajectories, and shower down in a diffuse, more or less uniform, pattern around the crater. Ejecta from large impact craters, on the other hand, are expected (by analogy with nuclear explosion craters) to be thrown out along both high and low trajectories, leaving a pattern containing distinct streaks or rays. From the ray pattern and the trajectories of the fragments that form the rays (the exterior ballistics) it is possible to reconstruct the fragmentation pattern of the ground (the interior ballistics of crater formation).

* * *

One major feature of lunar craters observable from the earth that may permit discrimination between impact craters and volcanic craters is the distribution pattern of the ejecta. The ejecta from a maar type of volcano (a volcano whose crater resembles lunar craters) are almost invariably thrown out along high-angle trajectories, and shower down in a diffuse, more or less uniform, pattern around the crater. These trajectories are the result of entrainment of the fragments in the volcanic gas jets, which are predominantly vertical. The ejecta from large impact craters, on the other hand, are thrown out along both high and low trajectories.

The ejecta patterns around all known large terrestrial impact craters, beyond the immediate vicinity of the rim, have been destroyed by erosion. The general nature of the pattern to be expected, however, is revealed by the debris

deposited around nuclear explosion craters. Far-flung ejecta from nearly every shallow underground explosion crater, whether the explosion is nuclear or chemical, are laid down in distinct streaks or rays (Fig. 1). The position and shape of the rays are governed in turn by the pattern in which the ground breaks up as it is engulfed by shock. From the ray pattern and the trajectories of the fragments that form the rays (the exterior ballistics) it is possible to reconstruct the fragmentation pattern of the ground (the interior ballistics of crater formation).

Ray pattern of Copernicus. Many craters on the moon are surrounded by a system of rays resembling the ejecta patterns around nuclear- and high-explosive craters. The ray pattern of Copernicus is especially suited for detailed analysis. Copernicus is favorably located near the center of the lunar disk; the ray system surrounding the crater is not only widespread but also extends in large part over dark, relatively smooth maria surfaces. Many of the fine details of the system can therefore be deciphered (Fig. 2).

The crater itself is somewhat polygonal in outline (Fig. 3). It is about 90 kilometers across, and about 3500 meters deep, measured from rim crest to floor. The rim rises about 1000 meters above the surrounding lunar surface. The interior walls of the crater comprise a series of terraces, scarps, and irregular sloping surfaces that descend stepwise from the crest to the crater floor, a roughly circular area of generally low relief 50 kilometers in diameter. A few low peaks rise above the floor near the center of the crater.

The outer slopes of the rim are a scaled-up version of the outer slopes of the rims of the Jangle U and Teapot ESS nuclear-explosion craters. To a lesser extent the rim of Copernicus resembles the rim of Meteor Crater, Arizona. Rounded hills and ridges are combined in a distinctive hummocky array that consists of humps and swales without obvious alignment near the crest of the rim and passes gradually outward into a system of elongate ridges and depressions with a vague radial alignment. The relief of the ridges gradually diminishes until it is no longer discernible at a distance of about 80 kilometers from the crest of the rim. Beyond this distance the rim passes gradationally into the ray system.

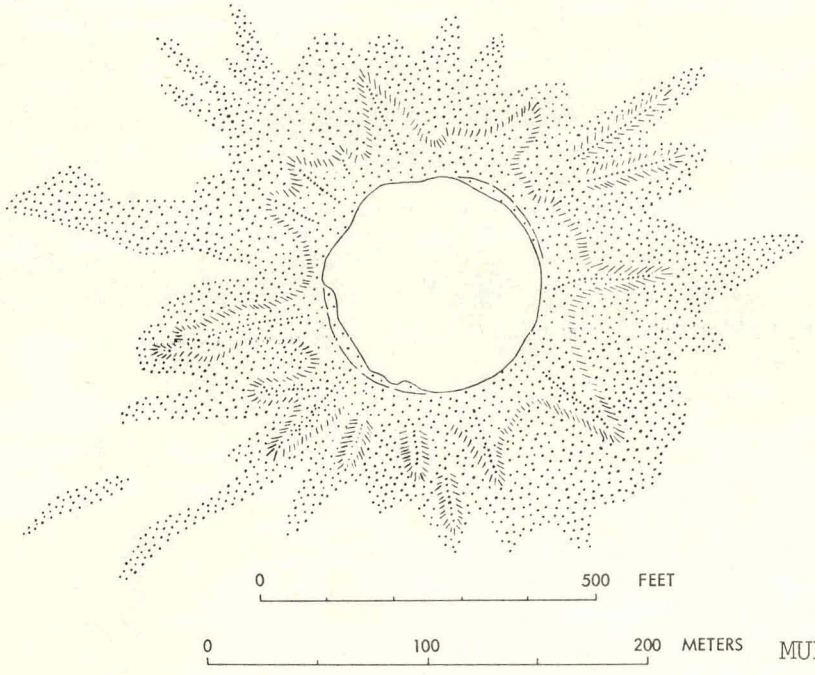

Fig. 1. Ejection pattern at Teapot ESS nuclear explosion crater.

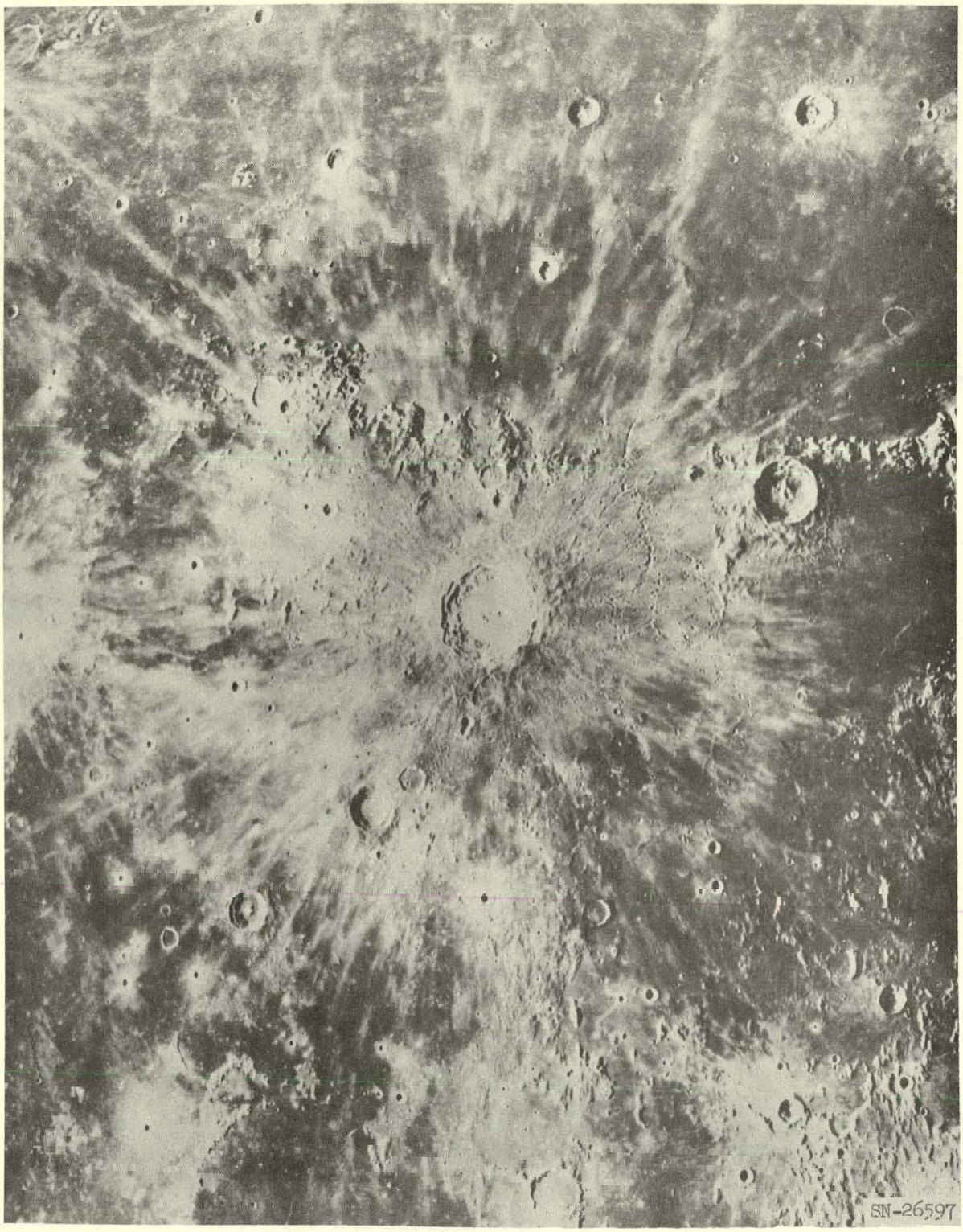

Fig. 2. The region of Copernicus (photograph by F. G. Pease, Mount Wilson Observatory).

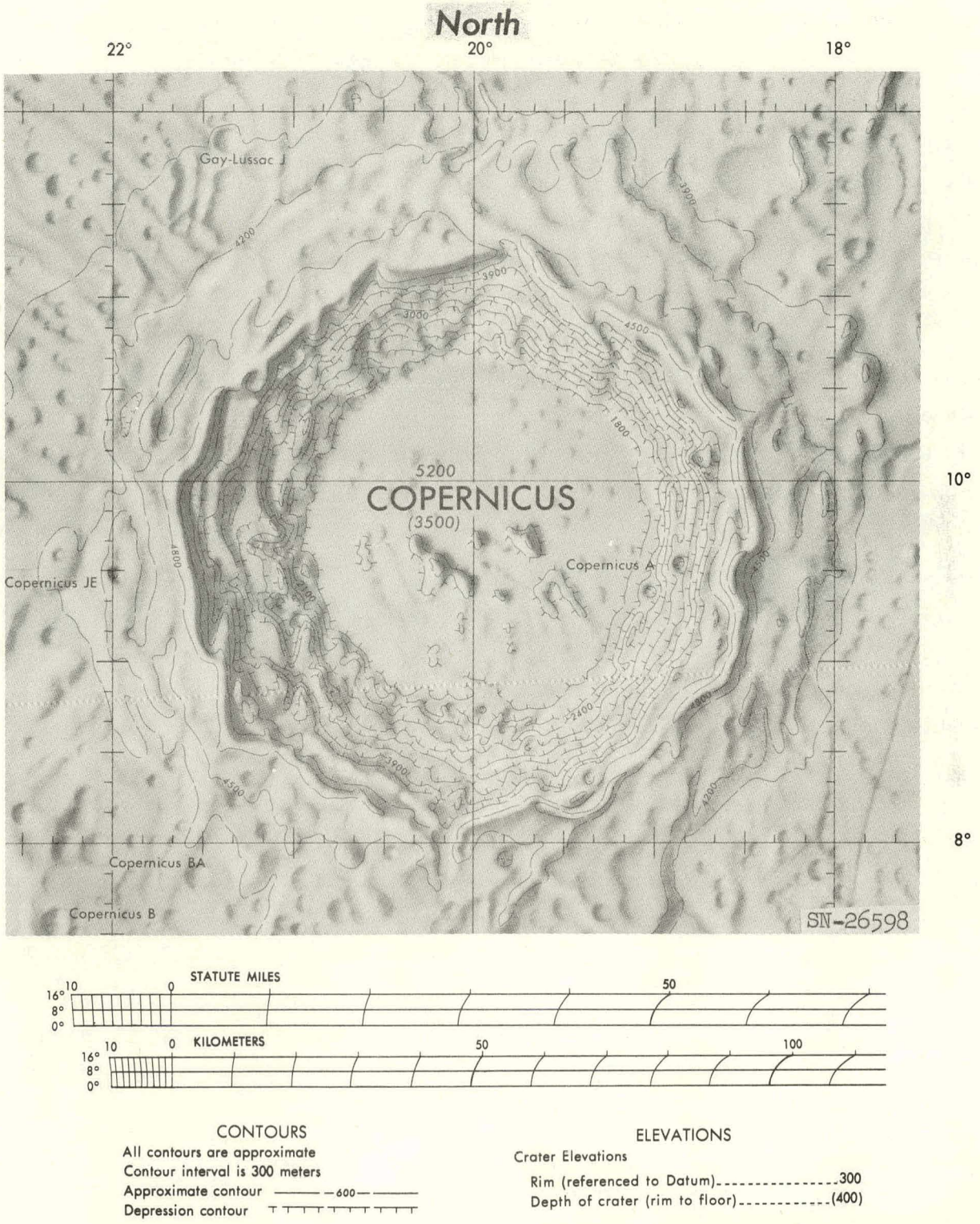

Fig. 3. Topographic map of Copernicus (from Lunar Chart LAC 58, Aeronautical Chart and Information Center, U. S. Air Force).

The ray system, which extends over 500 kilometers from Copernicus, consists mainly of arcuate and loop-shaped streaks of highly reflective material on a generally dark part of the moon's surface. In reflectivity characteristics, the rays are essentially an extension of the crater rim and cannot be sharply delimited from it. The major arcs and loops can be locally resolved into en echelon feather-shaped elements, ranging from 15 to 50 kilometers in length, with their long axes approximately radially arranged with respect to the center of the crater.

The pattern of the ray system roughly resembles the pattern of lines of force in a dipole magnetic field in a plane containing the dipole. The "dipole" axis of the Copernican rays trends northwest-southeast. Major arcuate rays curve away from the axis on either side, and a large closed elliptical loop extends southwest toward Mösting.* The ray system has a rough bilateral symmetry about a line coincident with the long axis of this loop, which is perpendicular to the "dipole" axis. Within the main loop extending toward Mösting are subsidiary loops. North of Copernicus are two so-called cross-rays. Both cross-rays consist of a series of vaguely defined loops linked end to end. Near or along the "dipole" axis the rays are mainly straight and radially arranged with respect to Copernicus; in some places, only individual feather-shaped ray elements are present.

Within the rays, and preponderantly near the concave or proximal margins of the major arcs and loops, are numerous elongate depressions or gouges in the lunar surface ranging in length from the limit of telescopic resolution to about 8 kilometers. A peculiar feature of the gouges is their alignment, which is radial from Copernicus in some places but is commonly at an angle to the radial direction. The alignment varies erratically from one gouge to the next. Visible depressions or gouges lie at the proximal ends of many ray elements, though there is not a 1:1 correspondence between gouges and distinguishable ray elements.

---

* The astronomical convention for east and west on the moon is opposite to the convention used for the earth.

It is commonly stated in the literature that there is no determinable relief of the lunar surface associated with the rays. This is not strictly true. At very low angles of illumination the moon's surface along the rays is visibly rough (see Kuiper, 1959, p. 289-291). The roughness is due, at least in part, to the presence of the gouges and very low rims around the gouges.

The interpretation is here adopted that lunar rays are thin layers of ejecta from the crater about which they are distributed. This interpretation dates back at least to the 19th century and is probably older. The gouges are interpreted as secondary impact craters formed by individual large fragments or clusters of large fragments ejected from Copernicus. Distinct ray elements are interpreted as splashes of crushed rock derived chiefly from the impact of individual large fragments or clusters of fragments. Partial verification of these interpretations is obtained if a full explanation of the ray pattern and associated gouges can be given in terms of the required ballistics.

In order to reduce the ballistic problem of the Copernican rays to a series of discrete points that can be treated mathematically, a compilation has been made of 975 secondary impact craters (Fig. 4). This is a conservative compilation and far from complete. The problem of compilation lies in finding the craters, many of which barely exceed the lower limit of resolution on good lunar photographs, and also in distinguishing secondary impact craters belonging to the ray system of Copernicus from other craters of about the same size that are common in this region. Three criteria were used to identify secondary impact craters, and the compilation includes only craters that satisfy at least two of these crateria: (1) markedly elongate shape, (2) shallow depth compared to most small craters outside of ray system, (3) absence of visible rim or extremely low rim. Most small craters in the region around Copernicus that fit these criteria occur in well-defined rays or ray elements, and nearly all such craters that do not lie in the Copernican rays appear to belong to another system of secondary impact craters around the major crater Eratosthenes. The identification of the secondary impact craters is based mainly on one photograph taken by F. G. Pease at the Mount Wilson Observatory, though other photographs from Mount Wilson and Lick Observatories were used as a check.

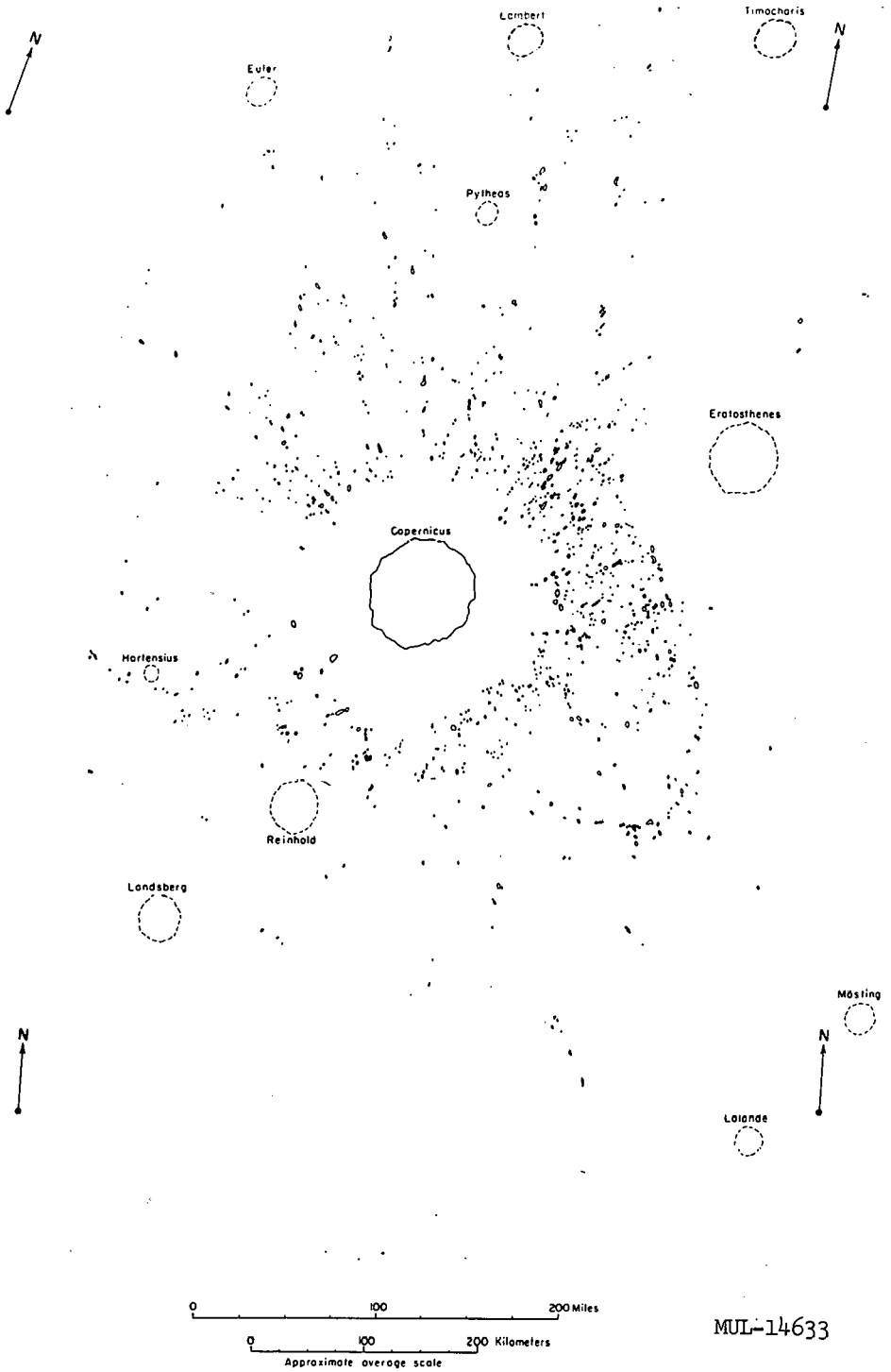

Fig. 4. Secondary impact craters in the Copernicus ray system.

Two deficiencies in particular should be noted in the present compilation. First, there is a gap in the area around Eratosthenes where no secondary impact craters have been plotted. This gap is due not to the absence of craters but to difficulty in distinguishing with certainty the secondary impact craters belonging to the Copernican ray system from craters produced by fragments ejected from Eratosthenes. All craters in the area around Eratosthenes have therefore been omitted. The second deficiency is a relative incompleteness of the compilation on the east side of Copernicus as revealed by the much lower areal density of craters in that area. This defect is due to the fact that in the principal photographs used for the compilation the terminator lay to the west of Copernicus and the small secondary impact craters can be distinguished with much higher confidence on the side nearest the terminator.

Ranges of all the secondary impact craters plotted on Fig. 4 were measured from the Mount Wilson photographs. The distance measured was from the tip of the centermost peak on the floor of Copernicus, which is almost precisely at the center of the circular crater floor, to the nearest point on the rim of each secondary impact crater. These measurements are strictly preliminary and have significant systematic proportional errors in certain directions. The purpose in making the measurements is simply to find the general nature of the fragmentation pattern that controlled the Copernican rays.

The frequency distribution of the secondary impact craters by range shows a sharp mode near 100 miles (about 160 kilometers) from the center of Copernicus (Fig. 5). At greater distances the frequency drops off rapidly, but the histogram reveals several subordinate maxima. Toward the outer extremity of the ray system the frequency drops gradually to zero. Coming closer to Copernicus from the modal distance, the frequency drops off very rapidly, owing to the fact that toward the main crater the gouges in the preexisting lunar surface tend to be covered up or smothered under an increasingly thick deposit of material making up the crater rim. The smothering effect begins about 80 kilometers from the edge of the crater, and from this point inward there is essentially a continuous blanket of ejecta.

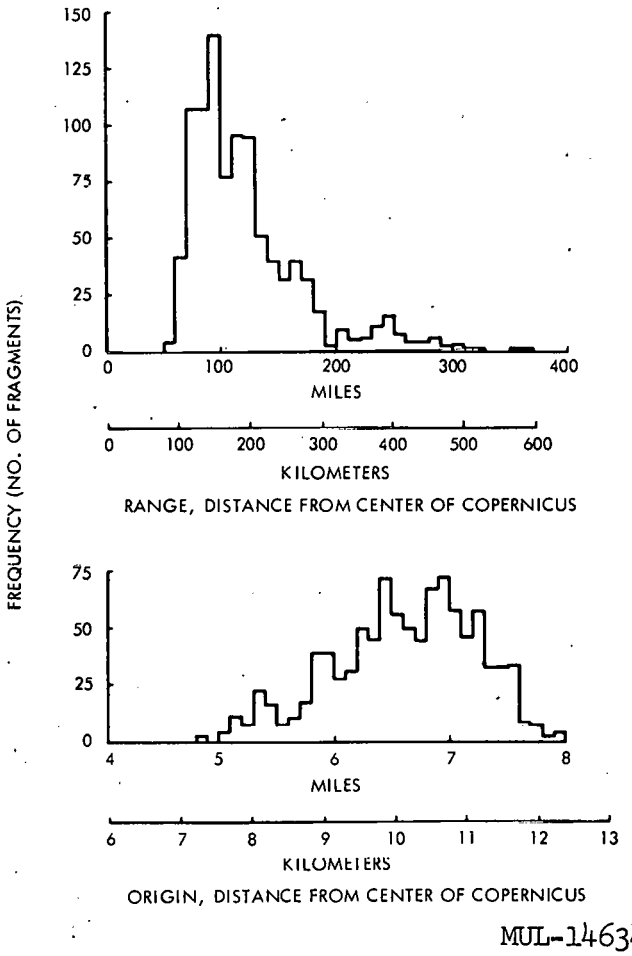

Fig. 5. Frequency distribution of secondary impact crater-forming fragments by range and by calculated original position in Copernicus.

The problem at hand is to deduce the trajectories of the fragments or clusters of fragments that have formed the secondary impact craters and to solve for the original position of these fragments within the crater. We wish to see if the special pattern of the ray system of Copernicus can be related to a relatively simple pattern of breakup of the rocks within the area of the crater and whether this interior ballistic pattern reflects any of the structural features of the moon's crust that can be seen in the region around Copernicus. If such a relationship can be found it will strengthen not only the ballistic interpretation of the rays but also the general features of the cratering theory upon which the numerical computations are based.

Cratering theory and exterior ballistics. To find the trajectories for individual fragments ejected from Copernicus we require a theory of cratering that gives the relation between ejection velocities and angle of elevation of ejection. A series of approximations and an idealization of the cratering problem will be used to obtain a relation in closed form.

First the shock generated by impact will be treated as having an apparent origin at a point some distance below the surface of the ground, corresponding to the center of gravity of the energy delivered during penetration of the meteorite. This approximation becomes seriously in error within a narrow cone with an axis coincident with the penetration path, but at angles to the probable penetration path that are of interest in explaining the observable features of the Copernican rays the approximation is held to be valid within the limits of variation introduced by inhomogeneities of the surface of the moon. The exterior ballistics can then be expressed in terms of the geometrical parameters shown on the following diagram.

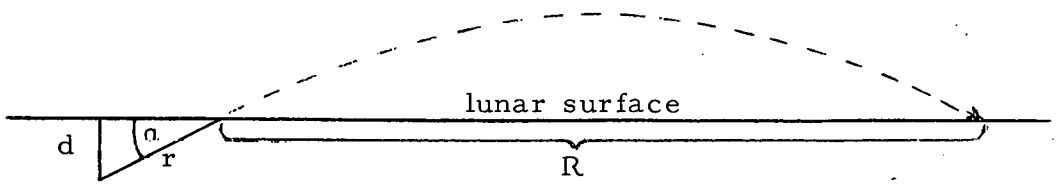

d = depth of apparent origin of shock,

r = slant radius from apparent origin of shock to surface,

α = angle of the slant radius to the horizontal,

R = range of trajectory of ejected fragment.

From the Rankine-Hugoniot condition we have the following relations across the shock front:

$$U\rho_0 = (U - \mu)\rho \qquad \text{(conservation of mass)}, \qquad (1)$$

$$P = \rho_0 U\mu \qquad \text{(conservation of momentum)}, \qquad (2)$$

$$e = P/2(1/\rho_0 - 1/\rho) \qquad \text{(conservation of energy)}, \qquad (3)$$

where U is the shock velocity, μ is the particle velocity behind the shock front, ρ_0 is the initial density of the lunar crust, ρ is the density behind the shock front, P is the pressure increment across the shock front, and e is the internal energy increment across the shock front. Combining equations (1), (2), and (3) we have

$$e = (1/2)\mu^2 . \qquad (4)$$

Now we shall make an approximation employed successfully by Griggs (Griggs and Teller, 1956, p. 8-9) to predict shock arrival times in the Jangle U underground explosion in the region of strong shock,

$$E = 2cM , \qquad (5)$$

where E is the total shock energy and M is the mass engulfed by shock. This approximation can be derived by assuming that the energy is uniformly distributed in the material behind the shock. Such a distribution is impossible, but the relation gives a fair approximation for the rates of decay of energy, pressure, and shock and particle velocities for shock propagation in rock. E can be written as

$$E = (1/2)mv^2 , \qquad (6)$$

where m is the mass of the meteorite or impacting bolide and v is its velocity. Combining (4), (5), and (6) we have

$$\frac{v^2}{\mu^2} = \frac{2M}{m} . \qquad (7)$$

Partly for algebraic simplicity M will be taken as

$$M = (4/3)\pi r^3 \rho_r \ , \tag{8}$$

where ρ_r is the initial density of the lunar crustal material. This relation will minimize the estimate of v. We also may write

$$m = (4/3)\pi x^3 \rho_m \ , \tag{9}$$

where x is the radius of the bolide and ρ_m its density, and

$$r = d/\sin\alpha \ . \tag{10}$$

Combining (7), (8), (9), and (10) we have

$$v = \mu(2\rho_r/\rho_m)^{1/2} (d/x)^{3/2}/\sin^{3/2}\alpha \ . \tag{11}$$

For an elastic wave the particle velocity for a point on the surface would be $2\mu \sin\alpha$, but the velocity of a large fragment ejected from a rock surface by shock will be close to μ. This means simply that the kinetic energy imparted by the rarefaction wave reflected from the ground surface is minor, and that the angle of ejection of a fragment from the horizontal lunar surface would be close to α. These relations are consistent with experimental results that have been obtained from large underground explosions.

In order to evaluate equation (11) numerically we must make some assumptions about ρ_r/ρ_m and d/x, and an accessory relationship is required relating μ and α. Some minimum requirements of this accessory relationship can be drawn from the ray system of Copernicus.

First, from (4), (5), and (8) we have

$$\mu = \frac{3E}{4\pi\rho_r r^3} \ . \tag{12}$$

For a first approximation let us ignore radial variation in the lunar gravitational potential and the departure of the lunar surface from a sphere and employ the simple classical ballistic formula

$$R = \frac{\mu^2 \sin 2\alpha}{g} \ , \tag{13}$$

where g is the gravitational acceleration at the surface of the moon (167 cm/sec^2). We will return to a more precise treatment of the trajectory later. Substituting (10) and (12) into equation (13) we have

$$R = \frac{3E \sin^3 a \sin 2a}{4\pi \rho_r d^3 g} \tag{14}$$

where

$$\frac{3E}{4\pi \rho_r d^3 g} = K \text{ (a constant).}$$

Now the greatest distance that the Copernican rays can be traced is a little more than 500 km. In order to set a minimum value for v let us suppose that this distance actually represents the greatest range of fragments. This supposition is demonstrably false, but we will examine it in more detail later. Under this supposition there are two possible trajectories for any range less than the maximum, one for ejection angles higher than the ejection angle for the maximum range and one for lower ejection angles. For the maximum range we have

$$\frac{dR}{da} = K(\cos a \, 4 \sin^3 a \cos a - \sin^4 a \sin a) = 0 , \tag{15}$$

$$\cos a_{max} = \sqrt{1/5} , \quad a_{max} = 63°26' . \tag{16}$$

Substituting the value of a obtained in (16) and R = 500 km into equation (13), we have

$$\mu = \sqrt{\frac{167 \times 5 \times 10^7}{0.80}} \text{ cm/sec} = 1.02 \text{ km/sec} . \tag{17}$$

We are now in a position to evaluate minimum values of v from equation (11). For Meteor Crater, Arizona, a value of d/x of about 8 to 10 was found for $\rho_r/\rho_m = 1/3$ and v = 15 km/sec (Shoemaker, 1960, p. 430). For the surface of the moon and likely compositions of the impacting bolide, values of ρ_r/ρ_m between 1/2 and 1 are more probable. For these higher ratios of the densities, lower values of d/x may be anticipated for the same impact velocities.

Let us adopt two pairs of values for numerical evaluation: (a) $\rho_r/\rho_m = 1/2$, $d/x = 4$; and (b) $\rho_r/\rho_m = 1$, $d/x = 2$. For the velocities that are derived from equation (11), these pairs of values are realistic for the case of Copernicus. Substituting them successively in (11), we have

$$\text{(a)} \quad v = \frac{1.02 \times 8}{0.846} \text{ km/sec} = 9.6 \text{ km/sec}, \tag{18}$$

$$\text{(b)} \quad v = \frac{1.02 \times 1.414 \times 2.83}{0.846} = 4.8 \text{ km/sec}. \tag{19}$$

The interesting thing about these results is that the cratering and ballistic theory presented here leads to the conclusion that the bolide that formed Copernicus was probably an independent member of the solar system and not a planetesimal or moonlet orbiting the earth (compare with Kuiper, 1954, p. 1108-1111). The value 4.8 km/sec for the impact velocity obtained in (19) is a minimum.

It may be noticed from (14) that the range, as defined, can be set independent of the total energy E and the size of the crater if the linear dimensions of the shock scale as the cube root of the energy. Thus we would expect practically just as long trajectories from small craters formed by small bolides as from large craters formed by large bolides if the impact velocities are similar. But, in point of fact, there is a rough correlation between size of crater and length of observable rays on the moon. This can be interpreted to mean that the rays are visible only out to the point where the areal density of ejected material is so sparse that it can no longer be photographed or seen, and smaller craters have shorter observable rays because the quantity of ejected debris is less. Close examination of photographs reveals that the rays die out gradually. There is rarely any suggestion of increase in ray density near the end, such as would be predicted by the maximum range hypothesis. Thus the Copernican rays are formed only by material that was ejected at low angles, and the material ejected at high angles went into escape trajectories.

Employing equation (14), one may express the total range R_T of a fragment from the epicenter of the shock as

$$R_T = K \sin^3 \alpha \sin^2 \alpha + d/\tan \alpha \, . \qquad (20)$$

The form of equation (20) indicates that the total range, as defined, must pass through a minimum. For a large crater this minimum will be slightly less than the radius of the initial crater produced by ejection of material. As α decreases to values sufficiently low that the total range starts to rise due to rapid increase of the second term, pieces will no longer be thrown out of the crater but will be simply displaced a short distance laterally and vertically. A series of thrust sheets may be formed at values of α where the total range passes through the minimum. In a large crater the final radius of the crater is increased by slumping.

From equation (12) we may write

$$\mu_2^2 = \frac{\sin^3 \alpha_2}{\sin^3 \alpha_1} \mu_1^2 \, . \qquad (21)$$

Thus if d and any pair of values of μ and α are specified, we may draw a curve for R_T. By successive approximation it may be found that an ejection velocity of 0.4 km/sec for an ejection angle of 12° will lead to the formation of a crater of the lateral dimensions of Copernicus if the center of gravity of the energy released is at 3.2 kilometers (2 miles) depth. The crater is taken as having been enlarged 25 kilometers by slumping, as measured by the cumulative width of the terraces on the crater walls. From equation (11) the impact velocity is found to be 17 km/sec. At this velocity the center of gravity of the energy released will be about equal to the linear dimensions of the bolide if the bolide is composed of the same material as the surface of the moon (calculated from methods given by Shoemaker, 1960). Adopting $d/x = 2$ and a density of 3 for the impacting bolide, the kinetic energy is found to be 7.5×10^{28} ergs or 1.8×10^9 kilotons TNT equivalent. This may be compared with 1.2 kilotons for the Jangle U experiment; the cube root of the ratio of the energies is $1.1_4 \times 10^3$. As the ratio of the diameters of the two craters is 1.1×10^3, the cratering theory employed gives good agreement with a cube root scaling

law for the diameters of nuclear craters (Glasstone, 1957, p. 198). It should be noted that the scaled depth for the Jangle U shot is slightly greater than that calculated for Copernicus.

The precise equation for the range of the trajectory on a spherical body can be written in the form

$$\theta = \tan^{-1}\left[\frac{\mu^2 \sin\alpha \cos\alpha}{\ell g - \mu^2 \cos^2\alpha}\right] , \qquad (22)$$

where θ is half the angular distance of travel along the surface and ℓ is the radius of the sphere (Giamboni, 1959). For ranges up to 100 km, or about 3° on the lunar surface, the error of equation (13) is small.

Given μ = 0.4 km/sec at 12° ejection angle, the ejection velocity may be specified for all ejection angles from equation (20) (see Fig. 6). From equation (22) and the tangent of α, the range of individual fragments initially at the surface may then be expressed as a function of the distance of these fragments from the epicenter of the shock (Fig. 7). Fragments ejected at angles ranging from about 8° to 16° form the continuous ejecta blanket mantling the rim of Copernicus. The ejected fragments follow a series of overarching trajectories, as required to form the inverted stratigraphy of the rim at Meteor Crater, Arizona (Shoemaker, 1960). Fragments ejected at angles ranging from about 16° to about 24° form secondary impact craters (the gouges) and the rays (Fig. 8). Between ejection angles of 24° and 43° the smaller volume of material ejected is so widely scattered over the surface of the moon that it is lost. Above 43° the fragments are ejected into escape trajectories.

Interior ballistics. The formation of rays depends upon a departure from the idealized cratering model in the real case. Fragments are not ejected precisely along the radii from the apparent shock origin but are thrown out in distinct clusters or clots. The shape and orientation of these clots as they are first formed in the crater can be found by using the theoretical trajectories to replace the fragments in their approximate original positions.

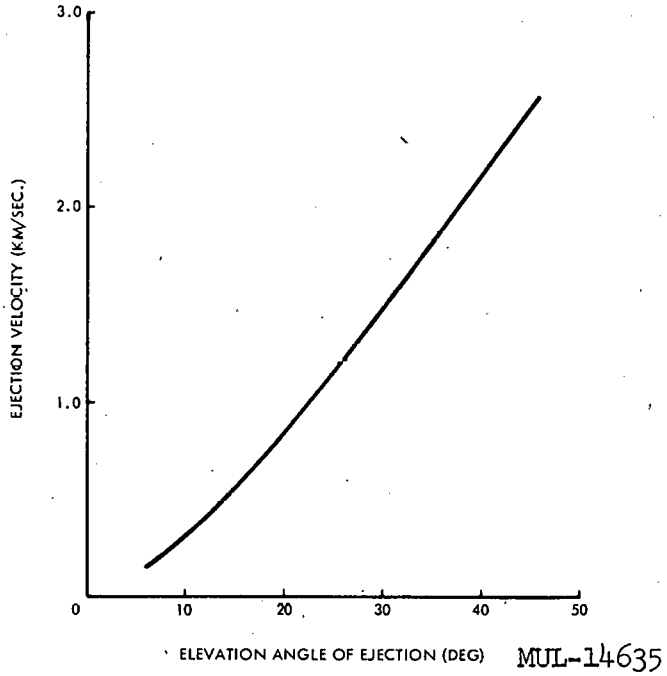

Fig. 6. Ejection velocity as a function of elevation angle of ejection for Copernicus.

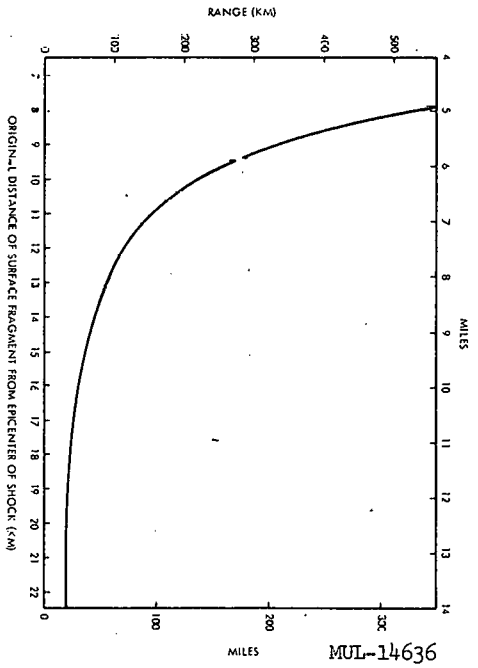

Fig. 7. Range of fragments as a function of original position in crater (Copernicus).

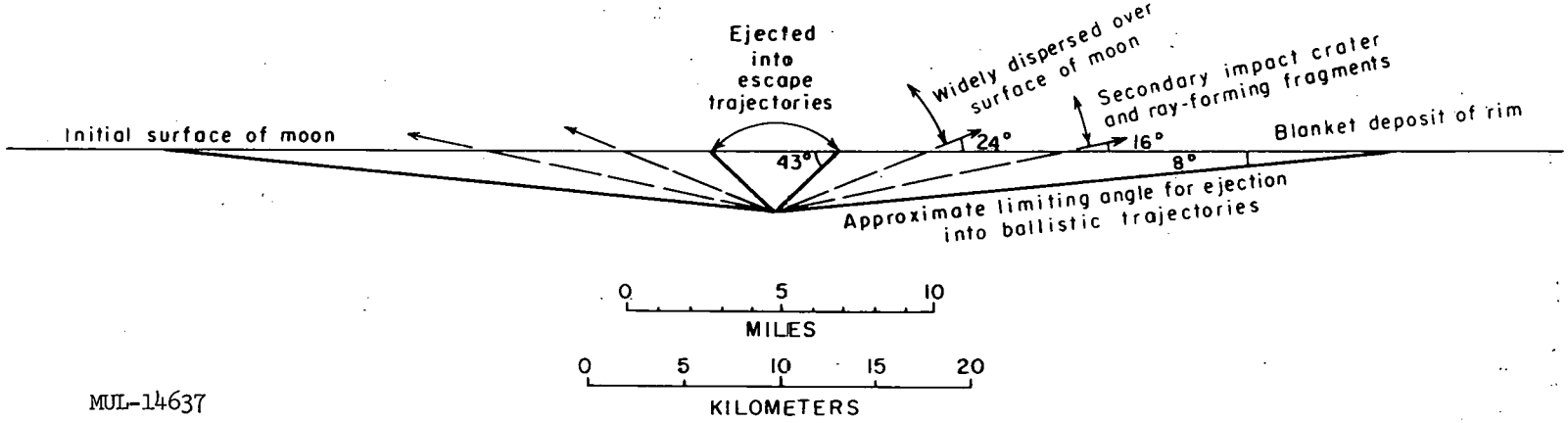

Fig. 8. Provenance of material ejected from Copernicus.

In order to plot positions within Copernicus for the approximate original loci of the fragments that produced the secondary impact craters, the provisional hypothesis is made that each secondary impact crater was formed by one main fragment and that the fragments all came from a near-surface layer. By use of the curve in Fig. 6 all the fragments are then transposed back into Copernicus along radii from the central point, which is taken as the shock epicenter. In the provisional transposition, the fragments are all found to originate from a circular belt around the shock epicenter (Fig. 9) with an inside radius just under 8 kilometers (5 miles) and an outside diameter of 13 kilometers (8 miles). The farthest thrown fragments are derived from the inner margin of the belt.

The large loop-shaped ray extending toward Mösting is found to have originated from a linear cluster of fragments about 7 kilometers long within Copernicus. The trend of this cluster is essentially parallel with the "dipole" axis of the whole ray system. It is also parallel with a northwest-trending linear system of prominent ridges in the Carpathian Mountains and with the dominant trend of linear topographic features in the general vicinity of Copernicus. These ridges and linear features are structural elements of the lunar crust that at least in part clearly predate the formation of Copernicus, as will be shown in a later section. The fragmentation pattern thus appears to have been influenced by pre-existing lines of weakness; individual clots of fragments evidently pulled apart along faults and fractures already present in the lunar crust. The linear cluster of fragments that formed the loop-shaped ray toward Mösting is interpreted as a pre-existing structural block that maintained its identity momentarily as it was engulfed by shock. In this way the major features of the ray pattern, the "dipole" axis and axis of symmetry, are controlled by the dominant structural grain of the lunar crust in the vicinity of Copernicus.

Subordinate structural trends also influenced the ray pattern. A prominent arcuate ray that curves around just north of Hortensius is derived from a linear cluster of fragments parallel with a subordinate set of north-northwest-trending linear features north of Copernicus and a north-northwest-trending

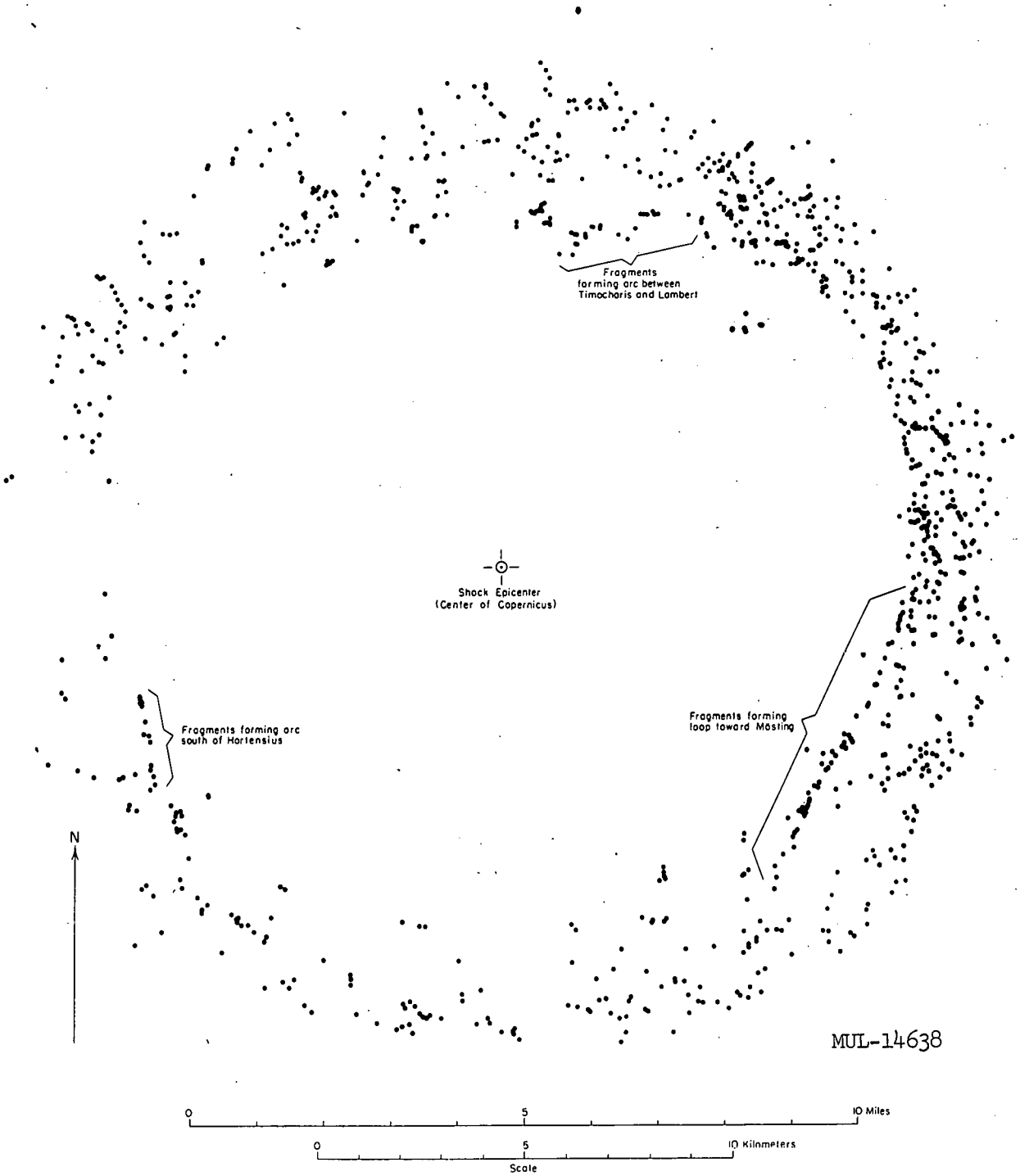

Fig. 9. Provenance of fragments which formed the secondary impact craters in the ray system of Copernicus.

set of terraces on the eastern crater wall (Fig. 3). Other linear clusters are also present in the interior ballistic pattern which are parallel with still other linear structures in the crater wall and the region around Copernicus.

The significance of these results is that a simple genetic relationship between the main features of the Copernican ray pattern and other observable features of the lunar crust is found by use of the idealized theory of cratering. The theory accounts quantitatively for both the crater dimensions and the distribution of ejecta. The transposition of rays into linear fragment clusters, however, is not a sensitive test of precision of the computed trajectories. The main features of the interior ballistic pattern would not be significantly changed by minor modification of the relation between the angle of elevation and ejection velocity that was derived from a series of approximations.

We may return now to examine the provisional hypothesis that all the secondary impact crater-forming fragments were derived from a near-surface layer. Material derived from deep positions close to the origin of the shock will be ejected at the same angles as fragments close to the surface. Because the near-surface fragments are farthest from the shock origin along any given slant radius and therefore experience the lowest peak shock pressure, it is reasonable to expect the largest fragments to come from near the surface. The question is whether any fragments or clusters of fragments large enough to form secondary impact craters may have originated at significant depth beneath the surface. The frequency distribution of the secondary impact crater-forming fragments in the reconstructed internal ballistic pattern provides some evidence bearing on this question.

The radial frequency distribution of fragments, after transposition into the crater, shows a series of pronounced maxima and minima that correspond to maxima and minima in the original range frequency distribution of the secondary impact craters (Fig. 5). This distribution has been broken down into three sectors around Copernicus (Fig. 10), and the individual maxima may then be identified with major rays or belts of secondary impact craters. In nearly all cases it is found that a maximum in one sector coincides fairly closely in radial position with a maximum in one of the other sectors. Such

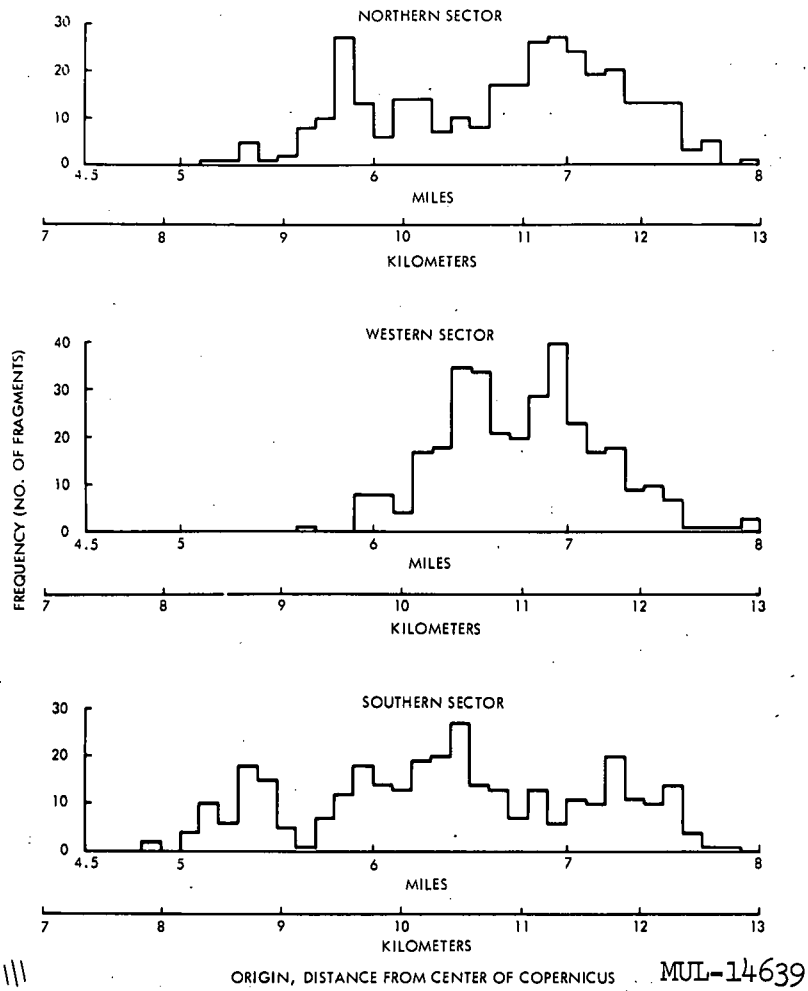

Fig. 10. Frequency distribution (by sectors) of secondary impact crater-forming fragments according to calculated original position in Copernicus.

a coincidence suggests that the interior fragmentation pattern has elements of concentric symmetry around the shock epicenter. A concentric pattern would be found if the lunar crust were layered and clusters of fragments were formed by the separation or pulling apart of layers. This implies that clusters which are separated radially in the fragmentation pattern as plotted in Fig. 9 may actually have been separated vertically in the crater.

Some features of the ray pattern seem easiest to explain by a combination of vertical and horizontal separation of fragment clusters. The very long ray trending north between Timocharis and Lambert, for example, is intersected or joined by two east-west-trending cross-rays, one that crosses north of Pytheas, and one that runs just north of Turner. The greatest density of visible secondary impact craters along the north-south ray occurs near the intersections. Such relations could be explained as follows: The north-trending ray was formed by an elongate cluster of fragments with the approximate shape and orientation shown in Fig. 9, but one end of the cluster originally lay at a deeper level than the other in the lunar crust and thus more than two separable layers were included in the cluster. The uneven distribution of secondary impact craters along the ray would be due to the tendency of the fragments of each layer to hang together momentarily on ejection. This interpretation implies that the fragments of the Turner cross-ray are derived from a different layer than those of the Pytheas cross-ray.

It is not immediately evident which of the two cross-rays, in this interpretation, would represent the deeper layer. Shock propagation theory suggests that, along a given slant radius, the upper layer should have the higher ejection velocity, in which case the Pytheas cross-ray would represent the higher layer. Empirical evidence from high-explosives cratering experiments, on the other hand, suggests that along certain slant radii fragments from the deeper layer would go farther (Sakharov and others, 1959). The high-explosives data may not be applicable because the fragments are ejected more by the impulse derived from expansion of the explosion gases than by the shock.

Keeping in mind the factors that may influence fragmentation, we may examine the question of the actual size of the fragments that formed the

secondary impact craters. A total of at least 975 fragments are derived from an annular segment of the lunar crust with an area of about 330 square kilometers and an unknown depth. If the fragments are assumed to be of equidimensional shape and all derived from one layer, the maximum mean diameter of the fragments would be about 600 meters. If the depth from which the large fragments are derived were about three times the mean diameter of the fragments, then the maximum mean diameter would be closer to 1 kilometer. But probably very few, if any, of the fragments that formed the secondary impact craters were as much as a kilometer across. In the first place, a mean diameter of a little less than 1 kilometer would require that essentially all the material ejected at ray-forming angles (Fig. 8) was in large fragments, whereas empirical data on the size frequency distribution of fragments produced by shock shows that about 50 percent of the material will be in size classes more than an order of magnitude smaller than the maximum size. Secondly, there is a much larger number of secondary impact craters in the visible size range than has actually been compiled. A better guide to the actual size of the fragments is probably provided by the length of the cluster of fragments that was ejected toward Mösting to form the loop-shaped ray. At least 50 fragments were derived from a cluster which was only 7 kilometers long. The mean size of the fragments that formed the visible secondary impact craters in the loop-shaped ray was probably in the range of 100 to 200 meters in diameter.

These results have an immediate bearing on the origin of the elongate secondary impact craters, many of which are oriented at angles to the radial direction from Copernicus and thus cannot be attributed simply to plowing or skidding of the low-angle missile on the lunar surface. Arbitrarily oriented craters could be formed by arbitrarily oriented elongate fragments; but the length required for the fragments is unreasonably great, for some of the secondary impact craters are more than 5 kilometers long. All of the markedly elongate craters are, therefore, probably compound craters formed by the impact of two or more fragments traveling closely together. All graduations can be found, especially along the inner margin of the ray system between

short chains of secondary impact craters and compound craters in which the partially merged components can still be recognized. The formation of these chains and compound craters is simply a smaller scale manifestation of the phenomenon of clustering of fragments which is responsible for the broad scale pattern of the rays. Ejection of fragments from large primary impact craters thus provides another mechanism in addition to volcanism by which chains of small craters can be formed on the moon.

Thickness of the ejecta blanket. The theoretical model of cratering may be used to estimate the thickness of the ejecta blanket surrounding Copernicus. The differential volume of material ejected from the crater at the angle α may be given as

$$d(v_c) = (2/3)\, d\pi\, x\, d(x)\,, \tag{23}$$

where $d(v_c)$ is the differential volume of a cone with height d and radius x, and

$$x = d/\tan\alpha\,. \tag{24}$$

This differential volume will be deposited at the distance R_T from the center of the crater as a differential increment of a cylinder of slowly varying height h, given by

$$d(v_r) = 2\pi h R_T\, d(R_T)\,, \tag{25}$$

where $d(v_r)$ is the differential volume of the cylinder.

As $d(v_r)$ is equal to $d(v_c)$ but opposite in sign, h, the thickness of the deposit, is given by

$$h = -\frac{d}{3}\,\frac{x\, d(x)}{R_T\, d(R_T)}\,. \tag{26}$$

Differentiating and combining equations (20), (24), and (26) we have

$$h = \frac{d}{3}\left(\frac{d}{\sin^2\alpha}\right)\left\{\frac{d}{\tan\alpha\left(2K\sin^4\alpha\cos\alpha + \frac{d}{\tan\alpha}\right)\left[2K(4\sin^3\alpha\cos^2\alpha - \sin^5\alpha) - \frac{d}{\sin^2\alpha}\right]}\right\}, \tag{27}$$

and, expanding and collecting terms,

$$h = \frac{d^3}{3(-d^2 + 6Kd \sin^5 \alpha - 10Kd \sin^7 \alpha + 16K^2 \sin^{10} \alpha - 20K^2 \sin^{12} \alpha)} . \quad (28)$$

This function is illustrated graphically in Fig. 11. It should be noted that, from the geometry of the derivation, the function loses meaning below the ejection angle where R_T passes through the minimum. For Copernicus, this angle is approximately 8 degrees.

From simultaneous solutions of equations (20) and (28) the calculated thickness of ejecta may be plotted as a function of distance from the center of Copernicus (Fig. 12) and compared with an approximate mean profile of the rim obtained from the Aeronautical Chart and Information Center. It is clear that uplift of the lunar crust beneath the ejecta must be called upon if the theoretical model of cratering is to be considered consistent with the observed volume of the rim. Such uplift was predicted on the basis of the theoretical model and is well illustrated in some of the larger terrestrial craters, such as the New Quebec crater of Canada (Millman, 1956) where the bedrock under the rim is extensively exposed (Shoemaker, unpublished data). In addition, it is likely that the angles of ejection derived from the simplified theoretical model are somewhat low for the materials deposited near the crest of the rim. Near the periphery of the crater some material is probably ejected from beneath the theoretical limiting cone of ejection and is deposited near the crest of the rim, thus forming a thicker deposit than would be predicted from the simplified cratering theory.

Toward the extremity of the continuous ejecta blanket the calculated thicknesses are probably fairly realistic. The average distance at which the continuous ejecta blanket breaks up into discrete rays is about 90 miles from the center of Copernicus, or 145 km. At this distance the calculated thickness of the ejecta deposit is 7 feet (2 meters). At 125 km from the center of Copernicus, the outer limit of low but visible subradial ridges in the ejecta, the average thickness is 4 meters. At 80 km, the approximate inner limit at

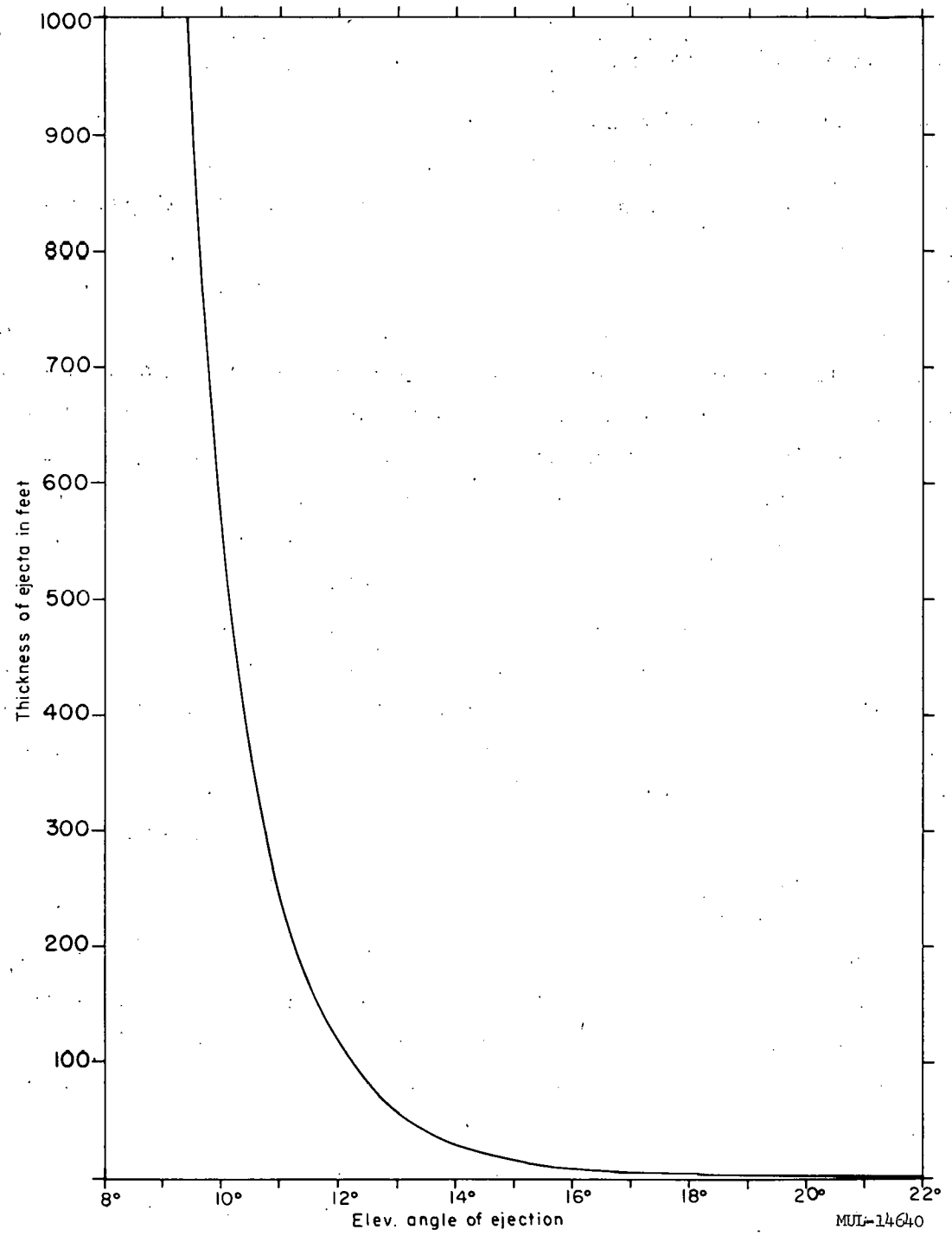

Fig. 11. Thickness of ejecta deposit as a function of angle of ejection from Copernicus.

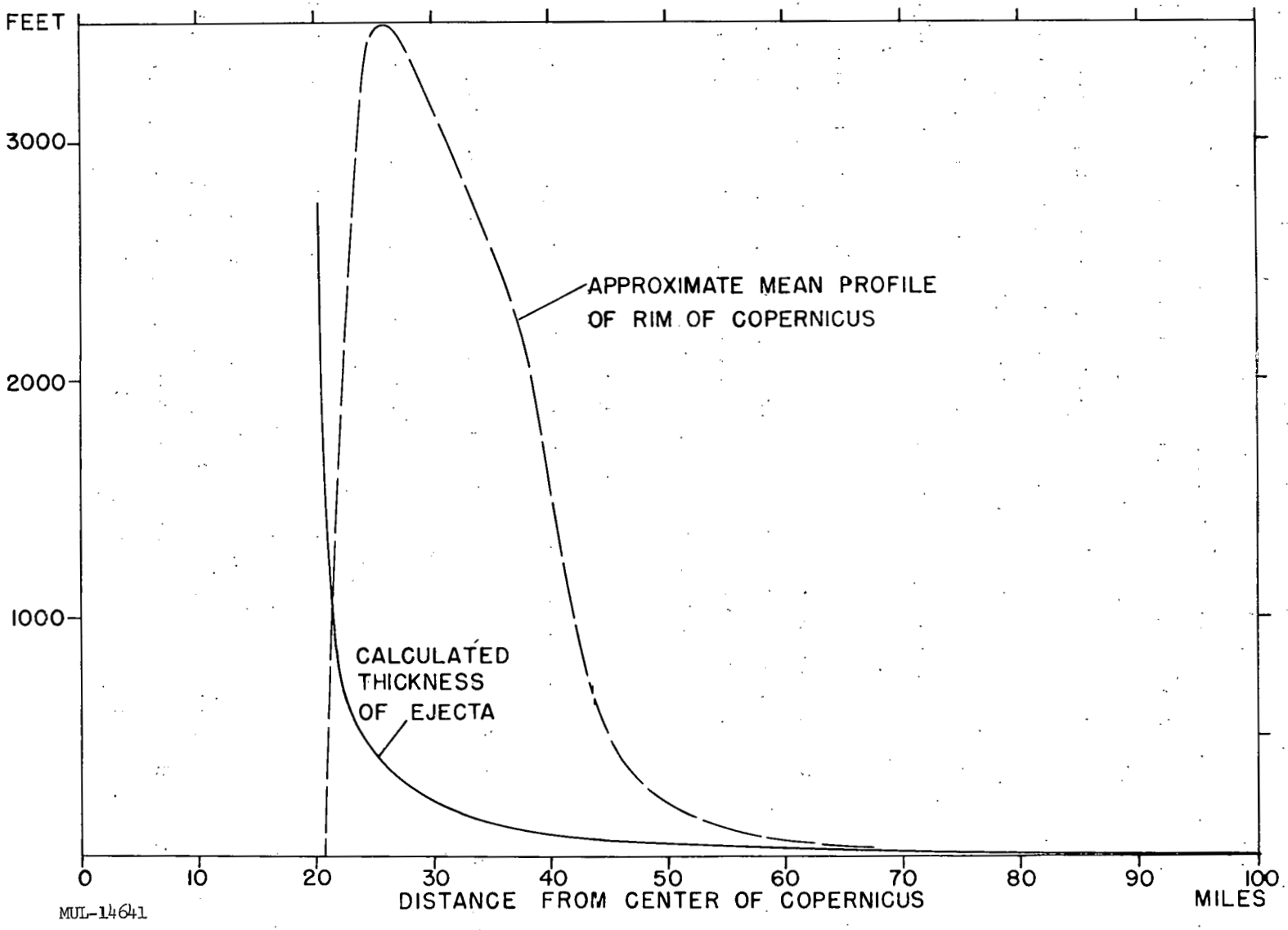

Fig. 12. Calculated thickness of ejecta as a function of distance from the center of Copernicus.

which secondary impact craters may be recognized with confidence, the calculated thickness of the ejecta blanket is 15 meters. Closer to the crest of the rim, many subdued depressions are present in the surface of the ejecta, but the ejecta deposit is of such thickness that the outlines of secondary impact craters are too blurred for certain identification.

West of Copernicus is a very low north-trending ridge that has been covered by the ejecta blanket. The ridge is part of a ridge system that extends farther north and is exposed in the Mare Imbrium where many similar low ridge systems are developed on the mare surface. Though covered by ejecta and partly scored by secondary impact craters, the outline of the ridge west of Copernicus can be traced to within 20 miles of the rim crest, or 80 kilometers of the center of the crater. Similar ridges in the ridge systems on the mare surfaces are about ten to a few tens of meters high. The fact that a surface feature of such low relief was not completely obscured by the superimposed ejecta tends to support the calculations which show the ejecta form only a thin veneer at this distance from the crater.

REFERENCES CITED

Giamboni, L. A., 1959, Lunar Rays: Their Formation and Age: Astrophys. J., v. 130, p. 324-335.

Glasstone, Samuel, ed., 1959, The effects of nuclear weapons: Washington, D. C., U. S. Atomic Energy Comm., 579 p.

Griggs, D. T., and Teller, Edward, 1956, Deep underground test shots: Univ. California Radiation Lab. Rept. UCRL-4659, 9 p.

Kuiper, G. P., 1954, On the origin of the lunar surface features: Proc. Natl. Acad. Sci. U. S., v. 40, no. 12, p. 1108-1111.

_____1959, The exploration of the moon, in Vistas in astronautics, 2d ann. astronaut. symposium: New York, Pergamon Press, v. 2, p. 273-312.

Millman, P. M., 1956, A profile study of the New Quebec Crater: Ottawa, Dominion Observatory Publ., v. 18, no. 4, p. 61-82.

Sakharov, V. N., Kolesnikov-Svinarev, V. I., Nazarenko, V. A., and Zabidarov, E. I., 1959, Local distribution of earth thrown up by underground explosions: Doklady Akad. Nauk S. S. S. R., v. 124, p. 21-22.

Shoemaker, E. M., 1960, Penetration mechanics of high velocity meteorites, illustrated by Meteor Crater, Arizona: Intern. Geol. Congr., 21st, Copenhagen, 1960, Rept., pt. 18, p. 418-434.

Paper R

ORIGIN OF LUNAR SURFACE FEATURES AND OF TERRESTRIAL OCEAN BASINS AND CONTINENTS

J. J. Gilvarry

Research Laboratories, Allis-Chalmers Manufacturing Company
Milwaukee, Wisconsin

ABSTRACT

Both cosmic and geological evidence indicate that the terrestrial atmosphere and hydrosphere are secondary in origin, formed by exudation from the earth's interior. If a similar origin is postulated for a lunar atmosphere and hydrosphere, the amounts of constituents present initially at a primordial time on the moon can be inferred. The results indicate that the pristine lunar hydrosphere lasted a time of the order of two billion years, and once attained a depth of about 2 km over the lunar lowlands.

It follows that the rocks in the level floors of the lunar maria, formed by sediments deposited from the water on the moon in the course of its dissipation, should be softer than the rocks of the lunar highlands. This conclusion is borne out by a correlation of the dimensions of craters in the mare floors and in the lunar highlands with the dimensions of terrestrial craters (meteorite and explosion) in soft and hard rock, respectively. Accordingly, the lunar maria represent craters formed by explosive impact of large meteorites on the moon at a pristine time when an appreciable hydrosphere existed. In agreement with this view, the dimensions of the lunar maria show a correlation with the dimensions of craters formed by explosion of nuclear bombs in water. A meteoritic crater, Deep Bay, exists which one can argue strongly must have been formed in water, and its dimensions show the expected correlation with those of the lunar maria.

The points of analogy between the lunar maria and the basins of terrestrial oceans are pointed out, and it is postulated that both types of feature had a similar origin by explosive impact of large meteorites in the presence of a hydrosphere. The shallowness of ocean basins relative to the lunar maria is explained as the result of isostatic readjustment on the earth. The fact that the Mohorovičić discontinuity must have been level under both oceans and continents prior to the impact of the meteorites in question makes it possible to reconstruct the mensuration of the primordial oceans

before isostatic readjustment. These dimensions show the expected correlation with those of the lunar maria, the Deep Bay meteoritic crater, and the craters made by nuclear explosions in water. Accordingly, the terrestrial continents are structures corresponding to the rims of the meteorite craters forming the ocean basins.

* * *

I. INTRODUCTION

The dark and smooth appearance of the lunar maria has generally been viewed as sufficient evidence to identify their surfaces as lava flows. Interpretations on this basis, but differing in detail, have been given by Baldwin,[1] Urey,[2] and Kuiper.[3] Gold[4] has argued strongly against the presence of lava, in view of the consequent difficulty in correlating temporal sequences of crater origin and the paucity of definite volcanic features. The author[5] has pointed out that the known presence of a dust layer over the entire surface of the moon vitiates the reasoning for the presence of lava.

The arguments for lava presuppose the absence of a lunar atmosphere or hydrosphere lasting any significant length of time. During the last few decades, however, it has become increasingly clear that the terrestrial atmosphere and hydrosphere were formed by exudation from the earth's interior. One purpose of this paper is to consider the possibility of an analogous process in the case of the moon. It will be shown that the origin and nature of major surface features on the moon can be explained in terms of effects of the former presence of a lunar hydrosphere.[6] The salient conclusion which emerges is that the circular lunar maria are simply large meteoritic craters, with sedimentary floors, which were excavated by explosive impact of meteorites on the lunar surface in the presence of a hydrosphere. The argument depends, in part, on a correlation of the dimensions of the lunar maria with those of terrestrial explosion craters in water.[6]

Recent reviews of the problem of the origin of ocean basins and continents have been given by Howell,[7] and by Jacobs, Russell, and Wilson.[8] The classical hypotheses in this connection are the tidal resonance theory of Darwin,[9] involving creation of the Pacific Ocean by escape of the moon, the theory of migrating continents originated by Taylor[10] and Wegener,[11] and the various

theories based on thermal convection.[12] Most of such theories were devised without taking into account a discovery of the last decade that the Mohorovičić discontinuity rises from its depth of about 33 km under the continents to within about 5 km from the floors of the oceans. This fact implies a profound difference in the structures of ocean basins and continents,[13,14] which creates grave difficulties for most theories of the origin of these features, in particular for the theory of migration of continents.[15]

If the circular lunar maria are simply large meteoritic craters with sedimentary floors, formed in the presence of a hydrosphere, one can postulate an exactly analogous mode of formation of ocean basins, i.e., as the result of the explosive impact of large meteorites during pristine time when the hydrosphere covered the earth to a roughly uniform depth.[16] The demonstration will be based on a reconstruction of the dimensions of the pristine oceans, and a correlation of their dimensions with those of the lunar maria, lunar craters of a particular class, and meteoritic and explosion craters in water. The disparity in the levels of the Mohorovičić discontinuity under continents and oceans enters the theory as an integral part — as the consequence of isostatic readjustment of the rim and floor of a crater.[16]

Independently, Harrison[17] has hypothesized that the Pacific Ocean was created by impact of a planetesimal, a terrestrial satellite, or a satellite of the earth-moon system, and has conjectured a similar mode of formation for every ocean. His basic argument is that creation of the Pacific Ocean by such an impact is energetically possible. The present reasoning differs in the essential respect that it is based on a correlation of dimensions of craters formed in water.

II. LUNAR SURFACE FEATURES

The origin of the topographical features of the surface of the moon will be considered first.

A. Lifetime of the Lunar Hydrosphere

By considering the cosmic and terrestrial abundances of the inert rare gases, Brown[18] and Suess[19] have demonstrated that any element which existed primarily as a gas at the time of the earth's formation could not have

been retained to a significant extent in its atmosphere. It follows that the present atmosphere and hydrosphere of the earth are not residual from primordial antecedents, but are almost entirely of secondary origin. Rubey[20] has adduced purely geological arguments leading to precisely the same conclusion; he presents compelling evidence that the terrestrial atmosphere and hydrosphere were formed by leakage from the interior of the earth through its surface.

In view of the moon's smaller mass, the conclusion follows a fortiori that it could have retained no residue of any primordial atmosphere or hydrosphere, since it necessarily was formed at essentially the same distance from the sun, at approximately the same time, and under roughly the same conditions as the earth. Accordingly, the question of the lifetime of a lunar atmosphere or hydrosphere cannot be discussed without deciding the type of secondary atmosphere or hydrosphere formed by leakage of fluid through its surface, by a degassing process exactly analogous to that postulated for the earth. To answer this question, a scaling law must be assumed. It will be hypothesized that the total masses of a constituent in the secondary atmosphere and hydrosphere for the moon and earth should be proportional to the corresponding masses of these bodies. Let Q_i represent the number of molecules above unit area on the moon's surface for the ith constituent in its atmosphere and hydrosphere, and let Q_i^* be the corresponding quantity for the earth. If the difference in mean density between the moon and earth is ignored, this assumption yields

$$Q_i/Q_i^* = R/R^* , \qquad (1)$$

where R is the radius of the moon and R^* that of the earth. As will appear, the order of magnitude of resultant lifetimes is not sensitive to the precise choice of scaling law.

In determining the values of Q_i for fluids on the moon from equation (1), it clearly is necessary to consider in Q_i^* the total amounts on the earth of any compound of atmospheric or hydrospheric provenience. In the case of the hydrospheric H_2O, for example, one must include the contribution from

continental ice, and in the case of CO_2, the fossil quantity locked in sediments. Values of Q_i have been determined for H_2O, CO_2, O_2, and N_2 by equation (1) from data of Wildt.[21] The resulting Q_i for H_2O corresponds to a surface density of 79 kg/cm^2 and exceeds by a large factor those for the other fluids, as a consequence of the large mass of water in the terrestrial oceans.

For simplicity, it will be assumed that the secondary lunar atmosphere and hydrosphere were formed by exudation from the interior in a time short compared to the corresponding lifetime. The lifetime L_i of the ith constituent of the lunar atmosphere and hydrosphere is then fixed by

$$L_i = Q_i/j_i \, , \tag{2}$$

where j_i is the thermal escape rate of Jeans[22] and Spitzer.[23] Equation (2) applies to the atmosphere and hydrosphere combined, since it presupposes that loss of a constituent (water vapor, for example) from the atmosphere can be replenished by gain from the hydrosphere. Thus, the model presumes that the entire hydrosphere is gaseous; the fact that it is liquid lengthens the actual lifetime over that computed. It is unnecessary to consider the correction factor B of Spitzer[23] or A_i of the author[24] in connection with equation (2), since use of these parameters is obviated when a direct estimate of Q_i is available. The author has determined the height of the escape layer above the earth's surface from data obtained by observation of satellite orbits.[25] Theoretical relations[24] have been used to scale the result for night conditions to yield an approximate height of 2300 km for the escape layer above the lunar surface. The mean temperature of the critical level for the earth varies between 1000 and 2000°K diurnally.[25] An upper limit of 3000°K will be assumed for the escape layer of the moon, which is about the value apparently required to explain the loss of atmospheric He^4 from the earth.[24,25]

The lifetime L_i on the assumptions made is shown in Fig. 1 as a function of assumed temperature of the escape layer, for H_2O, CO_2, O_2, and N_2. One sees that the lifetime of H_2O is the longest by a large margin for any temperature above 1000°K. Moreover, this lifetime is measured in billions of years, and thus is comparable with the duration (of order 4.5×10^9 years) of

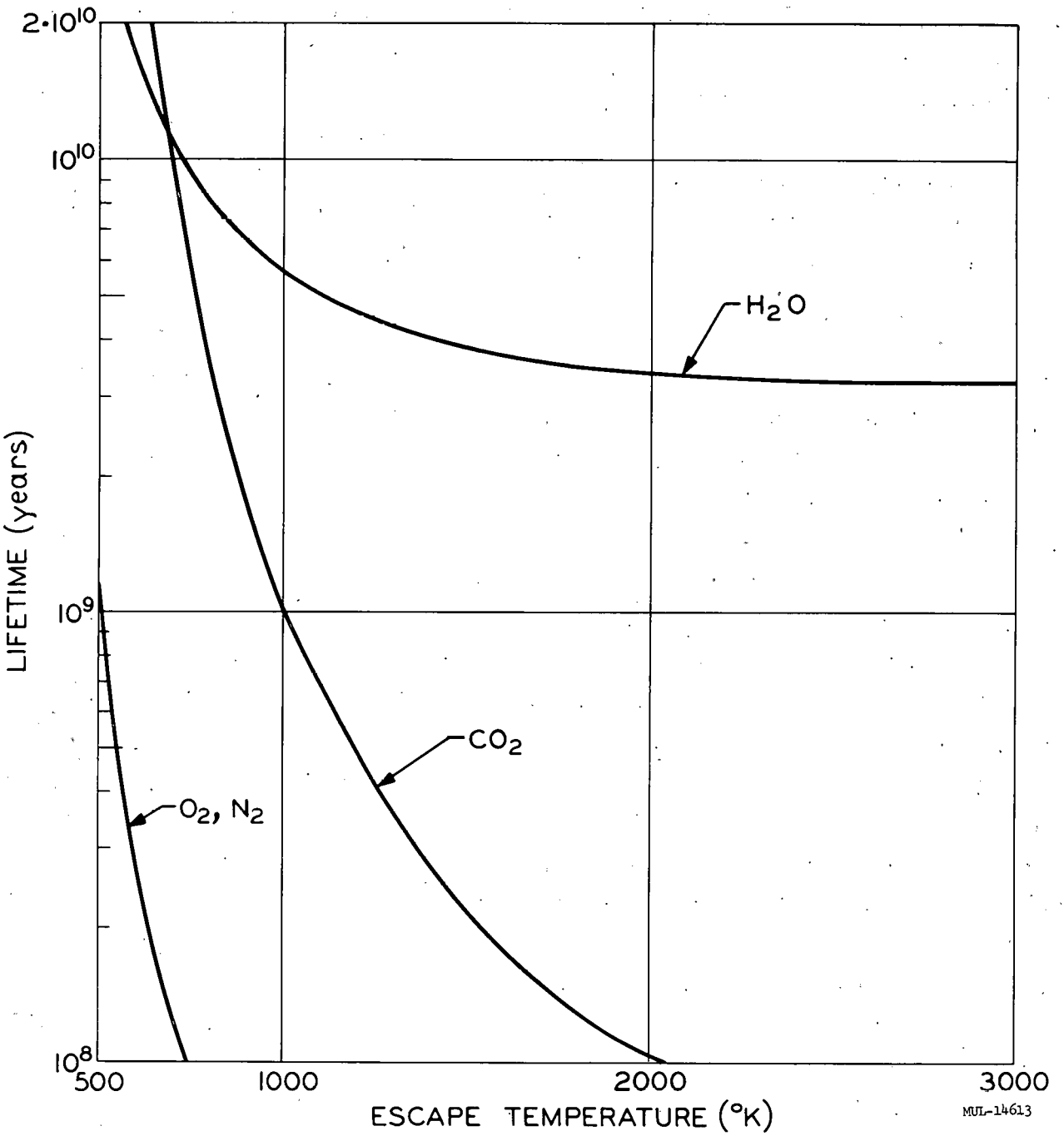

Fig. 1. Lifetime L_i of various constituents of the primitive lunar atmosphere and hydrosphere, as a function of assumed temperature in the escape layer. The curves for O_2 and N_2 are indistinguishable on the scale used.

the moon's lifetime. Corresponding to uncertainties in assumed initial conditions, the estimates shown can reasonably be increased or decreased by a factor of $10^{1/2}$, giving an overall spread of a factor of 10 in the results. The conclusion that the lunar hydrosphere lasted a period at least of the order of 10^9 years remains unaffected. Computations of the lifetime of H_2O on the moon have been made previously;[1,22] they yielded values insignificant on an astronomical scale because the possible existence of a lunar hydrosphere capable of continuously replenishing the atmosphere was ignored.

The maximum depth of the lunar hydrosphere can be estimated on the assumption that the time of its exudation from the interior was short compared to its lifetime. If the surface of the moon below the hydrosphere were smooth, the value of Q_i for H_2O would indicate a maximum water depth of about 1 km. However, about half the visible surface of the moon consists of highlands about 2 km higher on the average than the lowlands,[1] which, if true for the other face, would yield a mean water depth of roughly 2 km. Height estimates for the averted face, are not possible, since only a few crude photographs are available.[26] In spite of this uncertainty, it is clear that sufficient water once existed in the lunar hydrosphere to drown all the lowlands and to encroach significantly on the highlands.

On these considerations, a large part of the erosion evident for the lowland regions of the moon must have taken place subaqueously; a significant amount may have been done by turbidity currents.[27] Because of the relatively low surface gravity, small area available for watersheds, and thinness of the atmosphere (composed in later stages primarily of water vapor), erosion by flowing rivers and their tributaries should not have been very significant. Thus, dendritic drainage patterns should appear in the highlands but should not be prominent; Pickering[28] has shown observationally that such actually seems to be the case.

B. Craters on Land

If it is indeed true that the moon possessed an appreciable hydrosphere throughout a large fraction of its history, it follows that the level floors of the maria were formed by sediments deposited from the water in the course of its

dissipation. Compaction of these sediments should yield a softer rock than that forming the highlands, and this circumstance should be reflected systematically in the mensuration of the corresponding craters, to some degree. Evidence of a systematic difference between craters formed in the highlands and the maria will be sought in an extension of Baldwin's correlation of diameter and depth to include the effect of crater formation in hard or soft rock. Baldwin's curve of diameter versus depth for the lunar craters of Class I (presumably the youngest) exhibits a continuous variation through the analogous curve for terrestrial meteoritic craters into the corresponding curve for explosion craters on the earth. This correlation is one of the strongest arguments that the lunar craters were formed by explosion of meteorites on impact. It can be shown that such explosions necessarily occur close to the surface.[29]

It will be assumed that the relation between the diameter D and depth d of a crater can be written as the quadratic form

$$D = a_1 d[1 + (d/a_2)] \ , \qquad (3)$$

with the set of coefficients a_1 and a_2 different in the cases of hard and soft rock. The coefficients a_1 for hard and soft rock were determined from the results of measurements of the dimensions of craters formed by explosion of chemical charges in basalt and sedimentary rock, respectively.[30] These experiments were conducted under closely controlled conditions, with the center of mass of the charge at ground level. The resulting least-square linear relations $D = a_1 d$ for the two cases are shown (dashed in part) in Fig. 2. As a check, data points for the craters formed by the nuclear explosions Jangle (S) and Jangle (U) in compacted desert alluvium are shown also;[31] the latter was an underground explosion, but the scaled depth of burst was sufficiently small for it to approximate a surface explosion. One sees that agreement of the two points with the line for soft rock is excellent.

Of the craters in Baldwin's Class I, 80 have been classified in Class IH, occurring in the highlands, 84 in Class IS, occurring in the floors of the maria, and 30 as ambiguous on this score. With the value of a_1 fixed as above for hard and soft rock, the corresponding values of a_2 were determined by a

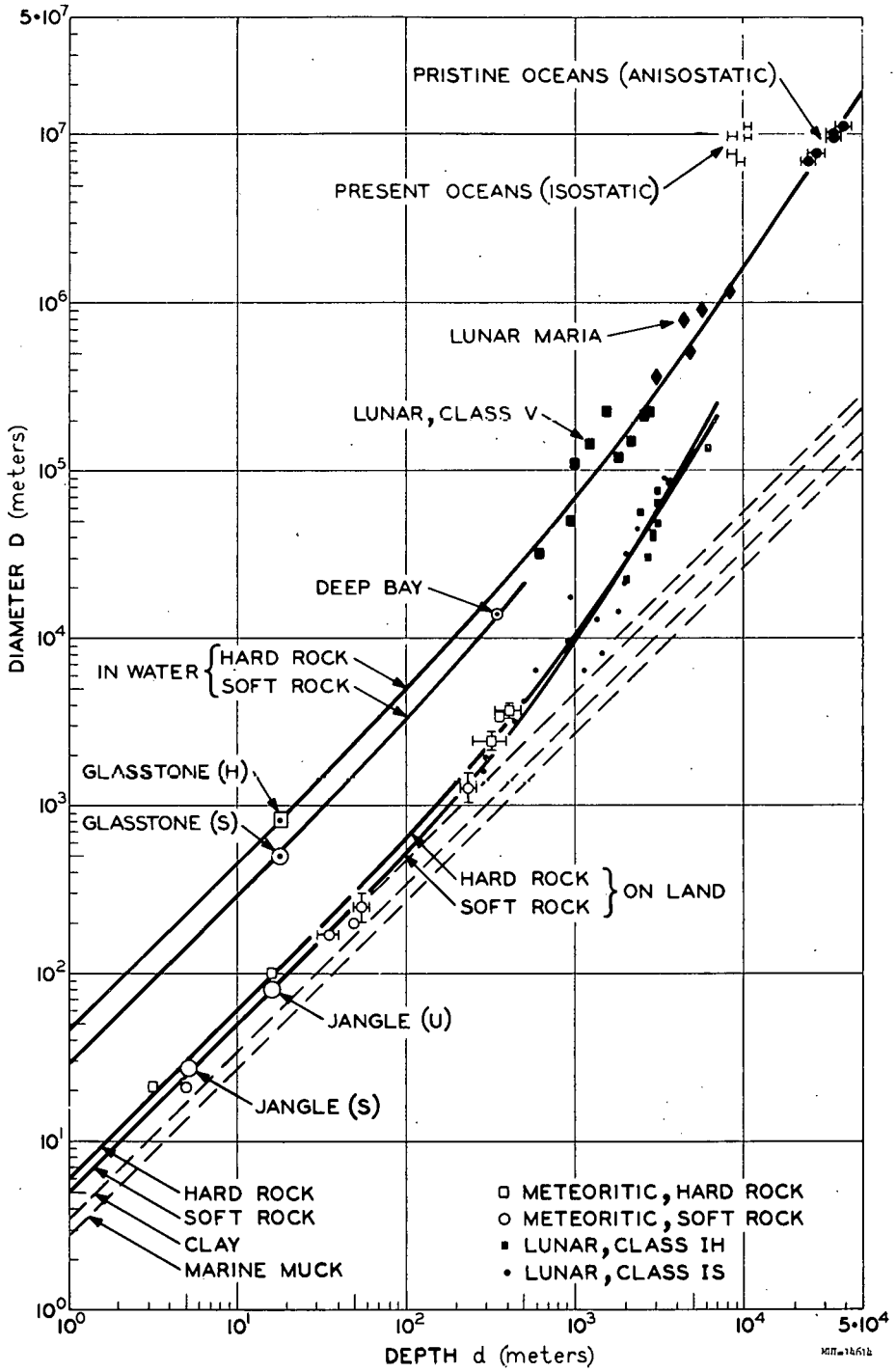

Fig. 2. Correlation of diameter versus depth for various classes of craters, lunar maria, and the pristine and present oceans. The solid curves correspond to fitted functions for craters on land and in water, for hard and soft rock. In general, points for only every tenth lunar crater in Classes IH and IS appear.

least-squares fit to the data of Baldwin for the dimensions of the craters of Class IH and IS, respectively. The resulting curves are shown in Fig. 2. They become nearly identical for large diameter and depth, as is clearly necessary, since the larger craters on the floor of a mare must extend into the harder rock below the sediments. The association of the lunar craters of Classes IH and IS with hard and soft rock, respectively, is inferential; one sees that the difference between the two curves computed on this assumption is too small in the region of large dimensions to be of diagnostic value.

However, a significant difference does appear for the two curves in question for the intermediate range of depth and diameter. To show that the difference is real, recourse will be made to the data for terrestrial meteoritic craters. Ten such craters for which dimensions are known with relative accuracy were classified in Class IH, formed in hard rock, and Class IS, formed in soft rock. The basis of distinction between hard and soft rock is primarily the shear strength; granite and dolomite are regarded as hard, and limestone and sandstone as soft. Schist and gneiss are considered soft, in view of their low shear strength along planes of foliation and banding, respectively. The craters of Class IH are Brent,[32] Chubb,[33] Holleford,[34] Sall,[35] and Dalgaranga;[36] those of Class IS are Barringer (Arizona),[1] Le Clot,[37] Merewether,[38] Odessa 1,[1] and Odessa 2.[1] The dimensions of these craters are plotted in Fig. 2, as differentiated into the two classes.

The close correlation between the data points for terrestrial meteoritic craters of Classes IH and IS, and the corresponding curves constructed on the assumption that the lunar craters of Classes IH and IS were formed in hard and soft rock, respectively, is obvious from the figure. Furthermore, one notes that no data on the dimensions of terrestrial meteoritic craters were used in the construction of the curves in question, as is not the case for Baldwin's curve. In spite of this fact, the curves yield a separation of the terrestrial meteorite craters into two classes, for hard and soft rock, correctly. When corresponding coefficients of correlation are obtained for each type of crater, one finds that the values from this work exceed or at least are equal to those obtained using Baldwin's equation, in all instances.

The considerations of this paper suggest strongly (but are insufficient to prove) that the rocks of the mare floors are sedimentary in origin. On this basis, they should be softer than the rocks of the highlands, and not basalt from lava flows. This view is diametrically opposed to those generally current. That the maria are vast pits filled with dust, as asserted by Gold,[4] is rendered highly unlikely by observed dimensions of craters formed in clay and marine muck.[30] Least-square lines for craters in these materials, analogous to those for hard rock and soft rock, appear in Fig. 2; the order of decreasing shear strength corresponding to the curves is to the right. Since dust has negligible shear strength, the points for the lunar craters of Class IS with smallest dimensions should be displaced far to the right in Fig. 2, if Gold's hypothesis were correct. Hence, the dust on the moon, the presence of which is revealed by analysis of eclipse and radio observations,[5] is superficial in distribution.

C. Craters in Water

Baldwin's correlation curve applies only to lunar craters of Class I, as do the curves discussed in the preceding section. The remaining craters have been classified by Baldwin in Classes II, III, and IV, in order of increasing age on the basis of apparent degree of erosion. When the dimensions of these craters are plotted in a diagram of the type of Fig. 2, the points lie in a broad band above the curves for Class I, at distances correlated roughly with the ordinal numbers of the classes. The nine craters of Class IV for which the representative points are displaced farthest from the curves for Class I have been placed in a separate Class V in this work. These craters are Hőrbiger, Grimaldi, Schickard, Hipparchus, Ptolemaeus, Neper, Letronne, Hansteen, and Encke. The locus of the corresponding representative points in Fig. 2 represents the upper bound of the band in which all the lunar craters lie.

Baldwin explained the upward progression of the representative points with ordinal class of the craters in a plot similar to Fig. 2 as purely an effect of some unknown erosive process, filling the bottom at the expense of the rim after crater formation. A similar explanation is inherent in Gold's arguments,[4] but suggested erosive agents[39] seem insufficient. It will be asserted that the

basic cause is a progressive change of the circumstances under which the craters were formed initially, corresponding to the gradual loss of the moon's hydrosphere. Specifically, the relative dimensions of a crater were fixed by the depth of the water in which the meteorite exploded to produce the crater. The craters of Class V are the oldest and were formed when the hydrosphere was at its maximum depth. The physical arguments of Gilvarry and Hill[29] can be used to show that the impinging meteorite must explode close to the surface of the water. It is not denied that erosion is of some consequence in modifying the relative dimensions of lunar craters, but the process is assigned a secondary role in this connection; however, the correlation of age and eroded appearance of a crater is assumed valid.

Glasstone[40] gives curves for the dimensions of craters formed by nuclear bombs in strata lying under water, with the seat of the explosion close to the water surface. The curves apply specifically to a water depth of 18 m for a bottom of soft rock, but conversion factors for a bottom of hard rock are given. It has already been established that the maximum depth of the lunar hydrosphere was at least 1 km and possibly 2 km. Inspection of Fig. 2 reveals that these figures represent the order of the depths for craters of Class V. Accordingly, the dimensionless parameter defined by

$$\mu = \delta/d \tag{4}$$

in terms of the water depth, δ, must have had nearly the value unity for these craters, on the assumption that they are among the oldest. Therefore, to relate the lunar craters of Class V with terrestrial explosion craters, it is reasonable to make the correlation with explosion craters for which $\mu = 1$. The dimensions of two craters satisfying this prescription, Glasstone (H) and Glasstone (S), for a bottom of hard and soft rock, respectively, have been obtained from Glasstone's data and plotted in Fig. 2.

Since the points in Fig. 2 for the lunar craters of Class V lie at an extreme displacement from the curves for Class I, it will be assumed that they were formed in hard rock, in agreement with the relative positions of the points for Glasstone (H) and Glasstone (S). Their dimensions were fitted by a

relation of the form

$$D = a_1 d \left[1 + (d/a_2)^n \right] , \qquad (5)$$

where a_1 was fixed by means of Glasstone (H), and the coefficient a_2 and exponent n were determined by a least-squares fit to the data. The corresponding curve is shown in Fig. 2 (labeled hard rock). One sees that the points for Glasstone (H) and Class V lie on one smooth curve, roughly parallel to those obtained for the craters of Class I. The curve is not changed greatly by an alternative choice of the dimensions of Glasstone (H), if the parameter of equation 4 lies in the range $1/12 < \mu < 2$, roughly.

The lunar maria can be divided into two broad classes. One class shows irregular borders. The other, of which Mare Imbrium is the archetype, is characterized by a nearly circular outline and the presence of an encircling ring of mountains, with an escarpment on the inner wall and a gradual slope on the outer face. It will be hypothesized that the maria of Imbrian type were formed by explosions of large meteorites, occurring at a time when the lunar hydrosphere exhibited roughly its maximum depth. If such were the case, the dimensions of these maria should show a correlation with those of the craters of Class V and Glasstone (H).

Values for the diameters of the maria have been given by Baldwin; the diameter was considered to extend fully to the encircling mountains (the Altai in the case of Mare Nectaris). The maximum height of these mountains can be taken as a first approximation to the corresponding crater depth; values were taken from results of Schmidt,[41] in general. This estimate can be improved by including a correction for the depth of the sediments in the mare basin. As an upper limit, Baldwin gives roughly 2 km as the depth in question for the maria; this value was adopted for the largest mare (Imbrium) and scaled linearly with diameter for the others. Representative points determined in this manner are shown in Fig. 2 for Mare Imbrium, Nectaris, Serenitatis, Crisium, and Humboldtianum. One sees that the points lie closely on the curve already determined from mensuration of Glasstone (H) and the craters of Class V.

As compared to the corresponding argument for the craters of Class I, the reasoning indicating that the Imbrian maria, the craters of Class V, and Glasstone (H) form one family lacks a link in the form of terrestrial meteorite craters. However, a meteoritic crater exists which one can argue reasonably must have been formed in water. This crater is Deep Bay,[42] which is a nearly circular appendage of Reindeer Lake in northern Saskatchewan, Canada, as shown in the map of Fig. 3. It has not been possible to fix the geological age of this crater with any degree of certainty. However, Reindeer Lake occupies the site of an extinct Pleistocene lake of considerably larger area, as Fig. 3 shows.[43] If Deep Bay actually is of Pleistocene age, it most probably was formed in water, and the spot elevations above the level of the present lake appearing in Fig. 3 indicate a value $\mu \approx 1/2$ for the parameter of equation (4).

Deep Bay was formed in schist and gneiss, and thus in soft rock on the criteria adopted. To construct a curve for meteorite craters formed in water for a bottom of soft rock, a_1 of equation (5) was fixed by the dimensions of Glasstone (S), and the values of a_2 and n were taken as already determined from the craters of Class V. The resulting curve is shown in Fig. 2 (labeled soft rock). One notes that the point for Deep Bay lies on it closely. The bottom of Deep Bay has not been bored, but would have to consist of roughly 1 km of glacial debris for the representative point in Fig. 1 to fall reasonably close to the curves for craters of Class I. Such a large value is inconsistent with the fact that at least one glacier passed over Chubb but left relatively little glacial deposit in the crater; it is necessary to presume that freezing of the lake in a crater protects it from glacial filling.[44] Note that the points for both Deep Bay and the lunar maria have been fitted without making use of their dimensions in constructing the fitting function.

If the dimensions of the lunar craters of Classes II, III, and IV (exclusive of V) are fitted separately in each case, the corresponding curves lie between those for Class I and the curve determined by Glasstone (H) and the craters of Class V, in a progression corresponding to ordinal number of the class. On the thesis of this paper, this progression corresponds to formation of craters at temporal stages in the dissipation of the lunar hydrosphere,

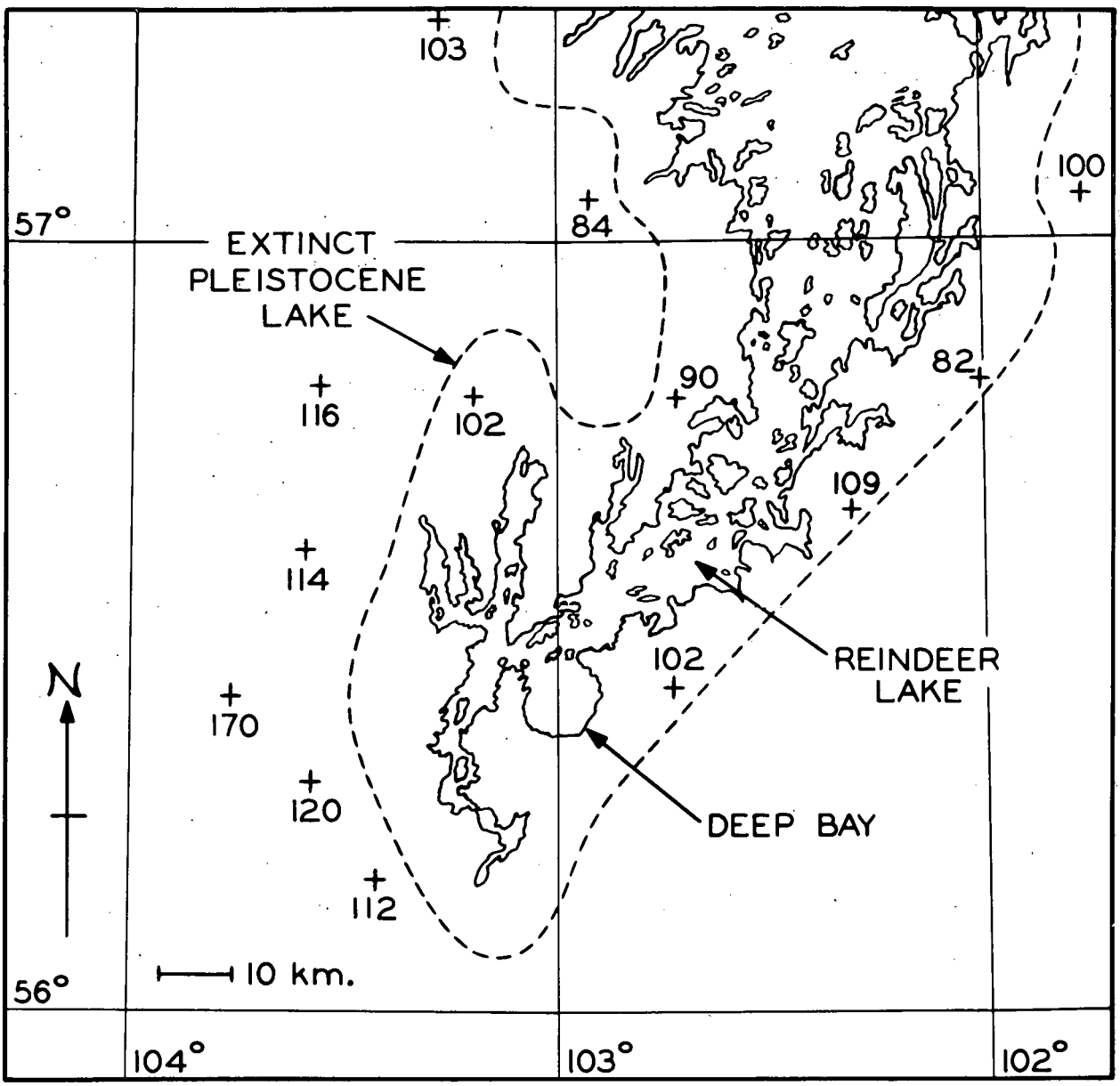

MUL-14615

Fig. 3. Map of the southern half of Reindeer Lake, showing Deep Bay and the outline of the extinct Pleistocene lake. The crosses indicate spot elevations, with heights in meters above the present level of Reindeer Lake.

where the average water level was below the maximum. Terrestrial analogs of these craters of intermediate type probably exist in the Campo del Cielo crater field[45] in Argentina. The meteorite fall occurred in marshland; the dimensions of one of the largest craters are known with reasonable accuracy from excavation and the corresponding point occupies an intermediate position relative to the curves of Fig. 2.

D. Discussion

It is clear that the presence of a lunar hydrosphere of the age calculated yields a direct explanation of the progression of relative dimensions of the craters in the various classes, of the origin of the maria, and of the nature of the mare floors. It is ironical that, on these views, the name mare is correct on the basis of provenance.

The considerations of this paper have a direct bearing on the problem of the origin of tektites. Nininger[46] has proposed that these glassy objects are fragments of rock fused initially by meteorite impact on the moon and ejected from the lunar surface by the force of the explosion. The second melting phase displayed by these objects then occurred during supersonic passage through the earth's atmosphere. Objections to the possibility of a swarm of bodies from the moon falling on the earth in a compact cluster seem to have been disposed of recently by Baker.[47] Thus, the theory yields properly two periods of fusion, the observed flow structure and shape of these objects, and the distribution over the earth's surface.

However, the chemical composition of most tektites is similar to that of argillaceous sedimentary rocks, and the view that such rocks could not be present on the moon has precluded general acceptance of Nininger's idea. This objection is met fully by the considerations of this paper. Erosion explains the presence of quartz particles in the lunar sediments, required to yield the lechatelierite observed in tektites. Thus the theory in question is the only one satisfying all the requirements laid down by Barnes.[48]

It remains to explain the dark color of the maria. Since only a small amount (less than 5 percent) of organic carbon in a sediment is sufficient to yield a dark rock of low reflectivity,[49] it will be postulated that a primitive

form of life existed in the lunar hydrosphere. All the requirements for biopoesis were once met on the moon,[50] in view of the existence for an extended time of an atmosphere and hydrosphere. Their presence would reduce the daily range of temperature below that presently observed;[5] if the albedo of the primitive atmosphere of the moon were comparable with that of the earth, the mean surface temperatures would be the same.[51] The time scale is favorable to the possibility in question, since the oldest known fossil plant (an alga) is at least 2.6×10^9 years old,[52] indicating that life began on the earth within a period less than 2×10^9 years after its origin. This maximum span for biopoesis to occur is less by 1×10^9 years than the minimum lifetime shown for H_2O in Fig. 2. Thus, one can speculate that life originated on the moon through the process postulated by Oparin.[53] The initial steps were the formation of fairly complex organic molecules through the action of solar ultraviolet radiation and lightning discharges on atmospheric gases, as reproduced to some extent in the laboratory.[54]

A positive clue exists that life once existed in the lunar hydrosphere. As this medium dissipated, the dark coloration in the maria of Imbrian type tended to recede from the bases of the encircling mountains, as is evident in the pattern of light and dark color in the mare basins. The retreat is most prominent in the case of Mare Nectaris, where the dark material has regressed about 100 km from the ring defined by the arc of the Altai Mountains,[55] but it appears also for Mare Crisium, Mare Serenitatis, and Mare Imbrium. It is characteristic of living matter to follow the retreat of its habitat in this manner.

The inferred presence of organic carbon in the maria and adjacent craters would explain in a natural way Kozyrev's observations[56] of the Swan bands of C_2, as the result of sublimation of carbon by the heat of a meteorite impact. Accordingly, the observations can be explained without the need to invoke volcanism on the moon, for which no visible evidence exists otherwise, on the thesis of this paper.

III. TERRESTRIAL SURFACE FEATURES

This section considers the origin of the major topographical features of the earth's surface, the ocean basins, and the continents.

A. Origin of Ocean Basins

The largest terrestrial ocean, the Pacific, can be divided geologically into two major basins, the North Pacific and the South Pacific, by prolongation to the coast of South America of an east-west line coinciding approximately with the andesite line north of Australia. On the side of the andesite line away from the Pacific the rocks tend to be continental in type. A similar natural division of the Atlantic into the North Atlantic and the South Atlantic can be made by a line joining South America and Africa at their closest points, roughly between Cape São Roque and Cape Palmas. With these divisions, each of the five oceans, the North Pacific, the South Pacific, the North Atlantic, the South Atlantic, and the Indian, possesses a roughly circular outline.

At the seaward limit of the continental shelf, the demarcation of each oceanic basin is an escarpment as precipitous as that forming the boundary of a lunar mare of the type of Mare Imbrium. Thus the terrestrial oceans possess at least two features, a roughly circular outline and an encircling scarp, in common with the lunar maria of Imbrian type. A third common feature exists: As is the case with the lunar maria, the floors of the oceans lie below the mean level of the land mass. In view of these similarities, it will be postulated that the terrestrial oceans and the lunar maria of Imbrian type were formed in the same manner, by explosive impact of large meteorites in the presence of a hydrosphere. At the outset, it should be emphasized that the hypothesized meteorite impacts occurred far back in the Pre-Cambrian era (a period of time lasting about 4 billion years).[57]

In the case of the lunar maria, the author's argument on the mode of formation was based on a correlation of their dimensions with those for explosion and meteoritic craters formed in water. For the present terrestrial oceans exclusive of marginal seas, the diameter D and depth d' are shown in Table I, as determined from data of Kossinna.[58] For simplicity, the line of division between the North Pacific and the South Pacific, and between the

Table I. Mensuration of Ocean Basins

Ocean	D (km)	d'(Isostatic) (km)	d(Anisostatic) (km)	ℓ(Anisostatic) (km)
S. Pacific	11,000	10.5 ± 0.5	39 ± 4	22 ± 2
Indian	9,700	8.5 ± 0.5	34 ± 3	19 ± 2
N. Pacific	9,500	10.5 ± 0.5	34 ± 3	19 ± 2
S. Atlantic	7,600	8.5 ± 0.5	27 ± 3	15 ± 2
N. Atlantic	6,800	9.5 ± 0.5	24 ± 2	14 ± 1

North Atlantic and the South Atlantic, has been taken as the earth's equator. Because of the inherent uncertainties, no effort has been made to correct the entries for the Pacific Oceans to take account of the location of the andesite line. The diameter D shown is an equivalent diameter fixed from the ocean area A by

$$(1/4)\pi D^2 = A \, . \tag{6}$$

The depth d' appearing in Table I corresponds to the maximum given by Kossinna for which a significant floor area of the ocean exists; it includes 1 km corresponding to the mean height (840 m) of the continents.[58]

The values of ocean dimensions in question cannot be made the basis of a correlation with the corresponding dimensions of the lunar maria, because the terrestrial ocean basins are and have been subject to isostatic compensation. On the other hand, the evidence is strong that the moon is not and never was in hydrostatic equilibrium, in view of its strongly triaxial shape. This shape reflects the strength of the component materials, and is consistent with a cold origin for the moon.[4,39] However, even if the earth were formed cold, radioactive heating certainly would be sufficient[59] to render the mantle plastic up to the present depth of isostatic compensation (roughly between 50 and 100 km). Thus, the ocean depths d' appearing in Table I must be corrected for the presence of isostasy.

For precision in terminology, the earth's crust will be defined as the region above the Mohorovičić discontinuity, and the solid region below will be referred to as the mantle. On the left (labeled "present") in Fig. 4 are shown standard sections through the earth's crust and mantle, for continental and ocean columns, as deduced by Worzel and Shurbet[60] by means of relatively accurate seismic data from explosions. The standard land column consists of 33 km of crustal rock of density 2.84 overlying mantle rock of density 3.27. The corresponding ocean column consists of 5 km of sea water (density 1.03), 1 km of sediments (density 2.30), and 4-1/2 km of crustal rock (density 2.84) over the mantle for a total depth of 10-1/2 km of crust. With these densities, the land and ocean columns are in isostatic equilibrium at a depth of 33 km, corresponding to the depth of the Mohorovičić discontinuity under the continents.

At the time of impact of the meteorites forming the ocean basins, the Mohorovičić discontinuity must have been level under the areas now corresponding to continents and oceans, as shown on the right (labeled "pristine") in Fig. 4. Its depth must have been intermediate between the present depths of this discontinuity below the oceans and continents. Using the data of Kossinna for the total area of the earth corresponding to continents (including marginal seas) and oceans, one computes from the volume balance that the level in question lay 14 km above the present depth of this discontinuity under the continents, as shown in Fig. 4. The standard land and ocean sections above the Mohorovičić discontinuity appear superposed on this base level (with the sedimentary layer omitted). The figure represents the proper relative position of the land and ocean columns immediately after meteorite impact, when anisostatic conditions prevailed, provided two conditions have been fulfilled. The first is that isostatic adjustment of oceans and continents, from pristine to present conditions, took place by horizontal flow of mantle rock at depths below the Mohorovičić discontinuity, as occurs in the isostatic balance of the present day. The second is that each standard column (land and ocean) above the Mohorovičić discontinuity has remained approximately the same throughout the earth's history since the oceans were first formed. This

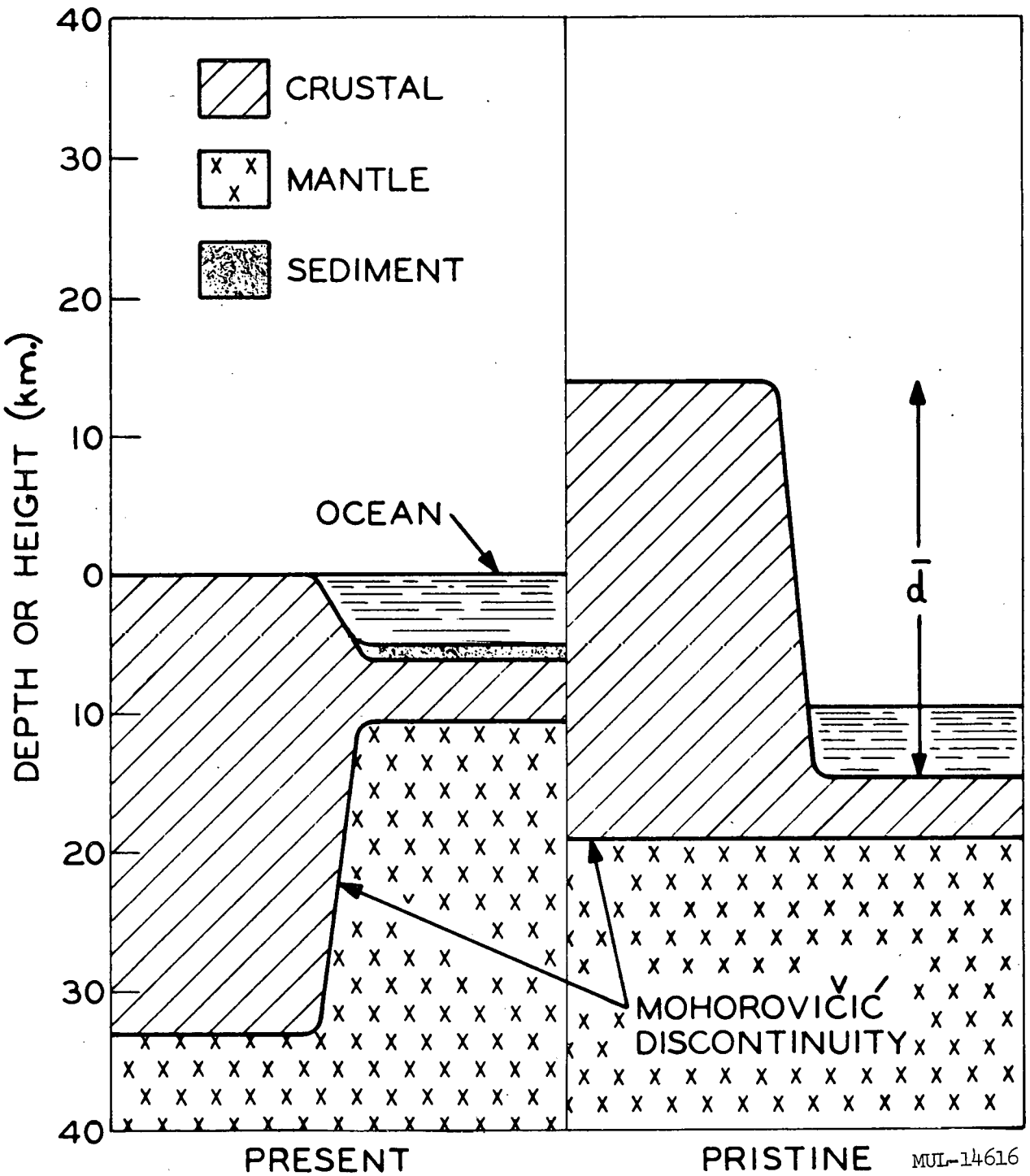

Fig. 4. Standard sections through rocks under continents and oceans at the present time (left), compared with corresponding pristine sections (right) immediately after the impacts of the meteorites forming the oceans.

assumption is reasonable in view of the small thickness and mass of oceanic sediments compared to the corresponding quantities for a total column, and implies that isostatic readjustment was fast compared to erosive processes.

On these assumptions, the mean depth $\overline{d}$ of the craters corresponding to the primordial ocean basins before isostatic adjustment is fixed approximately as the difference of the thickness of crustal rock in the standard continental and oceanic columns, with the sediment thickness ignored in the latter, as indicated in Fig. 4. This estimate can be improved in two respects. The first is to include in the estimate an additive correction for the ocean sediments, since primordially these deposits must have existed in the continental column. The present thickness (1 km) of such sediments yields 2 km for this correction, corresponding to the fact that the total area of the deep oceans is about twice that of the remainder of the earth. Secondly, to take account of the fact that the depths of the lunar maria were reckoned from the approximate maximum heights of the rims, one can include 1 km in $\overline{d}$ corresponding to the mean height (840 m) of the continents. The resulting value of $\overline{d}$ is entered in Table II with a possible error of $\pm 10\%$ of its value. The mean rim height $\overline{\ell}$ of the meteorite craters forming the primordial ocean basins can be obtained. Prior to the meteorite impact, the crustal rocks must have overlain the Mohorovičić discontinuity to an approximately uniform height, L. The value of L can be computed directly from the present thicknesses of crustal rock under the continents (including marginal seas) and oceans, and the corresponding areas[58] on the surface of the earth, as 15 km. The mean rim height $\overline{\ell}$ is then simply the difference of the height of the standard continental crustal column and L (the correction associated with the sediment thickness cancels approximately). The value of $\overline{\ell}$ appears in Table II with a possible error of $\pm 10\%$ of its value. The mean diameter $\overline{D}$ of the craters corresponding to the primordial ocean basins, given in Table II, was fixed from equation (6) with A taken as the mean area of a present ocean. These computations presume that a right circular cylinder represents a reasonable geometrical model for both the present and primordial ocean basins, and that isostatic adjustment leaves the diameter approximately the same.

Table II. Mensuration of Average Primordial Ocean Basin (Anisostatic)

$\overline{D}$ (km)	$\overline{d}$ (km)	$\overline{\ell}$ (km)	$\overline{r}$ (km)
9,000	32 ± 3	18 ± 2	2,900

To find the depth and rim height of an individual ocean basin under anisostatic conditions, it will be assumed as an approximation that each basin was geometrically similar to the average basin, primordially. Thus, the anisostatic depth d corresponding to the diameter D is given by

$$d = (\overline{d}/\overline{D})D\,, \tag{7}$$

and the anisostatic rim height ℓ is fixed by

$$\ell = (\overline{\ell}/\overline{D})D. \tag{8}$$

These primordial dimensions are shown in Table I for each ocean, with a possible error of ±10% of the value.

A sequence of events involving isostatic compensation, similar to that postulated here for the ocean basins, has been invoked by Daly[61] in explaining the Vredefort ring structure of South Africa as the result of a meteorite impact.

B. Correlations

Prior to the impact of the meteorites forming the ocean basins, water must have covered the earth to a uniform depth $\overline{\delta}$ above the roughly level surface of the crustal rock. On the assumption that the total volume of sea water has not changed greatly since the ocean basins were formed, the value of $\overline{\delta}$ is approximately 3 km. Accordingly, the parameter $\overline{\mu} = \overline{\delta}/\overline{d}$ corresponding to equation (4) had a value of roughly 1/11 for the crater corresponding to the average primordial ocean, and lies within the range for which the curves of Fig. 2 for craters in hard and soft rock under water apply. The diameter D as a function of the anisostatic depth d for each primordial ocean basin is plotted

in Fig. 2 from the data of Table I. One sees that the correlation of the data points with the curve for craters formed in hard rock under water is excellent, agreeing with the fact that the substratum of an ocean basin is basaltic. Clearly, the representative points for the pristine oceans, the lunar maria, the lunar craters of Class V, and the terrestrial explosion craters in hard rock under water all lie on one curve of correlation. Furthermore, no data on the dimensions of the lunar maria or terrestrial oceans were used in the construction of the curve in question. On the other hand, the points corresponding to the diameter D and present depth d' of an ocean show agreement with the curve only within an order of magnitude.

One might argue that the excellent correlation of crater diameter and depth obtained is fortuitous as regards the craters corresponding to the primordial oceans. To rule out this possibility, the correlation of diameter and rim height will be examined. It will be assumed that the relation between the diameter D and the rim height ℓ of a crater formed in water (for $\mu \approx 1$) can be written as the linear form

$$C = b_1 \ell \,, \tag{9}$$

with the coefficient b_1 fixed in the cases of hard and soft rock by the dimensions of Glasstone (H) and Glasstone (S), respectively. The corresponding straight lines appear in Fig. 5.

For the lunar craters of Class V, only a few uncertain rim heights are available[1] for comparison with the result of the corresponding line for hard rock. However, the rim heights of the lunar maria can be approximated as the maximum heights of the encircling mountains less the mean height (2 km) of the lunar highlands above the lowlands.[6] From the data of Schmidt,[41] this prescription yields the representative points for the lunar maria shown in Fig. 5. The agreement of the data points with the line for craters formed in hard rock under water clearly is good. Shown also are the diameters of the primordial ocean basins as a function of the anisostatic rim height ℓ, from the data of Table I. One sees that the correlation of the data points with the line for craters formed in hard rock under water is excellent. Furthermore, the

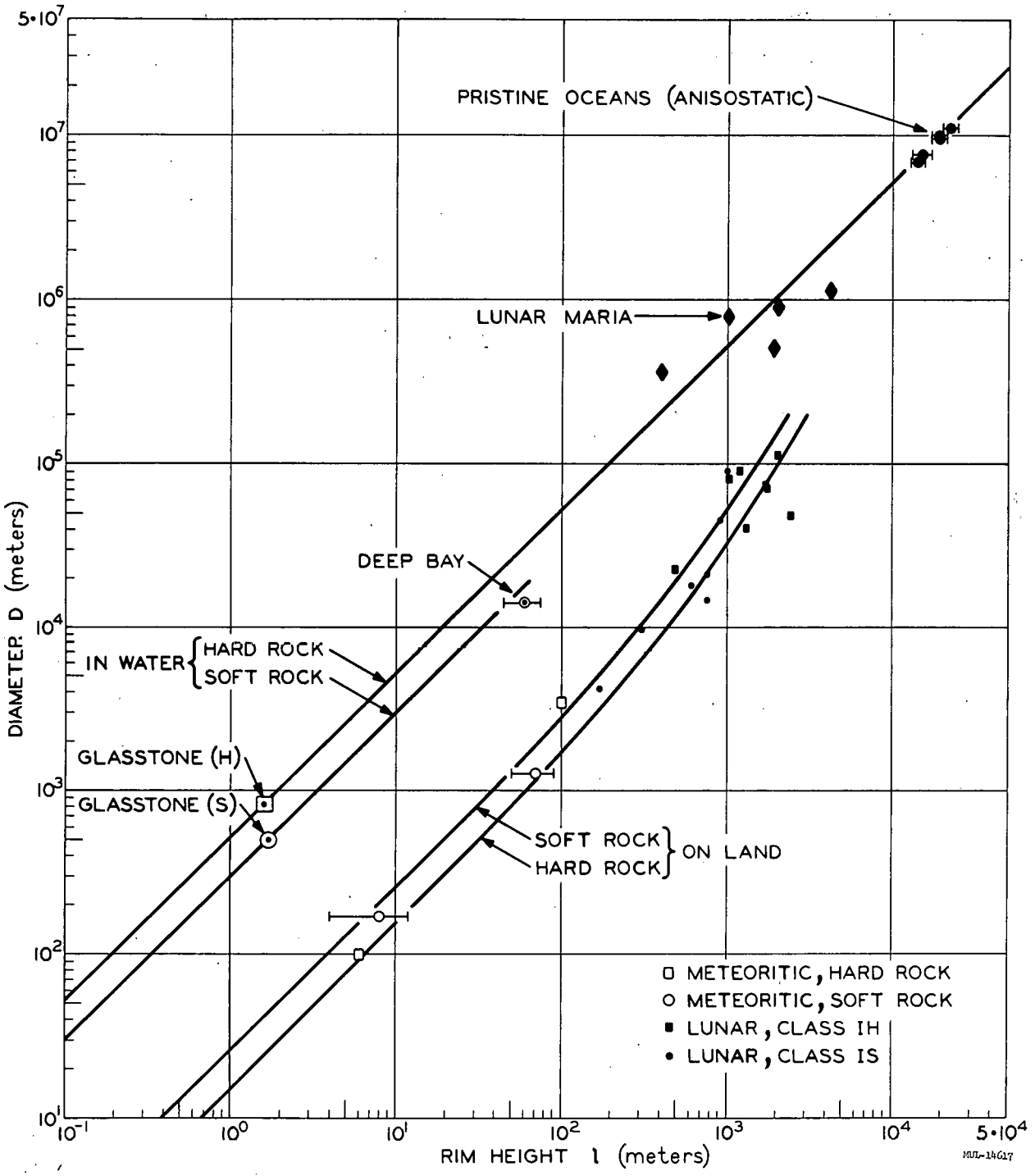

Fig. 5. Correlation of diameter versus rim height for the pristine oceans, the lunar maria, and various classes of craters. The curves correspond to fitted functions for craters on land and in water, for hard and soft rock.

fitting line was determined completely from the dimensions of Glasstone (H). As a final argument, one notes that the representative point[62] for the terrestrial meteoritic crater of Deep Bay (formed in soft rock) lies reasonably well on the proper straight line.

Analogous curves for craters in hard and soft rock on land are shown also in Fig. 5. The two curves were determined from dimensions of explosion craters in basalt and sedimentary rock,[30] and of lunar craters[1] in Classes IH and IS, respectively. The correlation of the data points for terrestrial meteoritic craters in hard and soft rock with the corresponding individual curves is not close, because of the sparsity and inaccuracy of the data. The general similarity of Fig. 2 and Fig. 5 is obvious.

In general, one sees that the correlation of the pristine dimensions of the terrestrial oceans with those of the lunar maria is excellent.

C. Origin of Continents

If the primordial ocean basins were large meteoritic craters, it follows that the primordial continents were simply structures corresponding to the rims of these craters. To see if the model is adequate quantitatively, one can calculate the average width of the rim of a crater corresponding to a primordial ocean. It will be assumed that the rim cross section is a right triangle in the plane of the crater's axis of symmetry, with the hypotenuse forming the outer slope, and one side parallel and one perpendicular to the axis. The altitude of the triangle is the rim height ℓ, and the length of the base will be designated by r. The average value $\bar{r}$ of the rim base can be calculated from the data of Table II by invoking Schröter's rule[1,63] for lunar craters, that the volume of the material displaced from the crater equals the volume of the rim. One obtains

$$\bar{r} = (3/4)\bar{D}\left\{\left[1 + 4(\bar{d} - \bar{\ell})/3\bar{\ell}\right]^{1/2} - 1\right\} \qquad (10)$$

on these assumptions, and the average value of the rim base is entered in Table II. It can be noted that Schröter's rule is a necessary consequence of explosive origin of a crater.[29,64]

For the continents regarded as circular in plan, one can determine an average diameter from equation (1) by taking A as one-sixth of the total area of the continents (considering Eurasia as a single continent). The corresponding average diameter is approximately 5600 km. From the result of Table II for $\bar{r}$, one sees that two abutting rims from adjacent craters corresponding to primordial oceans yield an average width of 5800 km for a continent. Thus, the hypothesis is closely consistent with the mean linear dimension of a continent in plan, as observed.

At the time of formation, the primordial crater rims were mountains of lunar type, and not of the folded type characteristic of present terrestrial topography. Further, these primordial mountains reared to heights above the earth about twice that observed today for the highest peak (Mount Everest). The eroded remnants of these mountains are the continental shields of crystalline igneous and metamorphic rock of Pre-Cambrian age, forming the nuclei of the continents. The view that the continental shields are simply the eroded roots of ancient mountain systems has been expressed by Collins[65] and Wahl,[66] and seems to have gained general acceptance.[67]

These ideas yield a direct and natural explanation of Wegener's law.[68] This law states that the frequency curve of elevation on the earth shows two pronounced maxima, corresponding to the ocean floor and to the continents. On the thesis of this paper, one maximum arises from the floor level of the craters forming the primordial oceans, and the other corresponds to the crater rims. Over the time since these rims first reached continental level, the processes of erosion, deposition, and diastrophism have maintained a balance, to yield a roughly constant mean height of the continents. The possibility of explaining the law in question was a major motivation of Wegener in formulating his theory of floating continents.

D. Discussion

It is clear that the hypothesis proposed yields a direct explanation of the origin of ocean basins and continents. The correlation of the pristine dimensions inferred for the ocean basins with those for lunar features and terrestrial craters formed in water represents a strong argument for the general

validity of the ideas. The disparity in the depths of the Mohorovičić discontinuity under continents and oceans appears directly as an essential element in the argument, without the need for ad hoc assumptions. Furthermore, the theory is consistent with the observed average diameter of a continent, and Wegener's law follows naturally.

The considerations of this paper have an important bearing on the meteoritic impact theory of the formation of lunar craters. In the view of Baldwin,[1] Urey,[2] and Kuiper.[3] the prevalence of craters formed by meteoritic impact on the moon is not a feature peculiar to that body, but implies a similar bombardment of the earth by meteorites in the past. However, the lunar craters obviously extend over a wide spectrum of sizes and ages. On the other hand, only 17 craters or clusters of craters were known at the time of Baldwin's work, and all these craters were small (of diameter less than 2 km) by lunar standards, and were of recent geological age.

Over the last decade, the situation has changed markedly. Discoveries of meteoritic craters in this period have enlarged significantly the total number known.[6,69] The age horizon has been extended to Early Paleozoic (Brent and Holleford Craters) and the crater size to a diameter of about 14 km (Deep Bay). Furthermore, the discovery of coesite in Barringer Crater[70] in Arizona and in the Rieskessel[71] in Austria has reinforced strongly the contention that cryptoexplosive features[1,72] are in fact meteoritic in origin. If this view is accepted, the Vredefort structure[61] provides an example of a meteoritic crater which is roughly 130 km in diameter and is Pre-Carboniferous in age. Finally, two large circular arcs which may be meteoritic in origin[69] have been noted in Canada. One has a diameter of 400 km.

Since the meteorite impacts forming the ocean basins occurred far back in Pre-Cambrian times, it is implicit in the thesis of this paper that the bombardment of the earth by meteorites has shown the same intensity throughout the ages as in the corresponding case of the moon. At the present time, the earth is experiencing merely the terminal phase of the process, marked by relatively sparse and small meteorites. In the past, the smaller craters on land vanished rapidly through erosion, sedimentation, and diastrophism. The

larger craters are relatively resistant to these processes, but another factor, isostatic readjustment, operates to make identification difficult, as in the cases of oceans and cryptoexplosive formations. Only for craters formed by impact of large meteorites in the hydrosphere is there hope of preservation over an extended period of time, because of the protection afforded by the water from subaerial erosion. In view of the enhanced rate of sedimentation in the shallow seas close to a land mass, the chance of preservation increases with the depth of the water.[73]

The primordial ocean basins were simply the largest meteoritic craters ever formed on the earth, entirely analogous to the circular lunar maria. They owe their preservation to their size, in spite of the effects of isostatic readjustment, mountain growth, erosion, and sedimentation in masking the characteristic features of a meteoritic crater. Because of their extent, transcending that of any other hydrospheric feature on the earth, it has been possible here to correct their dimensions for isostatic readjustment in a simple manner. This particular method cannot be applied in the case of a marginal sea of the ocean; it is possible that many such seas are meteoritic in origin, but demonstration of the fact may be difficult in an individual case. A possible example is the arm of the Gulf of St. Lawrence, outlined by the coasts of Nova Scotia and New Brunswick;[74] the diameter is 300 km.

Ideas similar to those above have been adumbrated by others. Chenoweth[75] has pointed out the close similarity between the Northern Canary Basin and Mare Crisium, and he has noted analogies in the features of the floor of the North Atlantic with structures in the basins of lunar maria. Gold[73] has speculated that the patterns of circular arcs in the zones of tectonic instability and gravity anomaly and in regions of earthquakes and volcanos on the earth may reflect the destruction of hydrostatically stratified balance by ancient meteorite impacts. A theory of Howell[7] bears a superficial resemblance to that presented here, but differs in that the meteoritic impacts considered are not explosive in nature.

IV. CONCLUSIONS

On the hypothesis of this paper, the early history of the moon and earth must have been very similar, as pertains to the origin of their main topographical features. At the pristine time when the largest meteoritic bodies were falling on their surfaces, the moon as well as the earth possessed an atmosphere and hydrosphere. The effect of the hydrosphere was to make the relative dimensions of the lunar maria and the primordial ocean basins different from those corresponding to lunar craters of Class I and to terrestrial meteoritic craters formed on land. Smaller bodies falling in later stages of evolution of the moon and earth produced craters either on land or in water, with a distinctive difference in relative dimensions for the two cases. These hypotheses permit complete correlation of the dimensions of the primordial oceans, lunar maria, lunar craters, terrestrial meteoritic craters, and terrestrial explosion craters. The relationships obtained go far beyond the partial correlations obtained by Baldwin, and, as in his argument, imply modes of crater genesis common to the moon and earth. One notes that an underlying idea of this paper is the extension of the geological doctrine of uniformitarianism to the moon as well as the earth.

The author wishes to thank E. W. Price, Dr. R. G. Greenler, and Dr. W. S. Rothwell for discussions, and Helen Jackson for computational work.

REFERENCES

1. Baldwin, R. B., "The Face of the Moon" (Univ. Chicago Press, Chicago, 1949).
2. Urey, H. C., "The Planets" (Yale Univ. Press, New Haven, 1952), p. 26.
3. Kuiper, G. P., Proc. Nat. Acad. Sci. U.S., 40, 1096 (1954).
4. Gold, T., Monthly Notices Roy. Astron. Soc., 115, 585 (1955).
5. Gilvarry, J. J., Astrophys. J., 127, 751 (1958).
6. Gilvarry, J. J., Nature, 188, 886 (1960).
7. Howell, B. F., "Introduction to Geophysics" (McGraw-Hill Book Co., New York, 1959), p. 256.

8. Jacobs, J. A., Russell, R. D., and Wilson, J. T., "Physics and Geology" (McGraw-Hill Book Co., New York, 1959), p. 342.
9. Darwin, G. H., "The Tides" (Houghton, Boston, 1898).
10. Taylor, F. B., Bull. Geol. Soc. Am., 21, 179 (1910).
11. Wegener, A., Geol. Rundschau, 3, 276 (1912).
12. Hills, G. F. S., Geol. Mag., 71, 275 (1934).
13. Hess, H. H., Proc. Roy. Soc. (London), A222, 341 (1954).
14. Bullard, E. C., Proc. Roy. Soc. (London), A222, 403 (1954).
15. Jacobs, J. A., Nature, 185, 231 (1960).
16. Gilvarry, J. J., Nature (in press).
17. Harrison, E. R., Nature, 188, 1064 (1960).
18. Brown, H., in Kuiper, G. P. (ed.), "The Atmospheres of the Earth and Planets" (2nd ed., Univ. Chicago Press, Chicago, 1952), p. 258.
19. Suess, H., J. Geol., 57, 600 (1949).
20. Rubey, W. W., in Poldervaart, A. (ed.), "Crust of the Earth" (Geol. Soc. Am., New York, 1955), p. 631.
21. Wildt, R., Revs. Modern Phys., 14, 151 (1942).
22. Jeans, J. H., "The Dynamical Theory of Gases" (3rd ed., Cambridge Univ. Press, Cambridge, 1921), p. 342.
23. Spitzer, L., in Kuiper, G. P. (ed.), "The Atmospheres of the Earth and Planets" (2nd ed., Univ. Chicago Press, Chicago, 1952), p. 211.
24. Gilvarry, J. J., Phys. Fluids, 4, 2, 8 (1961).
25. Gilvarry, J. J., Nature, 188, 804 (1960).
26. Sykes, J. B. (translator), "The Other Side of the Moon" (Pergamon Press, London, 1960), p. 32.
27. Ericson, D. B., Ewing, M., Heezen, B. C., and Woolin, G., in Poldervaart, A. (ed.), "Crust of the Earth" (Geol. Soc. Am., New York, 1955), p. 205.
28. Pickering, W. H., "The Moon" (Doubleday, Page, and Co., New York, 1903), p. 42.
29. Gilvarry, J. J. and Hill, J. E., Publ. Astron. Soc. Pacific, 68, 223 (1956); Astrophys. J., 124, 610 (1956).

30. Darling, T. A., Isthmian Canal Study Memoranda 283-P, 284-P, 286-P, 287-P (Dept. of Operation and Maintenance, Panama Canal, Canal Zone, 1948).
31. Vortman, L. J., Report SCTM 114-59 (51) (U.S. Department of Commerce, Washington, D.C., 1959).
32. Beals, C. S., Ferguson, G. M., and Landau, A., J. Roy. Astron. Soc. Can., 50, 203 (1956).
33. Millman, P. M., Publ. Dominion Astrophys. Observatory, Victoria, B.C., 18, 61 (1955).
34. Beals, C. S., Sky and Telescope, 16, No. 11 (1957).
35. Kraus, E., Meyer, R., and Wegener, A., Gerlands Beitr. Geophys., 20, 312 (1928).
36. Nininger, H. H., Science, 130, 1251 (1959).
37. Janssen, C. L., J. Roy. Astron. Soc. Can., 45, 190 (1951).
38. Meen, V. B., Proc. Geol. Assoc. Can., 9, 49 (1957).
39. Gilvarry, J. J., Nature, 180, 911 (1957).
40. Glasstone, S., "The Effects of Nuclear Weapons" (U.S. Atomic Energy Commission, Washington, D.C., 1957), p. 226.
41. Schmidt, J. F. J., "Charte der Gebirge des Mondes" (Reimer, Berlin, 1878); "Kurze Erläuterung zu J. Schmidt's Mondcharte" (Reimer, Berlin, 1878).
42. Innes, M. J. S., J. Roy. Astron. Soc. Can., 51, 235 (1957).
43. Dence, M. R., Falconer, G., and Falconer, J., (compilers), "Glacial Map of Canada" (Geol. Assoc. Canada, Toronto, 1958).
44. Harrison, J. M., J. Roy. Astron. Soc. Can., 48, 16 (1954).
45. Spencer, L. J., Geograph. J., 81, 227 (1933).
46. Nininger, H. H., "Chips from the Moon" (Desert Press, El Centro, California, 1947).
47. Baker, G., Nature, 185, 291 (1960).
48. Barnes, V. E., Geochim. et Cosmochim. Acta., 14, 267 (1958).
49. Pettijohn, F. J., "Sedimentary Rocks" (Harper and Brothers, New York, 1949), p. 175.

50. Huang, S., Publ. Astron. Soc. Pacific, 71, 421 (1959).
51. Möller, F., in Flügge, S. (ed.), "Encyclopedia of Physics," Vol. XLVIII (Springer-Verlag, Berlin, 1957), p. 155.
52. Holmes, A., Nature, 173, 612 (1954).
53. Oparin, A. J., "The Origin of Life" (Macmillan, New York, 1938).
54. Miller, S. L., Science, 117, 528 (1953).
55. Urey, H. C., Sky and Telescope, 15, No. 3 (1956).
56. Kozyrev, N. A., Priroda, 3, 84 (1959).
57. Wilson, J. T., in Flügge, S. (ed.), "Encyclopedia of Physics," Vol. XLVII (Springer-Verlag, Berlin, 1956), p. 288.
58. Kossinna, E., Veröffentl. Inst. Meereskunde Univ. Berlin, Neue Folge A. Geor.-naturwiss., 9, 1 (1921).
59. Birch, F., J. Geophys. Research, 56, 107, (1951).
60. Worzel, J. L., and Shurbet, G. L., in Poldervaart, A. (ed.), "Crust of the Earth" (Geol. Soc. Am., New York, 1955), p. 87.
61. Daly, R. A., J. Geol., 55, 125 (1947).
62. Beals, C. S., Sci. Am., No. 7 (1958).
63. Schröter, J. H., "Selenotopographische Fragmente" (Lilienthal and Helmst, Göttingen, 1791).
64. Hill, J. E., and Gilvarry, J. J., J. Geophys. Research, 61, 501 (1956).
65. Collins, W. H., Intern. Geol. Congress, 16th Session, 1, 271 (1936).
66. Wahl, W. A., Bull. Comm. Géol. Finlande, 115, 489 (1936).
67. Knopf, A., in Poldervaart, A. (ed.), "Crust of the Earth" (Geol. Soc. Am., New York, 1955), p. 685.
68. Wegener, A., "The Origin of Continents and Oceans" (translated from the the third German edition by Skerl, J. G. A.) (Dutton, New York, 1924), p. 30.
69. Beals, C. S., Nature, 181, 559 (1958).
70. Chao, E. C. T., Shoemaker, E. M., and Madsen, B. M., Science, 132, 220 (1960).
71. Shoemaker, E. M. and Chao, E. C. T., Bull. Geol. Soc. Am., 71, 2111 (1960).

72. Dietz, R. S., Science, 131, 1781 (1960).
73. Gold, T., Nature, 179, 121 (1957).
74. Willmore, P. L. and Scheidegger, A. E., Trans. Roy. Soc. Can., 50, 21 (1956).
75. Chenoweth, P. A., Bull. Geol. Soc. Am., 69, 1545 (1958).

Paper S

NOTES ON THE THEORY OF IMPACT CRATERS

E. J. Öpik*

Department of Physics, University of Maryland

College Park, Maryland

ABSTRACT

Quantitative consequences of a schematic theory of meteorite impact are studied. The interpolation formulae for penetration and mass eroded (crushed) are represented in standard form. From these formulae, and from independent consideration of the size of surviving fragments, consistent values of mass and velocity of the Canyon Diablo meteorite, around 2×10^6 tons and 15 km/sec, respectively, are obtained. The close order of magnitude of these estimates is further supported by the agreement between predicted and observed numbers of craters in Mare Imbrium. The observed mean ellipticity of lunar craters is compatible with low velocity impact into relatively soft material, as required by the writer's ideas on lunar cosmogony and structure, based on an independent array of observational data. Escape throwout and ejection of rock fragments from the moon by meteorite impact is considered. Impacts below 11 km/sec would lead to accretion; impacts above 11 km/sec would lead to depletion of lunar material. From consideration of survival of ejected fragments, it is concluded that meteorites of lunar origin must be less frequent than 1 for every 500 stony meteorites decending on earth. Breakup of stony meteorites by aerodynamic pressure prevents craters of less than 1 km diameter from being formed by them on earth. Tables for meteor and micrometeor frequencies and for the puncture risk of space vehicles are given.

* * *

* On leave from Armagh Observatory, Northern Ireland.

1. Introduction. The main purpose of this note is to consider some quantitative aspects of the theory of meteorite impact in their application to astronomical and cosmogonical problems such as the origin of lunar and terrestrial meteorite craters and the population of stray bodies in the solar system, as well as to the meteorite hazard and skin erosion of space vehicles.

A comprehensive review is not attempted here; the author rather prefers to apply his own simplified models[1,2] which, from a comparison with modern, more refined mathematical approaches and experimental data, appear to yield close order-of-magnitude approximations, being at the same time more expedient and flexible to handle. The different models used by the author serve different purposes, such as the separate estimates of penetration, volume of erosion and diameter of the crater, and the size of surviving fragments; the models are only used for "mathematical estimates" of a few characteristic quantities, and are not means to describe details of the process of impact. They may be somewhat contradictory between themselves, but the degree of divergence of the numerical results may even serve as a check on the consistency of the general picture. The intercomparison may be especially useful in assessing the somewhat arbitrary parameters of an unobserved event, such as the velocity and mass of the projectile, the effective strength of the materials, and the arbitrary definitions of the boundary conditions of penetration and cratering.

Much has been said about comparing terrestrial explosions with meteorite impact. Despite similarities in the process of cratering, there is a basic difference. The terrestrial explosion is the result of expansion of a gas ball without initial translational motion; its efficiency depends on the arbitrarily chosen depth of a planted charge and on the energy released in the explosion, which in underground nuclear explosions determines the initial mass of the gas ball without regard to the mass of the charge. In meteorite impact, the primary agent is the translational motion of the meteoric body, which itself, from mere inertia, is a powerful cratering factor and determines also the depth of penetration; at this predetermined depth, a gas ball develops as a secondary agent of cratering which may be missing at low velocities. The action of the

gas ball is similar in both cases, but its mass, in the case of impact, is not simply proportional to the kinetic energy of the projectile. There is no direct way of applying quantitative results of explosions to meteorite impact, although the geometry of the craters may be similar.

There is another difference between the two types of craters, namely in the spatial and temporal distribution of the source of the shock, due to the motion of the projectile as compared with the fixed position of the explosive charge. However, this kind of difference is of relatively minor importance.

Because of predetermined penetration, for given materials the volume efficiency of impact cratering is mainly proportional to the momentum of the projectile, and not to its kinetic energy, with some increase (doubling) of the factor of proportionality with increasing velocity (5 - 30 km/sec, cf. Table 2) due to the development of the gas ball. This circumstance has been overlooked by Wylie, Baldwin,[3] and others concerned with estimates of the mass of a meteoric projectile required to produce a certain size of crater.

2. The Arizona Meteorite. As a test case, the Canyon Diablo (Arizona) crater may be used. For the mass of the meteorite, Baldwin and Wylie suggest values of the order of 10^4 tons only,[3] the kinetic energy hardly accounting for the mechanical work of throwout and crushing of the crater material. This would imply almost 100 percent efficiency with respect to mechanical work. Considering that there is no "lid" to keep the material enclosed, and that most of the impact energy goes into heating and ejection of the central zone around the point of impact,[2] a mechanical efficiency of the order of 1 percent and a meteorite mass of the order of 10^6 tons appear more likely. The mass of sublimated nickel-iron, of a high nickel content (17%) and therefore chemically preserved in the form of small condensation globules, alone has been estimated by Rinehart[4] to amount to $1.0 - 1.5 \times 10^4$ tons spread over an area of 200 km^2 around the crater. The high nickel content of the condensate, about twice that for the large meteoritic fragments, points to a much greater amount of softer iron which has disappeared through oxidation, setting the total mass condensed from the vapors and deposited on the soil in the neighborhood of the impact at some 5×10^4 tons at least. Most of the meteor vapors and the

ensuing iron smoke must have been shot by the explosion mushroom high into the stratosphere and carried away by the winds as in the case of nuclear and volcanic explosions, so that the deposit left behind can represent but a small fraction of the whole. An initial mass of some 10^6 tons is not inconsistent with the observed residue.

From three independent models (penetration, crater volume, and size of fragments) the writer has derived a mass of 2.6×10^6 tons and a velocity of 15 km/sec for the meteorite.[2] However, this estimate is not currently accepted. There seems to exist a consensus of opinion that a mass of the order of 10^5 tons is more probable, although the low values proposed by Baldwin and Wylie are certainly out of the question.

In view of the importance of the scaling problem of impact craters, and with the purpose of checking the basis of the estimates, in the following sections the evaluation of the mass of the Arizona meteorite is critically reviewed.

3. A Simplified Theory of Impact. For the writer's theory of meteorite impact we refer to his Papers I[1] and especially to Paper II.[2] His first approach,[1] constructed on the model of inelastic incompressible liquid-drop impact into liquid, led to order-of-magnitude estimates of the penetration and mass eroded which appear to be in some accord with observation on meteor craters as well as with modern theory and experiment [see Ref. (2), p. 33].

Inelastic impact is defined here as a process where only momentum is transmitted in the shock, whereas the extra energy is converted into heat and into latent forms (ionization, dissociation, melting, vaporization). In meteorite shock, a spectrum of turbulence is originated which serves as an agent for dissipation of the energy. As a result, at the shock front for a given pressure the temperature is higher, the density lower, and the energy of compression smaller than in calculations with a reversible adiabatic equation of state. The latter would be valid for laminar flow, which certainly is not the case here. As to incompressibility, it is a formal approximation which does not affect the order of magnitude and, for the boundary conditions at low pressure, is well fulfilled.

The results were apparently more realistic than extrapolations from low-velocity missile data and terrestrial explosions used until quite recently by Baldwin,[3] Grimminger,[5] Whipple,[6] and others. The calculation of meteorite risk to space vehicles, based on these extrapolations and usually quoted in literature, are considerably overestimated, on account of the assumed too large penetration.

In Paper II the author revised and supplemented his former theory; in particular, backfiring from a "central funnel" partly vaporized by immediate contact with the meteoroid as well as by inelastic shock was taken into account as a factor increasing the radial momentum of the shock and the volume of destruction connected with it.

There are two main points of divergence between the author's approach (as well as that of modern calculations) and the aforesaid traditional extrapolations; (a) the plasticity and flattening of the projectile leads to a depth of penetration several times smaller than in the traditional estimates; and (b) it is shown that the volume of the crater is determined by the momentum of the projectile, and not by its kinetic energy as in the traditional approach. Hence, extrapolation to meteor velocities with kinetic energy as the argument leads to crater volumes which, for this reason alone, are too large by 1 to 2 orders of magnitude. The author's numerical results are cross-checked in several independent directions, such as the size of the largest surviving fragments of the Canyon Diablo meteorite, the frequency of craters in the lunar Mare Imbrium, and the penetration of shaped-charge jets, in addition to the depth and volume of the Canyon Diablo crater. Therefore, any considerable changes in these estimates do not seem to be likely.

The present simplified method consists of calculating mean values of pressure, velocity, etc., over certain idealized characteristic surfaces (schematic shock fronts) and volumes, and determining their variation by one-dimensional integration. The emphasis is on a realistic assessment of physical conditions, and not on mathematical precision. Integration of differential equations for continuous flow over the entire volume of the event will not lead to better results, unless all physical factors are taken into account; yet this is

usually not the case, and despite the great amount of work involved in numerical integrations, the results may not be closer to a real case than those of the simplified procedure. This is not meant to belittle the importance of hydrodynamic integrations which doubtless are needed to confirm the exploratory conclusions of a short-cut.

The author's scheme is not a purely liquid-drop case of infinitesimal cohesion, but the finite strength of the materials is incorporated in the model in such a manner that it actually defines the boundary conditions at the end of penetration, and the volume of the crater. Without this limitation, the purely liquid model would lead to infinite or indefinite penetration and volume.

Of course, a considerable uncertainty remains in defining the proper values of the strength of the materials, as well as in the specification of the crater boundaries to which they apply. In the application to cosmic craters, or to craters on earth which have not been properly studied, the rim-to-rim diameter of the crater wall is the only definitely established dimension; the theoretical formulae must then be adapted to yield expressly this dimension.

The mass eroded (crushed and displaced) at impact is estimated[2] to be

$$M = k\mu w\,(\rho/s)^{1/2}, \qquad (1)$$

where μ = mass of projectile, w = velocity at impact, ρ = density and s = crushing strength of the surface material; k is a nondimensional factor allowing for the extra momentum of backfiring. At high meteor velocities, the factor k feebly depends on the density ratio of projectile to surface material [see Ref. (2), Table 6]. It is expected to decrease to a minimum value of $k = 2$ at velocities below 5 km/sec, when vaporization virtually ceases (see below). In the first paper, $k \sim 1.5$ was used, without considering backfiring.

Equation (1) expresses the contention that the volume of crushed surface material is proportional to the momentum of the projectile. This is precisely also the outcome of more refined integrations.[7] Experiments with actual liquid drops[8] yield volumes of "craters" which for large drops (56 and 182 mg) are more or less in proportion to the momentum, but for small drops (11 mg) vary as the square of velocity (400 to 700 cm/sec); the latter result may be influenced by surface tension.

Absolute values of some crater parameters following from the author's simplified treatment are collected in Table 1; some of them are compared with Björk's calculations[7] when the materials of projectile and surface are identical.

Table 1. Crater Parameter Values.

M/μ = ratio of mass eroded to that of projectile; p = depth of erosion (penetration), D = crater diameter, both in units of equivalent spherical diameter of projectile; II = Paper II; I = Paper I; B = Björk, Ref. (7), Figs. 10 & 11; w = velocity of impact, km/sec. In II, $s = 2 \times 10^{10}$ dynes/cm^2 for iron, 4×10^9 for aluminum, 9×10^8 for stone (M/μ), and 2×10^9 for stone (p).

		Iron → Iron		Aluminum → Aluminum		Iron → Stone		Stone → Stone	
		w = 20	w = 60	w = 20	w = 60	w = 20	w = 60	w = 20	w = 60
$\frac{M}{\mu}$	II	180	530	230	690	500	1500	470	1400
	I	50	150	63	190	200	590	200	590
	B	72	216	150	450	-	-	-	-
p	II & I	2.14	2.30	-	-	4.00	4.30	2.32	2.50
	B	2.65	3.72	3.36	4.72	-	-	-	-
D	II	9.0	15.1	-	-	19.6	32.5	14.3	24.1
	I	4.9	8.0	-	-	12.1	20.3	9.2	14.9
	B	5.7	7.9	-	-	-	-	-	-

The comparison is inexact because the definitions of crater boundaries are not identical. Nevertheless, the table is sufficient to show that there is some general agreement between the different sets as to the order of magnitude, despite the different definitions of boundary conditions. The estimates of Paper I agree better with Björk's, apparently because neither considers backfiring by exploding vapors. Of the three approximations, the author would prefer those of Paper II. The depth of penetration (erosion) is smaller than Björk's, but this directly results from the consideration of the finite strength of the material (s) which in the purely "liquid" model is neglected.

The crater bowls of Paper II are shallow, with large D/p ratios as in the actual bedrock profiles of terrestrial meteor craters. As to lunar craters, only the apparent profiles are known, their bedrock outlines being concealed under the rubble. Because of throwout limitations in a gravitational field, the relative amount of debris ejected from the crater bowl decreases as absolute dimensions increase, so that large craters are more filled by material that has fallen back and appear shallower than small craters, despite the possible geometrical similarity of the impact processes and the true bedrock profiles.

This is borne out as the Baldwin Crater Relation,[3] or the depth-versus-diameter curve. However, beyond the terrestrial experimental range, the relation must contain the following discontinuities: (1) at velocities over 1.5 km/sec, the transition toward plasticity of iron projectiles leads to a decrease in penetration and crater depth; and (2) the fallback of rubble depends not only on crater size, but also on gravity, wherefore lunar craters must be deeper for a given diameter than terrestrial ones. A single relation cannot hold, nor can it be simply extrapolated or used indiscriminately.

4. Standardized Relations. In Paper II, a constant value of the coefficient k in Eq. (1) was considered. Actually it must vary somewhat with velocity and, to provide a conventional framework of reference for theory and experiment, its variation is to be allowed for.

In a "central funnel" of mass about 25μ overlying the final flattened outline of the projectile [Ref. (2), Figs. 1 & 4], the materials are in immediate contact with the passing projectile and are efficiently heated, chiefly by turbulent friction and transport. At $w \geq 35$ km/sec, the released energy is estimated to be sufficient to vaporize completely the material of the funnel and convert it into an exploding gas ball [Ref. (2), Table 5]. At lower velocities, the gas-ball fraction of mass, f_g, can be very roughly set equal to

$$f_g = 0.04\,(w/7 \times 10^5)^2 \qquad (2)$$

with $w \leq 35 \times 10^5$ cm/sec. We assume partial vaporization in this proportion,

and not uniform distribution of the released heat without vaporization. Equation (26) of Paper II then transforms into

$$k = 2f_g\lambda(1 - 0.04\,k^2)^{1/2} + 2\,, \tag{3}$$

which differs from the original equation by the factor f_g. Here, λ is a parameter "equal to the ratio of lateral surface to cross section of the central funnel."[2] With $\lambda = 4.0$ for the impact of iron into stone, and 2.6 for stone impact into stone, k can be calculated from the quadratic equation (3).

Assuming the average depth of the crater equal to two-thirds of the penetration, in notations and units of the preceding section we have

$$M/\mu = (\rho/\delta)\, p\, D^2\,, \tag{4}$$

where ρ and δ are the densities of bedrock and projectile, respectively.

With Eq. (1), this leads to

$$D = [kw(\rho/s)^{1/2}\,(\delta/\rho p)]^{1/2} \quad \text{(cgs units)}, \tag{5}$$

where s is the crushing strength of the bedrock.

Interpolation of the results of one-dimensional integrations for penetration (depth of erosion), summarized in the 8th line of Table 3 of Paper II, yields very closely

$$p = 2.30\left(\frac{\delta}{\rho}\right)^{1/2}\left(\frac{2\times 10^9}{s_p}\right)^{1/30}\left(\frac{w}{2\times 10^6}\right)^{1/15}, \tag{6}$$

with s_p denoting the plastic limit of the bedrock ($s_p > s$). The formulae are meant only to apply to the case of plastic deformation of the projectile, when

$$w \gg (2\,s_0/\rho)^{1/2}\,, \tag{7}$$

where s_0 is the plastic limit of the projectile. The lower limit of velocity is about 1.5 km/sec for iron impact into stone, and 0.5 km/sec for stone impact into stone.

From the standardized equations (2), (3), (5), and (6), the sample data of Table 2 have been calculated. With the aid of Eqs. (6) and (5), and k

interpolated directly with log (δ/ρ) as argument (the condition $2 < k < 5$ being observed), the cratering parameters for other values of δ/ρ and s can be easily derived from the table.

Table 2. Sample Characteristics of Meteorite Impact.

	Iron Impact into Stone $\delta/\rho=3$; $\rho=2.6$; $s=9\times10^8$; $s_p=2\times10^9$				Stone Impact into Stone $\delta/\rho=1$; $\rho=2.6$; $s=9\times10^8$; $s_p=2\times10^9$			
w km/sec	k	p	D	D/p	k	p	D	D/p
6	2.22	3.69	7.64	2.07	2.14	2.12	5.72	2.70
8	2.36	3.76	9.01	2.40	2.24	2.16	6.69	3.10
10	2.56	3.82	10.4	2.72	2.36	2.20	7.60	3.45
12	2.80	3.86	11.9	3.08	2.54	2.22	8.60	3.88
15	3.12	3.93	13.9	3.54	2.78	2.26	9.96	4.41
20	3.75	4.00	17.4	4.35	3.31	2.30	12.4	5.39
25	4.21	4.06	20.5	5.05	3.79	2.33	14.8	6.35
30	4.52	4.11	23.5	5.73	4.18	2.37	16.9	7.13
35	4.70	4.15	25.3	6.10	4.44	2.39	18.7	7.82
40	4.70	4.19	27.0	6.44	4.44	2.41	19.9	8.26
50	4.70	4.26	29.9	7.03	4.44	2.45	22.1	9.02
60	4.70	4.31	32.5	7.55	4.44	2.48	24.1	9.72
75	4.70	4.37	36.2	8.29	4.44	2.51	26.7	10.64

The angle of incidence has probably a very small effect on the D and p values of the present model unless the incidence is very oblique; this apparently follows from the actual curvature of the shock-wave front (Paper II, Fig. 2), as well as from refraction of the shock wave entering the surface of the medium.

If B is the rim-to-rim diameter of the crater, and H the depth of erosion (penetration), the spherical equivalent diameter of the projectile, d, is given by one of the two expressions

$$d = B/D, \tag{8a}$$

$$d = H/p, \tag{8b}$$

and the mass of the meteorite is

$$\mu = (1/6)\pi\, d^3 \delta\,. \tag{9}$$

For an arbitrary velocity, the two values of d may be different. They will coincide when

$$B/H = D/p\,, \tag{10}$$

which condition thus defines the proper velocity (cf. Table 2). The main uncertainties involved in applying these standardized relations to the estimate of the size and velocity of the projectile are: (a) in the assumed value of s, allowing perhaps a range from -50 to + 100%, which would correspond to a relative error in D of about ±18%, according to Eq. (5); (b) in the identification of the observed depth, H, with that defined theoretically through p, perhaps involving an error of ±10%; and (c) in the theory itself, which may be considerably off the mark with respect to both penetration and the effective value of k. It is almost impossible to assess a priori the last-named uncertainty. Assuming the model to be correct in principle, a numerical uncertainty from the first two sources remains, amounting to ±20% in the ratio D/p, and to ±10% in d as derived from Eq. (8b), or ±18% when derived from Eq. (8a).

In applying these data to the Arizona crater, we have B = 1200 meters and H = 320 meters, whence D/p = 3.75 ± 0.75. From Table 2 (iron impact into stone), this gives

$$w = 16 \text{ km/sec},$$

with a range from 11.5 to 21 km/sec, and

$$p = 3.94$$

with a very small range of uncertainty. From Eq. (8b) we obtain then

$$d = 81 \pm 8 \text{ meters},$$

and

$$\mu' = 4.08\, d^3 = 2.2 \times 10^6 \text{ tons},$$

with a range from 1.6 to 2.9 million tons.

5. Ellipticity of Craters. Oblique incidence has not been considered in the foregoing estimates. Generally, the circular symmetry of the crater is known to be little affected by the angle of incidence, but some ellipticity must result. If z is the angle of incidence, there will be a component of elongation of the crater diameter in the plane of impact equal to the difference between the axes of the elliptic shadow of the projectile; in units of the equivalent spherical diameter of the projectile, this is sec z - 1. Another component equals p' sin z, where p' = (1/3)p is the penetration to one-half momentum [Ref. (2), Fig. 1]. The effective elongation of the source of the shock wave can be set equal to two-thirds of the sum of the two components, whence the ellipticity of the crater is approximately

$$\epsilon = (a - b)/a = 2\left[\sec z + (1/3)p \sin z - 1\right]/3D, \qquad (11)$$

the mean diameter, D, as well as p, being in units of the equivalent diameter of the projectile as before. Table 3 contains the values of ellipticity according to Eq. (11), calculated with the parameters of Table 2.

Table 3. Ellipticities of Impact Craters.

z	0°	30°	45°	60°	75°
	Iron → Stone ($\delta = 7.8$, $\rho = 2.6$, $s = 9 \times 10^8$)				
w = 60	ϵ = 0.000	0.017	0.029	0.046	0.087
w = 20	ϵ = 0.000	0.030	0.052	0.082	0.159
w = 6	ϵ = 0.000	0.064	0.112	0.180	0.353
	Stone → Stone ($\delta = \rho = 2.6$, $s = 9 \times 10^8$)				
w = 60	ϵ = 0.000	0.015	0.028	0.048	0.101
w = 20	ϵ = 0.000	0.027	0.051	0.089	0.193
w = 6	ϵ = 0.000	0.055	0.106	0.188	0.413

The observed rms ellipticity of lunar craters is from 0.070 to 0.096,[9] which may be satisfied by the figures for $w \approx 10$ km/sec according to the table, with a median angle of incidence of 45°, more or less corresponding to a weight factor in Eq. (11) equal to sin z cos z dz. However, from indirect yet persuasive evidence[9] it appears that the majority of lunar craters must have been formed by low-velocity impact of the order of 3 km/sec, slightly above the velocity of escape, and the figures of the table would not apply except perhaps to the craters in the lunar maria[10] which apparently are of a later origin and are caused by impact of interplanetary bodies at velocities of the order of 20 km/sec. Furthermore, the material of the lunar crust appears to be softer than ordinary stone, probably because of its origin from fragmentation, low thermal conductivity, and high temperature at small depths.[9] The bottom of the largest lunar craters is about 4.8 km below the rim.[3] If we assume a density of $\rho = 2.6$ and an acceleration of gravity $g = 162$ cm/sec^2, this depth corresponds to a pressure of 2.0×10^8 dynes/cm^2, which may also be the plastic limit, s_p, of the lunar material at the time of formation of the craters. With $k = 2$, $s = 1.0 \times 10^8$, $\delta/\rho = 1$, and $w = 3 \times 10^5$ cm/sec, Eqs. (5) and (6) give $D = 6.64$ and $p = 2.19$, and Eq. (11) yields $\epsilon = 0.092$ at $z = 45°$, in satisfactory agreement with the observed average value. It may be added that, contrary to some beliefs, the projectiles falling on the moon will hit the surface isotropically from all directions, and not radially, even when their velocity is close to that of escape.

6. Survival of Fragments. In Paper II (pp. 30, 31), formulae were derived for the maximum mass of meteorite fragments which survive the impact when riding on the rear side of the meteorite and retaining their original crystal structure. Unlike Eqs. (5) and (6), these independent formulae are free from hypothetical elements except for the proper value of the crushing strength to be used. The large fragments of the Canyon Diablo meteorite, preserved in the Museum of Natural History, Washington, D.C., and elsewhere, all show an outer surface smoothed by fusion marks, and an inner ragged surface without traces of fusion, apparently torn off the main mass by enormous shearing stresses. Their appearance very well corresponds to our description of the mechanism of survival.

The explicit general formula for the mass of largest surviving fragments, $\Delta\mu$, in relation to μ, the mass of the meteorite, is

$$\Delta\mu = 2.43 \times 10^{30}\ \mu w^{-6}\left(\frac{p}{4.31}\ \frac{s_0}{2 \times 10^{10}}\ \frac{7.8}{\delta}\right)^3, \qquad (12)$$

in former notations and c.g.s units. Here, s_0 is the plastic limit (for ductile materials) or the crushing strength (for brittle substances) of the meteorite, and p is the penetration parameter defined by Eq. (6) or Table 2, regardless of whether the equation correctly represents the actual penetration.

For iron meteorite impact into stone ($\rho = 2.6$), with sufficient approximation the formula becomes

$$\Delta\mu_i/\mu = 2.43\ w_k^{-6}\ (s_0/2 \times 10^{10})^3, \qquad (13)$$

and for stone impact into stone ($\delta = \rho = 2.6$)

$$\Delta\mu_s/\mu = 1.16 \times 10^{-3}\ w_k^{-6}\ (s_0/9 \times 10^8)^3, \qquad (14)$$

w_k denoting the velocity in km/sec.

For the Canyon Diablo meteorite, $\Delta\mu_i = 0.7$ ton, whence the meteorite's mass in tons equals

$$\mu_t = 0.29\ w_k^6\ (2 \times 10^{10}/s_0)^3. \qquad (15)$$

The microhardness of this particular meteorite has been measured by Dalton;[11] his figures, translated into compressive strength, yield 1.5×10^{10} dynes/cm^2 for the kamacite and 3.4×10^{10} for the taenite of the meteorite [Ref. (12), p. 157]; with an upper limit of 25% of taenite and hard transition region, this yields $s_0 = 2.0 \times 10^{10}$ as an upper limit to the compressive strength. With this, and $w_k > 12$ km/sec as close to escape velocity, a lower limit to the mass of the meteorite is obtained,

$$\mu_t > 9 \times 10^5 \text{ tons}.$$

For short periods of time and excessive pressure, the effective ultimate strength may be higher, but it will hardly attain the double value, 4×10^{10}; in this case, the overall improbable lower limit becomes

$$\mu_t \gg 10^5 \text{ tons} .$$

At $s_0 = 2 \times 10^{10}$ and $\mu_t = 2.2 \times 10^6$, as estimated in Section 4, Eq. (15) yields

$$w_k = 14 \text{ km/sec}$$

for the probable impact velocity of the Arizona meteorite, in close agreement with the value of 16 km/sec previously arrived at independently. The coincidence supports the quantitative results of the theory.

With $\mu_t < 2.9 \times 10^6$ and $s_0 < 4 \times 10^{10}$, Eq. (15) also yields an upper limit to the velocity of the meteorite,

$$w_k < 21 \text{ km/sec} ,$$

which is also the upper limit indicated by the first method.

In case of a collision with the earth, the impact velocities of the six known asteroids of the Apollo Group, including the earth's gravitational action, are 20, 28, 18, 32, 18, and 16 km/sec; the Arizona object with 14 to 16 km/sec would fit into the lower limit for the group. A velocity as low as 12 km/sec appears extremely improbable, as it would imply a heliocentric orbit of small inclination and eccentricity close to the orbit of the earth — a type not yet observed among bodies of the relevant size.

In brief, the cross-check by different methods significantly supports the quantitative validity of our simplified theory of impact, to a close order of magnitude.

7. Frequency of Craters in Lunar Maria. The lunar maria have been exposed to the bombardment of interplanetary projectiles since their formation, some 4.5 billion years ago. Having erased the traces of earlier, more numerous craters (which are still preserved in the lunar continents), the maria have registered all subsequent collisions. The present distribution of stray bodies

of crater-producing size (comet nuclei, asteroids of the Apollo group, and asteroids deflected by cumulative perturbations in close approaches to Mars) in the vicinity of the earth's orbit, and their probability of collision with the earth and the moon, have been evaluated by the writer.[13, 14] There are good reasons to believe that the number of these objects remained more or less constant over all this time. It turns out that, with a crater-to-projectile diameter ratio of D = 20, the number and size distribution of craters in Mare Imbrium (733 craters down to B = 1.19 km over an area of 465,000 square kilometers) almost exactly corresponds to the expected number of collisions (at a relative velocity of 20 km/sec) during 4.5×10^9 years.[10]

The surfaces of the maria are most probably hard rock — solidified lava covered with a thin layer of dust; $\rho = 2.6$, $s = 9 \times 10^8$, $s_p = 2 \times 10^9$ can be assumed. For stony meteorite projectiles, which are expected to prevail among the interplanetary stray bodies, $\delta = 3.9$ is a fair guess. Eq. (5) with p from Eq. (6) yields then, at constant velocity,

$$D \sim (\delta/\rho)^{1/4} \quad \text{(stone} \rightarrow \text{stone)}. \tag{16}$$

At $w \cong 25$ km/sec as in the actual average for the interplanetary complex of stray bodies, and $\delta/\rho = 1.5$, from Table 2 we find

$$D = 14.8 \times (1.5)^{1/4} = 16.4$$

for stone projectiles, and D = 20.5 for iron meteorites. An average value of about D = 18 would thus follow from the standardized formulae, close enough to that assumed in the Mare Imbrium statistics. The latter can now be used as another check on the predicted value of D.

Consider two cases, that of D = 20 which is close to the prediction, and D = 40 which would correspond to a greater efficiency of impact and a mass of the Arizona meteorite ten times smaller than estimated or about 2×10^5 tons. Table 4 contains the comparison of the observed and predicted numbers of craters in Mare Imbrium.

Table 4. Cumulative Number of Impacts on Mare Imbrium (465,000 km^2) in 4.5×10^9 years.

Crater diameter lower limit, km	1.19	2.48	5.40	12.7	34.3	70.6
Observed number from limit to ∞	733	208	35	10	3	1
Predicted number, D = 20	1050	202	35	5.0	0.44	0.10
Predicted number, D = 40	6000	1080	190	25	2.0	0.46

For D = 20, or a value near that predicted by the author's theory, there is definite agreement with observation, whereas D = 40 would require about five times more craters than observed. If in the past the population of stray bodies was greater (it could not have been smaller), the discrepancy would become worse. Whatever the uncertainties in these estimates, the statistics of lunar craters can be regarded as further confirmation of the close order of magnitude of the scaling equation.

8. Lunar Escape Throwout. In a meteorite impact, some of the material will be ejected with velocities exceeding that of escape and will not return to the lunar surface. Because of the absence of a lunar atmosphere, the loss to space is unhindered and all material with sufficient initial velocity directed outwards will escape, irrespective of particle size. Most of the escaping material will be in the form of gas or finely divided dust and smoke. Very few of the large fragments would survive the excessive pressures and accelerations (cf. next section).

The energy of escape from the moon is

$$q_0 = 2.8 \times 10^{10} \text{ erg/gram}; \tag{17}$$

this exceeds the thermal kinetic energy of the vaporized substance at 3000-5000°K. However, the released vapors, while expanding, will reclaim some of the latent energy of vaporization while condensing into smoke, and this will lead to almost isothermal expansion. In such a case, the expanding gas gains in kinetic energy per gram an amount of

$$q_e = (RT/m) \ln (\rho_1/\rho_2), \tag{18}$$

where R = gas constant, T = temperature, m = mean molecular weight.

Although the initial temperature of the vapors may be high, 5000°K or more, it drops at first, and Eq. (18) is to be used with a lower effective value of the iosthermal temperature, $T \cong 3000°K$; with m = 50 [Ref. (12), p. 160],

$$RT/m = 5 \times 10^9 \text{ erg/gram}. \tag{19}$$

The thermal translational energy of the gas molecules is $1.5\ RT/m \cong 8 \times 10^9$, so that for escape an additional amount,

$$q_e = q_0 - 8 \times 10^9 = 2.0 \times 10^{10} \text{ erg/gram},$$

is required. From Eq. (18) this is obtained with quite a moderate expansion ratio of $\rho_1/\rho_2 \cong 55$. Hence we conclude that all the released vapors will escape. The latent heat of vaporization of stone being 6.0×10^{10} erg/gram,[12] about one-third of the vapor is to be converted into smoke for the mixture to attain escape velocity; further condensation into smoke will continue, and the material will be ejected into space as a mixture of smoke and gas molecules, at a velocity well exceeding the escape velocity.

From the geometry of the expansion of the vapors leaving the central funnel,[2] the gas-kinetic mean free length of path at expansion to 64 initial volumes is

$$7 \times 10^{-7}/f \text{ (cm)},$$

where f is the vaporized fraction of the material of the central funnel. This is so small that the expanding gas will be always in thermodynamic equilibrium, and Eq. (18) will apply to the smallest micrometeors.

The escape loss can thus be assumed equal to the amount of vaporized material. The vaporized fraction can be set equal to

$$f = (q - h_1)/h, \tag{20}$$

where $h_1 \cong 2 \times 10^{10}$ is the heat of fusion, $h \cong 6 \times 10^{10}$ erg/gram the latent heat of vaporization, and q the heat per gram generated by the shock.

From Eq. (22) of Paper II, with $y = M/\mu > 25$, the condition $f = 0$ or $q = h_1$ leads to

$$y = y_0 = \frac{1}{2} kw\, h_1^{-1/2} \tag{21}$$

as the mass boundary where vaporization ends. The total mass vaporized outside the central funnel is then

$$y_e = \int_{25}^{y_0} f\, dy . \tag{22}$$

The total heat released outside the central funnel is obtained by integration of Eq. (22) of Paper II from $y = 25$ to ∞ and equals $k^2/50$, in units of the kinetic energy of the meteor, whence the energy released and retained in the central funnel becomes

$$q_c = (50 - k^2)w^2/2500 \text{ (erg/gram)}. \tag{23}$$

When $y_0 < 25$, i.e., when vaporization is limited to the central funnel, the amount vaporized and ejected equals

$$M_{ec} = 25 f_c \mu , \tag{24}$$

where f_c is defined by Eq. (20) with $q = q_c$ from Eq. (23), and μ is the mass of the meteorite as before.

When $y_0 > 25$, the total mass vaporized and ejected is

$$M_{ec} = (y_e + 25)\mu . \tag{25}$$

With the integration of Eq. (22) performed [q in Eq. (20) being defined by Eq. (22) of Paper II], the resulting space throwout equations are

$$\frac{M_e}{\mu} = \frac{(50 - k^2)\, w^2}{6 \times 10^{12}} - 7.6 \tag{26}$$

for $y_0 < 25$, and

$$\frac{M_e}{\mu} = 33.3 + \frac{k^2 w^2}{6 \times 10^{12}} \left(1 - \frac{7 \times 10^6}{k w}\right) - \frac{k w}{8.4 \times 10^5} \qquad (27)$$

for

$$y_0 = k w / 2.8 \times 10^5 > 25 . \qquad (28)$$

The gain of mass by the moon is evidently

$$G = 1 - M_e/\mu \qquad (29)$$

in units of the mass of the meteor. $G > 0$ corresponds to accretion, $G < 0$ to depletion of the lunar mass.

The results of sample calculations according to Eqs. (26) through (29) are contained in Table 5.

Table 5. Impact Accretion (+G) or Depletion (-G) of Lunar Surface (in units of meteorite mass).

w, km/sec		≤ 10.7	11.1	12	15	20	25	30	40	60
G, stone meteorite	+	1.0	-0.5	-1.7	-6.5	-16.7	-24.9	-28.5	-43.7	-92.1
G, iron meteorite	+	1.0	+1.0	-0.8	-5.8	-14.6	-24.0	-31.2	-47.0	-98.5

The condition of starting vaporization, $f = 0$, corresponds to $w = 10.5$ km/sec for stone, and 10.7 km/sec for iron impact.

The total amount of vaporized material is $1 - G$, and this applies to terrestrial events as well, although the vapor does not escape from earth. For the Arizona meteorite at $w = 14$ km/sec, $G = -4.6$ and $1 - G = 5.6$; thus, the amount of vaporized material is likely to have exceeded several times the mass of the meteorite; all the mass of the projectile must have been vaporized (except for odd fragments from the rear), and, in addition, perhaps five times its mass of terrestrial rock.

The data of Table 5 imply that accretion of the lunar mass, and of other similar small bodies without an atmosphere, could have proceeded only at

impact velocities below 11 km/sec. Higher velocities would sputter the mass, instead of accreting, as has been pointed out by the writer on former occasions.[10,9]

9. Lunar Meteors. It has been suggested by Urey and others that fragments of the lunar surface ejected in meteorite impact may reach the earth as stony meteorites.

The conditions of ejection of sizable solid fragments in a cratering impact are quite similar to those of the survival of fragments of the meteorite. In both cases, the fragments must withstand acceleration to, or deceleration from, a certain velocity, w, over a length of the order of the depth, pd, of the crater; s of the rock materials must be substituted for s_0, ρ for δ, and w_e, the velocity of ejection, must be used for w in Eq. (12). This equation defines the condition of survival of lunar fragments from the top layer of the lunar surface; when $w_e > 2.3 \times 10^5$ cm/sec, the fragments will escape the lunar gravitational field, and when $w_e > 3.0 \times 10^5$, they may also escape the earth's field and enter interplanetary space in orbits of small inclination and eccentricity, of the order of $\sin i \cong e \cong 0.05$. These particles will be ultimately swept up by the earth, after an average lifetime of about 2.8×10^6 years,[13][9] short as compared with the age of the solar system. Thus, the fragments with $w_e > 3$ km/sec will be ultimately collected by the earth, whereas those which remain in the earth-moon system will be mostly recaptured by the moon; the orbits of the ejected particles will return to the lunar orbit and will have a high probability of collision with the moon. Only a few might touch on the outskirts of the terrestrial atmosphere and begin spiralling inward in the manner of the artificial satellites, finally descending on earth in circular orbits (tektites, according to O'Keefe).

Instead of Eq. (12), Eq. (14) as for stone can be used directly; for $w_e \geq 3$ km/sec, $s_0 = 9 \times 10^8$, it yields $\Delta\mu_s/\mu \cong 10^{-6}$ as a rough average, and a maximum diameter of the surviving fragments of the order of 0.01 of that of the projectile. As an upper limit, assume that the entire surface layer around the point of impact, of thickness 0.01 and diameter 3 in units of the projectile diameter [top of "central funnel"[2]], is ejected in fragments of the maximum size. (The inner layers are subject to higher pressures and are pulverized.)

This gives an upper limit of the total mass of uncrushed stone ejected and escaped to interplanetary space of the order of 0.05μ, broken up into 50,000 fragments of the maximum size 10^{-6}μ. With the observed distribution of interplanetary meteoritic, asteroidal, and cometary objects which, for the relevant interval of sizes (meteorites of Appollo Group), requires the cumulative numbers to vary as the 0.9 power of mass,[14] and with the smaller collision cross section of the moon (about 0.05 that of the earth at 20 km/sec velocity) for each 100 meteorites 100 cm in diameter or greater directly hitting the earth, there can be only one meteorite of lunar origin, as an upper limit.

Although this is a very rough estimate, it would indicate that lunar fragments may, indeed, be expected to occur among stony meteorites, but that their relative frequency must be very small, especially because there is another limitation. Solid particles cannot be accelerated by a gas jet to velocities exceeding that of the jet and, moreover, the acceleration must be completed during the first stage of the explosion, before the gas has passed the solid fragments and left them behind. The advantages of near-isothermal expansion are here of no avail, and it appears to be safe to assume that, to be able to accelerate the fragments to a velocity of 3 km/sec, the mean gas-kinetic velocity of the vapor molecules in the beginning should exceed 4 km/sec. With 8×10^{10} as the total energy of vaporization, and an equal amount in the translational energy of the molecules at 4 km/sec, a minimum release of

$$q_c = 1.6 \times 10^{11} \text{ erg/gram}$$

is required. Equation (23), with the proper values of k as from Table 2, yields then a lower limit of velocity for ejecting lunar meteors,

$$w > 2 \times 10^{7}/k \quad \text{(cm/sec)}, \tag{30}$$

or $w > 43$ for iron, and > 45 km/sec for stone impact. The main sources of meteorite impact [Apollo Group and Mars asteroids[14]] are in such a case not active, and only comet nuclei remain; their relative frequency of collisions, at the indicated inferior limit of velocity and diameter range of around 100 m, is estimated at about 20% of the total.[14] Hence, our upper limit must be

further revised downwards, to about one lunar meteorite in the 1-meter diameter range for every 500 general background meteorites of equal size directly intercepted by the earth.

10. Meteor Craters from Stony Projectiles. Terrestrial meteorite craters are definitely known to be associated with only one of the two principal meteorite species, the iron meteorites. This may be ascribed partly to nickel-iron cores surviving in asteroidal collisions which have shattered the stony mantles, so that large iron and small stone fragments may prevail in interplanetary space [Ref. (12), pp 23-24]. Also, fragments of large stony meteorites produced in a cratering impact will be much smaller, and will yield to chemical action much faster than their nickel-iron counterparts, so that, for ancient falls, the remnants of stony meteorites are unlikely to have been preserved.

However, there is another reason intrinsically connected with the physical conditions of the meteor phenomenon which would prevent the formation of small meteor craters by stony projectiles. As suggested by its behavior during flight, meteoric stone in its pre-terrestrial setting has a relatively low crushing strength of about 1.7×10^8 dyne/cm^2 [Ref. (12), p. 26], possibly as a consequence of injury in the original collision or explosion which sent it into space; the museum specimens may be stronger, as a result of natural selection. This explains why, under aerodynamic pressure in air, stony meteorites usually break up at altitudes of from 4 to 23 km.

The broken-up stony aggregate may be treated more or less as a liquid. The aerodynamic pressure on the front surface causes sideways flow and flattening. The rate of increase of the radius, w_r, depends on the aerodynamic pressure, $\frac{1}{2}\rho w^2 = P_a$,

$$w_r \cong (2 P_a/\delta)^{1/2} = w(\rho/\delta)^{1/2},$$

where ρ = density of the atmosphere, δ = that of the meteorite. The total increase in the diameter of the projectile, Δd, relates then to the total length of flight, L, from the breakup point to surface, as

$$\Delta d/L = 2(\rho/\delta)^{1/2} \cong 0.02 .$$

With $L = 20$ km, $\Delta d \cong 200$ meters.

To retain a sufficiently high velocity for cratering, the ultimate mass load per cm^2 of the flattened stony sheet must be of the order of the atmospheric mass traversed, or 10^3 gram/cm^2 at least, which corresponds to a thickness of about 3 meters. The volume of the projectile is

$$\frac{1}{4}\pi H(d + 200)^2 = \frac{\pi}{6} d^3,$$

with H denoting ultimate thickness. Hence

$$H = \frac{2}{3} d^3/(d + 200)^2. \qquad (31)$$

The ultimate thickness, as a function of initial diameter, then becomes:

d, meters	50	80	100	200
H, meters	1.3	4.2	11	33

We conclude (using D = 12 as for 20 km/sec) that at d = 50m, no craters produced by stony meteorites could be expected. At d = 80m, meteorite craters of 1 km diameter could be formed, but perhaps of a peculiar shallow contour. Only craters with diameter from 1.2 km up, or about the size of the Arizona crater, can be expected to have been produced on earth by the impact of stony meteorites. As most of the known craters are below this limit of diameter, it is not contrary to expectation that they are, as a rule, found to be associated with nickel-iron meteorites.

The Siberian fall of 1908 could well have been a stony object which disintegrated before hitting the ground. The Chubb crater in northern Quebec could be the result of impact of a large stone, some 200 meters in diameter, whose momentum no longer was significantly reduced by atmospheric resistance.

11. Skin Puncture and Erosion of Interplanetary Vehicles. With the penetration and erosion figures of Paper II (or practically those of Table 2 of this note), and a revised frequency of interplanetary dust and meteoric particles as follows from the author's research, Tables 6 through 8 have been calculated.

As compared with a former publication,[15] some arithmetical errors are removed. The figures are based on our knowledge of the population of interplanetary space and do not take into account the possibility of "dust belts" around the earth. Whereas the smaller penetration values, as compared with former estimates,[5][6] lead to smaller figures for the vehicle risk, the frequency of meteors has been usually underestimated. Usually, the total number of visually observed meteors has been taken as a basis, without regard to the distribution of velocities and masses among objects of the same apparent magnitudes (luminosity). Actually, visual meteors represent a nonhomogeneous aggregate, among which a certain group of objects of low relative velocity, moving in direct orbits of the asteroidal type, are inconspicuous in the statistical records on account of selection effects; yet the actual number and mass per volume of space of this "E-component" represents about 90 per cent of the total,[16][17] and the total number of meteoric particles down to a given mass limit is considerably greater than has been assumed. This partly counterbalances the overestimate of vehicle risk, caused by overrating penetration.

Allowance is also made for the different penetration ability of "dustballs" which make up the bulk of visual meteors; they are aggregates of smaller grains, of an average density estimated to be about 0.6, and a penetration of 0.35 to 0.4 of that of compact stone, in units of the appropriate diameters [see Eq. (6)].

Table 6. Penetration (p) in Equivalent Projectile Diameters at 20 km/sec.

	Compact Stone	Compact Stone	Dustball	Dustball
Skin Material	Mg	Steel	Mg	Steel
p	4.0	1.4	1.4	0.6

Table 7. Cumulative Number Density, $N(cm^{-3})$, from the Largest Down to an Inferior Limit of Diameter, d(cm), or Mass, μ(gram).

(a) Micrometeor grains or zodiacal dust particles near orbit of earth (δ = 3.4 gram/cm^3)

$d \geq$	3×10^{-5}	10^{-4}	10^{-3}	10^{-2}	0.03	0.06	0.07
$\mu \geq$	5×10^{-14}	2×10^{-12}	2×10^{-9}	2×10^{-6}	5×10^{-5}	4×10^{-4}	7×10^{-4}
N	4×10^{-12}	4×10^{-13}	6×10^{-15}	8×10^{-17}	8×10^{-18}	7×10^{-19}	0

(b) Dustballs or visual and telescopic meteors near orbit of earth (δ = 0.6 gram/cm^3)

(the stellar magnitude is at 100 km distance and w = 20 km/sec)

$d \geq$	0.03	0.1	0.3	1.0	3.0
$\mu \geq$	8.5×10^{-6}	3.1×10^{-4}	0.0085	0.31	8.5
Magnitude $\leq$	+13.2	+9.3	+5.7	+1.6	-2.5
N	3×10^{-18}	3×10^{-20}	3×10^{-22}	3×10^{-24}	3×10^{-26}

Table 8. Frequency of Punctures (n, per 100 m^2 and year).

Skin thickness, cm, Mg	0.040	0.12	0.14	0.42	1.4	4.2
Skin thickness, cm, Fe	0.014	0.042	0.05	0.15	0.5	1.5
Low-flying satellite, n	2300	240	0.4	0.004	4×10^{-5}	4×10^{-7}
Interplanetary vehicle, n	400	40	0.3	0.003	3×10^{-5}	3×10^{-7}

As to the acoustic method of calibration of micrometeor impacts, the effective momentum transfer is $k_n \mu w$; it is proposed to calculate the recoil coefficient, k_n, from Eq. (32) of Paper II which leads to an almost constant value:

k =	2	2.5	3	4	5
k_n =	3.5	3.5	3.5	3.3	3.0

The absorbed momentum, with the recoil from the ejected fragments, is thus expected to equal about 3.5 times the translational momentum of the micrometeor.

REFERENCES

(1) E. J. Öpik, "Theory of Formation of Meteor Craters," Acta et Comm. Univ. Tartu, A 30 (1936); Tartu Obs. Publ. 28, No. 6 (1936). Referred to as Paper I.

(2) E. J. Öpik, "Meteor Impact on Solid Surface," Irish Astron. J. 5, 14 (1958); Armagh Observ. Contrib. No. 24. Referred to as Paper II.

(3) R. B. Baldwin, "The Face of the Moon" (The University of Chicago Press, 1949).

(4) John S. Rinehart, "Distribution of Meteoric Debris About the Arizona Meteorite Crater," Smithsonian Contrib. to Astrophysics 2, 145 (1958).

(5) G. Grimminger, "Probability That a Meteorite Will Hit or Penetrate a Body," J. Appl. Phys. 19, 947 (1948).

(6) F. L. Whipple, "The Meteorite Risk to Space Vehicles," in "Vistas in Astronautics," p. 115, (Pergamon Press, London-New York, 1958).

(7) R. L. Björk, "Effects of a Meteoroid Impact on Steel and Aluminum in Space," The RAND Corporation, Report P-1662 (December 16, 1958).

(8) Olive G. Engel, "Collisions of Liquid Drops With Liquids, Part I." National Bureau of Standards, WADD Report 60-475, June 1960 (Preprint copy).

(9) E. J. Öpik, "Tidal Deformations and the Origin of the Moon," Astron J. 66, 60 (1961).

(10) E. J. Öpik, "The Lunar Surface as an Impact Counter," Monthly Notices Roy. Astron. Soc. 120, 404 (1960).

(11) F. K. Dalton, "Microhardness Testing of Iron Meteorites," Monthly Notices Roy. Astron. Soc. Can. 44, 1 and 185 (1950).

(12) E. J. Öpik, "Physics of Meteor Flight in the Atmosphere" (Interscience Publ. Inc., New York, 1958).

(13) E. J. Öpik, "Collision Probabilities With the Planets," Proc. Roy. Irish Acad. A 54, 165 (1951); Armagh Observatory Contrib. No. 6.

(14) E. J. Öpik, "On the Catastrophic Effects of Collisions With Celestial Bodies," Irish Astron. J. 5, 34 (1958); Armagh Observ. Contrib. No. 24.

(15) E. J. Öpik, "Artificial Satellites," Irish Astron. J. 4, 201 (1957); Armagh Observ. Leaflet No. 47.

(16) E. J. Öpik, "Statistical Results From the Arizona Expedition for the Study of Meteors," Armagh Observ. Contrib. No. 26 (1958). Also "Concluding Results From the Arizona Expedition," Irish Astron. J. 4, 49 (1956); Armagh Observ. Leaflet No. 44.

(17) E. J. Öpik, "Interplanetary Dust and Terrestrial Accretion of Meteoric Matter," Irish Astron. J. 4, 84 (1956); Armagh Observ. Contrib. No. 19.